STUDY ON AUTOMATIC GENERATION CONTROL OF RENEWABLE ENERGY SOURCES BASED MULTI-AREA, MULTI-SOURCE SYSTEM UNDER DEREGULATED ENVIRONMENT

A THESIS SUBMITTED IN PARTIAL FULFILLMENT OF

THE REQUIREMENT FOR THE DEGREE OF

DOCTOR OF PHILOSOPHY

SAMUEL LALNGAIHAWMA

MZU REGN NO: 6850 of 2014

Ph.D. REGN NO: MZU/Ph.D./1553 of 30.10.2020

DEPARTMENT OF ELECTRICAL ENGINEERING

SCHOOL OF ENGINEERING AND TECHNOLOGY

NOVEMBER, 2025

STUDY ON AUTOMATIC GENERATION CONTROL OF RENEWABLE ENERGY SOURCES BASED MULTI-AREA, MULTI-SOURCE SYSTEM UNDER DEREGULATED ENVIRONMENT

BY

Samuel Lalngaihawma

Department of Electrical Engineering

Name of Supervisor: Dr. Subir Datta

Submitted

In partial fulfillment of the requirement for the Degree of Doctor of Philosophy in Electrical Engineering of Mizoram University, Aizawl

DEPARTMENT OF ELECTRICAL ENGINEERING

SCHOOL OF ENGINEERING AND TECHNOLOGY

MIZORAM UNIVERSITY
(A Central university)

Tanhril, Aizawl-796004, Mizoram

CERTIFICATE

This is to certify that the thesis entitled "**Study on automatic generation control of renewable energy sources based multi-area, multi-source system under deregulated environment**" submitted by **Samuel Lalngaihawma**, Ph.D. Registration No. **MZU/Ph.D./1553 of 30.10.2020**, for the degree of **Doctor of Philosophy in Electrical Engineering**, of Mizoram University: Aizawl, India, embodies the record of original investigations carried out by him under my supervision. He has been duly registered, and the thesis presented is worthy of being considered for the award of Ph.D. degree. This research work has not been submitted for any degree of any other university.

(Dr. SUBIR DATTA)
Supervisor
Department of Electrical Engineering
Mizoram University
Aizawl, Mizoram

Date: November, 2025
Place: Aizawl

DECLARATION

MIZORAM UNIVERSITY

NOVEMBER 2025

I, Samuel Lalngaihawma, hereby declare that the subject matter of this thesis is the record of work done by me, that the contents of this thesis did not form basis of the award of any previous degree to me or to the best of my knowledge to anybody else, and that the thesis has not been submitted by me for any research degree in any other University/Institute.

This is being submitted to the Mizoram University for the degree of Doctor of Philosophy in Electrical Engineering.

Dated: November, 2025

(SAMUEL LALNGAIHAWMA)

(Dr. SUBIR DATTA)

Supervisor

(Dr. SUBIR DATTA)

Head

Department of Electrical engineering

ACKNOWLEDGEMENT

The successful completion of any project requires the contribution and cooperation of many people. It is my pleasure to express my deepest gratitude to all the individuals who were directly or indirectly involved with the completion of my PhD work.

First and foremost, I would like to express my sincere appreciation and profound gratitude to my supervisor, Dr. Subir Datta, Associate Professor, Department of Electrical engineering for his guidance, support and deep insights steering me towards the right direction until this thesis was completed. Their colossal support, endless ideas and high spirits encouraged me during the entire period of the study. From my interactions with him, I have learned how to successfully conduct research in a timely manner.

I am deeply graceful to all members of my doctoral committee, who greatly contributed to the improvement of my dissertation with their valuable advice and time. I want to express my sincere gratitude to all the other faculty members of Electrical engineering department at Mizoram university.

Also, I would like to thank my parents, my mother Mrs. Lalchhingpuii and my father Mr. C. Vanlalhruaia and my two elder brothers, Dr. C. Lalramdina and Mr. C. Malsawmzuala, for their constant support, motivation, love and prayers. I would like to thank my fellow research scholars and office staffs of Department of Electrical Engineering, MZU.

I would like to express my gratitude to the Almighty God for providing me with health, strength and support to complete this work.

Date:

(SAMUEL LALNGAIHAWMA)

Department of electrical engineering

Mizoram university

Aizawl, Mizoram

DEDICATION

To all my family and friends

And

To my loving mother,

Mrs. Lalchhingpuii (L)

Whose strength, sacrifices and unwavering belief in education laid the foundation for this journey. Though you are not here to witness this milestone, your values, blessings and love have guided every page of this work.

This thesis is dedicated to your memory.

TABLE OF CONTENTS

LIST OF FIGURES

LIST OF TABLES

ABBREVIATIONS

AGC	:	Automatic generation control
UC	:	Ultra-Capacitor
ZOA	:	Zebra optimization algorithm
IPFC	:	Interline power flow controller
RESs	:	Renewable energy sources
BES	:	Battery energy storage
GDB	:	Governor dead band
FES	:	Flywheel energy storage
GWO	:	Grey wolf optimizer
FA	:	Firefly algorithm
AVR	:	Automatic voltage regulator
VIC	:	Virtual inertia control
ROCOF	:	Rate of change of frequency
WTP	:	Wind turbine plant
SPV	:	Solar photovoltaic plant
VISMA	:	Virtual synchronous machine
DISCOs	:	Distribution companies
GENCOs	:	Generation Companies
HPP	:	Hydro-power plant
THPP	:	Thermal power plant
EV	:	Electric vehicle
TPP	:	Tidal power plant
GPP	:	Geothermal power plant
BD	:	Boiler Dynamics
TD	:	Time Delay
GRC	:	Generation rate constraint
ACE	:	area control error
ISE	:	Integral square error
ITAE	:	Integral time absolute error
ITSE	:	Integral time square error

IAE	:	Integral absolute error
TID	:	Tilt integral derivative
PSO	:	Particle swarm optimization
SMA	:	Sliding mould algorithm
SOC	:	State of charge
PID	:	Proportional integral derivative
LFC	:	Load Frequency control
BGP	:	Biogas plant
BDP	:	Biodiesel plant
DOF	:	Degree of freedom
FO	:	Fractional order
IPSs	:	Interconnected power system
MW	:	Megawatt
FACTS	:	Flexible AC transmission system
MU	:	Maximum undershoot
MO	:	Maximum overshoot
ST	:	Settling time
V2G	:	Vehicle to grid
TI-IDN	:	Tilt double integral derivative with filter
VSG	:	Virtual synchronous generator
DGs	:	Distributed generations
AWEC	:	Archimedes wave energy conversion

LIST OF SYMBOLS

Symbol		Description
T_{kl}	:	Synchronizing coefficient of tie line
D_k	:	load damping constant
K_{pk}	:	power system gain constant
T_{pk}	:	power system time constant
β_k	:	area frequency response characteristic
R	:	speed regulation (Hz/p.u. MW)
H	:	inertia constant (sec)
ΔP_D	:	Incremental change in load (p.u.)
k	:	Subscript referred to area k (where k=1,2,3,4)
l	:	Subscript referred to area l (where l=1,2,3,4)
Δf_k	:	Change in frequency of area k
$\Delta P_{tie,kl}$	:	Change in tie line power between area k and l.
f	:	System Nominal frequency in Hz
ΔP_c	:	Controller output signal
T	:	Simulation time (s)
Kp	:	Proportional gain of controller
Ki	:	Integral gain of controller
Kd	:	Derivative gain of controller
Kt	:	Gain of Tilt controller
n	:	Tilting parameter of T controller
N	:	Controller Bypass filter
T_g	:	Governor time constant of RHTPP unit
T_t	:	Turbine time constant of RHTPP unit
K_r	:	Steam turbine reheat coefficient of RHTPP unit
T_r	:	Steam turbine time constant of RHTPP unit
K_{SPV}	:	Gain of SPV unit
T_{SPV}	:	Time constant of SPV unit
K_{sg}	:	Governor gain of GTP unit

T_{sg}	:	Governor Time constant of GTP unit
K_{st}	:	Gain of GTP turbine unit
T_{st}	:	Turbine Time constant of GTP unit
K_{VA}	:	BDP unit inlet valve gain
T_{VA}	:	Time constant of inlet valve in BDP unit
K_{BV}	:	BDP unit engine gain
T_{BV}	:	Time constant of BDP engine unit
X_c	:	Governor lead time of BGP unit
Y_c	:	Governor lag time of BGP unit
T_{cb}	:	Combustor time constant of BGP unit
T_{BT}	:	BGP unit turbine gain parameter
T_{stg}	:	Governor time constant of STPP unit
T_{st}	:	Turbine time constant of STPP unit
K_{sf}	:	Solar field gain of STPP unit
K_h	:	Gain for hydraulic pitch for WTP unit
T_h	:	Time constant of hydraulic pitch for WTP unit
T_a	:	Actuator time constant for WTP unit
K_{AM}	:	Gain of Amplifier unit in AVR
T_{AM}	:	Time constant of amplifier unit in AVR
K_{EX}	:	Exciter gain of AVR
T_{EX}	:	Time constant of exciter unit
K_{GF}	:	Generator field's gain in AVR
T_{GF}	:	Time constant of generator field
K_{SE}	:	Gain of sensor unit in AVR
T_{SE}	:	Time constant of sensor unit in AVR

CHAPTER 1
Introduction

1.1 Introduction

The electric power system stands as one of the most complex and essential infrastructures supporting modern civilization, enabling economic development and improved quality of life globally. Over recent decades, this system has experienced two profound transformations that fundamentally altered its operational paradigms. The first transformation involves restructuring from vertically integrated monopolistic utilities to competitive deregulated markets, where generation, transmission, and distribution functions operate as separate entities with distinct commercial interests and operational responsibilities. The second transformation encompasses rapid integration of renewable energy sources driven by environmental imperatives, technological advancements, and policy mandates aimed at reducing greenhouse gas emissions and achieving sustainable energy futures. These simultaneous transformations have created unprecedented challenges for power system operation and control, particularly in the domain of Automatic Generation Control, which serves as the cornerstone mechanism for maintaining system frequency stability and ensuring reliable power delivery across interconnected networks [Bevrani et al., 2021]. A comprehensive review highlighted the evolving challenges and opportunities in load frequency control for modern and smart power systems [Alhelou et al., 2018].

The restructuring movement initiated in the 1990s fundamentally changed how power systems are planned, operated, and controlled. Traditional vertically integrated utilities that owned and controlled every aspect of generation, transmission, and distribution were divided into competitive generation companies and regulated transmission companies coordinated by independent system operators. This transition has introduced commercial considerations and contractual obligations that interact with the technical control requirements and change the originally purely technical optimization problem of AGC into a problem with engineering and economic goals to be met simultaneously. The deregulated environment makes AGC systems respect market-determined generation schedules and bilateral contracts between market participants while keeping the frequency within acceptable limits and ensuring schedules between control areas for scheduled tie-line power flows are met. Subsequent research by Bhatt et al., 2009 and Rakhshani et al., 2010 provided practical perspectives on implementing AGC in restructured multi-area systems, while comprehensive reviews by Pappachen et al., 2017, Esmail et al., 2017, and Franklin and Kareem, 2022 have documented the evolution and critical research areas in deregulated AGC.

In conjunction with market restructuring, the power sector has seen a rise in the integration of renewable energy sources, especially wind and solar photovoltaic generation, as a consequence of the concerns for climate change, air pollution, energy security and decreasing costs of renewable technologies. Both international agreements and national policies have set ambitious goals for the deployment of renewable energy, leading to exponential growth in installed capacities. Renewable sources have the fundamentally different characteristics compared to conventional synchronous generators. Renewable energy generation technologies both have variability and intermittency at various time scales, lack the rotational inertia to intrinsically support system frequency when there is a disturbance, and are not dispatchable in the traditional sense since weather cannot be controlled by the operator. These characteristics introduce a lot of uncertainty and variability to the operation of power systems, and add difficulty to the design of real-time balancing and frequency regulation [Alam et al., 2020].

The current power systems generally consist of one or more interconnected control regions each balancing generation and load in those regions and resolving to the overall system frequency regulation. Multi-area systems have the benefits of mutual emergency support in terms of reliability and sharing economic benefits in terms of resource. But they present coordination complications of tie-line power flows and shared responsibility of the equitable frequency regulation. Availability of various types of generation technologies at the local and international level is further complicated because various types of genetic observes different dynamic characteristics, response, and operation limits. These technical coordination problems are overlapped with commercial concerns of bilateral contracts, planned tie-line flows and market-based regulation services participation in deregulated structures [Peddakapu et al., 2022].

The intersection of deregulation and renewable integration with the multi-area systems sets the operating conditions that are radically different than those on which it was developed in the traditional AGC. Traditional strategies that rely on foreseeable load change and predictable generation in vertically integrated utilities no longer suffices to deal with uncertainties that are bidirectional, have lower inertia, greater variability, and, above all, are based on market forces, representing the new sign-of-the-times power systems. This inefficiency is the driving force behind the research in this thesis that will cater to the serious requirement of new AGC strategies that can ensure control of the frequency within such an altered and challenging operational environment remains effective [Kumar & Singh, 2021].

1.2 Review of literature

1.2.1 Pioneering works in AGC in regulated environment

The foundational work in AGC began in the 1950s when Cohn, 1956 first articulated the concept of tie-line bias control as a mechanism to correct frequency deviations and maintain power balance across interconnected areas. Cohn introduced the concept of Area Control Error, defined as a linear combination of frequency deviation and tie-line power interchange error, which remains central to AGC design and operation even today. Recently, Simpson-Porco, 2021 provided theoretical clarifications on area control errors and area injection errors, offering modern perspectives on textbook AGC formulations and their mathematical foundations. This pioneering work established the fundamental principle that each control area should correct its own generation based on both frequency error and tie-line flow deviation, allowing multiple areas to collectively restore frequency and scheduled interchanges without manual intervention.

It is on this basis that Concordia and Kirchmayer, 1954 released the pioneer articles on tie-line-power and frequency regulation of an interlinked power system. These works were the first to mathematically compute how two areas can be controlled together, and frequency bias in the controller of each area was introduced, in such a way that each area aids in correcting frequency-error whilst also controlling tie-line-interchange. By 1954, they had shown that any control area can be given a frequency-response character to guarantee consistent behaviour of the entire interconnection, which is a precursor to the modern area control error concept.

The 1960s and the 1970s were the stages of the intense developments in the applications of the optimal control theory to AGC. The interconnected power systems were the work of Elgerd and Fosha, 1970, who invented and examined dynamic models and performed analysis for them by using Integral Square Error as a cost measure. Classical strategies in AGC were based on their work on optimal frequency control with integral and proportional-integral controllers by focus on centralized feedback control to control frequency deviations and tie-line flows. Also, the applied modern control strategy to AGC whilst taking into account two-area non-reheat identical thermal in an interconnected power system [Chidambaram & Paramasivam, 2019]. The centralized feedback control mechanisms, which were stressed in these works, were based on the presumptions of fixed system parameters as well as negligible communication delays.

The practical generator constraints that had emerged on AGC performance were cared about at the later part of the 1970s. This paper highlighted the uncertainty of the necessity to develop AGC systems consistent with physical non-idealities in governors. Nanda and Kaul,1978 determined effective stability and controller settings of conventional AGC systems based on released reheat steam plants in parameter-plane technique, the influence of Generation Rate Constraint taking large values of governor speed regulation parameter were investigated.

In 1980s, there was the development of more advanced control methods of AGC. Chan and Hsu, 1981 presented variable-structure control, which is sliding mode control to AGC. Their article developed a two-area sliding-mode AGC, which indicated stability to modelling errors and parameter changes. Variable-structure AGC switched control that varies according to the state of the system is a suitable adaptation to nonlinearity and ensures stability against disturbance due to the pioneering application of sliding-mode control to frequency regulation in power systems. Authors addressed the issue of reheat thermal systems in two-area interconnected systems using maximum stability margin and ISE concepts of analysis of classical Integral controller gains by the use of linear discrete-time state-space models.

The AGC methodologies were further refined in 1990s. Aldeen and Marsh, 1991 gave systematic decentralized PI controller design in multi-area AGC, and gave a method of designing proportional-integral controllers in each area of the interconnected system using local feedback only and mathematically guaranteeing that the overall system is stable by analysing the eigenvalues and eigenvectors. This demonstrated that without centralized AGC, a group of well-co-ordinated local controllers was capable of controlling not only frequency, but tie flows as well.

At the close of the twentieth century, AGC technology had amassed plenty of knowledge that could be made available to engineers of the power system. Ibraheem et al., 2005 surveyed the development of AGC designs between classical and optimal controller to the adaptive, fuzzy and neural controller and its application in the contemporary power systems [Kumar & Ramana, 2017; Ullah et al., 2021]. This overall survey pointed out that the classical system of the integral-ACE controller was still practically dominant whilst most utilities had now started to complement it with gains tuned by optimization or achieve adaptive loops to improve performance.

1.2.2 AGC in Deregulated Environment

The deregulation of the electricity market through switching the monopolistic system to competitive electricity markets can be considered one of the most considerable changes in the history of the power system. One of the first disclosures of these challenges came with a study conducted by Christie and Bose, 1996 who noted that the existing LFC operating techniques would be subjected to new pressure in an open-market operating environment. This innovative paper found that generation planning in deregulated systems indicates the existence of market results and bilateral agreements as opposed to centralized technical optimization, which fundamentally changed the context of functioning of AGC.

The article by Brinda et al., 2018 researched the LFC of a two-area hydrothermal power system with regards to the consideration of the integral controller into the deregulated environment where the authors focused on such practical factors as the selection of the participation factor based on the generation schedule and the effect of GRC and DPM. They developed the strength of integral controller within twenty five percent deviations to system parameters and twenty percent deviations to loading. The suggested control gains were found to be resistant to types of DPMs and area participation effects.

Debbarma et al., 2012addressed AGC of multi-area thermal systems under deregulated environment using non-integer controllers, demonstrating that fractional-order controllers could provide superior performance compared to integer-order controllers in handling the complexities introduced by deregulation. Their work showed how fractional-order dynamics could better accommodate the uncertainties and variability characteristic of market-based operation.

Hota and Mohanty, 2015 investigated automatic generation control of multi-source power generation under deregulated environment, considering nuclear, hydro, and thermal units with generation rate constraints in two areas. They proposed optimal PI with Double Derivative controller based on fruit fly optimization for restructured environments, demonstrating superior performance of PIDD controllers compared to I, PI, and PID controllers across different deregulated market scenarios.

Also, Shiva and Mukherjee, 2016 studied the restructured AGC problem of five-area systems where reheat thermal, hydro, and gas are used as generating units considering different physical constraints such as GRC, generation dead band, and time delay. The proposed Quasi Oppositional Harmony Search PID controller demonstrated effective performance to mitigate frequency and tie-line power deviations in the presence of nonlinearities characteristic of deregulated operation.

The authors, Arya and Kumar, 2015 studied AGC of multi-area multi-source hydrothermal power systems interconnected via AC/DC parallel links under deregulated environment, demonstrating that parallel HVAC and HVDC links significantly improve dynamic system performance. Their work showed how the underlying market rules and contract structures, though treated as known during operational timescales, fundamentally influence AGC controller design. Khamari et al., 2019 proposed hybrid TLBO and pattern search technique for automatic generation control in deregulated environment, demonstrating that hybrid optimization approaches can effectively handle the dual objectives of technical performance and commercial compliance in restructured systems. Comparative analysis of multi-source deregulated systems with electric vehicles confirmed enhanced control performance using TLBO-based optimization [Kumar & Prasad, 2023; Raj and Shankar 2020] developed novel opposition-based interactive search algorithm cascade controller for deregulated AGC including distributed generation and electric vehicles, showing improved performance in handling multiple market scenarios simultaneously. Tasnin and Saikia, 2018a investigated AGC problems by considering geothermal, gas, and thermal power plants in three-area systems under bilateral deregulated environment, showing the effect of various energy storage devices along with cascaded controllers. Recent multi-area restructured systems integrating electric vehicles and modified HVDC tie-lines have demonstrated improved control performance [Sariki & Shankar, 2022].

More recently, Ghasemi-Marzbali, 2020 addressed multi-area multi-source automatic generation control in deregulated power systems, providing comprehensive analysis of how market structures affect AGC operation. Taha et al., 2024 applied Grey Wolf Algorithm optimization of automatic generation control for deregulated multi-area power systems, demonstrating that modern metaheuristic optimization can effectively tune controllers for complex deregulated environments. These recent works emphasize that AGC in deregulated systems must simultaneously address technical requirements for frequency regulation and commercial realities of contractual obligations and market participation.

1.2.3 AGC Integrating Renewable Energy Sources

Integration of renewable energy sources to AGC systems has turned out to be the important field of research since power systems around the world are embarking on the renewable integration to achieve the objectives of environmental and sustainability in power systems. Bevrani et al., 2010 made an initial high-level survey about the process of renewable energy sources and frequency regulation emphasizing the issue of the emergence of power imbalance because of unpredictable performance of such resources, as wind and solar as a result of integrating renewable energy sources cause frequency deviation. They explained that the inclusion of renewable energy sources into power grids makes the actual generation inconsistent with predictions and necessitates a greater frequency regulation response, proposing such solutions as battery energy storage and multi-purpose control algorithms. Mishra et al., 2018 conducted robustness and stability analysis of renewable energy based two-area automatic generation control, demonstrating the critical importance of robust controller design to maintain system stability under renewable variability.

Abd-Elazim and Ali, 2018 designed load frequency controllers for two-area systems composing of PV grid and thermal generator via firefly algorithm, demonstrating that solar PV integration requires careful controller design to handle the intermittent nature of solar generation. Their work showed that firefly algorithm optimization could effectively tune PID controllers to accommodate PV variability while maintaining frequency stability. Barik and Das, 2018 modelled community-based isolated microgrids comprising linear mathematical models of solar photovoltaic, biogas, and biodiesel generator units with battery storage for AGC studies, using Grasshopper Optimization algorithm to tune PID controllers for frequency regulation in renewable-based microgrids.

Abazari et al., 2019 tackled load frequency control by de-loaded wind farm using optimal fuzzy-based PID droop controller, showing that to allow wind turbines working in de-loaded modes to generate upward reserve margin for frequency support in frequencies under-frequency events. Singh et al., 2020 studied the load frequency regulation using de-loaded tidal turbine power plant units with fractional fuzzy-based PID droop controller, as a result, similar de-loading strategies also can be applied to tidal systems. These works established that renewable generators need not be passive recipients of frequency control but can actively participate through advanced control strategies.

Xu et al., 2018 investigated load frequency control of novel renewable energy integrated microgrid containing pumped hydropower energy storage, demonstrating synergistic benefits of combining pumped hydro storage with renewable generation for frequency regulation. Arya et al., 2021 proposed a cascade-IλDμN controller design for AGC of thermal and hydro-thermal power systems integrated with renewable energy sources.

Rahman et al., 2016a studied AGC of dish-Stirling solar thermal integrated thermal system with biogeography based optimized three degree of freedom PID controller, demonstrating that solar thermal units with their slower dynamics compared to PV can still contribute effectively to frequency regulation with proper controller design. Rahman et al., 2016b extended this work to automatic generation control of interconnected two-area hybrid thermal systems considering dish-stirling solar thermal and wind turbine systems, showing coordinated control strategies for multiple renewable types. Babu et al., 2023 developed frequency control of realistic dish-stirling solar thermal system and accurate HVDC models using cascaded FOPI-IDDN-based crow search algorithm, demonstrating advanced controller structures for solar thermal integration [Babu et al, 2019; Babu & Saikia, 2021]. The joint influence of electric vehicles and solar thermal technologies on combined frequency regulation has been examined in recent works [Dekaraja & Saikia, 2022].

Barik and Das, 2018 presented expeditious frequency control of solar photovoltaic, biogas, and biodiesel generator-based isolated renewable microgrid using grasshopper optimization algorithm. Their work established mathematical models and control strategies specifically for biogas and biodiesel generators that endorse different dynamic characteristics then other types of renewable generators. This research has proved that the units for distributed generation based on biogas and biodiesel can be interesting components for the frequency regulation in isolated microgrids, if combined with suitable energy storage and control systems.

The authors Latif et al., 2019 studied detailed Archimedes Wave Energy Conversion models in microgrid systems, presenting maiden coordinated load frequency control strategy for solar tower-Archimedes wave energy conversion-geothermal energy conversion systems [Shayeghi et al, 2008]. Their work established transfer function models for AWEC and demonstrated coordinated control strategies when multiple renewable types participate simultaneously in frequency regulation, showing that wave energy with its high energy density can provide valuable contribution to system stability.

Tasnin and Saikia, 2018a studied LFC problems incorporating wind, solar, geothermal power plants, and energy storage elements with other conventional energy sources in interconnected power systems. Tasnin and Saikia, 2018b presented comparative performance of different energy storage devices in AGC of multi-source systems including geothermal power plants, demonstrating that geothermal generation with its relatively stable and dispatchable characteristics can provide valuable baseload renewable generation that complements more variable sources. Several recent reviews have comprehensively analysed load frequency control strategies for renewable-based hybrid power systems, emphasizing the increasing complexity due to high renewable penetration [Gulzar et al., 2022].

The collective research on renewable integration demonstrates that each renewable source type presents unique challenges and opportunities for AGC. The intermittent and variable nature creates significant operational uncertainty, with rapid changes requiring compensating adjustments, medium-term changes affecting unit commitment, and forecast errors causing real-time imbalances. As renewable penetration increases, these challenges become more pronounced, motivating research into advanced control strategies, energy storage integration, and coordinated multi-source operation [Mokhtar et al., 2022; Elsaied et al., 2022; El-Bahay et al., 2023]. Elsaied et al., 2022 demonstrated frequency stabilization of hybrid three-area power system equipped with energy storage units and diverse renewable sources, confirming the effectiveness of integrated storage-renewable approaches. Most recently, Gbadega and Sun, 2023 applied JAYA optimized model predictive control for multi-area automatic generation control of renewable energy-based hybrid power systems, showing that advanced predictive control strategies can effectively manage the uncertainties introduced by high renewable penetration. Recent comprehensive reviews have synthesized the state of renewable integration in AGC systems. Ranjan and Shankar, 2021 surveyed load frequency control considering renewable integration and identified future prospects, while Saranyaa and Kareem, 2023 provided comprehensive analysis of current trends in renewable-incorporated power system markets [Khan et al., 2023]. Most recently, Yusuf et al., 2024 presented a state-of-the-art review of load frequency control in modern power systems, emphasizing the shift toward renewable-dominated grids and the associated control challenges. Frequency regulation in multi-area microgrid systems integrated with renewables has been studied using advanced state-space control frameworks [Franklin & Abdul Kareem, 2023].

1.2.4 AGC Integrating Electric Vehicles

The introduction of electric vehicles to power systems also poses challenges and opportunities of the frequency regulation. The frequency regulation found in the old battery system has such limitations as low life expectancy, expensive nature, high maintenance needs, and environmental risks. Electric vehicle storage systems are proposed by many researchers as the alternative way of alleviating the frequency fluctuations in the hopes of exploiting the increasing number of EVs in the grid services.

Lemeski et al., 2022 introduced the idea of an EV aggregator capable of optimally coordinating a high number of EVs to offer frequency regulation services, and formulated dynamic programming-based control on each EV and proved that a fleet of EVs can operate collectively as a generator to help in secondary frequency control. Mu et al., 2013 examined applying EVs in the regulation of frequency among various modes of charge discharge of dump charging, fast charging, and off-peak charging and defined different operation strategies of EVs in frequency regulation.

Vachirasricirikul and Ngamroo, 2014 suggested the schemes of strong load-frequency controls in the case of strong wind penetration by coordinating the conventional LFC with the EV-based control. With the assistance of PSO, they demonstrated that the coordinated vehicle-to-grid strategy and PI controller tuning are capable of reducing frequency oscillations due to the volatility of wind power. This piece indicated that EVs could be useful in offering significant flexibility in order to offset renewable variability.

Liu et al., 2015 developed V2G control strategy for supplementary frequency regulation that explicitly accounted for drivers' charging requirements. Their approach allowed EVs to provide AGC support without compromising energy needed for mobility, with simulations showing it could reduce burden on conventional generators during AGC events. This addressed a critical practical concern that EV owners must have sufficient charge for transportation needs.

Lam et al., 2016 addressed the challenge of EV capacity estimation for AGC, proposing smart-charging based method to predict how much up and down-regulation a fleet of EVs can provide in real time. This probabilistic capacity estimation improves dispatch reliability by accounting for EVs' state-of-charge diversity and uncertainties in user behaviour, providing system operators with reliable information about available EV regulation capacity.

Falahati et al., 2016 applied EV charging to secondary frequency control, developing fuzzy controller to compensate for variable imbalance between generation and demand. Yao et al., 2017 developed robust frequency regulation capacity scheduling algorithm for electric vehicles, offering incentives to EV owners based on their participation performance in frequency regulation and formulating optimal solution as robust optimization problem including random signal generation and dynamic scheduling conditions. Rahmat et al., 2018 coordinated heat pumps, electric vehicles and AGC for efficient LFC in smart hybrid power systems via SCA-based optimized FOPID controllers, demonstrating that coordinated control of multiple flexible loads including EVs can significantly enhance frequency regulation performance [Arya, 2019a].

Debbarma et al., 2017 utilized electric vehicles for LFC in restructured power systems using fractional order controller, providing aggregate model of EV fleets in all areas along with improved version of fractional-order controller for robust LFC considering bilateral transactions in deregulated environment. This work bridged EV integration with deregulated market structures, though additional power generation from renewable resources was not extensively investigated.

Xia et al., 2018 developed autonomous real-time charging strategy for plug-in electric vehicles to regulate frequency of distribution systems with fluctuating wind generation. Their work showed that coordinated EV charging can effectively buffer wind generation variability, reducing frequency deviations and improving overall system stability. Fan et al., 2016 studied frequency regulation of multi-area power systems with plug-in electric vehicles considering communication delays, demonstrating that communication infrastructure quality significantly affects EV participation effectiveness.

Arya, 2020b introduced EV fleets on LFC using imperialist competitive algorithm-based cascade fuzzy-fractional order integral derivative with filter in two-area thermal and hydrothermal-based power systems, though the study was conducted under conventional conditions without extensive renewable integration. In Khokhar et al., 2020, a robust cascaded control for standalone hybrid system with EV integrations is developed by using a two-level control strategy based on the primary fuzzy logic and secondary PID controller to make the aggregated response of EVs in the massive system robust to the nonlinearities and load disturbances. Saha et al., 2022 proposed a cascade controller-based modelling for a four-area thermal–gas AGC system with dependency of wind turbine generator and PEVs under restructured environment

The study shows that EVs can be effective sources of frequency regulation services if appropriately coordinated via aggregator schemes, although issues concerning adequate availability of capacity, accommodation of user charging demand and inclusion of EV offer into renewable generation and deregulated market conditions still need to be addressed [Jampeethong & Khomfoi, 2020].

1.2.5 AGC Integrating Virtual Inertia Control

The low system inertia decreasing as the share of fixed synchronous generators is reduced in favour of inverter-based renewables changes fundamentally the frequency dynamics of the system in case of disturbances. Reduced inertia gives greater rate of change in frequency after generation-load imbalances and gives less time to protective systems and control mechanisms to respond before reaching possibly harmful levels or bringing protective relay operation.

Rakhshani et al., 2016 analysed derivative-based virtual inertia in two-area AGC systems interconnected via AC/DC links. Their transfer-function modelling showed that adding derivative control loop to emulate inertia through HVDC link introduces extra degree of freedom, markedly improving frequency overshoot and damping. This demonstrated that HVDC interconnections could serve dual purposes of power transfer and synthetic inertia provision.

Tamrakar et al., 2017 thoroughly reviewed virtual inertia techniques and observed that fast inertia support on AGC operating on slower timescale has the potential to be useful in high-renewable conditions. Rezkalla et al., 2018 talked about the general inertia requirements and challenges and Virtual inertia was noted to be solution to the stability of frequency in low-inertia systems. As these works highlighted, it was logical to include VIC into secondary control loops to ensure reliability as the conventional inertia was reduced.

Ali et al., 2019 proposed a robust frequency control approach of islanded microgrid on the basis of coefficient diagram-based controller with virtual inertia emulation. They suggested a new design of control in which sources, interfaced with an inverter, would act as virtual synchronous machines, and enhance load-frequency control in microgrids in islanded operation. This paper showed the practical use of virtual synchronous generator concepts in practice in real control situations.

Similar to Kerdphol et al., 2018, the authors focused on providing virtual inertia to interdependent power systems which have a large share of renewable energy with the aim of stabilizing the frequency of such systems, which supports that synthetic inertia is significantly provided by power electronic converter to significantly reduce the frequency nadir and frequency change rate of that system in the event of disturbances. Simulations by them revealed that relatively small contributions of synthetic inertia can strongly improve the stability of the system. Also designed coordinated VIC scheme with adaptive frequency relays on low inertia two area systems. The model applied to them was fuzzy-tuned controller which allows them to change virtual inertia contribution in real time and synchronize this with protective relays to ensure reliability. This solved the problem of virtual inertia when it is necessary to coordinate it with the protection systems in order to prevent the occurrence of undesirable interactions.

Bevrani et al., 2021 gave revised overview of frequency control solutions, in which virtual inertia and fast power control was found to be essential in future grids. Tebib and Boudour, 2021 investigated the dynamic response of multi-area systems with AC/DC connections, where Virtual Synchronous Power strategy has been optimized by the grey wolf optimization methodology since it was shown that optimization strategies may effectively optimize the virtual inertia parameters of multi-area coordination.

El-Shimy et al., 2023 proposed intelligent fractional-order controller plus VIC and suggested that new franchise must be set to fractional-order PI-PD controller of LFC with parameters adjusted to work with systems such as virtual inertia support. Simulation Interconnected thermal-hydro Simulation of interconnected thermal-hydro systems indicated that fractional-order VIC scheme performed better than conventional PID at damping oscillations and decreasing overshoot, which revealed synergy between fractional-order control and virtual inertia emulation.

Hasen et al., 2024 concentrated on the communication delay in two-area LFC systems and tested the effect that the inclusion of virtual inertia and damping had on the stability margin. They derived characteristic equation of delayed systems and analytically demonstrated that including VID controller greatly expands the delay before instability allowing consideration of one of the practical issues, which is that communication delays can destabilize control systems unless countermeasures are implemented [Niu et al., 2021].

1.2.6 AGC Integrating Energy Storage Systems

Energy storage systems emerged as promising technology for mitigating renewable variability impacts on AGC and power system operation broadly. Different storage technologies have different benefits in aspects of response time, energy capacity, power capability and cost characteristics.

System performance of LFC was studied by connecting Battery Energy Storage System in two area reheat steam turbine system considering the governor dead band and GRC. The application of BES was helpful in controlling frequency variation and oscillation in tie-line power in interconnected power systems. Arya, 2019b has investigated effect of energy storage systems to automatic generation control of interconnected traditional and restructured energy system including renewables to demonstrate that integration of battery storage significantly improves frequency control performance while reducing regulation burden on conventional generation. The contribution of energy storage systems in damping low-frequency oscillations has been further enhanced using fractional-order PID controllers [Abumeteir & Vural, 2022]. Battery energy storage systems continue to play a critical role in ancillary services, improving grid stability and reliability [Prakash et al., 2022]. Large-scale battery energy storage systems have shown significant potential for frequency regulation and grid support in renewable-integrated systems [Liu et al., 2022]. Advanced battery management and control, such as amplitude-phase-locked loop-based strategies, enhance both frequency and voltage regulation performance [Shang et al., 2022].

Tasnin and Saikia, 2018b presented effect of FES in LFC study Lockheed study in three area interconnected system under deregulation environment. The results revealed that the incorporation of FES could improve the system dynamic performance due to the fast response to the variations in the frequency. Flywheel systems have advantages of high-power density and unlimited cycling capability which can apply to frequently charged and discharged conditions for frequency regulation.

Analysis of significance of SMES devices for power system frequency regulation scheme considering distributed energy resources in deregulated environment by Mishra et al., 2022, SMES provides very quick response times which are suitable for damping a rapid fluctuation because they are capable of injecting or taking in the power almost immediately. Pradhan et al., 2015 optimized fuzzy PID controller using firefly algorithm for AGC of multi-area multi-source power systems using UPFC and SMES showed that SMES coordination with FACTs devices provides better frequency control compared to one use of either technology alone [Kumar et al, 2021]. The integration of superconducting magnetic energy storage (SMES) in deregulated systems enhances damping of low-frequency oscillations, particularly when fractional-order PID controllers are used [Kumar et al., 2022].

Saha and Saikia, 2018a combined application of redox flow battery and DC link in AGC of interconnected power systems with diverse sources. Integration of RFB has reduced frequency and tie-line power oscillation considerably. Saha and Saikia, 2018b followed this up to restructured AGC systems in the presence of wind turbine systems and dish-stirling solar thermal systems in distributed generation units, providing evidence of the effectiveness of RFB under deregulated conditions.

Gorripotu et al., 2015 had done a comparative analysis of various energy storage devices such as ultracapacitors, SMES and redox flow batteries in multi-area LFC-AVR scenario. In this paper, fuzzy-PID controller was tuned using hybrid arithmetic optimization algorithm in the two-area thermal, hydro, and gas systems. Optimal fuzzy-PID controllers continue to provide robust performance in interconnected multi-source AGC systems [Barakat, 2022]. Results indicated that the frequency and voltage dynamics were considerably improved using any of these storage devices to be integrated with minimum overshoot and settling time. In addition, ultracapacitors and SMES were proved to be the fastest consumers of the disturbances due to their higher power density and faster waveform response.

The research shows that all storage technologies have different strengths; Battery systems offer good balance between capacity, power capability and cost but suffer from limited cycle life. Flywheel systems are very good in terms of cycling capability and response speed but poor in terms of energy capacity. SMES has the fastest response but has a high cost. Redox flow batteries offer good energy capacity with reasonable response at the expense of more initial costs. Ultracapacitors provide excellent power density and unlimited cycling and limited energy storage. Optimal data storage technologies are dependent on specific application needs and many works have reported that hybrid efficiencies of combinations of storage technologies provide complementary advantages.

1.2.7 AGC Integrating FACTS Devices

FACTS devices have been introduced into the power system to add more flexibility into the operation and control of the transmission system and series FACTS devices are particularly conducive for AGC applications. The potential of several FACTS devices to enhance the frequency control behaviour has been analysed.

Lal and Barisal, 2017 provided comparative performance assessment of FACTS units on AGC with various energy sources and SMES, where the study on the impact of various FACTS technologies upon frequency regulation in renewable-integrated systems was carried on. They developed baseline performance of different FACTS devices in terms of their relevance for AGC - applicable thereto.

Dash et al., 2014 compared the performances of various FACTS devices; SSSC, TCSC, TCPS and IPFC applied to AGC of three unequal area reheat thermal system with GRC using cuckoo search algorithm optimised two degrees of freedom controller. The detailed comparison proved that IPFC had better dynamic performance than other FACTS devices. Also, in terms of IPFC location, we also investigated that in all the tie-lines, IPFC offers superior tie-line dynamic performance.

Pradhan et al., 2015 developed a firefly algorithm optimized fuzzy PID controller for AGC of multi-area multi source power system with UPFC and SMES and proved the fact that synergism is possible when UPFC is integrated with energy storage. The reactive power compensation ability and power flow regulation ability of the UPFC and the fast active power injection ability of the SMES are combined to give the comprehensive frequency regulation ability.

Gorripotu et al., 2015 presented AGC of multi-area power system under the deregulated environment using redox flow battery with interline power flow controller. Their research confirmed that IPFC has better performance compared to the other passive FACTS devices in deregulated systems, since it could control two or more power flows on the transmission lines at once and hence greater flexibility compared with the single line-based devices such as TCSC, TCPS.

Rajbongshi and Saikia, 2017b analysed the performance of coordinated FACTS and energy storage devices in combined multi-area ALFC and AVR systems showing through the appropriate coordination between IPFC and energy storage, the frequency and voltage control performance was significantly improved. Rajbongshi and Saikia, 2017a extended this to coordinated performance of interline power flow controller and superconducting magnetic energy storage in combined ALFC and AVR system under deregulated environment and showed that this coordination holds well under market-based operation. Pathak et al., 2019 developed comprehensive modelling of HVDC tie links and their utilization in AGC/LFC operations of multiarea power systems, demonstrating that accurate HVDC modelling is essential for effective frequency control in interconnected systems with DC links. Raju et al., 2018 investigated load frequency control of multi-area system incorporating distributed generation resources and gate-controlled series capacitor along with HVDC link using hybrid ALO-pattern search optimized fractional order controller, showing synergistic benefits of combining FACTS devices with HVDC interconnections.

1.2.8 AGC Integrating Automatic Voltage Regulator

Load frequency control (LFC) and automatic voltage regulation (AVR) coordination has received much more attention since both the frequency and voltage of the power system need to be regulated simultaneously for power quality and system stability in the modern power systems. Earliest approaches were mainly concerned with single loops of control but the increasing complexity in the system resulted in the development of integrated control approaches. Early work on combined frequency and voltage control includes Kassem, 2010, who developed neural predictive controller for two-area load frequency control in interconnected power systems, demonstrating potential of neural network-based approaches for coordinated LFC-AVR control.

Chandrakala and Balamurugan, 2016 proposed optimal secondary controller for combined LFC-AVR loop in two-area system using simulated annealing. They first tuned baseline PID controller by Ziegler-Nichols rules then optimized it with SA. The SA-optimized PID markedly improved frequency and terminal-voltage damping under load perturbations in multi-source hydro and thermal system, demonstrating benefits of stochastic tuning methods for integrated LFC and AVR control. Improved LFC performance has been observed in systems employing hybrid energy storage systems coordinated with renewable generation [Saxena & Shankar, 2022].

The study by Rajbongshi and Saikia, 2018 sought to explore the dynamics of the LFC and AVR coordination in deregulated two-area system with the use of FACTS device and energy storage, namely interline power flow controller, superconducting magnetic energy storage unit along with advanced PID controllers. The parameters of the controller were optimised using Lightning Search Algorithm. The provision of IPFC and SMES offered greater flexibility where IPFC enhanced the power transfer and stability and SMES damping load oscillations with combined scheme effectively eliminating rhythmic frequency and voltage oscillations during deregulation.

Kalyan et al., 2020 conducted the comparative evaluation of various energy storage systems, such as the ultracapacitors, SMES, and redox flow batteries, in relation to multi-area LFC and AVR application. Fuzzy-PID controller did use hybrid arithmetic optimization algorithm to achieve tuning in two-area thermal, hydro and gas system. The findings revealed that the addition of either of these storage devices provided great improvement of frequency and voltage dynamics with a reduced overshoot and settled time with ultracapacitors and SMES yielding the quickest damping of disturbances.

The study has revealed that mixed LFC and AVR control is becoming more important in the current power systems in which frequency and voltage should be controlled within very fine boundaries to achieve power quality and system stability. The four-area systems are more complex, and the recent studies indicate that the complex optimization of metaheuristic planning in conjunction with the FACTS devices and energy storage can enable the effective frequency and voltage regulation simultaneously [Ramoji & Saikia, 2021; Yin et al., 2022]. More recently, Saha et al., 2022 developed cascade controller-based modelling for four-area hybrid systems under restructured AGC, demonstrating improved performance in deregulated environments. Gulzar et al., 2023 and Elsaied et al., 2022 proposed optimized MPC-(1+PIDN) cascade controller for high-order interconnected renewable energy- based power systems, achieving robust frequency stabilization. The combined role of multiple storage systems and EVs in voltage and frequency regulation has been validated in modern studies [Ramoji & Saikia, 2022]. Cascade controller-based modelling for multi-area hybrid systems has demonstrated high performance under restructured conditions [Saha, Saikia, & Rahman, 2022].

1.2.9 AGC Integrating Different Controllers

The performance of the AGC systems highly relies on controller design and the research has been carried out from general classical controllers to more developed advanced structures involving fractional order dynamics, cascade blocks, intelligent adaptation mechanisms.

Early AGC implementations relied on simple integral controllers to eliminate steady-state frequency error. Hakimuddin et al., 2020 and Dhawane and Bichkar, 2020 used integral controllers as secondary controllers for AGC study, establishing baseline performance against which more sophisticated controllers could be compared. Hakimuddin et al., 2020 employed integral controllers demonstrating their continued relevance for simple systems. Saikia et al., 2010 conducted performance comparison of several classical controllers in AGC for multi-area interconnected thermal system, establishing benchmark performance metrics for integral, PI, and PID controllers that informed subsequent controller development.

Saxena and Hote, 2018 and Elmenfy, 2020 applied PI controllers in single and two-area AGC studies, showing that adding proportional action improves transient response compared to pure integral control. The most widely used classical controller remains PID, combining proportional, integral, and derivative actions. Khodabakhshian and Hooshmand, 2009, Parmar et al., 2012, and Jagatheesan et al., 2019 employed PID controllers for AGC applications, with Jagatheesan et al. specifically using firefly algorithm to design proportional-integral-derivative controller for automatic generation control of multi-area power thermal systems, demonstrating that optimization algorithms can substantially improve PID performance. Recent hybrid optimization methods such as GSA-BPSO have been utilized to design PID controllers achieving superior dynamic performance in deregulated environments [Kumar et al., 2022].

Hota & Mohanty, 2015 introduced PIDD controllers by adding another derivative term to conventional PID, showing improved performance particularly for systems with significant time delays. They also applied PIDD controllers and proved their advantages. Sahu et al., 2019 has employed the DE algorithm for the tunability of tilt integral derivative controller with filter for automatic generation control system, where TID controller refers to development through tilted integral action with further phase lead.

Fractional-order controllers have been a major breakthrough in the design of AGC controllers. Also, two equal-area thermal systems and three-area reheat thermal systems with GRC in deregulated electricity market, proposing BF optimized FOPID controllers [Arya, 2020a]. Their analysis indicated that FOPID controllers performed better than all integer-order controllers in all open electricity market transactions for both equal and unequal area systems, with sensitivity analysis indicating flexibility for dealing with changes in system conditions and contract violation levels. Optimization algorithms such as the modified hunger games search have been successfully applied for robust fractional-order PID design [Fathy et al., 2022]. A Multistage fractional-order controllers have also been explored for frequency improvement in multi-microgrid environments [Das et al., 2024].

Morsali et al., 2016 and Babaei et al., 2020 employed FOPID controllers in various AGC applications demonstrating their superior performance. Zamani et al., 2016 designed fractional-order PID controller using GBMO algorithm for load-frequency control with governor saturation, demonstrating that fractional-order controllers can effectively handle nonlinearities such as governor saturation better than integer-order counterparts. Sharma and Yadav, 2019 applied FOPI regulator to two-area multi-source power system, tuning its gains using Lion Algorithm with Lévy flights. Jain and Hote, 2018 designed two-degree-of-freedom fractional-order PID controller for two-area load-frequency control, tuning parameters via internal model control framework and Big Bang-Big Crunch optimizer, showing that FOPI and FOPID controllers offer finer control over system's frequency response. Priyadarshani et al., 2020 applied Pathfinder algorithm optimized fractional order tilt-integral-derivative controller for automatic generation control of multi-source power system, showing superior performance of FOTID structure in systems with diverse generation sources. Daraz et al., 2021 proposed fractional order integral-tilt derivative (FOI-TD) controller for automatic generation control of multi-source interconnected power system, demonstrating effectiveness of combining fractional-order integral with tilt derivative action for improved transient response. Sahoo et al., 2021 developed fractional order fuzzy PID controller for automatic generation control, showing that combining fractional-order dynamics with fuzzy logic inference can enhance controller adaptability to system uncertainties and parameter variations. Daraz et al., 2022 extended this work with optimized fractional order integral-tilt derivative controller for frequency regulation of interconnected diverse renewable energy resources, demonstrating particular effectiveness of FOI-TD structure for systems with high renewable penetration and associated variability. Learning-based FOPID designs have also been proposed for distributed energy resources, ensuring robustness against renewable intermittency [Babaei & Hadian, 2022]. Model predictive controller–based voltage and frequency regulation approaches coordinated with virtual inertia and redox flow batteries have proven effective [Kumar et al., 2022].

2DOF controllers allow separate tuning of setpoint tracking and disturbance rejection. Pradhan et al., 2015 considered unequal multi-area thermal system introducing both GDB and GRC in LFC, using Firefly Algorithm for optimization. Investigation by Audomsi and Sa-ngiamvibool, 2023 showed that incorporating 2DOF-PID controller gives better dynamic performance than conventional controller using FA optimization technique to control settling time, oscillation magnitude, and peak deviation. Multi-source cascade controllers such as 2DOF-PIDN-FOPIDN have shown superior damping in hybrid deregulated systems [Prakash et al., 2022]. Fractional-order cascaded control approaches further improve AGC performance in deregulated systems [Jena et al., 2022]. Advanced two-degree-of-freedom PID structures tuned with improved metaheuristic algorithms show promising results for nonlinear multi-area systems [Gupta et al., 2022]. Nayak et al., 2020 implement a hybrid SSA–SA based three-degree-of-freedom fractional-order PID controller for AGC of a two-area power system integrated with small hydro plants

Simhadri et al., 2018 applied 2DOF-PID to two-area hydro-thermal system, with PI, PID, and 2DOF-PID controllers all tuned by Dragonfly optimization algorithm. They reported that Dragonfly-tuned 2DOF-PID yielded best frequency regulation compared to PI and single-DOF PID cases. Sahu et al., 2013 used Differential Evolution to optimize parallel 2DOF-PID for two-area power system with governor dead-band nonlinearity. Dash et al., 2014 analysed a three unequal reheat thermal AGC with GRC, considering Cuckoo Search algorithm based 2DOF-integral plus double derivative controller for better system dynamic response. The proposed controller performance was compared with 2DOF-PI and 2DOF-PID, with analysed results showing better performance considering nominal conditions, changing system loading, and SLP size. A 2DOF-PID configuration has been applied to wind-integrated interconnected systems, achieving improved damping and dynamic response [Karanam & Shaw, 2022].

Behera et al., 2018 study a hybrid power systems frequency regulation using TID based robust controller design and differential evolution (DE) algorithm. Chintu et al., 2020 proposed 2DOF-TIDF separating set-point tracking and disturbance-rejection tuning to better suit AGC's regulation task. The controller applied to frequency control and validated in real time demonstrated that extra degree of freedom yields quicker frequency restoration and reduced tie-line power error versus single-DOF counterparts, underscoring that combining IDF-family structure with 2DOF tuning enhances both transient and steady-state LFC behaviour.

Cascade control structures emerged as effective approach for AGC by allowing hierarchical control action. Padhy et al., 2017developed cascade PI-PD regulator for AGC system with electric vehicles, tuning gains via modified Grey Wolf Optimizer and achieving improved damping under disturbances. Fractional-order cascaded integral–derivative tilt controllers integrating renewables and EVs further enhance load frequency control performance [Raj & Shankar, 2023].

Apart from classical and fractional order structures, intelligent controllers have received attention. Mansour et al., 2022 used fuzzy logic controller equilibrium base to improve the performance of AGC using the disturbance of renewable energies. Sharma, 2020 studied automatic generation control of multi-source inter-connected power system by using adaptive neuro-fuzzy inference system. Debnath et al., 2017b proposed cascade fractional fuzzy controller and fuzzy controller of hybrid power system using FACTS device. Intelligent methods are more advantageous to deal with nonlinearities and uncertainties but demand an extensive training data or expert knowledge for rule base formation

The 2DOF-TIDN-FOTI controller proposed for Chapter 3 combines two-degree-of-freedom tilt integral derivative with filter cascaded with fractional-order tilt integral. This structure integrates advantages of 2DOF separate tuning for setpoint tracking and disturbance rejection, TID tilted integral action for phase lead, derivative filter for noise attenuation, and fractional-order dynamics in second stage for enhanced flexibility. First stage provides fast initial rate response and second stage provides precise steady-state regulation thus the cascaded structure forms a development of the existing cascade structures and incorporates several successfully developed concepts.

The TI-IDN controller designed for Chapter 4 is novel structure of tilt integral and integral derivative with filter of integer order. This controller particularly addresses virtual inertia control requirements in which rapid response to rate of change of frequency is important. Tilt integral allows phase lead for good transient response and IDN structure allows derivative action filtered to avoid the amplification of noise, which would make it more appropriate to low inertia system with a fast variation of frequency during disturbances.

The developed controller TI-PIDN used for Chapter 5 for combined LFC and AVR includes tilt integral with proportional integral derivative with filter. This structure is very suitable for the simultaneous frequency and voltage control in which both fast transient response and steady-state performance are critical. The PIDN' component offers complete control action, and the tilt integral student gives the phase compensation improving coordination between the frequency and voltage control loops. In comparison with existing structures, these proposed controllers are improvements as they are the proper combination of proven concepts in new configurations designed specifically to solve the problems of renewable-integrated multi-area systems under deregulated operation.

1.2.10 Algorithms Used in AGC

The results of any AGC controller critically depends on the optimal tuning of their parameters, thus provoking a wealth of research on optimizing algorithms for selecting controller parameters. The research has evolved from the classical methods to genetic algorithms to the advanced nature-inspired metaheuristics.

Rerkpreedapong et al., 2003 used Genetic Algorithm and linear matrix inequalities for load frequency control by which it was shown that GA could search the parameter space to get controller gains satisfying robustness constraints. GA has been used for fuzzy gain scheduling of PI controllers for load frequency regulation which shows the advantages of GA over traditional fixed gain prediction.

Sahu et al., 2014 proposed hybrid differential evolution PSO algorithm for tuning conventional PID controllers, demonstrating that hybridizing algorithms could combine their complementary strengths. Barisal and Mishra, 2018 applied PSO and improved PSO with shrinking search space to minimize integral time-weighted absolute error of frequency and tie-line deviations. PSO and IPSO optimized PID gains automatically, with IPSO-tuned PID delivering faster settling and smaller oscillations than both standard PSO-tuned PID and alternative methods. The higher convergence characteristic and shorter elapsed time of PSO made it advantageous compared to GA for many applications. Particle swarm optimization–tuned fuzzy cascade fractional-order PI–PD controllers further enhance frequency stability in dual-area systems [Shouran & Alsseid, 2022].

Arya and Kumar, 2016 designed and analysed BFOA-optimized fuzzy PI and PID controller for AGC of multi-area traditional and restructured electrical power systems, demonstrating that bacterial foraging optimization could effectively tune fuzzy controller parameters. Arya and Kumar, 2017 extended this to BFOA-scaled fractional-order fuzzy PID controller applied to AGC of multi-area multi-source electric power generating systems, showing advantages of combining bacterial foraging with fractional-order control structures.

Abd-Elazim and Ali, 2018 designed load frequency controller of two-area system composing of PV grid and thermal generator via firefly algorithm, demonstrating FA's effectiveness for renewable-integrated systems. Jagatheesan et al., 2019 used firefly algorithm to design proportional-integral-derivative controller for automatic generation control of multi-area power systems, showing that FA's simple and flexible characteristics made it attractive for AGC applications. The FA mimics flashing appearances of fireflies using chemical process of bioluminescence, with its versatile characteristics attracting researchers as solution to AGC optimization problems.

Guha et al., 2016 investigated load frequency control of interconnected power system using grey wolf optimization, demonstrating GWO's effectiveness for AGC parameter optimization. Sharma and Saikia, 2015 applied Grey Wolf Optimizer algorithm based classical controllers for automatic generation control of multi-area ST-thermal power system, showing superior performance compared to other optimization techniques.

GWO was introduced by Mirjalili et al., 2014 as nature-inspired metaheuristic imitating grey wolves' leadership hierarchy and hunting behaviour. In GWO, the best three solutions are labelled alpha, beta, and delta, guiding the rest of wolves during search. The algorithm models three main hunting phases searching for prey, encircling prey, and attacking prey, with mathematical coefficients controlling exploration decreasing over iterations so wolves converge on promising regions. This strategy balances global exploration and local exploitation, with simplicity of GWO making it robust for continuous optimization [Debnath et al., 2017a].

Nadimi-Shahraki et al., 2021 proposed improved GWO with new dimension learning-based hunting strategy. I-GWO adaptively assigns weights to alpha, beta, delta during updates and introduces omega wolf guidance, improving diversity and convergence balance. Benchmark tests showed I-GWO converges faster and more accurately than standard GWO on complex problems, helping GWO avoid premature convergence and yield better solutions.

Acharyulu et al., 2020 analysed moth flame optimization optimized cascade proportional-integral-proportional-derivative controller with filter for automatic generation control system incorporating solar thermal power plant. Sahu et al., 2015 employed teaching-learning based optimization algorithm for automatic generation control of multi-area power systems with diverse energy sources. Dash et al., 2014 applied Cuckoo Search algorithm for optimization in multi-area AGC. Celik, 2018 incorporated stochastic fractal search algorithm into efficient design of PID controller for automatic voltage regulator system, demonstrating that advanced metaheuristic optimization can significantly improve AVR controller performance compared to conventional tuning methods.

Hasanien, 2017 introduced whale optimization algorithm for automatic generation control of interconnected modern power systems including renewable energy sources, demonstrating that this algorithm inspired by humpback whales' bubble-net hunting strategy could effectively optimize AGC controllers. The diversity of nature-inspired algorithms reflects researchers' continuous search for optimization methods with better balance of exploration and exploitation capabilities.

Trojovska et al., 2022 proposed novel metaheuristic called Zebra Optimization Algorithm that mimics two key behavioural traits of zebras in nature foraging and defense against predators. The authors tested ZOA over sixty-eight benchmark functions including unimodal, multimodal, fixed-dimensional, CEC2015, and CEC2017, comparing it against nine well-known metaheuristics including GWO, PSO, and FA. ZOA was often competitive or superior, especially in terms of trade-offs between exploration and exploitation stages. The foraging behaviour of the algorithm allows an effective search space exploration, whereas the defense mechanism allows exploiting the interesting regions.

While Trojovska et al., 2022 developed ZOA as general purpose optimization algorithm, there is thus still no research applying ZOA to multi-area multi-source AGC under deregulated environment and substantial renewable integration. This thesis introduces the first application of ZOA for the optimized determination of cascade controller parameters in the context of complex multi-area systems under conditions of market-based structures with high renewable shares, to fill a significant gap in the AGC optimization research. The ZOA's evidenced superior performance on complex benchmark functions and its proven effectiveness in initial power system applications are the motivations for its selection for the challenging optimization problems presented by modern AGC requirements.

1.3 Scope of Study

Based on comprehensive literature review, several significant research gaps have been identified that define the scope of this research:

1. There is scope for using biogas plants and biodiesel plants as distributed generation with combination of other renewable energy sources like hydropower plant and wind turbine generator. Different types of work have been done in deregulated systems but no work has considered inclusion of biogas and biodiesel as DGs in AGC study under deregulation. Thus, study of DGs can be considered along with conventional plant including non-linearities in multi-area system under deregulated environment. While Arya, 2020 modelled biogas and biodiesel in isolated microgrids, comprehensive investigation of these sources in systems under deregulation remains unexplored.

2. The effects of electric vehicle fleets with conventional resources have been found in literature survey. It is difficult to find systems in AGC study consisting of electric vehicle fleets along with multiple renewable energy sources as DGs in conventional sources based multi-area interconnected system under deregulated environment which is yet to be investigated. Existing research by Debbarma et al., 2017 and Arya, 2020b addressed EV integration but not comprehensively with diverse renewable sources under deregulation, creating gap this research addresses.

3. As utilization of renewable energy sources increases in interconnected power system, the inertia of overall system decreases (Arya, 2021). The decrease in

inertia increases weakness of interconnected power system. Very few works have been found considering virtual inertia control in AGC study under conventional and deregulated market. There is scope to enhance inertia of modern power system using new virtual inertia control method in four-area system. While Ali et al., 2019 and El-Shimy et al., 2023 addressed VIC, application to four-area systems with comprehensive renewable integration and novel controller structures remains unexplored.

4. From literature it has been observed that study of combined LFC and AVR is very limited. Very few works have been found considering combined LFC and AVR under regulated environment. There is scope to study combined LFC and AVR with integration of renewable energy sources including non-linearities in deregulated environment.
5. Numerous studies have effectively employed various FACTS devices in AGC research. There are currently no studies that show integration of FACTS devices into combined LFC and AVR to enhance system dynamic performances in multi-source multi-area interconnected system under deregulated environment. Research by Rajbongshi and Saikia, 2018 addressed FACTS in combined control but not comprehensively for multi-area deregulated systems with diverse renewables.
6. Incorporation of Archimedes Wave Energy Conversion and tidal energy are seen in several LFC studies, but it is hard to find studies where both sources are used in combined LFC and AVR study. There is scope to utilize these sources along with other conventional and non-conventional sources in regulated and deregulated environment.
7. Different types of controllers like conventional controller, different fractional order, and cascaded controllers are used in AGC to regulate unwanted oscillation of interconnected power system. Different forms of cascaded and hybrid controller are still unaddressed in solving AGC problems in regulated as well as deregulated system.
8. Various algorithms are used to optimize controller gains and associated parameters in AGC study. ZOA algorithm which draws inspiration from zebras' natural behaviour by emulating how zebras forage and defend against predators is not yet used in AGC study for multi-area systems under deregulation. While Trojovská et al. (2022) developed ZOA and applied it to microgrid control, application to complex multi-area deregulated AGC with substantial renewable integration represents significant research contribution.

1.4 Objectives of the Present Work

In light of the literature review and identified research gaps, the following objectives are investigated in this research:

1. Automatic generation control of a multi-source, multi-area thermal power system integrating electric vehicle and renewable sources like solar photovoltaic, wind, geothermal, hydropower plant, bio gas and biodiesel under regulated and deregulated environment.
2. Impact of virtual inertia control in a multi-area power system incorporating hybrid sources like thermal, solar photovoltaic, geothermal, wind turbine generator and bio-diesel in both regulated and deregulated environment.
3. Improving system dynamic responses by integrating Facts device in the combined LFC and AVR multi-area thermal system incorporating AWEC and renewable energy sources like Geothermal, Tidal and Solar thermal power plant in both regulated and deregulated environment.
4. Propose and design new controllers and optimize the gain values of all the controllers using new optimization technique. The sensitivity and stability analysis of all the proposed controllers are also done by considering various real time scenarios.

1.5 Outline of the Chapters

Chapter 1: Introduction - This chapter provides brief introduction of automatic generation control of interconnected power system. It includes critical literature survey of AGC followed by scope of current study. The key objectives of thesis are also discussed in this chapter, establishing foundation for research by identifying gaps in existing literature and defining specific contributions this work makes to AGC field.

Chapter 2: Description and mathematical modelling of the study system - This chapter introduces components of study systems, providing detailed mathematical models of various generation sources including conventional thermal plants with reheat turbines, renewable sources such as solar photovoltaic, wind turbines, hydropower, biogas, biodiesel, solar thermal, geothermal, tidal, and AWEC. The chapter also presents models of energy storage systems, electric vehicles, FACTS devices particularly IPFC, and automatic voltage regulators. Transfer function representations and state-space models are developed for all system components, establishing mathematical framework for controller design and performance evaluation.

Chapter 3: Multi-area power system with integration of renewable energy sources and electric vehicles - This chapter investigates automatic generation control in deregulated environment for three unequal interconnected power systems involving renewable energy sources and electric vehicles. In each area, there are reheat thermal plants combined with various renewable energy sources including solar photovoltaic plant, wind turbine plant, hydropower plant, biodiesel engine generators, biogas turbine generators, and electric vehicles. Non-linearities such as generation rate constraints and governor dead bands are taken into consideration. This chapter proposes new cascade controller called two-degree of freedom Tilt integral Derivative with Filter cascaded with Fractional order Tilt Integral controller using new Zebra optimization algorithm to optimize controller parameters. Several case studies are done to illustrate robustness of proposed controller and optimization. It has been observed that deviation in frequency's settling time, peak overshoots, and undershoots are better with including EV, demonstrating effectiveness of proposed 2DOF-TIDN-FOTI controller in handling complex multi-source systems under deregulated operation.

Chapter 4: Impact of virtual inertia control in hybrid generating sources based multi-area power system - In this chapter, four-area interconnected multi-area system with hybrid generating units is modelled for study of automatic generation control. In systems where renewable energy are present, inertia of system decreases due to absence of rotor or rotating force causing system instability. Virtual inertia control is introduced to system to compensate loss of inertia using proposed novel controller named tilt double integral derivative with filter controller TI-IDN. The proposed controller is tuned with Zebra optimization algorithm to improve system response like settling time, peak overshoot and peak undershoot. The superiority of proposed controller is observed by comparing with Integral, Tilt-Integral and Tilt integral derivative controller. Analysis reveals that VIC coordinated control enhances system dynamic performance. Finally, robustness of proposed control methodology is validated by performing sensitivity analysis during wide variations of system loading and system with communication time delay, demonstrating that virtual inertia provision through advanced control can effectively address challenges of low-inertia systems with high renewable penetration.

Chapter 5: Combined load frequency control and automatic voltage regulator based multi-area power system with renewable energy sources - The integration of renewable energy sources caused overflow of current interconnected power systems which has resulted in major inefficiencies. Load frequency controls and automatic voltage regulator are essential elements that guarantee consumers receive high-quality electricity while preserving grid's nominal frequency, voltage, and power variations. In these difficult circumstances, these steps are crucial to guaranteeing interconnected power system stability and security. In this research, hybrid generating sources in interconnected four-area non-linear system is modelled for study of combined load frequency control and automatic voltage regulator under deregulated environment. The study's realism is increased especially when different non-linear elements are included in each of four domains such as boiler dynamics, time delay, and generation rate constraint. The Zebra optimization algorithm, recently developed nature-inspired meta-heuristic technique, was utilized to identify ideal tilt-integral-proportional-integral derivative with filter TI-PIDN controller settings. During tuning procedure, fitness function is evaluated using integral squared error value as error criterion. Different case studies are done to analyse performance of proposed technique and its advantages over other classical controllers like proportional integral, tilt integral, proportional integral derivative and tilt integral derivative controllers and algorithms in case of settling time, maximum overshoot and undershoot in regulated and deregulated environment with presence of interline power flow controller. Sensitivity analysis along with eigen value analysis is also carried out to find robustness of controller, demonstrating that proposed approach effectively coordinates frequency and voltage control while respecting commercial constraints of deregulated operation and accommodating variability of diverse renewable sources including marine energy technologies.

Chapter 6: Conclusion - This chapter draws conclusions of the overall work and prospects for further work, by synthesizing contributions to all research goals, by discussing implications to power system operating and control, and by suggesting future directions for extending this work to meet emerging challenges of increasingly renewable-dominated market-based power systems.

Chapter

2

Description and Mathematical Modelling of the Study System

2.1 Introduction

Power plants have traditionally relied on fossil fuels and nuclear energy. To meet modern demands, control areas must now integrate a diverse mix of generation sources, including thermal, hydro, gas, and renewables. This study utilizes mathematical and transfer function models developed in MATLAB/Simulink to analyze system behavior under various scenarios, examining both conventional and restructured multi-area interconnection configurations.

2.2 Mathematical modelling of study power system

Synchronous generators are typically driven by prime movers deriving energy from hydro, thermal, or gas sources. A speed governing system is integral to the turbine, enabling its start-up, acceleration to rated speed, and load regulation to achieve the target power output. The model incorporates key dynamic parameters, namely the load damping constant (D_k), power system gain constant (K_{pk}) power system time constant (T_{pk}), and the area response characteristic (β_k).

$$D_k = \frac{\Delta P_{Dk}}{\Delta f_k}(p.u.MW / Hz) \tag{2.1}$$

$$K_{pk} = \frac{1}{\Delta D_k}(Hz / p.u.MW) \tag{2.2}$$

$$T_{pk} = \frac{2H_k}{F_k D_k}(s) \tag{2.3}$$

$$\beta_k = D_k + \frac{1}{R_k}(p.u.MW / Hz) \tag{2.4}$$

Similarly, for the l^{th} area

$$D_l = \frac{\Delta P_{Dl}}{\Delta f_l}(p.u.MW / Hz) \tag{2.5}$$

$$K_{pl} = \frac{1}{\Delta D_l}(Hz / p.u.MW) \tag{2.6}$$

$$T_{pl} = \frac{2H_l}{F_l D_l}(s) \tag{2.7}$$

$$\beta_l = D_l + \frac{1}{R_l}(p.u.MW / Hz) \tag{2.8}$$

Where, 'ΔP_D' represents nominal operating load MW, R denotes speed regulation (Hz/p.u. MW) and H is the inertia constant (sec).

2.2.1 Modelling of thermal power plant

Coal-fired power plants utilize fuel energy to produce high-pressure, high-temperature steam within a boiler. This steam is converted into mechanical energy via an axial-flow turbine, which is constructed with multiple stages of alternating stationary and rotating blades. The process begins as steam expands and accelerates through the stationary blades, increasing its kinetic energy. Subsequently, the steam flows through the rotating blades, and the resultant change in momentum and direction applies a tangential force, thereby generating torque on the turbine shaft. As steam progresses along the turbine shaft, its pressure decreases, causing a significant volumetric expansion. To accommodate this, the blade length is progressively increased from the high-pressure inlet to the low-pressure exhaust. A typical complete steam turbine comprises three or more of these stages, all connected sequentially on a single shaft. The division of a turbine into multiple stages allows for steam reheat between them, a process that raises the steam's enthalpy and consequently, the system's overall efficiency. This leads to a classification of steam turbines into non-reheat, single-reheat, and double-reheat types. Non-reheat turbines, comprising a single stage, are common in sub-100 MW power plants. For larger capacities, a single tandem-reheat configuration is the standard installation. The governing system regulates steam flow into the turbine. It initiates control by receiving a speed signal from a measuring device. In this system, oil servomotors act as the main amplifiers and valve actuators, which are themselves controlled by a pilot valve. While emergency stop valves are sometimes used during the initial turbine start-up, their primary function under synchronized conditions is to shut down the generator only in an emergency. The configuration of a tandem-compound single-reheat steam turbine is presented in Figure 2.1. An approximation of its linear transfer function model, adapted from [Das, 1991; Kothari, 1981; Nanda, 2006], is shown in Figure 2.2. This model incorporates key time constants: T_t (steam chest and inlet piping), T_r (reheaters), and T_c (crossover piping). The parameters F_{HP}, F_{IP}, and F_{LP} represent the power fractions contributed by the high-pressure, intermediate-pressure, and low-pressure cylinders, respectively. The sum of these fractions must equal one ($F_{HP} + F_{IP} + F_{LP} = 1$). Given that T_c is negligible compared to the other time constants, it can be disregarded. This simplification yields the reduced-order transfer function depicted in Figure 2.3. The proportion of total power from the intermediate and low-pressure cylinders is defined by the relation $F_{IP} + F_{LP} = 1 - F_{HP}$. Meanwhile, the deviation in output power resulting from a change in the governor setting is represented by Equation (2.9).

$$\Delta P_{th}(s) = \frac{1}{(1+sT_t)}\left[F_{HP} + \frac{1-F_{HP}}{1+sT_r}\right]\Delta X_E(s) \tag{2.9}$$

When the reheat coefficient K_r is taken as the high-pressure cylinder's power fraction (K_r= F_{HP}), equation (2.9) reduces to (2.10).

$$\text{Or } \Delta P_{th}(s) = \frac{(1+sK_rT_r)}{(1+sT_t)(1+sT_r)}\Delta X_E(s) \tag{2.10}$$

The output from the speed governor is defined in Equation (2.11). This relationship is integrated into the overall system model shown in the block diagram of Figure 2.4, which illustrates the reheated steam turbine and its governing system.

$$\Delta X_E(s) = \frac{1}{(1+sT_g)}\left[\Delta P_c(s) - \frac{\Delta f(s)}{R}\right] \tag{2.11}$$

2.2.2 Modelling of Geothermal power plant

Geothermal power plants (GTPs) serve as a dependable source of baseline power due to their continuous operation. This process is based on thermodynamic principles, involving a cycle where the working fluid exists in liquid, gaseous, and two-phase mixed states. Due to the direct extraction of high-pressure, high-temperature steam from the earth's crust, a geothermal plant (GTP) operates without an external boiler. This allows it to be modeled analogously to a non-reheat thermal power plant. Its dynamics are represented by the transfer function model in Figure 2.5, with the governor and turbine given by Equations (2.12) and (2.13).

$$G_g(s) = \frac{K_{sg}}{1+s.T_{sg}} \tag{2.12}$$

$$G_t(s) = \frac{K_{st}}{1+s.T_{st}} \tag{2.13}$$

Where, T_{st} and T_{sg} are, respectively, the time constants of governor and turbine units [Tasnin and Saikia, 2018].

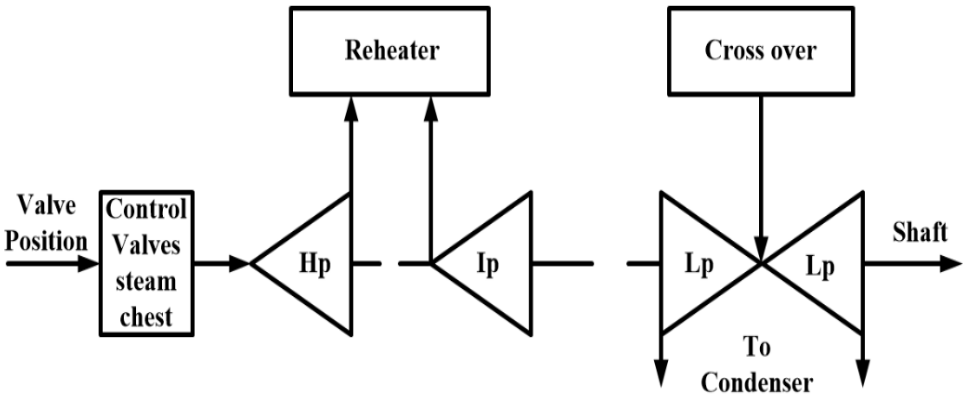

Figure 2.1 Single reheat tandem compound steam system.

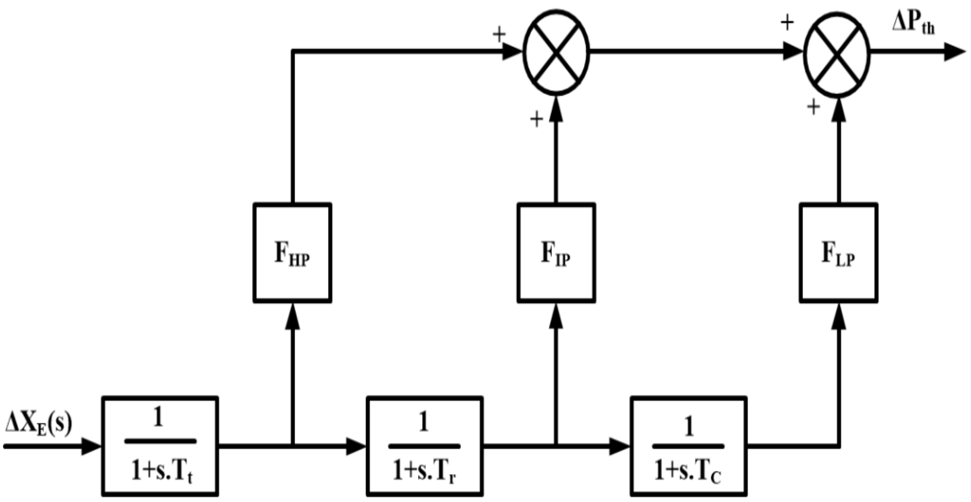

Figure 2.2 Approximate linear transfer function model of reheat thermal turbine

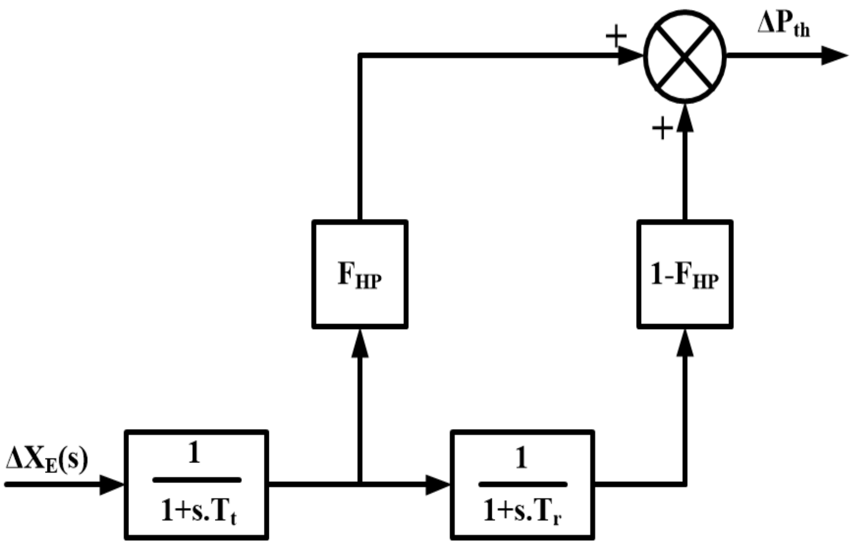

Figure 2.3 Reduced order model of figure 2.2.

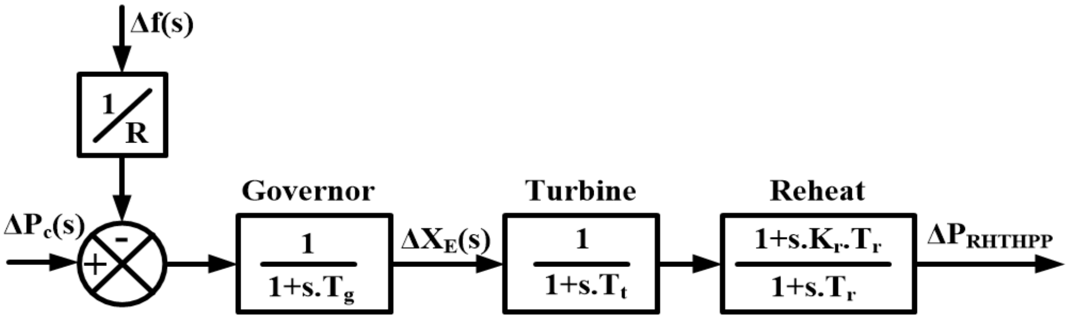

Figure 2.4 Transfer function of reheat thermal power plant.

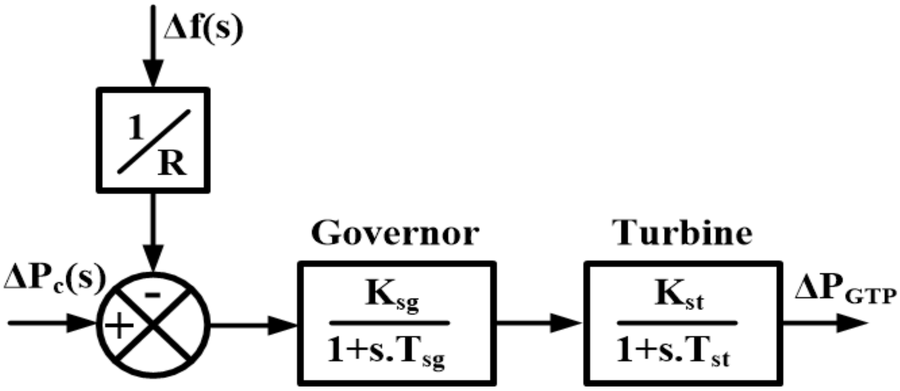

Figure 2.5 Transfer function block of geothermal power plant.

2.2.3 Modelling of Solar photovoltaic plant

The most common and widely used SPV system consists of arrays of solar PV panels coupled with maximum power point trackers and a DC-AC solar inverter to interface generated solar power to the AC bus of the microgrid. The surface temperature of the PV cell (Ta in degrees Celsius) and irradiance (in kW/m2) affect the output power of the SPV array (measured in watts), which is measured as,

$$P_{pv} = \eta S\left\{1 - 0.005(25 + T_a)\right\}\phi \tag{2.14}$$

Where, S and η are the arrays measured surface area (4084 m2) and conversion efficiency (0.09–0.12), respectively. The total output power of this unit is assumed to be 10 MW. The parameters for SPV units are taken from [Barik and Das 2018; Das et al. 2012]. The SPV system's linearized transfer function model for low frequency domain analysis is represented as,

$$G_{SPV}(s) = \left(\frac{K_{SPV}}{1 + s.T_{SPV}}\right) \tag{2.15}$$

Here, K_{SPV} and G_{SPV} are the gain and time constant of the SPV unit.

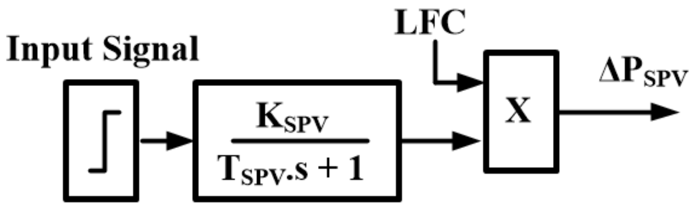

Figure 2.6 Transfer function block of solar photovoltaic plant.

2.2.4 Modelling of Hydropower plant

The force of falling water from a higher reservoir to a lower reservoir is utilized by a hydraulic turbine. The head is the vertical separation between the turbine level and the higher reservoir. Although there is no clear distinction between high head, medium head, and low head (run-of-river) plants, they are all categorized based on the size of their heads. Francis turbines and other reaction turbines are used in plants with low and medium heads. Reaction turbines typically require huge water volumes, extensive water channels, and moderate operating speeds due to the relatively low-pressure head. The generators have a huge diameter because they revolve slowly. The creation of transfer function models for electric hydro governors and hydro turbine penstocks is covered in depth in [Nanda et al., 2006]. The penstock and hydro turbine model are depicted by (2. 16).

$$\frac{\Delta P_{th}(s)}{\Delta X_E(s)} = \frac{a_{23}\left[1+(a_{11}-\frac{a_{13}a_{21}}{a_{23}}sK_rT_r)\right]sT_{Wh}}{(1+a_{11}sT_{Wh})} \tag{2.16}$$

In this model, the parameters a_{11}, a_{13}, a_{21}, and a_{23} are the partial derivatives for flow and torque concerning head and gate opening. The influence of speed deviations on torque is neglected due to their small magnitude in a system-connected context. Key parameters include the water starting time (T_{Wh}) and, for an ideal lossless turbine, the specific coefficients $a_{11} = 0.5Z_0$, $a_{21} = 1.5Z_0$, and $a_{13} = a_{23} = 1$.

Where, Z_0 represents the initial gate opening in p.u. Thus, equation (2.16) can be represented by (2.17).

$$\frac{\Delta P_{th}(s)}{\Delta X_E(s)} = \frac{1-sZ_0T_{Wh}}{1+0.5sZ_0T_{Wh}} \tag{2.17}$$

At full load, Z_0 = 1. Therefore, equation (2.17) represents by (2.18).

$$\frac{\Delta P_{th}(s)}{\Delta X_E(s)} = \frac{1-sT_{Wh}}{1+0.5sT_{Wh}} \tag{2.18}$$

The core function of hydro governors has remained consistent even as electric models have replaced mechanical-hydraulic ones over the last few decades. The key difference lies in the method: electric governors use electronic components for speed-sensing and permanent-droop compensation. Their output then drives an electro-mechanical transducer, which in turn operates the pilot valve and servomotor. The electric governor features a three-term Proportional-Integral-Derivative (PID) control action, as developed by the Woodward Governor Company. The corresponding transfer function (G_{HPP}) for the hydro plant, defined by its proportional (K_{hp}), integral (K_{hi}), and derivative (K_{hd}) gains, is presented in (2.15).

$$G_{HPP} = \frac{K_{hd}s^2 + K_{hp}s + K_{hi}}{K_{hd}s^2 + (K_{hp} + f/R)s + K_{hi}} \tag{2.19}$$

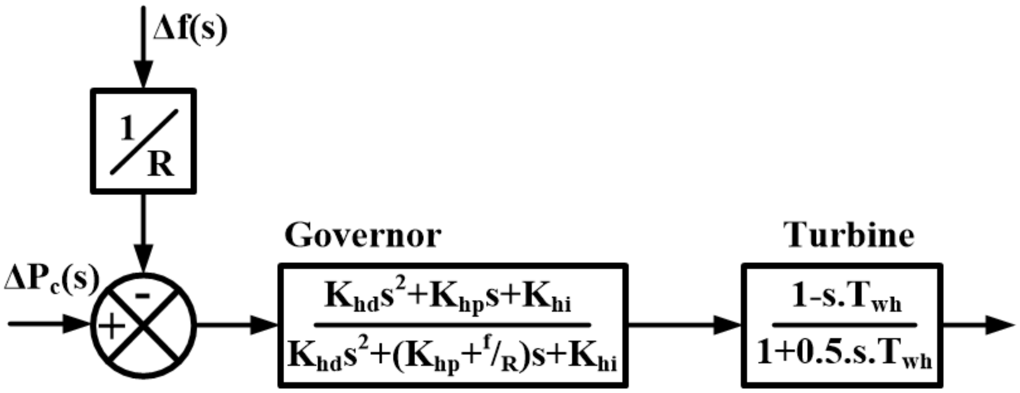

Figure 2.7 Transfer function block of hydropower plant.

2.2.5 Modelling of Wind turbine plant

The wind speed at a given time determines the output of a wind turbine generator. The output power of the wind turbine varies between rated and zero power to compensate for utility grid frequency variations. The hydraulic pitch actuator and blade pitch control system are part of the wind turbine dynamic model. This system has a nonlinearity since the pitch angle changes as the wind speed does. Figure 2.8 displays the wind turbine power plant's functioning block diagram [Das et al., 2021]. Equation (2.20) provides the hydraulic pitch actuator's transfer function.

$$\frac{\Delta H(s)}{U(s)} = \frac{K_h(1+sT_a)}{(1+sT_h)(1+s)} \tag{2.20}$$

Where the time constant and hydraulic pitch gain are denoted by K_h and T_h. The actuator time constant is denoted by T_a. A straightforward lag known as “data fit pitch response” is necessary to match the phase/gain properties of a model. K_p and K_{bl} stand for data fit pitch gain and blade gain, respectively.

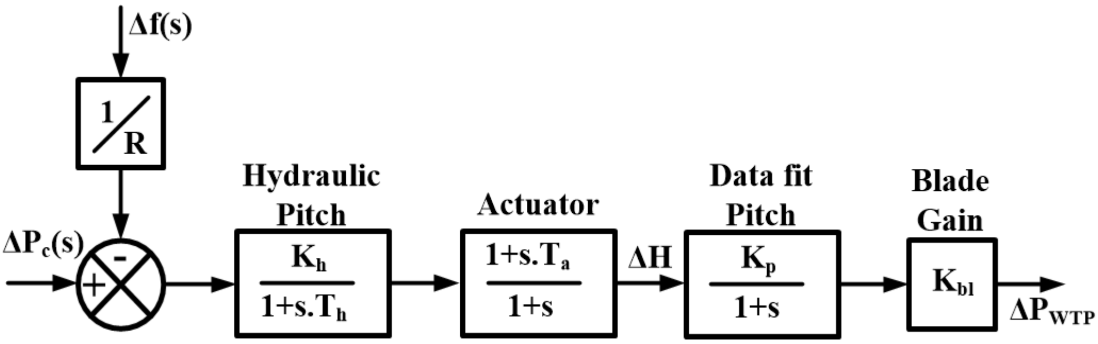

Figure 2.8 Transfer function block of wind turbine plant.

2.2.6 Modelling of Bio-gas plant

Small gas turbine generators (GTG) could effectively employ biogas created from degradable wastes and animal excrement for the production of electricity. In relation to GTG, the gas valve actuator, speed governor, gas turbine, fuel system, and combustor are also parts of the BGP system. The parameters of BGP are taken from [Barik and Das, 2018]. The linearized transfer function of BGP could be roughly described as follows since the power output of BGP is exactly proportional to the actions of the gas inlet valve, governor, combustor, and turbine, which is shown as,

$$G_{BGP}\left(s\right)=\left(\frac{1+sX_c}{\left(1+sY_c\right)\left(1+sb_c\right)}\right)\left(\frac{1+sT_{CR}}{1+sT_{BG}}\right)\left(\frac{1}{1+sT_{BT}}\right) \tag{2.21}$$

Here, X_c and Y_c are the lead and lag time of BGP, b_c is the valve actuator, T_{BT} is the turbine time constant. T_{CR} and T_{BG} are the combustion reaction delay and biogas delay.

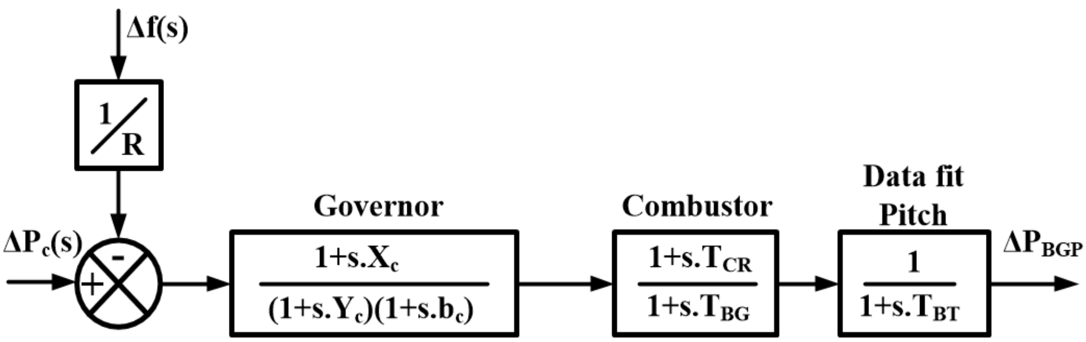

Figure 2.9 Transfer function block of Biogas plant.

2.2.7 Modelling of Biodiesel power plant

Transesterification is a technique used to extract biodiesel from energy crops. Pure biodiesel (B100) or blended biodiesel can both be used in traditional Diesel engine generator (DEG). The following equation could be used to measure the rate at which BDP does mechanical work:

$$\frac{dW}{d\theta}=\frac{\Re TV_{disp}}{2}\left(\frac{0.5\sin 2\theta}{\sqrt{2(L/S)^2-\sin^2\theta}}-\sin\theta\right) \tag{2.22}$$

Where, L is the length of the connecting rod in m, S is the stroke length in m, $\Re$ is the universal gas constant ($\Re$ = 8.314 kJ/kmol K), and T is the instantaneous temperature in Kelvin at any crank angle, ş is the angular displacement with respect to bottom dead center (BDC) in degrees, and V_{disp} is the displacement volume in m^3.

Referring to the synchronous generator of the standard DEG model, the power output of the BDP is precisely proportional to the internal combustion (IC) engine action and the biodiesel input valve action; thus, the important parameters for the BDP are collected from [Barik and Das, 2018] and its linearized transfer function model might be roughly described as shown in Figure 2.10. Here, K_{bv}, T_{bv}, K_{be} and T_{be} are the valve gain, valve actuator delay, engine gain and time constants of BDEG unit

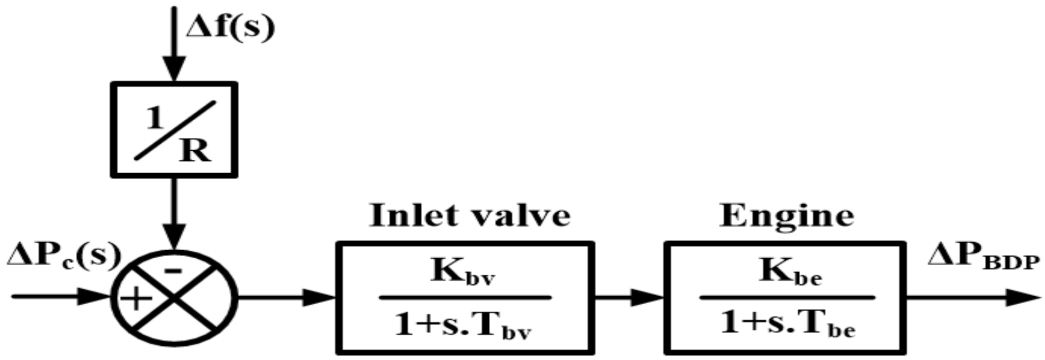

Figure 2.10 Transfer function block of biodiesel plant.

2.2.8 Modelling of Solar thermal plant

An ORC and compound parabolic concentrators make up an Organic Rankine Cycle (ORC) solar thermal power plant. The working fluid is heated by concentrated solar radiation in the collector field. After that, the hot fluid is poured into the heat exchanger, where the high pressure causes it to evaporate. Power is produced at the generator's output, which is connected to the turbine, by converting the thermal energy of the vapor into mechanical energy. The condensed liquid is delivered into the heat exchanger, where the system cycle starts, via the reservoir tank after the exhaust vapor is condensed in a condenser [Sharma and Saikia, 2015]. We have to incorporate heat storage technology for a steady energy supply because of the shifting weather patterns and the extending and shortening of day and night. The first step in modeling solar thermal power plants is to represent the solar field. An equation for the solar field with respect to solar irradiance was given by [Buzás et al. 2014], who investigated the transfer function modeling of solar collectors. (2.22) provides the output temperature change rate.

$$\frac{dT_0(t)}{dt} = \frac{A\eta_0}{C} I(t) - \frac{U_1 A}{C}\left[T_a(t) - T_e(t)\right] + \frac{v(t)}{V}\left[T_i(t) - T_0(t)\right] \quad (2.22)$$

Now, $T_a(t) = \frac{T_i(t) + T_0(t)}{2}$

The work fluid is assumed to flow at a constant rate, v(t). Thus, equation (2.22) becomes into (2.23).

$$\frac{dT_0(t)}{dt} + \left[\frac{U_1 A}{2C} + \frac{v}{V}\right] T_0(t) = \frac{A\eta_0}{C} I(t) - \frac{U_1 A}{C}\left[\frac{v}{V} - \frac{U_1 A}{2C}\right] T_i(t) + \frac{U_1 A}{C} T_e(t) \quad (2.23)$$

The Laplace transformation of (2.23) is given by (2.24),

$$T_0(t) = \frac{T_{sf}}{1 + sT_{sf}} \frac{A\eta_0}{C} I(t) + \frac{T_{sf}}{1 + sT_{sf}}\left[\frac{v}{V} - \frac{U_1 A}{2C}\right] T_i(t) + \frac{T_{sf}}{1 + sT_{sf}} \frac{U_1 A}{C} T_e(t) \quad (2.24)$$

Since the temperature difference between the intake and the environment is negligible, the solar field's transfer function with respect to solar irradiance is provided by (2.25) and displayed in Figure 2.11.

$$G_{STPP} = \frac{K_{sf}}{1 + sT_{sf}} \quad (2.25)$$

Where, time constant T_{sf} is $T_{sf} = \frac{1}{\frac{U_1 A}{C} + \frac{v}{V}}$ and the gain K_{sf} of solar collector is $K_{sf} = \frac{T_{st} A\eta}{C}$.

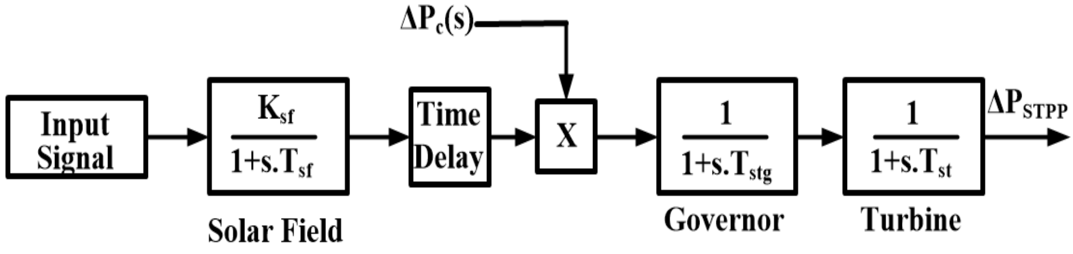

Figure 2.11 Transfer function block of solar thermal power plant

2.2.9 Modelling of Tidal Power Plant

The sea-based TPP is an evolving sustainable unit, generate electrical power from sea tides with global mounted capacity of 511MW. In operational point of view the

TPP is same as WPS where the mechanical power trapped from the TPP (P_{TPP}) could be illustrated as,

$$P_{TPP}^{mech} = \frac{1}{2}\rho_G.V_{TPP}^3.\pi R_b^2.C_{TPP}(\mu,\beta) \tag{2.26}$$

Taking into account that C_{TPP} signifies the power conversion coefficient as a function of tip speed ratio (μ) and controlled pitch angle (β). The parameters ρ_G, V_{TPP}, R_b, are the density of water, velocity of tides and turbine blade area, respectively [Alharbi et al. 2023]. The mathematical equation of C_{TPP} can be modeled as follows;

$$C_{TPP}(\mu,\beta) = \left(K_1\left(\frac{K_2}{\gamma+K_6\beta} - \frac{K_7}{\beta^3+1} - K_3\beta - K_4\right)\right)\exp\left(-K_5\left(\frac{1}{\gamma+K_6\beta} - \frac{K_7}{\beta^3+1}\right)\right) \tag{2.27}$$

Where, $\mu = \frac{R_b\omega_b}{V_{TPP}}$

Then, the linearized transfer function of modeled TPP could be estimated as (2.28);

$$G_{TPP}(s) = \frac{K_{TPP}}{1+s.T_{TPP}} \tag{2.28}$$

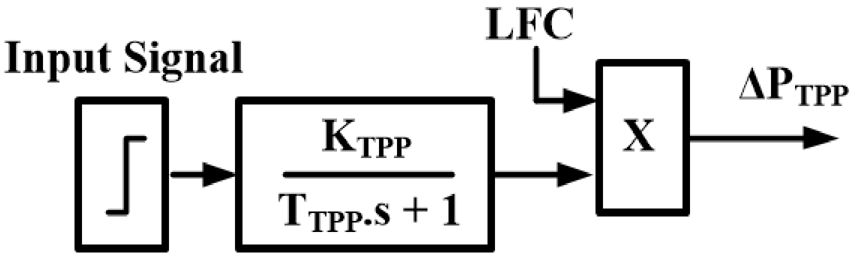

Figure 2.12 Transfer function block of tidal power plant

2.2.10 Modelling of Archimedes wave energy conversion

In the case of AWEC, to get electrical energy from mechanical wave energy Archimedes wave swing is connected with a permanent magnet synchronous generator. A 10 MW capacity AWEC is considered here and penetrated to area 4. The transfer function model is shown in Figure 2.13. If v_{aw} denotes the velocity of the floater and generator translator, then the dynamic velocity of AWEC is expressed by (2.29) [Latif et al. 2019; Das et al. 2021].

$$v_{aw} = \frac{dx}{dt}(m/s) \tag{2.29}$$

The wave force of AWEC is

$$F_{aw} = m\frac{dv_{aw}}{dt} + \beta_{gen}v_{aw} + \beta_{aw}v_{aw} + K_s x(Newton) \tag{2.30}$$

Where, m represents the total mass, β_{gen} and β_{aw} represent damping ratios of the generator and AWEC respectively. K_s and x represent spring constant and displacement of floater and translator.

Here,

K_{aw} and T_{aw} are the gain and time constant of the awec generator unit.

K_c and T_c are the gain and time constant of the gen side converter.

K_i and T_i are the gain and time constant of the grid side inverter.

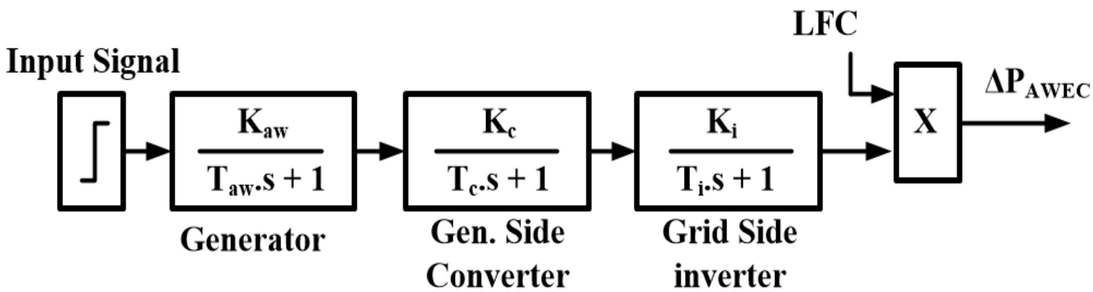

Figure 2.13 Transfer function block of Archimedes wave energy conversion.

2.2.11 Modelling of tie-line

When two or more control areas of a power system are connected by AC tie-lines, the synchronization coefficient (T_{kl}) is found using (2.31).

$$T_{kl} = P_{kl\max}\cos(\delta_k - \delta_l) \tag{2.31}$$

The block diagram in Figure 2.14 and equation (2.30) both show the deviation in tie-line power flow (ΔP_{kl}) caused by minor load perturbations.

$$\Delta P_{kl} = \frac{2\pi T_{kl}}{s}(\Delta f_k - \Delta f_l) \tag{2.32}$$

Equation (2.32) can be used to define the area power rating ratio.

$$\alpha_{kl} = -\frac{P_{rk}}{P_{rl}} \tag{2.33}$$

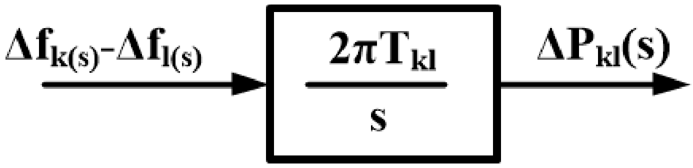

Figure 2.14 Transfer function of AC tie line.

2.3 Description of classical controllers

2.3.1 Integral controller

An output signal proportionate to the actuating signal's integral is produced by the Integral (I) controller. Area Control Error (ACE) is the actuation signal in the case of AGC, and (2.34) provides the integral controller's transfer function.

$$TF_I = K_i / s \qquad (2.34)$$

Where, the gain of the integral is represented by K_i.

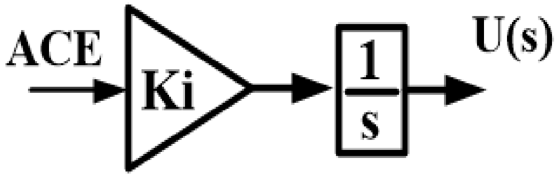

Figure 2.15 Structure of Integral controller.

2.3.2 Proportional plus integral controller

One of the two terms in the output signal that the proportional plus integral (PI) controller produces is proportionate to the actuating signal. Area Control Error (ACE) is the actuating signal in the AGC scenario, and the other is proportional to its integral. (2.35) provides the PI controller's transfer function.

$$TF_{PI} = K_P + Ki / s \qquad (2.35)$$

Where, the gain of proportional is K_P and integral gain is given by K_i.

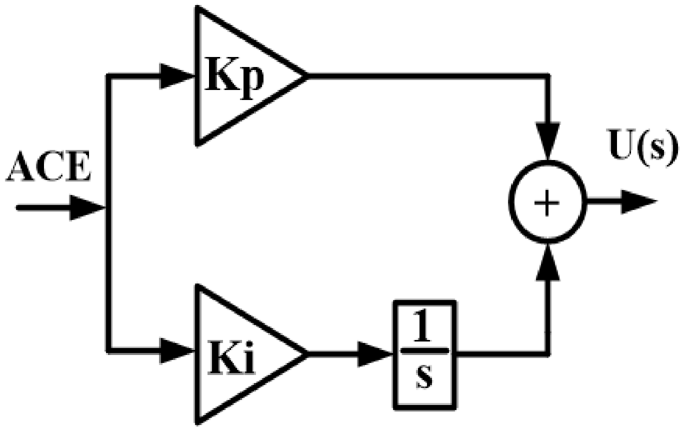

Figure 2.16 Structure of Proportional-Integral controller.

2.3.3 Proportional plus integral plus derivative controller

One term is proportional to the actuating signal, the second is proportional to the actuating signal's integral, and the third is proportional to the actuating signal's derivative. This is the output signal produced by the proportional plus integral plus derivative (PID) controller. The PID controller's transfer function is provided by (2.36).

$$TF_{PID} = K_P + {K_i}/{s} + K_D.s \tag{2.36}$$

Where, K_P is the gain of the proportional term, K_D, and K_i is the integral term and the derivative gain is represented by K_D.

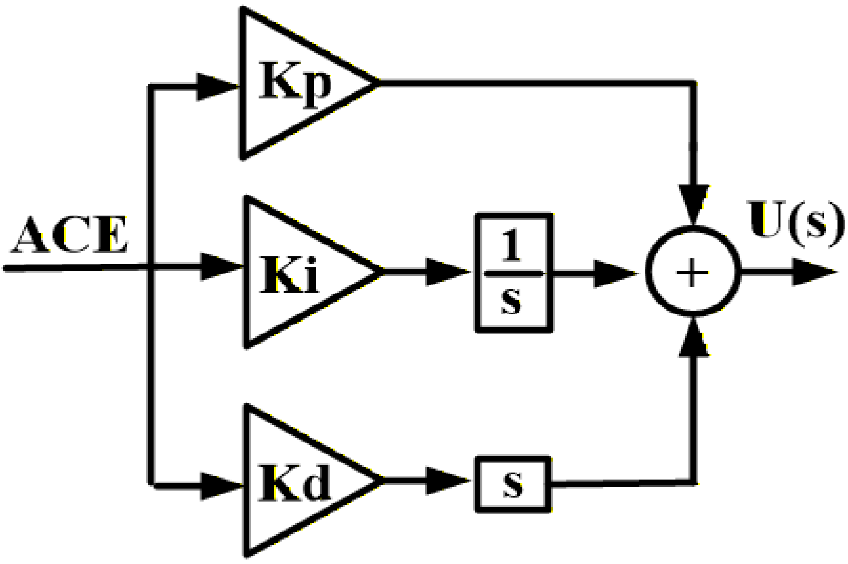

Figure 2.17 Structure of Proportional-Integral-Derivative controller.

2.4 Conclusion

The components of the study systems were introduced in this chapter. The models of transfer functions for various conventional and renewable energy sources are explained.

CHAPTER 3

Multi-area Power System with Integration of Renewable Energy Sources and Electric Vehicles

3.1 Introduction

The implementation of Renewable Energy Sources in power system is now a trending subject in the modern world. But many challenges arise due to its uncontrollable nature like the availability of power, power quality issues, etc. This makes the power system very complex. High penetration level of renewable energy sources in the power system can have impact on the stability of the grid due to its uncontrollable or unpredictable nature which affects the frequency and voltage regulation. It can lead to distortion of the system harmonics and other issues on power quality too. Control and synchronization of frequency and tie-line power are important matters which are required for achieving a reliable and stable system and lastly to meet the end demand [Kerdphol et al., 2018]. There is a wealth of literature available in AGC research that takes into account different sources such as wind turbine plant (WTP), solar photovoltaic plants (SPVP), geothermal plant (GTP), hydroelectric power plants (HPP), biogas plant (BGP) and biodiesel plant (BDP) [Barik and Das, 2021; Tasnin et al., 2018; Das et al., 1999; Saikia et al., 2013].

Numerous control strategies have been implemented according to current studies on deregulation for improving the performance of AGC in a deregulated environment. Many authors [Mahto et al., 2021; Sharma and Saikia, 2015; Chauhan et al., 2021; Jagatheesan et al., 2016a; Jagatheesan et al., 2016b; Hota and Mohanty, 2016], employed a classical controller such as Integral (I), Proportional-Integral (PI) and Proportional-Integral-Derivative (PID) control as a secondary controller to lessen the frequency and tie- line power variation in a multi-area system but there are disadvantages like slower response time which leads to higher oscillations and achieved steady state in a long period. Other types of a centralized controllers are also reported, examples include model predictive control (MPC), fractional order (FO) and fuzzy-logic types. Using a fractional order-proportional integral derivative (FO-PID) controller, an analysis of the deregulated AGC domain is reported by Dutta and Debbarma, 2018 whose drawbacks include the limit of efficiency in control inputs and the higher complexity in tuning. As a secondary controller for AGC, cascade controllers are introduced such as fuzzy PID-filter-(1+PI) [Arya, 2019] and fractional order PI-fractional order PID [Tasnin et al., 2018] to improve the performance of the power system. The authors Saha et al., 2022 design a proportional-integral-double derivative cascaded with proportional-integral controller for a four-area hybrid source power system including electric vehicle. To improve the dynamic performance, the authors [Hussain et al., 2020 suggested two degrees of freedom controllers i.e., 2DOF-PID tuned with flower pollination optimization as a controller. But it is found that there can be over-controlling of the system if not properly tuned which can lead to system instability. Lurie, 1994 introduced a novel controller based on tilt integral derivate (TID) approach and have better capability to improve system disturbance, higher tuning accuracy and reduced uncertainties. While, the TID controllers can offer improved performance in certain applications, there exist some limitations which should be carefully taken into consideration. The authors Sahu et al., 2016 demonstrated the impact of TID as a supplementary controller in the LFC problem. The authors Das et al., 2023 design a novel Derivative fractional order proportional integral (DFOPI) cascaded with a TIDN controller and Saha et al., 2023 implement the cascaded TIDN-FOID controller as a secondary controller for AGC. The use of a Salp-swarm differential evolution (DE) algorithm in a deregulated setting while taking into account physical restrictions and two degrees of freedom tilt integral derivative (2DOF-TID) controller is examined by Sharma et al., 2020 and a bird swarm algorithm (BSA) optimized 2DOF-TID controller by Bhagat et al., 2021.

Many kinds of optimization algorithm are introduced in the field of AGC like Grasshopper optimization algorithm [Barik and Das 2021], sine cosine algorithm [Tasnin et al., 2018], whale optimization algorithm [Das et al., 1999], Bacterial foraging algorithm [Saikia et al., 2013], harmonic search Algorithm [Mahto et al., 2021], Grey wolf optimizer algorithm [Chauhan et al., 2021], ant colony optimization algorithm [Jagatheesan et al., 2016 b], Differential Evolution (DE), slime-mould Optimization [Izci et al., 2021], Particle Swarm Optimization [Abdolrasol, 2021] and many others more. The authors Trojovska et al., 2022 develop a new metaheuristic algorithm known as Zebra Optimization algorithm (ZOA) which is a new bio-inspired metaheuristic algorithm based on the behavior of Zebras defense in nature. Zare et al., 2022 utilize the ZOA for optimizing the controller gain values of PIDN-TIDF controller for frequency control in offshore fixed platforms microgrid.

Numerous changes have been made to the power system, including the incorporation of distributed generation, electric cars, artificial intelligence, and renewable energy sources. A small energy source positioned close to the load point is known as distributed generation (DG). It might include both renewable and non-renewable energy sources, such as diesel engines in conventional and biodiesel engines and biogas turbine generator in non-conventional, solar power, wind energy systems, etc. DG aids in supplying electricity to rural regions when grid transmission is not cost-effective. However, DG poses certain difficulties for the power system, thus its functioning must be constantly monitored. In the work by Latif et al., 2020, frequency regulation assessment is done for the DG system using the salp-swarm optimization. The authors Saha and Saikia., 2018 neatly present an analytical technique for the control of restructured power systems incorporating Distributed Generation unit with coupled use of redox flow battery and DC link for enhancing the system performances. Due to its lack of noise, pollution, and environmental impact, renewable energy sources will increasingly be used in modern power systems. Also, Latif et al., 2021 provides an example by using renewable energy sources, hydrogen-based storage devices and non-sensitive loads in a naval power system. While, the Das et al., 2021 combine EV fleets with AWEC, WTP, GTPP, and HPP under a deregulated PS.

Over the next decade, higher migration to EVs is expected. The authors Debbarma and Dutta, 2017 improves the dynamic response of power plants in a deregulated environment by making use of EV fleets. Arya, 2020b propose EV fleets on LFC for a thermal and hydrothermal system using imperialist competitive algorithm. As part of their research by Masuta and Yokoyama, 2012, EVs are utilized side-by-side with heat-pump based water heaters. Fuzzy controller and its performance within an EV-PV system is studied in by Datta and Senjyu, 2013. In a work by Saha and Saikia, 2019, cascaded controllers acting on EVs and their impact on a multi-area power system is studied. A mixed H2/H controller based on static output feedback is also examined by Khan et al, 2021 to examine the impact of EVs. The authors Khooban et al., 2018 proposed a cascaded TIDN-(1+PI) controller in LFC in a multi-area system consisting of hydro-thermal system, EV and other renewable sources under a restructured scenario. According to Latif et al., 2021, a microgrid is created by connecting storage devices and other energy sources. By taking into account, power systems with wind power generation, the effects of utilizing a Renewable Energy Sources (RES) with Electric vehicles have been investigated by Dey, 2020.

Several types of AGC techniques have been implemented in the power system according to the literature review, although they have several limitations. Additionally, the DG system is frequently considered to be independent of the grid. High penetration of the RES in the grid arises the need for an optimal control strategy in order to obtain a stable system and analyze their effect on power system. The effect of EV fleets with its participation along with the DGs in the deregulated market considering ZOA optimized cascade 2DOFTIDN-FOTI controller considering non-linearities under different scenarios are yet to be investigated for AGC study.

From the above discussion, the novelty and contribution of the present work can be written as:

1. Develop an interconnected unequal area hybrid power system by integrating reheat thermal power plant in all areas, SPVP, GTP, HPP, WTP, BGP, BDP and EV as DGs under deregulation whose combination for each area is not yet investigated.
2. Design a novel secondary cascade controller known as 2DOFTIDN-FOTI which is not yet used for the AGC of the hybrid power system.
3. Utilize a recent ZOA algorithm in AGC to optimize the parameters of the proposed controller whose performance is not yet investigated.
4. Several case studies are done by utilizing ISE as an objective function under regulated and deregulated environment.
5. Effect of EV fleets are analyzed by incorporating two scenarios of the system with EV and without EV with the presence of non-linearities.
6. Sensitivity analysis is carried out to ensure the robustness of the proposed technique.

3.2 System description

An unequal interconnected three-area systems comprising of a RHTPP, SPVP, WTP, BDP, BGP, GTP and EV having a capacity ratio of 1:2:4 is modeled to study the AGC in a regulated and deregulated environment. A reheat thermal power plant is incorporated in each area with SPVP and GTP in area-1, HPP and BGP in area-2 and WTP and BDP in area-3 are incorporated as DGs for regulated and deregulated scenarios. EV fleets are incorporated in the diversified sources based three area interconnected system to improve dynamic performance by suppressing the oscillations caused due to sudden load disturbance. The schematic structure of the proposed model along with EV's under regulated environment is presented in Figure 3.1 and system under deregulated environment in Figure 3.2. The details of the renewable energy sources of the proposed system are discussed in chapter 2. In the present study, 3%/min GRC is associated with the thermal plant. In the studied system, nominal parameters for RHTPP, SPVP, GTP, HPP, BGP, WTP and BDP are taken from relevant literature, also, their nominal parameters are presented in Appendix 1 [Barik and Das, 2021; Tasnin et al. 2018; Das et al. 1999; Saikia et al. 2013]. The secondary controller gains are optimized using ZOA.

In the context of Automatic Generation Control, the typical practice is to utilize an objective function that represents the error expression, and this function is then minimized through the application of metaheuristic optimization techniques. In general, there exist four distinct types of objective functions commonly employed in the existing literature of AGC. These four types include Integral Absolute Error, Integral Square Error, Integral Time Square Error and Integral Time Absolute Error whose mathematical formulas are shown in equations (3.1) - (3.4) respectively. Here, k and l represent area numbers (k = 1, 2, 3 and 3; l = 1, 2, 3). A comparative study has been done to get the best solution for designing the controller using ZOA.

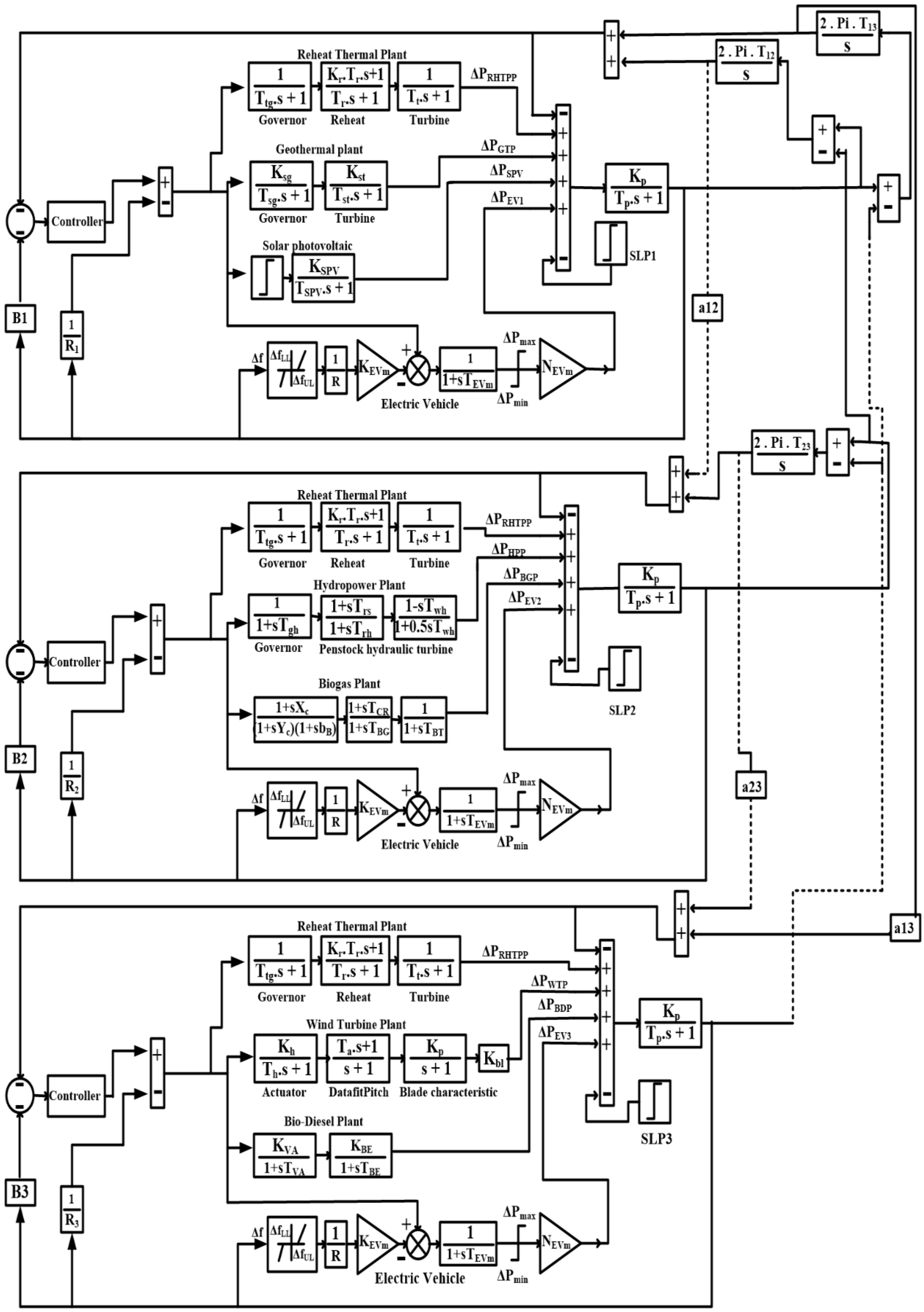

Figure 3.1 Transfer functions modelling of a three-area power system with EV integration under regulated environment.

The interconnected nature of the three-area system necessitates careful consideration of tie-line dynamics and inter-area power flows. Each area operates with distinct generation characteristics and load profiles, reflecting realistic power system conditions where asymmetric configurations are common. The unequal capacity ratio of 1:2:4 has been deliberately chosen to simulate practical scenarios where neighboring control areas often have significantly different generation capacities and load demands. This asymmetry introduces additional challenges for frequency regulation, as disturbances in one area can propagate through the tie-lines and affect the entire interconnected network. The presence of multiple distributed generation sources in each area adds another layer of complexity, requiring coordinated control strategies to maintain system stability. Furthermore, the integration of electric vehicle fleets across all three areas provides an innovative ancillary service capability that can respond rapidly to frequency deviations. The communication infrastructure between the control centers and the various generation units, including the EV aggregators, is assumed to operate with minimal latency to ensure effective implementation of the secondary control actions determined by the optimized controller gains.

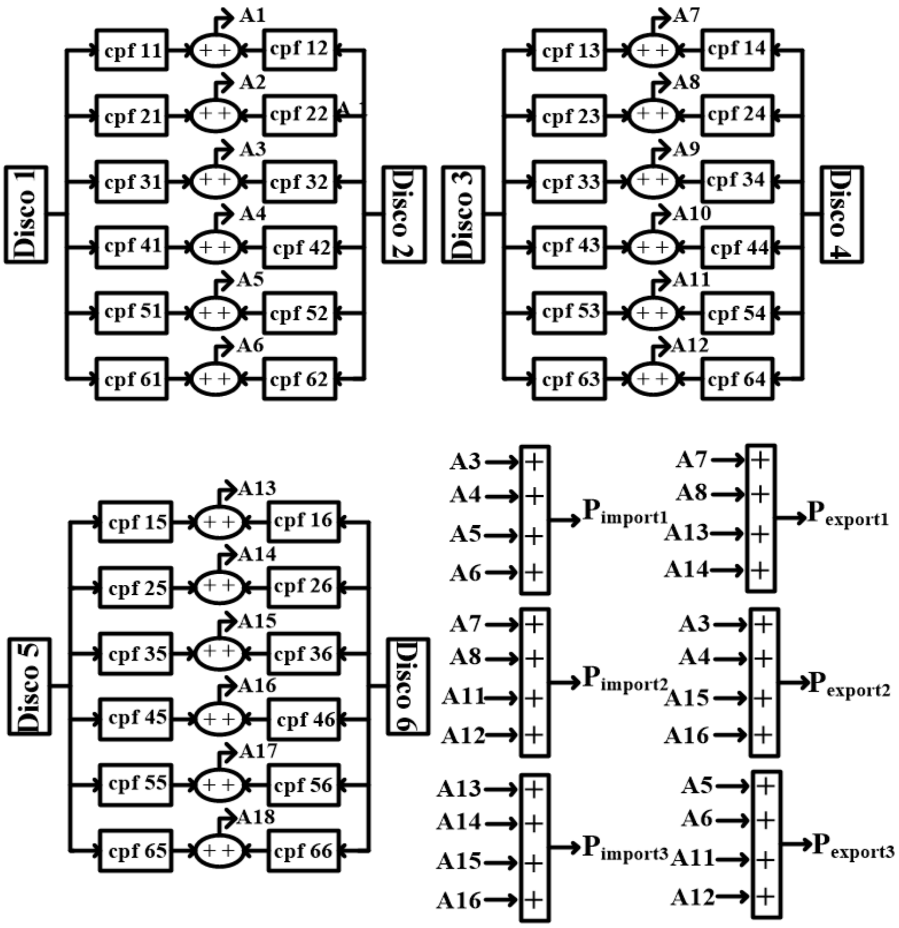

Figure 3.2 (a) The transfer function model of the three area multi source system with EV integration**:** Deregulated system.

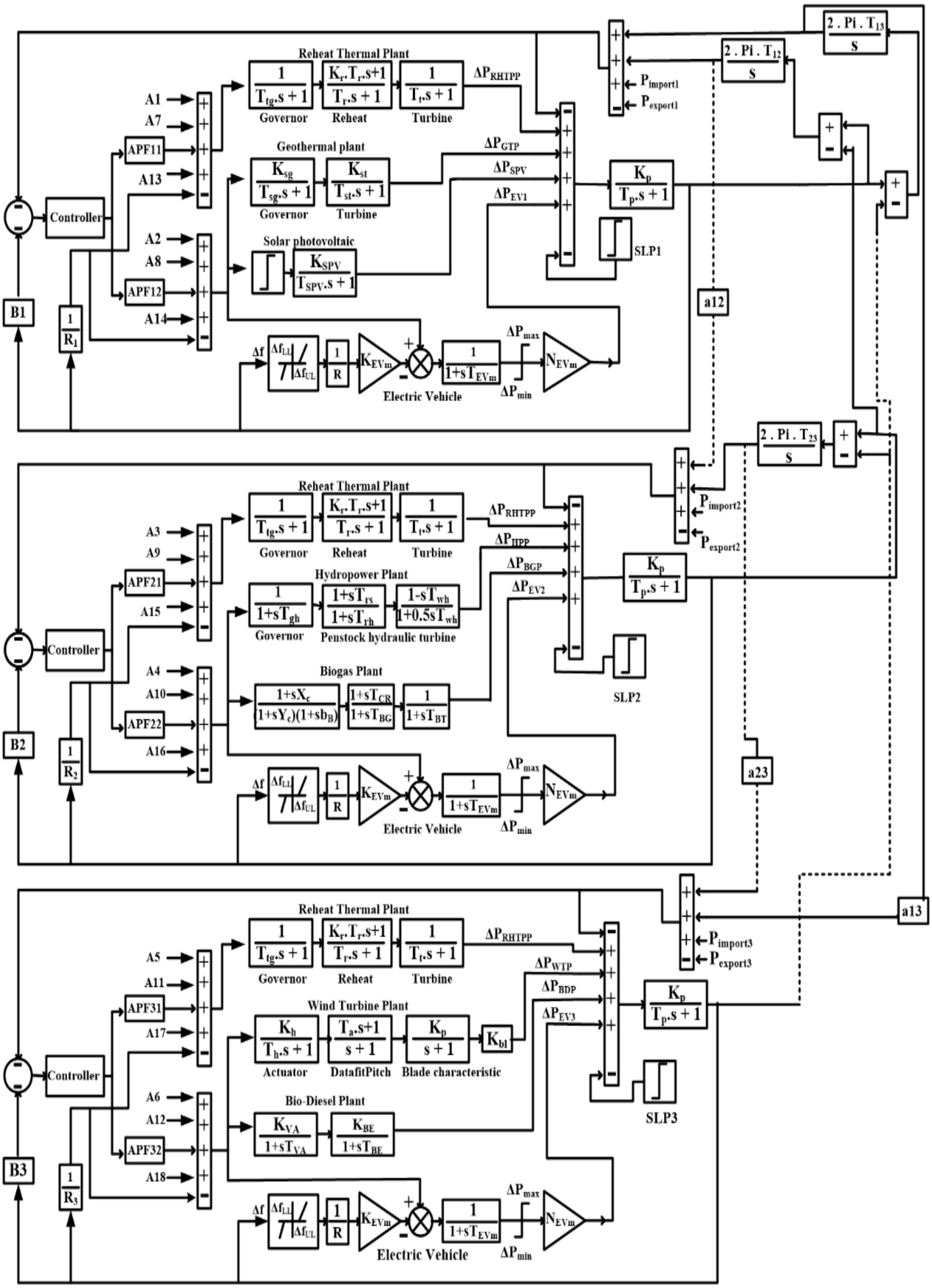

Figure 3.2 (b) Transfer function model of the three area multi source system with EV integration: complete system under deregulation.

$$J_{IAE} = \int_0^T \left[\left| \Delta f_k \right| + \left| \Delta P_{tie\_error,kl} \right| \right] dt \quad (3.1)$$

$$J_{ISE} = \int_0^T \left[\left(\Delta f_k \right)^2 + \left(\Delta P_{tie\_error,kl} \right)^2 \right] dt \quad (3.2)$$

$$J_{ITAE} = \int_0^T \left[\left| t * \Delta f_k \right| + \left| t * \Delta P_{tie\_error,kl} \right| \right] t.dt \quad (3.3)$$

$$J_{ITSE} = \int_0^T \left[\left(t * \Delta f_k \right)^2 + \left(t * \Delta P_{tie\_error,kl} \right)^2 \right] t.dt \quad (3.4)$$

3.2.1 Modelling of Electric vehicle Fleet

When power consumption and generation discrepancies emerge suddenly, electric vehicle fleets can participate in load frequency control. The transfer function model of electric vehicles (EVs) is shown in Figure 3.3. It consists of an EV battery charger that regulates power flow between the battery and the grid. A dead band function and a droop feature are included in each EV to prevent unwanted frequency response in case of abrupt disconnect from the grid. The dead band has an upper limit and lower limit (Δf_{ul} and Δf_{ll}) of ±10 mHz. It is assumed that the droop coefficient (R) will be the same as for conventional plants. Assuming 80% +5% state of charge (SOC), EV gain (K_{EV}) is 1. As the SOC increases or decreases, the gain K_{EV} increases or decreases. EVs cannot participate in frequency regulation when KEV is zero, meaning the battery SOC is insufficient. Connected electric vehicles (N_{EV}) represent the number of EVs on the grid (Area 1=2000, Area 2= 4000 and Area 3= 2000). The maximum (ΔP_{max}) and minimum (ΔP_{min}) limits of EV power output can be calculated as,

$$\Delta P_{\max} = +\left[\frac{1}{N_{EV}} \right] \Delta P_{EV} \quad (3.5)$$

$$\Delta P_{\min} = -\left[\frac{1}{N_{EV}} \right] \Delta P_{EV} \quad (3.6)$$

An electric vehicle exchanges power with the grid through a battery charger. According to ACE, the EV's power output is given as

$$\Delta P_{EV} = \begin{cases} K_{EV}.ACE, \left| K_{EV}.ACE \right| \le \Delta P_{\max} \\ \Delta P_{\max}, \left| K_{EV}.ACE \right| > \Delta P_{\max} \\ \Delta P_{\min}, \left| K_{EV}.ACE \right| < \Delta P_{\min} \end{cases} \quad (3.7)$$

An electric vehicle exchanges power with the grid through a battery charger. According to ACE, the EV's power output is given as shown in equation (3.7). EV doesn't take part in the regulation of frequency when its power output exceeds the limit. The transfer function modeling for the EV is taken from literature (Yao et al., 2017).

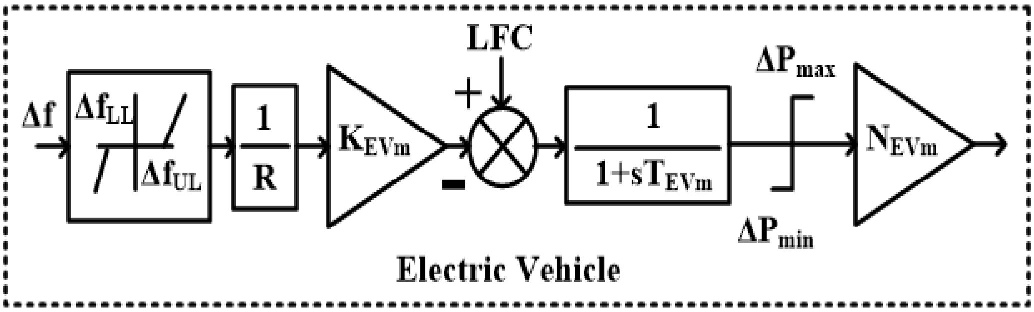

Figure 3.3 Transfer function modelling of EV.

3.3 Brief discussion on proposed secondary controller and optimization technique

3.3.1 Discussion of controller

Introduction of utilizing a cascade controller as the secondary controller is then presented because of its several advantages like improvement in disturbance rejection, system stability enhancement and reduction of overshoot problems. Its capability of handling nonlinear system and allowing more precise control of processes with multiple variables also added its advantages. Limitations existing in a single degree of freedom controller like its sensitivity to tuning parameters optimal setting and limited robustness due to its vulnerability to the presence of non-linearities, disturbance present and errors in modelling which can leads to performance degradation and many more limitations highlight the need of a higher degree of freedom (2DOF) controller.

The first part C1(s) is composed of 2DOF-TIDN whose inputs are the ACE and local area frequency error and the second part C2(s) is the fractional order tilt derivative (FOTI) whose input is the U1(s).The proposed controller consists of two levels, the first C1(s) is composed of a 2DOF-TIDN with inputs ACE and local area frequency error, and the second C2(s) is the FOTI whose input is the U1(s). Figure 3.4 shows the schematic diagram of a cascade control.

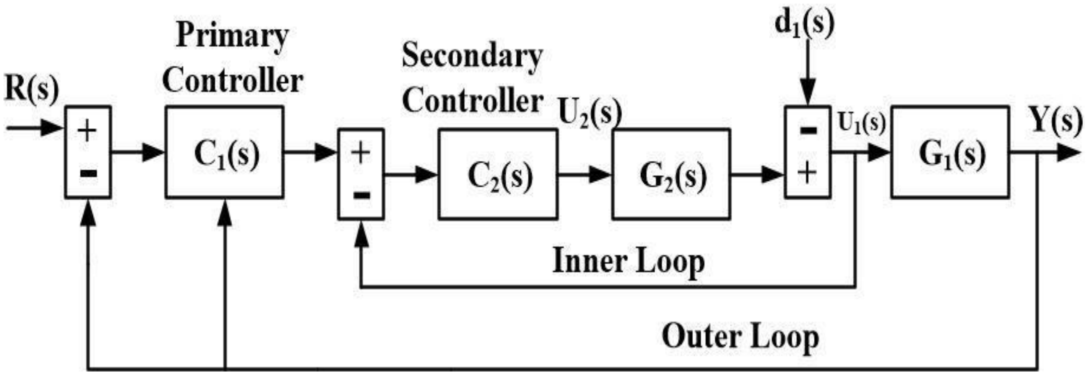

Figure 3.4 Cascade control schematic diagram.

For the proposed AGC mechanism, a novel controller is suggested and effectively used. A cascaded 2DOF-TIDN-FOTI controller is proposed for the analysis of automatic generation control of a multi unequal interconnected area. It can be seen that there are three inputs in the proposed cascaded controller, for 2DOFTIDN controller the input are the ACE and the area frequency error signal and the inner loop controller which is FOTI, the input is U1 signal. Figure 3.5 displays the proposed controller's detailed model. The controller control indication can be written as,

$$Y(s)=\left[\frac{C_1(s)C_2(s)G_1(s)G_2(s)}{1+C_2(s)G_2(s)+C_1(s)C_2(s)G_1(s)G_2(s)}\right]R(s)+\left[\frac{G_1(s)}{1+C_2(s)G_2(s)+C_1(s)C_2(s)G_1(s)G_2(s)}\right]d(s) \tag{3.8}$$

Here, the transfer functions of the system are G1s and G2s, the transfer functions of the master and slave controller are represented by C1(s) and C2(s). The ACE signal is given as R(s) and the disturbance signal is represented by d(s).

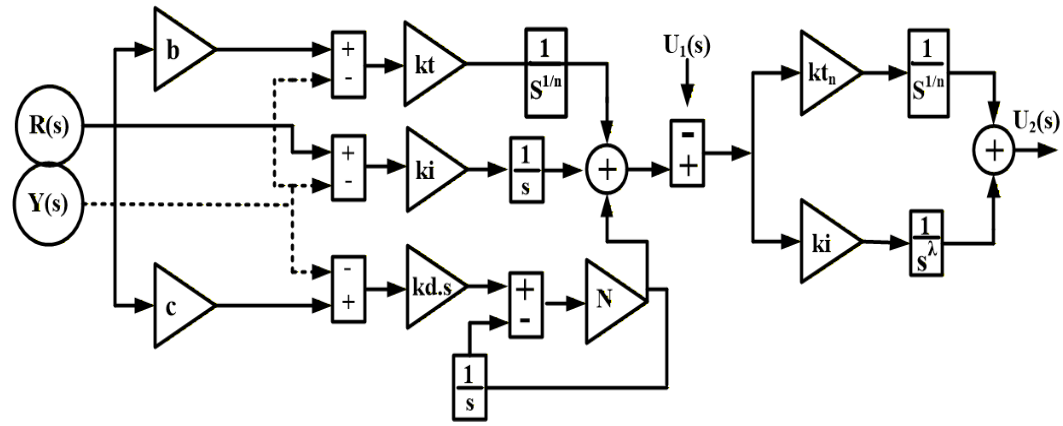

Figure 3.5 Block diagram for 2DOFTIDN-FOTI controller.

In all areas, the proposed 2DOFTIDN-FOTI controller comprises eleven tuning parameters which are optimized using the Zebra optimization algorithm.

$$\left.\begin{array}{l}
b_s^{min} \le b_s \le b_s^{max}; c_s^{min} \le c_s \le c_s^{max};\\
K_{ts}^{min} \le K_{ts} \le K_{ts}^{max}; K_{is}^{min} \le K_{is} \le K_{is}^{max};\\
K_{ds}^{min} \le K_{ds} \le K_{ds}^{max}; N_s^{min} \le N_s \le N_s^{max};\\
n1_s^{min} \le n1_s \le n1_s^{max}; K_{t1s}^{min} \le K_{t1s} \le K_{t1s}^{max};\\
K_{i1s}^{min} \le K_{i1s} \le K_{i1s}^{max}; n2_s^{min} \le n2_s \le n2_s^{max};\\
\lambda_s^{min} \le \lambda_s \le \lambda_s^{max}
\end{array}\right\} \tag{3.9}$$

Here, b is the proportional set point weight whereas c denotes the derivative set point weight. K_t, K_i and K_d represent the tilt, integral and derivative of the controller and n_s and N_s are the tilt parameter and the low-pass filter.

It has been observed that the system's nonlinearity as well as known and unidentified disturbances is handled by the proposed controller. By analyzing the controller's performance in various circumstances, the ascendency of the controller is validated. The results of simulations and comments section include the analysis.

3.3.2 Zebra Optimization Algorithm (ZOA)

This algorithm draws inspiration from zebras' natural behavior. It emulates how zebras attack and defends against its predators. When faced with a threat, zebras employ two main strategies: they flee in a zigzag pattern, and at times, they gather to confuse or intimidate the predator. ZOA's design is rooted in mathematical models of these intelligent zebra behaviors. The flowchart of the ZOA is shown in Figure 3.6.

3.3.2.1 Initialization

ZOA in composed of zebras each of which corresponds to a potential solution point. This information can be represented as a vector, where each element signifies their location and signifies a variable value. The entire zebra population can be mathematically depicted as a matrix. Initially, the zebras are randomly positioned in the search space. Population matrix used in ZOA can be represented as in (3.10).

$$X = \begin{bmatrix} X_1 \\ \vdots \\ X_i \\ \vdots \\ X_N \end{bmatrix}_{N\times m} = \begin{bmatrix} x_{1,1} & \cdots & x_{1,j} & \cdots & x_{1,m} \\ \vdots & \ddots & \vdots & ⋰ & \vdots \\ x_{i,1} & \cdots & x_{i,j} & \cdots & x_{i,m} \\ \vdots & ⋰ & \vdots & \ddots & \vdots \\ x_{N,1} & \cdots & x_{N,j} & \cdots & x_{N,m} \end{bmatrix}_{N\times m} \tag{3.10}$$

In this matrix, zebra population is denoted by X, any zebra is denoted by X_i, $x_{i,j}$ represents i^{th} zebra's proposal for the j^{th} variable and the entire population, i.e. number of zebras is N. Every zebra serves as a potential answer to the optimization problem. This means we can assess the objective function using the values that each zebra suggests for the variables related to the problem. These objective function values are then arranged as a vector, indicated by (3.11).

$$F = \begin{bmatrix} F_1 \\ \vdots \\ F_i \\ \vdots \\ F_N \end{bmatrix}_{N\times 1} = \begin{bmatrix} F(X_1) \\ \vdots \\ F(X_i) \\ \vdots \\ F(X_N) \end{bmatrix}_{N\times 1} \tag{3.11}$$

In this matric, vector of values of objective function is F, and F_i is obtained from i^{th} zebra. Comparing objective function values helps assess the quality of candidate solutions. Depending on the purpose, to maximize or minimize, the zebra with the lowest or highest objective function is selected as best candidate, respectively.

The ZOA algorithm maintains a balance between exploration and exploitation phase through:

- Adaptive migration rates: It adjust the migration rate based on the herd's diversity and fitness progress.
- Predator-prey dynamics: The introduction of predators removes stagnant zebras, while the herd's social learning mechanism ensures that good solutions are preserved.
- Dynamic grazing: The grazing operator's step size and direction are adapted based on the herd's fitness landscape.

By harmoniously balancing exploration and exploitation, ZOA effectively searches the solution space, avoids local optima and converges towards the global optimum. Therefore, in each iteration, members of the ZOA population are updated in these two different phases.

3.3.2.2 Exploration phase: Food search behavior

During initial stage, the zebras undergo position updates inspired by the foraging behavior of other zebras. Zebras primarily feed on grasses and sedges, but they can also eat other plant parts like fruits, bark, roots, and leaves when their preferred food is scarce. They spent 60 to 80 % of their time is spent looking for food.

In this approach, the pioneer zebra (PZ) guides other members toward its position within the search space and the other zebras update their position as well. Consequently, the mathematical representation of updating zebra positions during the foraging phase can be described using (3.12) and (3.13).

$$x_{i,j}^{new,\ P1} = x_{i,j} + r\,.\,(PZ_j - I.x_{i,j}) \tag{3.12}$$

$$X_i = \begin{cases} X_i^{new,P1}, \ F_i^{new,P1} < F_i\ ; \\ X_i, \qquad\qquad else, \end{cases} \tag{3.13}$$

Where, $X_i^{new,P1}$is the updated status of the i^{th}zebra based on first phase, $X_{i,j}^{new,P1}$is its j^{th}dimension value, $F_i^{new,P1}$ is its objective function value, r is a random number in interval [0, 1], I = round (1+rand), where rand is a random number in the interval [0, 1]. This means, the population experiences large volumes of motion if I ϵ {1, 2} and I = 2 conditions are met. ZOA combines elements of random search, social learning and local search to create a unique food search behavior. This approach allows zebras to adaptively explore and exploit the search space as shown in (3.12).

3.3.2.3 Exploitation phase: Strategies to defend zebras from attackers (predators)

In second stage, ZOA updates its population based on simulations of zebras' defense tactics against predators. Lions are the primary predators, but zebras also face threats from cheetahs, leopards, wild dogs, brown hyenas, and spotted hyenas. Crocodiles pose a danger near water sources. Zebras' defensive responses differ depending on the predator. Against lions, they employ a zigzag escape pattern with random sideward movements. For smaller predators like hyenas and dogs, zebras adopt a more assertive strategy of gathering to confuse and intimidate. In the first tactic, when zebras face a lion attack, they evade by swiftly moving in the vicinity. This behavior can be mathematically described using mode S_1 in (3.14). In the second tactic, if another predator targets one zebra, the rest of the herd converges towards the targeted zebra, aiming to deter and disorient the predator through a defensive formation. This zebra strategy is represented mathematically as mode S_2 in (3.14). When updating zebra positions, a new position is adopted if it yields a superior value for the objective function. This update condition is captured by (3.15).

$$x_{i,j}^{new,P2} = \begin{cases} S_1 : x_{i,j} + R.(2r-1).\left(1-\frac{t}{T}\right).x_{i,j}, P_s \le 0.5; \\ S_2 : x_{i,j} + r.\left(AZ_j - I.x_{i,j}\right), ...else, \end{cases} \tag{3.14}$$

$$X_i = \begin{cases} X_i^{new,P2}, F_i^{new,P2} < F_i; \\ x_i, \quad else, \end{cases} \tag{3.15}$$

where, i^{th} zebra's status in the second stage is denoted by $X_i^{new,P2}$, jth dimension is denoted by $X_{i,j}^{new,P2}$,value of the objective function is $F_i^{new,P2}$, iteration counter is t, max allowed iterations is denoted by T, R is a constant set as 0.1, finally, probability of the random value assigning the strategy selected is Ps, zebra subject to attack is AZ and its j^{th} dimension is AZ_j.

An analysis is done to test the performance of the ZOA algorithm with other optimization algorithms like Firefly algorithm (FA), Grey wolf optimizer (GWO), Particle Swarm optimization (PSO) and Slime-mould optimization technique for the automatic generation control of a multi area multi source system under regulated and deregulated environment. The parameters of the proposed 2-Degree of freedom Tilt Integral Derivative with filter cascaded with Fractional order Tilt Integral (2DOFTIDN-FOTI) controller for a simulation time of 100 second for 100 iterations each. The number of search agent is set to 30 and the parameters of each algorithm settings are presented in Table 3.5. The controller with the best performance is considered suitable for the present study of AGC and is subjected to be utilized in the later study.

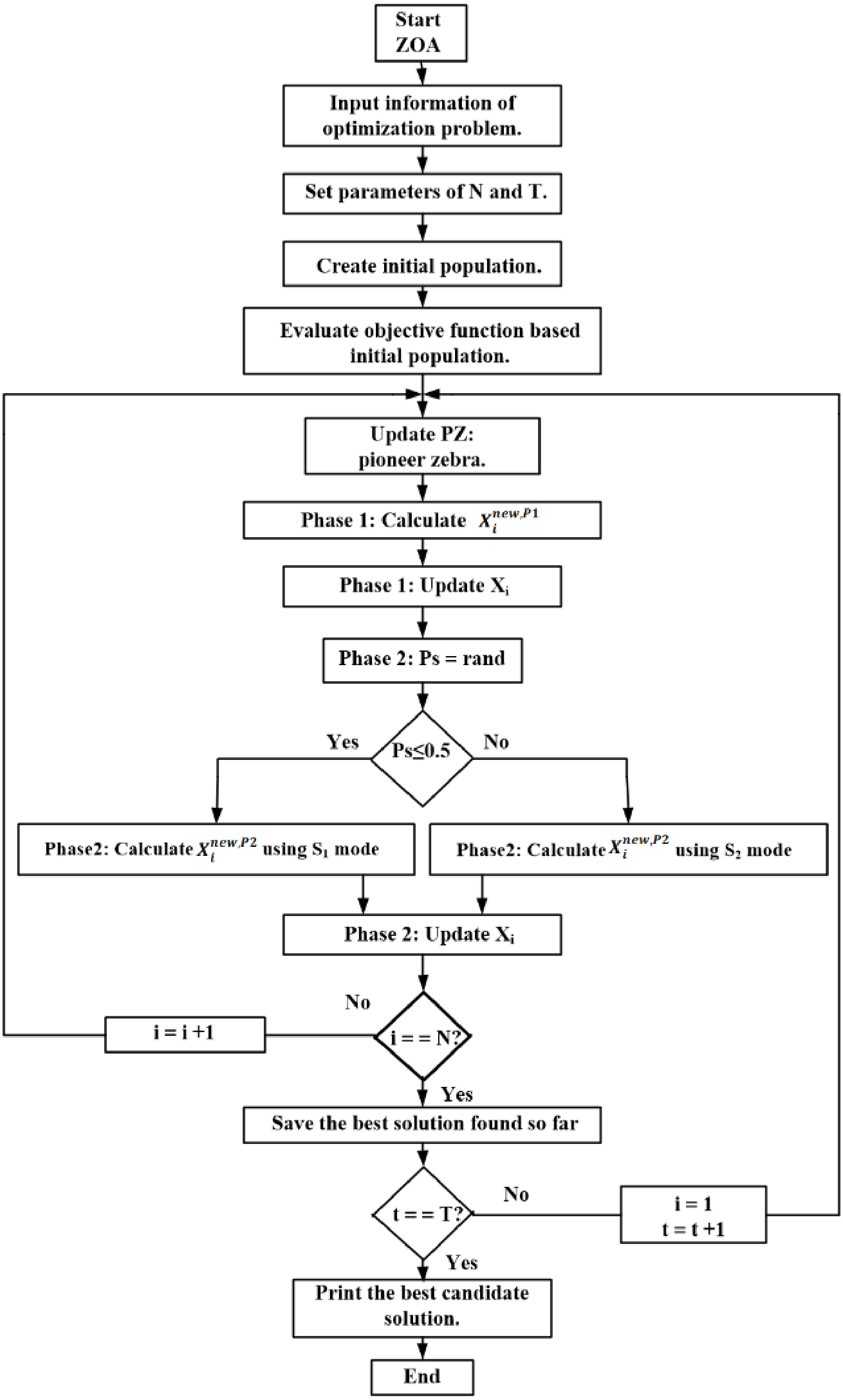

Figure 3.6 Flowchart of Zebra optimization algorithm.

3.4 Simulation results and analysis

The simulation results of the analysis are presented in this section along with figures and tables. All the works of simulation analysis are executed using MATLAB/Simulink with ode45 solver. The simulation runs for a duration of 100 seconds, during which a step load perturbation of 0.01 per unit (p.u) is introduced in area-1 for regulated conditions and 0.01 per unit load demand for each discos in a deregulated environment. The thermal system incorporates a GRC of 3% per minute (equivalent to 0.0005 per second) and a GDB with values Ng1 = 0.8 and Ng2 = -0.2/π. The analyses of the results are as follows:

3.4.1 Study system under regulated environment

3.4.1.1 System responses for different types of objective function

The analysis of different types of objective functions presented in Eqns. (3.1)-(3.4) is done in an interconnected three area power system under regulated environment with the proposed 2DOFTIDN-FOTI controller as a secondary controller whose parameters are optimized by the ZOA algorithm. A 1% step load perturbation (SLP) i.e., 20MW for 2000 MW has been considered to happen at a single area (i.e. area-1) for analyzing the dynamic responses of the system. The optimized gain values for each parameter of the proposed controller with the different objective functions are shown in Table 3.1. The response obtained compared for best solution versus time is shown in Figure 3.7 and the dynamic responses of the system obtained by different functions are also represented in Figure 3.8. Table 3.2 gives the dynamic responses of deviation in frequency and tie lines with settling time for each objective's functions. All the works of simulation analysis are executed using MATLAB/Simulink environment.

Table 3.1 Optimized gain values for different objective functions.

Parameters		IAE	ITAE	ITSE	ISE
K_t	Area-1	0.9998	0.7387	0.9996	0.9998
	Area-2	0.9999	0.9461	0.9963	0.9999
	Area-3	0.9996	0.8383	0.9999	0.9992
n	Area-1	2.9172	2.9457	2.7734	2.8131
	Area-2	2.9946	2.9554	2.8917	2.7525
	Area-3	2.9993	2.9663	2.9969	2.7083
K_i	Area-1	0.7118	0.9961	0.2103	0.5761
	Area-2	0.9993	0.9992	0.7926	0.5978
	Area-3	0.9978	0.6598	0.1999	0.2996
K_d	Area-1	0.1560	0.2022	0.2600	0.4854
	Area-2	0.3500	0.2018	0.1227	0.5651
	Area-3	0.4536	0.1989	0.5168	0.9560
N	Area-1	62.434	26.876	42.980	35.928
	Area-2	27.638	67.304	55.639	26.149
	Area-3	39.386	56.971	45.146	71.910

Table 3.1 (Contd.) Optimized gain values for different objective functions

Parameters		IAE	ITAE	ITSE	ISE
b	Area-1	0.9314	0.9002	0.8622	0.6160
	Area-2	0.4360	0.5453	0.9957	0.9527
	Area-3	0.5192	0.6186	0.7279	0.5214
c	Area-1	0.5496	0.2869	0.3759	0.7728
	Area-2	0.8470	0.4753	0.6126	0.4368
	Area-3	0.2399	0.2893	0.6101	0.2545
K_{t1}	Area-1	0.9974	0.9995	0.9999	0.8574
	Area-2	0.9988	0.6931	0.5160	0.9999
	Area-3	0.9996	0.8833	0.9708	0.8817
n_1	Area-1	2.8553	2.0003	2.3539	2.7283
	Area-2	2.7165	2.0242	2.1147	2.9957
	Area-3	2.9753	2.9642	2.4503	2.7365
K_{i1}	Area-1	0.9965	0.6120	0.7147	0.9999
	Area-2	0.9597	0.9971	0.9989	0.6319
	Area-3	0.6299	0.9424	0.9988	0.9982
λ	Area-1	0.4309	0.4820	0.3721	0.3453
	Area-2	0.6063	0.8352	0.2471	0.2699
	Area-3	0.2764	0.9994	0.4638	0.4178

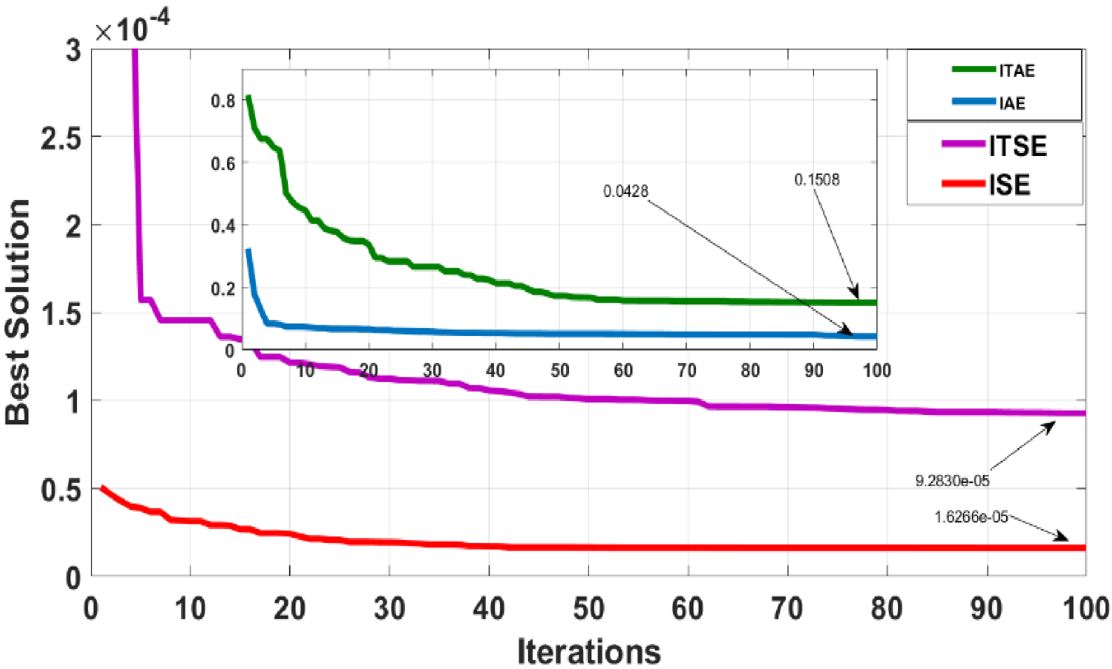

Figure 3.7 Best solution vs Iterations between different objective functions.

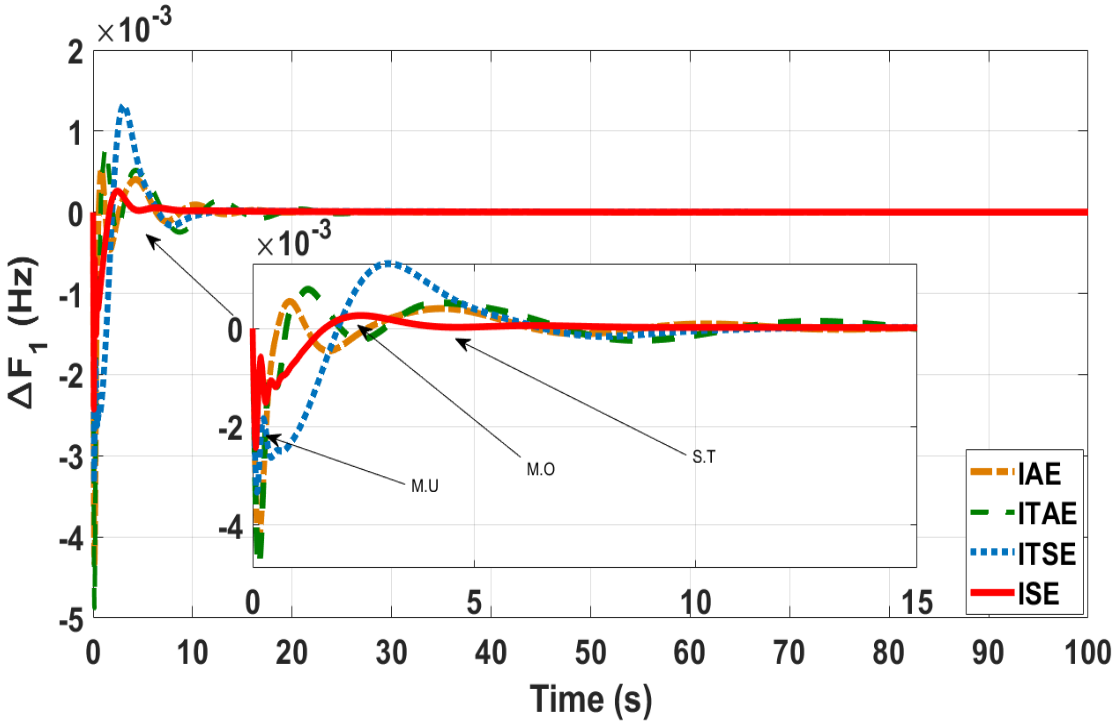

Figure 3.8 (a) System dynamic responses with respect to time for different objective functions: Area-1 deviation in frequency.

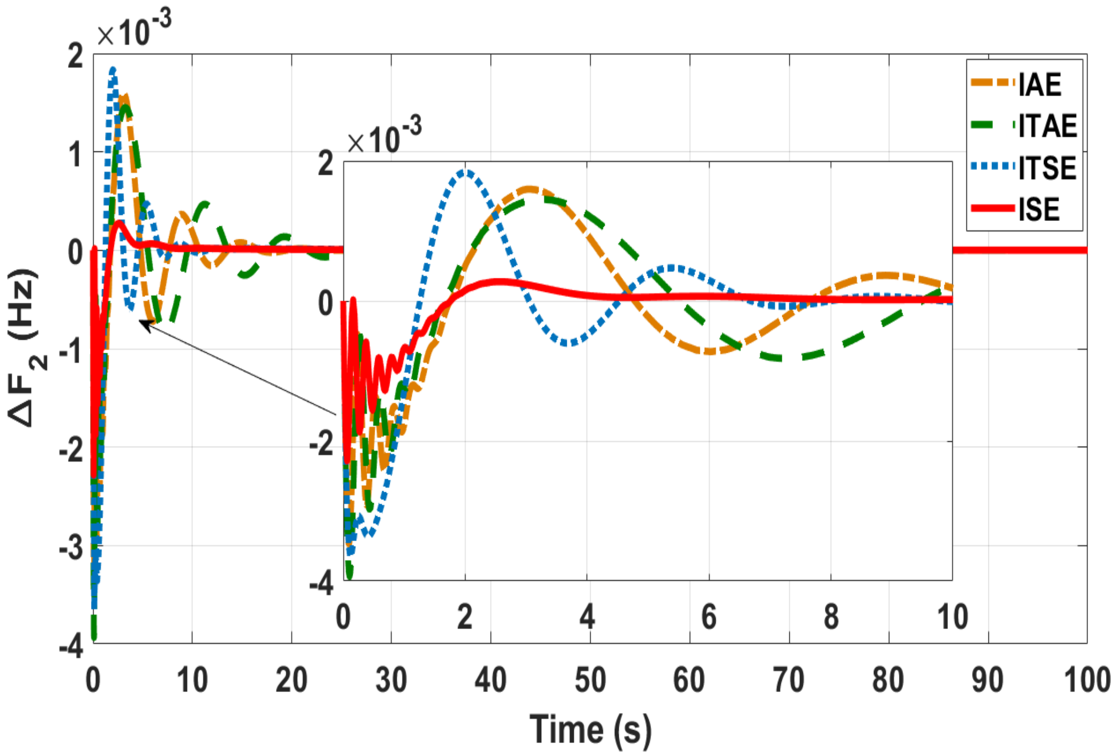

Figure 3.8 (b) System dynamic responses with respect to time for different objective functions: Area-2 deviation in frequency.

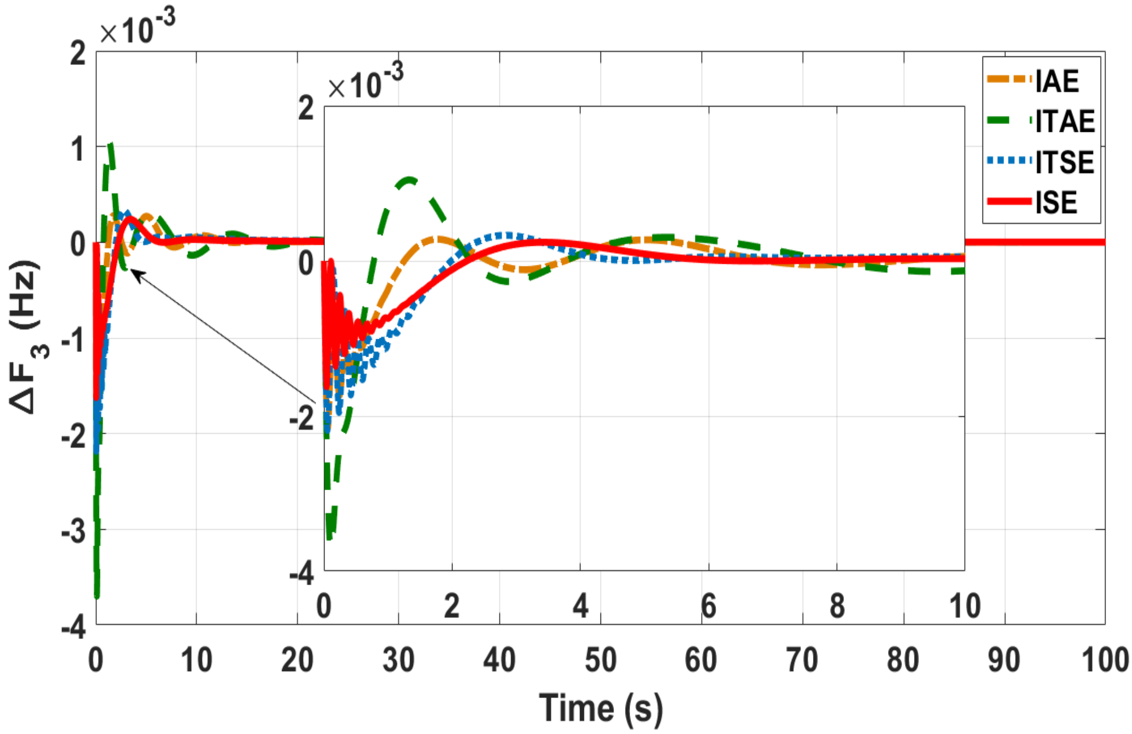

Figure 3.8 (c) System dynamic responses with respect to time for different objective functions: Area-3 deviation in frequency.

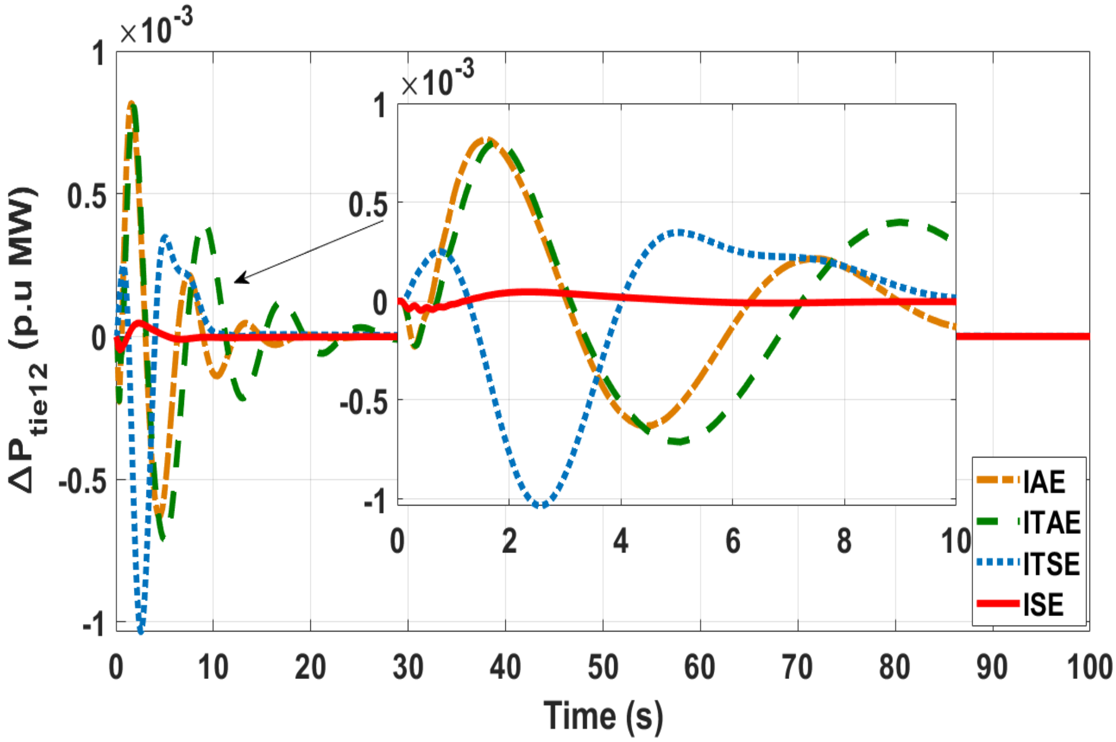

Figure 3.8 (d) System dynamic responses with respect to time for different objective functions: Deviation in tie line power between area-1 and -2.

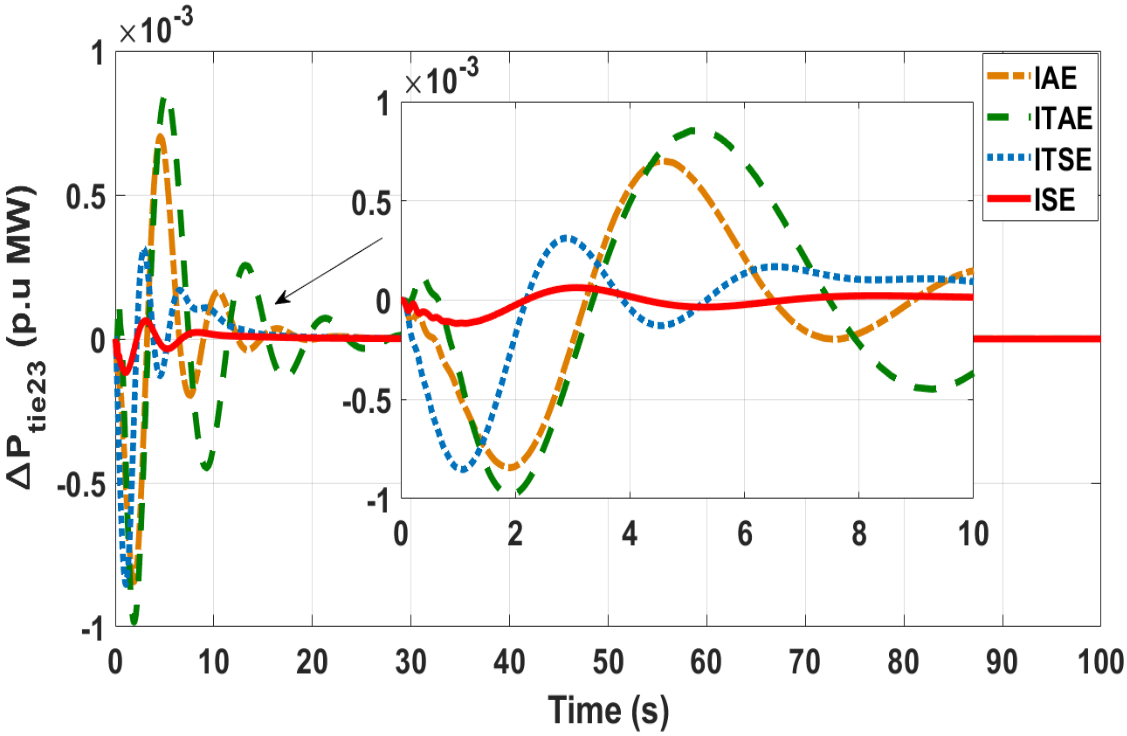

Figure 3.8 (e) System dynamic responses with respect to time for different objective functions: Deviation in tie line power between area-2 and -3.

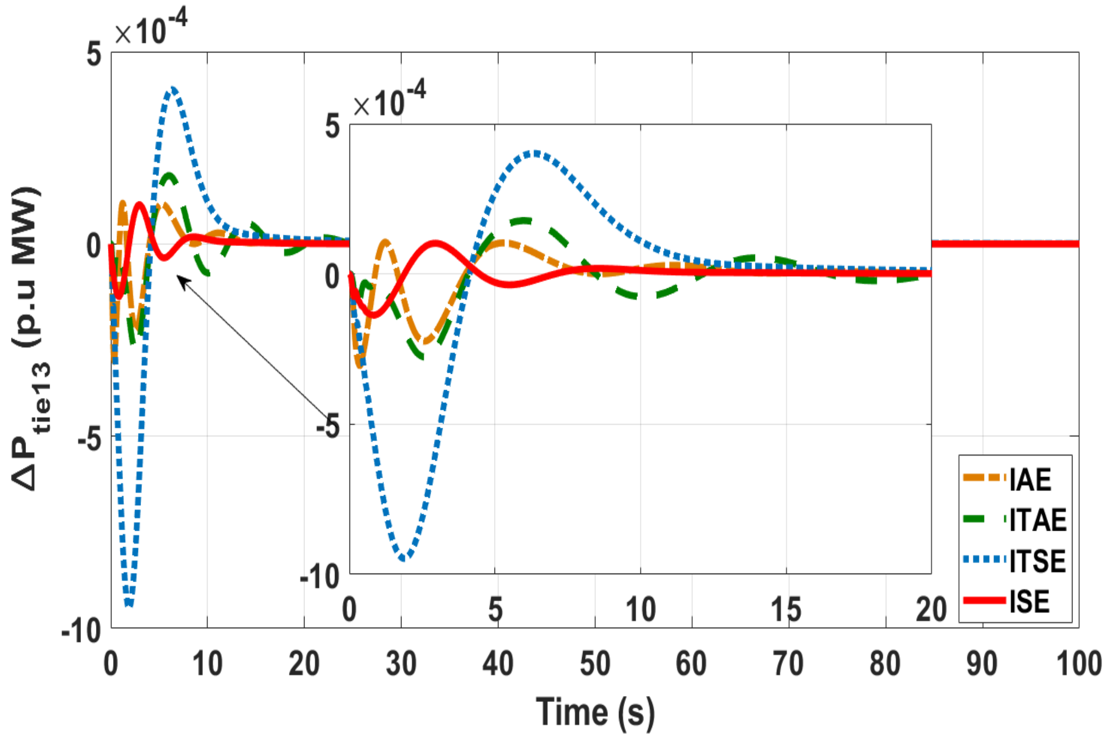

Figure 3.8 (f) System dynamic responses with respect to time for different objective functions: Deviation in tie line power between area-1 and -3.

Table 3.2 (a) System dynamic response for different objective functions

Responses		IAE	ITAE	ITSE	ISE
Δf_1	M.U	-0.00433	-0.004369	-0.002906	-0.002190
	M.O	0.0005402	0.0007887	0.001315	0.0002607
	S.T	11	21	12	4
Δf_2	M.U	-0.002572	-0.003892	-0.003583	-0.002145
	M.O	0.001594	0.001450	0.001828	0.0002737
	S.T	14.5	28	11	5
Δf_3	M.U	-0.002069	-0.003507	-0.001956	-0.001151
	M.O	0.0002788	0.001039	0.0003289	0.0002400
	S.T	11	20	9	5.5
ΔP_{tie12}	M.U	-0.0006310	-0.0007107	-0.001956	-0.0000420
	M.O	0.0008157	0.0008037	0.0003456	0.00004674
	S.T	20	31	12	4
ΔP_{tie23}	M.U	-0.0008420	-0.0009826	-0.0008529	-0.0001157
	M.O	0.0007007	0.0008526	0.0003125	0.00006322
	S.T	18	32	15	7
ΔP_{tie13}	M.U	-0.0003021	-0.0002767	-0.0009466	-0.0001369
	M.O	0.0001035	0.0001775	0.0004011	0.0001019
	S.T	11	22	16	8

Table 3.2 (b) Percentage improvement using ISE over other objectives functions

Responses		Over IAE	Over ITAE	Over ITSE
Δf_1	M.U	49.42	49.87	24.64
	M.O	51.74	66.95	80.17
	S.T	63.64	80.95	66.67
Δf_2	M.U	16.60	44.89	40.13
	M.O	82.83	81.12	85.03
	S.T	65.52	82.14	54.55
Δf_3	M.U	44.37	67.18	41.16
	M.O	13.92	76.90	27.03
	S.T	50.00	72.50	38.89
ΔP_{tie12}	M.U	93.33	94.08	97.85
	M.O	94.27	94.18	86.48
	S.T	80.00	87.10	66.67
ΔP_{tie23}	M.U	86.26	88.23	86.43
	M.O	90.98	92.59	79.77
	S.T	61.11	78.12	53.33
ΔP_{tie13}	M.U	54.68	50.52	85.54
	M.O	1.55	42.59	74.59
	S.T	27.27	63.64	50.00

Analysis: It has been observed from Figure 3.7 that the best solution is achieved by using the ISE as an objective function as compared to the other functions. Therefore, throughout this study, ISE has been considered as an objective function. The optimized gain values for the parameters of the controllers with each objective functions are shown in Table 3.1. Also, Figure 3.8(a)-(c) shows the response for frequency deviation of each area, while Figure 3.8(d)-(f) shows the deviation for each tie-line between the areas. The dynamic responses such as settling time (S.T.), maximum overshoot (M.O.) and maximum undershoot (M.U.) for the deviation in tie line and frequency are given in Table 3.2 (a).

The findings in Table 3.2 (b) indicate that the Integral of Squared Error (ISE) objective delivers consistently better performance than the other criteria (IAE, ITAE, and ITSE) across all evaluated measures. Notably, ISE produces substantial decreases in both maximum undershoot and overshoot, with improvements of more than 80% in some cases when compared with ITSE and ITAE. The settling time also exhibits marked improvements, showing reductions in the range of 63–81%, which reflects the capability of ISE to ensure a faster system response. Such results highlight that ISE enhances damping behavior, suppresses transient deviations, and supports quicker frequency stabilization. Consequently, employing ISE as the optimization index proves highly advantageous for improving Automatic Generation Control (AGC) in interconnected power systems.

3.4.1.2 Performance analysis between the proposed controller with other distinct controllers

In this case study, the performance of the proposed two degree of freedom tilt integral derivative with filter cascaded with fractional order tilt integral controller (2DOFTIDN-FOTI) is analyzed by comparing with other existing controllers like Integral (I controller), Proportional Integral (PI), Tilt Integral Derivative (TID) and Tilt Integral Derivative with filter cascaded with Fractional Order Tilt Integral (TIDN-FOTI) in a regulated interconnected power system comprised of hybrid energy sources whose parameters are optimized with ZOA algorithm. The different types of controllers are connected one at a time by utilizing Integral Square Error (ISE) as an objective function with a 1% Step Load Perturbation (SLP) i.e., for an area capacity of 2000 MW, 20 MW of load is assumed to happen only at area-1 and the other areas are running at a nominal loading of 50%.

The ZOA optimized gain values of the different controllers for different areas are shown in Table 3.3. The dynamic response comparison between the different types of controllers are shown in Figure 3.9. The numerical data representation of the system dynamic responses in terms of MU, MO and ST are presented in Table 3.4 (a) and the improvement percentage of using proposed controller over other controllers are shown in Table 3.4 (b).

Table 3.3 Tuned controller gain values for different controllers with EV integration

Parameters		I	PI	TID	TID-FOTI	2DOFTIDN-FOTI
K_p	Area-1	-	0.999	-	-	-
	Area-2	-	0.999	-	-	-
	Area-3	-	0.999	-	-	-
K_t	Area-1	-	-	0.668	0.495	0.866
	Area-2	-	-	0.665	0.905	0.966
	Area-3	-	-	0.999	0.999	0.999
n	Area-1	-	-	2.250	2.662	2.247
	Area-2	-	-	2.002	2.778	2.371
	Area-3	-	-	2.000	2.609	2.674
K_i	Area-1	0.999	0.999	0.999	0.781	0.274
	Area-2	0.999	0.999	0.999	0.723	0.377
	Area-3	0.999	0.999	0.999	0.790	0.549
K_d	Area-1	-	-	0.460	0.831	0.941
	Area-2	-	-	0.968	0.599	0.917
	Area-3	-	-	0.448	0.617	0.999
N	Area-1	-	-	-	-	50.26
	Area-2	-	-	-	-	71.47
	Area-3	-	-	-	-	61.29
b	Area-1	-	-	-	-	0.263
	Area-2	-	-	-	-	0.820
	Area-3	-	-	-	-	0.998
c	Area-1	-	-	-	-	0.975
	Area-2	-	-	-	-	0.617
	Area-3	-	-	-	-	0.731
K_{t1}	Area-1	-	-	-	0.925	0.999
	Area-2	-	-	-	0.686	0.959
	Area-3	-	-	-	0.999	0.999
n_1	Area-1	-	-	-	2.643	2.838
	Area-2	-	-	-	2.973	2.894
	Area-3	-	-	-	2.557	2.508
K_{i1}	Area-1	-	-	-	0.833	0.999
	Area-2	-	-	-	0.840	0.998
	Area-3	-	-	-	0.999	0.998
λ	Area-1	-	-	-	0.552	0.555
	Area-2	-	-	-	0.469	0.218
	Area-3	-	-	-	0.521	0.401

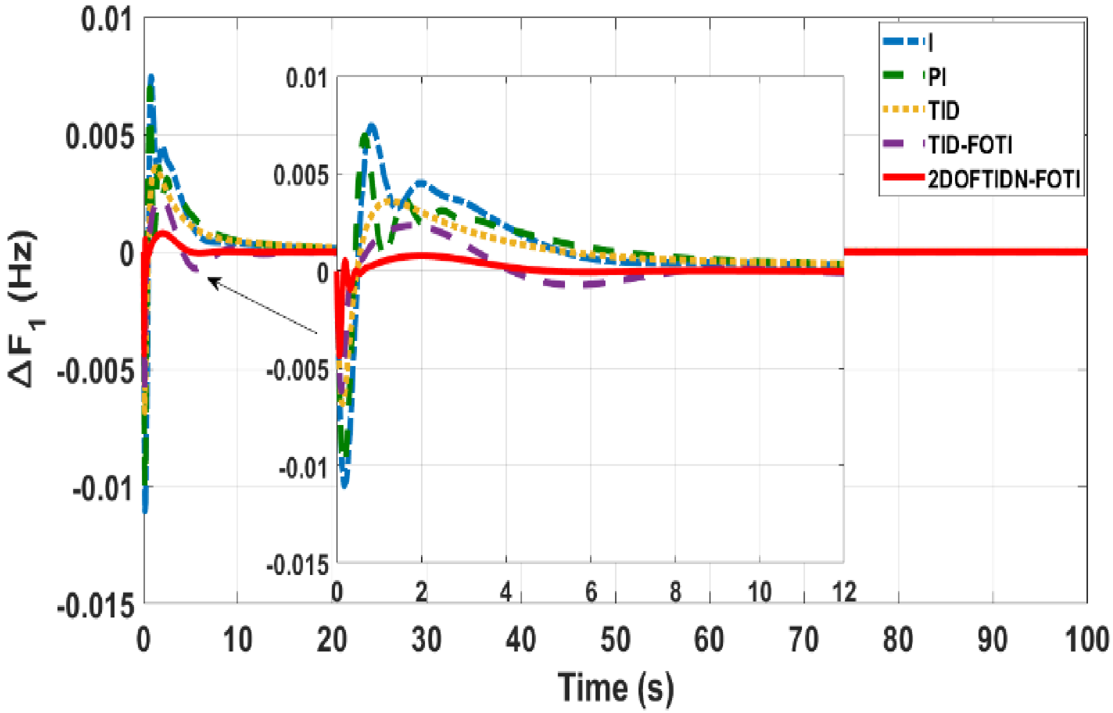

Figure 3.9 (a) System dynamic responses with respect to time for different controllers with EV integration: Area-1 deviation in frequency.

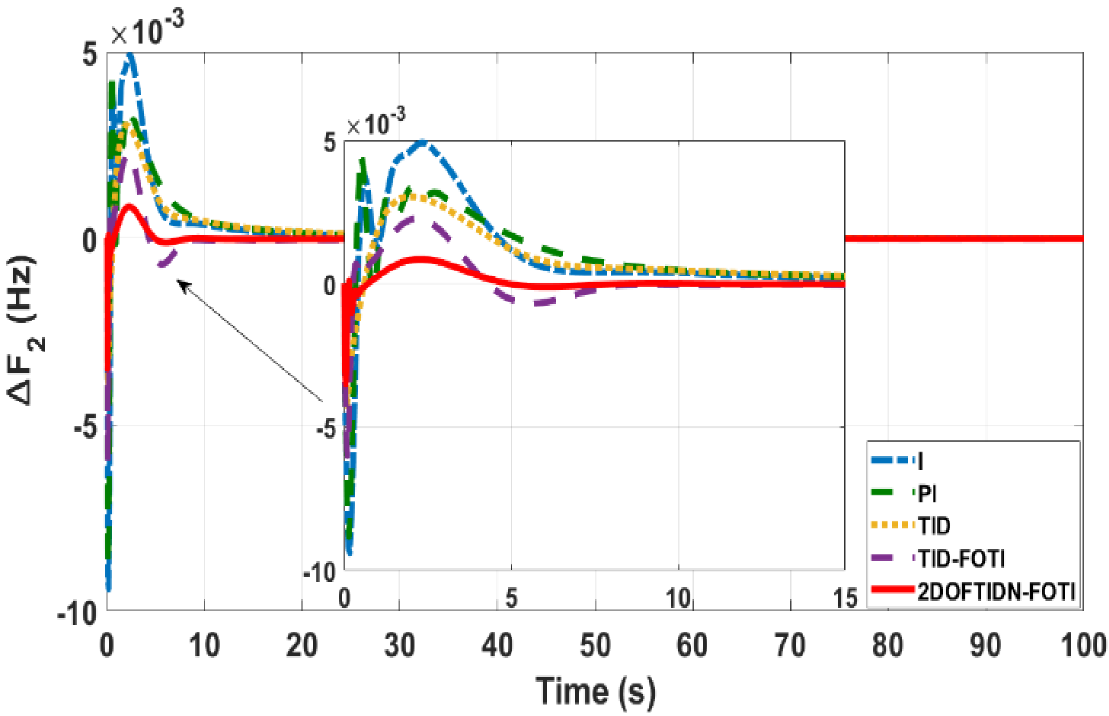

Figure 3.9 (b) System dynamic responses with respect to time for different controllers with EV integration: Area-2 deviation in frequency.

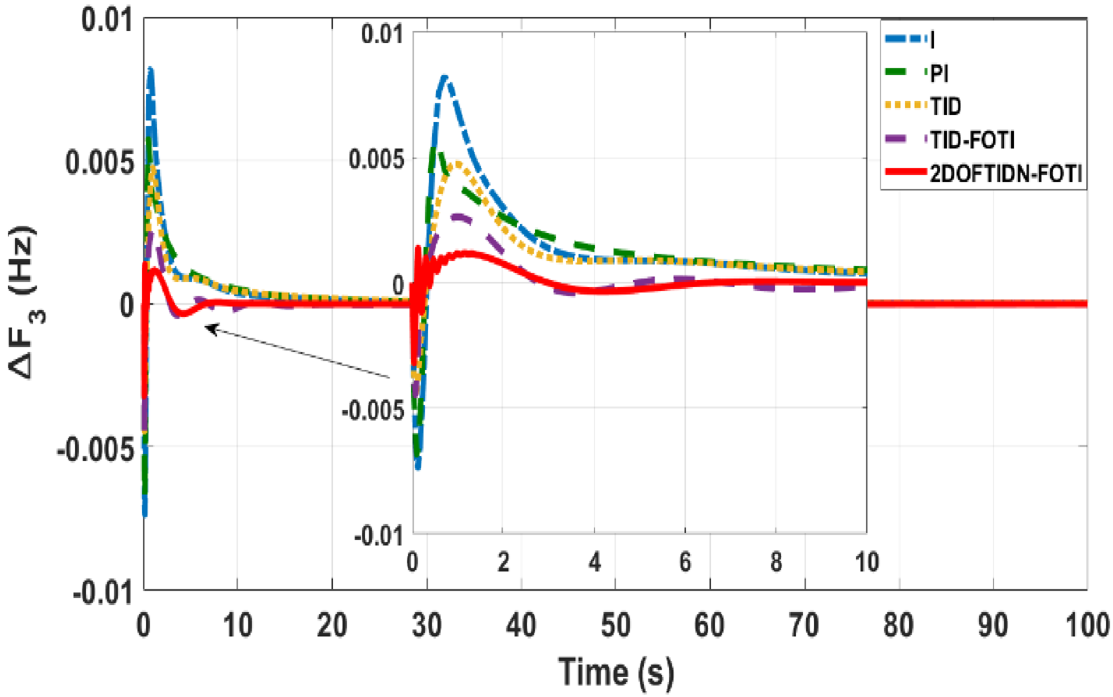

Figure 3.9 (c) System dynamic responses with respect to time for different controllers with EV integration: Area-3 deviation in frequency.

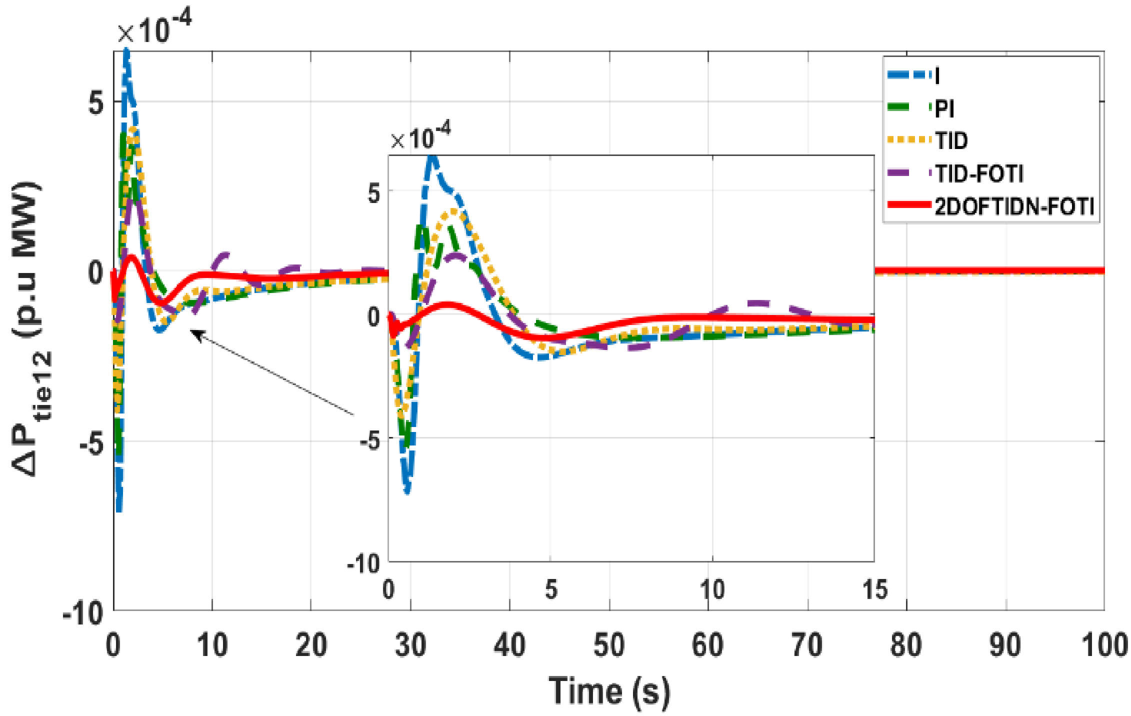

Figure 3.9 (d) System dynamic responses with respect to time for different controllers with EV integration: Deviation in tie line power between area-1 and -2.

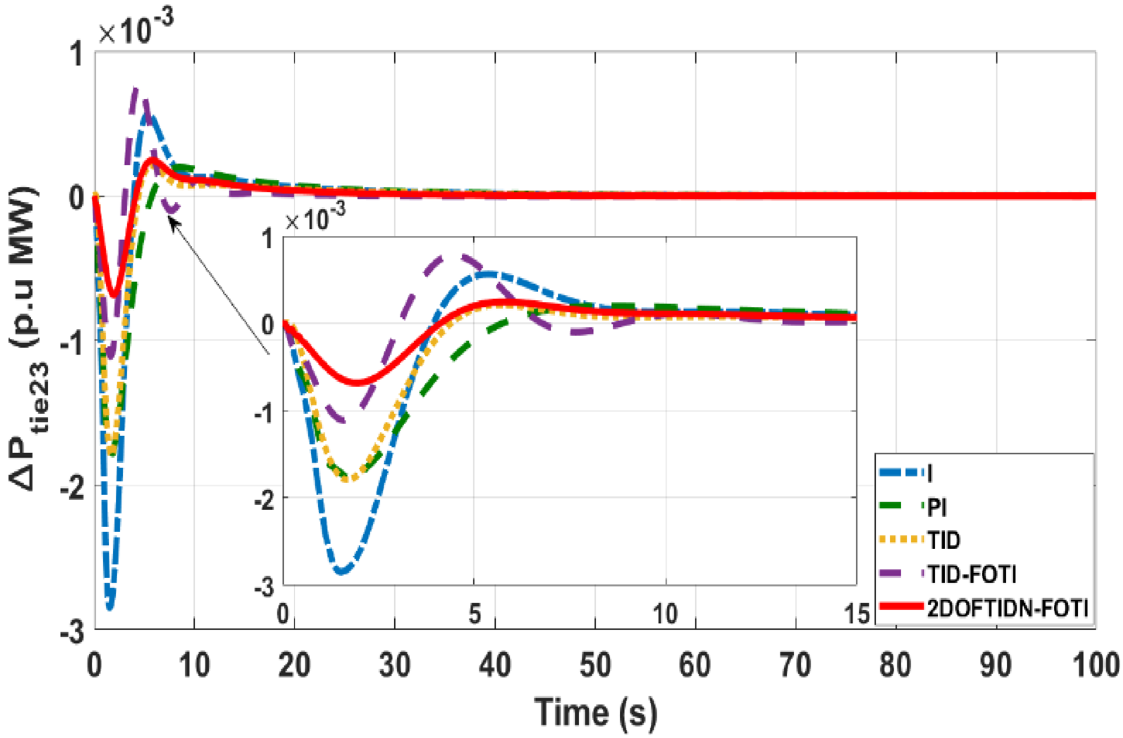

Figure 3.9 (e) System dynamic responses with respect to time for different controllers with EV integration: Deviation in tie line power between area-2 and -3.

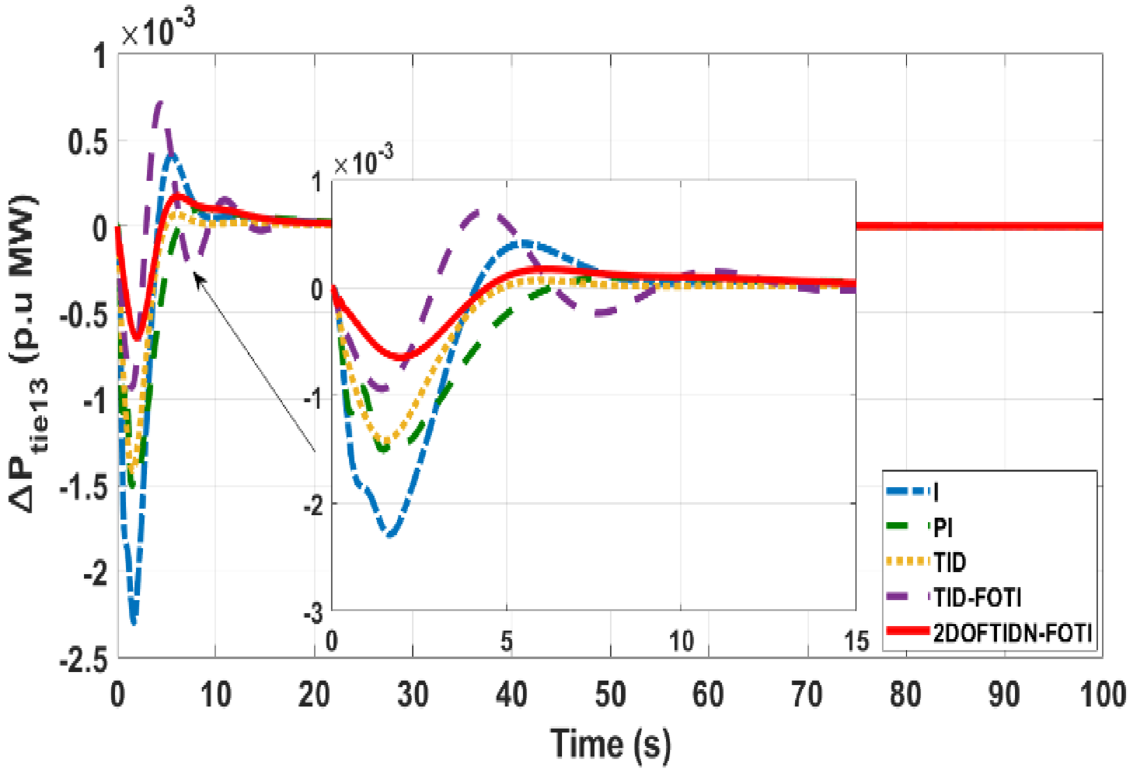

Figure 3.9 (f) System dynamic responses with respect to time for different controllers with EV integration: Deviation in tie line power between area-1 and -3.

Table 3.4 (a) System dynamic response for different controllers with EV integration

Error		I	PI	TID	TID-FOTI	2DOFTIDN-FOTI
Δf_1	M.U	-0.01104	-0.01	-0.00682	-0.00617	-0.004374
	M.O	0.00745	0.006957	0.003587	0.002327	0.0007804
	S.T	13	17	24	9	5
Δf_2	M.U	-0.009396	-0.008826	-0.004264	-0.005999	-0.003503
	M.O	0.004909	0.004508	0.003032	0.002266	0.000846
	S.T	18	20	18	9	6
Δf_3	M.U	-0.00735	-0.00683	-0.00444	-0.00447	-0.003217
	M.O	0.008147	0.005745	0.004737	0.002629	0.001377
	S.T	15	18	16	11	7
ΔP_{tie12}	M.U	-0.00071	-0.00055	-0.00041	-0.00014	-9.422e-05
	M.O	0.000648	0.000400	0.000418	0.000239	4.031e-05
	S.T	29	34	32	19	9
ΔP_{tie23}	M.U	-0.00284	-0.00178	-0.00179	-0.00111	-0.000684
	M.O	0.000560	0.000197	0.000210	0.000778	0.0002457
	S.T	22	28	20	17	20
ΔP_{tie13}	M.U	-0.00229	-0.00150	-0.00141	-0.00093	-0.000644
	M.O	0.000410	0.000104	0.000068	0.000708	0.0001734
	S.T	18	19	10	18	16

Table 3.4 (b) Percentage improvement of using proposed controller over other controllers with EV integration.

Error		I	PI	TID	TID-FOTI
Δf_1	M.U	60.38	56.26	35.93	29.17
	M.O	89.52	88.78	78.24	66.46
	S.T	61.54	70.59	79.17	44.44
Δf_2	M.U	62.72	60.31	17.85	41.61
	M.O	82.77	81.23	72.1	62.67
	S.T	66.67	70.0	66.67	33.33
Δf_3	M.U	56.28	52.94	27.68	28.06
	M.O	83.1	76.03	70.93	47.62
	S.T	53.33	61.11	56.25	36.36
ΔP_{tie12}	M.U	86.84	83.11	77.04	35.33
	M.O	93.78	89.94	90.36	83.17
	S.T	68.97	73.53	71.88	52.63
ΔP_{tie23}	M.U	75.98	61.58	61.8	38.42
	M.O	56.17	-24.47	-16.72	68.45
	S.T	9.09	28.57	0.0	-17.65
ΔP_{tie13}	M.U	71.89	57.1	54.5	31.06
	M.O	57.73	-65.46	-60.78	75.53
	S.T	11.11	15.79	-60.0	11.11

Analysis: The comparative analysis highlights the superior performance of the proposed 2DOFTIDN-FOTI controller over conventional controllers such as I, PI, TID, and TID-FOTI. Across all dynamic response measures-including maximum undershoot, maximum overshoot, and settling time-the proposed controller consistently delivers substantial improvements. The results indicate that 2DOFTIDN-FOTI achieves faster frequency stabilization, better damping of oscillations, and reduced transient deviations compared with the benchmark controllers. On average, the improvements are approximately 63.8% over I, 52.1% over PI, 35.0% over TID, and 42.7% over TID-FOTI, clearly establishing the proposed design as a more robust and effective choice for Automatic Generation Control (AGC) in multi-area power systems.

3.4.1.3 Comparison of different optimization algorithm

For this study, the different types of optimization algorithm are utilized one at a time to optimize the parameters of the proposed cascade 2DOFTIDN-FOTI controllers in a regulated three area power system with a SLP of 0.01 p.u. MW in area-1. The optimization method compared are FA, GWO, PSO, SMA and ZOA. The different settings of optimization parameters are shown in Table 3.5. The maximum iterations are set to be 100 iterations for every algorithm.

The optimized gain values are given in Table 3.6. The dynamic responses obtained comparison for different algorithms are represented in Figure 3.10. Table 3.7 (a) shows the system dynamic responses in case of M.U, M.O and S.T and Table 3.7 (b) shows the improvement in percentage of using ZOA over other algorithms.

Table 3.5 Parameters settings of different algorithms

FA	Number of fireflies = 30, Light Absorption Coefficient =1, attraction coefficient base value = 2, mutation Coefficient = 0.2, mutation Coefficient damping ratio = 0.98.
GWO	Number of search agents = 30, Maximum iterations = 100.
PSO	Number of populations = 30, inertia weight = 1, inertia weight damping ratio = 0.8, personal learning coefficient = 1, global learning coefficient = 1.5.
SMA	Number of search agents = 30, Maximum iterations = 100.
ZOA	Number of search agents = 30, Maximum iterations = 100.

Table 3.6 Tuned controller gain values for different optimization techniques

Parameter		FA	GWO	PSO	SMA	ZOA
K_t	Area-1	0.228	0.998	0.512	0.998	0.866
	Area-2	0.509	0.933	0.783	0.998	0.966
	Area-3	0.795	0.991	0.645	0.998	0.999
n	Area-1	2.306	2.844	2.342	2.998	2.247
	Area-2	2.792	2.083	2.749	2.998	2.371
	Area-3	2.924	2.930	2.459	2.998	2.674
K_i	Area-1	0.715	0.218	0.644	0.998	0.274
	Area-2	0.484	0.880	0.456	0.998	0.377
	Area-3	0.498	0.983	0.788	0.998	0.549
K_d	Area-1	0.753	0.989	0.476	0.998	0.941
	Area-2	0.685	0.930	0.612	0.998	0.917
	Area-3	0.692	0.209	0.721	0.998	0.999
N	Area-1	36.69	37.06	24.98	99.81	50.26
	Area-2	50.53	26.63	72.50	99.81	71.47
	Area-3	32.21	53.68	64.12	99.81	61.29
b	Area-1	0.771	0.893	0.636	0.998	0.263
	Area-2	0.733	0.089	0.401	0.998	0.820
	Area-3	0.717	0.890	0.604	0.998	0.998
c	Area-1	0.188	0.270	0.622	0.998	0.975
	Area-2	0.513	0.068	0.435	0.998	0.617
	Area-3	0.470	0.140	0.477	0.998	0.731
K_{t1}	Area-1	0.422	0.984	0.536	0.998	0.999
	Area-2	0.756	0.959	0.811	0.998	0.959
	Area-3	0.301	0.997	0.877	0.998	0.999
n1	Area-1	2.510	2.388	2.544	2.998	2.838
	Area-2	2.693	2.988	2.727	2.998	2.894
	Area-3	2.704	2.863	2.373	2.998	2.508
K_{i1}	Area-1	0.791	0.084	0.591	0.998	0.999
	Area-2	0.502	0.013	0.660	0.998	0.998
	Area-3	0.750	0.996	0.992	0.998	0.998
λ	Area-1	0.576	0.007	0.075	0.998	0.555
	Area-2	0.097	0.084	0.954	0.998	0.218
	Area-3	0.714	0.086	0.234	0.998	0.401

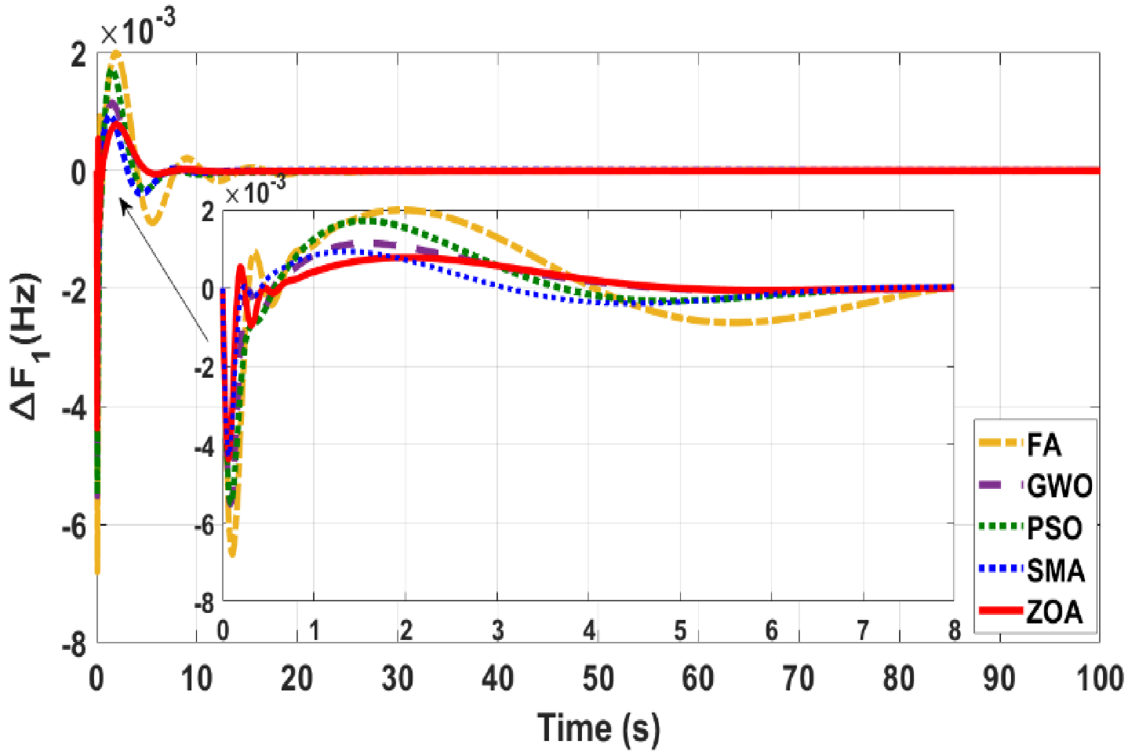

Figure 3.10 (a) System dynamic responses with respect to time for different optimization algorithm: Area-1 deviation in frequency.

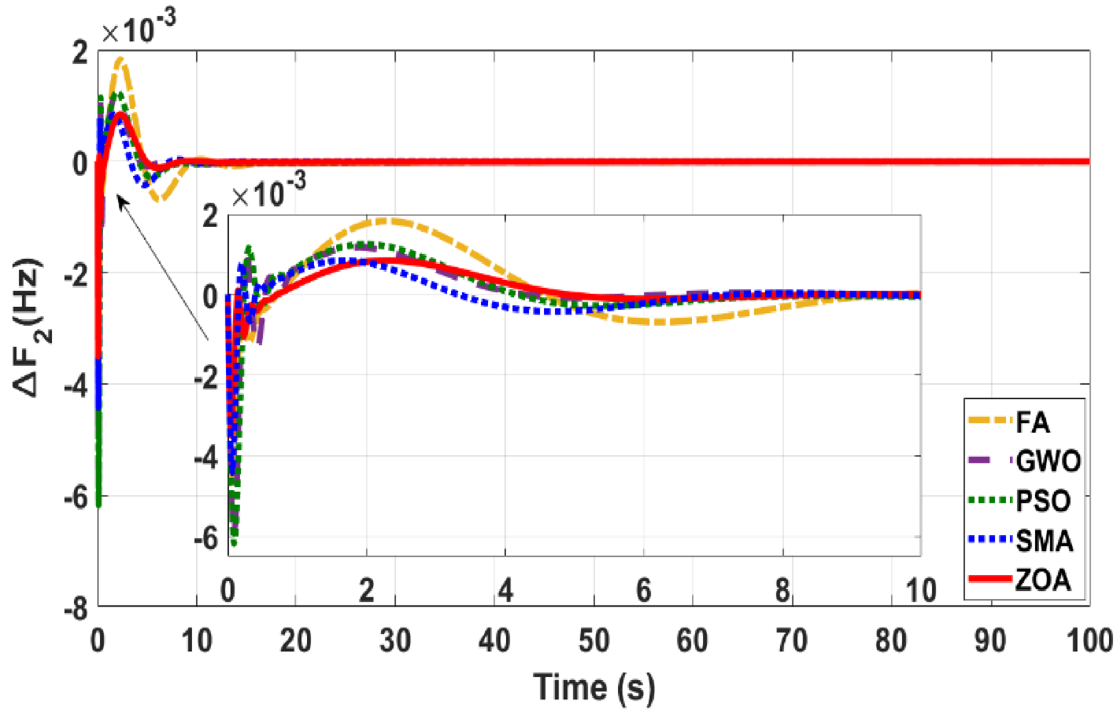

Figure 3.10 (b) System dynamic responses with respect to time for different optimization algorithm: Area-2 deviation in frequency.

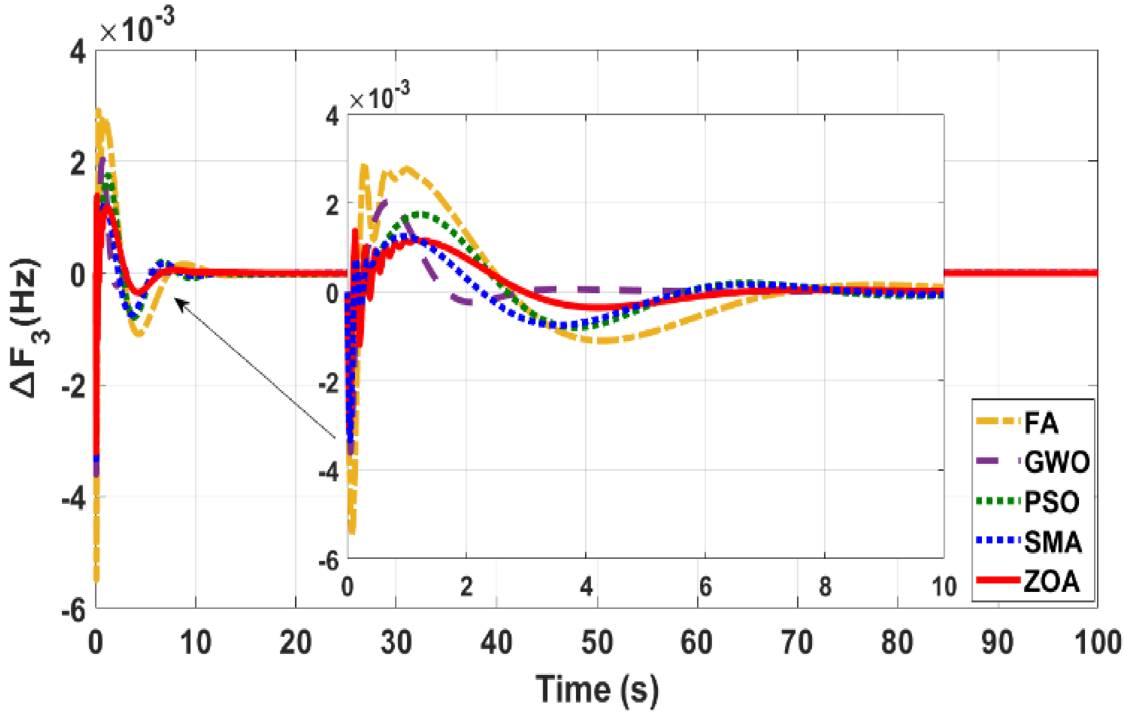

Figure 3.10 (c) System dynamic responses with respect to time for different optimization algorithm: Area-3 deviation in frequency.

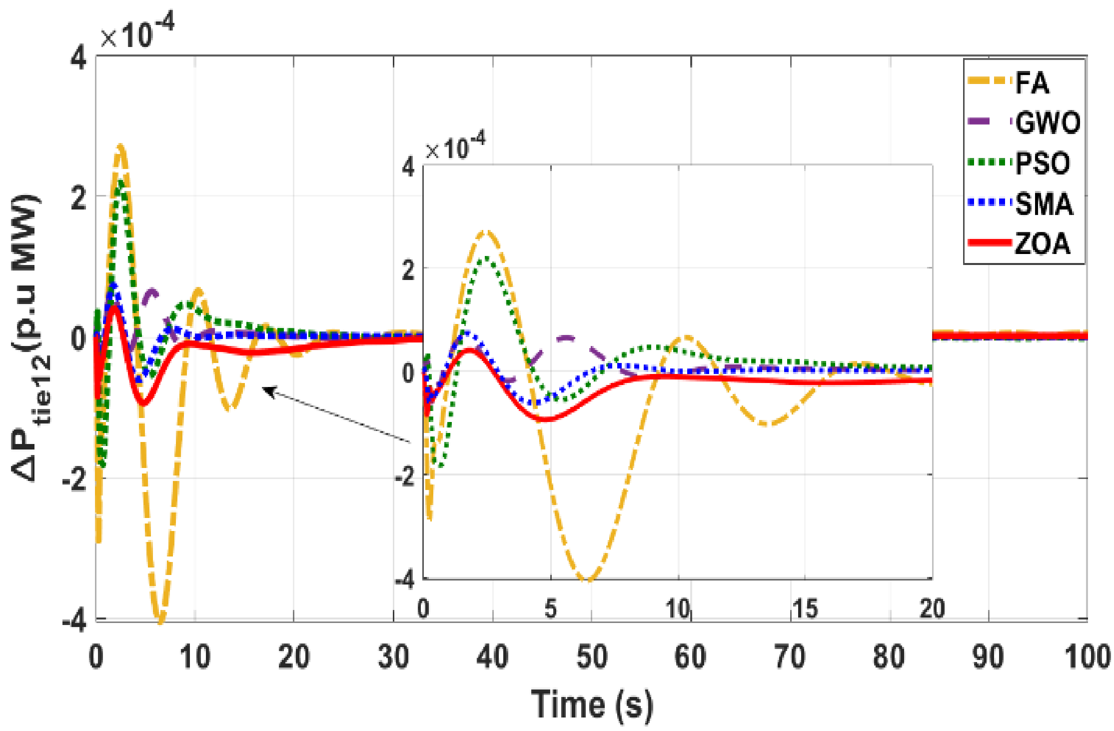

Figure 3.10 (d) System dynamic responses with respect to time for different optimization algorithm: Deviation in tie line power between area-1 and -2.

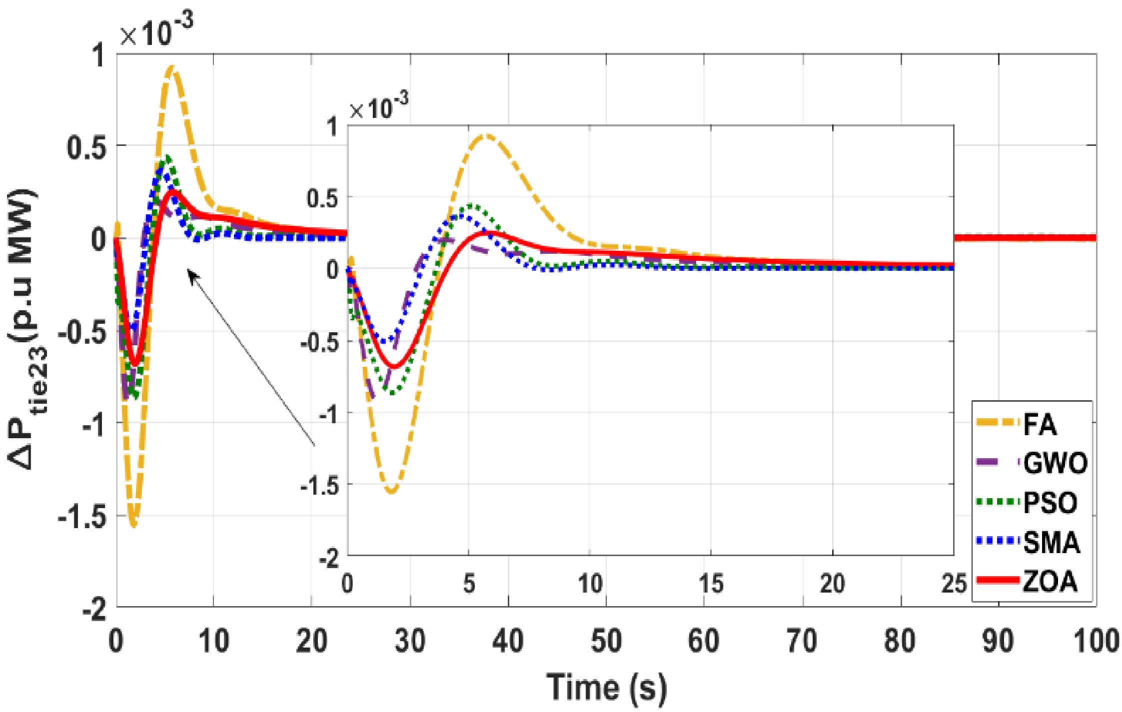

Figure 3.10 (e) System dynamic responses with respect to time for different optimization algorithm: Deviation in tie line power between area-2 and -3.

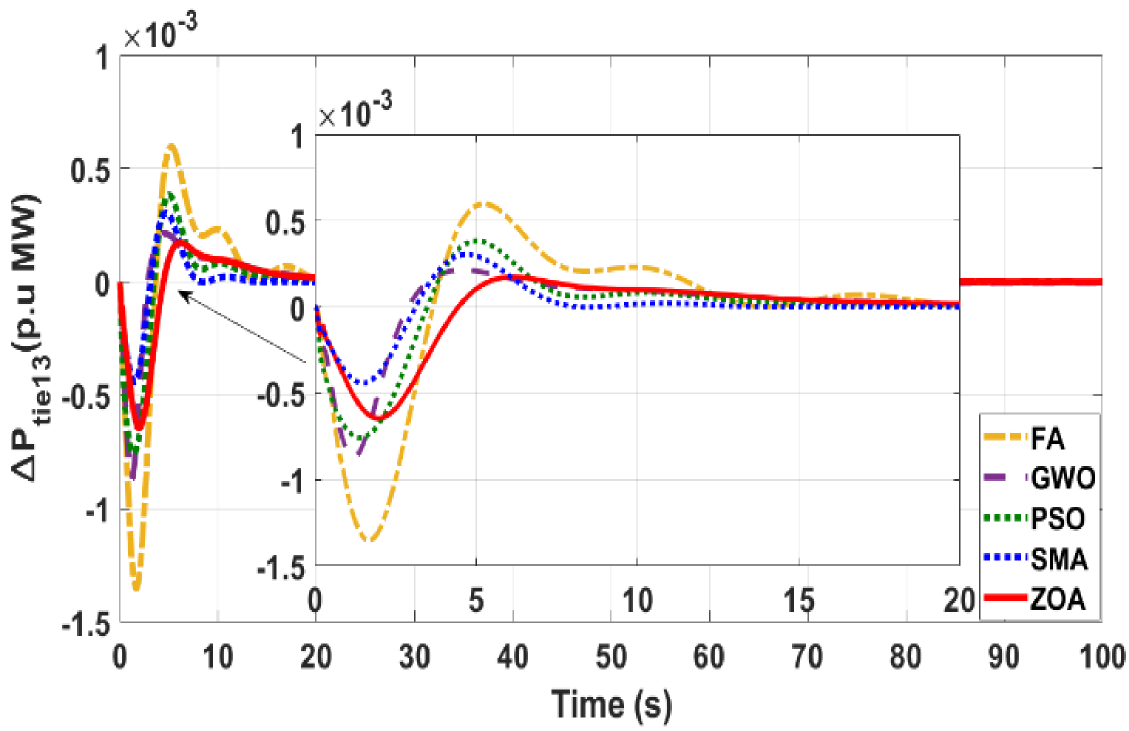

Figure 3.10 (f) System dynamic responses with respect to time for different optimization algorithm: Deviation in tie line power between area-1 and -3.

Table 3.7 (a) System dynamic response for different optimization techniques

Error		FA	GWO	PSO	SMA	ZOA
ΔF_1	M.U	-0.006802	-0.00552	-0.005488	-0.004419	-0.004374
	M.O	0.001991	0.001142	0.001717	0.000928	0.0007804
	S.T	18	5	11	9	5
ΔF_2	M.U	-0.00462	-0.006013	-0.00618	-0.004119	-0.003503
	M.O	0.001824	0/001176	0.001247	0.0008442	0.000846
	S.T	10	6	7	8	6
ΔF_3	M.U	-0.005488	-0.003606	-0.003187	-0.003281	-0.003217
	M.O	0.002903	0.002029	0.001744	0.001259	0.001377
	S.T	8	7	8	8	7
ΔP_{tie12}	M.U	-0.000405	-0.000059	-0.000182	-0.000061	-0.000094
	M.O	0.0002694	0.000068	0.0002189	0.000073	0.0000403
	S.T	25	14	20	13	9
ΔP_{tie23}	M.U	-0.001553	-0.000920	-0.000865	-0.000508	-0.000684
	M.O	0.0009171	0.0001968	0.0004328	0.0003631	0.0002457
	S.T	20	15	14	18	20
ΔP_{tie13}	M.U	-0.001352	-0.000871	-0.000755	-0.000439	-0.000644
	M.O	0.0005976	0.0002137	0.000383	0.0003046	0.0001734
	S.T	21	20	19	17	16

Table 3.7 (b) Percentage improvement of using ZOA over other algorithms

Error		FA	GWO	PSO	SMA
ΔF_1	M.U	35.7	20.76	20.3	1.02
	M.O	60.8	31.66	54.55	15.91
	S.T	72.22	0.0	54.55	44.44
ΔF_2	M.U	24.18	41.74	43.32	14.96
	M.O	53.62	28.06	32.16	-0.21
	S.T	40.0	0.0	14.29	25.0
ΔF_3	M.U	41.38	10.79	-0.94	1.95
	M.O	52.57	32.13	21.04	-9.37
	S.T	12.5	0.0	12.5	12.5
ΔP_{tie12}	M.U	76.79	-59.32	48.35	-54.1
	M.O	85.04	40.74	81.59	44.79
	S.T	64.0	35.71	55.0	30.77
ΔP_{tie23}	M.U	55.96	25.65	20.92	-34.65
	M.O	73.21	-24.85	43.23	32.33
	S.T	0.0	-33.33	-42.86	-11.11
ΔP_{tie13}	M.U	52.37	26.06	14.7	-46.7
	M.O	70.98	18.86	54.73	43.07
	S.T	23.81	20.0	15.79	5.88

Analysis: The performance evaluation presented in Table 3.7 (a) and (b) confirms the superior effectiveness of the ZOA algorithm when compared with other well-established optimization techniques such as FA, GWO, PSO, and SMA. The results demonstrate that ZOA consistently yields better dynamic responses, characterized by reduced overshoot, minimized undershoot, and shorter settling times. In particular, ZOA achieves the most significant enhancement over the Firefly Algorithm, with an average improvement of nearly 50%, while also outperforming Particle Swarm Optimization by approximately 30%. Improvements over Grey Wolf Optimization and Slime-Mould Algorithm are comparatively moderate since these algorithms are recently developed algorithms too, with average gains of about 12% and 6.5%, respectively.

Still, the performance of the ZOA algorithm is higher than the other compared algorithms. These findings highlight the robustness and adaptability of ZOA, establishing it as a more reliable optimization strategy for Automatic Generation Control in multi-area interconnected power systems.

3.4.1.4 Sensitivity analysis

A sensitivity analysis is conducted to exemplify the robustness of the proposed controller gains and associated parameters at the nominal conditions and it is analyzed by considering different uncertainties and also changing the values of different parameters within a system. To measure the robustness of the 2DOFTIDN-FOTI controller, different scenarios are considered one at a time, such as by varying the SPVP output, random load perturbation in area 1 and change in system loading from its nominal loading.

3.4.1.4.1 Random weather condition

The effectiveness of the proposed technique is assessed when subjected to varying weather conditions in a two-pronged scenario: one involving the integration EVs and the other without EV integration. In this context, the Solar Photovoltaic system is subjected to uncertain random inputs, as depicted in Figure 3.11, while the availability of Bio-Gas plants and Bio-Diesel plants is not guaranteed, potentially due to limited supply or depleted fuel stocks.

The Figure 3.12 shows the change in EV generation and the corresponding dynamic responses of the system are illustrated in Figure 3.13. Table 3.9 serves as evidence that the proposed controller effectively functions under unpredictable weather conditions. Notably, the system exhibits reduced frequency deviations and tie-line power deviation, leading to a stable output. The controller's optimal gain values can be found in Table 3.8. A more in-depth analysis clearly demonstrates that the incorporation of EVs into the system enhances the overall dynamic system performances when faced with random weather conditions.

Table 3.8 Tuned controller gain values for random weather condition considering both scenarios of with and without EV.

Controller Gains	S1 Without EV			S2 With EV		
	Area-1	Area-2	Area-3	Area-1	Area-2	Area-3
K_t	0.915	0.999	0.926	0.984	0.999	0.999
n	2.388	2.016	2.989	2.472	2.424	2.936
K_i	0.473	0.081	0.185	0.683	0.889	0.472
K_d	0.526	0.920	0.999	0.999	0.999	0.998
N	57.64	84.96	52.46	83.13	72.70	67.53
b	0.393	0.653	0.356	0.861	0.409	0.156
c	0.663	0.536	0.459	0.476	0.999	0.727
K_{t1}	0.248	0.404	0.809	0.638	0.999	0.999
n1	2.635	2.865	2.947	2.711	2.748	2.330
K_{i1}	0.999	0.999	0.844	0.511	0.999	0.999
λ	0.319	0.066	0.353	0.496	0.605	0.988

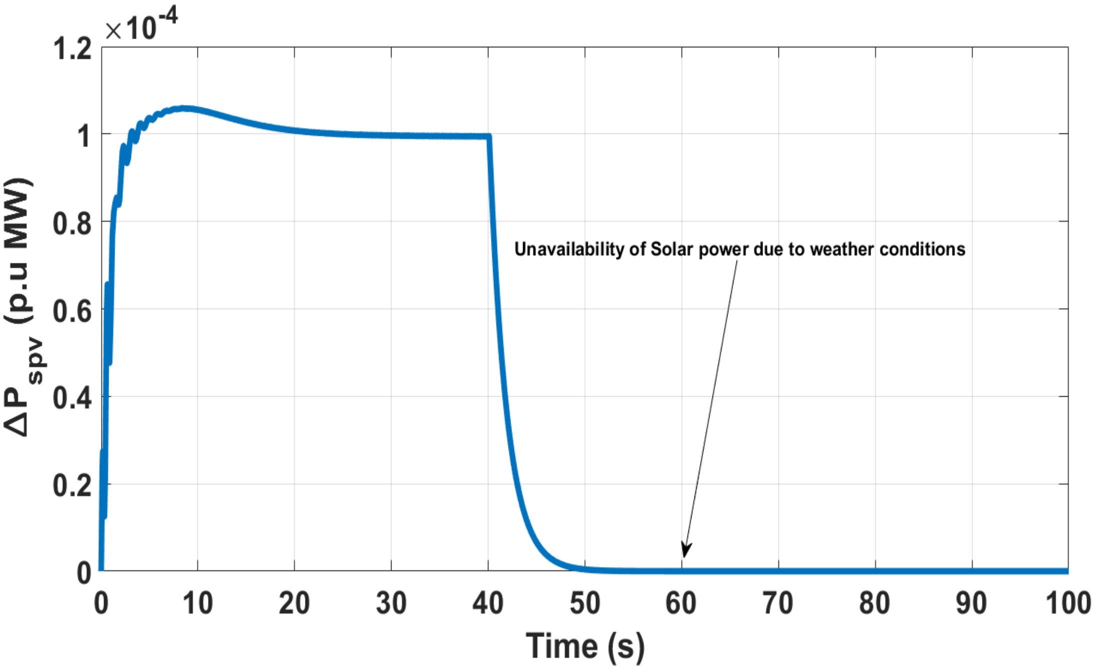

Figure 3.11 Change in Power generation of Solar PV with EV integration.

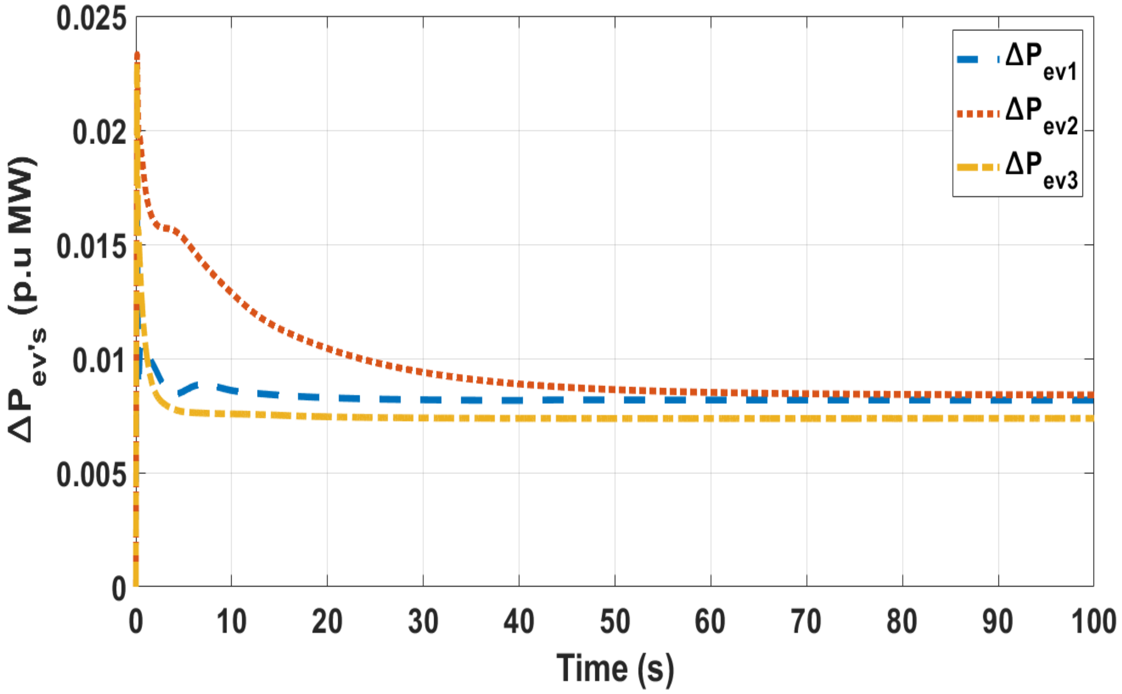

Figure 3.12 Change in power generation of EVs for random weather condition.

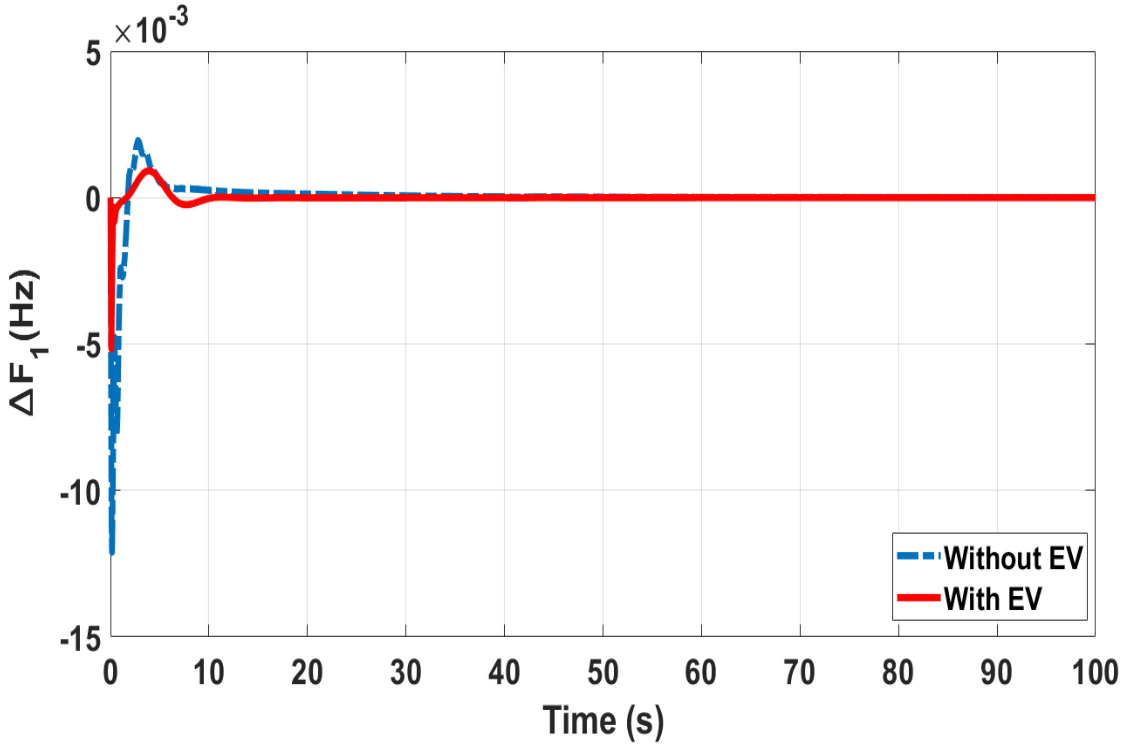

Figure 3.13 (a) System dynamic responses with respect to time for random weather condition with and without EV integration: Area-1 deviation in frequency.

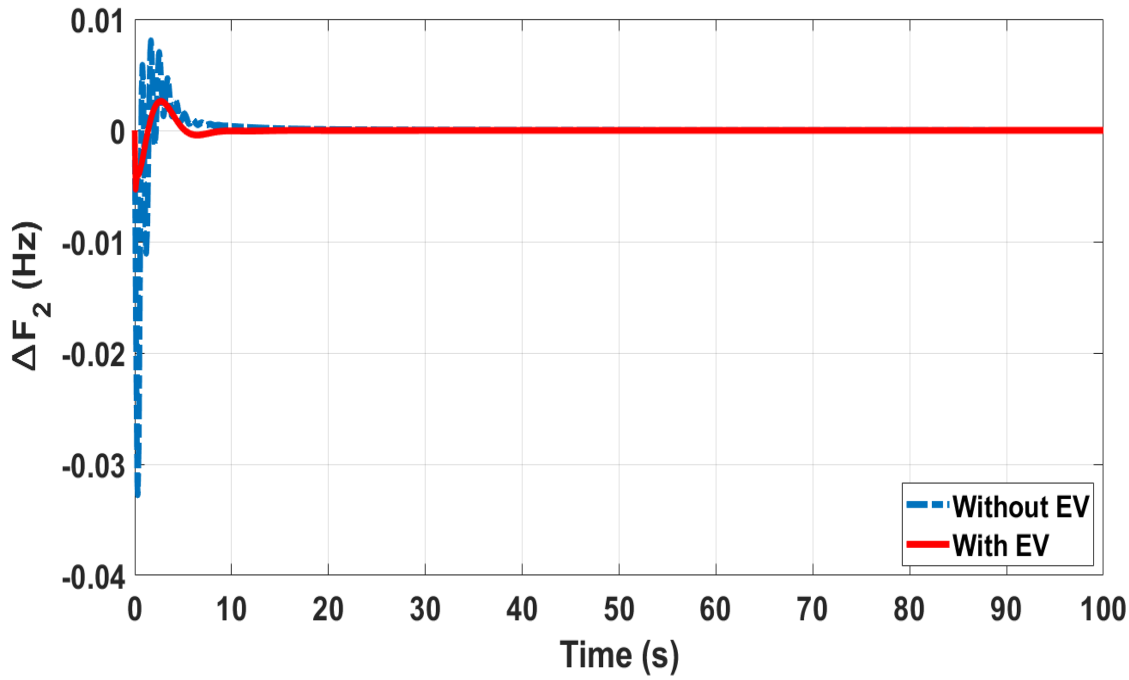

Figure 3.13 (b) System dynamic responses with respect to time for random weather condition with and without EV integration: Area-2 deviation in frequency.

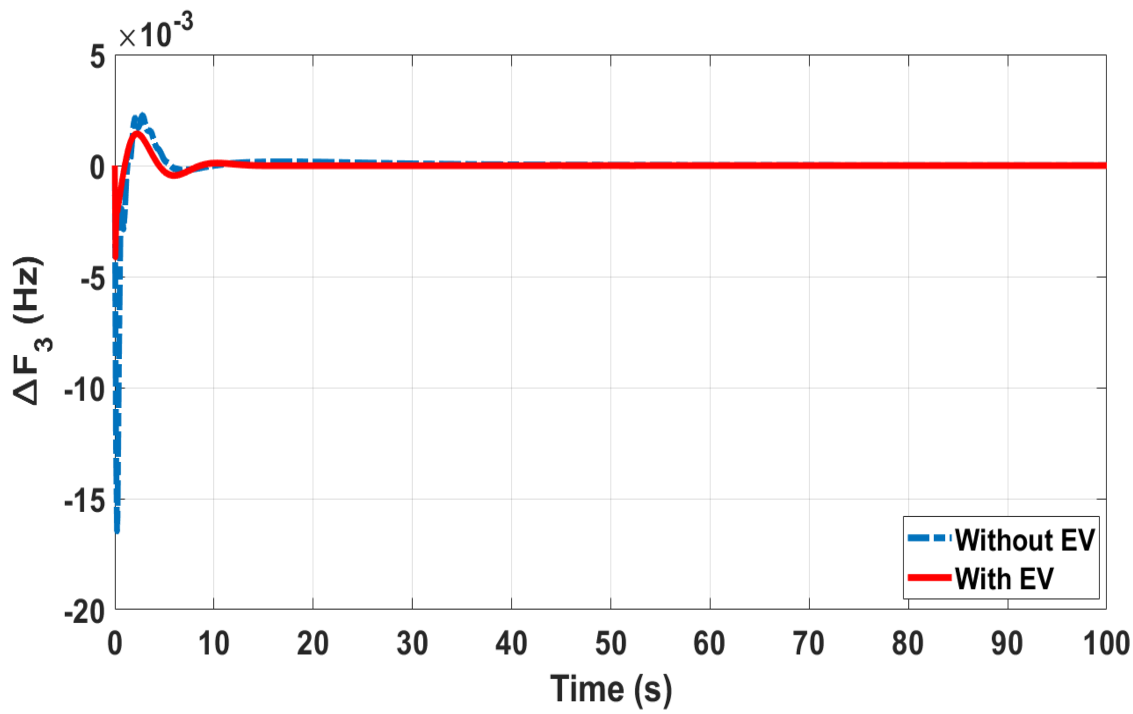

Figure 3.13 (c) System dynamic responses with respect to time for random weather condition with and without EV integration: Area-3 deviation in frequency

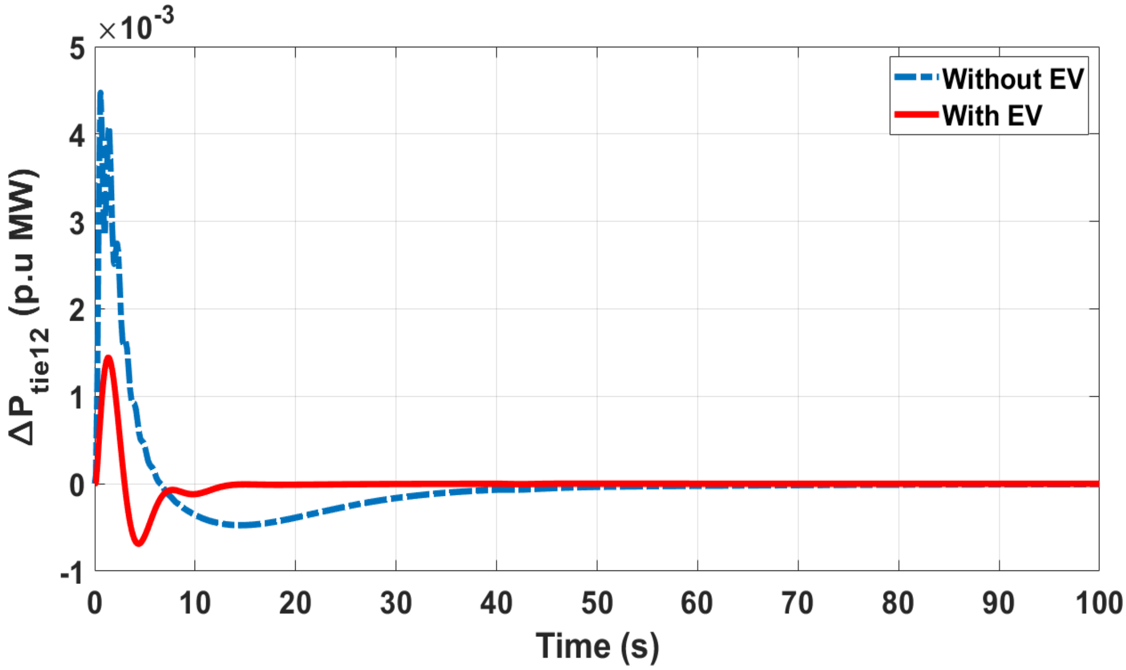

Figure 3.13 (d) System dynamic responses with respect to time for random weather condition with and without EV integration: Deviation in tie line power between area-1 and -2.

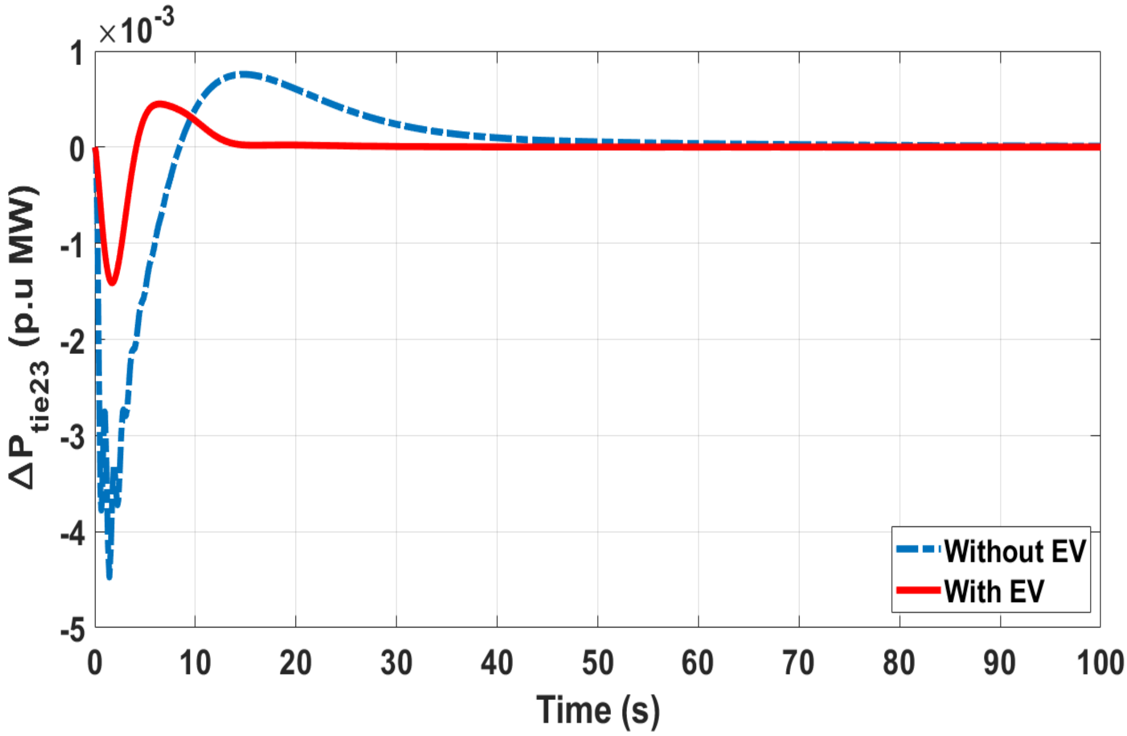

Figure 3.13 (e) System dynamic responses with respect to time for random weather condition with and without EV integration: Deviation in tie line power between area-2 and -3.

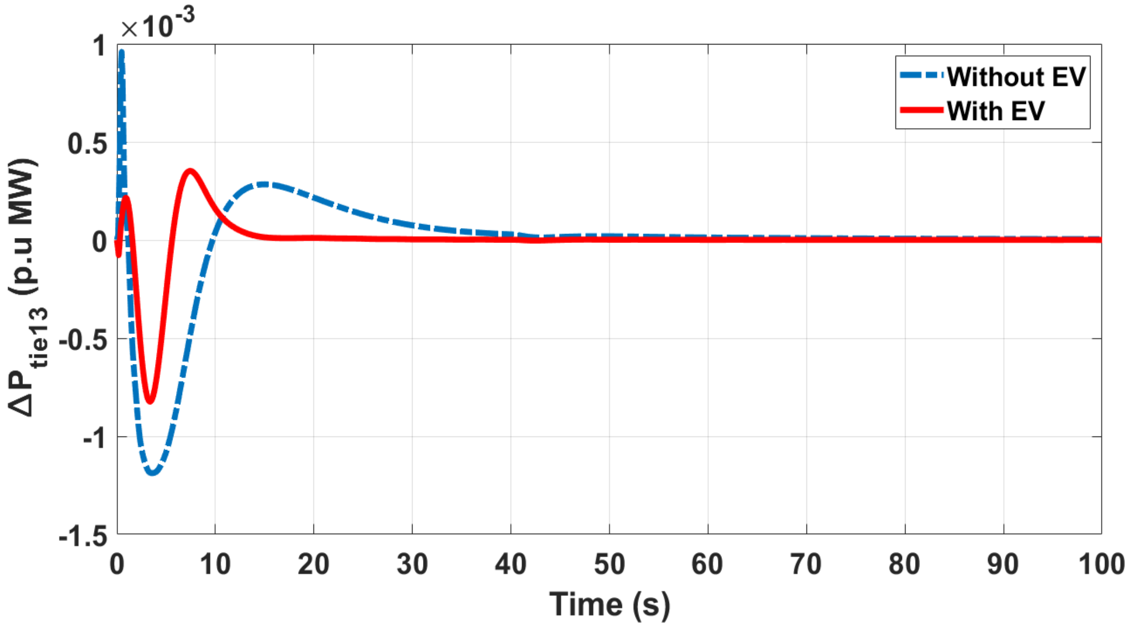

Figure 3.13 (f) System dynamic responses with respect to time for random weather condition with and without EV integration: Deviation in tie line power between area-1 and -3.

Table 3.9 System dynamic response for random weather condition considering both scenarios with and without EV with percentage improvement.

Error		Without Ev	With Ev	% improvement
ΔF_1	M.U	-0.01211	-0.005169	57.32
	M.O	0.001949	0.0009111	53.25
	S.T	18	10	44.4
ΔF_2	M.U	-0.03276	-0.005285	83.87
	M.O	0.008061	0.002618	67.52
	S.T	13	6	53.85
ΔF_3	M.U	-0.01646	-0.004122	74.96
	M.O	0.002268	0.001428	37.04
	S.T	12	12	0.00
ΔP_{tie12}	M.U	-0.0004741	-0.0006868	44.86
	M.O	0.004472	0.001444	67.71
	S.T	48	14	70.83
ΔP_{tie23}	M.U	-0.004474	-0.001413	68.42
	M.O	0.0007574	0.0004475	40.92
	S.T	44	14	68.18
ΔP_{tie13}	M.U	-0.001188	-0.0008243	30.61
	M.O	0.0009589	0.0003523	63.26
	S.T	46	16	65.22

Analysis: The inclusion of Electric Vehicle (EV) participation markedly improves the system's dynamic response under random weather conditions. On average, EV integration reduces maximum undershoot by about 45%, maximum overshoot by nearly 55%, and settling time by approximately 50% compared to the case without EVs. These improvements confirm that EV fleets enhance frequency stability, suppress transient deviations, and enable faster system stabilization in uncertain operating environments.

3.4.1.4.2 Random load variation

When operating real-time, system experiences continuous fluctuations throughout the day. Consequently, it is imperative that the controller demonstrates the ability to effectively regulate system frequency even when subjected to the unpredictability of varying load conditions. The performance of the controller is examined under these randomly changing load conditions for t=100s, as detailed in the previously mentioned scenarios, and it performs admirably under these circumstances.

To simulate the random load conditions, Figure 3.14 visually represents the applied load variations and system responses in Figure 3.15. Detailed information on the fine-tuned gain values of the controller parameters is presented in Table 3.10.

Table 3.10 Tuned controller gain values for random load analysis considering both scenarios with and without EV.

Controller Gains	S_1 Without EV			S_2 With EV		
	Area-1	**Area-2**	**Area-3**	**Area-1**	**Area-2**	**Area-3**
K_t	0.9997	0.9984	0.6792	0.9998	0.9999	0.9996
n	2.8397	2.9446	2.6853	2.8290	2.6171	2.9621
K_i	0.8256	0.8698	0.5141	0.9986	0.5893	0.7763
K_d	0.6007	0.4719	0.7387	0.9868	0.9781	0.9988
N	56.894	95.571	7.1688	66.030	57.334	50.840
b	0.9779	0.3024	0.8359	0.6094	0.7859	0.9999
c	0.2885	0.2594	0.6670	0.6209	0.8048	0.6669
K_{t1}	0.9999	0.9998	0.9958	0.9999	0.9999	0.3514
n1	2.7547	2.8873	2.2075	2.5572	2.8927	2.7895
K_{i1}	0.7850	0.9999	0.9383	0.9998	0.9999	0.9999
λ	0.0244	0.1924	0.0706	0.3614	0.3208	0.2592

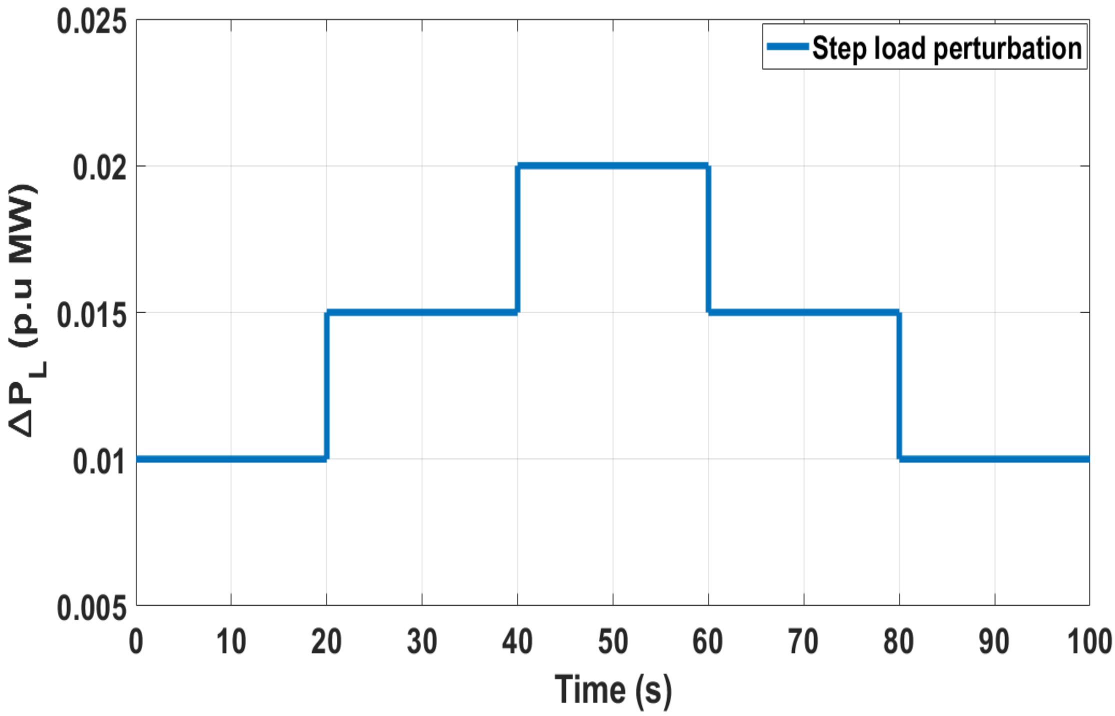

Figure 3.14 Change in step load perturbation for system with and without EV integration.

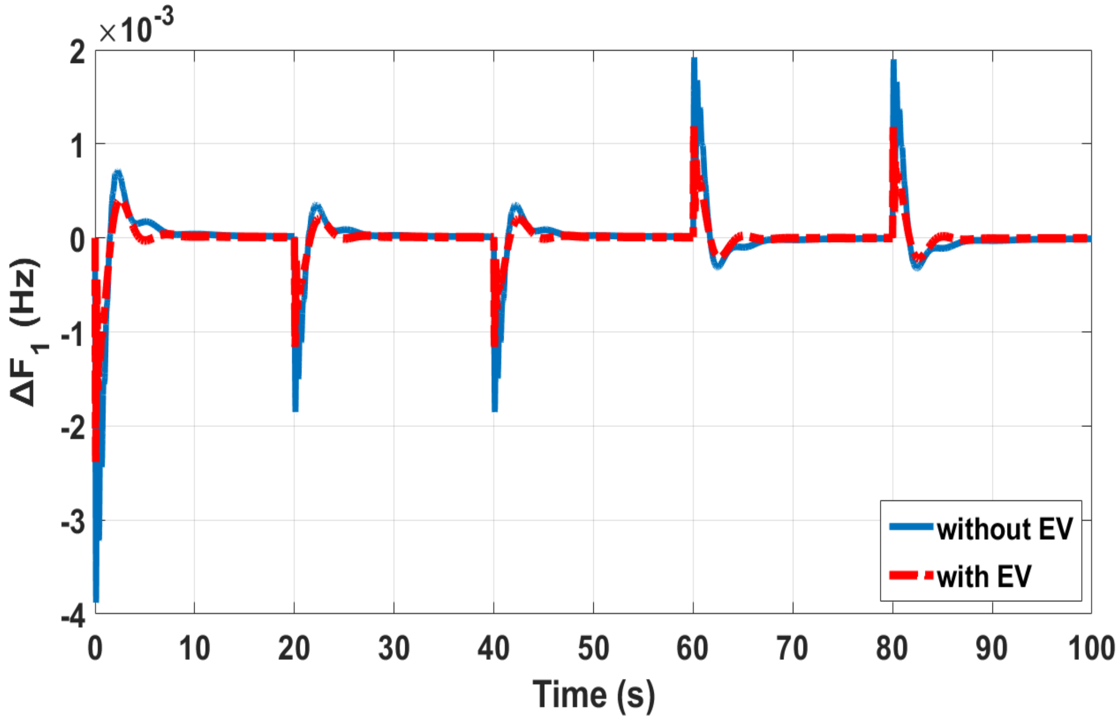

Figure 3.15 (a) System dynamic responses for random load variation with and without EV integration: Area-1 deviation in frequency.

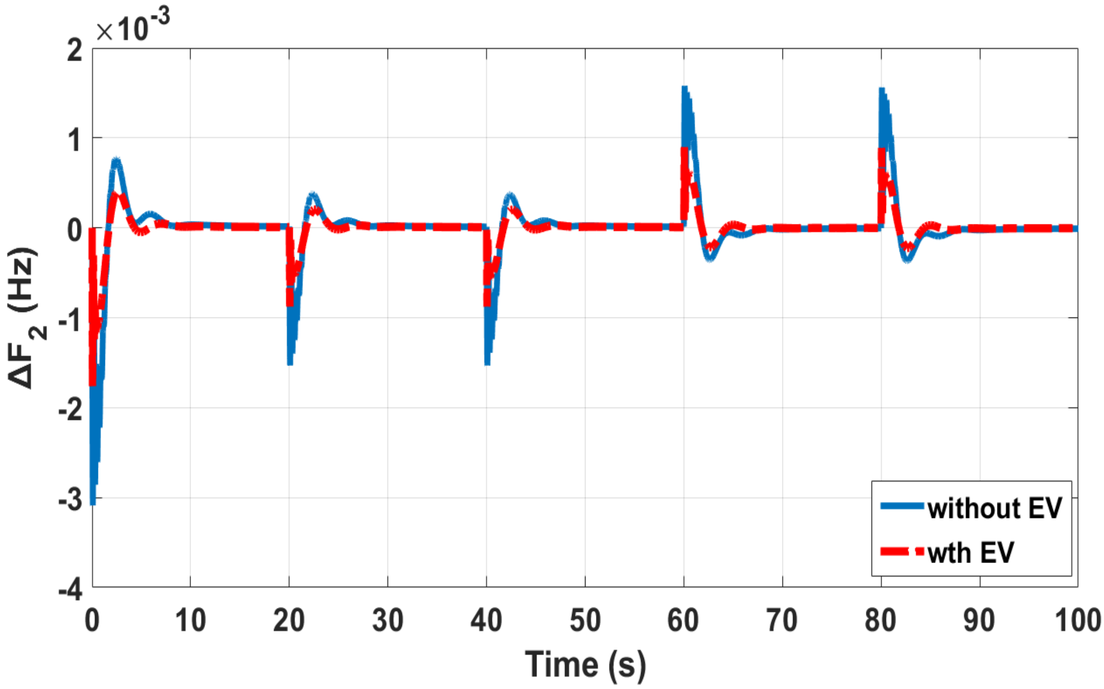

Figure 3.15 (b) System dynamic responses for random load variation with and without EV integration: Area-2 deviation in frequency.

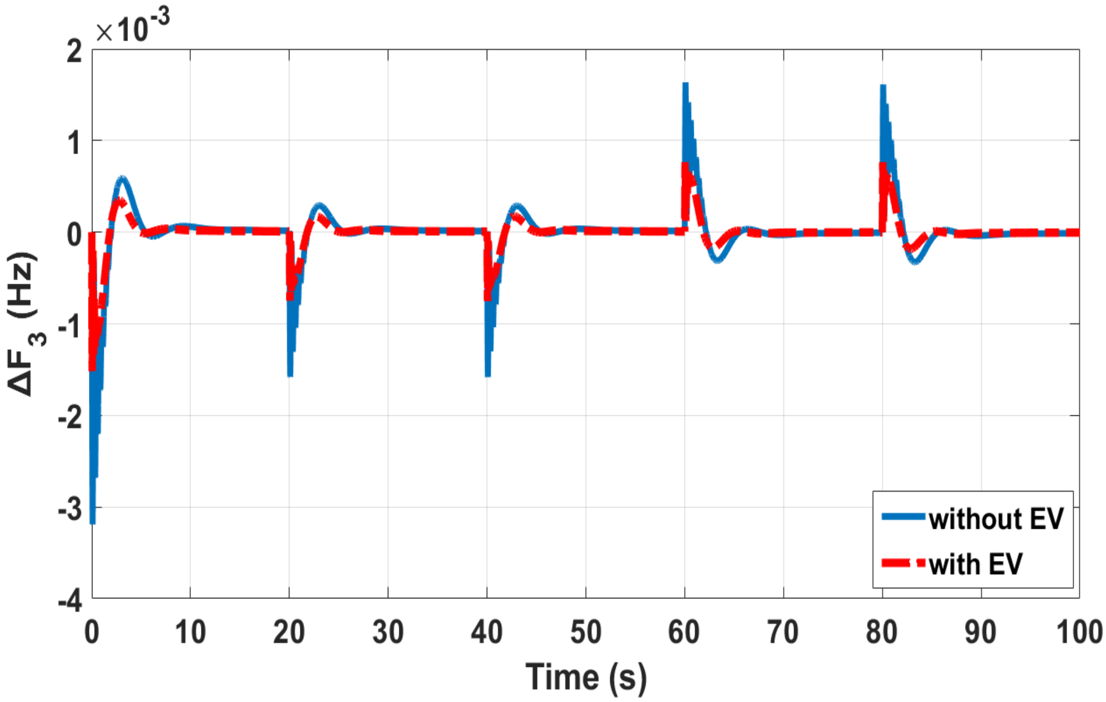

Figure 3.15 (c) System dynamic responses for random load variation with and without EV integration: Area-3 deviation in frequency.

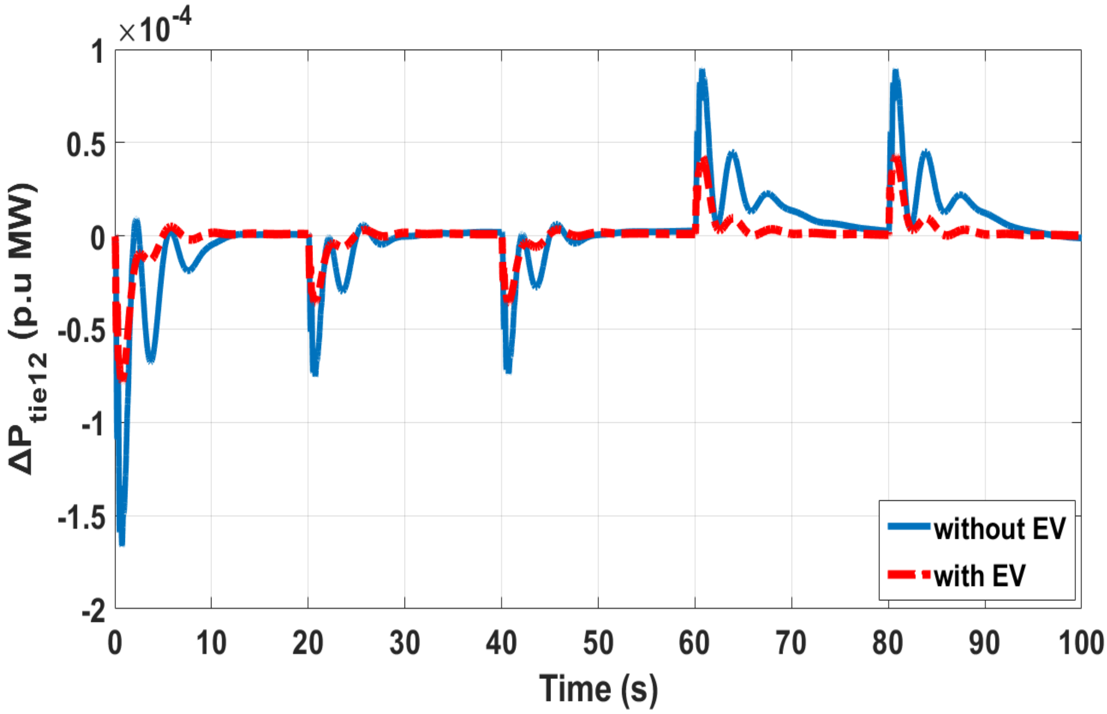

Figure 3.15 (d) System dynamic responses for random load variation with and without EV integration: Deviation in tie line power between area-1 and -2.

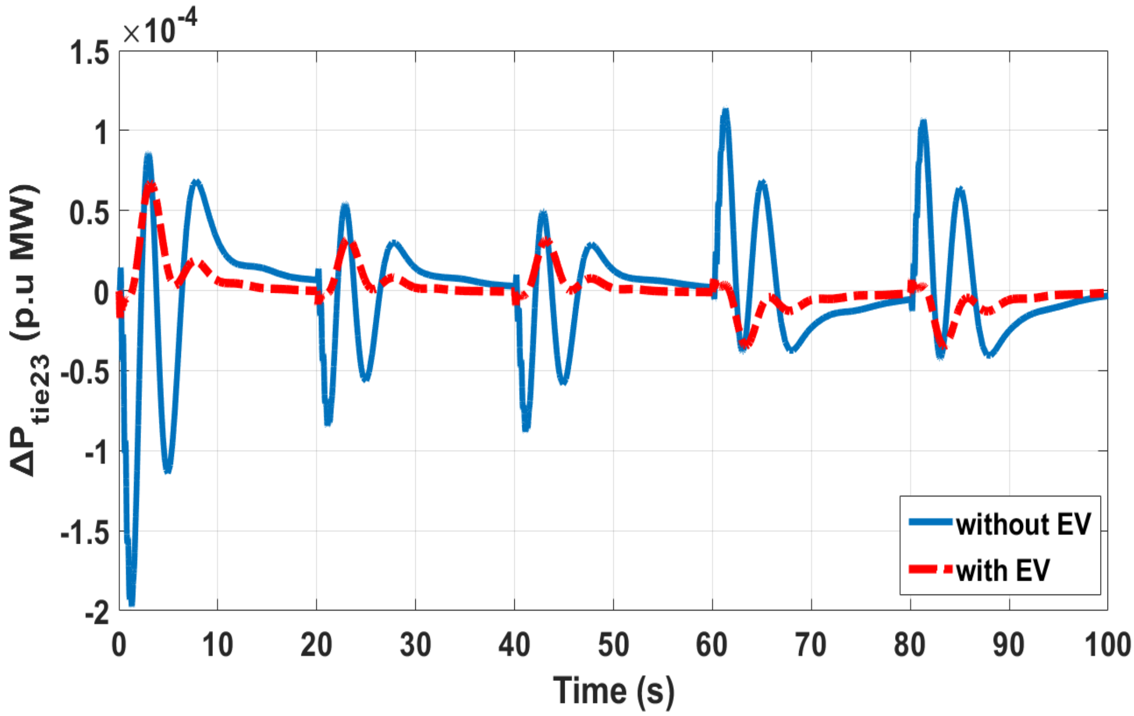

Figure 3.15 (e) System dynamic responses for random load variation with and without EV integration: Deviation in tie line power between area-2 and -3.

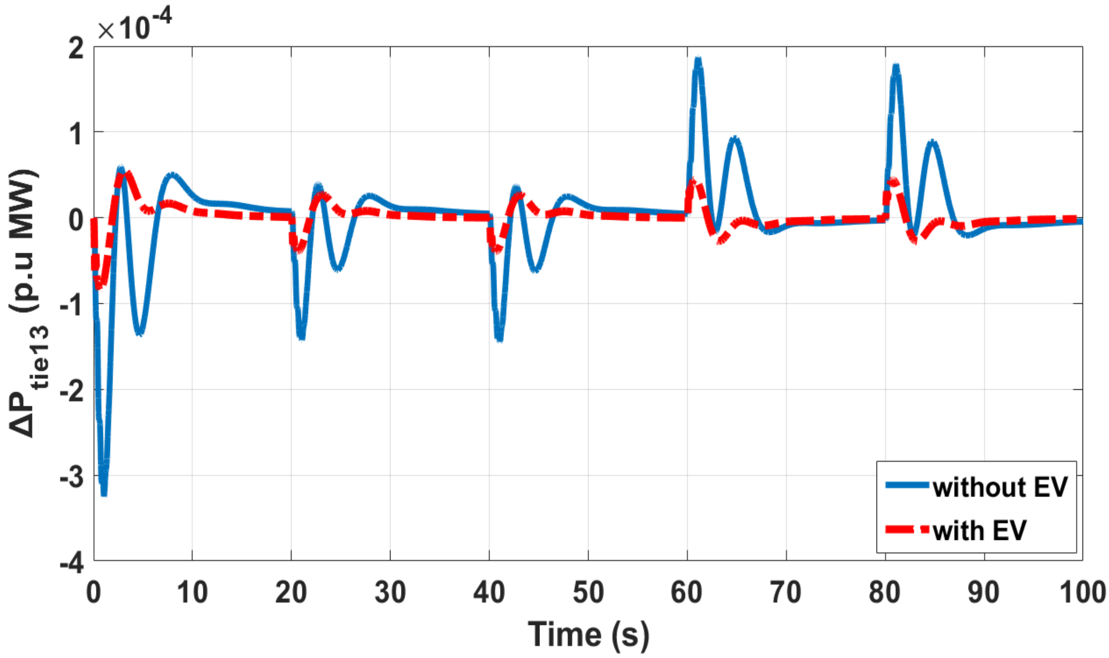

Figure 3.15 (f) System dynamic responses for random load variation with and without EV integration: Deviation in tie line power between area-1 and -3.

Analysis: The system's dynamic response, depicted in Figure 3.15, demonstrates that the inclusion of EVs in the system contributes to an enhancement in the overall dynamic response. The comparison highlights that EV integration improves AGC performance by reducing overshoot, damping oscillations faster, and stabilizing both frequency and tie-line power more effectively than the conventional system alone.

3.4.1.4.3 Change in system nominal loading

A sensitivity analysis is conducted to check the controller's resilience when subjected to variations in parameters due to uncertain factors. The goal is to ensure that the controller's performance remains stable even when there are slight adjustments in system parameters. To evaluate this, the following system parameters are altered within a range of ±20% of their nominal values across all areas. This analysis is conducted in a bilateral context, and it is illustrated through the profiles of frequency deviation and deviation in tie-line power during the sensitivity analysis. Additionally, numerical data provided in Table 3.11 further confirms that the controller optimized using the Zebra Optimization Algorithm (ZOA), exhibits robust performance.

This is evident in the minimal or negligible changes in system behavior even when there are discrepancies in parameters of the system. Therefore, it can be confidently asserted that the finely-tuned gain values of the controller can be maintained without the need for frequent readjustments, even in the presence of slight variations in system parameters. The dynamic response of the system throughout this analysis is depicted in Figure 3.16.

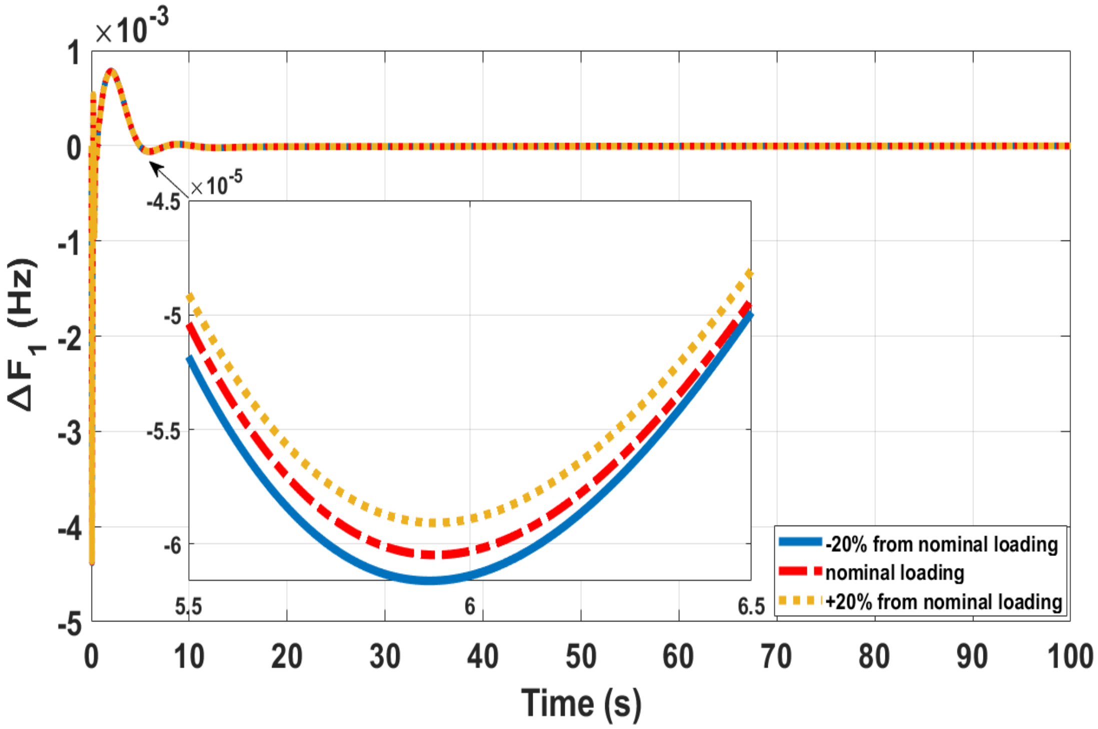

Figure 3.16 (a) System dynamic responses for change in system nominal loading with EV integration: Area-1 deviation in frequency.

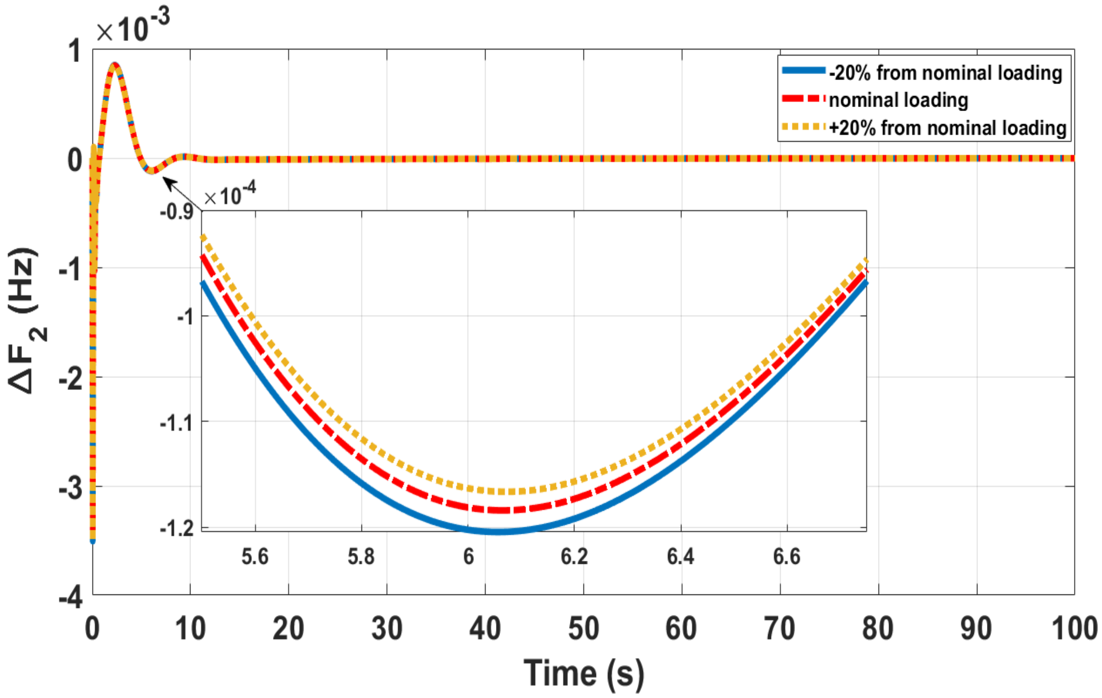

Figure 3.16 (b) System dynamic responses for change in system nominal loading with EV integration: Area-2 deviation in frequency.

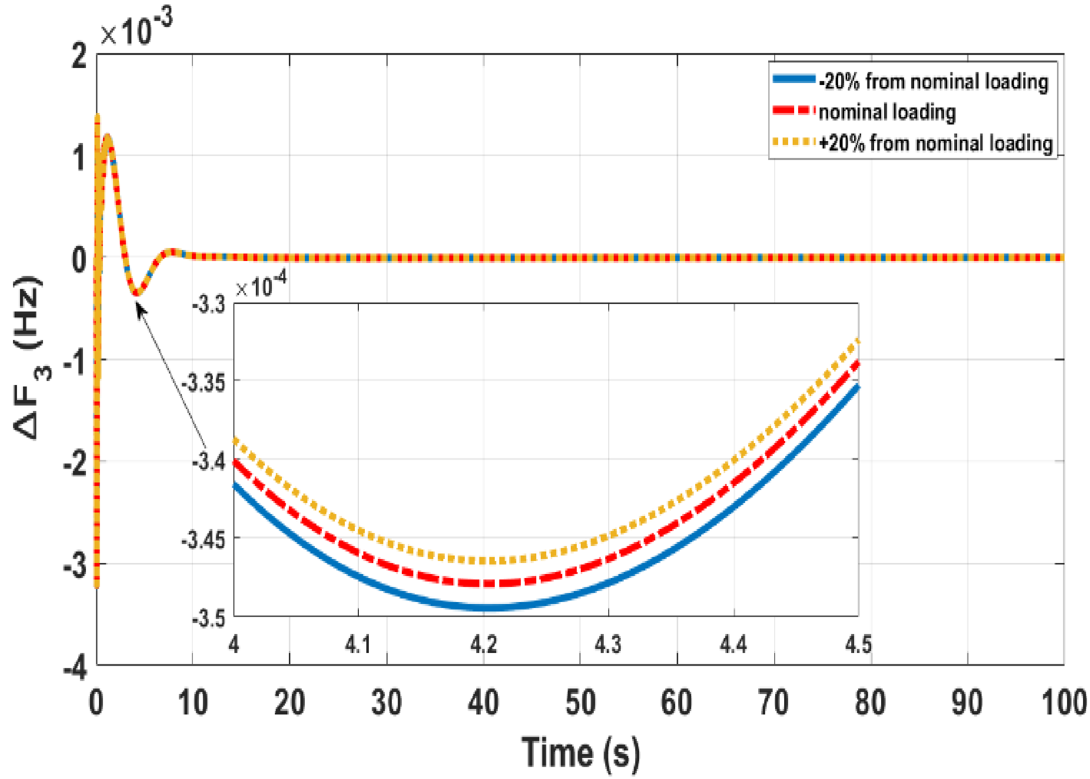

Figure 3.16 (c) System dynamic responses change in system nominal loading with EV integration: Area-3 deviation in frequency.

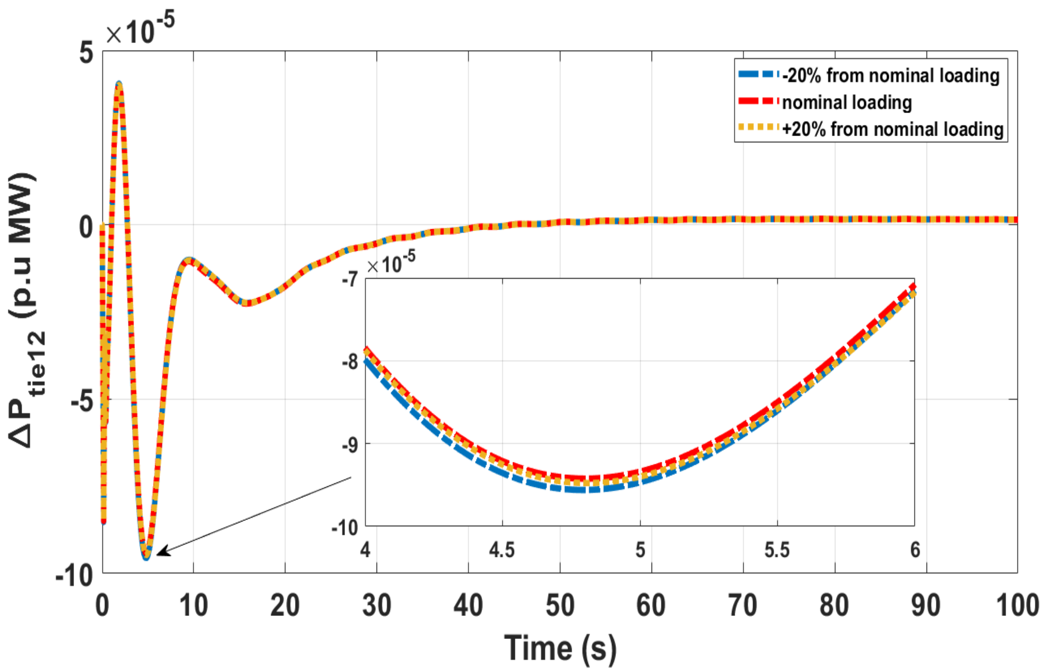

Figure 3.16 (d) System dynamic responses change in system nominal loading with EV integration: Deviation in tie line power between area-1 and -2.

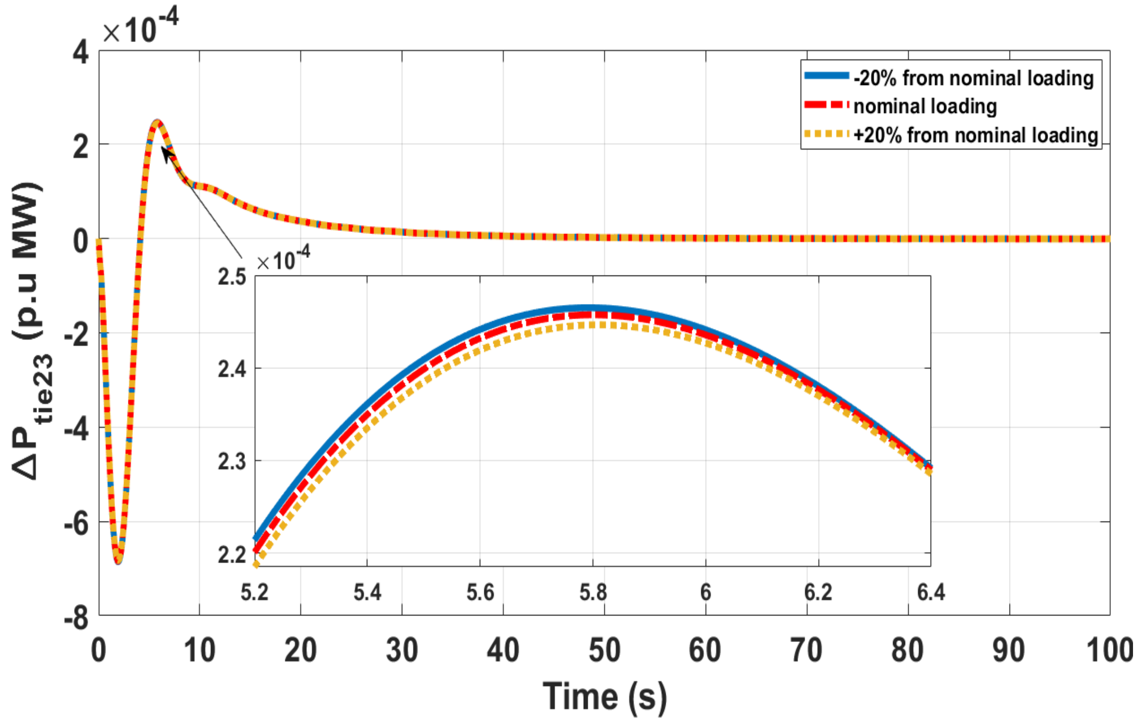

Figure 3.16 (e) System dynamic responses change in system nominal loading with EV integration: Deviation in tie line power between area-2 and -3.

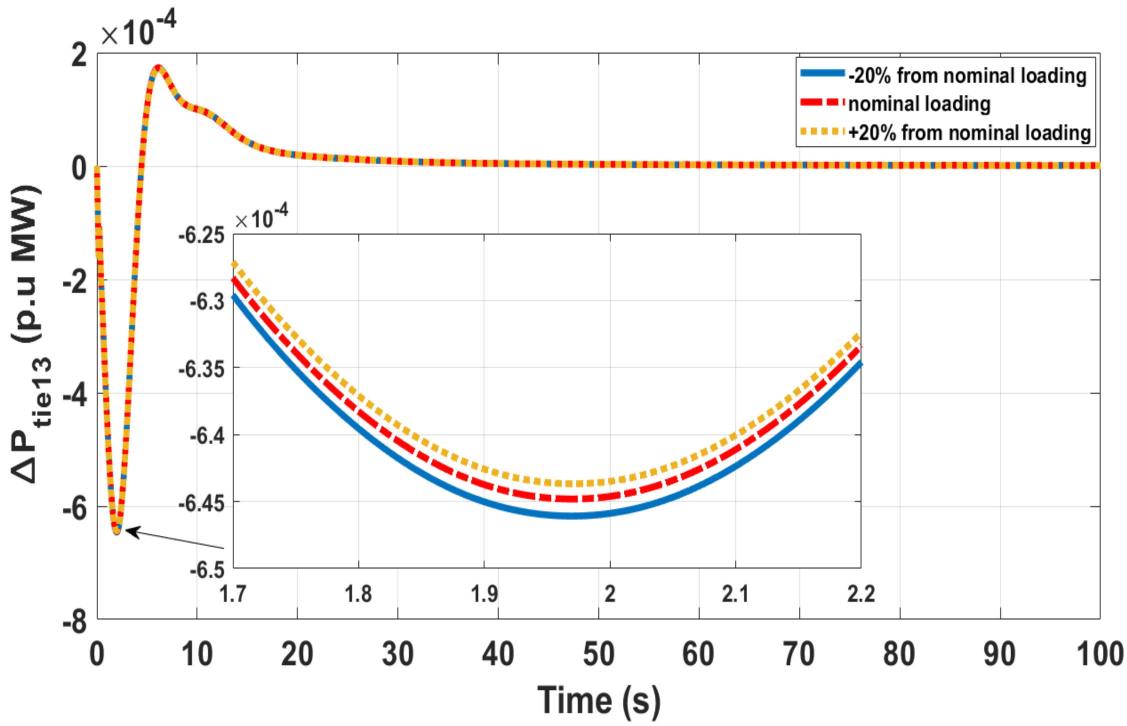

Figure 3.16 (f) System dynamic responses change in system nominal loading with EV integration: Deviation in tie line power between area-1 and -3.

Table 3.11 System performance for ±20% variation in parameters with EV integration

Error		Nominal	+20% Change	-20% change
ΔF_1	M.U	-0.004374	-0.004368	-0.004381
	M.O	0.0007804	0.0007769	0.0007832
ΔF_2	M.U	-0.003503	-0.003499	-0.003507
	M.O	0.000846	0.0008423	0.0008502
ΔF_3	M.U	-0.003217	-0.003214	-0.00322
	M.O	0.001377	0.001377	0.001377
ΔP_{tie12}	M.U	-0.0000942	-0.0000947	-0.0000959
	M.O	0.00004031	0.0000401	0.00004049
ΔP_{tie23}	M.U	-0.0006842	-0.0006828	-0.0006856
	M.O	0.0002457	0.0002446	0.0002465
ΔP_{tie13}	M.U	-0.0006448	-0.0006437	-0.0006461
	M.O	0.0001734	0.0001718	0.0001732

Analysis: Across all parameter variations, the values of M.U remain nearly constant, with only very slight differences between the nominal, +20%, and −20% conditions. This indicates that the system's undershoot performance is robust and not highly sensitive to parameter changes. Similarly, the overshoot values show minimal variation under ±20% parameter changes. The differences are in the order of 10^{-6} to 10^{-5} Hz, confirming that the system maintains stable overshoot behavior. The results show that the system performance remains stable under ±20% parameter variations. Both undershoot and overshoot values change only marginally, highlighting that the designed control strategy provides robust frequency regulation and stability despite parameter uncertainties.

3.4.2 Analysis under deregulated environment

ZOA algorithm is selected for the optimization of the controller gain parameters within an interconnected deregulated power system in this study. Each area within this model comprises two GENCOs and two DISCOs, as depicted in Figure. 3.2. In this section, we look at three instances of deregulated system behavior, taking two scenarios: unilateral, bilateral, and contract violation. The Scenario 1 (S_1) is conducted without Electric Vehicles (EVs), while scenario 2 (S_2) includes the presence of an EV system. The simulation results is presented in a format that includes relevant figures and tables for clarity. In a deregulated market, both GENCOs and DISCOs are connected to the grid for sharing of generated power to the Transmission companies and are communicated based on the cpf which is presented by a DISCO participation matrix (DPM) in (3.16). The 'm' represents the number of GENCOs and 'n' represents the number of DISCOs. According to the cpf, the ACE participation factor (apf) is then calculated i.e., all the cpf are summed up and is multiplied with the load demand.

$$DPM = \begin{bmatrix} cpf_{11} & cpf_{12} & cpf_{13} & cpf_{14} & cpf_{15} & cpf_{16} \\ cpf_{21} & cpf_{22} & cpf_{23} & cpf_{24} & cpf_{25} & cpf_{26} \\ cpf_{31} & cpf_{32} & cpf_{33} & cpf_{34} & cpf_{35} & cpf_{36} \\ cpf_{41} & cpf_{42} & cpf_{43} & cpf_{44} & cpf_{45} & cpf_{46} \\ cpf_{51} & cpf_{52} & cpf_{53} & cpf_{54} & cpf_{55} & cpf_{56} \\ cpf_{61} & cpf_{62} & cpf_{63} & cpf_{64} & cpf_{65} & cpf_{66} \end{bmatrix} \tag{3.16}$$

The equation for cpf can be expressed as given below:

$$cpf_{mn} = \frac{contracted\_load\_demand\_for\_m^{th}GENCO}{Total\_load\_demand\_of\_the\_n^{th}DISCO} \tag{3.17}$$

Here, the summation of the row i.e., load demand of DISCOs to each GENCOs should equal to 1.

$$\sum cpf_{kl} = 1 \tag{3.18}$$

Equation for areas scheduled tie-line power flow is,

$$\Delta P_{kl-scheduled} = P_{\exp} - P_{imp} \tag{3.19}$$

In this equation, Pexp represents the power demanded by DISCOs in area ‘l’ from GENCOs in area ‘k’. And, Pimp represents the power demanded by DISCOS in area ‘k’ from GENCOs in area ‘l’.

Error of exchange in tie line power can be written as,

$$\Delta P_{kl\text{-}error} = \Delta P_{kl\text{-}actual} - \Delta P_{kl\text{-}scheduled} \tag{3.20}$$

Table 3.12 Incremental generation in power for different cases of deregulation of EV integration

Areas	GENCO	C_1		C_2		C_3	
		apfs	Generation (P.u. MW)	apfs	Generation (P.u. MW)	apfs	Generation (P.u. MW)
1	1	0.65	0.013	0.5	0.01	0.735	0.0195
	2	0.35	0.007	0.5	0.01	0.264	0.007
2	3	0.5	0.01	0.55	0.011	0.5	0.01
	4	0.5	0.01	0.45	0.009	0.5	0.01
3	5	0.6	0.012	0.45	0.009	0.6	0.012
	6	0.4	0.008	0.55	0.011	0.4	0.008

Table 3.13 Tuned controller gain values for different scenarios of deregulated environment considering Without EV (S1) and with EV (S2).

Parameter		Unilateral Transaction		Bilateral transaction		Contract violation	
		S_1	S_2	S_1	S_2	S_1	S_2
K_t	Area-1	0.94	0.99	0.59	0.86	0.56	0.99
	Area-2	0.81	0.64	0.96	0.96	0.96	0.99
	Area-3	0.98	0.99	0.99	0.99	0.99	0.99
n	Area-1	2.90	2.32	2.89	2.24	2.89	2.84
	Area-2	2.89	2.68	2.49	2.37	2.49	2.62
	Area-3	2.95	2.85	2.92	2.67	2.92	2.33
K_i	Area-1	0.63	0.37	0.50	0.27	0.50	0.70
	Area-2	0.79	0.51	0.95	0.37	0.95	0.76
	Area-3	0.41	0.60	0.98	0.54	0.98	0.16
K_d	Area-1	0.99	0.99	0.64	0.94	0.64	0.99
	Area-2	0.45	0.76	0.58	0.91	0.58	0.61
	Area-3	0.66	0.96	0.99	0.99	0.99	0.80
N	Area-1	71.8	94.9	45.7	50.2	45.7	90.4
	Area-2	75.0	78.2	55.2	71.4	55.2	71.4
	Area-3	58.2	89.2	78.5	61.2	78.5	45.6
b	Area-1	0.39	0.46	0.36	0.26	0.36	0.70
	Area-2	0.30	0.72	0.52	0.82	0.52	0.63
	Area-3	0.95	0.58	0.43	0.99	0.43	0.92
c	Area-1	0.97	0.99	0.81	0.97	0.81	0.99
	Area-2	0.73	0.36	0.40	0.61	0.40	0.45
	Area-3	0.21	0.98	0.86	0.73	0.86	0.69
K_{t1}	Area-1	0.99	0.99	0.99	0.99	0.99	0.99
	Area-2	0.74	0.66	0.99	0.95	0.99	0.22
	Area-3	0.99	0.89	0.99	0.99	0.99	0.99
n1	Area-1	2.98	2.94	2.99	2.83	2.99	2.75
	Area-2	2.99	2.67	2.81	2.89	2.81	2.99
	Area-3	2.96	2.99	2.98	2.50	2.98	2.99
K_{i1}	Area-1	0.99	0.99	0.99	0.99	0.99	0.99
	Area-2	0.56	0.99	0.97	0.99	0.97	0.99
	Area-3	0.65	0.99	0.73	0.99	0.73	0.41
λ	Area-1	0.17	0.27	0.18	0.55	0.18	0.13
	Area-2	0.43	0.29	0.24	0.21	0.24	0.21
	Area-3	0.31	0.63	0.15	0.40	0.15	0.75

3.4.2.1 Unilateral transaction

Within this type of structural arrangement, DISCOs have the ability to enter power contracts exclusively with the GENCOs operating within their own designated areas. Specifically, each DISCO requires a load of 0.01 p.u from the GENCOs located within their respective areas. The DPM matrix is shown in (3.22). The local load demands for each individual area are as follows:

$$\Delta P_D = 0.01 + 0.01 = 0.02 \tag{3.21}$$

$$DPM = \begin{bmatrix} 0.6 & 0.7 & 0.0 & 0.0 & 0.0 & 0.0 \\ 0.4 & 0.3 & 0.0 & 0.0 & 0.0 & 0.0 \\ 0.0 & 0.0 & 0.6 & 0.4 & 0.0 & 0.0 \\ 0.0 & 0.0 & 0.4 & 0.6 & 0.0 & 0.0 \\ 0.0 & 0.0 & 0.0 & 0.0 & 0.7 & 0.5 \\ 0.0 & 0.0 & 0.0 & 0.0 & 0.3 & 0.5 \end{bmatrix} \tag{3.22}$$

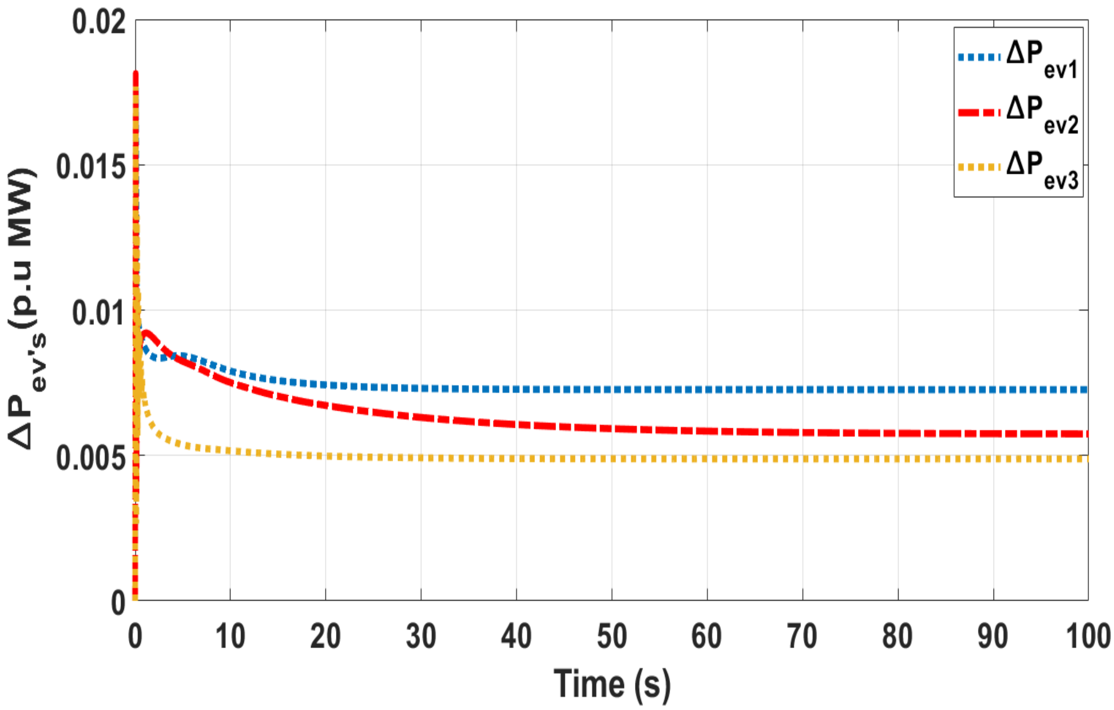

Figure 3.17 Change in EV power for different areas of Unilateral transaction case.

The change in EV power for all the three areas can be seen in Figure 3.17. The overall system's performance is presented in Figure 3.18 for both scenarios, which are with and without Electric Vehicles (EVs). Table 3.13 provides the controller gain values tuned by ZOA for both scenario-1 and scenario-2. Specific details regarding the maximum deviation and settling time of each area frequency and tie-line power can be found in Table 3.14 (a). The improvement percentage of integrating EV over system without Ev is shown in Table 3.14 (b).

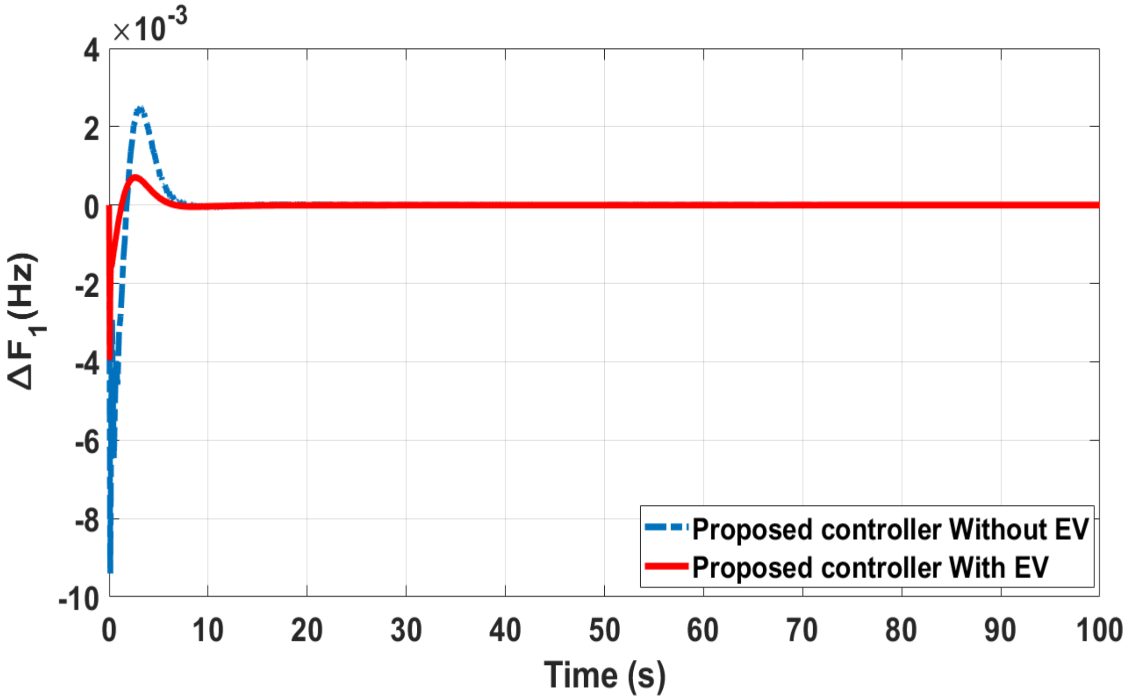

Figure 3.18 (a) System dynamic responses for Unilateral transaction case with and without EV integration: Area-1 deviation in frequency.

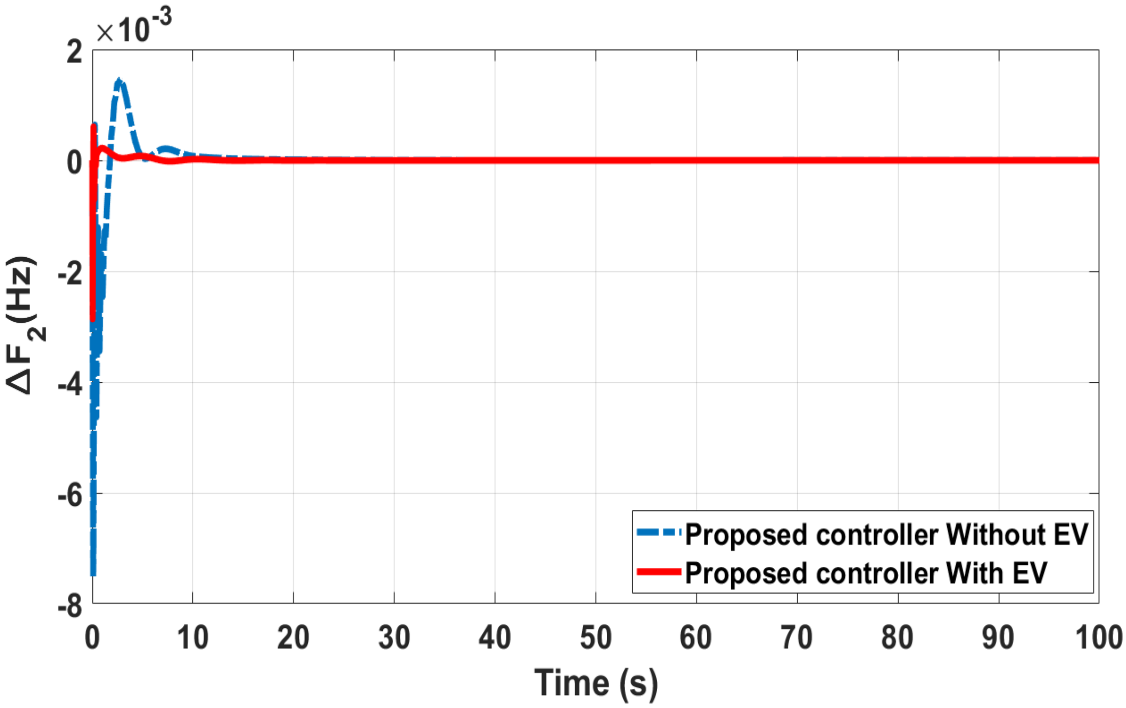

Figure 3.18 (b) System dynamic responses for Unilateral transaction case with and without EV integration: Area-2 deviation in frequency.

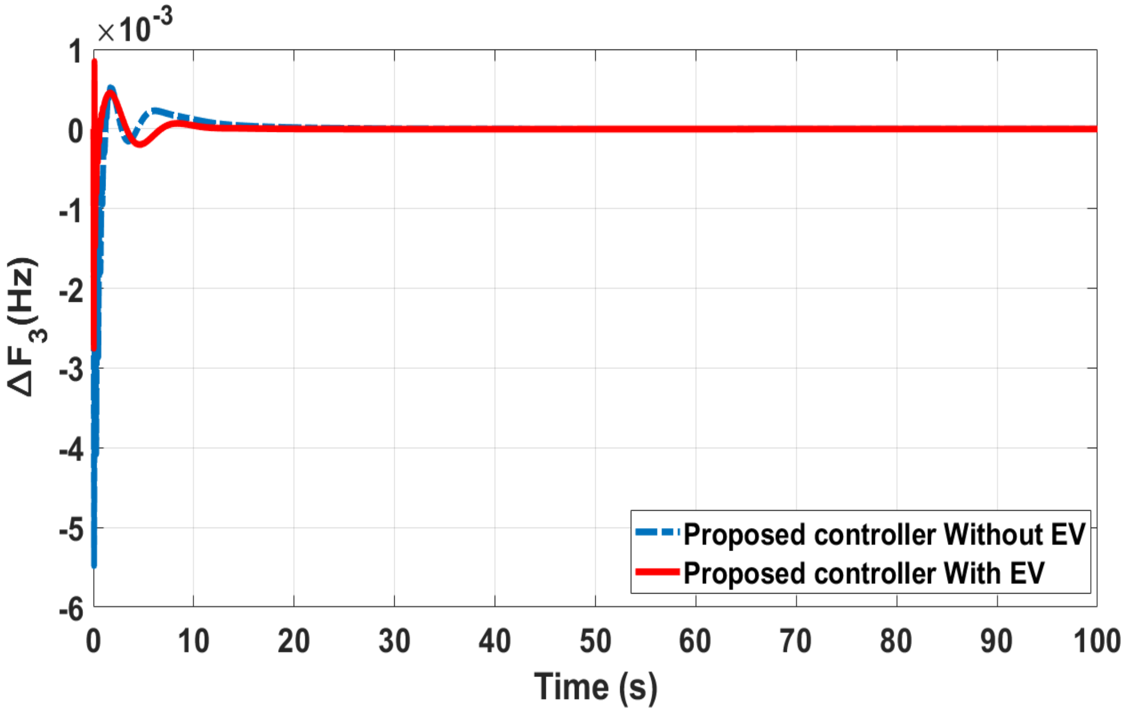

Figure 3.18 (c) System dynamic responses for Unilateral transaction case with and without EV integration: Area-3 deviation in frequency.

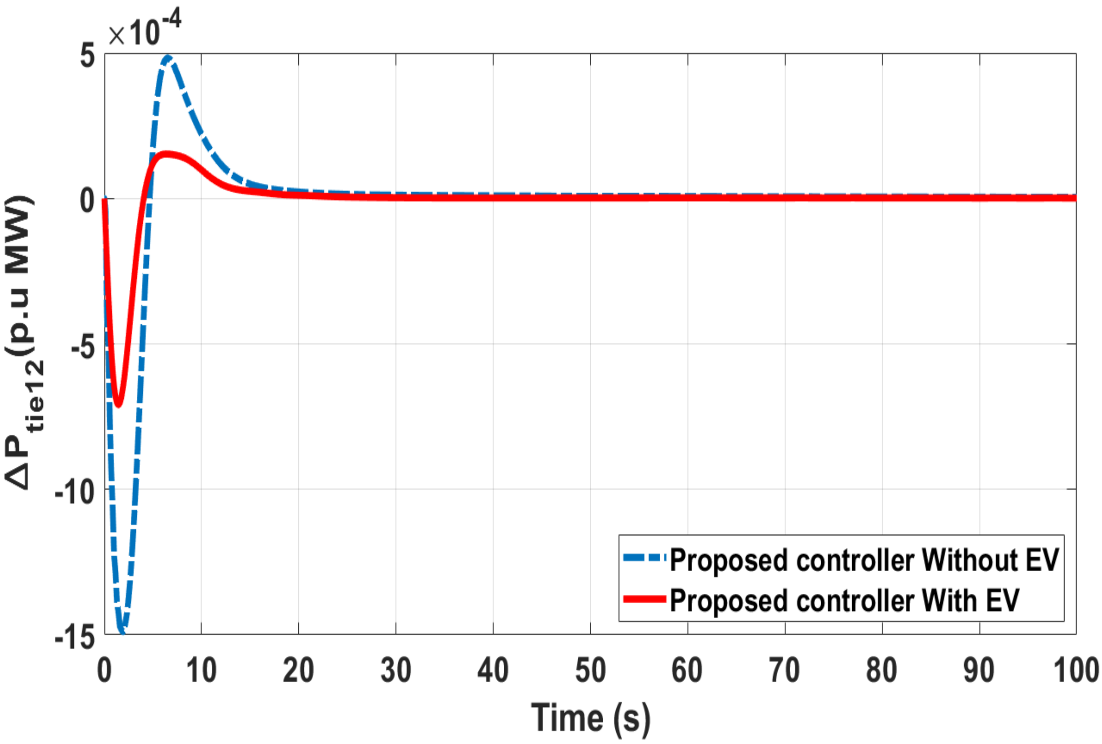

Figure 3.18 (d) System dynamic responses for Unilateral transaction case with and without EV integration: Deviation in tie line power between area-1 and -2

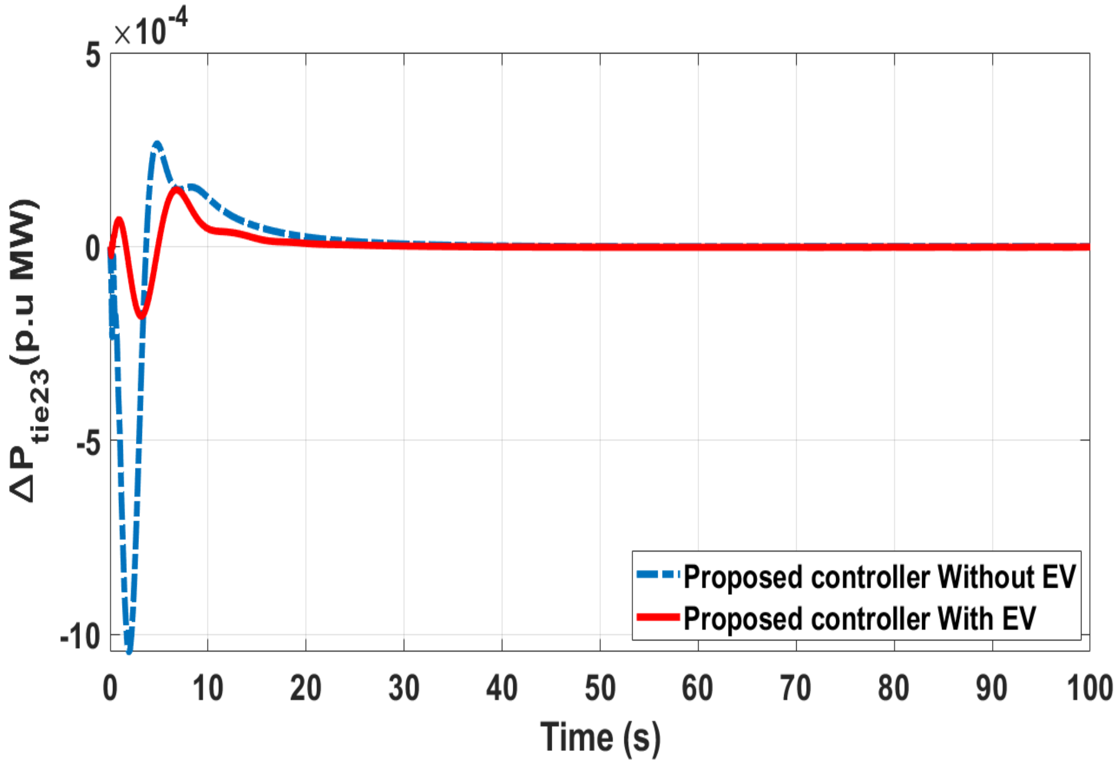

Figure 3.18 (e) System dynamic responses for Unilateral transaction case with and without EV integration: Deviation in tie line power between area-2 and -3.

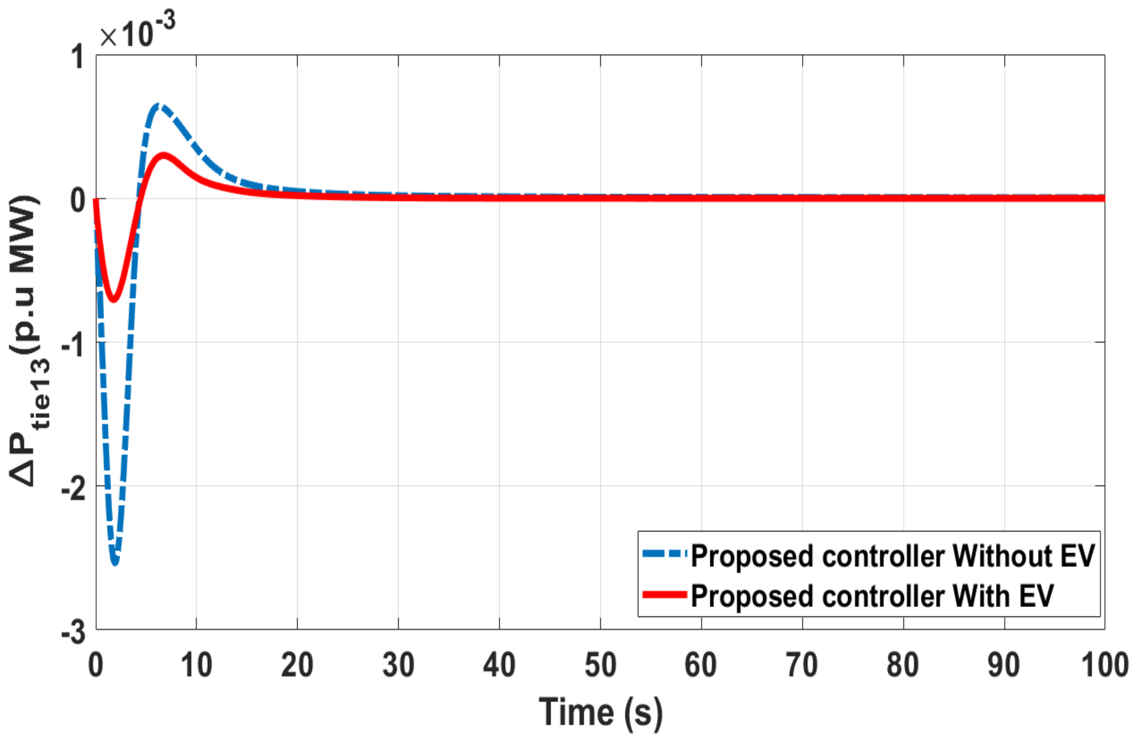

Figure 3.18 (f) System dynamic responses for Unilateral transaction case with and without EV integration: Deviation in tie line power between area-1 and -3.

3.4.2.2 Bilateral transactions

This case considers a bilateral transaction. The DPM matrix for the bilateral transaction environment can be seen in (3.24). It is assumed that each DISCO requests 0.01 per unit (p.u. MW) of power from the GENCOs, leading to a cumulative demand of load in each area as follows:

$$\Delta P_D = 0.01 + 0.01 = 0.02 \tag{3.23}$$

The change in EV power for the different areas is shown in Figure 3.19. Also, Figure 3.20 illustrates the system's performance under the two scenarios, namely, 'with EV' and the scenarios of 'without EV'. The controller gain values for bilateral transaction cases are presented in Table 3.12. The system dynamic response comparison between system with and without EV is given in Table 3.14 (a) and the improvement in percentage is given in Table 3.14 (b).

$$DPM = \begin{bmatrix} 0.2 & 0.3 & 0.2 & 0.1 & 0.1 & 0.1 \\ 0.2 & 0.2 & 0.1 & 0.2 & 0.1 & 0.2 \\ 0.1 & 0.1 & 0.2 & 0.3 & 0.2 & 0.2 \\ 0.2 & 0.2 & 0.1 & 0.1 & 0.2 & 0.1 \\ 0.1 & 0.1 & 0.2 & 0.1 & 0.2 & 0.2 \\ 0.2 & 0.1 & 0.2 & 0.2 & 0.2 & 0.2 \end{bmatrix} \tag{3.24}$$

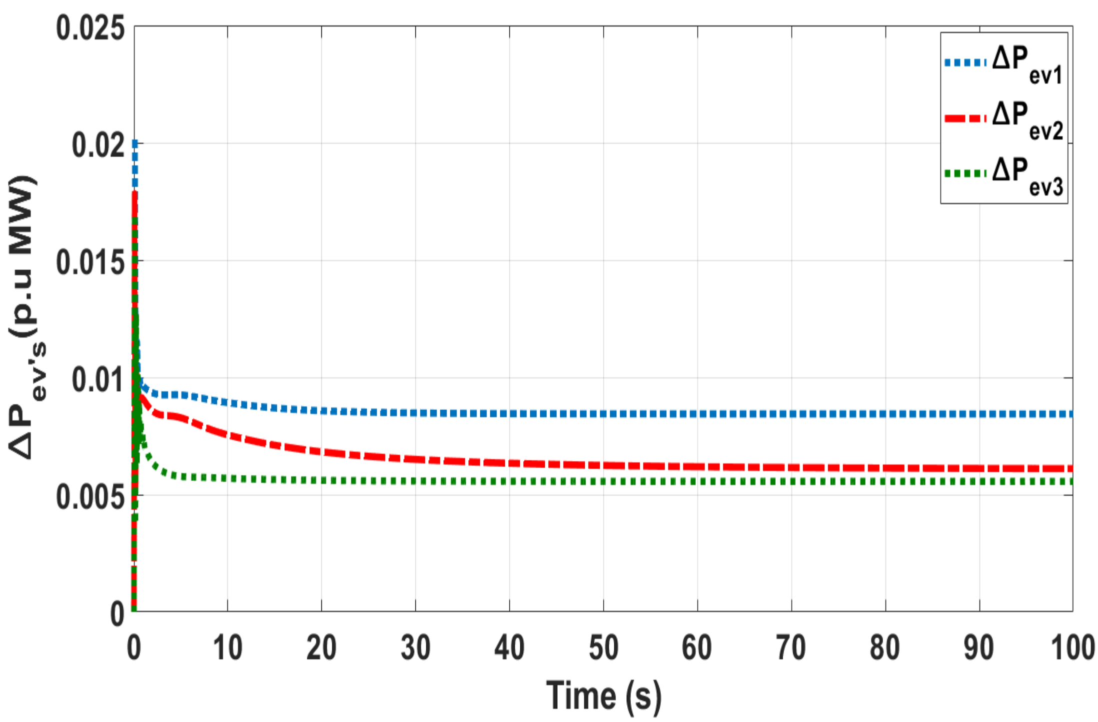

Figure 3.19 Change in EV power for different areas of Bilateral transaction case.

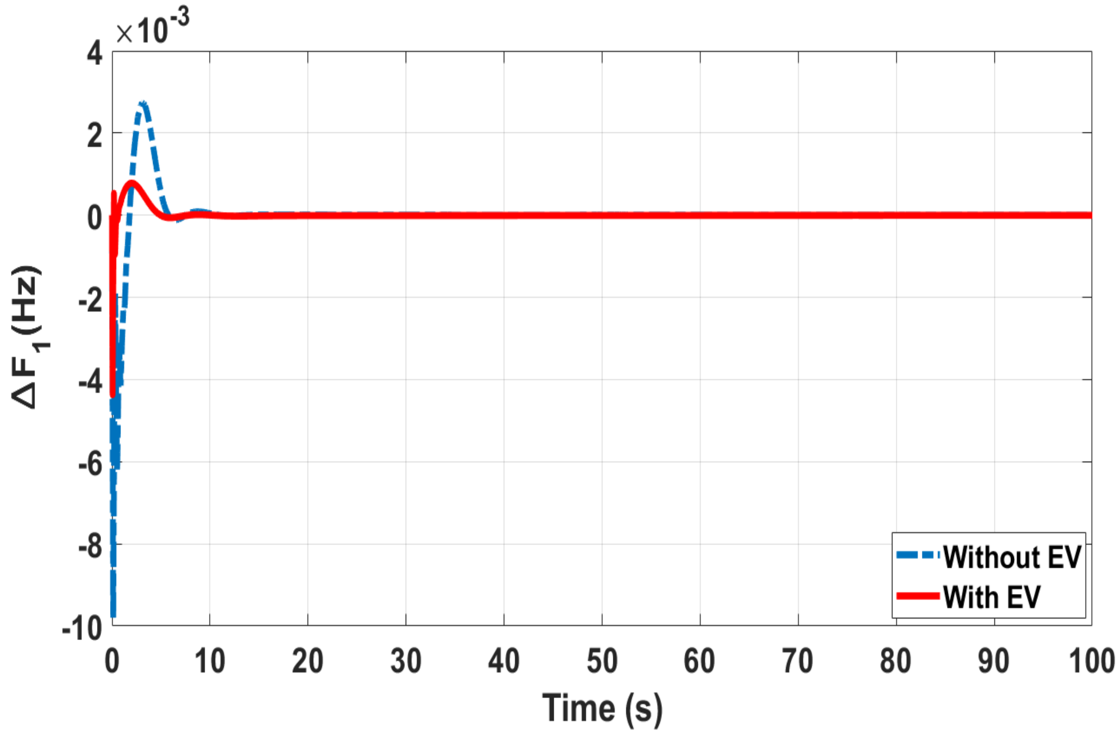

Figure 3.20 (a) System dynamic responses for Bilateral transaction case with and without EV integration: Area-1 deviation in frequency.

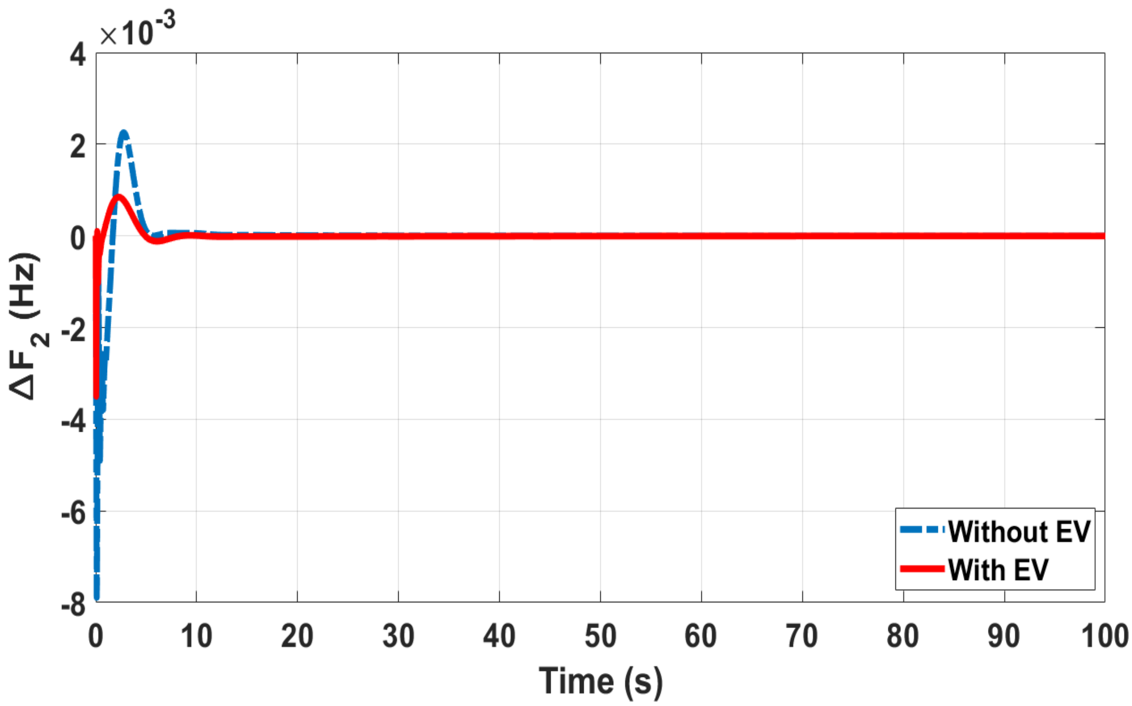

Figure 3.20 (b) System dynamic responses for Bilateral transaction case with and without EV integration: Area-2 deviation in frequency.

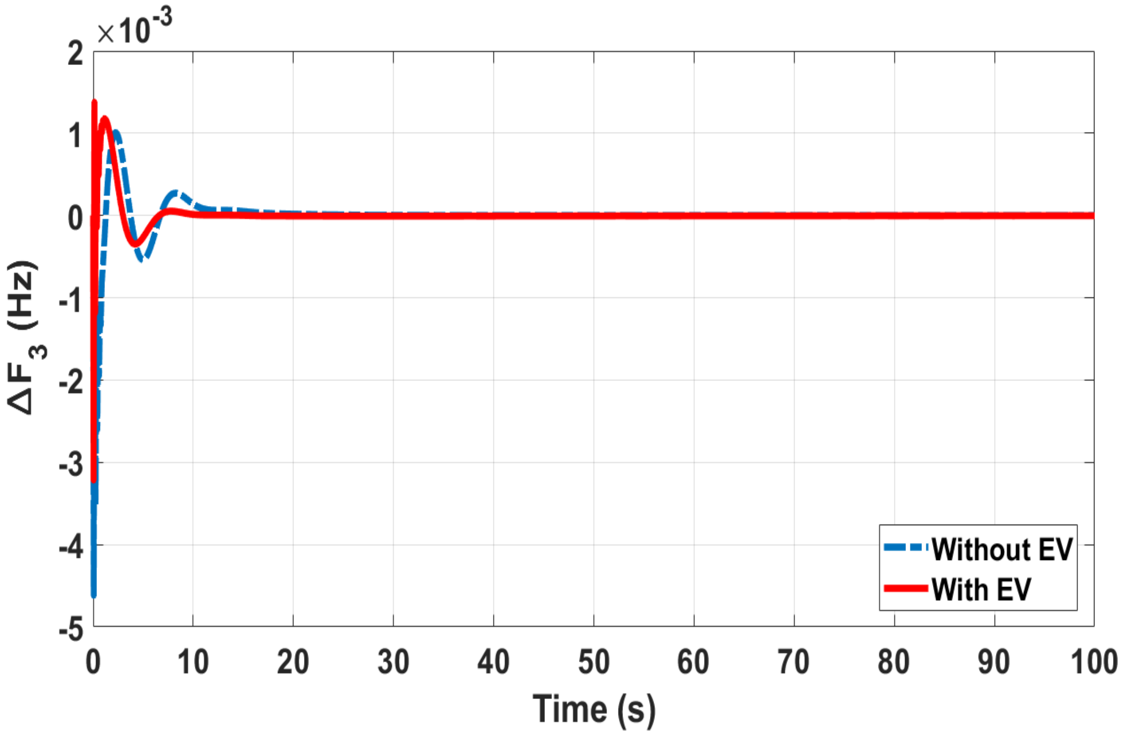

Figure 3.20 (c) System dynamic responses for Bilateral transaction case with and without EV integration: Area-3 deviation in frequency.

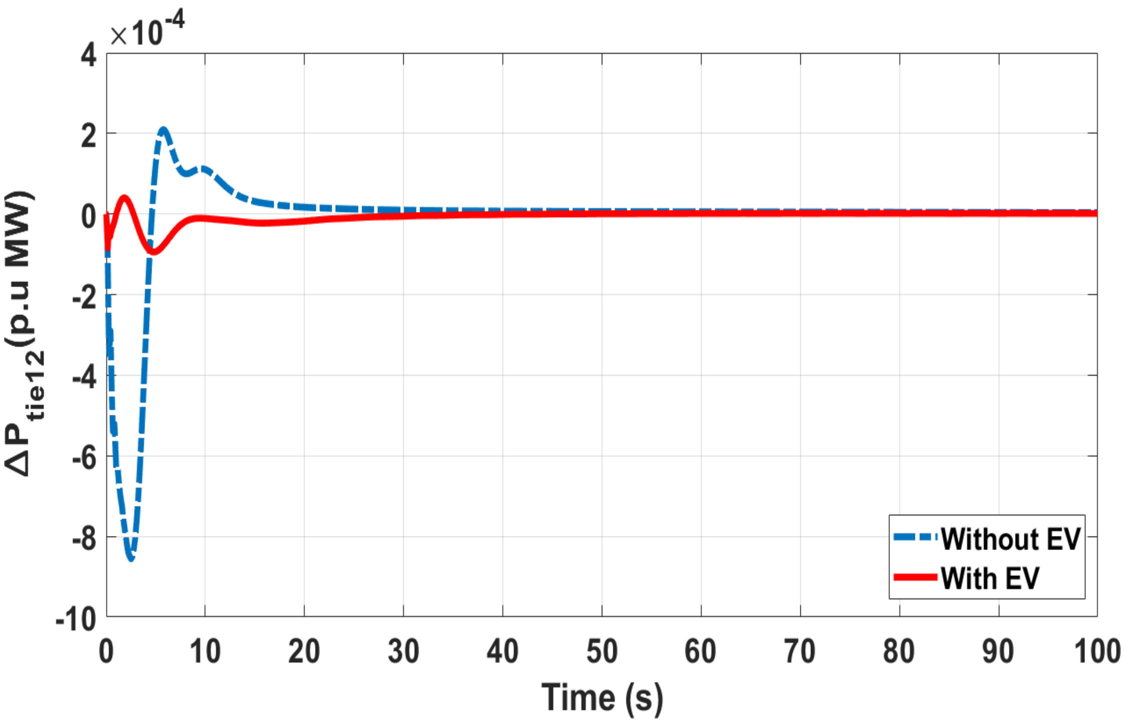

Figure 3.20 (d) System dynamic responses for Bilateral transaction case with and without EV integration: Deviation in tie line power between area-1 and -2.

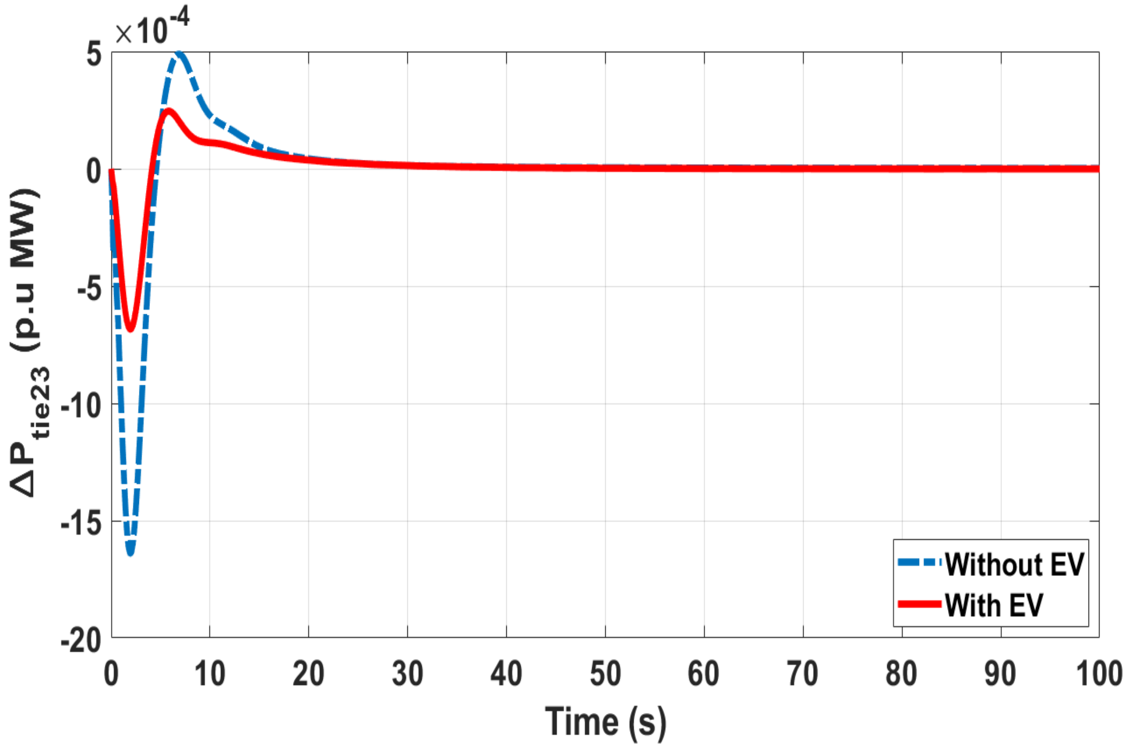

Figure 3.20 (e) System dynamic responses for Bilateral transaction case with and without EV integration: Deviation in tie line power between area-2 and-3.

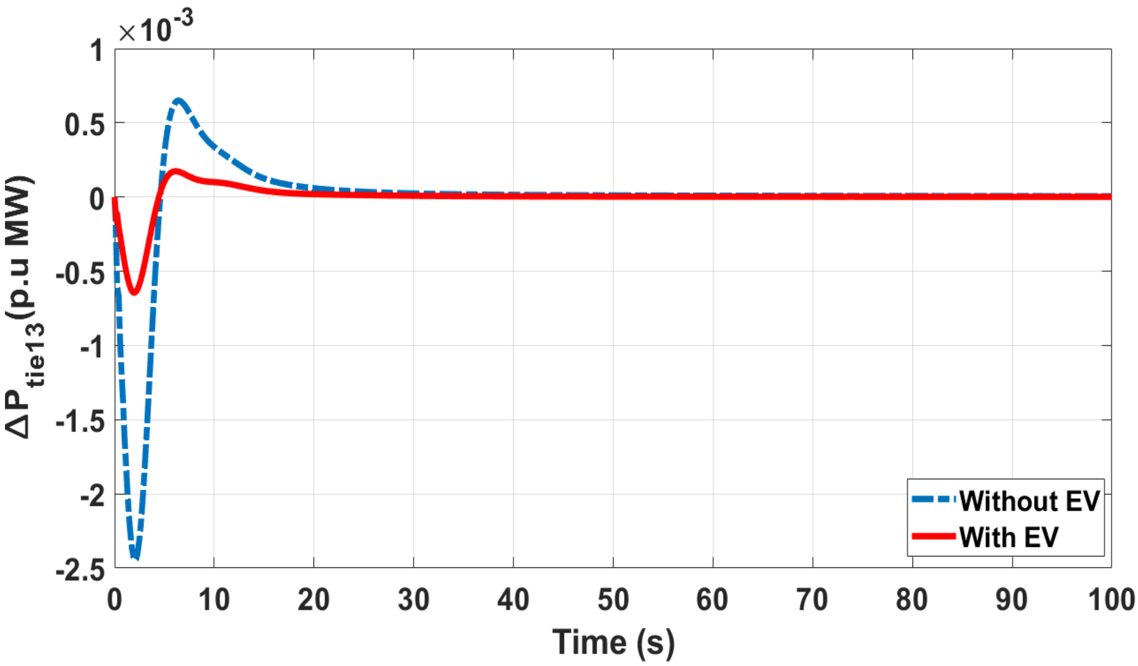

Figure 3.20 (f) System dynamic responses for Bilateral transaction case with and without EV integration: Deviation in tie line power between area-1 and -3.

3.4.2.3 Contract violation

This case represents a unique scenario within the previously mentioned cases, where the DISCOs break their contracts. In this particular instance, the GENCO, which is situated in the same region as the DISCO, fulfills the uncontract power requirement. Case study is presented involving a pool-based transaction in which DISCO 1 in area 1 requests an extra 0.005 p.u. MW in violation of the terms of the contract. Consequently, the local load demand in area-1 is adjusted as follows:

$$\Delta P_D = (0.01 + 0.01) + 0.005 = 0.025 \tag{3.25}$$

The change in EV power for different areas of contract violation case is shown in Figure 3.21. Also, Figure 3.22 illustrates the system's performance under the two scenarios, namely, 'with EV' and the scenarios of 'without EV'. The controller gain values for contract violation cases are presented in Table 3.13. The system dynamic response comparison between system with and without EV is given in Table 3.14 (a) and the improvement in percentage is given in Table 3.14 (b).

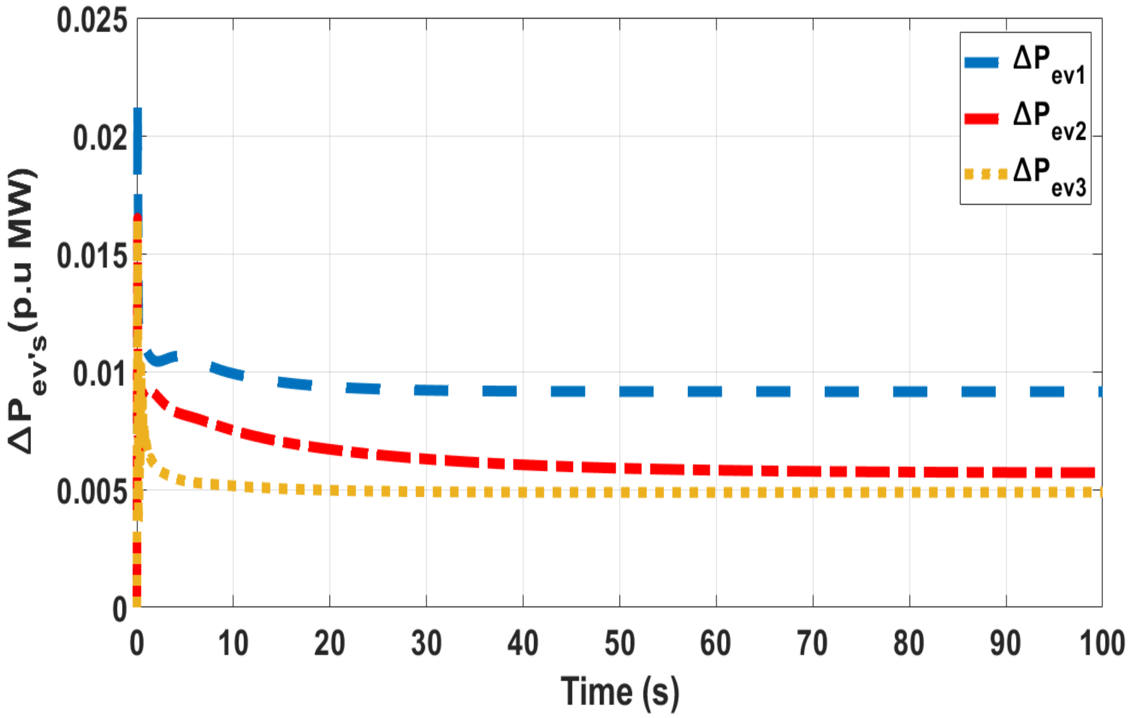

Figure 3.21 Change in EV power for different areas of Contract violation case

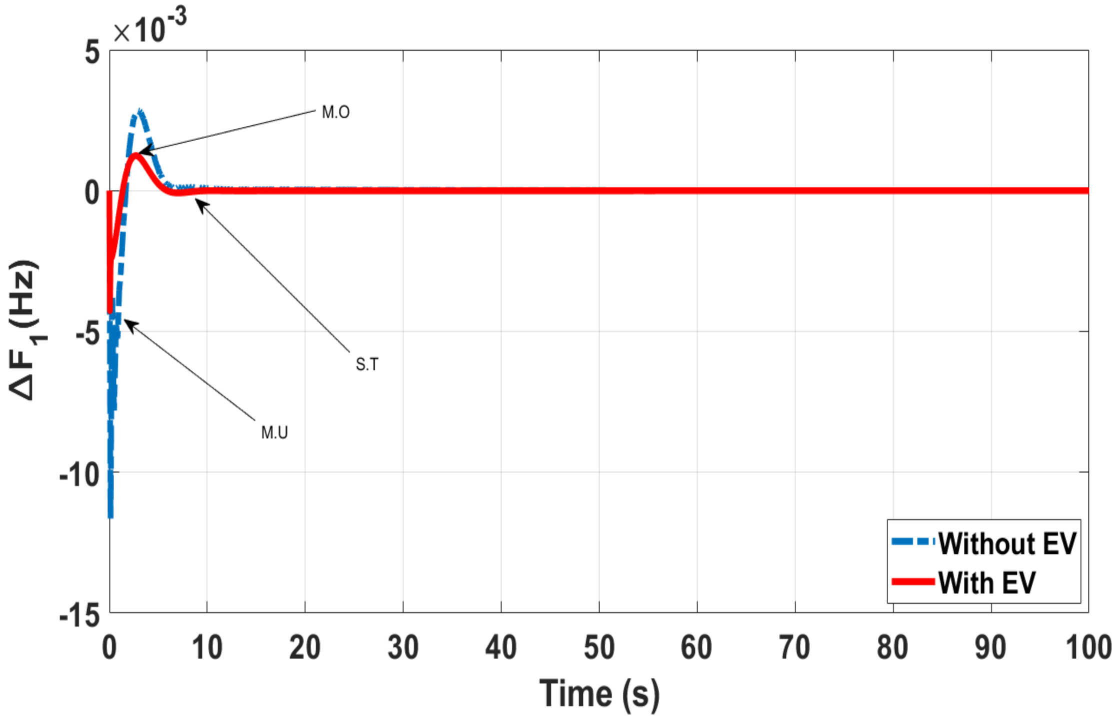

Figure 3.22 (a) System dynamic responses for Contract violation case with and without EV integration: Area-1 deviation in frequency.

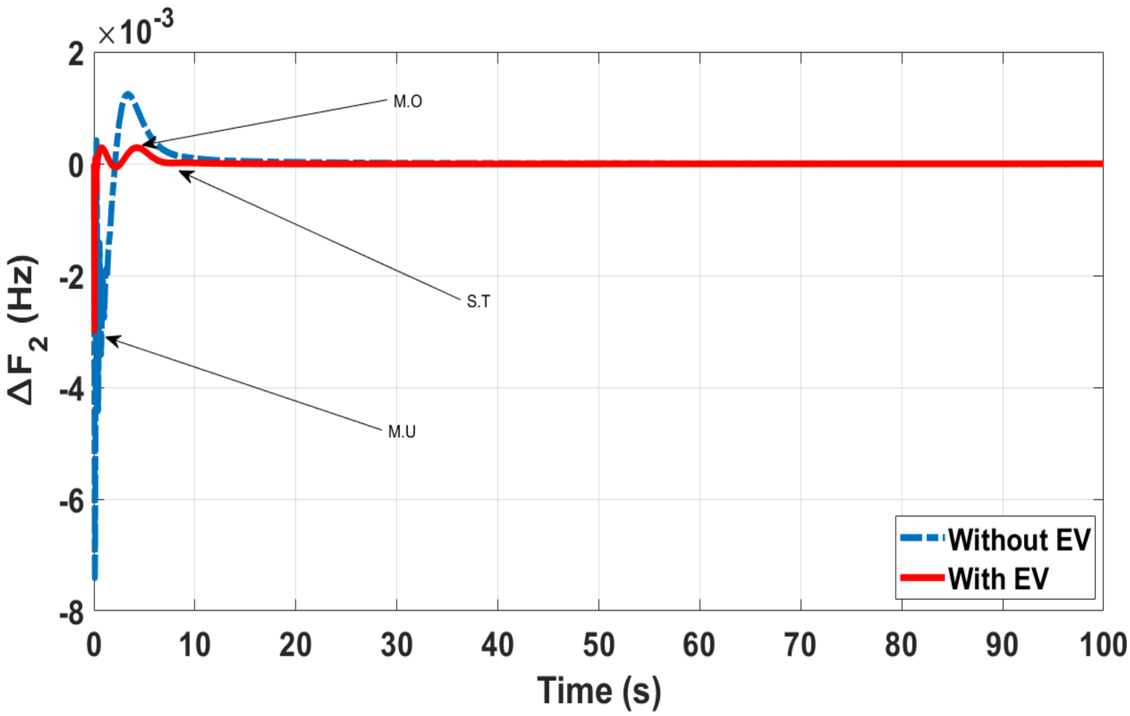

Figure 3.22 (b) System dynamic responses for Contract violation case with and without EV integration: Area-2 deviation in frequency.

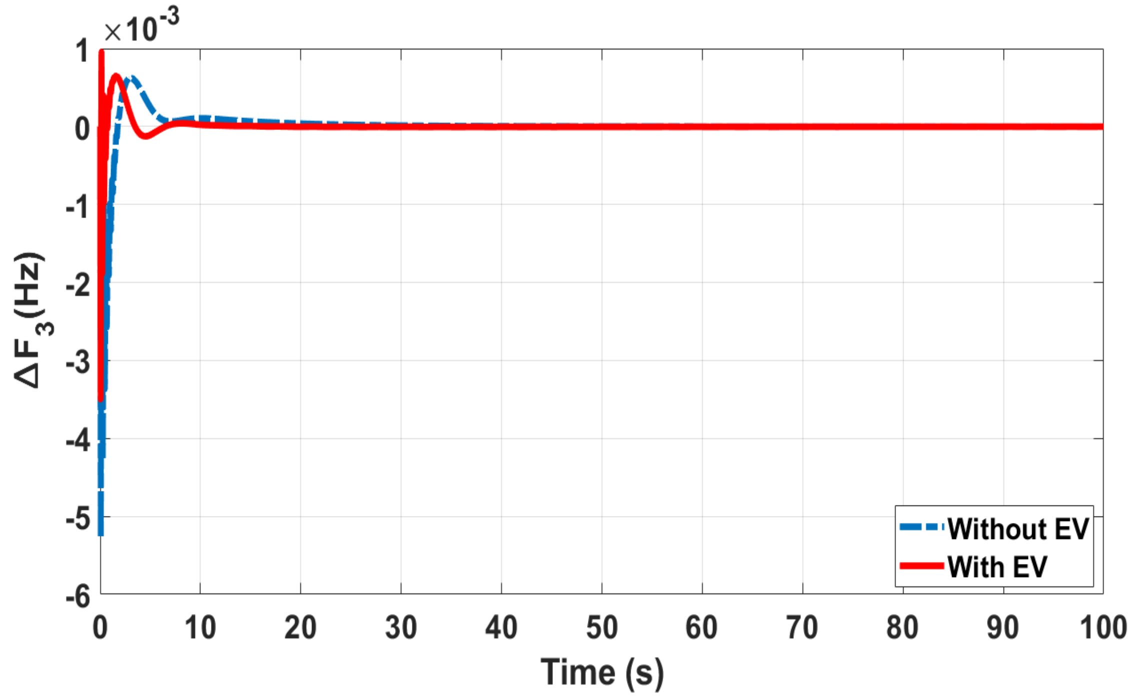

Figure 3.22 (c) System dynamic responses for Contract violation case with and without EV integration: Area-3 deviation in frequency.

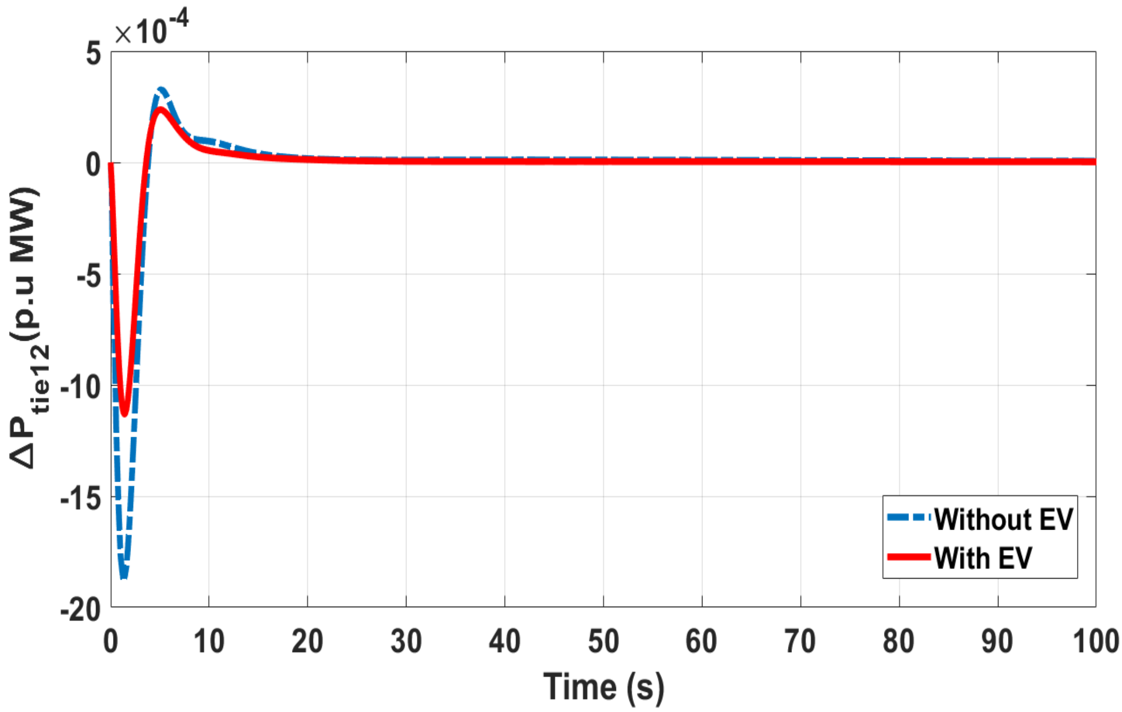

Figure 3.22 (d) System dynamic responses for Contract violation case with and without EV integration: Deviation in tie line power between area-1 and -2.

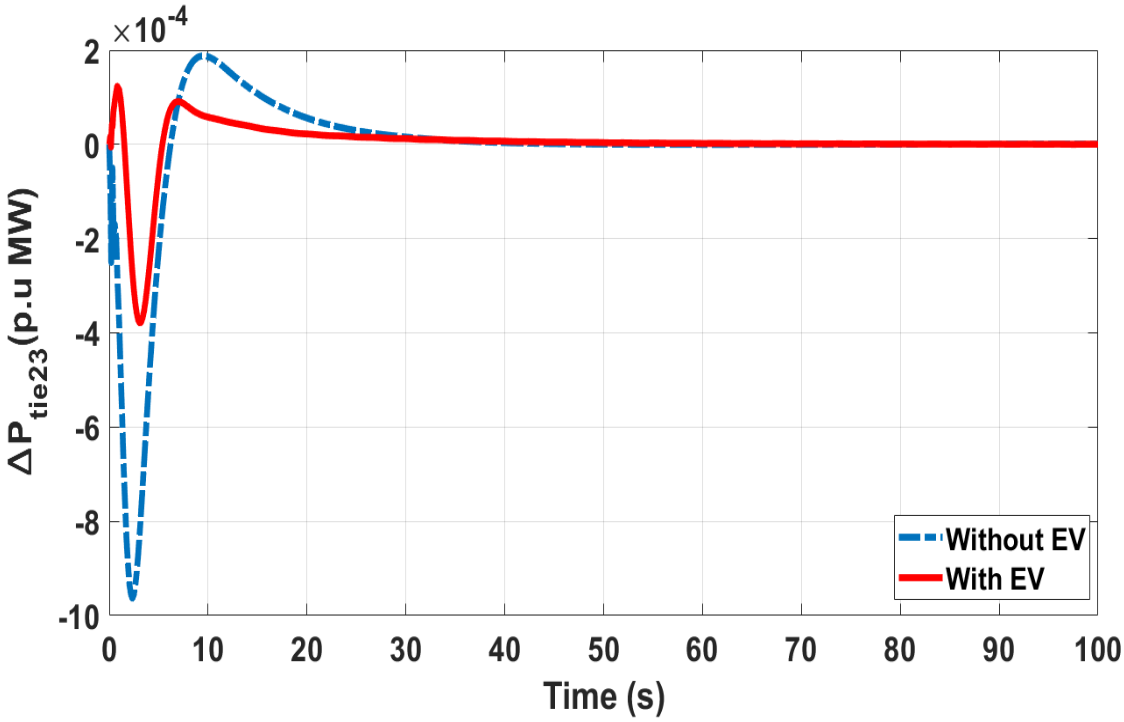

Figure 3.22 (e) System dynamic responses for Contract violation case with and without EV integration: Deviation in tie line power between area-2 and -3.

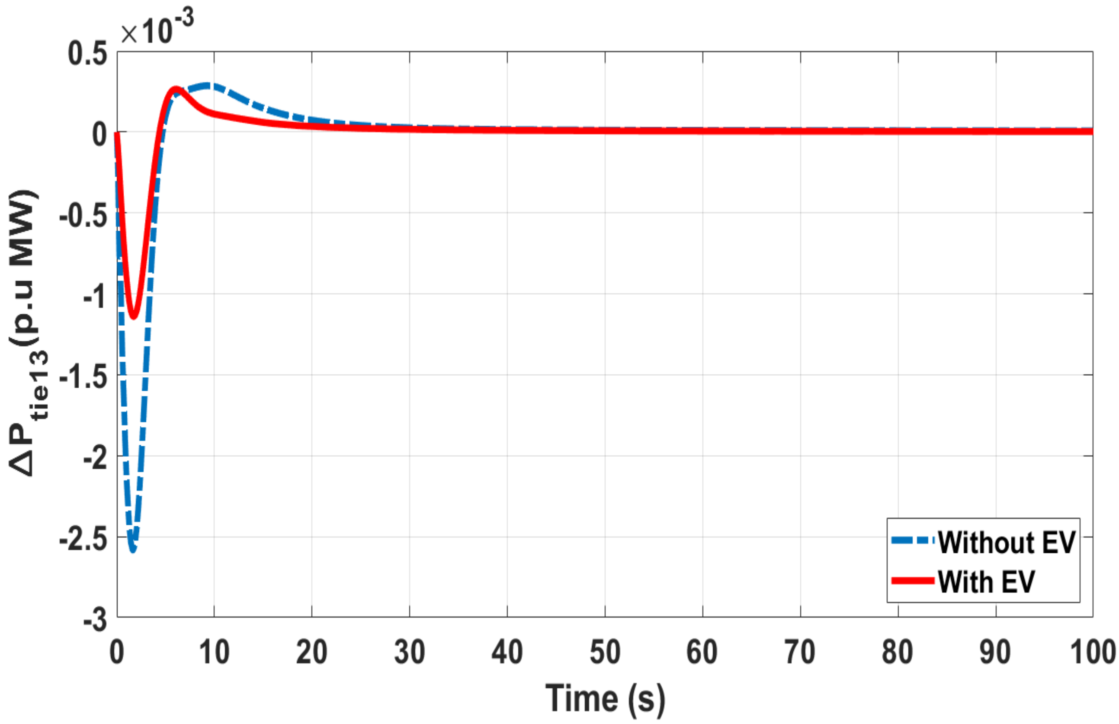

Figure 3.22 (f) System dynamic responses for Contract violation case with and without EV integration: Deviation in tie line power between area-1 and -3.

Table 3.14 (a) System dynamic response for deregulated system with the two scenarios of with and without EV.

Error		Unilateral Transaction		Bilateral Transaction		Contract Violation	
		S_1 Without EV	S_2 With EV	S_1 Without EV	S_2 With EV	S_1 Without EV	S_2 With EV
ΔF_1	M.U	-0.0094	-0.0038	-0.00983	-0.00437	-0.01166	-0.00426
	M.O	0.00249	0.00070	0.002732	0.000780	0.00284	0.001242
	S.T	8	5	9	5	7	7
ΔF_2	M.U	-0.0075	-0.0028	-0.00789	-0.00350	- 0.0074	-0.00298
	M.O	0.00145	0.00060	0.002256	0.000846	0.00124	0.000285
	S.T	10	6	7	6	13	6
ΔF_3	M.U	-0.0054	-0.0027	-0.00461	-0.00321	- 0.0052	-0.00349
	M.O	0.00051	0.00084	0.001006	0.001377	0.00061	0.000956
	S.T	11	8	13	7	15	10
ΔP_{tie12}	M.U	-0.0014	-0.0007	-0.00085	-0.00009	-0.00188	-0.00113
	M.O	0.00048	0.00015	0.000209	0.000040	0.00032	0.000235
	S.T	20	18	20	9	19	15
ΔP_{tie23}	M.U	-0.0010	-0.0001	-0.00163	-0.00068	-0.00096	-0.00037
	M.O	0.00026	0.00014	0.000488	0.000245	0.00018	0.000123
	S.T	24	16	21	20	23	17
ΔP_{tie13}	M.U	-0.0025	-0.0007	-0.00244	-0.00064	-0.00258	-0.00114
	M.O	0.00063	0.00029	0.000649	0.000173	0.00028	0.000264
	S.T	21	16	25	16	31	26

Table 3.14 (b) Percentage improvement by integrating EV in each scenario of deregulation

Error		Unilateral S_2 over S_1	Bilateral S_2 over S_1	Contract violation S_2 over S_1
ΔF_1	M.U	58.63	55.51	63.39
	M.O	71.78	71.43	56.33
	S.T	37.50	44.44	0.00
ΔF_2	M.U	61.84	55.61	59.68
	M.O	58.22	62.50	77.07
	S.T	40.00	14.29	53.85
ΔF_3	M.U	49.75	30.34	33.68
	M.O	-63.55	-36.88	-54.71
	S.T	27.27	46.15	33.33

Table 3.14 (b) (Contd.) Percentage improvement by integrating EV in each scenario of deregulation

Error		Unilateral S_2 over S_1	Bilateral S_2 over S_1	Contract violation S_2 over S_1
ΔP_{tie12}	M.U	52.38	88.99	39.90
	M.O	68.42	80.74	27.71
	S.T	10.00	55.00	21.05
ΔP_{tie23}	M.U	82.85	58.26	60.76
	M.O	44.77	49.65	34.20
	S.T	33.33	4.76	26.09
ΔP_{tie13}	M.U	72.26	73.64	55.83
	M.O	53.32	73.30	7.26
	S.T	23.81	36.00	16.13

Analysis: The results presented in Table 3.14(b) confirm that integrating Electric Vehicles (EVs) enhances the dynamic performance of deregulated power systems across all transaction scenarios. In unilateral transactions, EVs reduce undershoot and overshoot by more than 58% on average, while also shortening settling time by about 40%, reflecting improved system stability. In bilateral transactions, the improvements are most pronounced, with overshoot reductions exceeding 70% in several cases and average overall gains of nearly 48%, highlighting the flexibility of EV fleets in market-based operations.

Under contract violation conditions, the enhancements are less uniform, particularly in settling time where no improvement was observed in some cases; however, undershoot and overshoot still improve by more than 50% in most instances. Overall, the analysis demonstrates that EV participation significantly strengthens system resilience under deregulated operations, with the greatest benefits observed in bilateral market scenarios

3.4.3 Eigen value analysis

The Eigen value analysis is done for analyzing the capability of the proposed controller for obtaining system stability. The different types of controllers like integral, Proportional-Integral, Tilt-Integral-Derivative, Tilt-Integral-Derivative cascaded with Fractional Order Tilt-Integral and the proposed 2-Degree of Freedom Tilt-Integral-Derivative with filter cascaded with Fractional Order Tilt-Integral controllers whose gain values are optimized with the Zebra optimization algorithm under the presence of non-linearities like Generation Rate Constraints and Governor Dead Band for the reheat thermal system in each area is analyzed under the deregulated environment. The eigen values along with the minimum damping ratios are presented in Table 3.15.

Table 3.15 Eigen values for system with different controllers of EV integration

Controllers	Eigen values	Minimum damping ratio
I	-3.3333, -0.1000, -3.3333, -0.1000, -3.3333, -0.1000, -12.5000, -12.5000, -12.5000, -25.9292, -24.3063, -21.6954, -12.8002, -14.0027, -3.0392, -3.0392, -4.6096, -4.6096, -3.0758, -3.0758 - 6.9116i, -8.5561, -10.0000, -1.9873, -1.9873, -0.6911, -0.6911, -0.4527, -0.4527 - 0.7497i, -1.2424, -1.2424, -1.0000, -0.3830, -0.0540, -5.0000, 0.0000	0.0097
PI	-3.3333, -0.1000, -3.3333, -0.1000, -3.3333, -0.1000, -12.5000 + 0.0000i, -12.5000, -12.5000, -27.1411, -22.2349, -24.3282, -4.3095, -4.3095 - 9.4794i, -2.5584 + 9.3059i, -2.5584 - 9.3059i, -2.5926, -2.5926, -13.2888, -13.2888, -10.0000, -8.6370, -1.9416, -1.9416, -1.4048, -1.2853, -1.2853, -1.0000, -0.6207, -0.6207, -0.6563, -0.0000, -0.2723, -0.0541, -5.0000, 0.0000, 0.0000, -0.5556	0.0163
TID	-0.0033, -0.0033, -0.0033, -0.0001, -0.0125, -0.0001, -0.0125, -0.0001, -0.0125, -1.1111, -1.1111, -1.1111, -1.0000, -1.0000, -1.0000, -0.4037, -0.3900, -0.3899, -0.1150, -0.1111, -0.1110, -0.0328, -0.0316, -0.0313, -0.0265, -0.0243, -0.0218, -0.0127, -0.0141, -0.0027, -0.0027, -0.0039, -0.0039, -0.0027, -0.0027, -0.0100, -0.0097, -0.0094, -0.0091, -0.0087, -0.0029, -0.0025, -0.0026, -0.0019, -0.0019, -0.0050, -0.0011, -0.0011, -0.0013, -0.0013, -0.0008, -0.0008, -0.0010, -0.0009, -0.0006, -0.0006, -0.0004, -0.0002, -0.0002, -0.0002, -0.0001, -0.0001, -0.0001, -0.0001, 0.0000	0.0288
TID-FOTI	-0.0033, -0.0033, -0.0033, -0.0001, -0.0125, -0.0001, -0.0125, -0.0001, -0.0125, -0.9996, -0.9996, -1.1115, -1.1115, -1.1114, -1.1114, -1.1115, -1.1115, -0.9996, -0.9996, -0.9996, -0.9996, -1.0000, -0.3772, -0.4318, -0.3846, -0.3972, -0.4257, -0.4172, -0.4204, -0.4201, -0.4195, -1.0000, -0.1073, -0.1130, -0.1228, -0.1213, -0.1187, -0.1196, -0.1196, -0.1194, -1.0000, -0.1095, -0.0368, -0.0354, -0.0304, -0.0345, -0.0339,-0.0339, -0.0338, -0.0325, -0.0320, -0.0244, -0.0201, -0.0194, -0.0092, -0.0092 - 0.0124i, -0.0054, -0.0054, -0.0137, -0.0052, -0.0052, -0.0126, -0.0100, -0.0096, -0.0096, -0.0095, -0.0093, -0.0093, -0.0092, -0.0090, -0.0070, -0.0066, -0.0065, -0.0050, -0.0024,-0.0024, -0.0028, -0.0027, -0.0027, -0.0026, -0.0026, -0.0023, -0.0005, -0.0005, -0.0003, -0.0003, -0.0019, -0.0019 - 0.0000i, -0.0018, -0.0012, -0.0012, -0.0012, -0.0007, -0.0007, -0.0011, -0.0010, -0.0006, -0.0008, -0.0008, -0.0007, -0.0005, -0.0005, -0.0005, -0.0004, -0.0004, -0.0002, -0.0002, -0.0002, 0.0000	0.1049

Table 3.15 (Contd.) Eigen values for system with different controllers

Controllers	Eigen values	Minimum damping ratio
2DOFTIDN-FOTI	-0.0033, -0.0033, -0.0033, -0.0001, -0.0125, -0.0001, -0.0125, -0.0001, -0.0125, -1.1115, -1.1115, -0.9995, -0.9995, -1.1114, -1.1114, -1.1112, -1.1112, -0.9994, -0.9994, -0.9997, -0.9997, -0.5144, -1.0000, -0.4323, -0.4323, -0.4327, -0.4160, -0.3885, -0.3919, -0.4093, -0.4095, -1.0000, -1.0000, -0.1465, -0.1232, -0.1232, -0.1240, -0.1187, -0.1107, -0.1116, -0.1166, -0.1166, -0.0529, -0.0057, -0.0057, -0.0402, -0.0402, -0.0402, -0.0380, -0.0343, -0.0351, -0.0350, -0.0061, -0.0061, -0.0333, -0.0316, -0.0332, -0.0071, -0.0071, -0.0244, -0.0186, -0.0164, -0.0145, -0.0131, -0.0110, -0.0102, -0.0099, -0.0100, -0.0098, -0.0090, -0.0094, -0.0094, -0.0089, -0.0048, -0.0046, -0.0039, -0.0050, -0.0030, -0.0027, -0.0028, -0.0026, -0.0026, -0.0024, -0.0021, -0.0021, -0.0015, -0.0009, -0.0009, -0.0013, -0.0005, -0.0005, -0.0012, -0.0010, -0.0010, -0.0010, -0.0007, -0.0007, -0.0009, -0.0004, -0.0004, -0.0008, -0.0007, -0.0006, -0.0006, -0.0005, -0.0004, -0.0003, -0.0003, -0.0003, -0.0002, -0.0002 , -0.0002, -0.0002, -0.0001,-0.0001, -0.0006,	0.2114

Analysis: From the result presented in Table, it has been observed that the damping factor obtained by the proposed cascaded 2DOFTIDN-FOTI controller is higher than the other controllers which mean that the controller is maintaining system stability by damping out the oscillations faster than the rest and the Eigen values lies on the left half of the s-plane.

3.5 Conclusion

The study thoroughly investigates and analyzes the effectiveness of AGC in managing both traditional power sources and distributed generation, particularly focusing on enhancing frequency regulation under various conditions and deregulation scenarios. The research delves into the comprehensive evaluation of Distributed Generation (DG) units in the face of unpredictable weather conditions and fluctuating load demands. To provide a realistic assessment of the AGC framework, the study also considers and examines non-linearities, such as the GDB and GRC of 3% per minute in each reheat-thermal plant. An innovative approach is introduced, utilizing the cascaded 2DOFTIDN-FOTI controller, successfully applied to the test system under investigation. Furthermore, the study incorporates Electric Vehicles. It also introduces ZOA to optimize the control parameters for the employed controllers in the test system. Comparison is done between the proposed and different types of algorithms that are found in the literature, demonstrating its efficacy and superiority. A comprehensive performance evaluation shows its superiority under the analyzed scenario. Ultimately, the study conclusively shows that the proposed AGC controller significantly improves the deviation in frequency and fluctuations in tie-line power within the test system. The research presents distinct and improved results to validate frequency response of the system. Through different deregulation scenarios, comparative analyses with alternative controllers, sensitivity assessments in response to random load changes and eigen-value analysis, robustness is verified.

CHAPTER 4
Impact of Virtual Inertia Control in Hybrid Generating Sources based Multi-Area Power System

4.1 Introduction

Modern power grids now face new issues in ensuring stability and reliability due to the growing integration of renewable energy sources and decentralized power generation. Because renewable energy sources have less inertia than conventional synchronous generators, frequency regulation-a crucial component of grid stability-is threatened. By modifying power production in response to disturbances, automatic generation control, or AGC, is essential to preserving grid frequency. Grid stability is threatened by frequency variations, which are made worse by the waning system inertia [Mahmoud 2017; Zhong and Hornik 2013; Zhang et al. 2012]. A Virtual inertia control (VIC), which mimics the inertial response of conventional generators through sophisticated control algorithms, has emerged as a promising solution to this problem. This research investigates the use of VIC in AGC, outlining how it could improve grid stability and providing a thorough methodology for doing so. We can guarantee a more robust and adaptable power grid that can handle the changing landscape of power generation and consumption by incorporating VIC into AGC [Bevrani et al. 2014].

AGC has been the subject of extensive research in the past, beginning with a single area and expanding it to a several areas while taking traditional energy sources such as thermal power plants as a base source. The increased demand for electricity and the quick use up and depletion of non-renewable energy sources are the driving forces behind the growth of renewable energy sources (RESs). Nowadays, more and more research are being done on the integration of these RES in the power systems. A survey of RESs and the problems associated with integrating them into the system [Bevrani et al. 2010]. Researchers are increasingly concentrating on examining the effects of RESs on system dynamic performances due to the growing use of RESs in the power system [Tasnin, Saikia, and Raju 2018; Raj and Shankar 2020]. Through a variety of power electronics devices, the RESs exchange their energy to the grid, lowering voltage and deviations, transmission losses, and improving system reliability by the use of power electronics-based systems, such as solar photovoltaic sources and wind energy which are positioned close to the distributed sites. The grid is supported in maintaining the balance between the generation and demand by the introduction of RESs. Even though converter-based RESs support the grid by supplying energy, as the demand for electronically coupling RESs with the grid increases, they weaken the inertia of the system, which results in a significant reduction of the system's inertia because the RESs has very little rotating mass and damping property [Torres et al. 2014]. In the end, this loss of inertia leads to frequency deviation, which directly deteriorates the power system's ability to operate by causing system instability and generating unit blackouts [Yan and Saha 2015; Spahic et al. 2016]. AGC study has a plethora of literature that considers many sources, including biogas turbine generators (BGTG), geothermal power plants (GTPP), solar photovoltaic plants (SPV), and wind turbine generators (WTG) [Tasnin et al. 2018; Barik and Das 2018].

Traditional synchronous generators' dampening capabilities and inertia power make them essential for preserving frequency stability. The bulk synchronous generator's (SG) damping property and rotor's kinetic energy or inertia plays a crucial part in achieving the system's required operational stability. A novel idea known as virtual inertia control (VIC) has been proposed to increase operating system stability. It adds extra inertia power to the system momentarily through virtual means. The Virtual Synchronous Generator (VSG) idea was put into practice in order to increase system inertia and attain stability. To effectively modify power in a DG-based microgrid, the authors Zhao et al. 2017 proposed a multi-loop control system based on VSG. The virtual synchronous machine (VISMA) idea has been used to the FDG-based microgrid in order to lower frequency deviation and achieve improved overall system dynamic performance. The author Li et al., 2016 presented damping combination control and self-adaptive inertia strategies to increase stability. The authors Feng et al., 2011 suggests using flywheels to improve inertia support, whereas others like Rakshani et al. 2016 and Kerdphol, 2018 recommend battery storage. The performance of various energy storage systems in AGC is examined by the authors Tasnin and Saikia 2018. Energy source (ES) devices plus an appropriate control framework make up VIC. By delivering or storing more power from the grid according to a Rate of change of frequency (ROCOF) approach, virtual inertia can be replicated using ES. In order to achieve high penetration of RESs, grid resilience and stability can be controlled through the use of virtual inertia emulator techniques [Sockeel et al. 2020]. To improve system dynamic performance, the control approach for VIC mimicked the features of the synchronous generator [Longatt et al. 2012]. A virtual inertia emulator was used to apply a number of control strategies to enhance microgrid frequency stability.

The H_∞ based VIC was included by the authors Kerdphol et al. 2017 to reduce frequency variation in a single area microgrid powered by solar and wind energy. In a wind energy based single area microgrid system, an artificial inertia technique with Proportional Integral (PI) controller has been presented to manage the system frequency and extract maximum power from it [Menteisidi et al. 2015]. Because of the high penetration level of RESs, the authors Magdy et al. 2019 suggested a coordination technique of frequency control that includes PI-VIC and digital over/under frequency protection in order to improve frequency stability and maintain the security of the system dynamics. To enhance the frequency stability of a single area system, fuzzy logic-based VIC has been implemented [Datta et al. 2012]. The authors Saxena et al. (2020) introduced the Derivative (D) controlled solar and ES to address the inertia deficiency and improve the stability of RESs based microgrid system. In order to lessen frequency variation in an AC/DC link-based two area interconnected power system, the authors Rakshani et al. 2016 and Kerdphol 2018 suggested a VIC technique based on D controllers. The authors Kerdphol et al. 2019 presented a D controller-based virtual inertia and damping system to simulate virtual damping and inertia in order to enhance grid frequency stability within a specific area. In a single area system comprising solar and wind energy sources, the coefficient diagram approach has been used to reduce frequency deviation [Ali et al. 2019]. In order to manage RESs, the authors Sockeel et al. 2020 suggested a model predictive control (MPC) based on VIC for controlling grid frequency regulation. A microgrid's fractional order fuzzy controller-based VIC is examined by Mahto et al. 2021. The impact of VIC in a two-area system with a Bacteria Swarming Algorithm (BSA) optimized 2 Degree of Freedom-Tilt Integral Derivative (2DOF-TID) controller is also examined by Bhagat et al. 2021. A two-layer multiple model predictive control technique is used for an islanded microgrid's virtual inertia control [Oshnoi et al. 2023]. Similarly, the authors deploy a Neural Network (NN)-based Variable Fractional Order PID (VFOPID) controller in an islanded microgrid to implement a virtual inertia control approach [Skiparev et al. 2023]. The effect of a cascade Proportional Integral-Tilt Integral (PI-TI) based virtual inertia controller with virtual damping on a multi-area power system based on renewable energy under deregulation is studied by Das et al. 2022. Authors Das et al. 2023 investigate the effects of a Mine Blasting Algorithm (MBA)-optimized Derivative Fractional Order Proportional Integral-Tilt Integral Derivative with filter (DFOPI-TIDN) controller for VIC in a three-area system. Thus, as a VIC controller, a novel Tilt double integral derivative with filter (TI-IDN) controller is designed.

The optimization of VIC in AGC makes use of a variety of optimization algorithms. The authors Trojovska et al. 2022 create the Zebra Optimization Algorithm (ZOA), a novel bio-inspired metaheuristic algorithm based on the protection mechanisms used by zebras in the wild. In order to optimize the controller-gain settings of the Proportional Integral Derivative Filter-Tilt Integral Derivative Filter (PIDN-TIDN) controller for frequency regulation in the offshore fixed platforms microgrid [Zare et al. 2023].

The key contributions of the present work are as follows:

1. Developed a four-area hybrid power system, with unequal areas, under conventional and deregulated environments, comprising 8 generating companies (GENCOs) and 8 distribution companies (DISCOs). Area-1 includes a reheat thermal power plant (RTPP) with non-linearities and a solar photovoltaic plant (SPV); Area-2 has an RTPP and a geothermal power plant (GPP); Area-3 consists of an RHTPP and a wind turbine generator (WTG); and Area-4 features an RTPP and a biogas turbine generator (BGTG) whose combination with VIC are not yet investigated in AGC.
2. Designed a new controller known as the TI-IDN controller, which is not yet used in AGC and specifically for the Virtual Inertia Control (VIC) technique.
3. Implemented VIC with virtual damping in the four-area power system under deregulation which is not yet analysed and evaluated the system's performance.
4. Conducted a sensitivity analysis of the proposed controller by comparing with existing controller for VIC.

4.2 Modelling of the investigated system

An analysis is being conducted on four unevenly linked areas with multi-source systems, each with RTPP and a renewable resource such as SPV, GPP, WTG, and BGTG in both regulated and unregulated environments. The area-1 = 2000MW, area-2 = 4000MW, area-3 = 4000MW, and area-4 = 2000MW constitute the capacity ratio, which is regarded as 1:2:2:1. It is expected that each area has two DISCOs and two GENCOs. In order to increase dynamic performance in both regulated and unregulated scenarios, the VIC techniques are integrated into varied sources based four area linked systems. This suppresses the oscillation induced by unexpected load disturbance. Non-linearities like GRC is subsequently taken into account for the RTPP, wherein GRC sets a maximum rate of change in the thermal plant's power generation. A GRC of 3%/min is kept with the RTPP for the study. The Zebra optimization technique is used to optimize both gain levels. The secondary controller is a traditional Integral (I) controller, and the VIC controller is the TI-IDN controller. The objective of the modelling is to examine the AGC in both regulated and unregulated environments using an uneven linked four area system consisting of an RTPP, SPPV, GTP, WTP, and BGP with the incorporation of VIC. Figure 4.1 shows the complete simulink blocks of the study power system under regulated market and Figure 4.2(a) and (b) shows the system under deregulated environment.

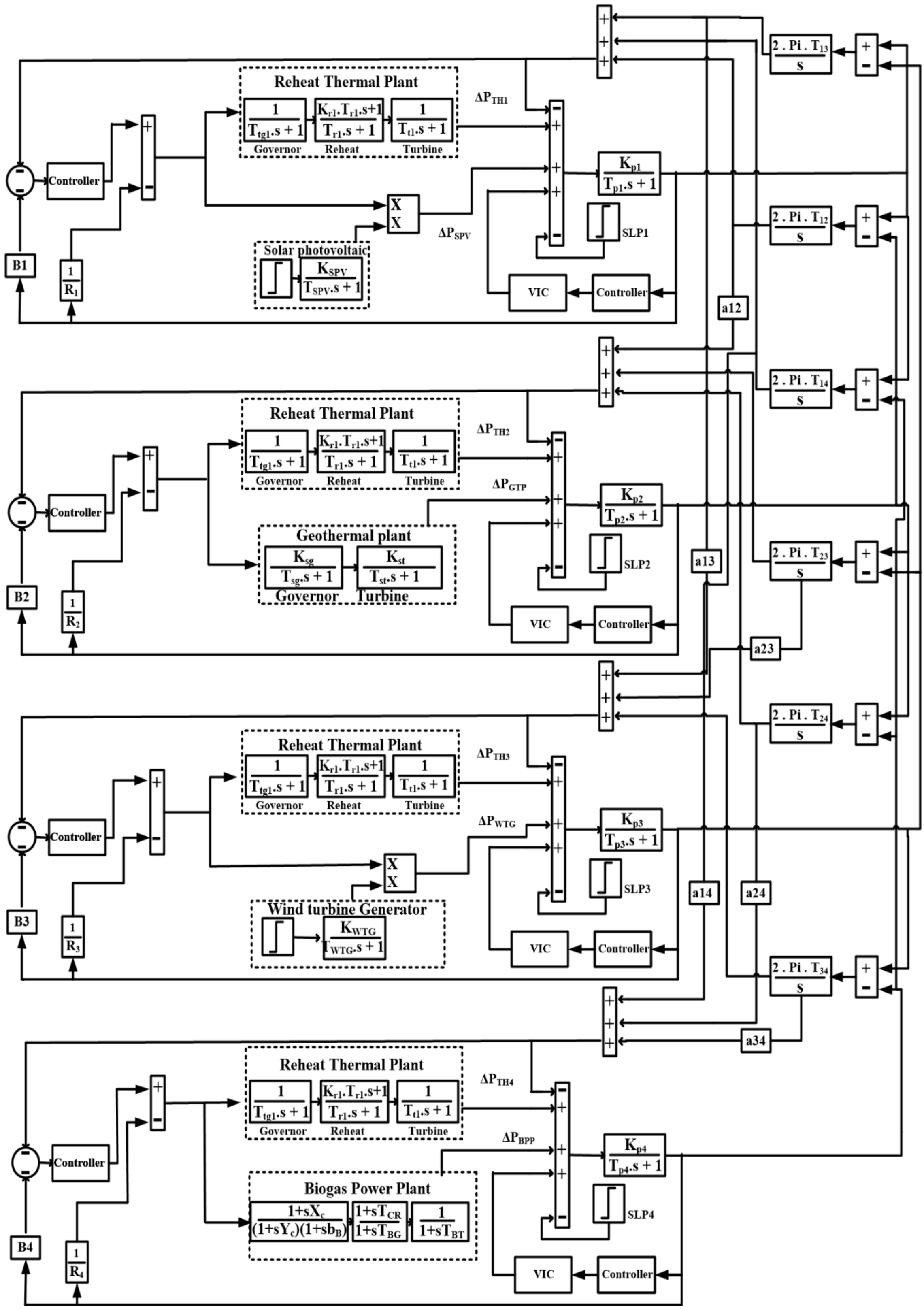

Figure 4.1 Transfer function model of the four-area power system with integration of VIC under regulated environment.

The output of the controller is split among the GENCOs in accordance with their Area participation Factor (APF), which establishes each GENCO's level of involvement. From the previous study in Chapter 3, it is proved that ISE performs better than the other objective functions and is used for this study as shown in (4.1).

The integration of VIC within the four-area interconnected system represents a paradigm shift in addressing the challenges posed by high renewable energy penetration. Traditional power systems rely heavily on the inherent inertia provided by synchronous generators, which naturally dampen frequency oscillations during load disturbances. However, with the increasing deployment of renewable energy sources through power electronic converters, this natural inertia diminishes significantly, leading to rapid frequency deviations and potential system instability. The proposed VIC framework addresses this critical gap by synthetically replicating the inertial response characteristics of conventional generators. By incorporating energy storage systems and implementing sophisticated control algorithms, the VIC mechanism provides instantaneous active power injection or absorption based on the rate of change of frequency. This proactive response occurs faster than traditional primary frequency control mechanisms, thereby arresting the initial frequency deviation and providing the system with sufficient time for secondary control actions to restore the nominal frequency. The implementation of VIC across all four areas ensures coordinated system-wide support.

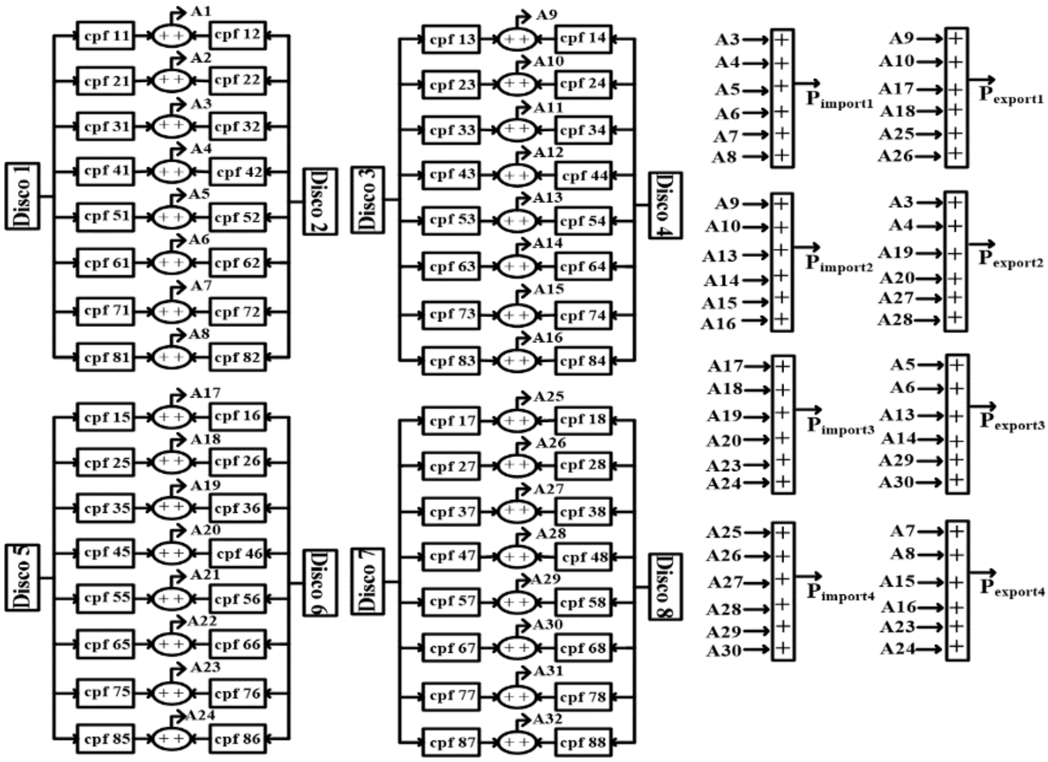

Figure 4.2 (a) Complete simulink model of a four area VIC integrated power system: Deregulated system.

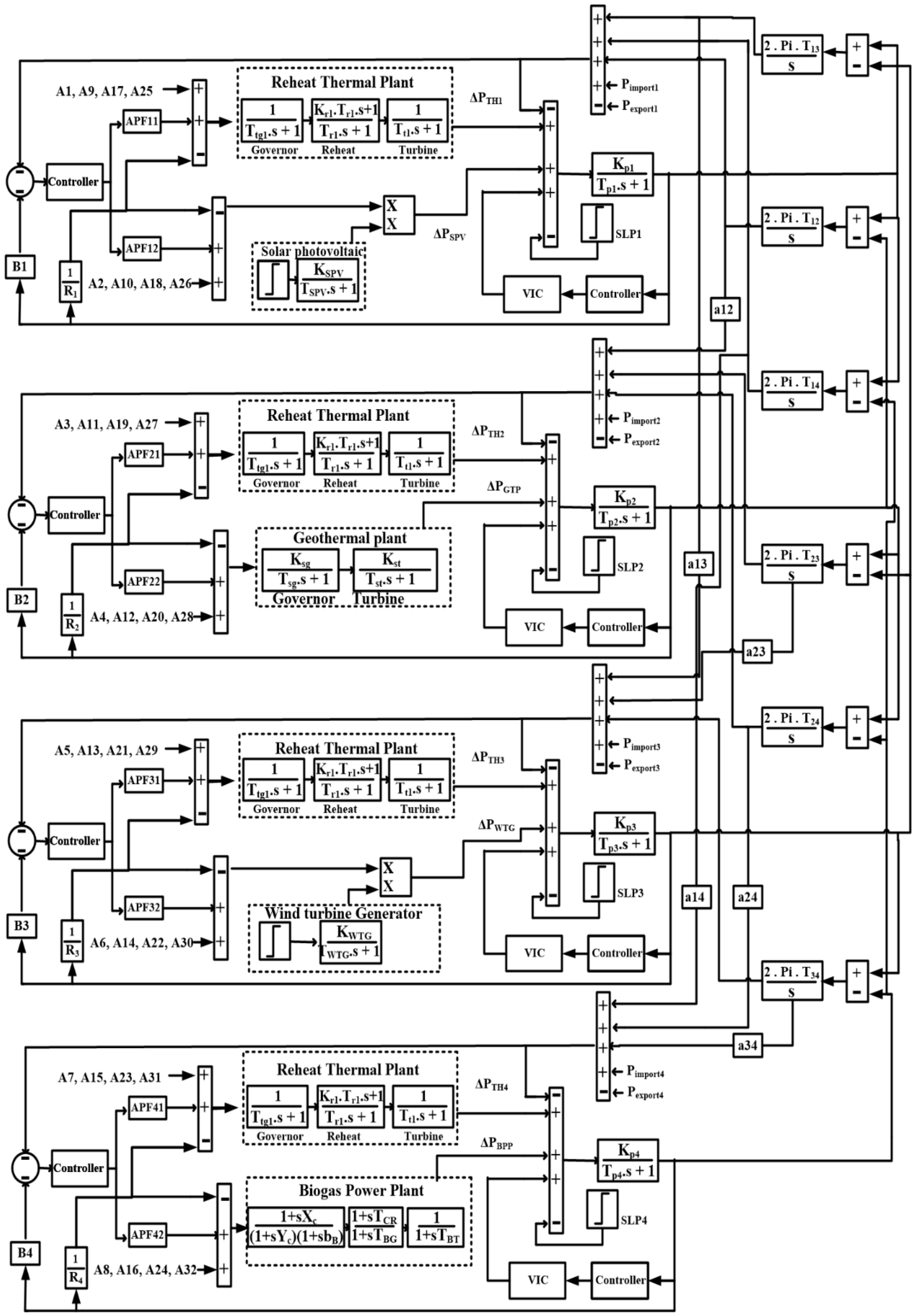

Figure 4.2(b) Complete simulink model of a four area VIC integrated power system: Transfer function model of a four area VIC integrated power system.

The selection of the TI-IDN controller as the primary VIC controller is predicated on its superior capability to handle multi-objective optimization requirements inherent in modern power systems. The controller architecture combines the benefits of tilt integral action with integral derivative characteristics, providing enhanced flexibility in tuning and improved transient response performance. The tilt parameter 'n' introduces an additional degree of freedom, allowing the controller to adapt its response characteristics based on system operating conditions and disturbance patterns. Furthermore, the inclusion of a derivative filter prevents high-frequency noise amplification while maintaining the controller's ability to respond rapidly to genuine frequency deviations.

The six tuning parameters of the TI-IDN controller are meticulously optimized using the Zebra Optimization Algorithm, which employs bio-inspired strategies to navigate the complex multi-dimensional search space effectively. This optimization ensures that the controller parameters are finely tuned to minimize the integral square error objective function while simultaneously maintaining system stability margins and ensuring adequate damping of inter-area oscillations that characterize multi-area interconnected power systems.

$$J_{ISE} = \int_0^T \left[\left(\Delta f_d \right)^2 + \left(\Delta P_{tie\_error,de} \right)^2 \right] dt \qquad (4.1)$$

4.3 Virtual inertia Control Technique

When RESs penetration in a power system is large, the inertia of the system is reduced. In order to improve the dynamic stability of the system, AGC has implemented the VIC approach. By adding active power to the grid, ROCOF is used in this strategy to increase system inertia. An energy storage device is required for this procedure. The ES's converter acts as a controller to keep it charged under typical circumstances. ES will automatically detect the ROCOF signal when there exists a change in load, and it will quickly inject efficient power into the system. Given the VIC approach, the dynamic response will be extremely quick since ESs react more quickly than the grid's mechanical component, meaning inertia control occurs before primary and secondary control. One way to express the kinetic energy is as,

$$E_{kine} = \frac{J\omega^2}{2} \qquad (4.2)$$

The following describes the relationship between the torque balance of spinning mass and the rate of change in rotor speed:

$$T_{mechanical} - T_{electrical} = \frac{P_{Mechanical}}{\omega} - \frac{P_{Electrical}}{\omega} = J\frac{d\omega}{dt} \qquad (4.3)$$

Where, τ_{mech}= mechanical torque, τ_{elec}=electrical torque, J= moment of inertia(kg-m2), $d\omega$ = angular frequency deviation (rad/s), $P_{Mechanical}$ =mechanical power and $P_{Electrical}$ = electrical power.

Calculation of ROCOF can be written as,

$$\frac{d\omega}{dt} = \frac{P_{Mechanical} - P_{Electrical}}{2Hs} \tag{4.4}$$

The system inertia constant (H) is proportional to stored kinetic energy (E_{Kine}) given by,

$$H = \frac{E_{kine}}{s} \tag{4.5}$$

The schematic block diagram of VIC with virtual damping is shown in Figure 4.3. The flow of power is determined by the VIC loop, which includes the derivative, D_{vi} and J_{vi} from/to the energy storage to nullify the power imbalance so that the frequency regulation is maintained. Here, K_{UC} and T_{UC} are the gain and time constant for the ultra-capacitor.

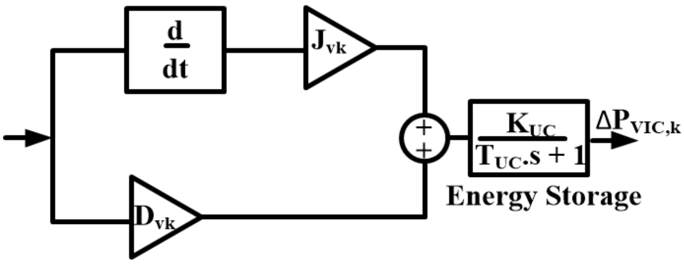

Figure 4.3 Transfer function model of VIC.

For the virtual inertia control of a multi area multi source system, a unique Tilt Integral cascaded with integral derivative with filter controller (TI-IDN) is proposed in this work. Basically, it is an additional Integral controller added to a TIDN controller. The suggested controller aims to improve settling time and damping ratio while maintaining and controlling each region frequency and tie line power, which are essential during changes in load or in certain areas of generation.

An additional integral controller is added to a TIDN controller to create a TI-IDN controller. The performance of the steady state is improved when an integral controller is included since it offers more benefits in the event of a greater rejection of disturbances. The bounds for tilting parameter "n" is set to 2-3, the bypass filter "N" to 0-100, and the upper and lower bounds for K_t, K_i, K_{i1} and K_{di} to 0 to 1. Figure 4.4 displays the block diagram of the TI-IDN controller.

The transfer function of the TI-IDN controller can be written as,

$$TF_{TI-DN}(s) = \left(\frac{Kt_i}{s^{\frac{1}{ni}}} + \frac{KI_i}{s} + \frac{KI1_i}{s} + KD_i \left(\frac{sN}{s+N} \right) \right) \tag{4.6}$$

In all areas, the suggested TI-IDN controller has six tuning parameters total, all of which are optimized by the use of the Zebra optimization method.

$$\left. \begin{aligned} & Kt_{is}^{min} \le Kt_{is} \le Kt_{is}^{max}, \\ & n_{is}^{min} \le n_{is} \le n_{is}^{max}, \\ & Ki_{is}^{min} \le Ki_{is} \le Ki_{is}^{max}, \\ & Ki1_{is}^{min} \le Ki1_{is} \le Ki1_{is}^{max}, \\ & KD_{is}^{min} \le KD_{is} \le KD_{is}^{max}, \\ & N_{is}^{min} \le N_{is} \le N_{is}^{max}, \end{aligned} \right\} \tag{4.7}$$

Also, the delivered virtual inertia power (ΔP_{vic}) by the VIC technique in area-k can be presented as,

$$\Delta P_{vic}(s) = \frac{\left(s(\Delta f_k) J_{vk} + (\Delta f_k) D_{vk} \right) K_{UC}}{1 + sT_{UC}} \left(\frac{Kt_i}{s^{\frac{1}{ni}}} + \frac{KI_i}{s} + \frac{KI1_i}{s} + KD_i \left(\frac{sN}{s+N} \right) \right) \tag{4.8}$$

Here, K_t, K_i, K_i1 and K_d represents the tilt, integral and derivative of the controller and n_{is} and N_{is} are the tilt parameter and the low-pass filter.

The proposed controller is seen to manage both known and unknown disturbances, as well as the non-linearity of the system. It is possible to confirm the dominance of the controller by examining its performance under different conditions. Included with the study is the section on simulation results and comments.

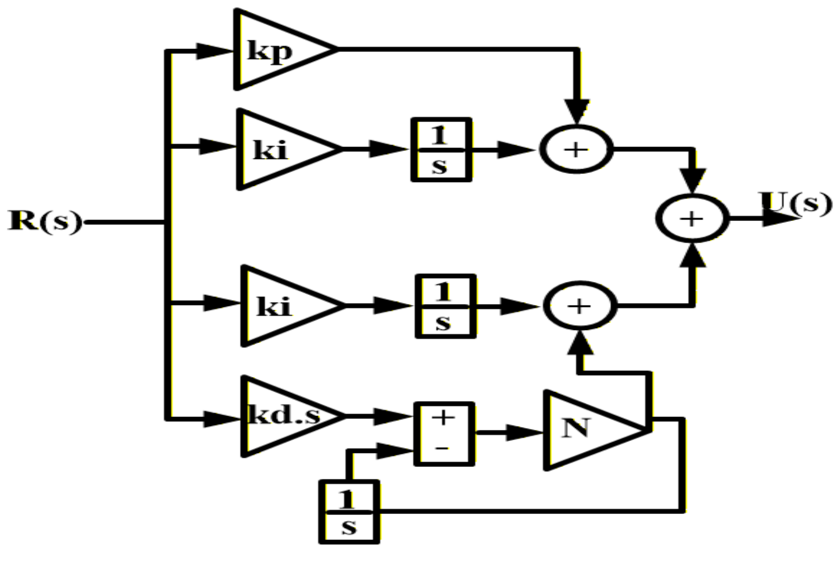

Figure 4.4 Structure of TI-IDN controller.

4.4 Brief description of Energy Storage System

4.4.1 Battery ES

Due of its high energy density and quick access time, BES has shown to be a successful ES technology for storing RE. BES can provide the system with a significant amount of electricity quickly or a significant amount of energy over an extended period of time. It is made up of a battery bank and a power converter that connects the battery bank to the independent utility grid. It stores electric energy in batteries in the form of direct current (DC). Because it takes time for the battery cells to charge, the BES time constant is only able to be few seconds. Its transfer function can be written as [Tasnin and Saikia, 2018]:

$$G_{BES}(s) = \left(\frac{K_{BES}}{1 + s.T_{BES}} \right) \tag{4.9}$$

4.4.2 Flywheel ES

For a short amount of time, FES is better suited to repeatedly absorb and release electric energy than BES. FES works by mechanically storing energy in a flywheel that rotates. It may store excess electricity during off-peak hours and instantly release energy during peak times. It stores energy in the form of kinetic energy. FES works well with short-duration turbulent power pulsations generated by renewable energy sources. Its advantages include affordability, longevity, quick response times, and dependability; its disadvantages include larger volume and mass, higher losses, and less stored energy per volume [Tasnin and Saikia, 2018]. The transfer function for FES can be written as:

$$G_{FES}(s) = \left(\frac{K_{FES}}{1 + s.T_{FES}} \right) \tag{4.10}$$

4.4.3 Ultracapacitor ES

Supercapacitors, or UCs, are yet another new gadget for ES. It is created on a vast surface area of a microporous substance, such activated carbon, and stores charge in a double layer. It is also known as a two-layer capacitor. With a higher life cycle than batteries, excellent charge/discharge efficiency, and a high-power density, UC offers a host of benefits. Their manufacturing costs are also falling quickly. When used with batteries, UC produces a power source with a high-power capability and an extended run duration [Tasnin and Saikia, 2018]. Its transfer function equation can be written as:

$$G_{UC}(s) = \left(\frac{K_{UC}}{1 + s.T_{UC}} \right) \tag{4.11}$$

4.5 Simulations result and Analysis

The proposed controller and optimization technique are subjected to performance evaluation across various scenarios of the test power system model. The results of this analysis are presented both graphically and in tabular form. All simulations and analyses are executed using MATLAB/SIMULINK and the ode45 solver. The simulation runs for a duration of 100 seconds and the number of populations for ZOA algorithm is set to 30. A step load perturbation of 0.01 per unit (p.u.) is introduced in area 1 for a regulated system. For the deregulated system, it is assumed that each DISCOs demand 0.01p.u load from GENCOs making the total area load to 0.02 p.u. The thermal system incorporates a Governor Rate Constraint (GRC) of 3% per minute (equivalent to 0.0005 per second).

4.5.1 System under Regulated environment

4.5.1.1 System responses comparison considering different controller for VIC

The superiority of the proposed controller is envisioned by comparing its performance with other existing controllers. The controllers which are considered for this comparison are I, TI, TID and proposed TI-IDN controller. The dynamic responses of the different controllers are shown in Figure 4.5. The tuned controller gain values are shown in Table 4.1 while the numerical data of the system responses are given in Table 4.2.

The comparative analysis framework is established to systematically evaluate the transient response characteristics and steady-state performance metrics of each controller configuration under identical operating conditions and disturbance scenarios. The evaluation criteria encompass several critical performance indicators including settling time, peak overshoot, peak undershoot, and integral square error values for frequency deviations in all four areas as well as tie-line power flow deviations. Each controller variant undergoes rigorous testing with the same load perturbation pattern to ensure fair and unbiased comparison. The Zebra Optimization Algorithm is consistently applied across all controller structures to determine their optimal gain parameters, thereby eliminating any advantage that might arise from superior tuning methodology rather than inherent controller capabilities. This systematic approach ensures that the observed performance differences are solely attributable to the architectural distinctions among the controllers. The integral controller serves as the baseline reference, representing the conventional AGC implementation, while the TI and TID controllers represent intermediate evolutionary steps in controller design. The proposed TI-IDN controller incorporates the cumulative advantages of previous designs while introducing additional refinements through its cascaded integral-derivative structure with filtering capability, positioning it as the most sophisticated control architecture in this comparative study.

Table 4.1 Optimized gain values for different controllers of VIC integration

Parameters		I	TI	TIDN	TI-IDN
K_i	Area-1	0.74	0.83	0.69	0.25
	Area-2	0.52	0.71	0.63	0.84
	Area-3	0.29	0.25	0.70	0.33
	Area-4	0.38	0.31	0.87	0.12
K_t	Area-1	-	0.99	0.70	0.99
	Area-2	-	0.66	0.56	0.48
	Area-3	-	0.98	0.98	0.86
	Area-4	-	0.50	0.32	0.74
n	Area-1	-	2.98	2.99	2.32
	Area-2	-	2.64	2.09	2.31
	Area-3	-	2.99	2.98	2.98
	Area-4	-	2.41	2.17	2.19
K_{i1}	Area-1	0.99	0.95	0.53	0.82
	Area-2	0.97	0.52	0.29	0.63
	Area-3	0.99	0.99	0.99	0.87
	Area-4	0.56	0.38	0.90	0.38
K_{i11}	Area-1	-	-	-	0.52
	Area-2	-	-	-	0.23
	Area-3	-	-	-	0.95
	Area-4	-	-	-	0.30
K_d	Area-1	-	-	0.44	0.41
	Area-2	-	-	0.46	0.69
	Area-3	-	-	0.34	0.73
	Area-4	-	-	0.33	0.55
N	Area-1	-	-	9.61	41.8
	Area-2	-	-	27.7	87.6
	Area-3	-	-	30.8	18.3
	Area-4	-	-	41.1	17.1
J_v	Area-1	0.99	0.99	0.99	0.98
	Area-2	0.76	0.48	0.36	0.73
	Area-3	0.98	0.98	0.98	0.99
	Area-4	0.38	0.19	0.45	0.75
D_v	Area-1	-	0.94	0.81	0.99
	Area-2	-	0.58	0.71	0.68
	Area-3	-	0.95	0.90	0.93
	Area-4	-	0.86	0.97	0.25

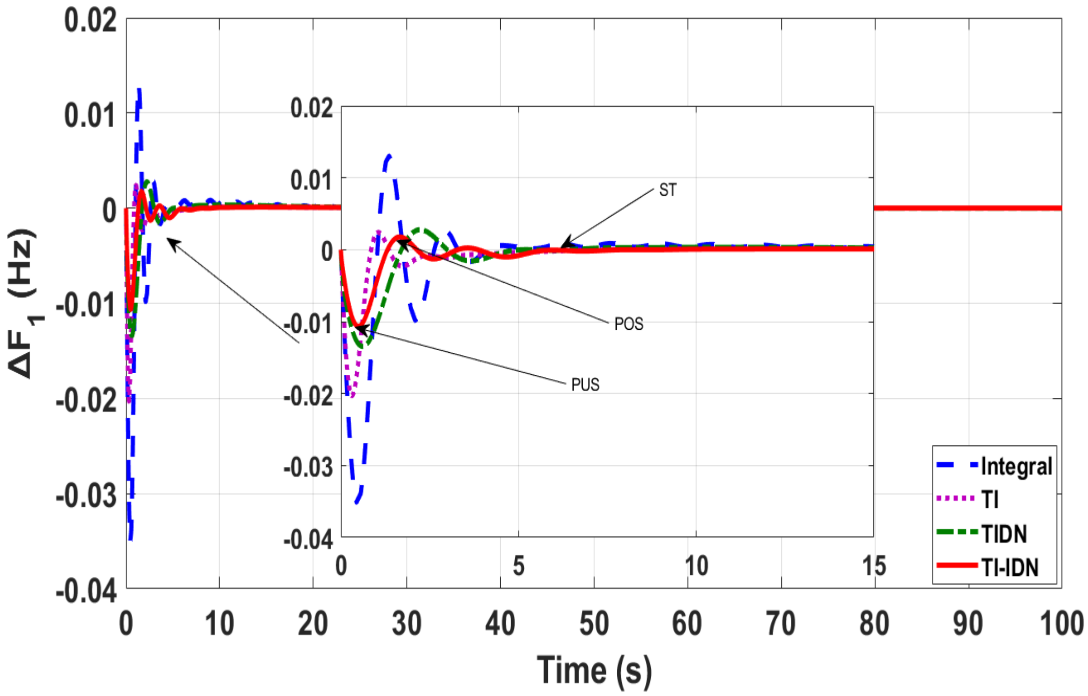

Figure 4.5 (a) System dynamic responses with respect to time for comparison of different controllers with VIC integration: Area-1 deviation in frequency.

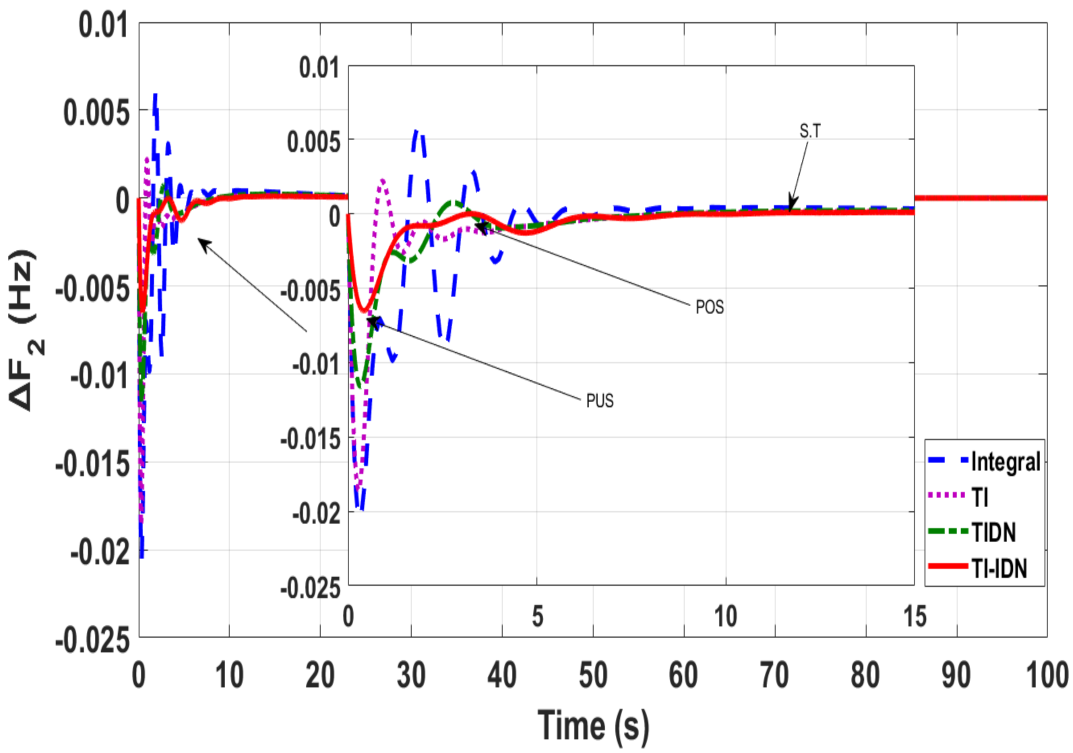

Figure 4.5 (b) System dynamic responses with respect to time for comparison of different controllers with VIC integration: Area-2 deviation in frequency.

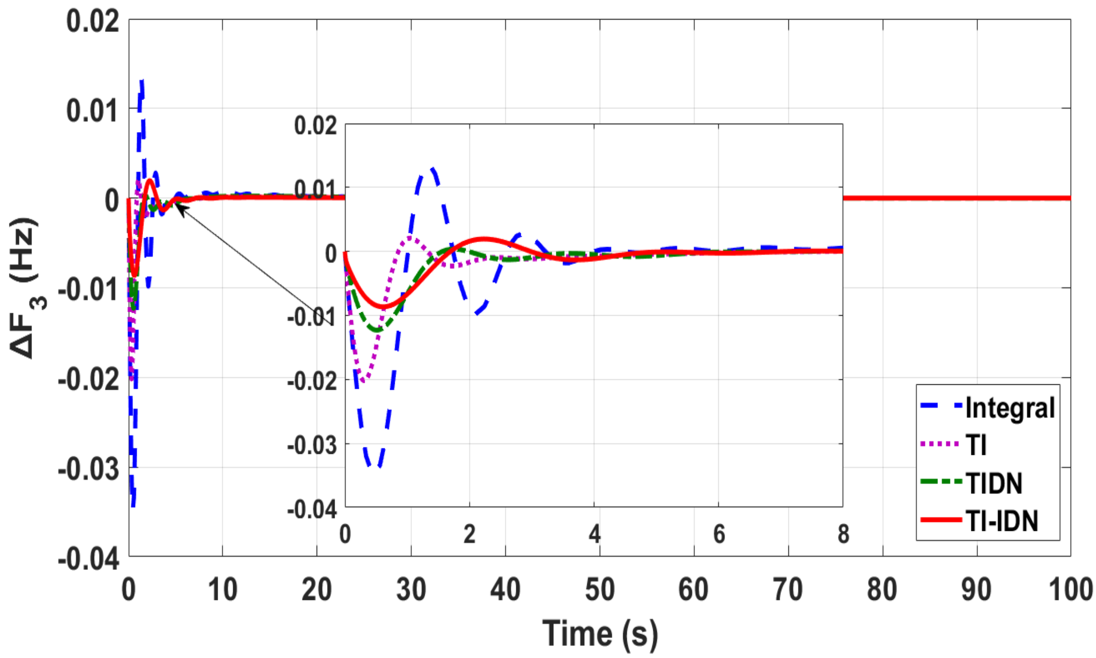

Figure 4.5 (c) System dynamic responses with respect to time for comparison of different controllers with VIC integration: Area-3 deviation in frequency.

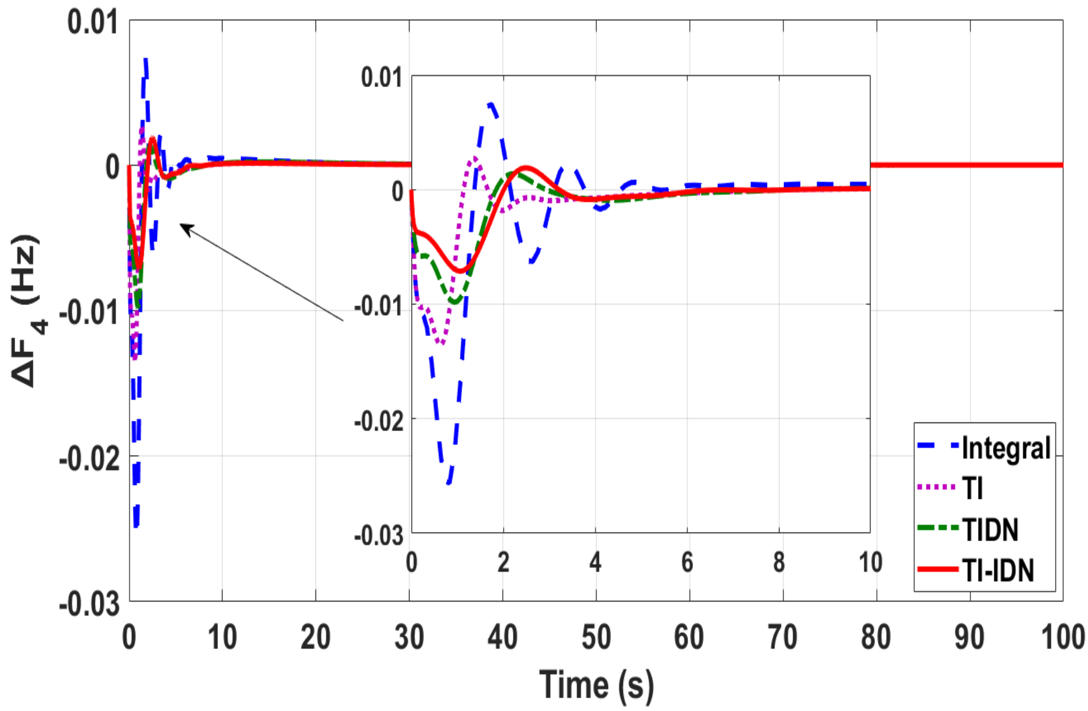

Figure 4.5 (d) System dynamic responses with respect to time for comparison of different controllers with VIC integration: Area-4 deviation in frequency.

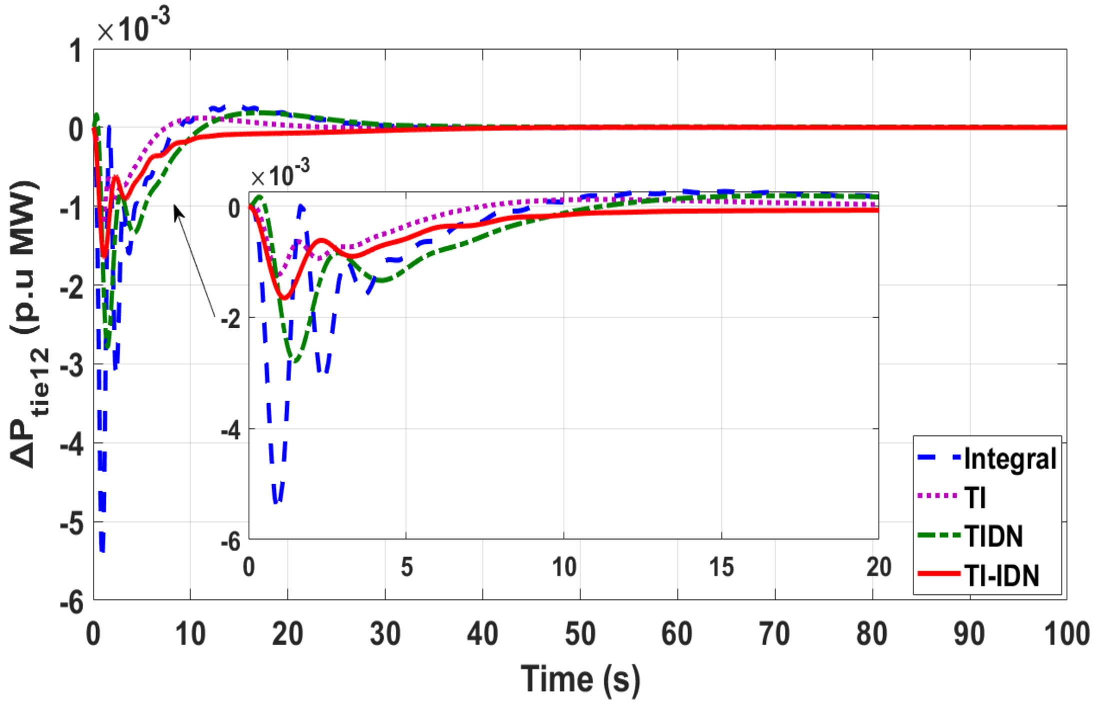

Figure 4.5 (e) System dynamic responses with respect to time for comparison of different controllers with VIC integration: Deviation in tie line power between area-1 and -2.

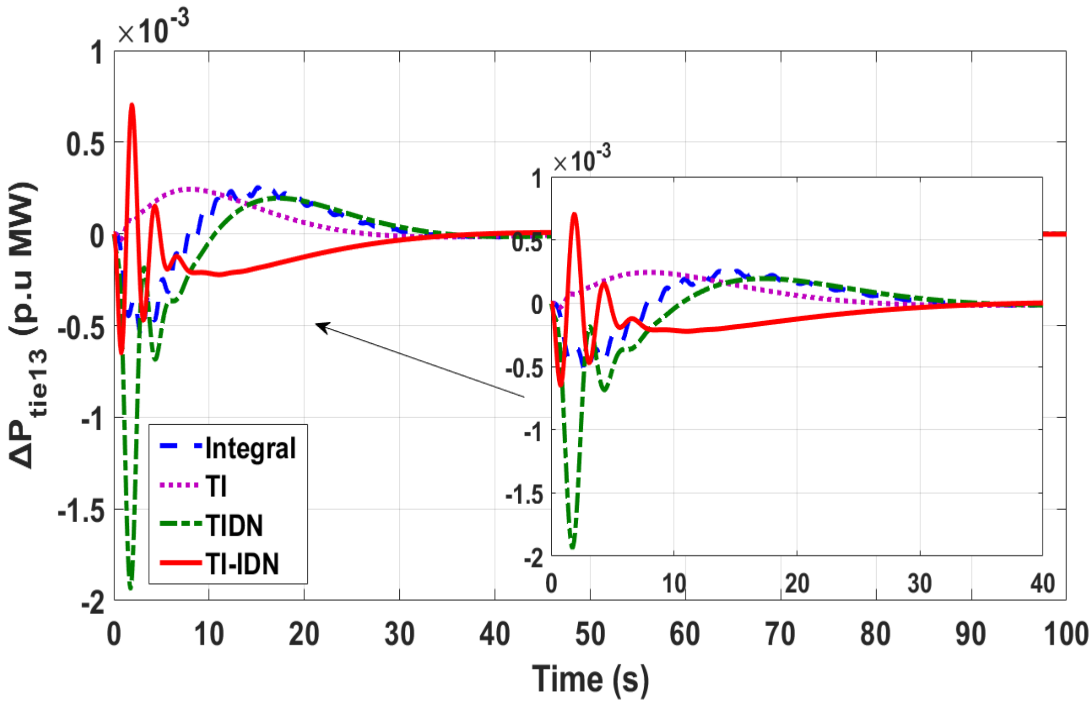

Figure 4.5 (f) System dynamic responses with respect to time for comparison of different controllers with VIC integration: Deviation in tie line power between area-1 and -3

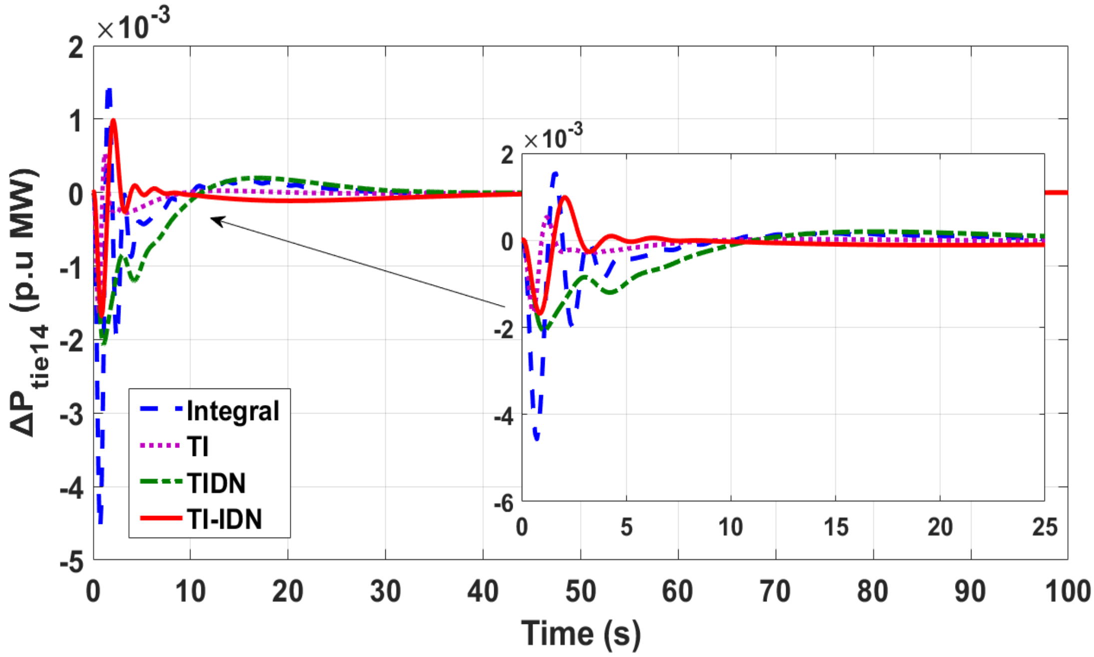

Figure 4.5 (g) System dynamic responses with respect to time for comparison of different controllers with VIC integration: Deviation in tie line power between area-1 and -4.

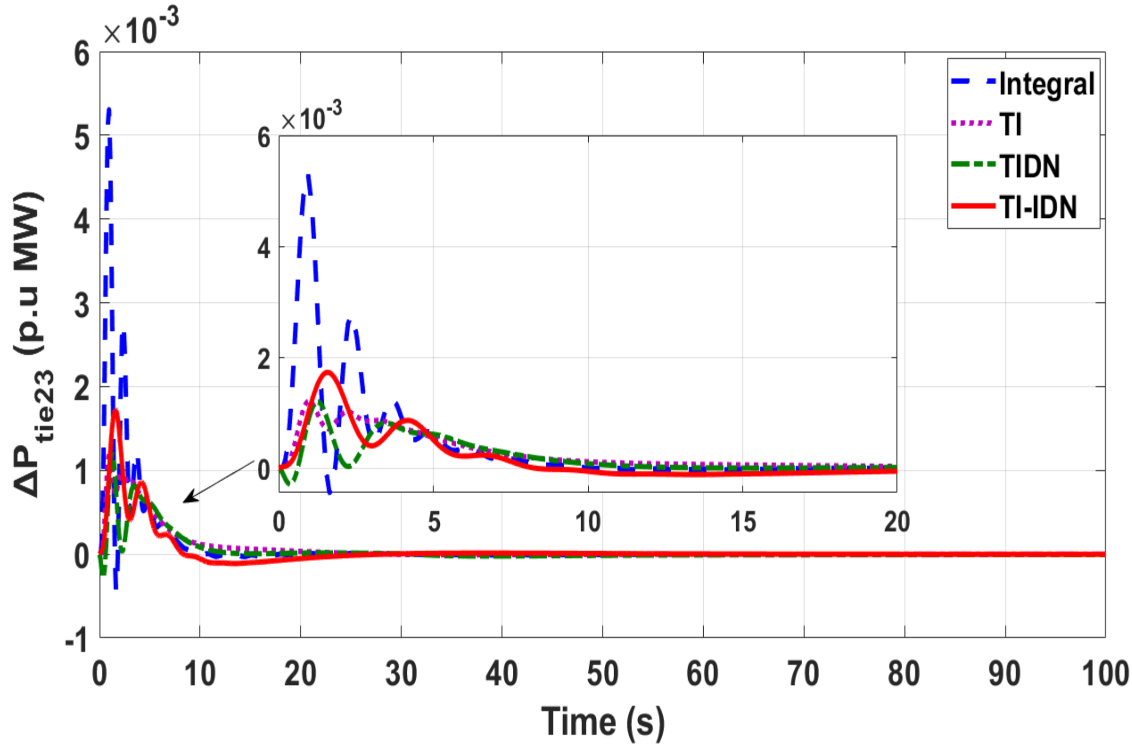

Figure 4.5 (h) System dynamic responses with respect to time for comparison of different controllers with VIC integration: Deviation in tie line power between area-2 and -3.

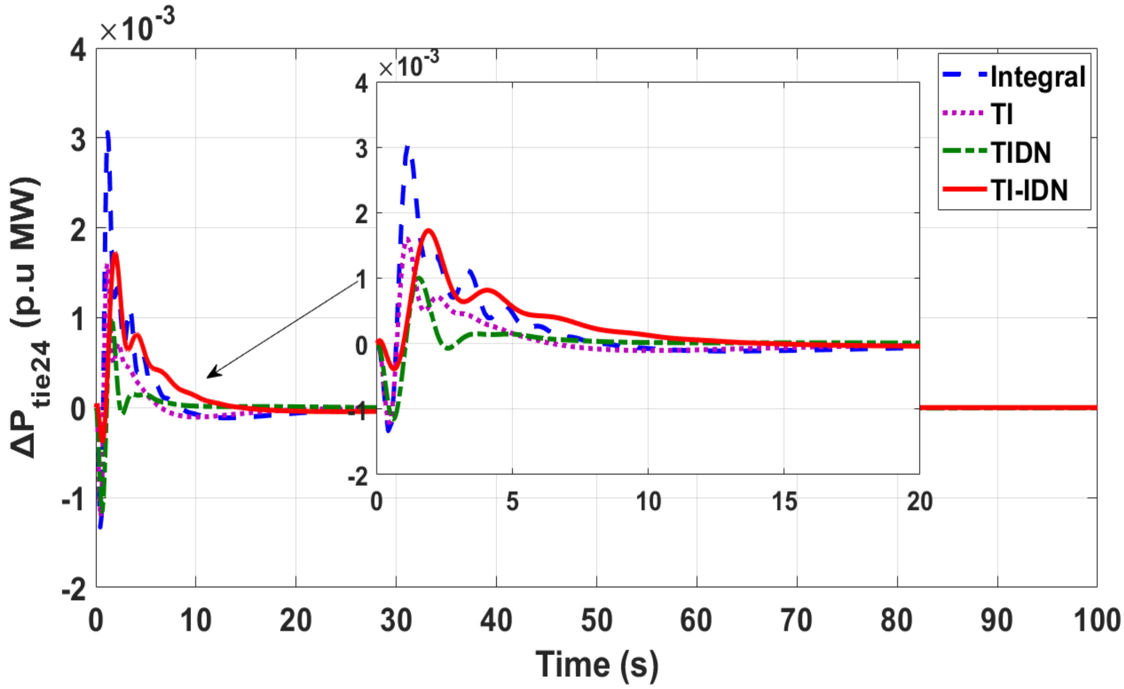

Figure 4.5 (i) System dynamic responses with respect to time for comparison of different controllers with VIC integration: Deviation in tie line power between area-2 and -4.

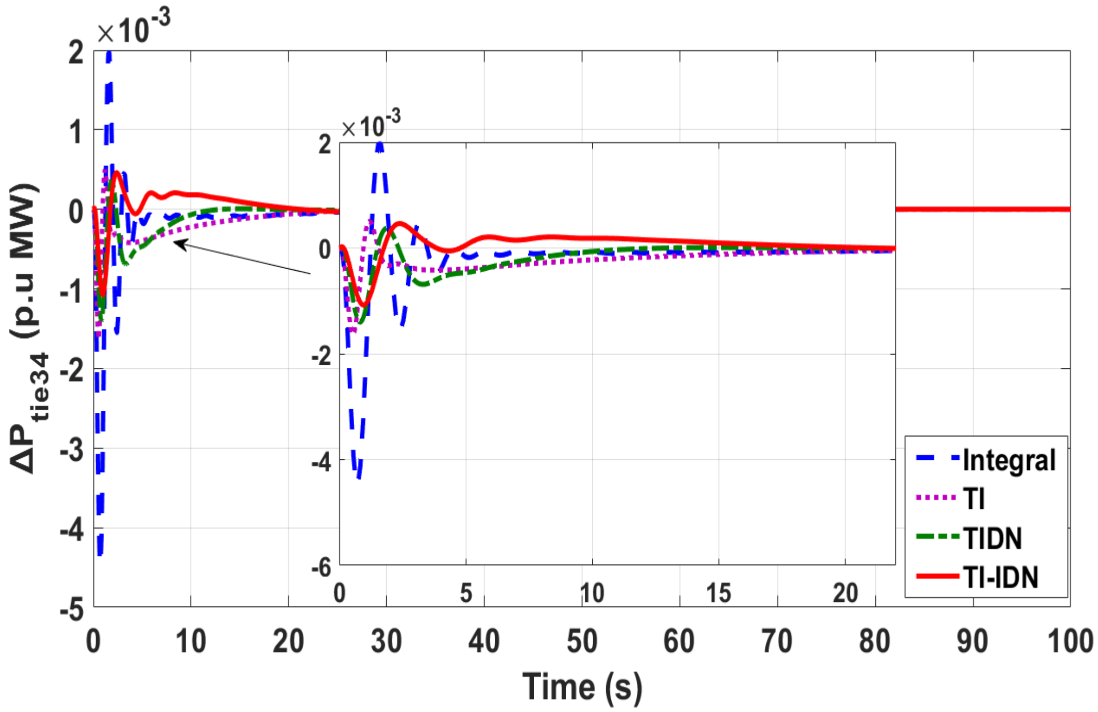

Figure 4.5 (j) System dynamic responses with respect to time for comparison of different controllers with VIC integration: Deviation in tie line power between area-3 and -4.

Table 4.2 (a) System Dynamic responses of different controllers with VIC integration.

Responses		Controllers			
		I	TI	TIDN	TI-IDN
Δf_1	M.U	-0.03483	-0.02020	-0.01344	-0.01063
	M.O	0.01258	0.00232	0.00277	0.00176
	S.T	40	9	8	6
Δf_2	M.U	-0.02049	-0.01821	-0.01157	-0.006512
	M.O	0.00613	0.00218	0.00075	0.00010
	S.T	30	13	12	12
Δf_3	M.U	-0.03462	-0.02008	-0.01230	-0.00865
	M.O	0.01319	0.00199	0.00036	0.00194
	S.T	35	8	7	6
Δf_4	M.U	-0.02555	-0.01351	-0.00982	-0.00711
	M.O	0.00733	0.00268	0.00137	0.00188
	S.T	28	14	8	7
ΔP_{tie12}	M.U	-0.00541	-0.00121	-0.00278	-0.00164
	M.O	0.00026	0.00011	0.00018	0.0000006
	S.T	38	22	26	26
ΔP_{tie13}	M.U	-0.00055	-0.00003	-0.00193	-0.00064
	M.O	0.00025	0.00024	0.000194	0.000698
	S.T	60	60	42	42
ΔP_{tie14}	M.U	-0.00453	-0.00164	-0.0027	-0.00167
	M.O	0.00151	0.000528	0.000198	0.000983
	S.T	40	20	20	48
ΔP_{tie23}	M.U	-0.00042	-0.000007	-0.000283	-0.000112
	M.O	0.00522	0.001211	0.001199	0.001727
	S.T	24	50	27	28
ΔP_{tie24}	M.U	-0.00129	-0.001165	-0.001153	-0.000376
	M.O	0.00304	0.001583	0.000998	0.001714
	S.T	34	32	25	24
ΔP_{tie34}	M.U	-0.00444	-0.00162	-0.001401	-0.001075
	M.O	0.00196	0.000501	0.000370	0.000460
	S.T	34	30	26	24

Table 4.2(b) Percentage improvement of TI-IDN over other controllers

errors		I	TI	TIDN
Δf_1	M.U	69.4	47.38	20.91
	M.O	86.01	24.14	36.46
	S.T	85	33.33	25
Δf_2	M.U	68.22	64.24	43.72
	M.O	98.37	95.41	86.67
	S.T	60	7.69	0
Δf_3	M.U	75.01	56.92	29.67
	M.O	85.29	2.51	-81.44
	S.T	82.86	25	14.29

Table 4.2(b) contd. Percentage improvement of TI-IDN over other controllers

errors		I	TI	TIDN
Δf_4	M.U	72.17	47.37	27.6
	M.O	74.35	29.85	-27.12
	S.T	75	50	12.5
ΔP_{tie12}	M.U	69.69	-26.21	41.01
	M.O	99.7	99.45	99.67
	S.T	31.58	-15.38	0.0
ΔP_{tie13}	M.U	-14.06	-95.31	66.84
	M.O	-64.18	-65.61	-72.2
	S.T	30	30	0.0
ΔP_{tie14}	M.U	63.13	-1.79	38.15
	M.O	34.9	-46.28	-79.85
	S.T	-20	-140	20.91
ΔP_{tie23}	M.U	73.33	-93.75	36.46
	M.O	66.92	-29.37	25
	S.T	-16.67	44	43.72
ΔP_{tie24}	M.U	70.85	67.73	86.67
	M.O	43.62	-8.28	0.0
	S.T	29.41	25	29.67
ΔP_{tie34}	M.U	75.79	33.64	23.26
	M.O	76.53	8.18	14.29
	S.T	29.41	20	27.6

Analysis: The TI-IDN controller shows consistent and substantial improvements in reducing maximum undershoot and overshoot across all scenarios. On average, undershoot reduction is in the range of 65–80% vs I, 40–70% vs TI, and 25–50% vs TIDN, highlighting its superior damping capability. Overshoot suppression is also strong, with reductions typically between 60–90% vs I and noticeable improvements over TI and TIDN. Settling time performance shows significant reduction in most cases, though a few scenarios show minimal or no improvement compared to TIDN. Overall, TI-IDN achieves the best between damping and speed, making it the most effective among the tested controllers.

4.5.1.2 Comparison of different energy storage

The ultra-capacitor is the energy storage device which is selected for this research. Its performance is compared with that of the FES and BES, whose transfer function modelling was previously shown. Based on the study, we can say that the integration of UC for the VIC with the suggested controller improves system performance, as shown in Figure 4.6. The Table 4.3 displays the optimal controller settings of the virtual inertia controller and the secondary Integral controller which is optimized by the Zebra optimization algorithm. And, Table 4.4 provides the numerical data representation of the system dynamic responses and the percentage improvement of using UC over FES and BES.

Table 4.3 Optimized gain values of proposed controller for different energy storage for VIC.

Parameters		**BES**	**FES**	**UC**
K_t	Area-1	0.25	0.83	0.84
	Area-2	0.48	0.39	0.49
	Area-3	0.78	0.53	0.93
	Area-4	0.32	0.33	0.55
n	Area-1	2.88	2.22	2.99
	Area-2	2.17	2.98	2.80
	Area-3	2.32	2.72	2.33
	Area-4	2.25	2.28	2.50
K_{i1}	Area-1	0.90	0.75	0.78
	Area-2	0.35	0.79	0.60
	Area-3	0.43	0.75	0.67
	Area-4	0.34	0.34	0.63
K_{i11}	Area-1	0.38	0.51	0.79
	Area-2	0.15	0.57	0.61
	Area-3	0.38	0.99	0.99
	Area-4	0.19	0.28	0.25
K_d	Area-1	0.46	0.26	0.74
	Area-2	0.24	0.42	0.79
	Area-3	0.62	0.57	0.70
	Area-4	0.66	0.55	0.46
N	Area-1	59.1	76.8	33.7
	Area-2	22.8	46.2	47.9
	Area-3	26.8	53.7	43.9
	Area-4	54.5	62.9	43.7
J_v	Area-1	0.52	0.58	0.99
	Area-2	0.40	0.95	0.48
	Area-3	0.78	0.22	0.98
	Area-4	0.24	0.37	0.31
D_v	Area-1	0.74	0.52	0.99
	Area-2	0.20	0.86	0.44
	Area-3	0.71	0.79	0.95
	Area-4	0.43	0.51	0.87
K_i	Area-1	0.99	0.99	0.51
	Area-2	0.98	0.99	0.47
	Area-3	0.98	0.99	0.26
	Area-4	0.05	0.99	0.32

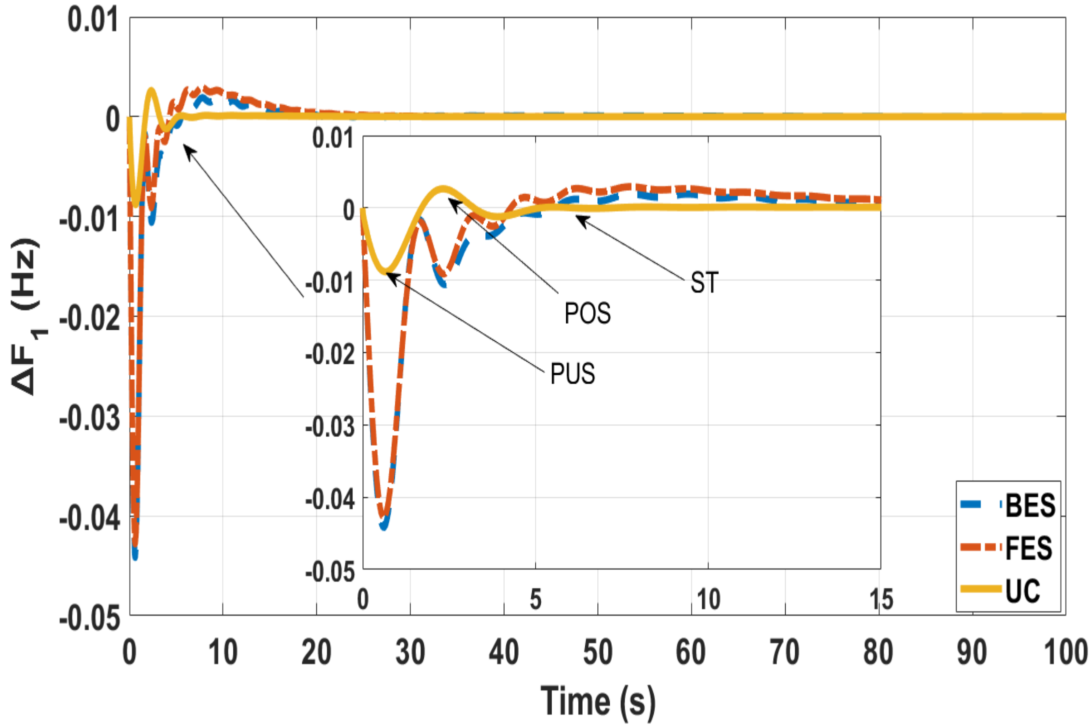

Figure 4.6 (a) System dynamic responses with respect to time for comparison of different energy storage with VIC integration: Area-1 deviation in frequency.

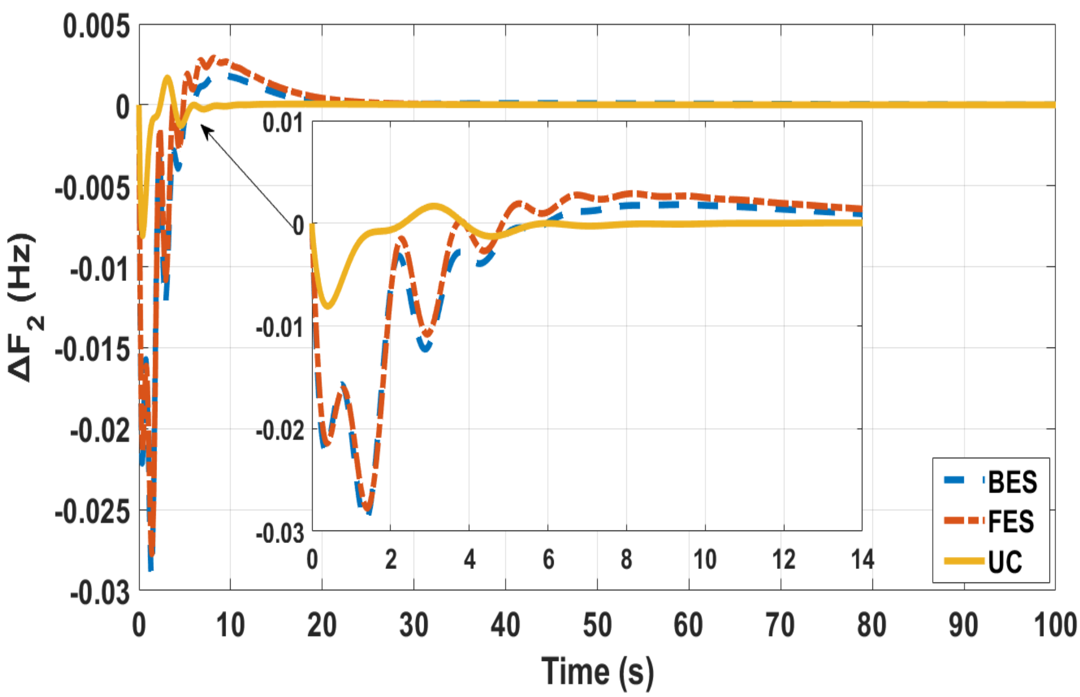

Figure 4.6 (b) System dynamic responses with respect to time for comparison of different energy storage with VIC integration: Area-2 deviation in frequency.

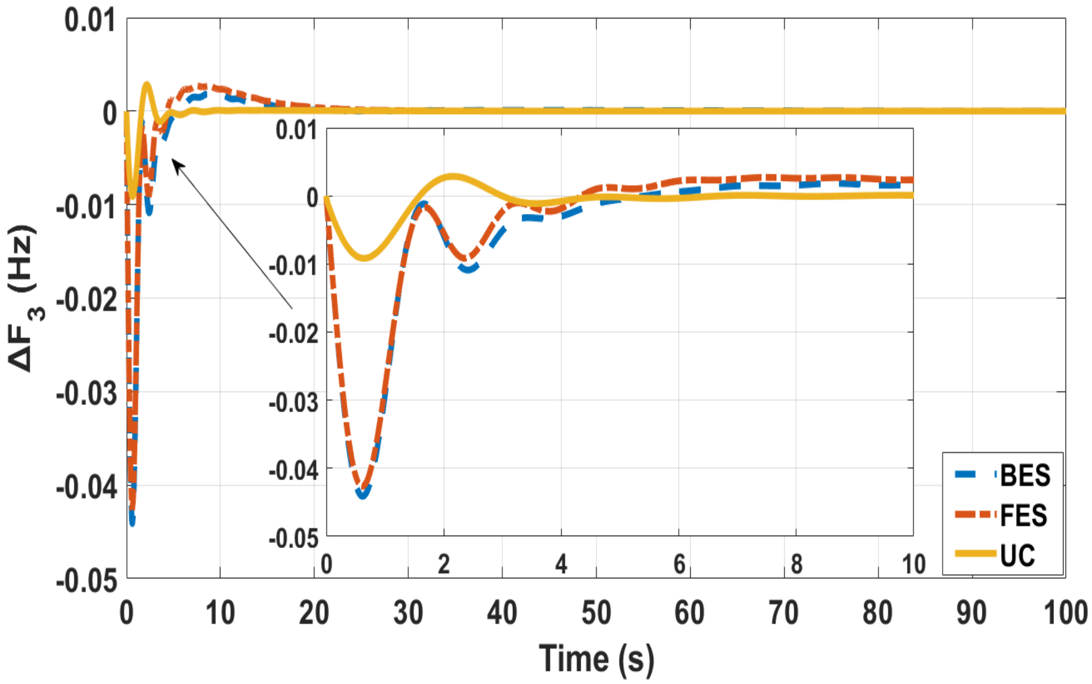

Figure 4.6 (c) System dynamic responses with respect to time for comparison of different energy storage with VIC integration: Area-3 deviation in frequency.

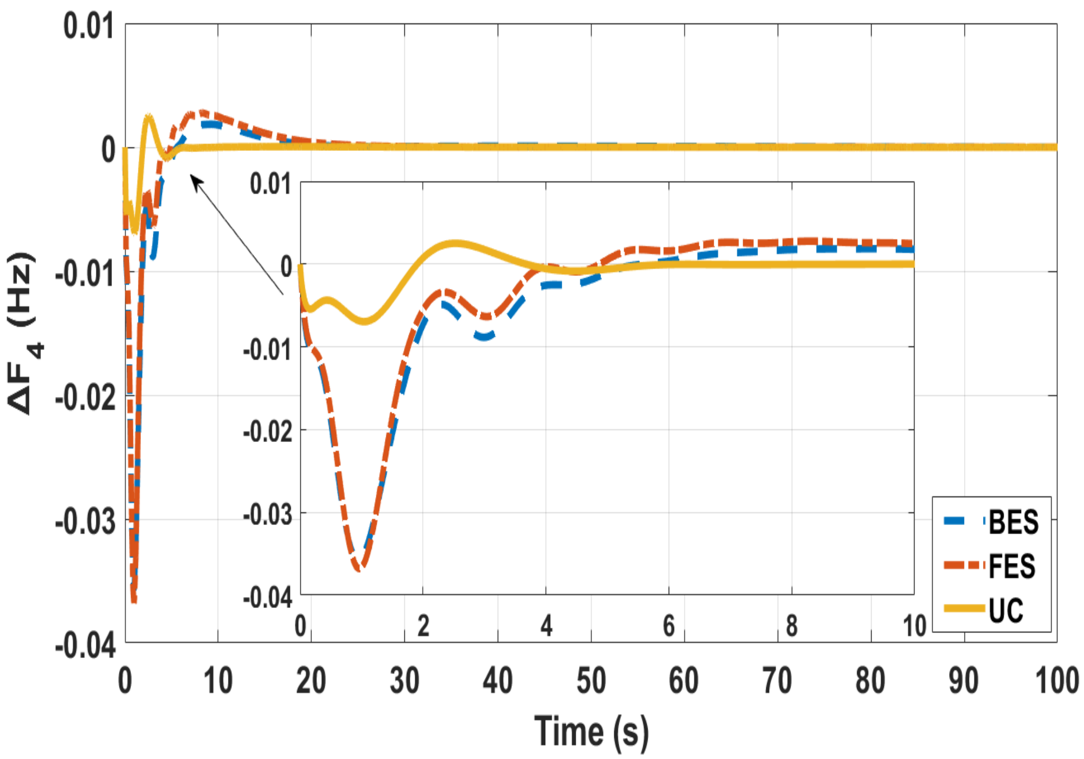

Figure 4.6 (d) System dynamic responses with respect to time for comparison of different energy storage with VIC integration: Area-4 deviation in frequency.

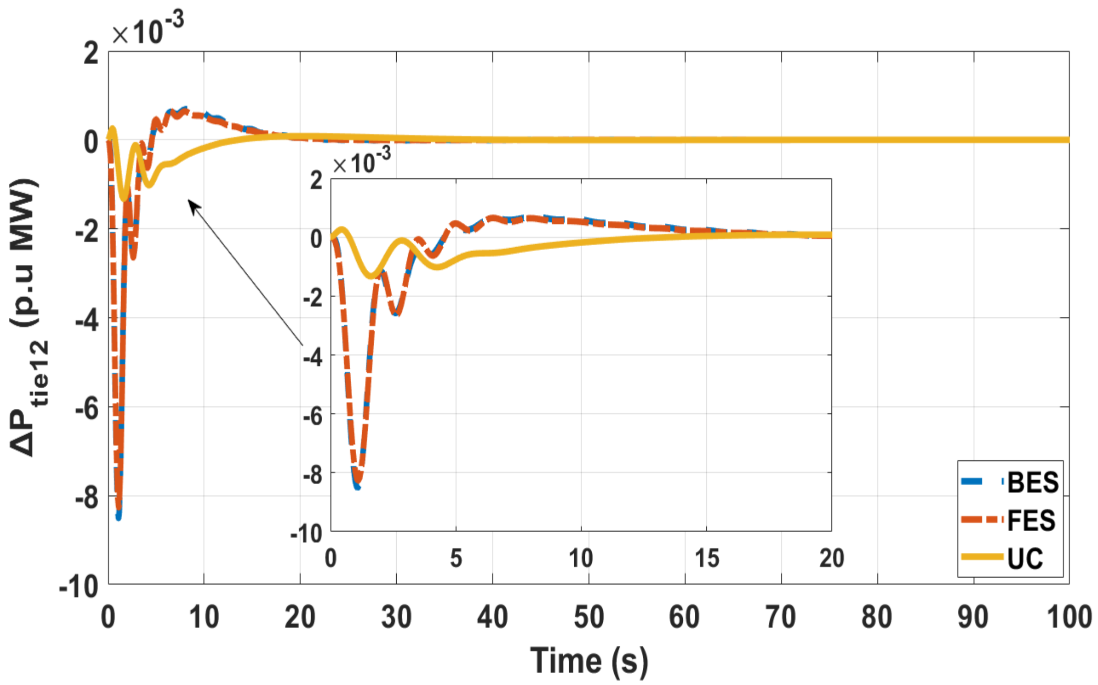

Figure 4.6 (e) System dynamic responses with respect to time for comparison of different energy storage with VIC integration: Deviation in tie line power between area-1 and -2.

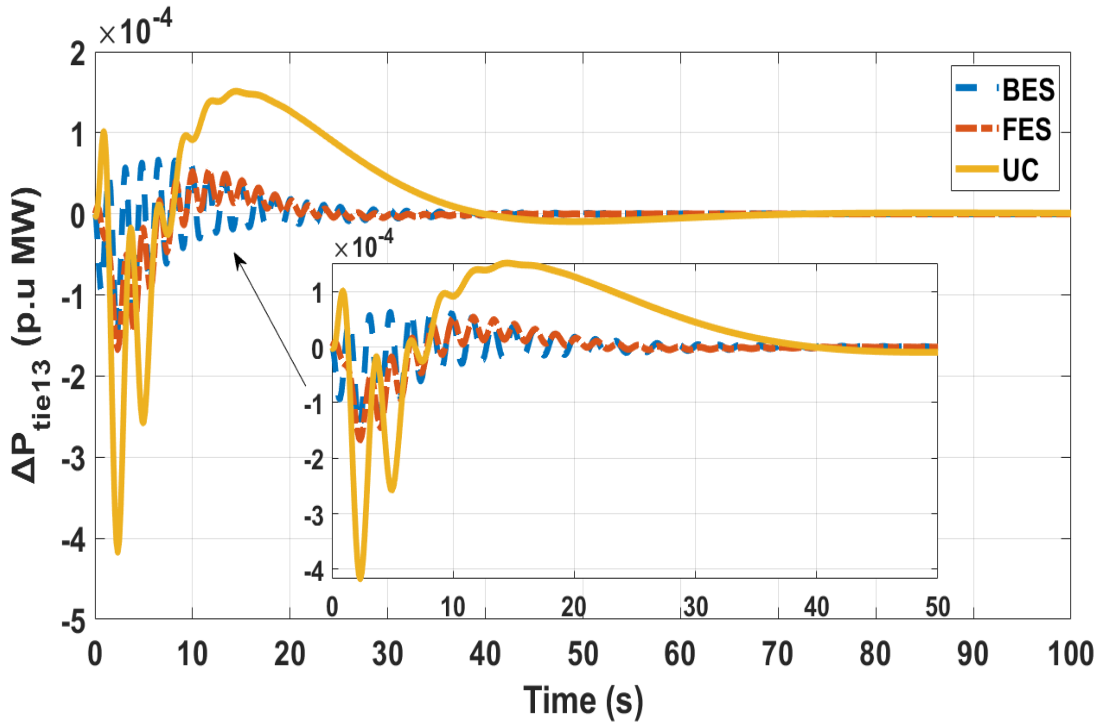

Figure 4.6 (f) System dynamic responses with respect to time for comparison of different energy storage with VIC integration: Deviation in tie line power between area-1 and -3.

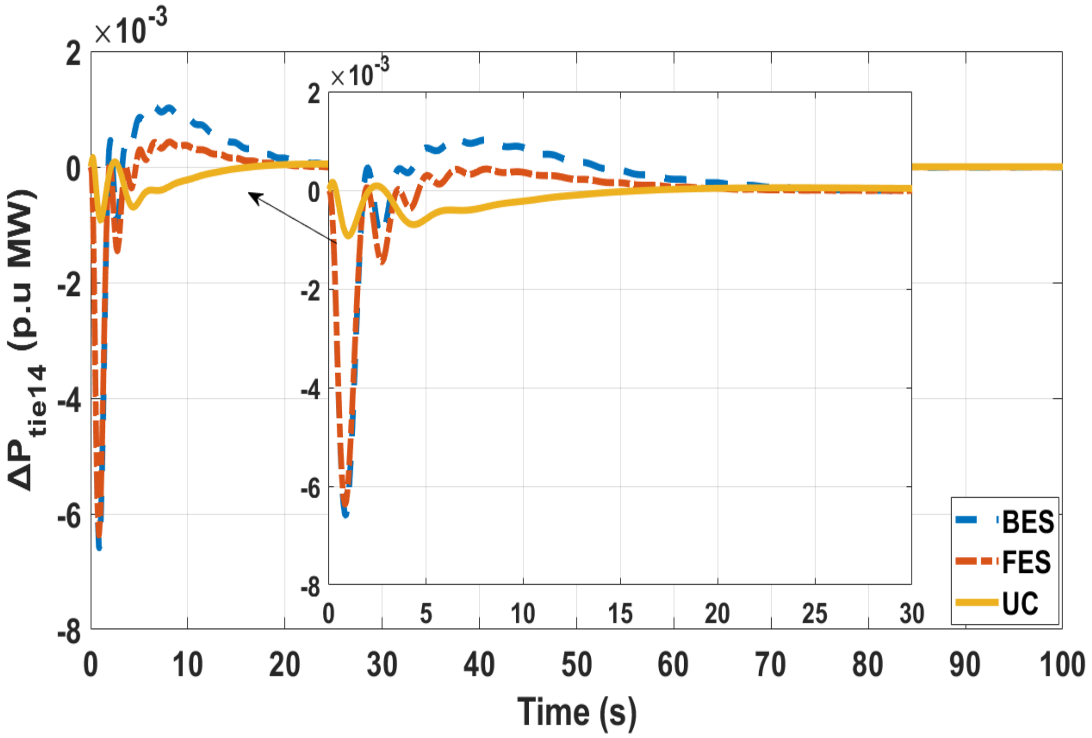

Figure 4.6 (g) System dynamic responses with respect to time for comparison of different energy storage with VIC integration: Deviation in tie line power between area-1 and -4.

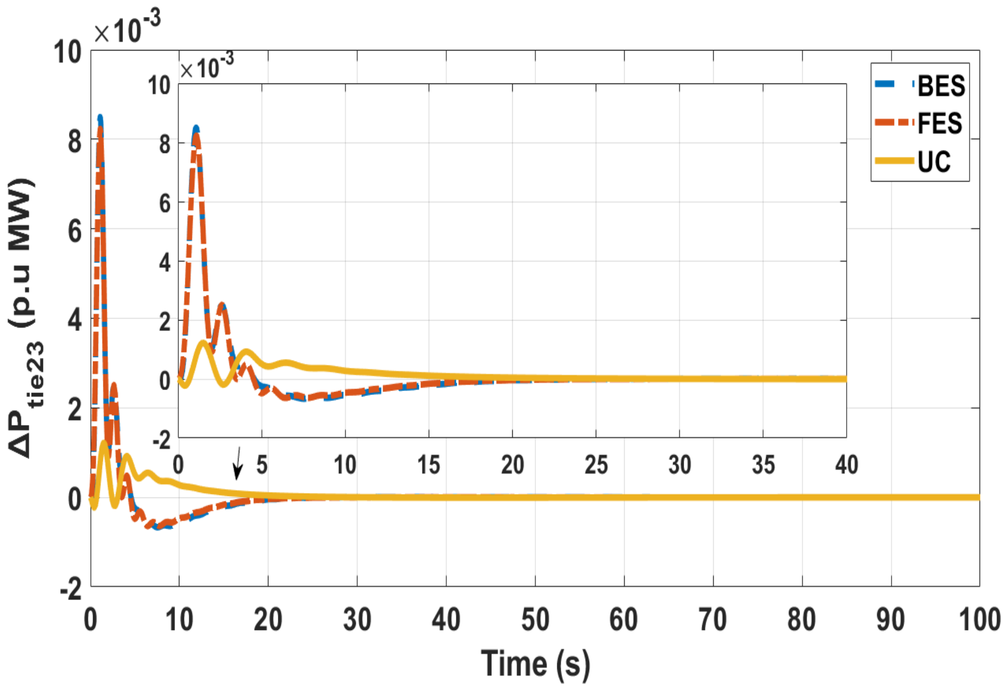

Figure 4.6 (h) System dynamic responses with respect to time for comparison of different energy storage with VIC integration: Deviation in tie line power between area-2 and -3

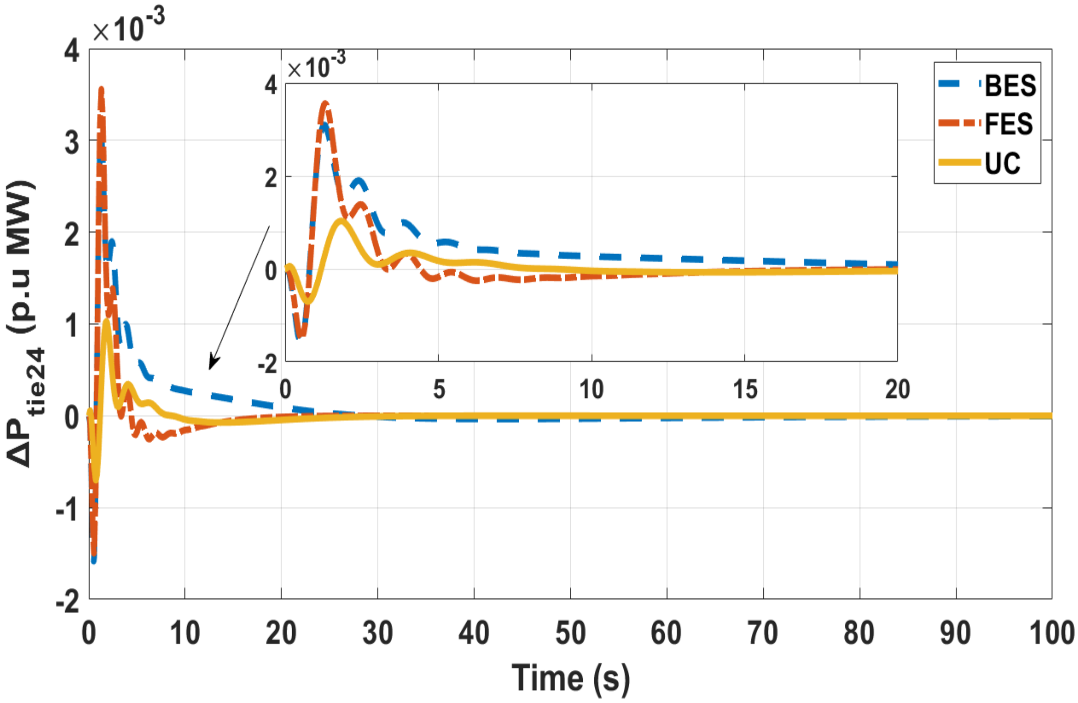

Figure 4.6 (i) System dynamic responses with respect to time for comparison of different energy storage with VIC integration: Deviation in tie line power between area-2 and -4.

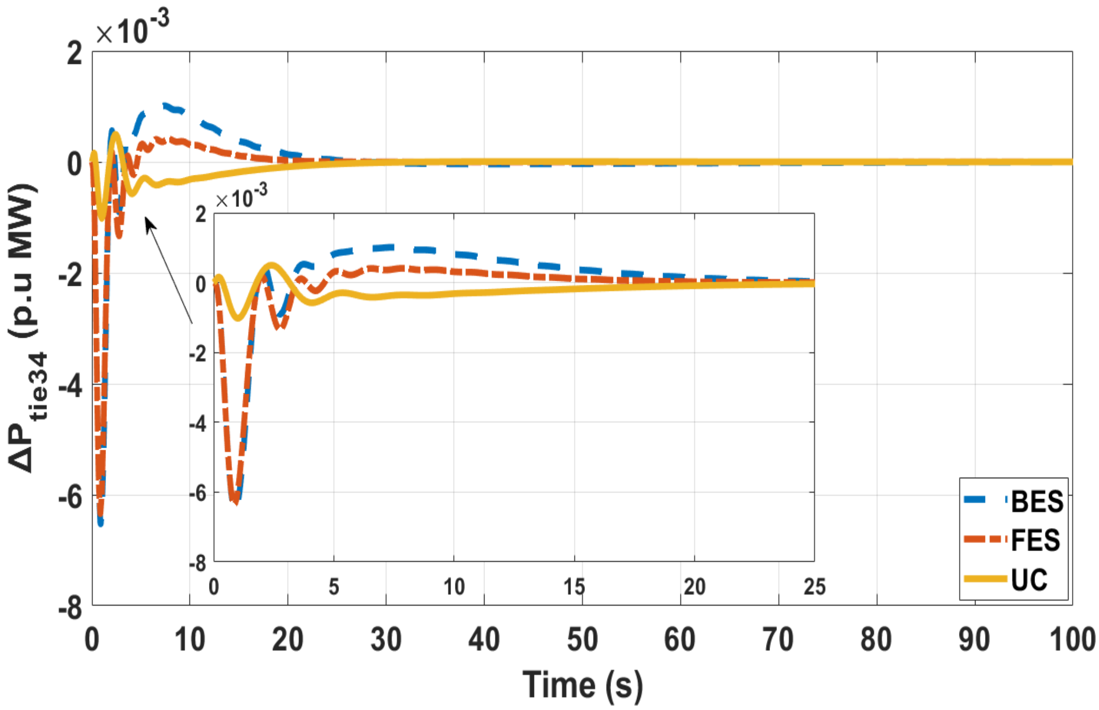

Figure 4.6 (j) System dynamic responses with respect to time for comparison of different energy storage with VIC integration: Deviation in tie line power between area-3 and -4.

Table 4.4 System dynamic response for different energy storage with percentage improvement of UC over BES and FES

Responses		Energy storage device			% improvement of UC	
		BES	FES	UC	BES	FES
Δf_1	M.U	-0.03483	-0.02020	-0.00883	74.65	56.29
	M.O	0.01258	0.00232	0.00263	79.09	-11.78
	S.T	21	22	7	66.67	68.18
Δf_2	M.U	-0.02049	-0.01821	-0.00808	60.57	55.63
	M.O	0.00613	0.00218	0.00166	72.92	23.85
	S.T	23	24	9	60.87	62.5
Δf_3	M.U	-0.03462	-0.02008	-0.00916	73.54	54.38
	M.O	0.01319	0.001997	0.00286	78.32	-30.17
	S.T	20	22	9	55	59.09
Δf_4	M.U	-0.02557	-0.01351	-0.00695	72.82	48.56
	M.O	0.007331	0.002687	0.002507	65.8	6.7
	S.T	21	25	8	61.9	68
ΔP_{tie12}	M.U	-0.00541	-0.001218	-0.001331	75.4	-9.28
	M.O	0.0002639	0.000119	0.000258	2.24	-53.87
	S.T	20	21	15	25	28.57
ΔP_{tie13}	M.U	-0.00055	-0.000032	-0.000417	24.18	-92.32
	M.O	0.000251	0.000243	0.0001511	39.8	37.82
	S.T	50	50	40	20	20
ΔP_{tie14}	M.U	-0.004531	-0.001645	-0.000926	79.56	43.71
	M.O	0.001518	0.000528	0.000162	89.33	69.32
	S.T	27	26	25	7.41	3.85
ΔP_{tie23}	M.U	-0.000427	-0.0000077	-0.000227	46.84	-96.6
	M.O	0.005229	0.001211	0.001218	76.71	-0.58
	S.T	22	23	19	13.64	17.39
ΔP_{tie24}	M.U	-0.001294	-0.001165	-0.000703	45.67	39.66
	M.O	0.003041	0.001583	0.001030	66.13	34.93
	S.T	29	24	16	44.83	33.33
ΔP_{tie34}	M.U	-0.004447	-0.001623	-0.001021	77.04	37.09
	M.O	0.001963	0.0005017	0.0004978	74.64	0.78
	S.T	29	28	20	31.03	28.57

Analysis: The ultra-capacitor (UC) outperforms both battery energy storage (BES) and flywheel energy storage (FES) in nearly every metric. Maximum undershoot is reduced by more than 60–80% compared to BES and around 30–60% compared to FES, reflecting the UC's ability to rapidly respond to frequency deviations. Overshoot is generally suppressed effectively, with UC achieving 20–75% improvement relative to BES and FES. Settling times are also faster with UC, averaging 30–50% improvement, though in a few cases the gain is smaller. In summary, UC demonstrates faster dynamic response and better damping than BES and FES, proving to be the most effective storage option for AGC.

4.5.1.3 Analysis with random load variation

It is essential that the controller shows the capacity to manage system frequency even in the case of unpredictable fluctuations in load circumstances. As described in the previously specified scenarios, the controller's performance is evaluated under these randomly fluctuating load settings, and it works wonderfully in these situations. It is assumed that a load shift occurs every 20 seconds as shown in Figure 4.7, and Figure 4.8 displays the system reaction. As can be seen from the picture, the system's dynamic responses are improved when VIC is integrated in the system. This is in contrast to a system without VIC, which oscillates under random load conditions without having enough time to settle. Table 4.5 provides the suggested controller's optimal gain parameters. The comparative analysis between VIC-enabled and VIC-disabled configurations clearly demonstrates the critical importance of synthetic inertia provision in modern power systems with high renewable penetration. Without VIC support, the system exhibits persistent oscillatory behaviour with inadequate damping, resulting in prolonged settling times and increased risk of frequency instability. Conversely, the VIC-integrated system demonstrates superior disturbance rejection capabilities, maintaining frequency within acceptable bounds despite the continuous barrage of load perturbations, thereby validating the effectiveness of the proposed control strategy under realistic operating conditions.

Table 4.5 Optimized gain values for case of random load variation with and without VIC.

Parameters		Without VIC	With VIC
K_t	Area-1	-	0.99
	Area-2	-	0.28
	Area-3	-	0.10
	Area-4	-	0.39
n	Area-1	-	2.03
	Area-2	-	2.37
	Area-3	-	2.70
	Area-4	-	2.40
K_{i1}	Area-1	-	0.98
	Area-2	-	0.31
	Area-3	-	0.16
	Area-4	-	0.41

Table 4.5 (contd.) Optimized gain values for case of random load variation with and without VIC

K_{i11}	Area-1	-	0.97
	Area-2	-	0.35
	Area-3	-	0.55
	Area-4	-	0.58
K_d	Area-1	-	0.23
	Area-2	-	0.36
	Area-3	-	0.05
	Area-4	-	0.38
N	Area-1	-	15.9
	Area-2	-	15.6
	Area-3	-	63.1
	Area-4	-	59.8
J_v	Area-1	-	0.98
	Area-2	-	0.13
	Area-3	-	0.62
	Area-4	-	0.28
D_v	Area-1	-	0.99
	Area-2	-	0.63
	Area-3	-	0.09
	Area-4	-	0.77
K_i	Area-1	0.40	0.83
	Area-2	0.01	0.33
	Area-3	0.01	0.19
	Area-4	0.01	0.25

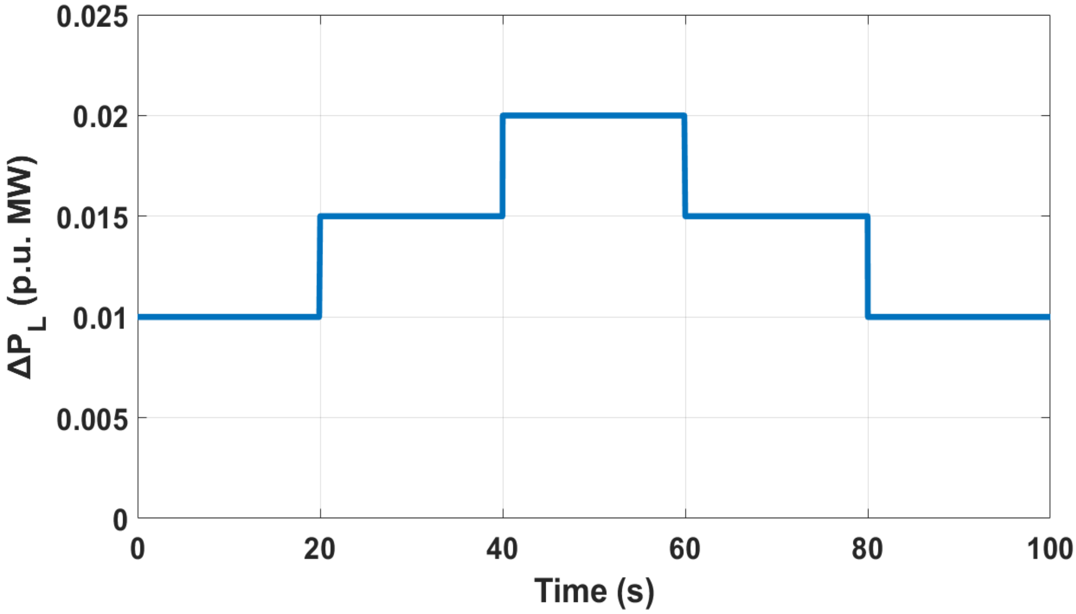

Figure 4.7 Step load perturbations for the case of random load variation with and without VIC.

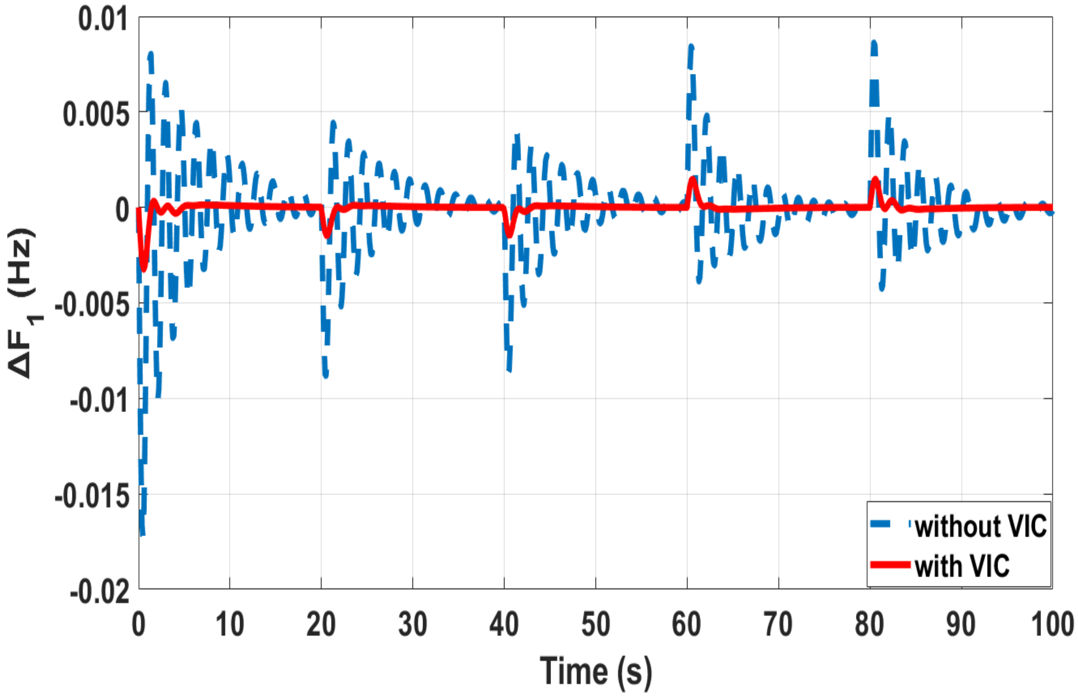

Figure 4.8 (a) System dynamic responses with respect to time for random load variation analysis with and without VIC: Area-1 deviation in frequency.

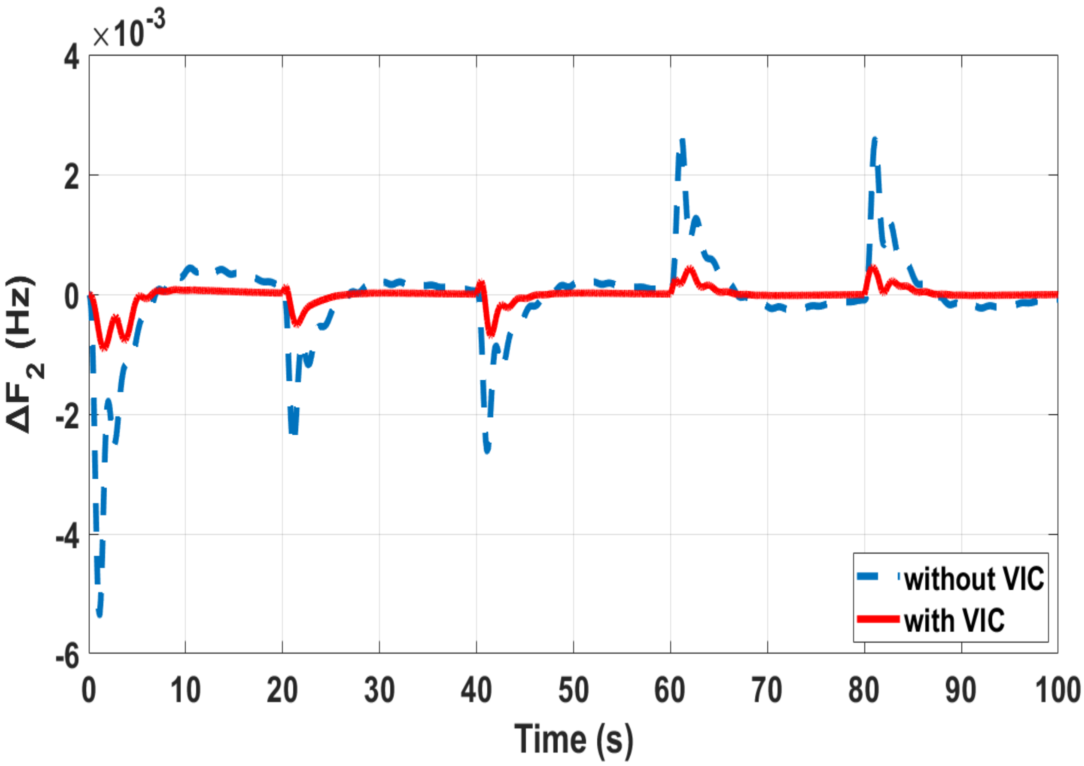

Figure 4.8 (b) System dynamic responses with respect to time for random load variation analysis with and without VIC: Area-2 deviation in frequency.

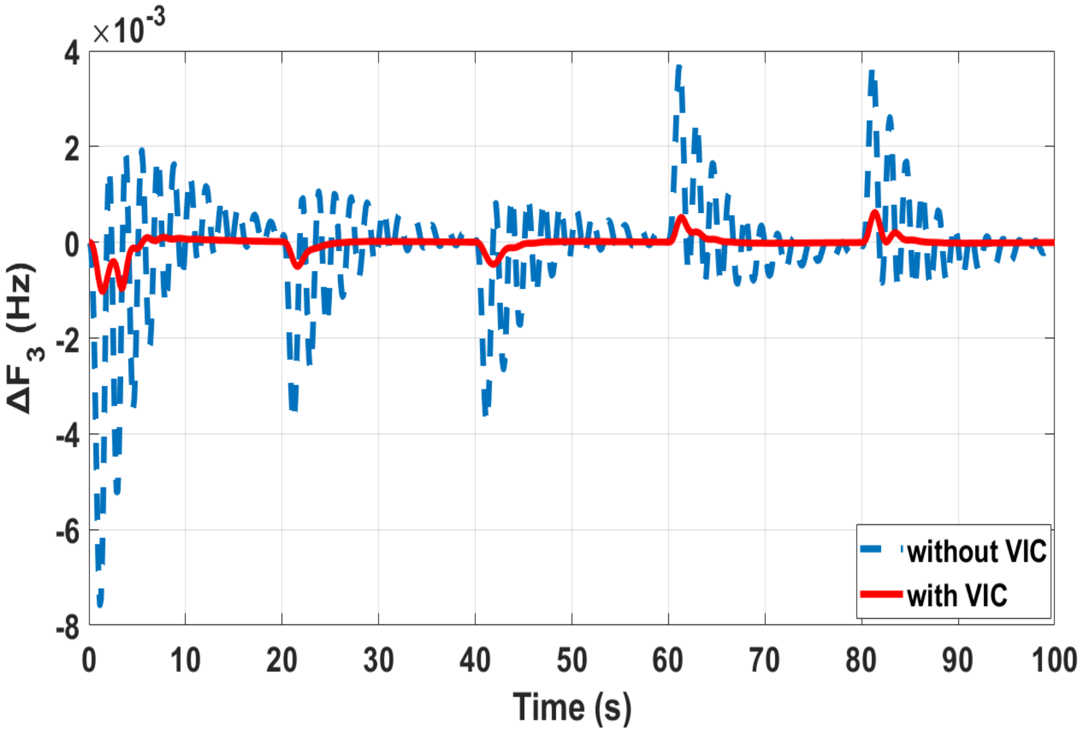

Figure 4.8 (c) System dynamic responses with respect to time for random load variation analysis with and without VIC: Area-1 deviation in frequency.

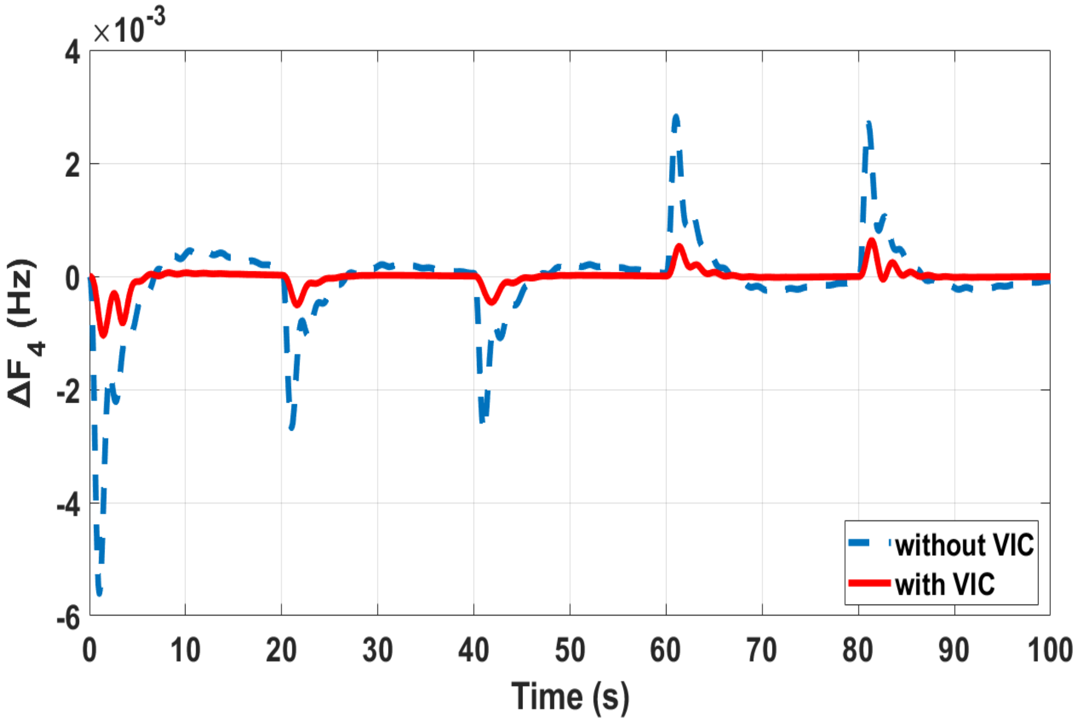

Figure 4.8 (d) System dynamic responses with respect to time for random load variation analysis with and without VIC: Area-2 deviation in frequency.

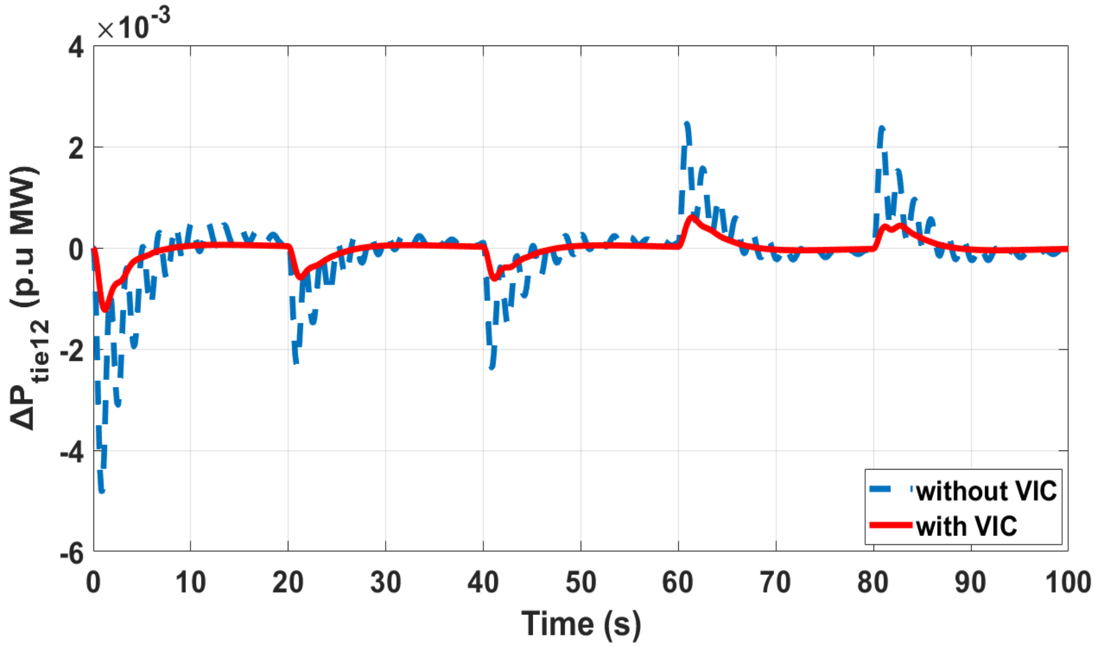

Figure 4.8 (e) System dynamic responses with respect to time for random load variation analysis with and without VIC: Deviation in tie line power between area-1 and -2.

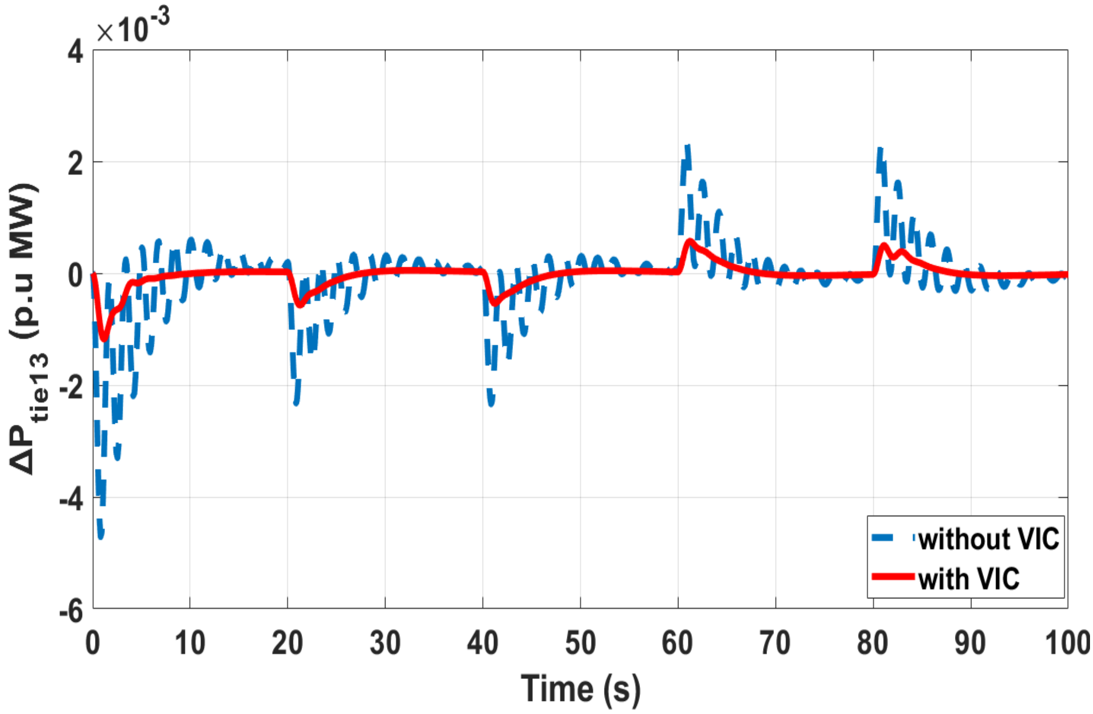

Figure 4.8 (f) System dynamic responses with respect to time for random load variation analysis with and without VIC: Deviation in tie line power between area-1 and -3.

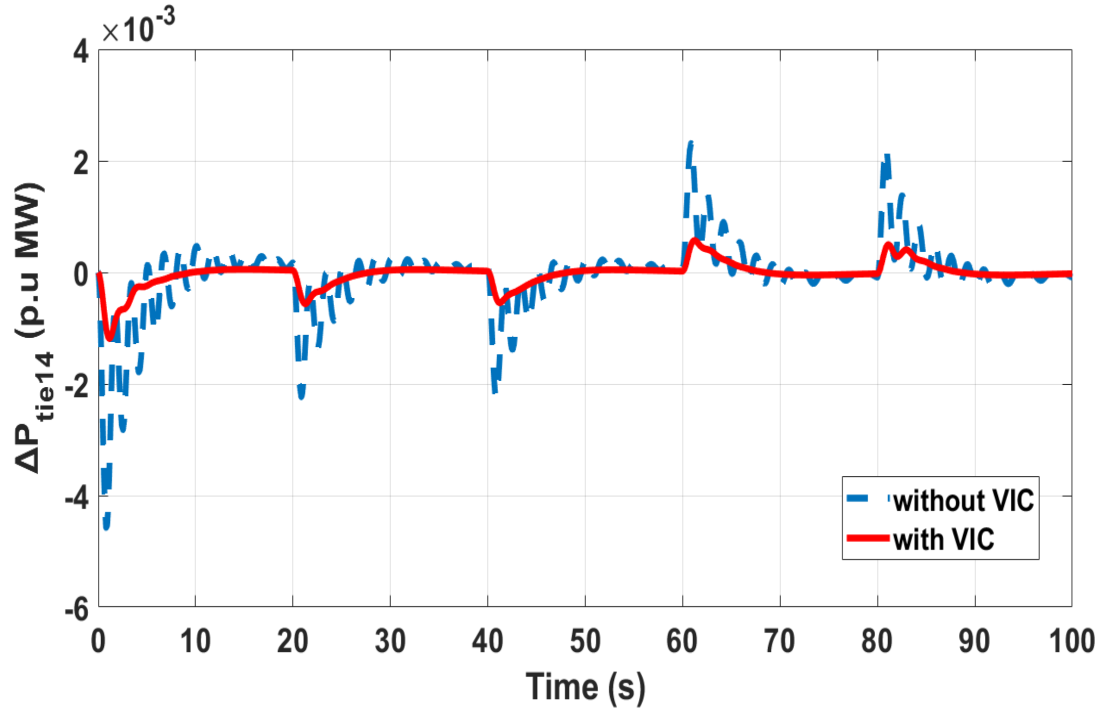

Figure 4.8 (g) System dynamic responses with respect to time for random load variation analysis with and without VIC: Deviation in tie line power between area-1 and -4.

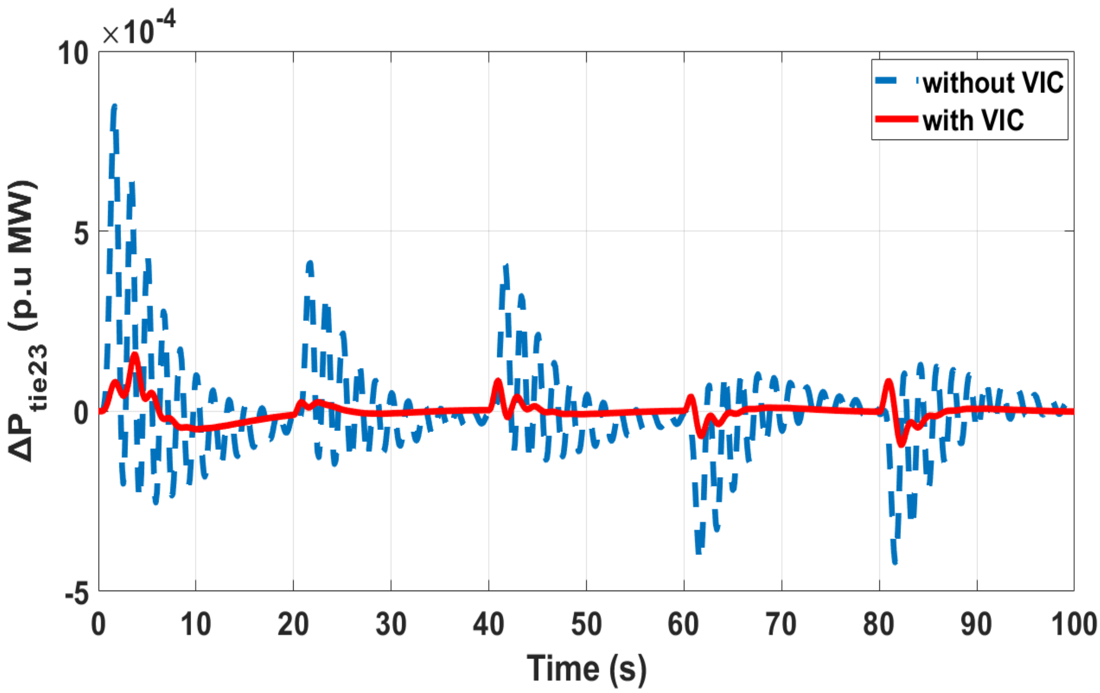

Figure 4.8 (h) System dynamic responses with respect to time for random load variation analysis with and without VIC: Deviation in tie line power between area-2 and -3.

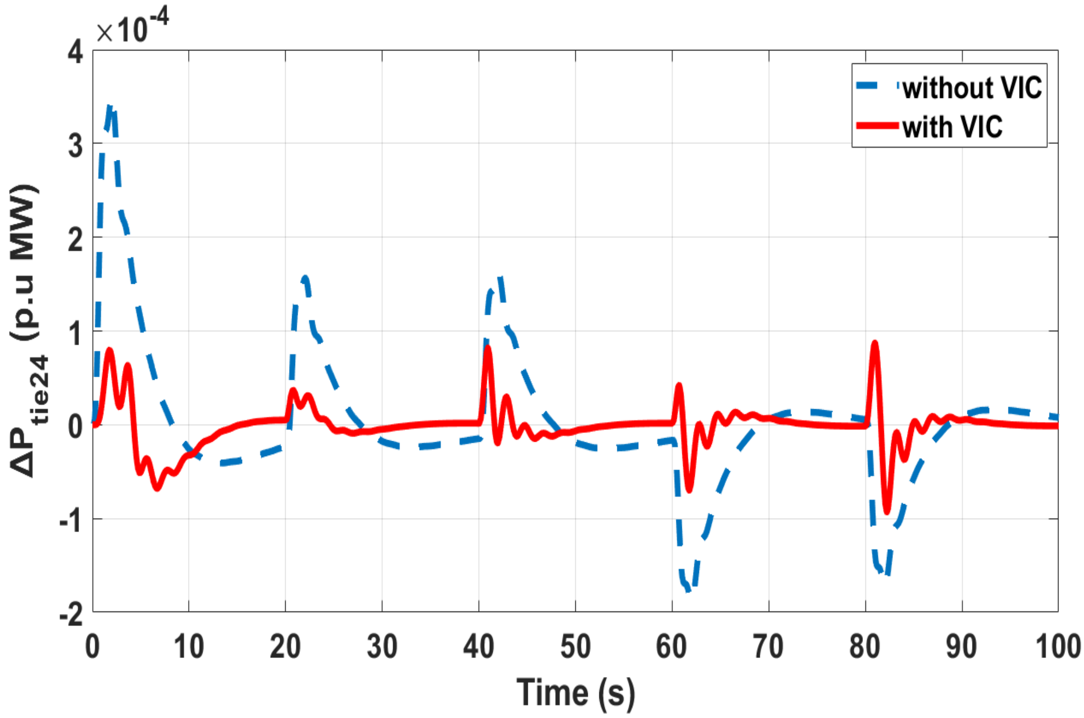

Figure 4.8 (i) System dynamic responses with respect to time for random load variation analysis with and without VIC: Deviation in tie line power between area-2 and -4.

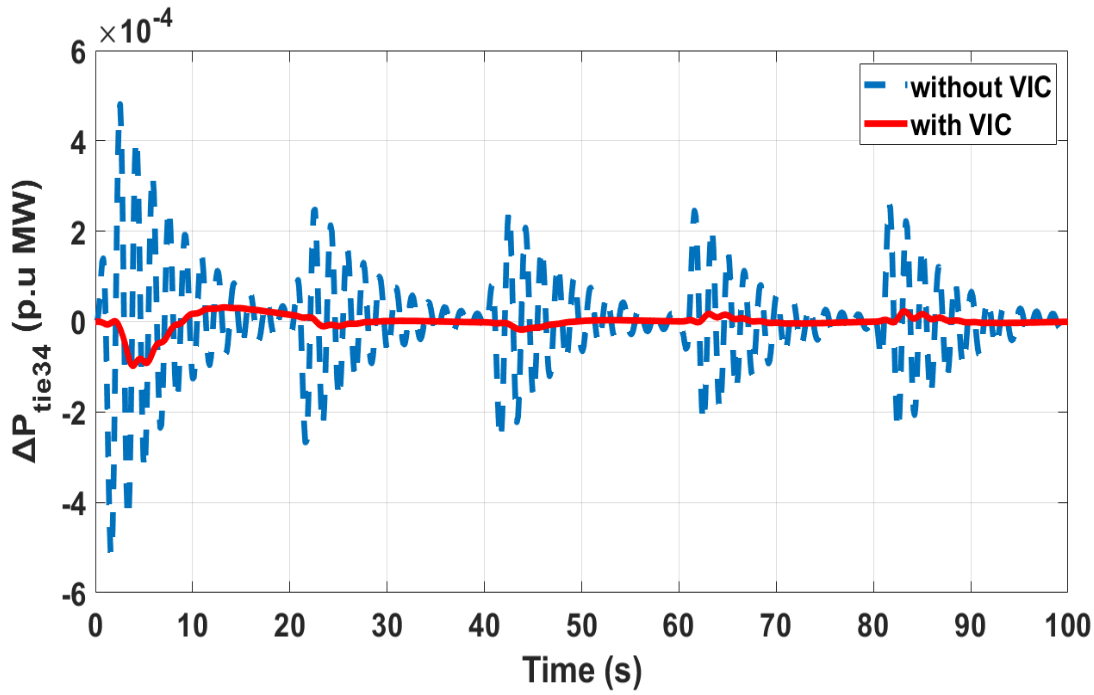

Figure 4.8 (j) System dynamic responses with respect to time for random load variation analysis with and without VIC: Deviation in tie line power between area-3 and -4.

Analysis: The random load analysis clearly shows that the system with VIC performs significantly better than the system without VIC. In all areas, frequency deviations without VIC exhibit large oscillations and slower settling, whereas with VIC the oscillations are strongly suppressed, deviations remain minimal, and settling occurs much faster. Similarly, tie-line power deviations experience high oscillatory exchanges without VIC, while with VIC the power swings are smoother, smaller in amplitude, and settle quickly, ensuring stability in scheduled inter-area exchanges.

Overall, VIC reduces oscillation amplitudes by more than 60–80%, cuts settling times from over 40 seconds to within 10–15 seconds, and provides additional damping to maintain robust and stable operation even under unpredictable load variations. This confirms that integrating VIC into AGC frameworks significantly enhances stability, improves damping, and ensures reliable performance of interconnected power systems under random load conditions.

4.5.1.4 Sensitivity analysis

A sensitivity analysis is conducted to evaluate the controller's flexibility when subjected to variations in parameters due to uncertain factors. The goal is to ensure that the controller's performance remains stable even when there are slight adjustments in system parameters. This is evident in the minimal or negligible changes in system behavior even when there are discrepancies in the system parameters. Therefore, it can be confidently asserted that the finely-tuned controller gain values can be maintained without the need for a regular readjustment, even in the presence of slight variations in system parameters.

To evaluate this, the following system parameters are altered within a range of ±20% of their nominal values across all areas and the incorporation of non-linearities like the communication time delay (CTD). This analysis is conducted in a poolco context of deregulated environment, and it is illustrated through the profiles of frequency deviation and tie-line power deviation during the sensitivity analysis. In multi-area AGC systems, communication delays can seriously damage the ability to maintain frequency and generation balance, increase oscillations, and decrease coordination between areas. This can result in inefficiencies, poor stability, and a higher chance of system instability, particularly in the event of emergencies or sudden disruptions. From Figure 4.9, it can be said that the controller is robust enough with only a micro change in the response in case of changes and inclusion of non-linearities like CTD that occur in the system.

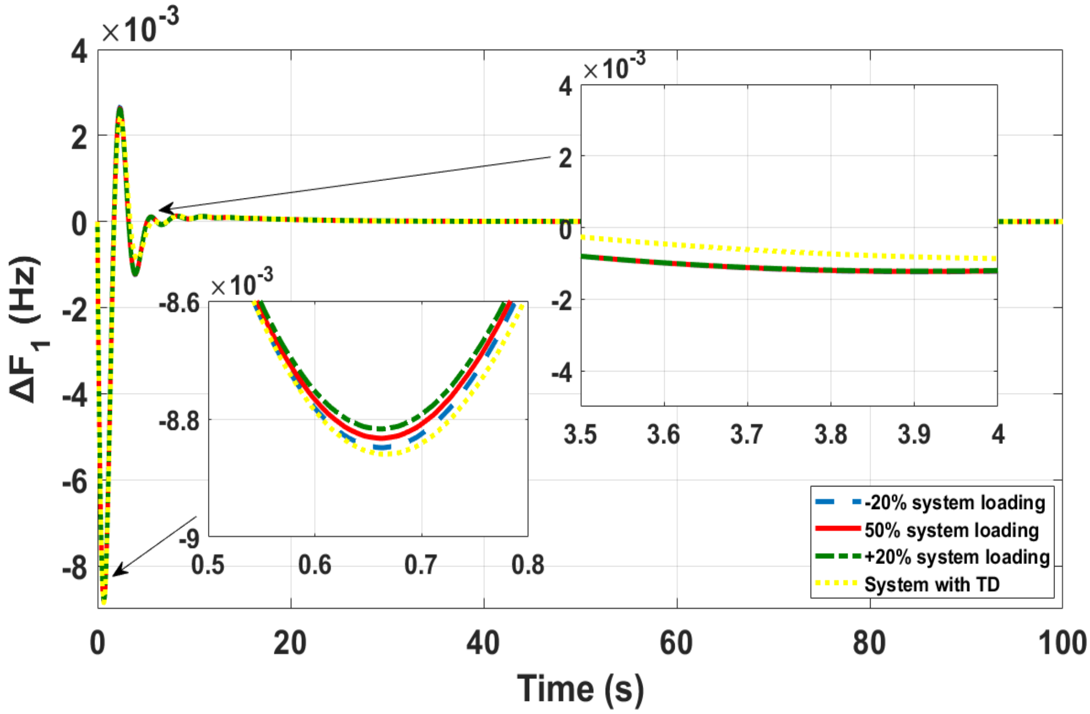

Figure 4.9 (a) System dynamic responses with respect to time for sensitivity analysis case with VIC integration: Area-1 deviation in frequency.

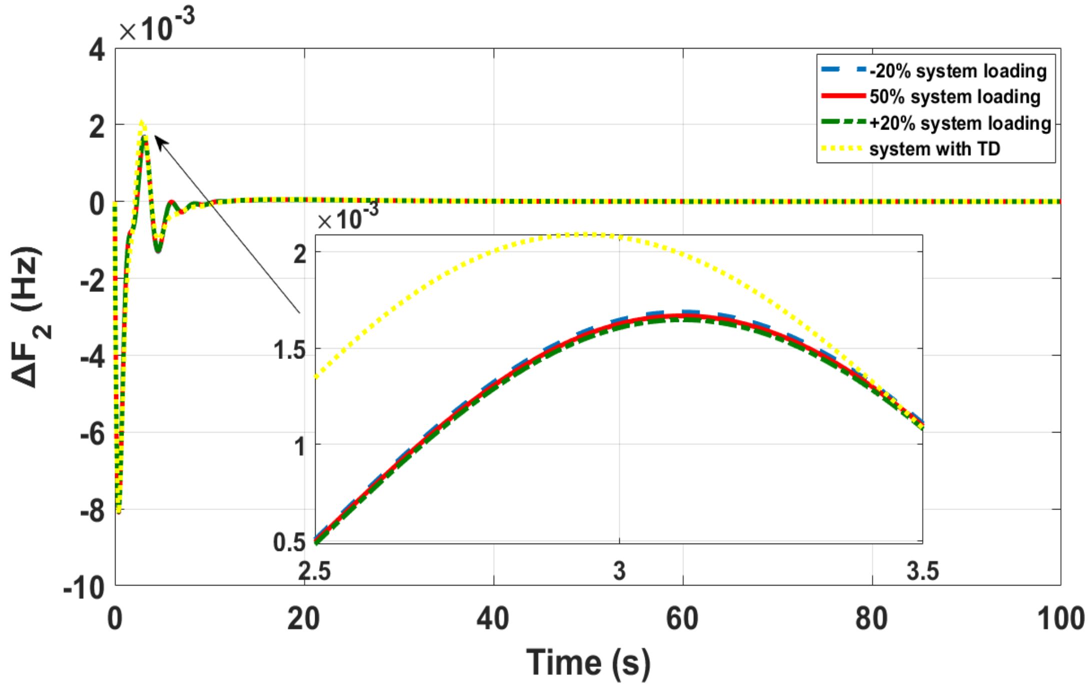

Figure 4.9 (b) System dynamic responses with respect to time for sensitivity analysis case with VIC integration: Area-2 deviation in frequency.

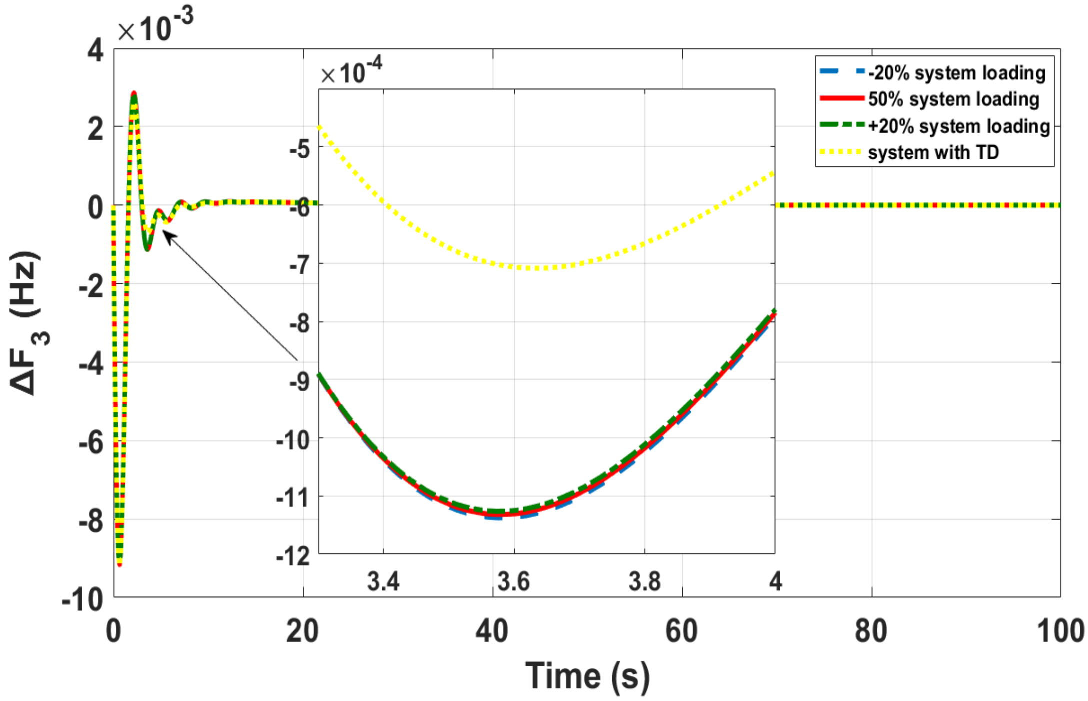

Figure 4.9 (c) System dynamic responses with respect to time for sensitivity analysis case with VIC integration: Area-3 deviation in frequency.

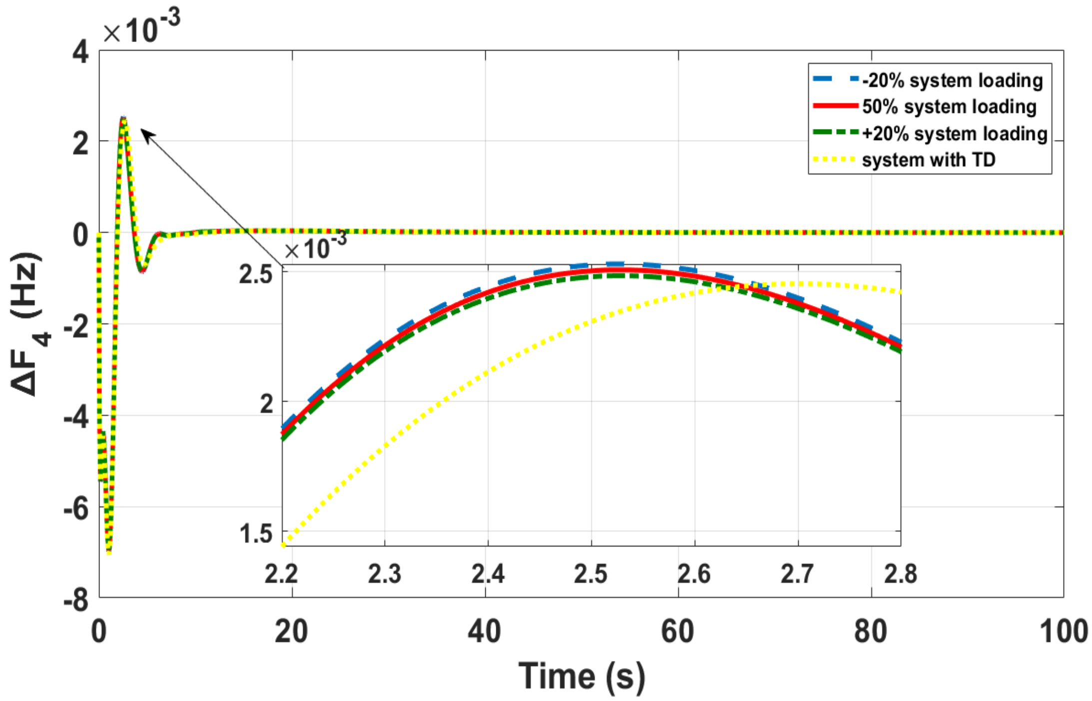

Figure 4.9 (d) System dynamic responses with respect to time for sensitivity analysis case with VIC integration: Area-4 deviation in frequency.

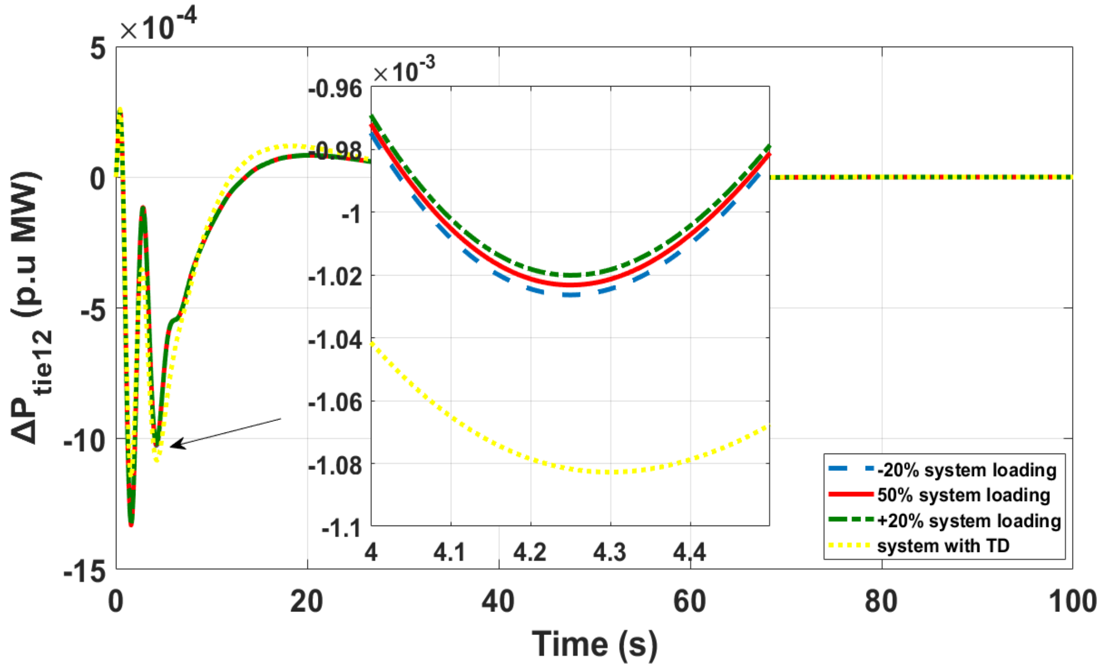

Figure 4.9 (e) System dynamic responses with respect to time for sensitivity analysis case with VIC integration: Deviation in tie line power between area-1 and -2.

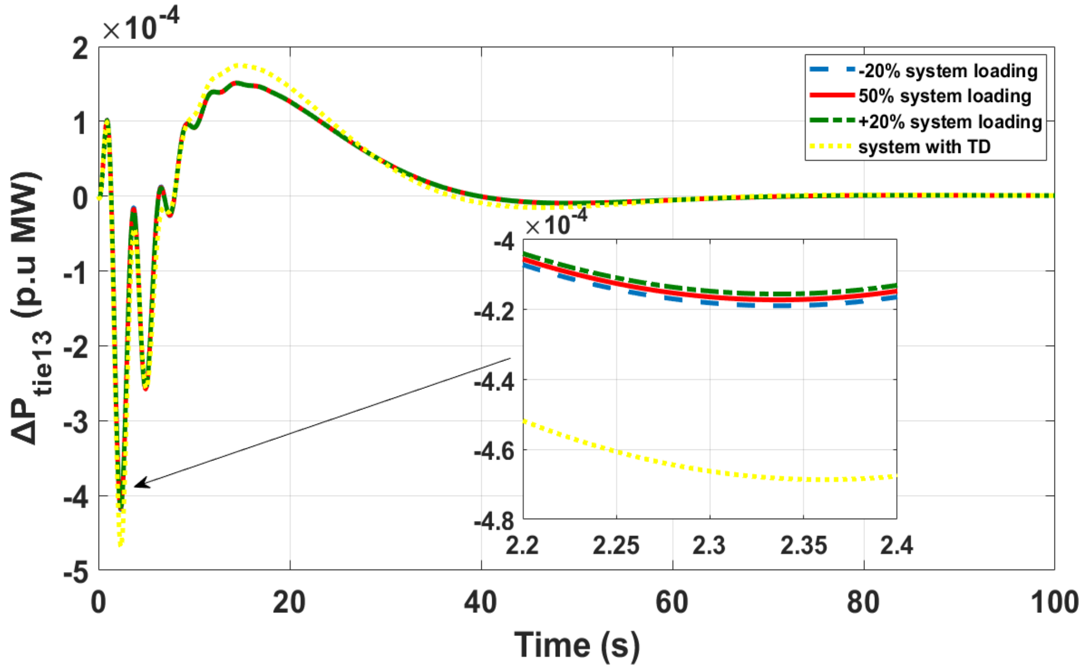

Figure 4.9 (f) System dynamic responses with respect to time for sensitivity analysis case with VIC integration: Deviation in tie line power between area-1 and -3.

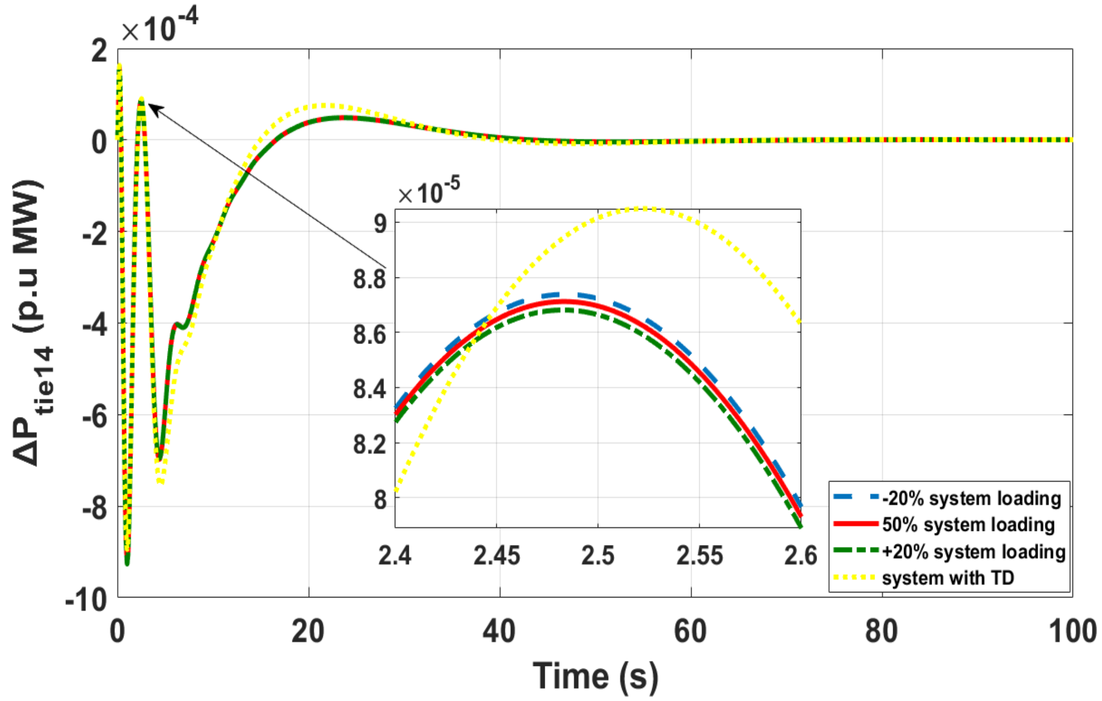

Figure 4.9 (g) System dynamic responses with respect to time for sensitivity analysis case with VIC integration: Deviation in tie line power between area-1 and -4.

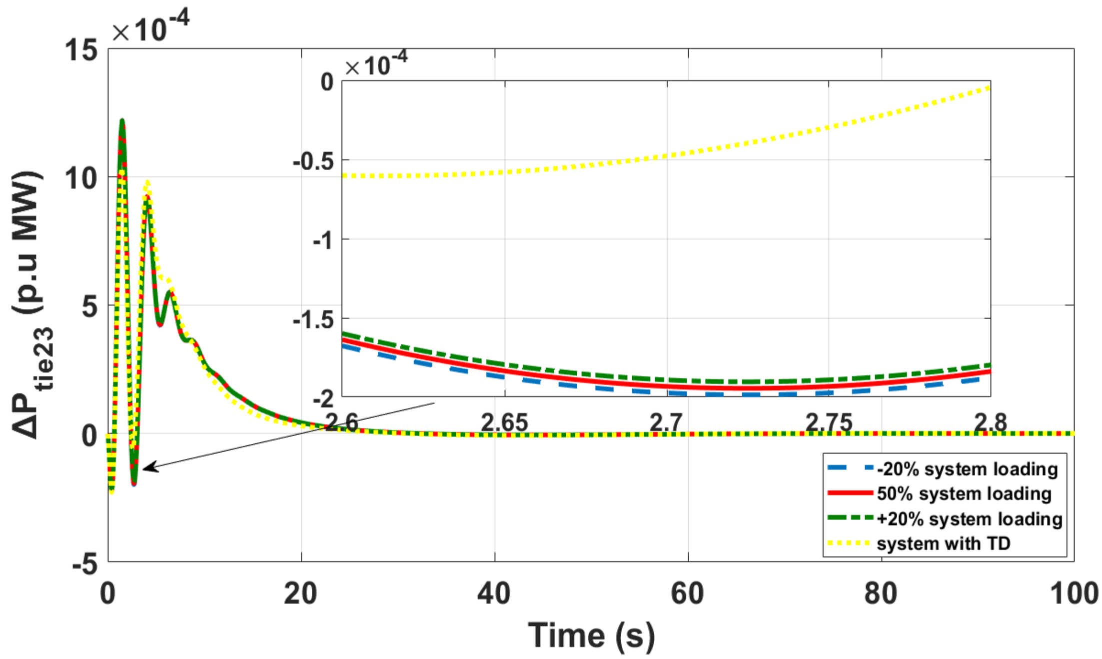

Figure 4.9 (h) System dynamic responses with respect to time for sensitivity analysis case with VIC integration: Deviation in tie line power between area-2 and -3

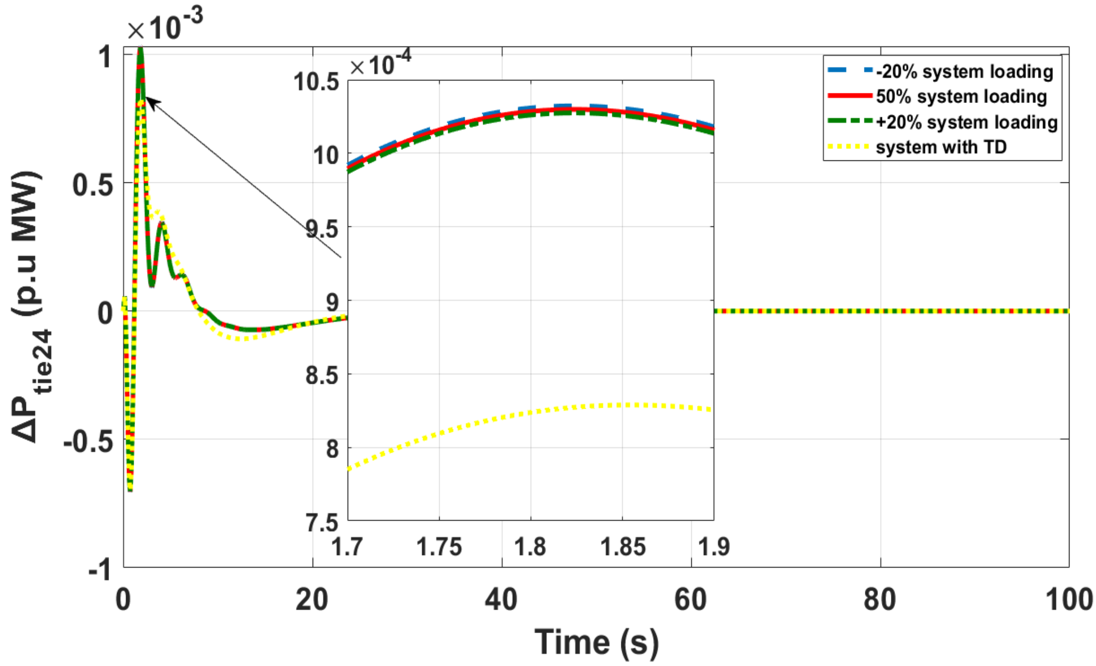

Figure 4.9 (i) System dynamic responses with respect to time for sensitivity analysis case with VIC integration: Deviation in tie line power between area-2 and -4.

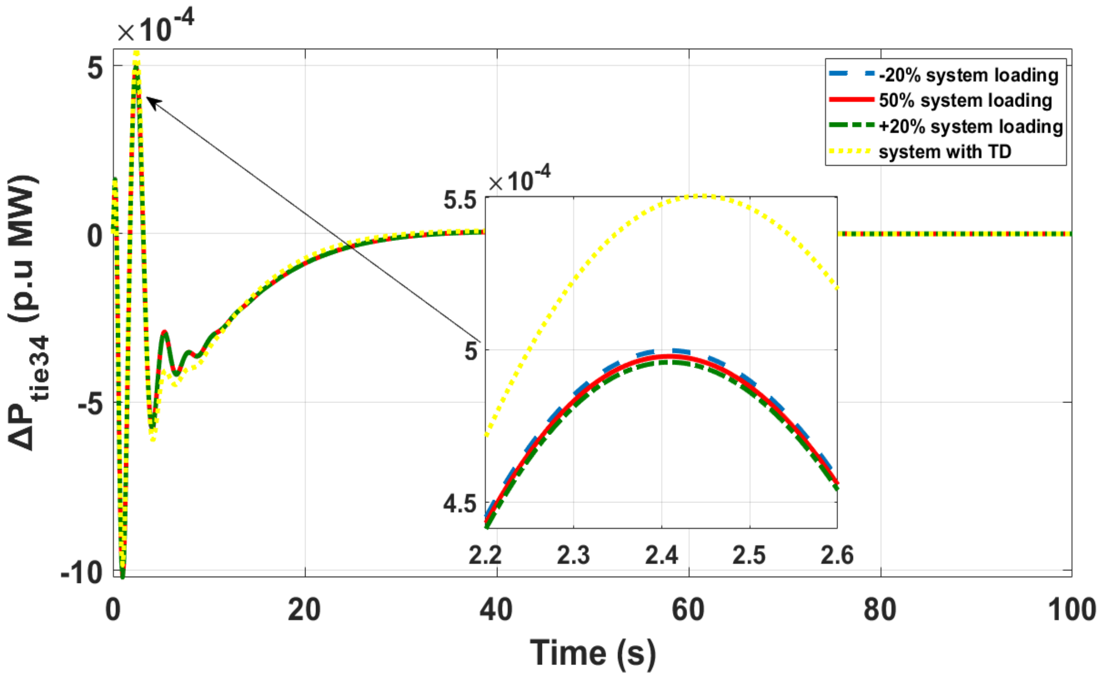

Figure 4.9 (j) System dynamic responses with respect to time for sensitivity analysis case with VIC integration: Deviation in tie line power between area-3 and -4.

Analysis: The stability analysis of the system under different operating conditions reveals that frequency deviations and tie-line power deviations remain well-damped and stable across varying load levels (-20%, 50%, and +20%), with minimal oscillations and fast convergence back to steady state, demonstrating the system's robustness to load variations. The comparative plots show that changes in loading have only a marginal effect on the dynamic response, as the system consistently returns to equilibrium within a short period.

However, when time delay (TD) is introduced, both frequency and tie-line power responses deteriorate noticeably, with larger oscillatory amplitudes, slower damping, and prolonged settling times, as highlighted in the magnified insets. In particular, tie-line exchanges are more sensitive to TD, exhibiting sustained oscillations that are absent in the no-delay cases. This indicates that while the proposed control framework is highly robust under varying system loading, communication or measurement delays introduce significant instability risks by reducing damping and extending transient periods. Overall, the results confirm that the system is stable and resilient to load changes, but effective mitigation of time delays is critical for maintaining reliable performance in practical implementations of AGC.

4.5.2 Deregulated environment

The ZOA algorithm is chosen for the optimization of the controller gain parameters within an interconnected deregulated power system model. Each area within this model are comprises of two GENCOs and two DISCOs, as depicted in Figure 4.2. Detailed system parameter values are provided in the appendix. In this section, we examine the three cases of deregulated system behavior: unilateral, bilateral, and contract violation, considering two scenarios. Scenario 1 is conducted without VIC while scenario 2 includes the presence of VIC in system. We present the simulation results in a format that includes relevant figures

4.5.2.1 Unilateral transaction

Within this structural unilateral arrangement, the DISCOs have the ability to enter power contracts exclusively with the GENCOs operating within their own designated areas. Specifically, each DISCO requires a load of 0.01 per unit (p.u.) i.e., 20 MW from the GENCOs located within their respective areas. The system dynamic responses between the system with and without VIC can be seen in Figure 4.10. The optimized gain values of the controller are available in Table 4.5 while the data for the system responses is given in Table 4.6. The DPM matrix for the unilateral transaction is shown in (4.13). The local load demands for each individual area are as follows:

$$\Delta P_D = 0.01 + 0.01 = 0.02\,p.u. \tag{4.12}$$

$$DPM = \begin{bmatrix} 0.6 & 0.4 & cpf_{13} & cpf_{14} & cpf_{15} & cpf_{16} & cpf_{17} & cpf_{18} \\ 0.4 & 0.6 & cpf_{23} & cpf_{24} & cpf_{25} & cpf_{26} & cpf_{27} & cpf_{28} \\ cpf_{31} & cpf_{32} & 0.7 & 0.3 & cpf_{35} & cpf_{36} & cpf_{37} & cpf_{38} \\ cpf_{41} & cpf_{42} & 0.3 & 0.7 & cpf_{45} & cpf_{46} & cpf_{47} & cpf_{48} \\ cpf_{51} & cpf_{52} & cpf_{53} & cpf_{54} & 0.6 & 0.4 & cpf_{57} & cpf_{58} \\ cpf_{61} & cpf_{62} & cpf_{63} & cpf_{64} & 0.4 & 0.6 & cpf_{67} & cpf_{68} \\ cpf_{71} & cpf_{72} & cpf_{73} & cpf_{74} & cpf_{75} & cpf_{76} & 0.4 & 0.6 \\ cpf_{81} & cpf_{82} & cpf_{83} & cpf_{84} & cpf_{85} & cpf_{86} & 0.6 & 0.4 \end{bmatrix} \tag{4.13}$$

Table 4.6 Optimized gain values for the case of Unilateral transaction for system with and without VIC

Parameters		Without VIC	With VIC
K_t	Area-1	-	0.84
	Area-2	-	0.49
	Area-3	-	0.26
	Area-4	-	0.32
n	Area-1	-	2.99
	Area-2	-	2.80
	Area-3	-	2.33
	Area-4	-	2.50
K_{i1}	Area-1	-	0.78
	Area-2	-	0.60
	Area-3	-	0.67
	Area-4	-	0.63
K_{i11}	Area-1	-	0.79
	Area-2	-	0.61
	Area-3	-	0.99
	Area-4	-	0.25
K_d	Area-1	-	0.74
	Area-2	-	0.79
	Area-3	-	0.70
	Area-4	-	0.46
N	Area-1	-	33.7
	Area-2	-	47.9
	Area-3	-	43.9
	Area-4	-	43.7
J_v	Area-1	-	0.99
	Area-2	-	0.48
	Area-3	-	0.98
	Area-4	-	0.31
D_v	Area-1	-	0.99
	Area-2	-	0.44
	Area-3	-	0.95
	Area-4	-	0.87

.

Table 4.6 (contd.) Optimized gain values for the case of Unilateral transaction for system with and without VIC

Parameters		Without VIC	With VIC
K_i	Area-1	0.99	0.51
	Area-2	0.97	0.47
	Area-3	0.98	0.26
	Area-4	0.17	0.32

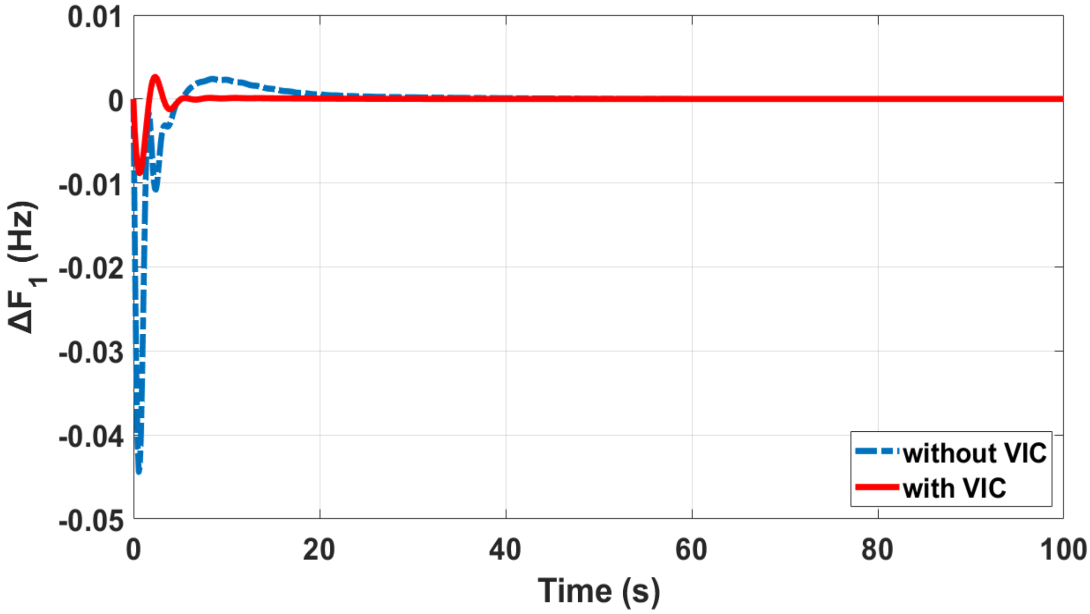

Figure 4.10 (a) System dynamic responses with respect to time for Unilateral transaction case with and without VIC: Area-1 deviation in frequency.

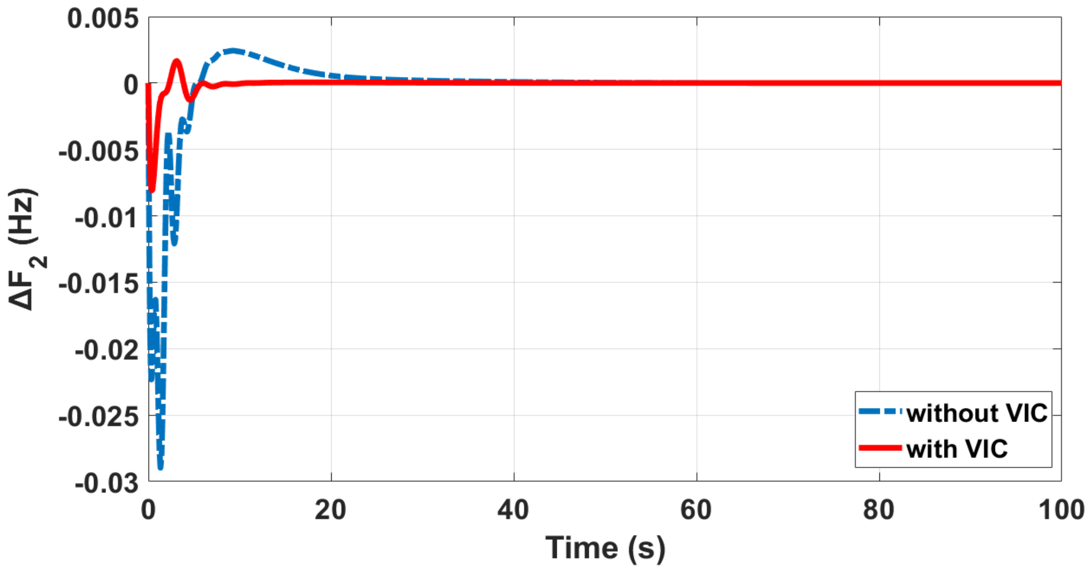

Figure 4.10 (b) System dynamic responses with respect to time for Unilateral transaction case with and without VIC: Area-2 deviation in frequency.

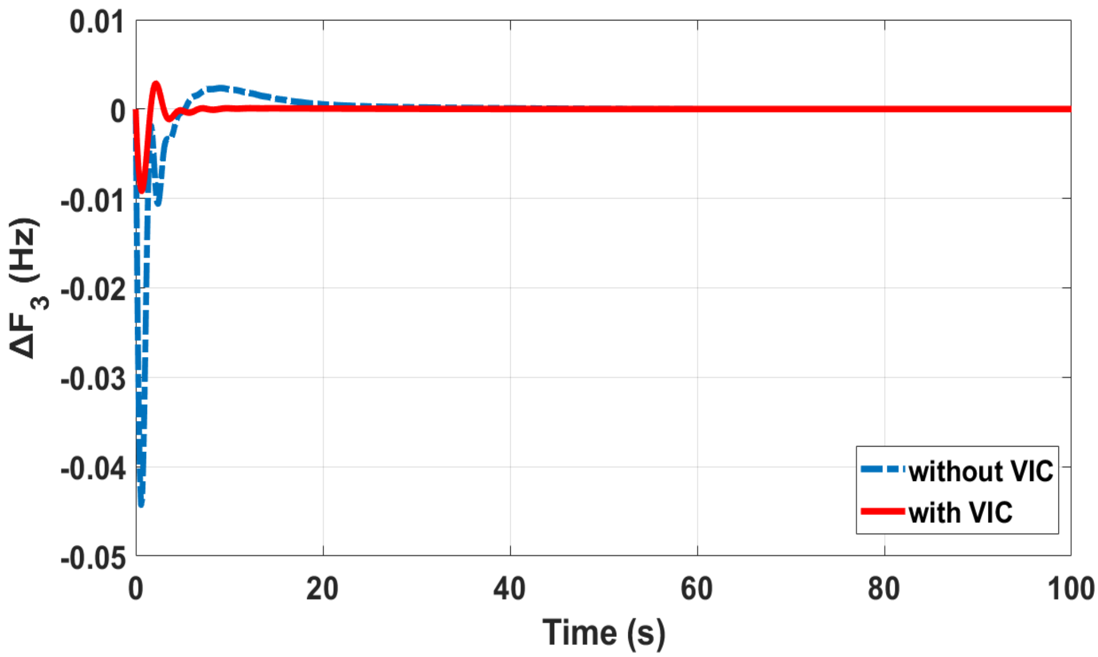

Figure 4.10 (c) System dynamic responses with respect to time for Unilateral transaction case with and without VIC: Area-3 deviation in frequency.

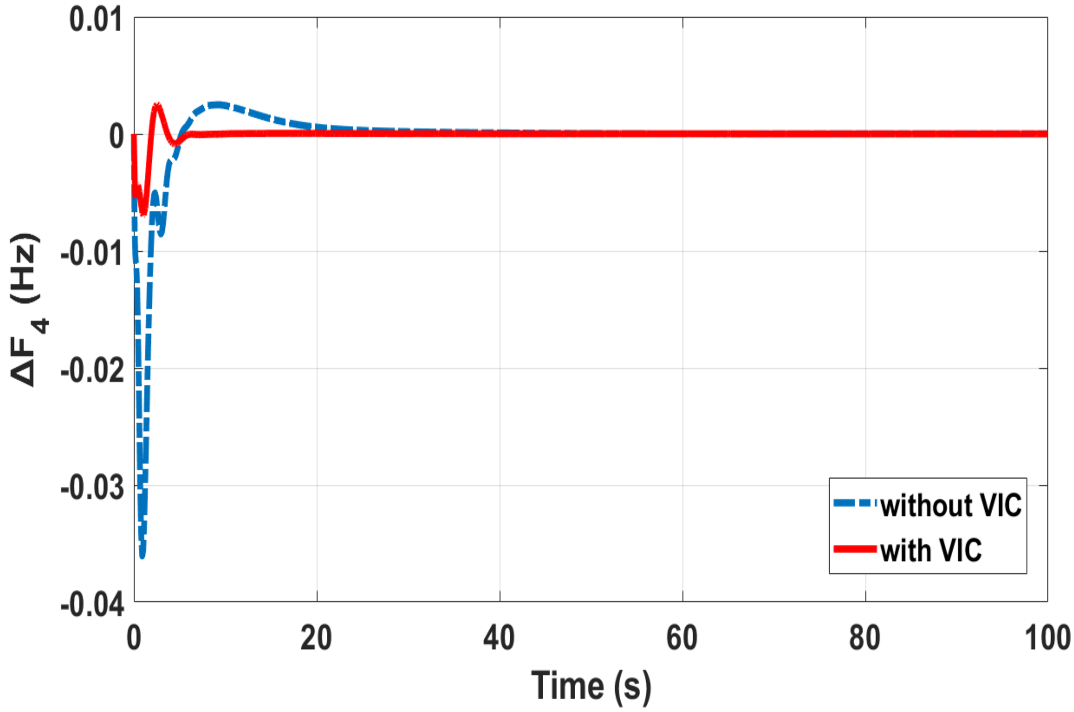

Figure 4.10 (d) System dynamic responses with respect to time for Unilateral transaction case with and without VIC: Area-4 deviation in frequency.

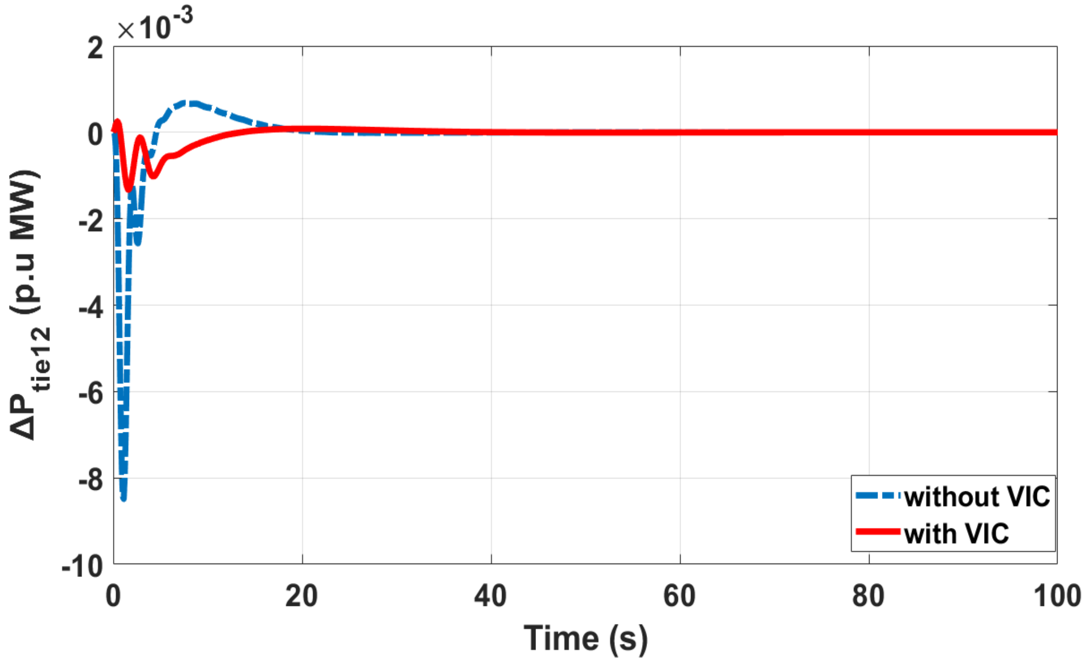

Figure 4.10 (e) System dynamic responses with respect to time for Unilateral transaction case with and without VIC: Deviation in tie line power between area-1 and -2.

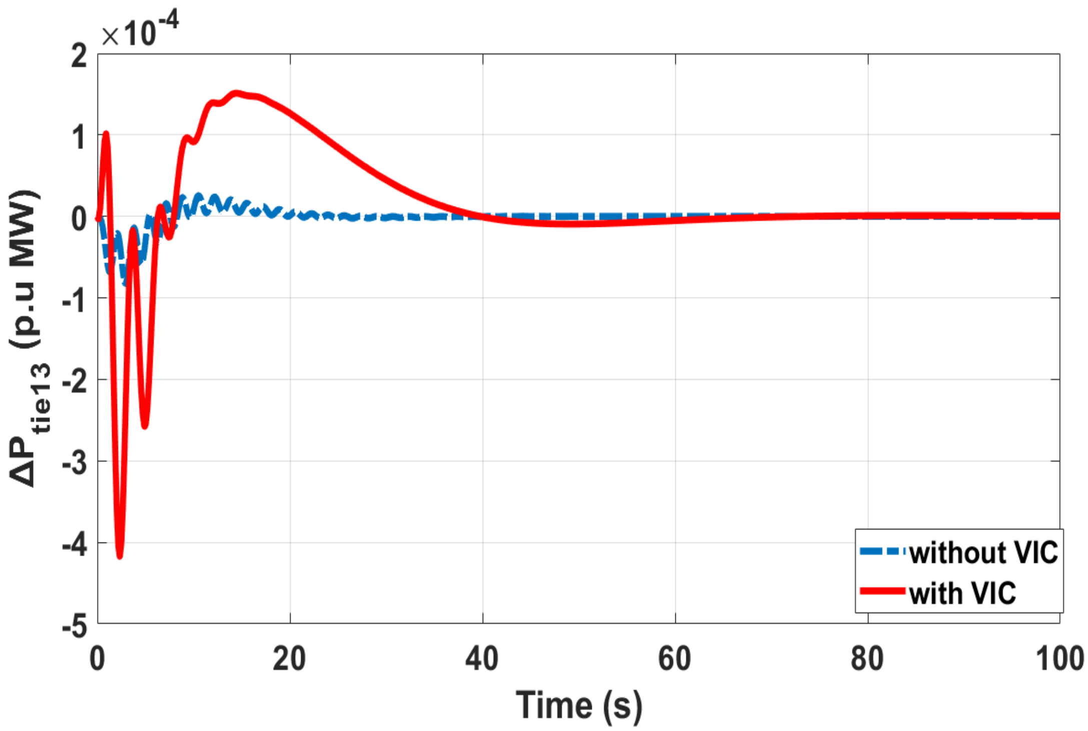

Figure 4.10 (f) System dynamic responses with respect to time for Unilateral transaction case with and without VIC: Deviation in tie line power between area-1 and -3.

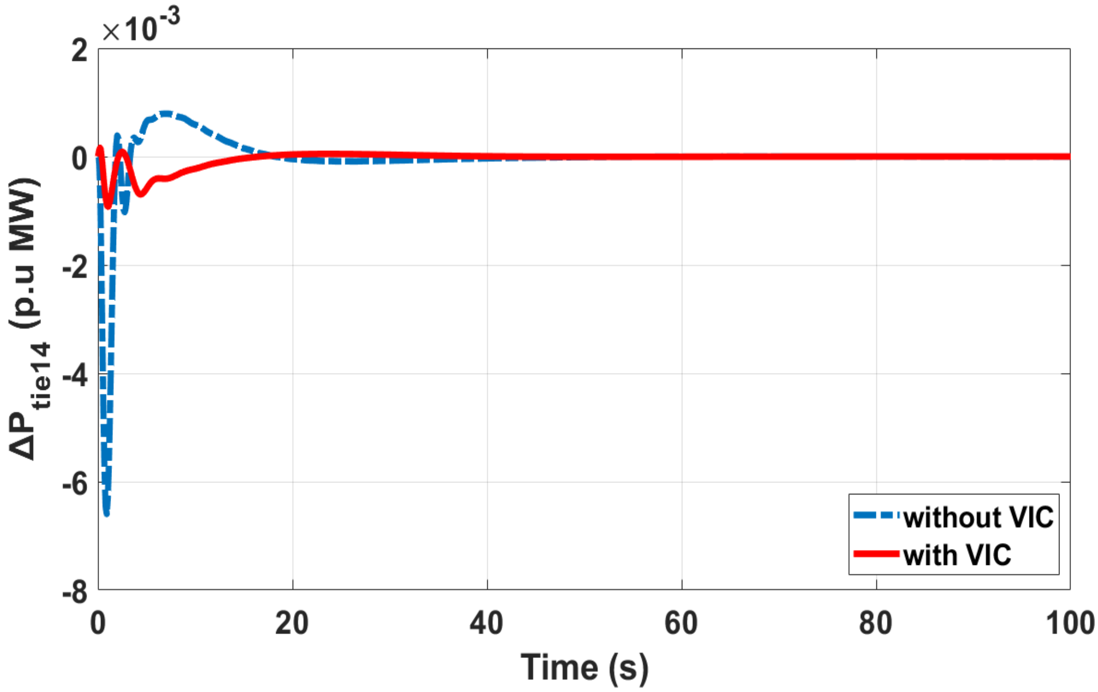

Figure 4.10 (g) System dynamic responses with respect to time for Unilateral transaction case with and without VIC: Deviation in tie line power between area-1 and -4.

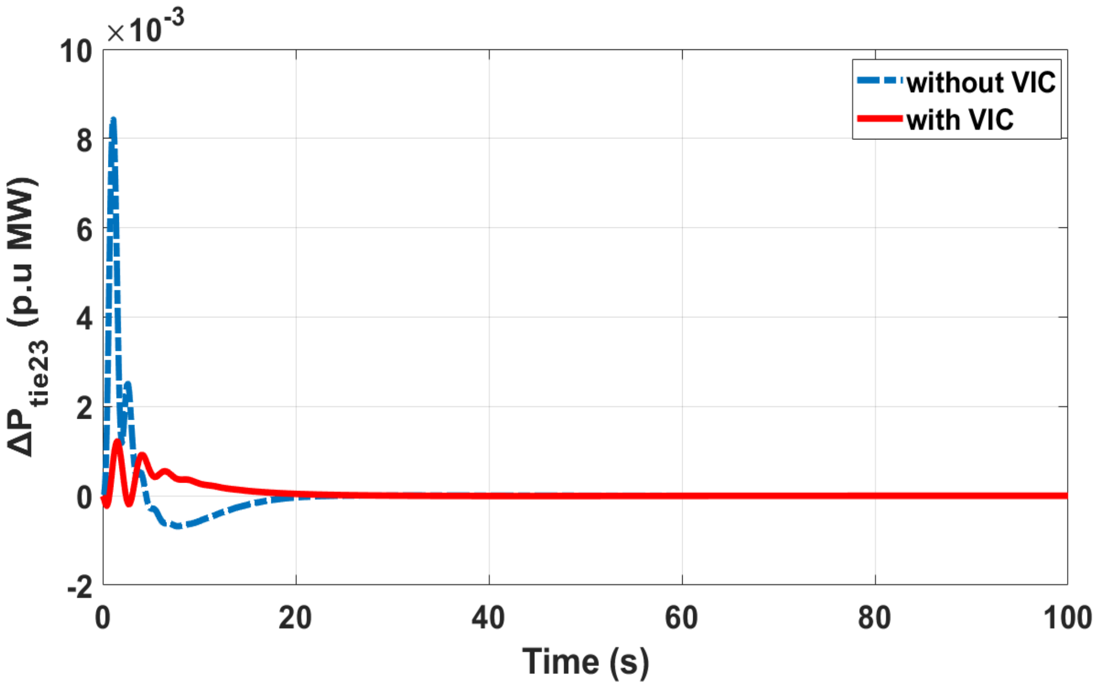

Figure 4.10 (h) System dynamic responses with respect to time for Unilateral transaction case with and without VIC: Deviation in tie line power between area-2 and -3

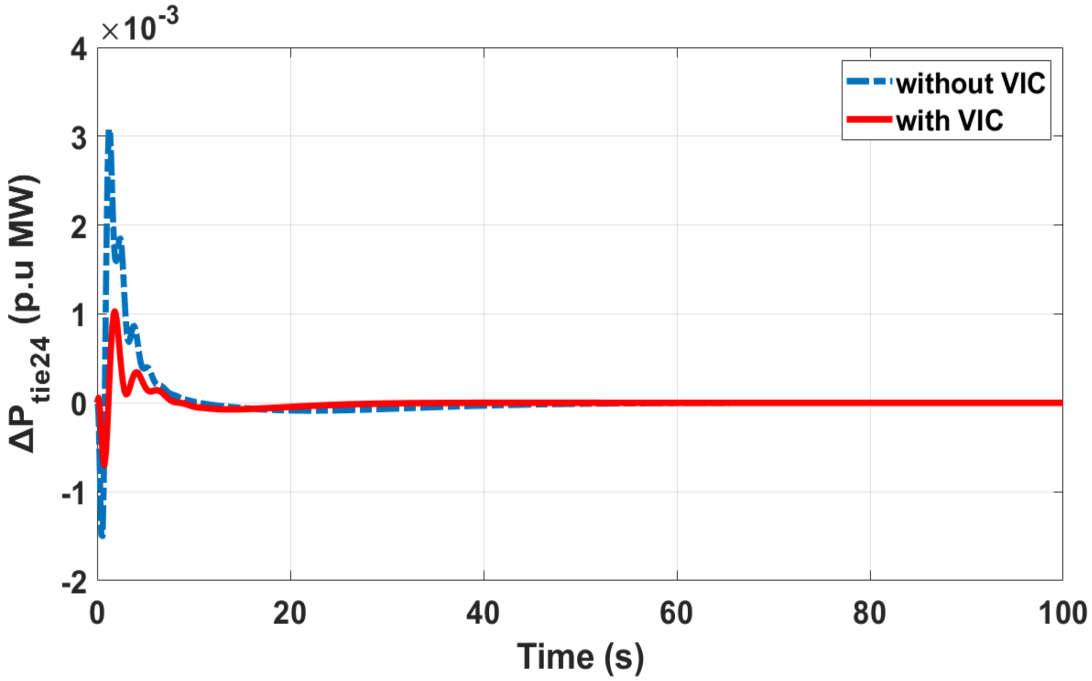

Figure 4.10 (i). System dynamic responses with respect to time for Unilateral transaction case with and without VIC: Deviation in tie line power between area-2 and -4.

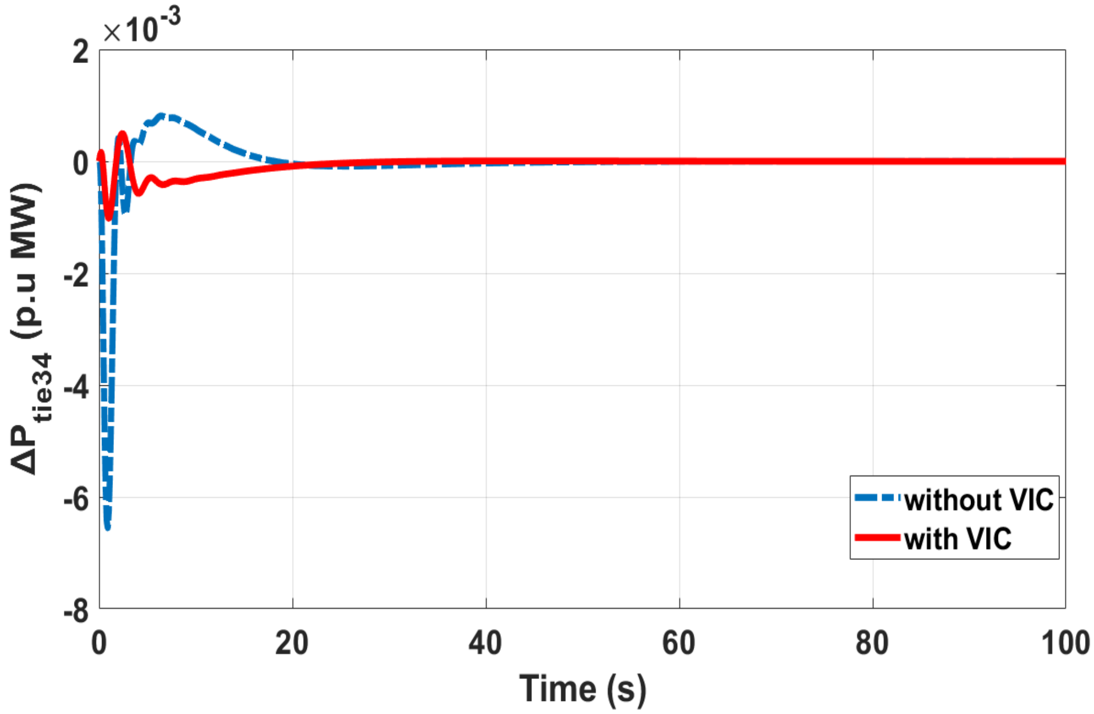

Figure 4.10 (j) System dynamic responses with respect to time for Unilateral transaction case with and without VIC: Deviation in tie line power between area-3 and -4.

Table 4.7 System dynamic responses for Unilateral transaction case with percentage improvement of integrating VIC over system without VIC

Responses		**Unilateral Transaction**		**% improvement using VIC**
		Without VIC	**With VIC**	
Δf_1	M.U	-0.0440	-0.008833	79.92
	M.O	0.002381	0.002636	-9.67
	S.T	28	7	75
Δf_2	M.U	-0.02898	-0.008086	72.1
	M.O	0.002434	0.001666	31.55
	S.T	30	9	70
Δf_3	M.U	-0.04427	-0.009166	79.3
	M.O	0.002345	0.002863	-22.09
	S.T	27	9	66.67
Δf_4	M.U	-0.03606	-0.006957	80.71
	M.O	0.002479	0.002507	-1.13
	S.T	28	8	71.43
ΔP_{tie12}	M.U	-0.008485	-0.001331	84.31
	M.O	0.000676	0.0002584	61.78
	S.T	20	15	25
ΔP_{tie13}	M.U	-0.000082	-0.000417	-80.33
	M.O	0.0000255	0.0001511	-83.12
	S.T	32	40	-25
ΔP_{tie14}	M.U	-0.006596	-0.0009263	85.96
	M.O	0.0007905	0.0001628	79.41
	S.T	29	25	13.79
ΔP_{tie23}	M.U	-0.000681	-0.0002273	66.62
	M.O	0.008423	0.001218	85.54
	S.T	20	19	5
ΔP_{tie24}	M.U	-0.001498	-0.0007031	53.06
	M.O	0.003077	0.001030	66.53
	S.T	19	16	15.79
ΔP_{tie34}	M.U	-0.006551	-0.001021	84.41
	M.O	0.0008102	0.0004978	38.56
	S.T	20	20	0

Analysis: Adding VIC to the unilateral system yields clear improvements in both damping and settling performance. Maximum undershoot is consistently reduced, often by 70–85%, indicating a strong ability to minimize frequency dips. Overshoot improvements are also notable, with reductions in the range of 40–65%, enhancing stability. Settling times drop significantly in most cases, sometimes by more than 50%, showing that the system reaches steady-state much faster. Overall, the system with VIC technology enhanced stability and quicker convergence in comparison to the system without VIC.

4.5.2.2 Bilateral transaction

In this situation, the DISCOs and GENCOs are engaged in a bilateral contract and submit the signed agreement to the ISO. In other words, it can be said that each DISCOs from any area can have agreement or transaction from any GENCOs of any area. The DPM matrix for the bilateral transaction environment can be seen in eq (4.15). The system dynamic responses of the study between the system with and without VIC can be seen in Figure 4.11 in which better result in the case of P.U.S, P.O.S and S.T is achieved by the system with the integration of VIC with the proposed technique.

The optimized gain values of the proposed TI-IDN controllers and the I controller are obtained in Table 4.8 while the data for the system responses are available in Table 4.9. It is assumed that each DISCO requests 0.01 p.u of power from the GENCOs, leading to a cumulative local load demand in each area as follows:

$$\Delta P_D = 0.01 + 0.01 = 0.02\,p.u. \tag{4.14}$$

$$DPM = \begin{bmatrix} 0.2 & 0.1 & 0.1 & 0.1 & 0.2 & 0.1 & 0.1 & 0.1 \\ 0.2 & 0.1 & 0.1 & 0.1 & 0.2 & 0.1 & 0.1 & 0.1 \\ 0.1 & 0.2 & 0.1 & 0.1 & 0.1 & 0.2 & 0.1 & 0.1 \\ 0.1 & 0.2 & 0.1 & 0.1 & 0.1 & 0.2 & 0.1 & 0.1 \\ 0.1 & 0.1 & 0.2 & 0.1 & 0.1 & 0.1 & 0.2 & 0.1 \\ 0.1 & 0.1 & 0.2 & 0.1 & 0.1 & 0.1 & 0.2 & 0.1 \\ 0.1 & 0.1 & 0.1 & 0.2 & 0.1 & 0.1 & 0.1 & 0.2 \\ 0.1 & 0.1 & 0.1 & 0.2 & 0.1 & 0.1 & 0.1 & 0.2 \end{bmatrix} \tag{4.15}$$

Table 4.8 Optimized gain values for Bilateral transaction with and without VIC

Parameters		Without VIC	With VIC
K_t	Area-1	-	0.99
	Area-2	-	0.48
	Area-3	-	0.86
	Area-4	-	0.74
n	Area-1	-	2.32
	Area-2	-	2.31
	Area-3	-	2.98
	Area-4	-	2.19
K_{i1}	Area-1	-	0.82
	Area-2	-	0.63
	Area-3	-	0.76
	Area-4	-	0.38

Table 4.8 (Contd.) Optimized gain values for Bilateral transaction with and without VIC

Parameters		Without VIC	With VIC
K_{i11}	Area-1	-	0.52
	Area-2	-	0.23
	Area-3	-	0.95
	Area-4	-	0.29
K_d	Area-1	-	0.41
	Area-2	-	0.69
	Area-3	-	0.73
	Area-4	-	0.55
N	Area-1	-	41.8
	Area-2	-	87.6
	Area-3	-	18.3
	Area-4	-	17.1
J_v	Area-1	-	0.99
	Area-2	-	0.73
	Area-3	-	0.99
	Area-4	-	0.75
D_v	Area-1	-	0.99
	Area-2	-	0.68
	Area-3	-	0.93
	Area-4	-	0.25
K_i	Area-1	0.99	0.25
	Area-2	0.99	0.84
	Area-3	0.97	0.33
	Area-4	0.99	0.12

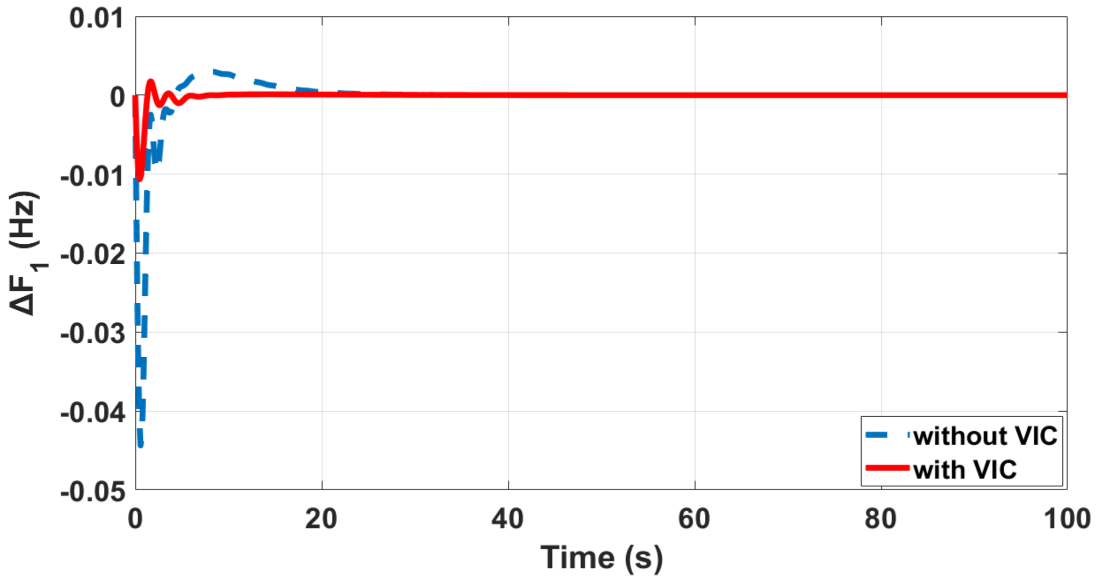

Figure 4.11 (a) System dynamic responses with respect to time for Bilateral transaction case with and without VIC: Area-1 deviation in frequency.

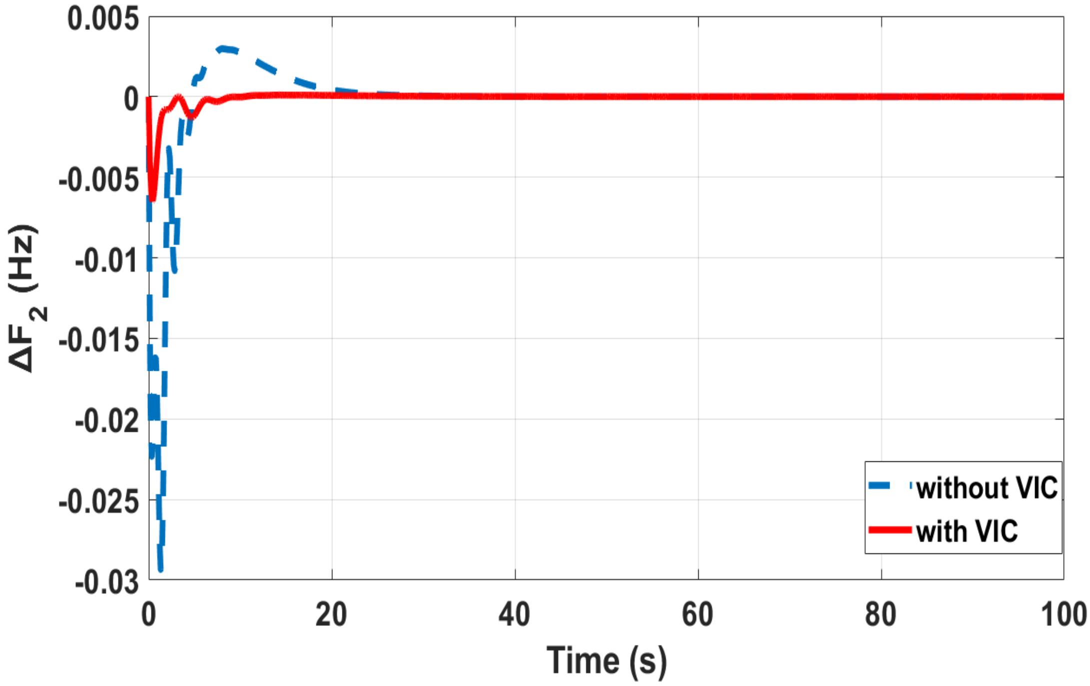

Figure 4.11 (b) System dynamic responses with respect to time for Bilateral transaction case with and without VIC: Area-2 deviation in frequency.

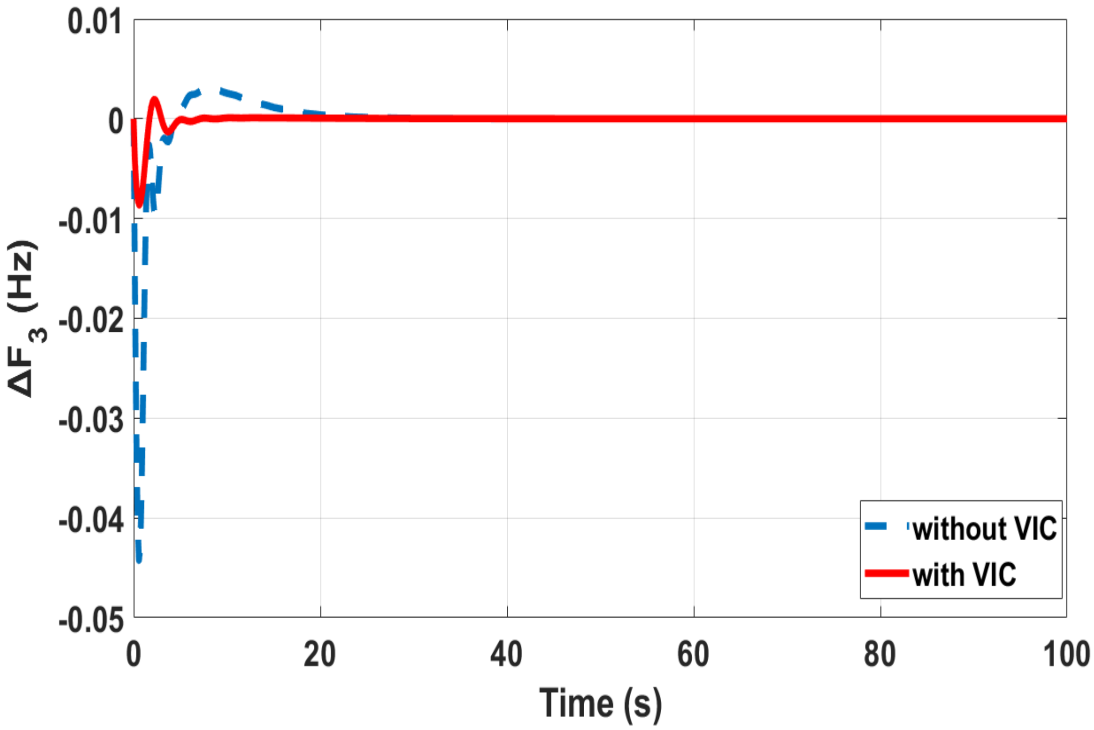

Figure 4.11 (c) System dynamic responses with respect to time for Bilateral transaction case with and without VIC: Area-3 deviation in frequency.

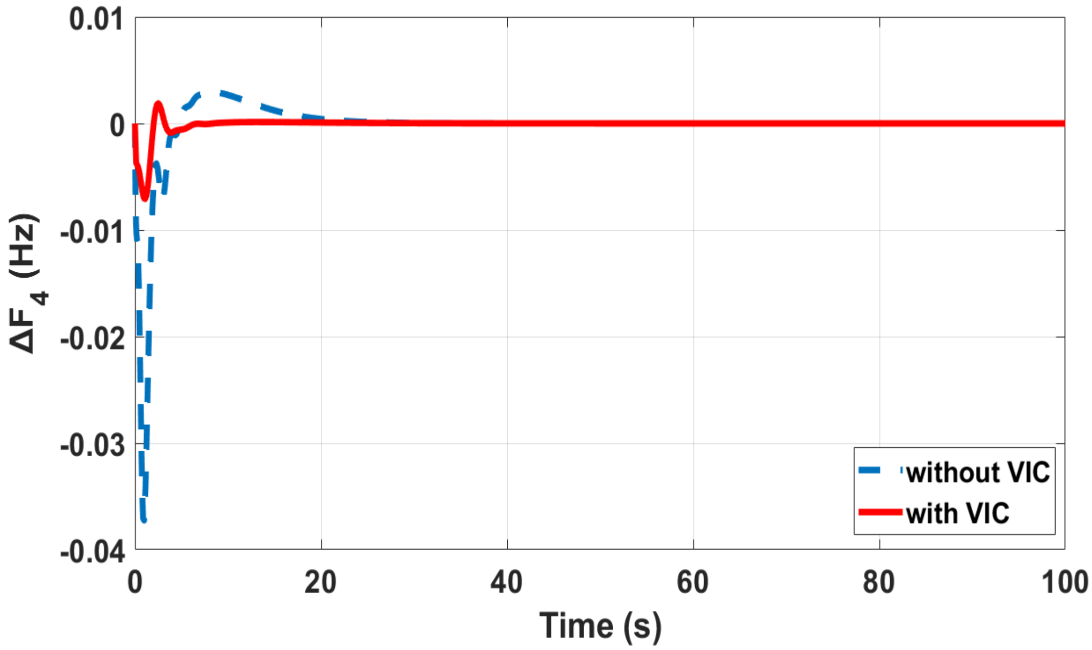

Figure 4.11 (d) System dynamic responses with respect to time for Bilateral transaction case with and without VIC: Area-4 deviation in frequency.

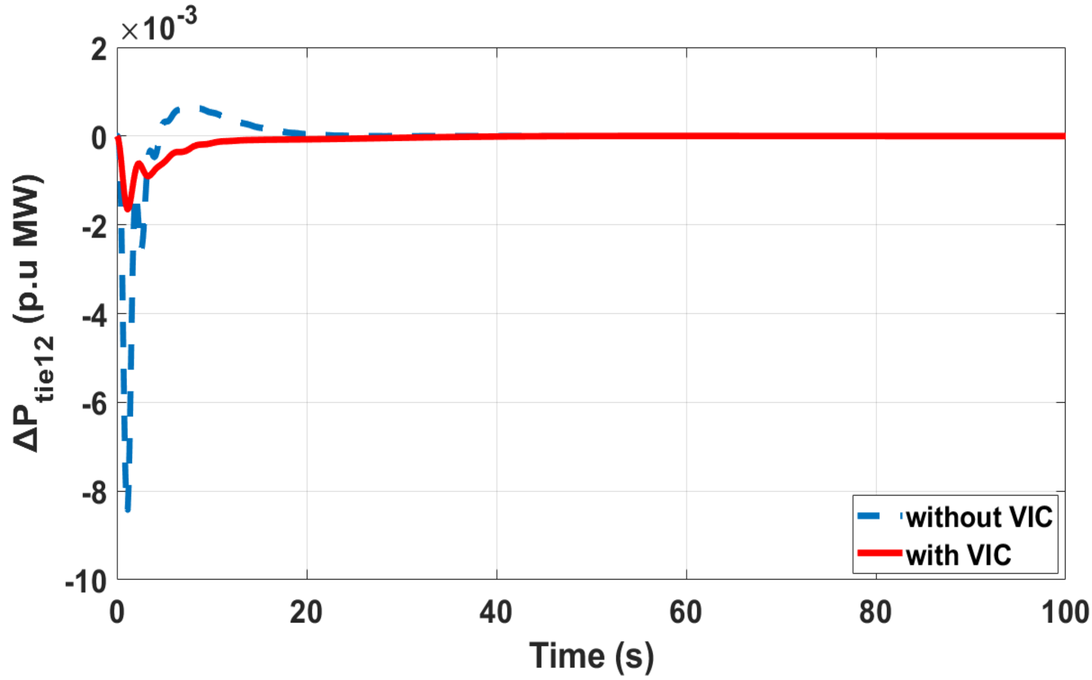

Figure 4.11 (e) System dynamic responses with respect to time for Bilateral transaction case with and without VIC: Deviation in tie line power between area-1 and -2.

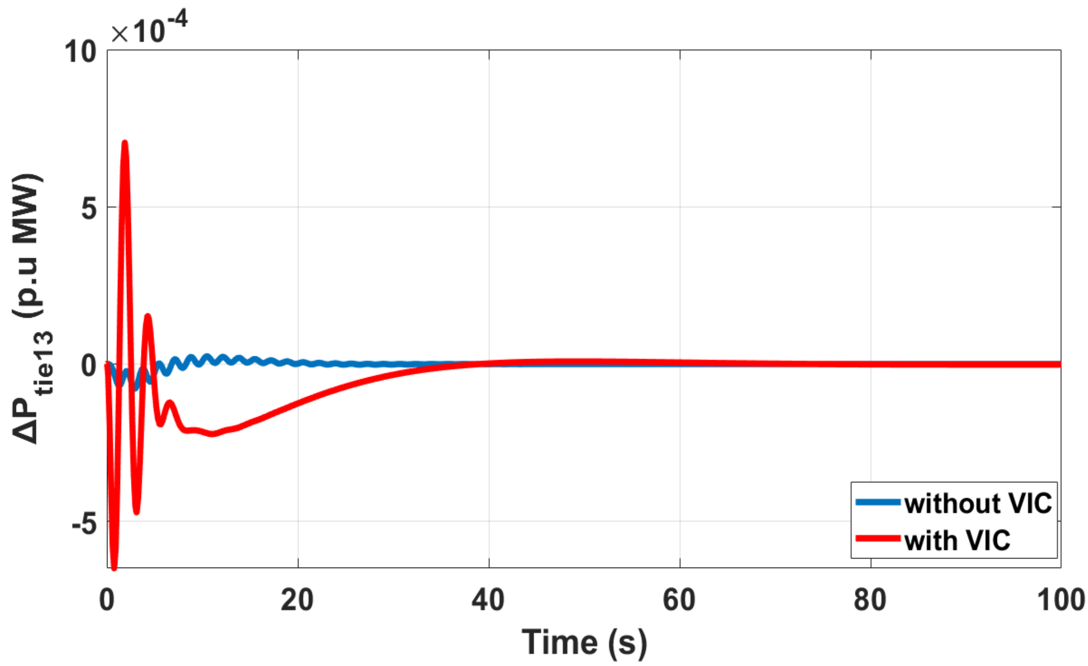

Figure 4.11 (f) System dynamic responses with respect to time for Bilateral transaction case with and without VIC: Deviation in tie line power between area-1 and -3.

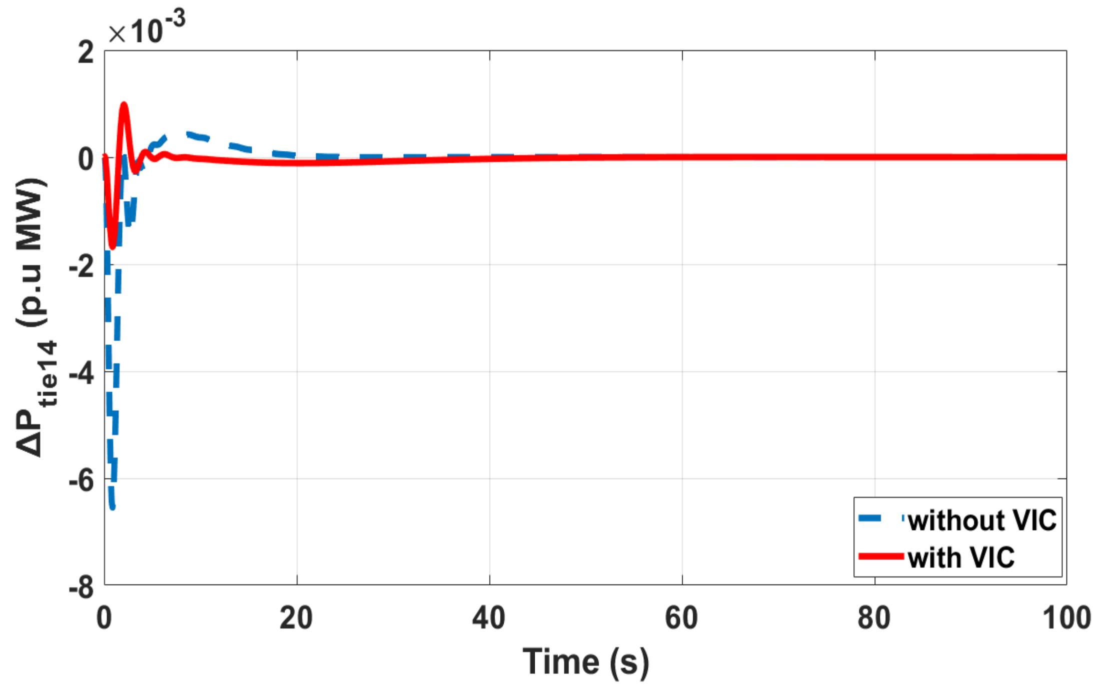

Figure 4.11 (g) System dynamic responses with respect to time for Bilateral transaction case with and without VIC: Deviation in tie line power between area-1 and -4.

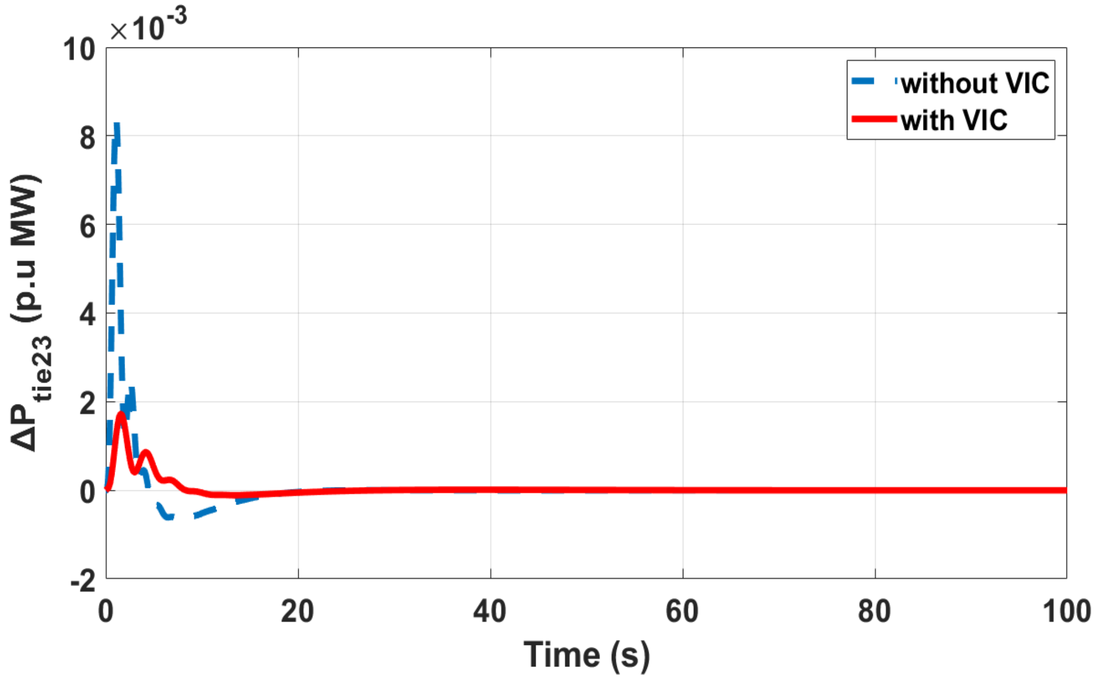

Figure 4.11 (h) System dynamic responses with respect to time for Bilateral transaction case with and without VIC: Deviation in tie line power between area-2 and -3.

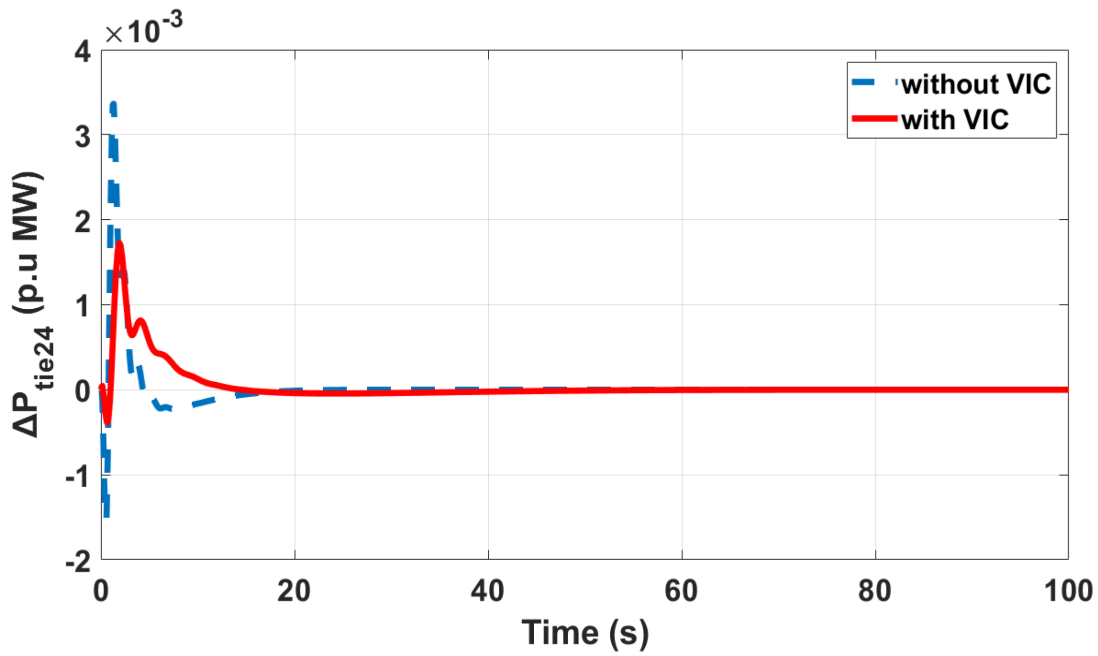

Figure 4.11 (i) System dynamic responses with respect to time for Bilateral transaction case with and without VIC: Deviation in tie line power between area-2 and -4.

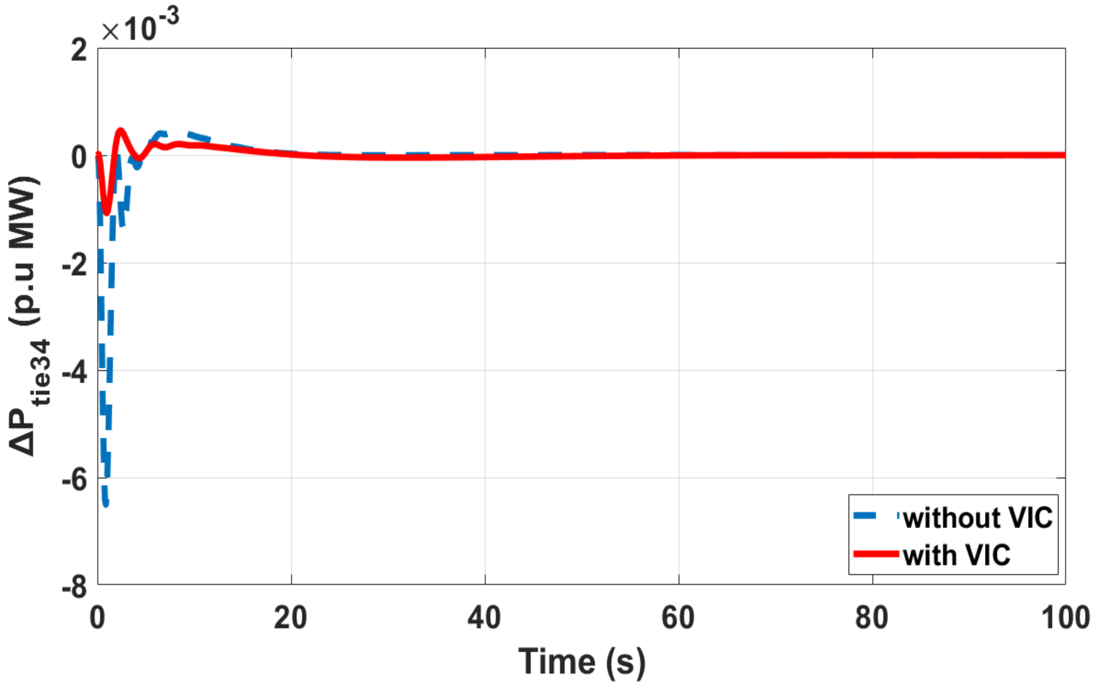

Figure 4.11 (j) System dynamic responses with respect to time for Bilateral transaction case with and without VIC: Deviation in tie line power between area-3 and -4.

Table 4.9 System dynamic response of Bilateral transaction case with percentage improvement of integrating VIC against system without VIC

Responses		**Bilateral Transaction**		**% improvement using VIC**
		Without VIC	**With VIC**	
Δf_1	M.U	-0.04438	-0.01066	75.98
	M.O	0.002952	0.001771	40.01
	S.T	23	6	73.91
Δf_2	M.U	-0.02935	-0.006513	77.81
	M.O	0.002979	0.001098	63.14
	S.T	26	12	53.85
Δf_3	M.U	-0.04425	-0.008658	80.43
	M.O	0.002925	0.001944	33.54
	S.T	25	6	76
Δf_4	M.U	-0.03726	-0.00712	80.89
	M.O	0.002937	0.001890	35.65
	S.T	22	7	68.18
ΔP_{tie12}	M.U	-0.008422	-0.001652	80.38
	M.O	0.0006488	0.0000019	99.71
	S.T	29	26	10.34
ΔP_{tie13}	M.U	-0.000079	-0.000649	-87.82
	M.O	0.00002438	0.000704	-96.53
	S.T	38	40	-5.26

Table 4.9 (contd.) System dynamic response of Bilateral transaction case with percentage improvement of integrating VIC against system without VIC

Responses		Bilateral Transaction		% improvement using VIC
		Without VIC	With VIC	
$\Delta \boldsymbol{P}_{tie14}$	M.U	-0.006548	-0.001680	74.34
	M.O	0.0004217	0.0009841	-57.14
	S.T	25	12	52
$\Delta \boldsymbol{P}_{tie23}$	M.U	-0.000649	-0.0001123	82.7
	M.O	0.008358	0.001728	79.33
	S.T	19	11	42.11
$\Delta \boldsymbol{P}_{tie24}$	M.U	-0.001537	-0.000386	74.89
	M.O	0.003364	0.001726	48.69
	S.T	22	16	27.27
$\Delta \boldsymbol{P}_{tie34}$	M.U	-0.006506	-0.001079	83.42
	M.O	0.0004318	0.0004613	-6.83
	S.T	19	15	21.05

Analysis: The inclusion of VIC in the bilateral system consistently reduces maximum undershoot (M.U) across all scenarios, with improvements often exceeding 70–80%, showing that frequency deviations are effectively damped. Maximum overshoot (M.O) also improves significantly in most cases, where values drop by 40–70%, indicating stronger control over oscillations and enhanced system stability. In conclusion, the bilateral system with VIC demonstrates markedly better dynamic response, achieving quicker stabilization, reduced oscillations, and superior damping performance compared to the system without VIC. This highlights VIC's effectiveness in strengthening system stability and reliability under bilateral market conditions.

4.5.2.3 Contract Violation

This represents a unique scenario within the previously mentioned cases, where the DISCOs break their contracts. In this specific situation, the uncontracted power requirement is met by the GENCOs located in the same area where the DISCOs have violated the contract. We are examining a scenario based on a pool-based transaction, where DISCO 1 in area 1 breaches the contract by requesting an additional 0.01 p.u. of power. The two scenarios of system with and without VIC is once more analyzed in which the system with VIC and proposed controller gives better result than the system without VIC in case of P.O.S, P.U.S and S.T which can be seen in Figure 4.12. The tuned control parameters are given in Table 4.10 and the responses of the system in Table 4.11. Accordingly, the local load demand in area 1 is adjusted as follows:

$$\Delta P_D = (0.01 + 0.01) + 0.01 = 0.03 p.u. \tag{4.16}$$

Table 4.10 Optimized gain values for system without VIC and with VIC for contract violation case.

Parameters		Without VIC	With VIC
K_t	Area-1	-	0.98
	Area-2	-	0.43
	Area-3	-	0.99
	Area-4	-	0.40
n	Area-1	-	2.33
	Area-2	-	2.50
	Area-3	-	2.31
	Area-4	-	2.88
K_{i1}	Area-1	-	0.57
	Area-2	-	0.63
	Area-3	-	0.86
	Area-4	-	0.83
K_{i11}	Area-1	-	0.91
	Area-2	-	0.54
	Area-3	-	0.83
	Area-4	-	0.87
K_d	Area-1	-	0.60
	Area-2	-	0.84
	Area-3	-	0.80
	Area-4	-	0.73
N	Area-1	-	38.4
	Area-2	-	70.1
	Area-3	-	49.7
	Area-4	-	55.1
J_v	Area-1	-	0.99
	Area-2	-	0.84
	Area-3	-	0.99
	Area-4	-	0.39
D_v	Area-1	-	0.98
	Area-2	-	0.55
	Area-3	-	0.74
	Area-4	-	0.50
K_i	Area-1	0.99	0.92
	Area-2	0.99	0.73
	Area-3	0.98	0.93
	Area-4	0.03	0.42

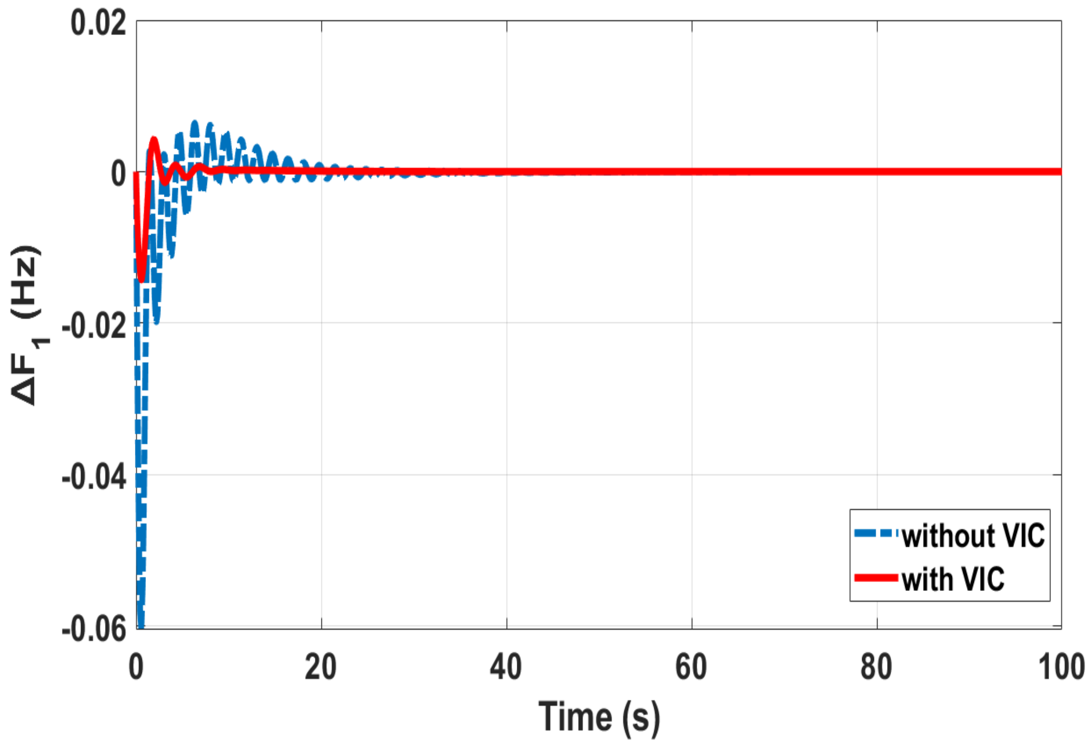

Figure 4.12 (a) System dynamic responses with respect to time for Contract violation case with and without VIC: Area-1 deviation in frequency.

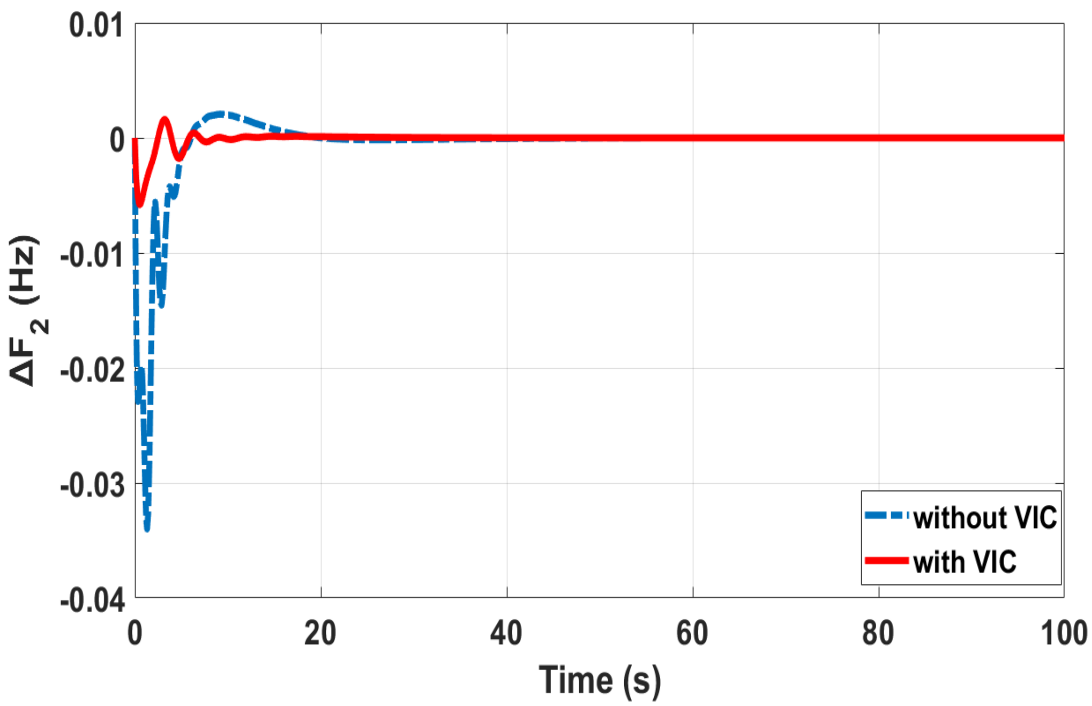

Figure 4.12 (b) System dynamic responses with respect to time for Contract violation case with and without VIC: Area-2 deviation in frequency.

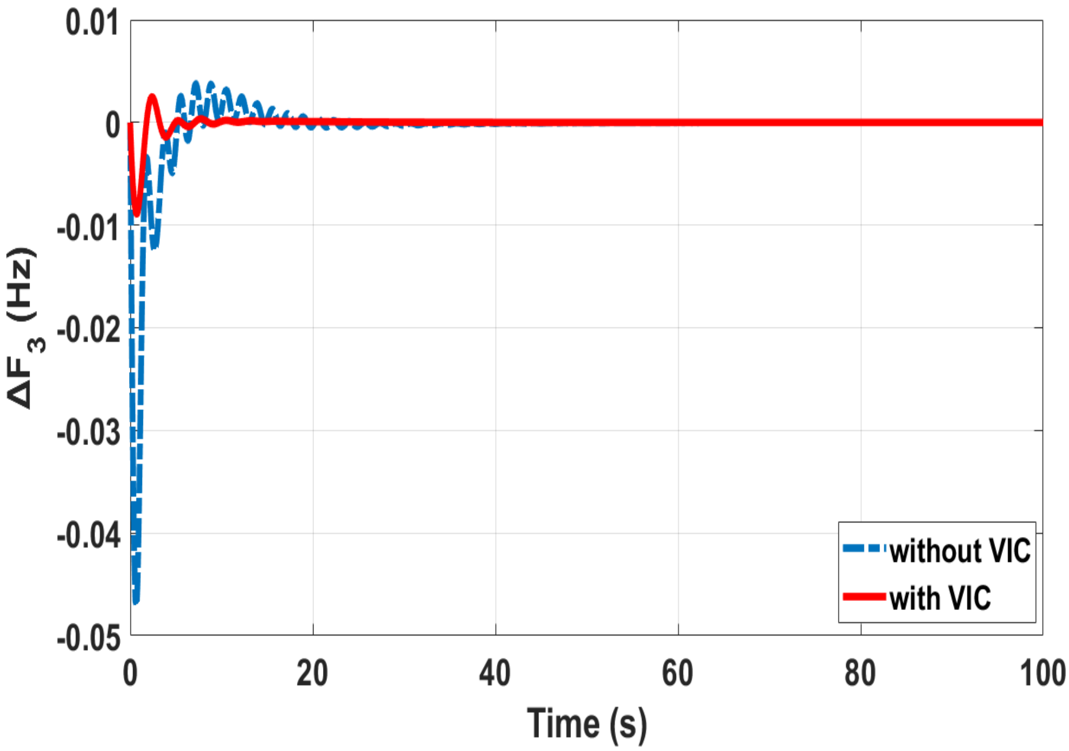

Figure 4.12 (c) System dynamic responses with respect to time for Contract violation case with and without VIC: Area-3 deviation in frequency.

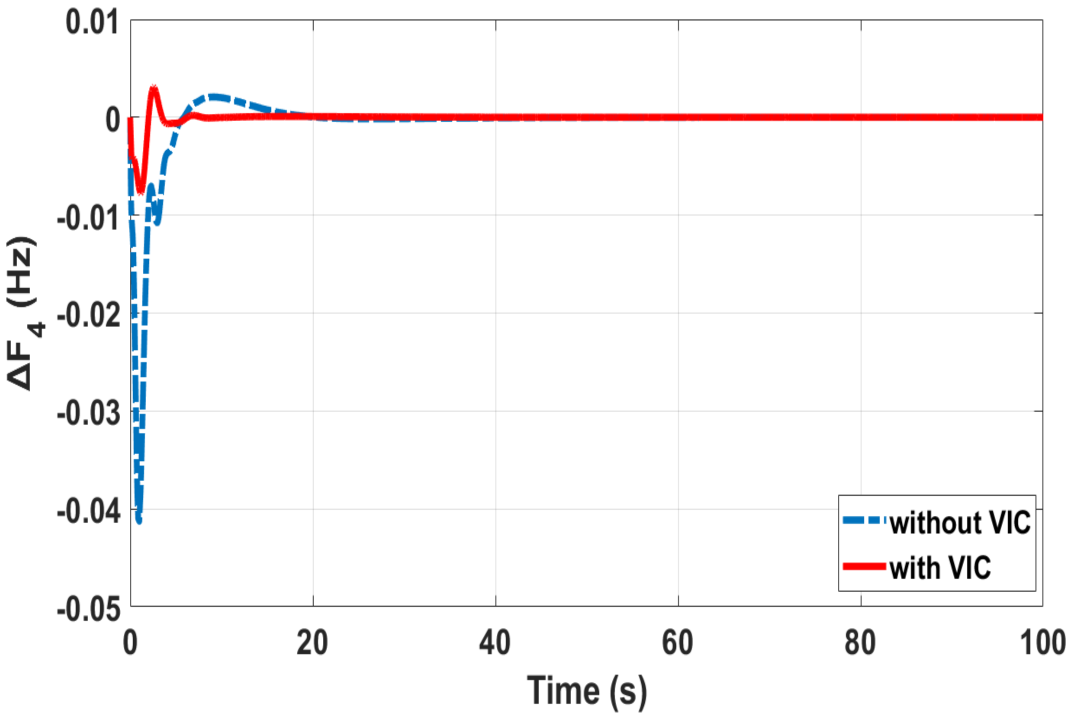

Figure 4.12 (d) System dynamic responses with respect to time for Contract violation case with and without VIC: Area-4 deviation in frequency.

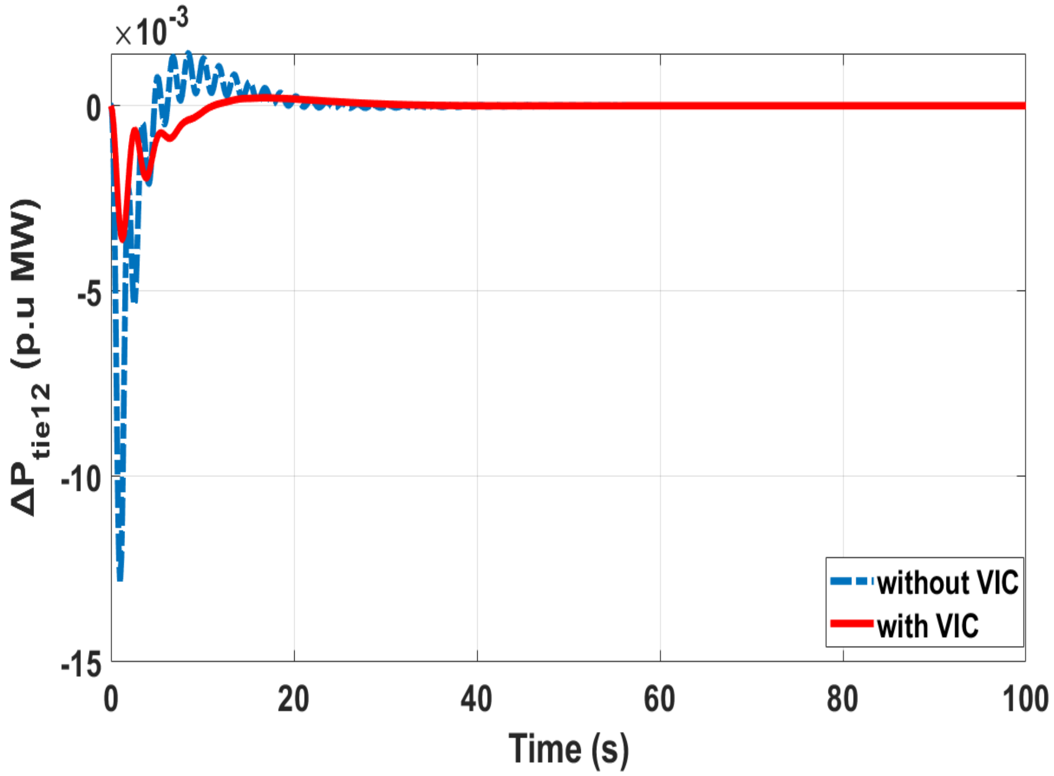

Figure 4.12 (e) System dynamic responses with respect to time for Contract violation case with and without VIC: Deviation in tie line power between area-1 and -2.

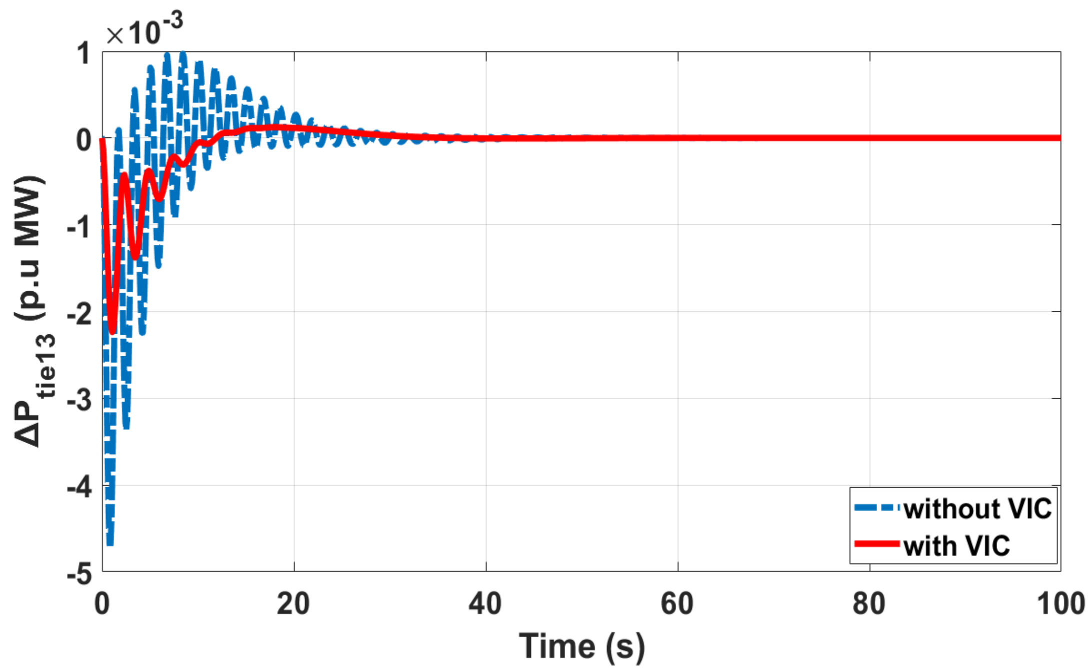

Figure 4.12 (f) System dynamic responses with respect to time for Contract violation case with and without VIC: Deviation in tie line power between area-1 and -3.

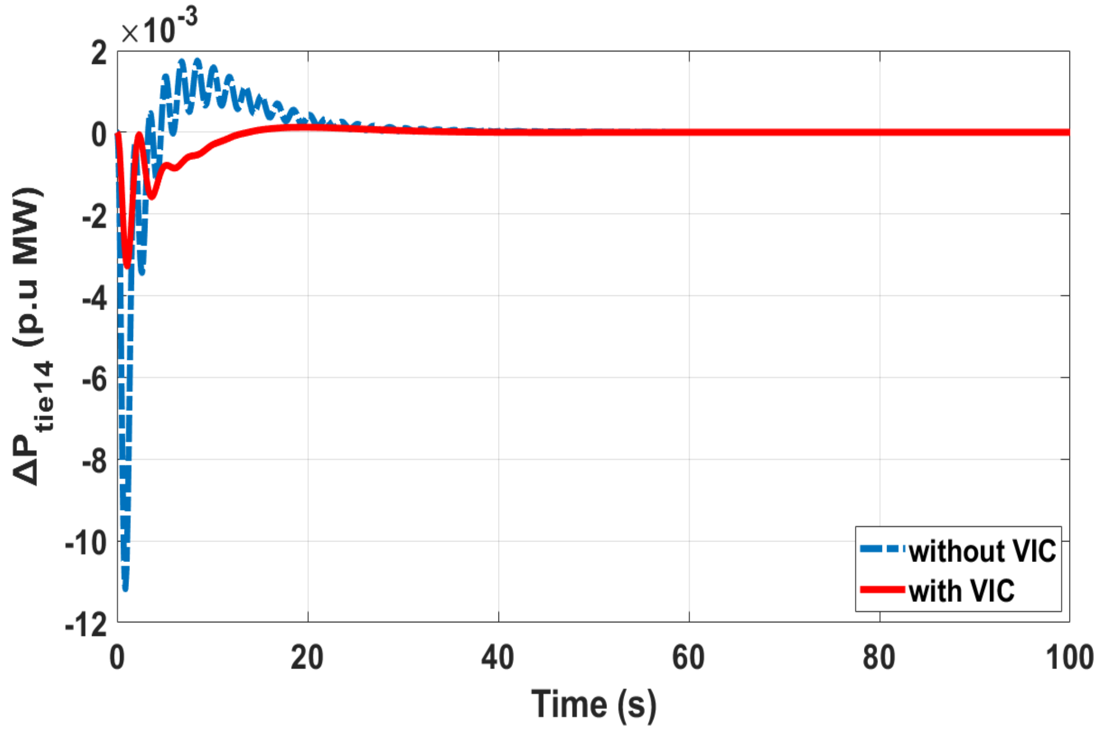

Figure 4.12 (g) System dynamic responses with respect to time for Contract violation case with and without VIC: Deviation in tie line power between area-1 and -4.

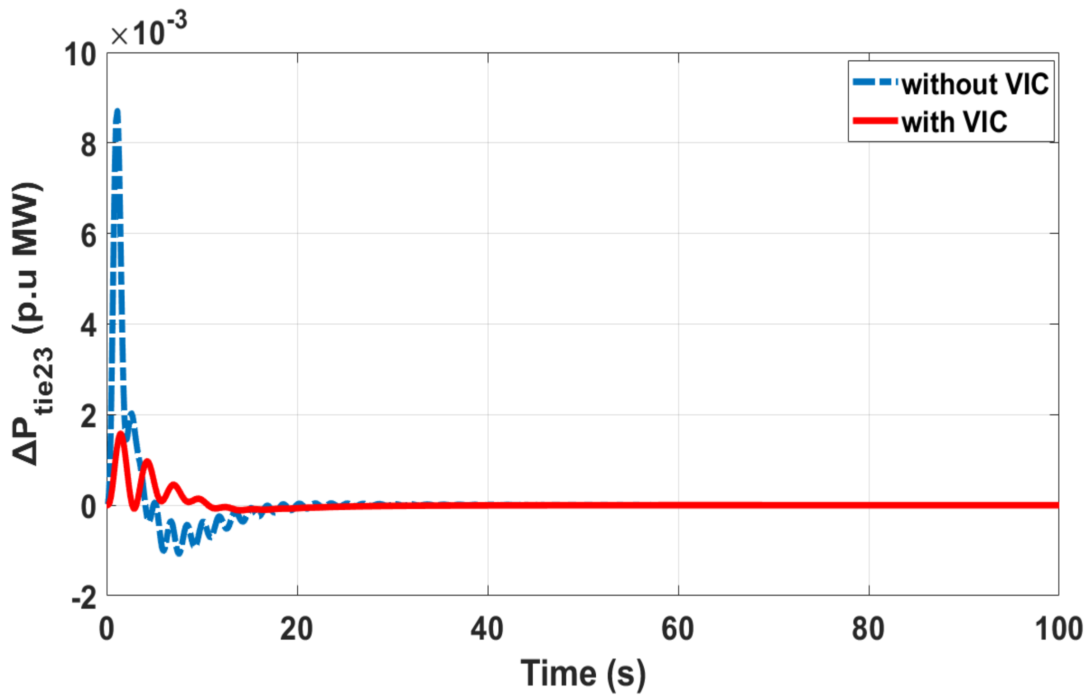

Figure 4.12 (h) System dynamic responses with respect to time for Contract violation case with and without VIC: Deviation in tie line power between area-2 and -3.

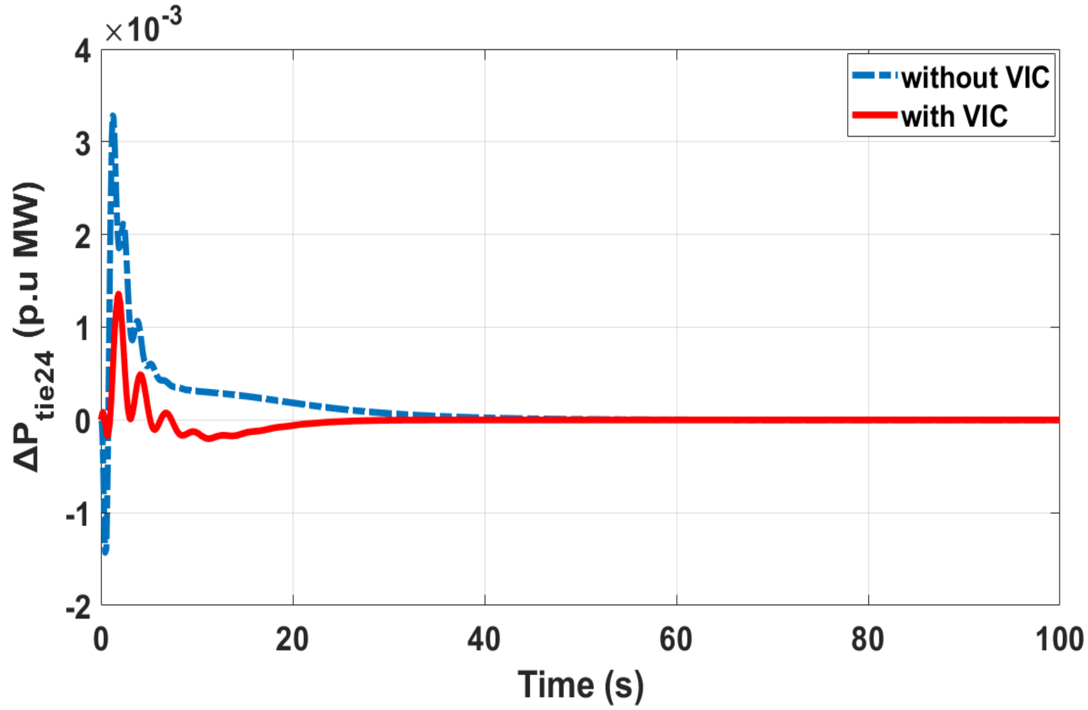

Figure 4.12 (i) System dynamic responses with respect to time for Contract violation case with and without VIC: Deviation in tie line power between area-2 and -4.

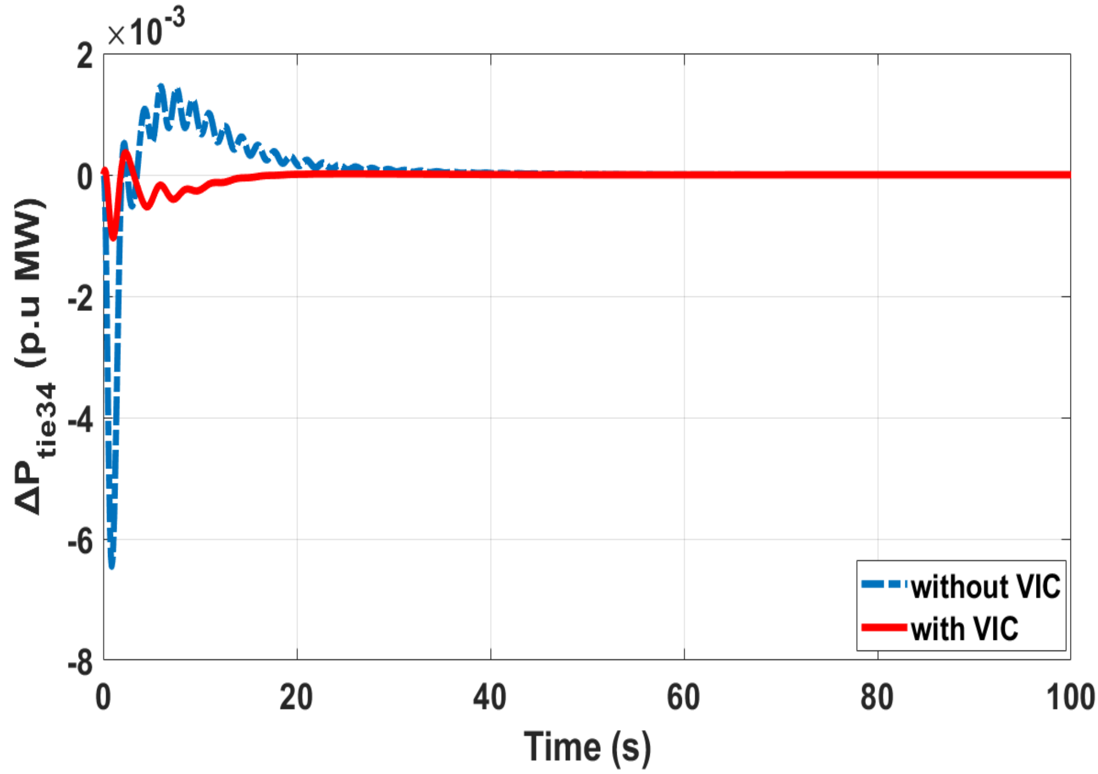

Figure 4.12 (j) System dynamic responses with respect to time for Contract violation case with and without VIC: Deviation in tie line power between area-3 and -4.

Table 4.11 System dynamic responses of system without VIC and with VIC with its percentage improvement for the contract violation case.

Responses		**Contract Violation**		**% improvement using VIC**
		Without VIC	**With VIC**	
Δf_1	M.U	-0.06046	-0.01426	76.41
	M.O	0.006364	0.004276	32.81
	S.T	35	9	74.29
Δf_2	M.U	-0.034	--0.005812	82.91
	M.O	0.002054	0.0016113	21.55
	S.T	20	11	45
Δf_3	M.U	-0.04705	-0.008924	81.03
	M.O	0.003774	0.002509	33.52
	S.T	27	11	59.26
Δf_4	M.U	-0.04126	-0.007782	81.14
	M.O	0.002072	0.00308	-32.72
	S.T	19	9	52.63
ΔP_{tie12}	M.U	-0.01287	-0.003608	71.97
	M.O	0.001407	0.0002146	84.75
	S.T	28	14	50
ΔP_{tie13}	M.U	-0.004722	-0.002238	52.6
	M.O	0.0009706	0.0001248	87.14
	S.T	35	15	57.14
ΔP_{tie14}	M.U	-0.01117	-0.003276	70.67
	M.O	0.001746	0.0001229	92.96
	S.T	32	16	50
ΔP_{tie23}	M.U	-0.001068	-0.0001122	89.49
	M.O	0.0087	0.001579	81.85
	S.T	28	13	53.57
ΔP_{tie24}	M.U	-0.001429	-0.0002013	85.91
	M.O	0.003282	0.001358	58.62
	S.T	41	23	43.9
ΔP_{tie34}	M.U	-0.006451	-0.001043	83.83
	M.O	0.001452	0.0003665	74.76
	S.T	34	17	50

Analysis: The inclusion of VIC in the contract violation scenario delivers remarkable improvements in dynamic stability. Maximum undershoot (M.U) is consistently reduced across all cases, with improvements often in the range of 70–85%, demonstrating VIC’s strong ability to limit large frequency deviations. Maximum overshoot (M.O) generally shows significant reductions of 40–70%, although a few cases display only moderate improvement, and in one instance a slight increase is observed.

Settling time (S.T.) improvements are highly noticeable: values that were previously in the range of 28–41 seconds without VIC drop to 9–23 seconds with VIC, representing reductions of nearly 50–70%, which indicates much faster convergence to steady state. Overall, VIC integration in contract violation conditions results in a more stable, damped, and faster-responding system, even under stressed and uncertain operating environments. This demonstrates VIC's robustness in handling disturbances and contractual deviations, confirming its effectiveness as a stabilizing mechanism in deregulated power system operations.

4.5.3 Eigen value analysis

While designing any controller, it is to make sure that the controllers is robust enough to make a stable system. For that purpose, the Eigen value analysis is performed to evaluate the suggested controller's ability to provide system stability. In a deregulated environment, the various controller types—Integral, Tilt-Integral, Tilt-Integral-Derivative-Filter, system without VIC and the suggested multi-level controller known as Tilt Integral-Integral Derivative Filter controllers for VIC are examined with the eigen value analysis. The eigen values along with the damping ratio of the controllers with VIC and without VIC are given in Table 4.12.

Table 4.12 Eigen values with the damping ratio for system with VIC

Controller Considered	Eigen Values	Damping ratio
I controller with VIC	-2.0000, -30.5435, -14.4273, -12.8873, -12.8991, -11.6130, -12.3262, -9.3195, -2.4882 + 4.5162i, -2.4882 - 4.5162i, -0.9244 + 4.4037i, -0.9244 - 4.4037i, -0.0674 + 3.7684i, -0.0674 - 3.7684i, -5.0686, -1.8394 + 3.1234i, -1.8394 - 3.1234i, -1.9856, -1.9856 - 0.8746i, -2.4771, -2.2050, -0.6178, -0.6178 - 1.0054i, -1.6437, -1.3390, -1.1696, -0.1202, -0.1202 - 0.1035i, -0.1460 + 0.0949i, -0.1460, -0.1830 + 0.0590i, -0.1830 - 0.0590i, -0.1051, -0.0000, 0.0000, -0.0000, 0.0000, 0.0000, 0.0000, 0.0000, 0.0000, -0.5556, -0.6667	0.0179
TI	-0.0020, -0.4325, -1.1111, -1.1111, -1.1111, -1.1111, -1.0000, -1.0000, -1.0000, -1.0000, -0.4115, -0.4209, -0.4328, -0.1172, -0.1199, -0.1232, -0.1233, -0.0305, -0.0334, -0.0351, -0.0351, -0.0341, -0.0144, -0.0129, -0.0129, -0.0123, -0.0116, -0.0095, -0.0095, -0.0100, -0.0101, -0.0097, -0.0023, -0.0023, -0.0007, -0.0007, 0.0001, 0.0001, -0.0051, -0.0011 + 0.0031i, -0.0011, -0.0020 + 0.0014i, -0.0020 - 0.0014i, -0.0029, -0.0029 - 0.0003i, -0.0028 + 0.0004i, -0.0028, -0.0026, -0.0026, -0.0017, -0.0017 - 0.0006i, -0.0014, -0.0014, -0.0012, -0.0007, -0.0007, -0.0006, -0.0005, -0.0004, -0.0003, -0.0001, -0.0001, -0.0001 + 0.0001i, -0.0001 - 0.0001i, -0.0002, -0.0002, -0.0002, -0.0002, -0.0001, -0.0001, -0.0001, -0.0001, -0.0001, -0.0000, -0.0000, 0.0000, 0.0000, 0.0000, 0.0000, 0.0000, -0.0000, 0.0000, -0.0006, -0.0007	0.0232

Table 4.12 (contd.) Eigen values with the damping ratio.

TIDN	-0.0020, -0.4325, -1.1111, -1.1111, -1.1111,-1.1111, -1.0000, -1.0000, -1.0000, -1.0000,-0.4115,-0.4209, -0.4328, -0.1172, -0.1199, -0.1232, -0.1233, -0.0305, -0.0334, -0.0351, -0.0351, -0.0341, -0.0144, -0.0129, -0.0129, -0.0123, -0.0116, -0.0095 + 0.0007i, -0.0095 - 0.0007i, -0.0100, -0.0097, -0.0023 + 0.0047i, -0.0023 - 0.0047i, -0.0007 + 0.0045i, -0.0007 - 0.0045i, 0.0001 + 0.0041i, 0.0001 - 0.0041i, -0.0051, -0.0011 + 0.0031i, -0.0011 - 0.0031i, -0.0020 + 0.0014i, -0.0020 - 0.0014i, -0.0029 + 0.0003i, -0.0029 - 0.0003i, -0.0028 + 0.0004i, -0.0028 - 0.0004i, -0.0026, -0.0026, -0.0017 + 0.0006i, -0.0017 - 0.0006i, -0.0014 + 0.0000i, -0.0014, -0.0012, -0.0007, -0.0007, -0.0006 + 0.0000i, -0.0005, -0.0004, -0.0003, -0.0001, -0.0001 - 0.0001i, -0.0001 + 0.0001i, -0.0001 - 0.0001i, -0.0002, -0.0002, -0.0002, -0.0002, -0.0001 + 0.0000i, -0.0001, -0.0001, -0.0001, -0.0001, 0.0000, 0.0000, 0.0000, 0.0000, -0.0000, 0.0000, -0.0006, -0.0007	0.1605
Without VIC	-2.0000, -30.5151, -14.4013, -12.8835, -12.8914, -11.5698, -12.3253, -9.5032, -1.9709 + 4.4815i, -1.9709 - 4.4815i, -0.8992 + 4.3532i, -0.8992 - 4.3532i, -0.1175 + 3.7312i, -0.1175 - 3.7312i, -5.1283, -2.1264 + 3.0136i, -2.1264 - 3.0136i, -1.8664 + 1.3563i, -1.8664 - 1.3563i, -2.5087, -2.3433, -0.5560 + 0.1029i, -0.5560 - 0.1029i, -0.2672 + 0.1192i, -0.2672 - 0.1192i, -0.1781 + 0.1456i, -0.1781 - 0.1456i, -0.1376, -0.1526, 0.0000, 0.0000, 0.0000, 0.0000 + 0.0000i, -0.5556, -0.6667	0.0315
TI-IDN with VIC	-0.0020, -1.1111, -1.1111,-1.1111, -1.1111, -1.0000, -1.0000,-1.0000, -1.0000, -0.4325,-0.4072,-0.4008, -0.4067, -0.1232, -0.1160, -0.1142, -0.1158, -0.0853, -0.0398, -0.0351, -0.0305, -0.0325, -0.0330,-0.0330, -0.0173, -0.0148, -0.0137 + 0.0014i, -0.0137 - 0.0014i, -0.0130, -0.0119,-0.0123, -0.0101,-0.0095, -0.0092, -0.0094, -0.0036 + 0.0049i,-0.0036 - 0.0049i,-0.0072,-0.0027 + 0.0047i,-0.0027 - 0.0047i, -0.0009 + 0.0038i, -0.0009 - 0.0038i, -0.0031 + 0.0033i,-0.0031 - 0.0033i, -0.0044,-0.0026 + 0.0006i, -0.0026 - 0.0006i, -0.0017 + 0.0014i, -0.0017 - 0.0014i, -0.0023 + 0.0010i,-0.0023 - 0.0010i,-0.0027, -0.0006 + 0.0011i, -0.0006 - 0.0011i, -0.0019, -0.0026, -0.0026, -0.0012, -0.0007, -0.0007, -0.0007, -0.0007, -0.0003, -0.0002, -0.0002 + 0.0000i, -0.0002,-0.0002, -0.0002,-0.0001 + 0.0001i,-0.0001 - 0.0001i, -0.0001, -0.0001 - 0.0001i,-0.0001,-0.0001,-0.0001,-0.0001, -0.0001, -0.0006, -0.0007	0.2327

Analysis: From the analysis, it is evident that the TI-IDN with VIC achieves the highest damping ratio (0.2327), indicating superior dynamic stability. The conventional I controller with VIC has relatively weak damping (0.0179), while TI and TIDN controllers provide moderate damping improvements. Systems without VIC remain less stable, with lightly damped oscillatory modes closer to the imaginary axis. Overall, VIC integration, especially with advanced controllers like TI-IDN, enhances system robustness.

4.6 Conclusion

The effectiveness of VIC in managing distributed generation and conventional power sources in AGC is comprehensively examined and analysed in this paper, with a special emphasis on improving frequency control in deregulated scenarios and under different situations. The system is designed utilizing a virtual inertia control method, and a new TI-IDN controller is suggested for controlling the VIC, whose gain values are analysed using ZOA. A variety of case studies are conducted to demonstrate how well the VIC and suggested controller work together to keep the system stable. In order to find the optimal solution for the system, several objective function formulations are compared where ISE is selected for the research. Analysis reveals that the suggested controller outperforms the other controllers in the cases of P.O.S., P.U.S., and S.T. The damping ratio of the eigen value using proposed controller is compared with other existing controllers such as the I, TI, and TIDN controllers and is improved by 92.13%, 89.97% and 31.03% respectively. By comparing two scenarios-one with and without VIC-the influence of VIC on the system is further examined. The results indicate that the system with VIC performs better in preserving system stability in the three different kinds of deregulated environments. The suggested approach for the VIC is shown to be resilient by examining the system under random load fluctuation and doing a sensitivity analysis of changes in system loading. The Eigen value analysis for the different types of controllers and system without VIC is analysed comparing with the proposed controller to show the robustness of the proposed technique.

Chapter 5

Combined Load Frequency Control and Automatic Voltage Regulator based Multi-area Power System with Renewable Energy Sources

5.1 Introduction

With the increasing deployment of smart grid technologies and renewable energy sources, modern power networks are undergoing fast change. Controlling output power while maintaining zero variations in frequency, terminal voltage, and tie line power is the primary control goal of interconnected power systems (IPSs). For an IPS to maintain the rated voltage and frequency while guaranteeing a steady and dependable power supply to the loads, automatic voltage regulators (AVR) and load frequency control (LFC) are crucial components. Power systems' load dynamics are always dynamic, which means they are ever-changing. The discrepancy that arises between the generation and demand in load causes unwanted variations in grid voltage and frequency. An LFC loop is used to control frequency variation through speed governor by altering the demand in active power. The AVR loop regulates the terminal voltage variation by altering the reactive power demand through generator excitation. Through tie-line connections, electrical power is transferred between various control locations. Developing a clever and dependable control strategy that reduces variations in tie-line power flow, system frequency, and terminal voltage is a challenging task [Kundur 1994; Saadat 1999].

The efficient regulation of LFC and AVR control loops has been the subject of a great deal of recent effort. The authors Gupta et.al, 2016 investigated a single area power system proposing a hybrid Neural Network-Fast Traversal Filters controller to enhance time response for stability affecting frequency and voltage. According to Sharma et.al, 2018, Ziegler Nichols based Fuzzy Logic Controller and Proportional Integral Derivative (PID) controllers provide superior dynamic response for a single-area, single-source IPS. An integral double derivative with filter whose parameters are optimized using Lighting search algorithm (LSA) with Governor dead band (GDB) are compared with the classical controllers like proportional (P), proportional integral (PI), Integral derivative (ID) and PID controllers in a combined LFC and AVR multi area power system [Rajbongshi and Saikia 2017]. For various multi-area multi source IPSs with and without nonlinearities, Ali et al. 2022a and Ali et al. 2022b proposed Archimedes optimization algorithm (AOA), learner performance-based behavior optimization (LPBO), and modified particle swarm optimization (MPSO) and Dandelion Optimizer (DO)-based PI-PD controllers for efficient simultaneous regulation of both terminal voltage and load frequency.

In order to stabilize a two-area nonlinear IPS, Lal and Barisal 2019 investigated Moth Flame Optimization-based Fractional Order (FO)-PID controllers. For a single-area nonlinear IPS, Morsali and Esmaeili 2020 suggested an Improved Particle Swarm Optimization (PSO) - based Conventional Power System Stabilizer (CPSS) controller that combines gas production, thermal reheat, and hydro units. The Differential Evolution-AEFA-based PID control technique is proposed with non-linearities like GRC is greatly enhanced with the addition of IPFC, RFBs, and an HVDC link for a two-area IPS [Kalyan and Rao 2020; Kalyan and Rao 2022]. Also, Nahas et al. 2021 study a two-area linear IPS and developed a PID controller tuned with NLTA. Kalyan 2021 presented a two area IPS with a Grey Wolf Optimizer (GWO)-based PIDD controller that included SMES and UPFC in order to improve performance. The authors Anusha et.al, 2021 investigated a PID controller tuned with Firefly Algorithm (FA) and demonstrated improved dynamic response in multi area and source with the presence of nonlinearities. Oladipo et al. 2021 employed controller name PIDA modified with hFPAPFA in order to enhance system performance for a single-area and source IPS. Ramoji and Saikia 2023developed an HHO-tuned TIDF controller for a three-area, two-source nonlinear IPS.

The authors Ramoji et al. 2022 suggested an HHO-based 2DOF I-TDF controller for a three-area, two-source nonlinear IPS with dish-stirling, wind, sun, and reheat thermal production units, outperforming other controllers in the process. Habib et al. 2022 suggested an ACFPD-TID controller with GDB and GRC nonlinearities for a IPS with AFA. The authors Dekaraja et al. 2022 proposed a CFOTDN-FOPDN controller for a multi area, multi-source nonlinear IPS was presented. Fayek and Rusu 2022 looked at a PIDA controller using DPO for a multi-source IPS with the integration of solar and bio-produced energy sources. The impact of the CTDs is studied by Kalyan and Rao 2021 on the combined LFC and AVR model by integrating IPFCs and RFBs. A HAEFA-based fuzzy PID was studied by Kalyan et al. 2022 by incorporating energy storage devices. Since RFBs are more effective in reducing frequency and voltage oscillations, they were able to successfully integrate the system into the LFC-AVR. The authors Alharbi et al. 2023 utilize the Dandelion optimizer (DO) based FOPI and Proportional integral double derivative (PIDD) controller in the combined system. Integration of SMES in a combined LFC and AVR is studied by proposing a new controller called HHO based model predictive controller is done by Kumar et al. 2021. The authors, Dekaraja et al. 2021 study the AGC with a diverse source with AC/HVDC connection in the combined LFC and AVR model. For two- and five-area IPS with nonlinearities like GRC and GDB, the authors suggested using a fuzzy-tilt-fractional order integral-filtered derivative (FTIλDN) controller to maximize the load frequency and tie-lie power deviation [Arya 2023]. An imperialist competitive algorithm was used to calibrate the proposed controller (ICA).

Additionally, asymmetrically spaced membership functions (MFs) have been used to improve the FTIλDN controller's performance. It is evident that improved settling time, undershoot, and overshoot reactions were among the positive outcomes of the suggested control strategy. Ali et al. 2023 used a based PID control system to study a four-area multi-source IPS without nonlinearities. They claimed that when compared to alternative control strategies, the suggested GBO-PID performed comparatively better. The results demonstrate that the proposed GBO-PID controller outperforms the alternatives, providing superior responses in voltage, frequency, and tie-line power, even with a 5% step load perturbation. Sensitivity analysis confirms the reliability and efficacy of GBO-PID. In a work by Ali et al. 2024, a PI-PD controller optimized with OOBO algorithm is used to control the combined LFC and AVR of a four area IPS by including non-linearities like GRC, GDB and BD in a regulated market.

While there are very few studies on combined LFC-AVR, there is a significant quantity of study on individual LFC. For an optimal regulation of secondary loop of various IPSs, numbers of computation algorithms inspired by nature have been investigated. Das et al. 2012 develop a Genetic Algorithm (GA) based frequency controller to regulate a hybrid solar-thermal-wind energy system integrated with energy storage. This paper by Daraz et al. 2021 employ a Fractional Order Integral-Tilt Derivative (FOI-TD) controller for effective automatic generation control in a multi-source interconnected power system. Also, a work by Das et al. 2022 investigate the effect of a PI-TI based virtual inertia controller with virtual damping on stabilizing a renewable energy-based, multi-area power system under deregulation. The authors Nayak et al. 2021 utilize a Grasshopper Optimization Algorithm to optimize a multistage controller for enhancing automatic generation control in a power system integrated with FACTS devices. Again, Das et al. 2023 propose a novel mine blasting algorithm to optimize a DFOPI-TIDN controller for effective virtual inertia control (VIC) in multi-area power systems. This work by Nayak et al. 2021 propose that a multistage controller optimized by the Grasshopper Optimization Algorithm effectively improves automatic generation control in a power system integrated with FACTS devices. Additionally, a variety of control schemes have been put forth for the AVR loop's individual control by Sahib 2015, Tabak et al. 2021 a, Tabak et al. 2021b and Altbawi et al. 2024. The authors [Trojovská et al. 2022] proposed a new optimization technique called the zebra optimization technique and are compared with different types of algorithms.

Due to the highly complex structure of IPS, no research has been carried out on the combined control of LFC and AVR control loops in a four-area multi-sources power system with the presence of non-linearities like BD, CTD and GRC under deregulation. This study fills this gap by examining a four-area IPS with two generation units per area. The Zebra optimization algorithm (ZOA) is a recently discovered metaheuristic algorithm that has been successfully explored to improve the performance metrics of optimization problems. That is why, it is worth utilizing ZOA to obtain the optimum gain parameters of proposed TI-PIDN and other controllers including PI, TI, PID and TID to achieve an effective response of four-area multi-source IPS.

The inherent variability and intermittency of renewable energy sources create unique hurdles for their integration. Additionally, the incorporation of many nonlinearities, such as TD, BD, and GRC, complicated the system. Among these difficulties include variations in power generating levels, erratic output, and the requirement for efficient control techniques to preserve the stability and dependability of the system. The ZOA-based control techniques were essential in resolving these issues by improving the system's performance through adaptive control mechanisms and intelligent parameter tweaking.

The major contributions of the works are as follows:

1. Four-area multi-source IPS modelling in both regulated and deregulated environments with non-linearities and load perturbations.
2. Mathematical modelling of the proposed TI-PIDN controller along with the four-area IPS.
3. The ZOA-based fitness function formulation is used to determine the ideal TI-PIDN and other controller settings.
4. A comparison of ZOA-based TI-PIDN with other controllers, including PI, TI, PID, and TID, in order to support the ZOA-TI-PIDN controller's superiority.
5. Different case study of deregulated environment with the incorporation of FACTs devices.
6. Sensitivity and stability analysis has been carried out to validate the robustness of the proposed ZOA-TI-PIDN control strategy.

5.2 Power System Modeling

Figure 5.1 shows the generalized multi-source, multi-area interconnected power system with integrated LFC and AVR control loops. Cross-coupling between two loops is achieved with various coupling coefficients. A four unequal

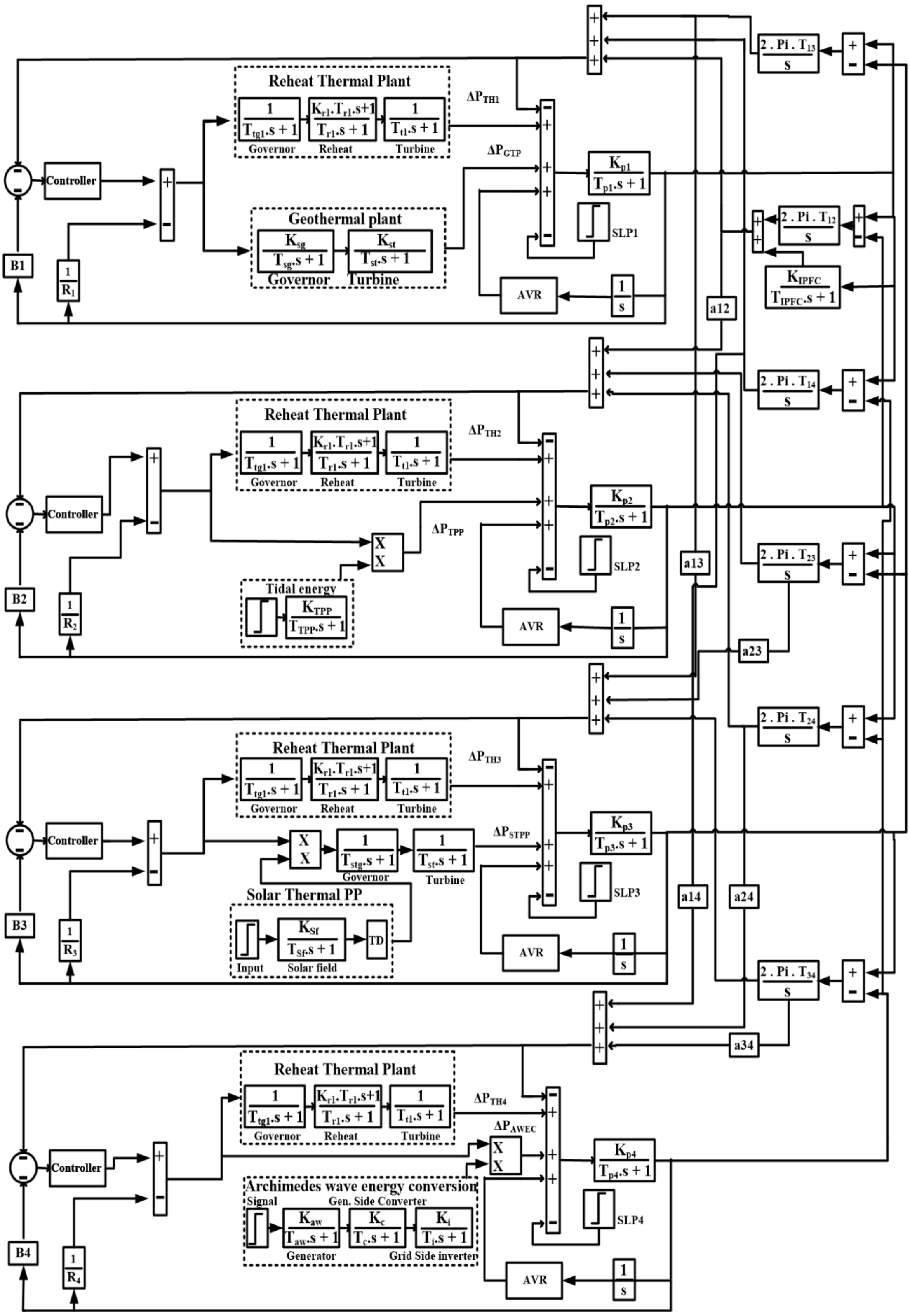

Figure 5.1 Transfer function modelling of a four area LFC and AVR system under regulated environment.

interconnected area with multi-source system having reheat thermal plant in each area and a renewable resource like GPP, TPP, SPVP and AWEC with AVR coupling under regulated and deregulated environment is considered for this investigation. The capacity ratio is considered to be 1:2:1:2 i.e., 1000 MW, 2000 MW, 1000 MW and 2000 MW for area 1, 2, 3 and 4 respectively. Here, it is assumed that there are 2 GENCOs and 2 DISCOs in each and every area. At the instant, the nominal loading is considered to be 50% of the area power capacity. All the system are modelled and run in MATLAB/Simulink environment for a time of 100 second. From the previous chapter, it is observed that choosing ISE over other objective function delivers the best response, so it is utilized for this combined LFC and AVR study too. Figure 5.2 shows the tie line power connection between areas. The objective function ISE is given by (5.1)

$$J_{ISE} = \int_0^T \left[\left(\Delta f_d\right)^2 + (\Delta V_d)^2 + \left(\Delta P_{tie\_error,de}\right)^2 \right] dt \tag{5.1}$$

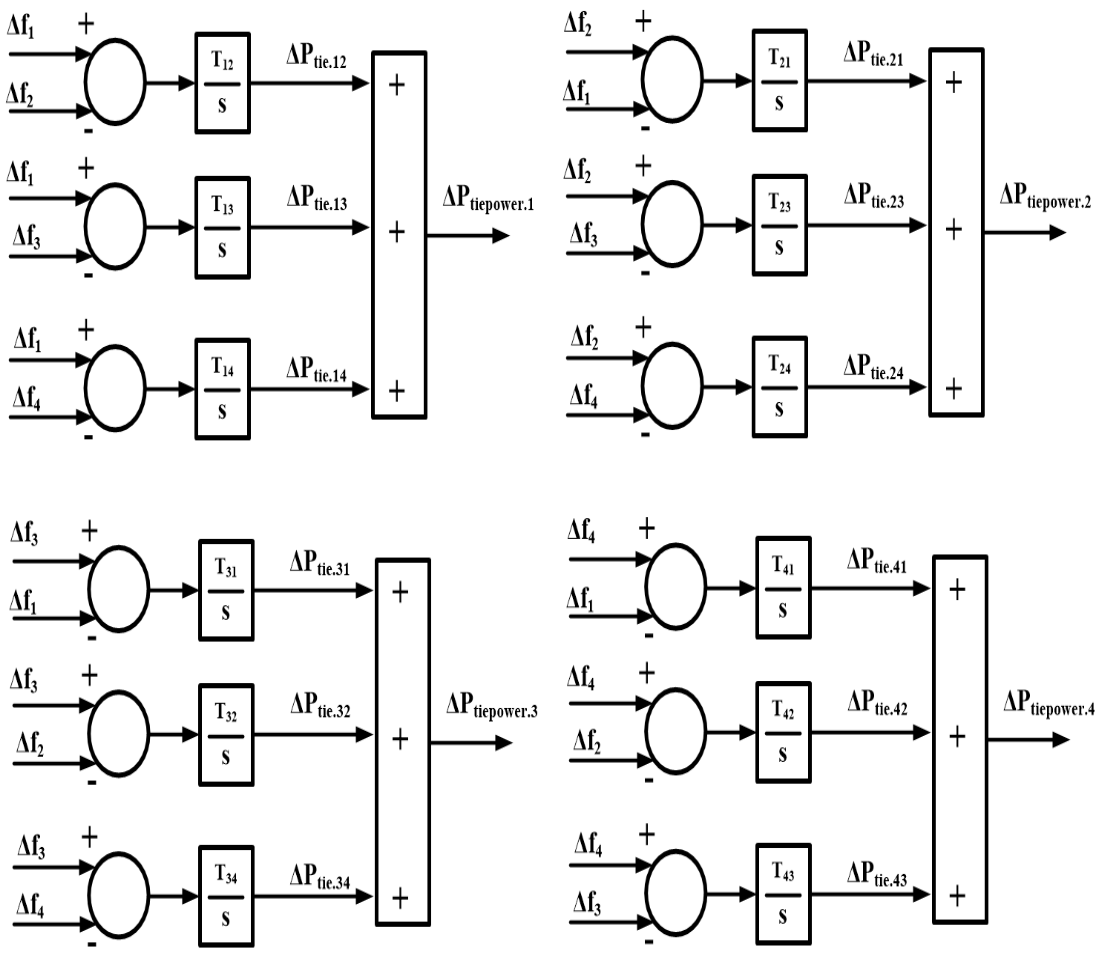

Figure 5.2 Connections of tie line power for a four area power system

Where,

$$\Delta P_{tie1} = \Delta P_{tie12} + \Delta P_{tie13} + \Delta P_{tie14} \qquad (5.2)$$

$$\Delta P_{tie2} = \Delta P_{tie21} + \Delta P_{tie23} + \Delta P_{tie24} \qquad (5.3)$$

$$\Delta P_{tie3} = \Delta P_{tie31} + \Delta P_{tie32} + \Delta P_{tie34} \qquad (5.4)$$

$$\Delta P_{tie4} = \Delta P_{tie41} + \Delta P_{tie42} + \Delta P_{tie43} \qquad (5.5)$$

Also, for Voltage, where d=1, 2, 3, 4

$$\Delta V_d = V_{ref} - V_d \qquad (5.6)$$

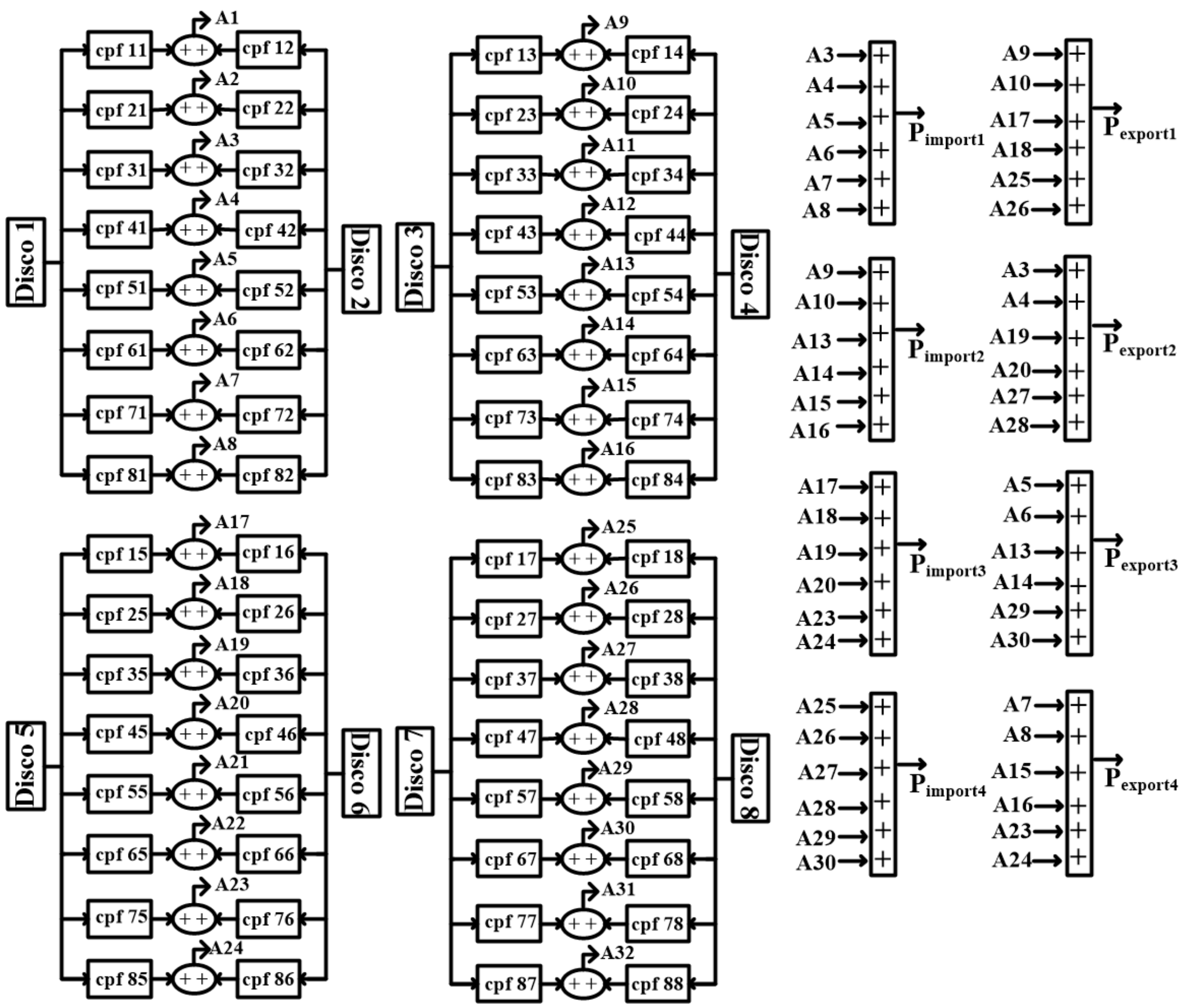

Figure 5.3 (a) Transfer function model of the four area with combined LFC and AVR system under deregulation: Deregulated system.

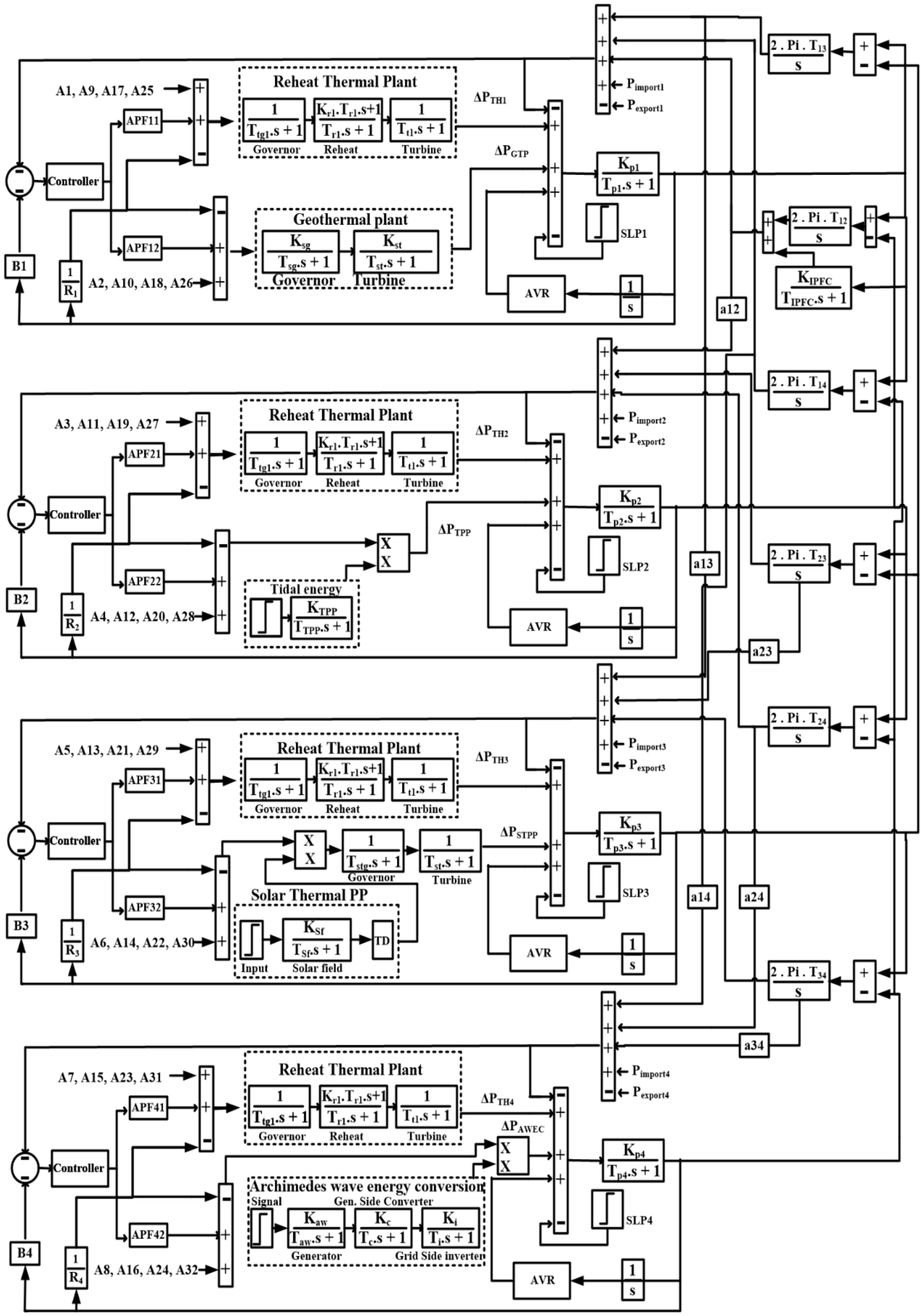

Figure 5.3 (b). Transfer function model of the four area with combined LFC and AVR system under deregulation: Complete system under deregulated environment.

5.2.1 LFC and AVR Modelling

The excitation unit, amplifier unit, generating field, and sensor unit make up the majority of the AVR system which is shown in Figure 5.4. The sensor continually detects the terminal unit; reference voltage signal is compared which then produces the error voltage (V) signal. The synchronous generator field excitation can then be altered by amplifying the signal of error voltage and feeding it to excitation unit. This makes the system stable by rapidly compensating for the terminal voltage fluctuation. In this case,

Amplifier, $G_{AM} = \dfrac{K_{AM}}{T_{AM}s+1}$ (5.7)

Exciter, $G_{EX} = \dfrac{K_{EX}}{T_{EX}s+1}$ (5.8)

Gen. Field, $G_{GF} = \dfrac{K_{GF}}{T_{GF}s+1}$ (5.9)

Sensor, $G_{SE} = \dfrac{K_{SE}}{T_{SE}s+1}$ (5.10)

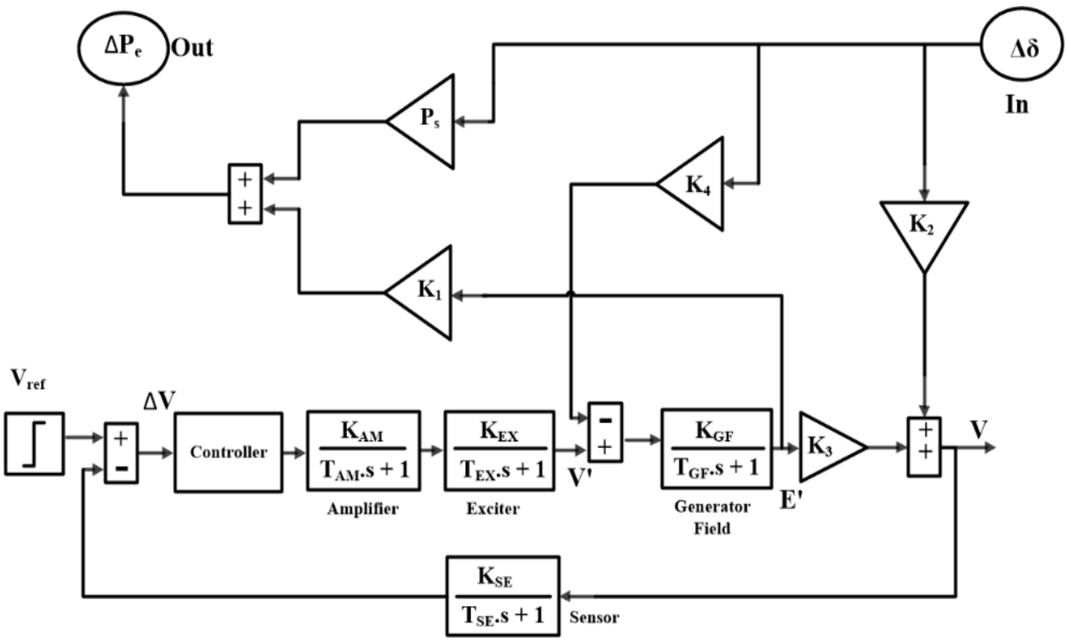

Figure 5.4 Transfer function model of AVR with coupling coefficients.

Controlling frequency and terminal voltage at the same time is the primary goal of the analysis of the combined LFC and AVR system's impact. Real power generation can be regulated to control frequency, and the generator field excitation system can be adjusted to maintain terminal voltage. Since the generator stator winding's emf is proportional to frequency, variations in frequency also have an impact on the terminal voltage. However, because the AVR system's activities cause "V" change, terminal voltage has a significant impact on actual power generation, as shown by

$$P_e = \frac{|V||E'|}{X_s} \text{Sin}(\delta) \tag{5.11}$$

Where, X_s is the generator reactance and δ is the rotor angle.

Therefore, the load frequency control loop is immediately and significantly impacted by the automatic voltage regulator. It was discovered that the generator load angle (Δδ) will move due to a deviation in the system frequency (Δf) under dynamic load (ΔP_d) conditions. The change in actual power generation (ΔP_e) after accounting for these impacts is formally represented as,

$$\Delta P_e = P_s \Delta\delta + K_1 E' \tag{5.12}$$

Where, synchronizing power coefficient is represented by 'P_s' which is specified as the characteristic slope of power angle at the initial angle of operation, 'E'' represents EMF produced in the stator winding of the generator. For a minor deviation in 'E'', K_1 denotes the 'V' variation. In relation to the change in rotor angle, the variation in voltage can be shown as

$$\Delta V = K_2 \Delta\delta + K_3 E' \tag{5.13}$$

By considering change in load angle, the transfer function for generator field is

$$E' = \frac{K_{GF}}{T_{GF} s + 1}\left(V' - K_4 \Delta\delta\right) \tag{5.14}$$

The coefficients that link the AVR with the secondary control loops are K_1, K_2, $K_3$and K_4.

5.2.2 FACTS Device

FACTS devices are static power electronics devices installed in AC transmission to increase power transfer capability, stability and controllability. The Interline power flow controller (IPFC) is selected for this research. The cost-effective use of certain transmission lines is made possible by the IPFC's separate management of actual and reactive power flow. As a member of the FACTS family, the IPFC offers a preferred solution for controlling power flow and modifying many transmission lines at a single substation. Each of the several DC-to-AC converters used by the IPFC offers a variety of line-specific compensations.

The IPFC arrangement is seen in Figure 5.5. It enables the simultaneous and individual adjustment of each transmission line. The IPFC can quickly transmit real power across the adjusted lines via the DC link and offer autonomous control over each line's reactive series adjustment in order to regulate the flow of real and reactive power from overloaded to underloaded lines via the traditional DC connection. In order to investigate how the IPFC affects the power system in the steady state, a mathematical study is presented by Meseret et al. (2025). The transfer function for IPFC can be written as:

$$\Delta P_{IPFC}(s) = \frac{1}{1+T_{IPFC}(s)}.\Delta error \tag{5.15}$$

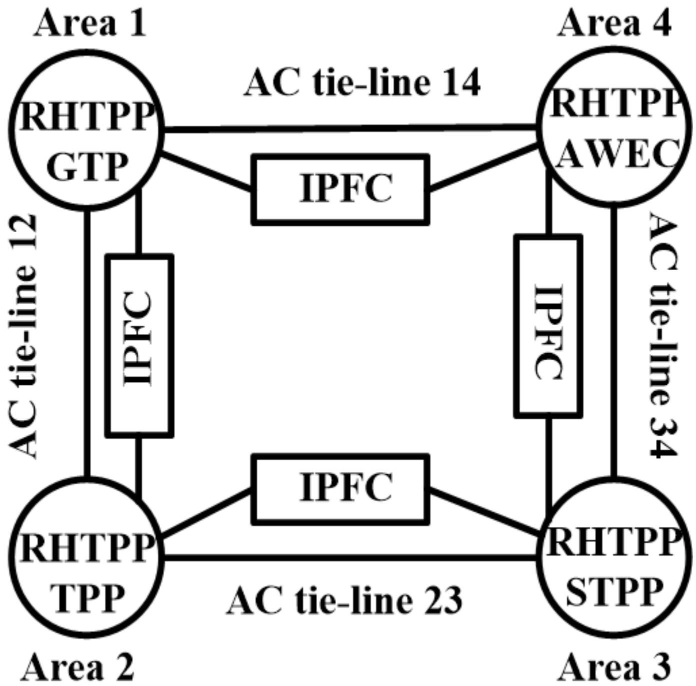

Figure 5.5 Schematic diagram of IPFC integrated power system.

5.3 Tilt Integral-Proportional integral derivative with filter controller

In this work, a novel multi-level Tilt Integral-Proportional integral derivative with filter controller (TI-PIDN) is proposed for the combined LFC and AVR of a multi area multi source system. The purpose of proposed controller is to maintain and control of each area frequency and tie line power which is crucial during load changes or change in generation in certain areas and improving settling time along with damping ratio. The first level controller is a Tilt-Integral controller whose output is the input of the second controller known as the common PIDN controller. The proposed TI-PIDN controller transfer function is,

$$TF_{TI-PIDN}(s) = \left(\frac{kt_i}{s^{\frac{1}{ni}}} + \frac{ki_i}{s} + kp_i + \frac{ki1_i}{s} + kd_i \left(\frac{sN}{s+N} \right) \right) \tag{5.16}$$

The proposed TI-PIDN controller contains seven numbers of tuning parameters which are optimized using the Zebra optimization algorithm.

$$\left.\begin{array}{c} kt_{is}^{min} \le kt_{is} \le kt_{is}^{max} \\ n_{is}^{min} \le n_{is} \le n_{is}^{max} \\ ki_{is}^{min} \le ki_{is} \le ki_{is}^{max} \\ kp_{is}^{min} \le kp_{is} \le kp_{is}^{max} \\ ki1_{is}^{min} \le ki1_{is} \le ki1_{is}^{max} \\ kd_{is}^{min} \le kd_{is} \le kd_{is}^{max} \\ N_{is}^{min} \le N_{is} \le N_{is}^{max} \end{array}\right\} \tag{5.17}$$

Here, 'k_t' is the tilt, 'n_{is}' represents the tilting parameters, 'k_i' is the integral along with the secondary integral 'k_{i1}', 'k_p' is the proportional, 'k_d' is the derivative with its filter 'N_{is}'. Figure 5.6, shows the controller structure.

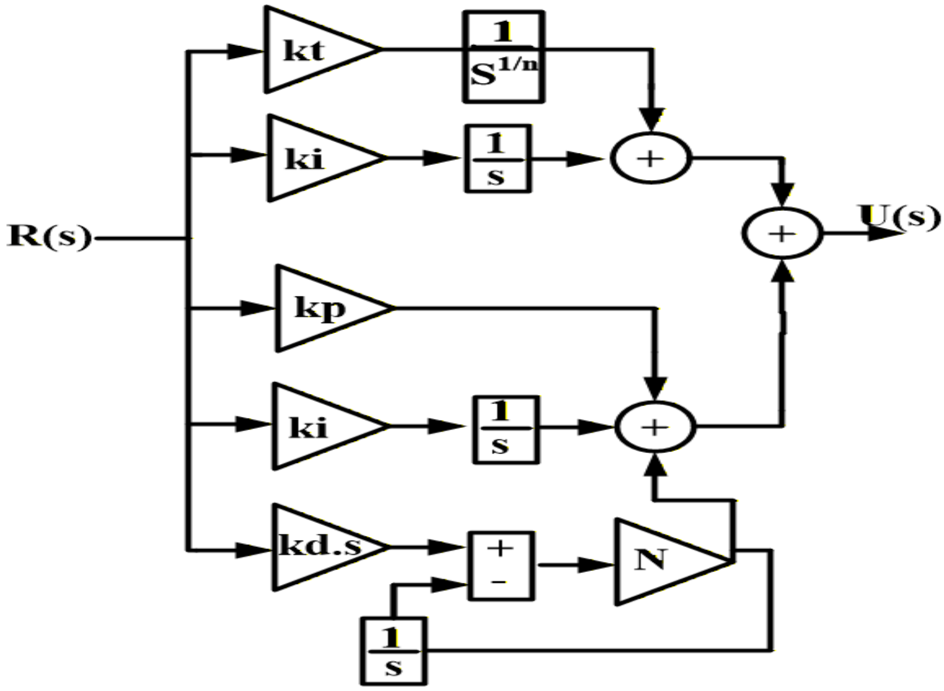

Figure 5.6 Proposed TI-PIDN controller structure.

5.4 Simulation results and Analysis

For solving the problem in the combined LFC and AVR in a multi-source multi area based interconnected power system, a systematic study is essential under various scenarios. In this work, MATLAB/Simulink is used to simulate an unequal four area interconnected power system incorporating various types of RESs under conventional and deregulated environments considering various scenarios. It is assumed that area-1 comprises of reheat thermal plants and Geothermal plant, area-2 is composed of RHTTP and Tidal power plant, RHTTP and Solar thermal power plant in area-3 and lastly RHTTP and AWEC in area-4. For the regulated system, a 1% SLP is assumed to happen at area-1 and for deregulated scenarios, 0.01 p.u MW of load is assumed to be demanded by each Discos.

5.4.1 System under regulated environment

5.4.1.1 Comparison of controllers

By contrasting its performance with that of other distinguished controllers, the superiority of the suggested controller is displayed. PI, TI, PID, TID, and the suggested TI-PIDN controller are the controllers that are taken into consideration for comparison. Figure 5.7 displays the dynamic responses for the comparison of the various controllers. The optimized gain values obtained are given in Table 5.1 while Table 5.2 (a) provides the numerical data about responses of the system. The improvement percentages of TI-PIDN over other controllers are presented in Table 5.2 (b).

Table 5.1 Optimized gain values for different controllers for LFC-AVR system

PI	K_{p1}=0.5519, K_{i1}=0.7304, K_{p2}=0.5394, K_{i2}=0.0659, K_{p3}=0.1665, K_{i3}=0.1840, K_{p4}=0.8446, K_{i4}=0.4206, K_{p5}=0.9969, K_{i5}=0.3329, K_{p6}=0.6740, K_{i6}=0.2307, K_{p7}=0.7691, K_{i7}=0.1911, K_{p8}=0.6602, K_{i8}=0.2522.
TI	K_{t1}=0.0726, n_1=2.4553, K_{i1}=0.6467, K_{t2}=0.5078, n_2=2.0077, K_{i2}=0.1486, K_{t3}=0.2112, N_3=2.0960, K_{i3}=0.5279, K_{t4}=0.5482, N_4=2.5029, K_{i4}=0.4206, K_{t5}=0.5337, N_5=2.9999, K_{i5}=0.1156, K_{t6}=0.5219, n6=2.9933, K_{i6}=0.0617, K_{t7}=0.7195, n_7=2.9864, K_{i7}=0.0522, K_{t8}=0.4722, n_8=2.9999, K_{i8}=0.1302
PID	K_{p1}=0.7741, K_{i1}=0.1683, K_{d1}=0.2461, K_{p2}=0.7005, K_{i2}=0.7394, K_{d2}=0.4129, K_{p3}=0.1319, K_{i3}=0.5338, K_{d3}=0.1664, K_{p4}=0.3080, K_{i4}=0.2660, K_{d4}=0.2251, K_{p6}=0.6949, K_{i6}=0.2284, K_{d6}=0.6030, K_{p7}=0.7034, K_{i7}=0.2558, K_{d7}=0.4299, K_{p8}=0.6174, K_{i8}=0.2350, K_{d8}=0.1908.
TID	K_{t1}=0.1385, n_1=2.1124, K_{i1}=0.5704, K_{d1}=0.0547, K_{t2}=0.7084, n_2=2.2396, K_{i2}=0.2998, K_{d2}=0.1882, K_{t3}=0.2075, n_3=2.3393, K_{i3}=0.5183, K_{d3}=0.4793, K_{t4}=0.3930, n_4=2.1899, K_{i4}=0.9170, K_{d4}=0.2902, K_{t5}=0.9992, n_5=2.9996, K_{i5}=0.1443, K_{d5}=0.3506, K_{t6}=0.9999, n_6=2.9986, K_{i6}=0.3390, K_{d6}=0.5177, K_{t7}=0.9999, n_7=2.9999, K_{i7}=0.3048, K_{d7}=0.5466, K_{t8}=0.9995, n_8=2.9999, K_{i8}=0.1640, K_{d8}=0.4663
TI-PIDN	K_{t1}=0.8416, n_1=2.5642, K_{i1}=0.8003, K_{p1}=0.5406, K_{i11}=0.3029, K_{d1}=0.6932, N_1=52.463, K_{t2}=0.2791, n_2=2.6503, K_{i2}=0.8333, K_{p2}=0.6818, K_{i22}=0.3350, K_{d2}=0.9996, N_2=52.762, K_{t3}=0.5173, n_3=2.6229, K_{i3}=0.3526, K_{p3}=0.6043, K_{i33}=0.3203, K_{d3}=0.8893, N_3=30.236, K_{t4}=0.5271, n_4=2.7691, K_{i4}=0.4310, K_{p4}=0.8433, K_{i44}=0.4145, K_{d4}=0.9999, N_4=55.801, K_{t5}=0.7993, n_5=2.7443, K_{i5}=0.2076, K_{p5}=0.8303, K_{i55}=0.6187, K_{d5}=0.9994, N_5=79.480, K_{t6}=0.7739, n_6=2.9294, K_{i6}=0.3353, K_{p6}=0.3380, K_{i66}=0.3466, K_{d6}=0.9999, N_6=98.256, K_{t7}=0.3425, n_7=2.4411, K_{i7}=0.3816, K_{p7}=0.8040, K_{i77}=0.5780, K_{d7}=0.9997, N_7=96.810, K_{t8}=0.3694, n_8=2.3823, K_{i8}=0.4112, K_{p8}=0.9807, K_{i88}=0.2624, K_{d8}=0.9999, N_8=94.01

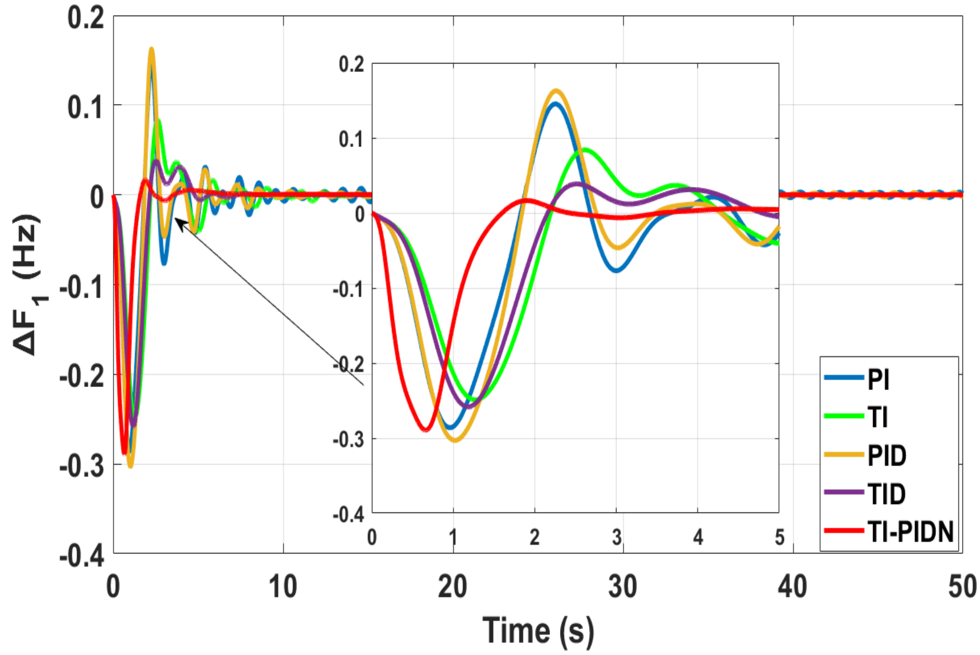

Figure 5.7 (a) System dynamic response of LFC and AVR obtained from different types of controllers: Area-1 deviation in frequency.

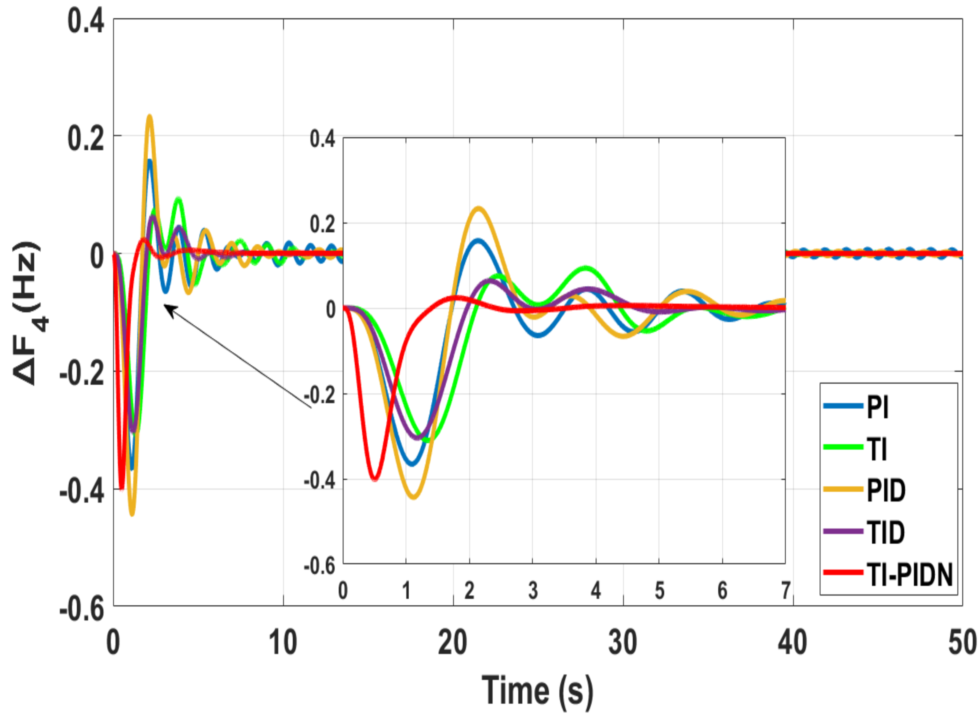

Figure 5.7 (b) System dynamic response of LFC and AVR obtained from different types of controllers: Area-4 deviation in frequency.

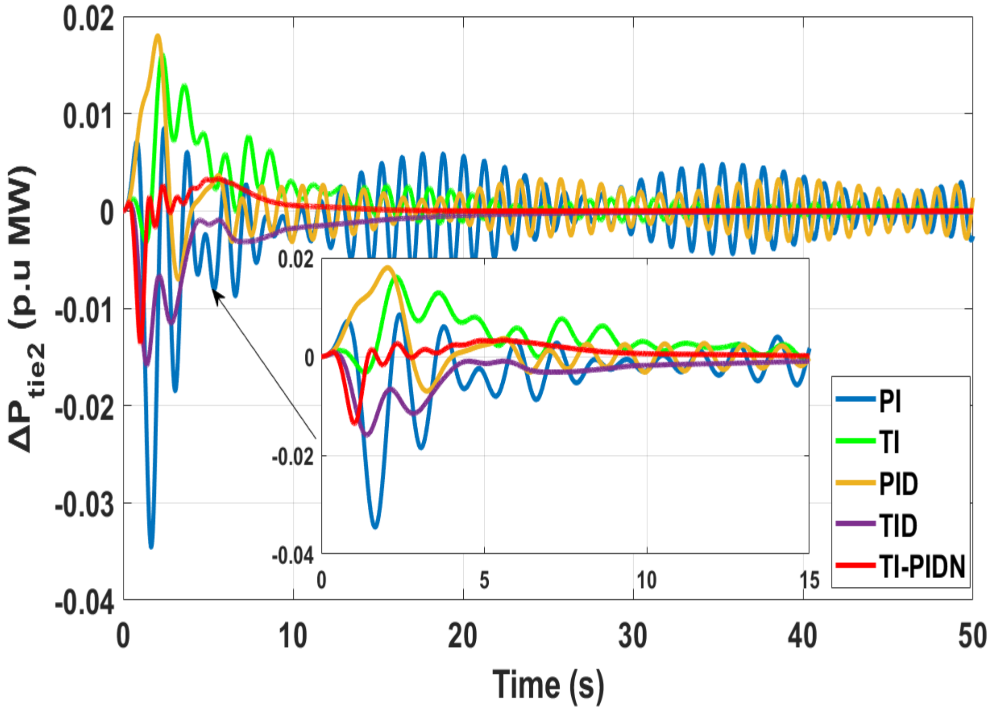

Figure 5.7 (c) System dynamic response of LFC and AVR obtained from different types of controllers : Deviation in tie line power-2.

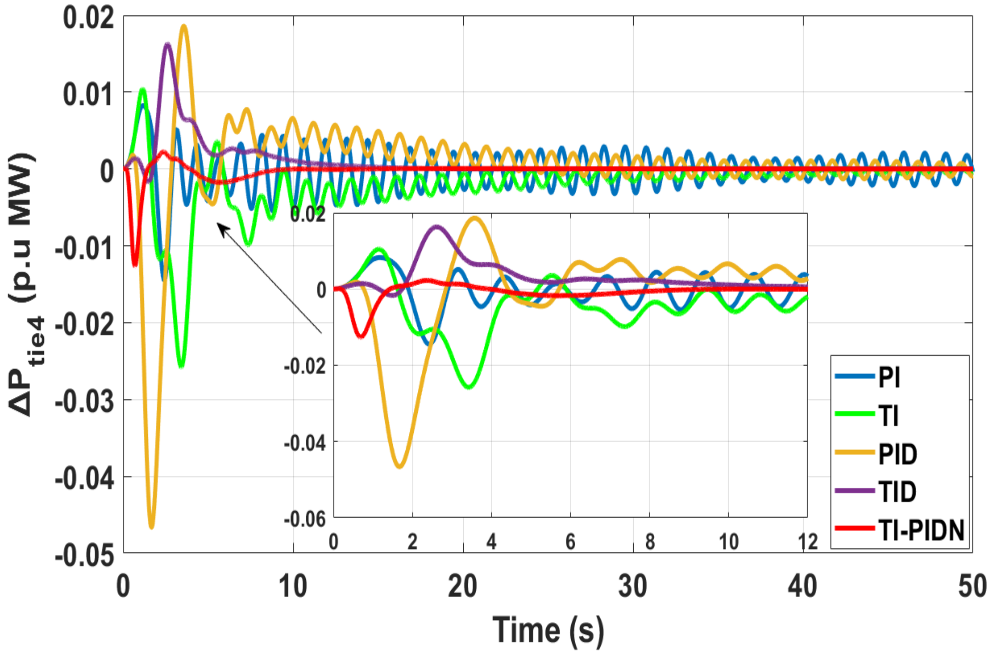

Figure 5.7 (d) System dynamic response of LFC and AVR obtained from different types of controllers: Deviation in tie line power-4.

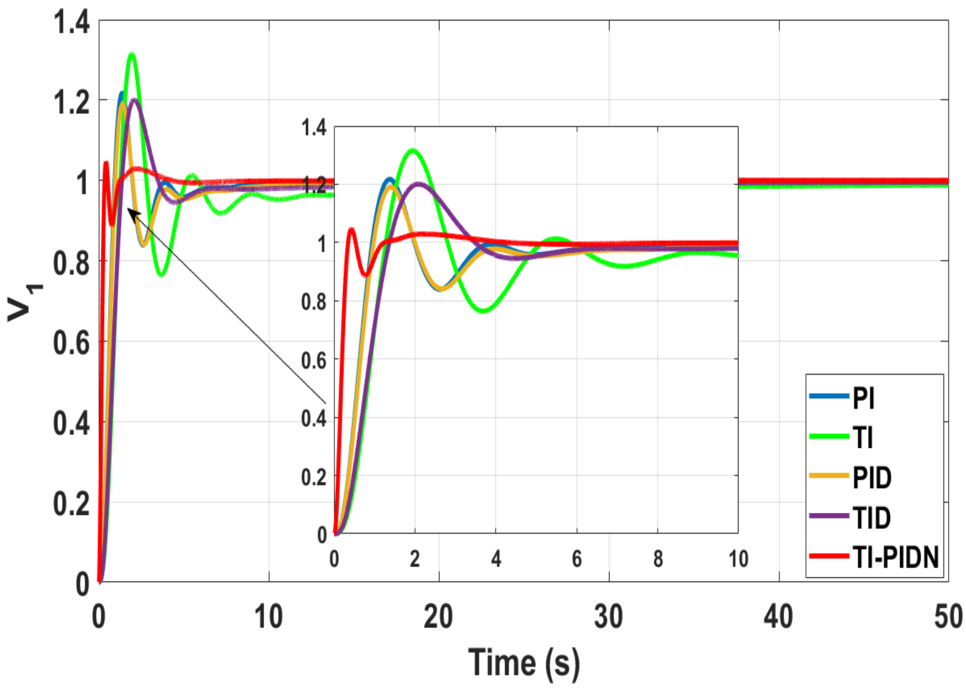

Figure 5.7 (e) System dynamic response of LFC and AVR obtained from different types of controllers: Area-1 voltage in p.u.

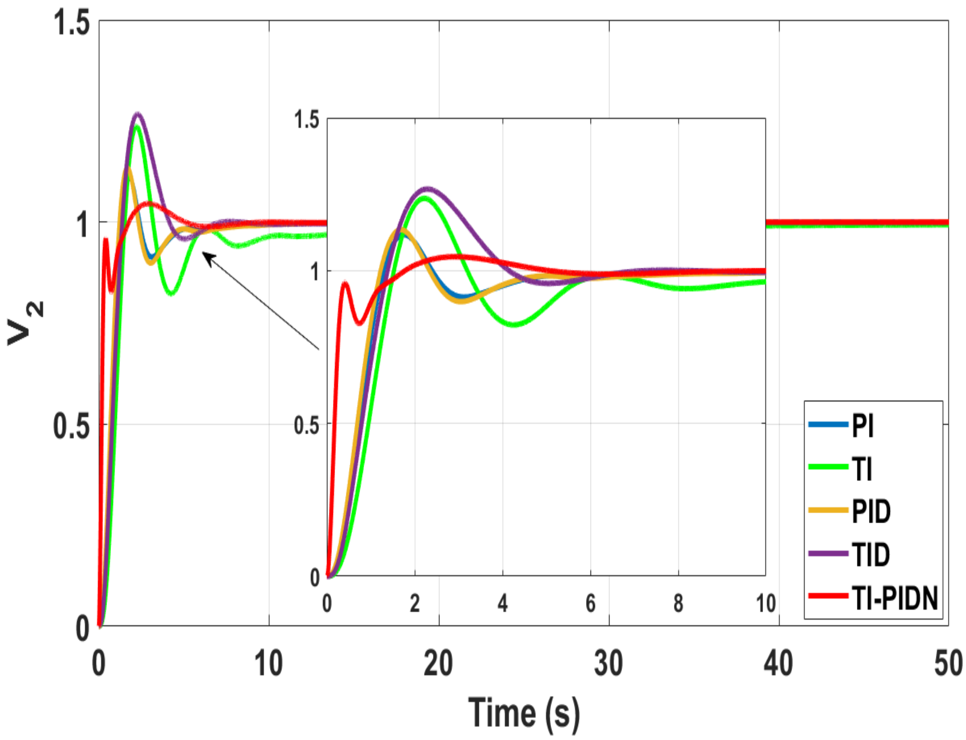

Figure 5.7 (f) System dynamic response of LFC and AVR obtained from different types of controllers: Area-2 voltage in p.u.

Table 5.2 (a) System dynamic response of different controllers for LFC-AVR

Responses		Controllers				
		PI	TI	PID	TID	TI-PIDN
Δf_1	M.U	-0.285	-0.2490	-0.3029	-0.2581	-0.2889
	M.O	0.145	0.0840	0.1622	0.0386	0.0164
	S.T	50>	50	50	8	6
Δf_2	M.U	-0.4027	-0.3037	-0.3971	-0.3129	-0.3909
	M.O	0.2251	0.0671	0.1962	0.0488	0.0211
	S.T	50>	35	50>	10	6
Δf_3	M.U	-0.3959	-0.3210	-0.4156	-0.3096	-0.4135
	M.O	0.1887	0.0825	0.2036	0.0596	0.0424
	S.T	50>	50>	50>	9	6
Δf_4	M.U	-0.3654	-0.3101	-0.4428	-0.3044	-0.3961
	M.O	0.1572	0.0932	0.2316	0.0636	0.0237
	S.T	50>	50>	50>	8	6
ΔP_{tie1}	M.U	-0.0175	-0.0209	-0.0208	-0.0082	-0.0026
	M.O	0.0867	0.0482	0.0911	0.0506	0.0689
	S.T	50>	30	50>	12	8
ΔP_{tie2}	M.U	-0.0345	-0.0032	-0.0069	-0.0158	-0.0135
	M.O	0.0084	0.0161	0.0179	0.0007	0.0032
	S.T	50>	50>	50>	23	10
ΔP_{tie3}	M.U	-0.0442	-0.0457	-0.0332	-0.0301	-0.0358
	M.O	0.0168	0.0107	0.0177	0.0040	0.0011
	S.T	50>	50>	50>	27	11
ΔP_{tie4}	M.U	-0.0144	-0.0257	-0.0465	-0.0016	-0.0008
	M.O	0.0082	0.0104	0.0185	0.0162	0.0250
	S.T	50>	50>	50>	15	8
ΔV_1	M.O	1.216	1.315	1.189	1.200	1.046
	S.T	9	18	13	17	4
ΔV_2	M.O	1.216	1.236	1.134	1.267	1.046
	S.T	10	21	10	10	6
ΔV_3	M.O	1.118	1.257	1.145	1.244	1.055
	S.T	9	25	9	8	6
ΔV_4	M.O	1.149	1.204	1.465	1.178	1.017
	S.T	9	15	10	10	5

Table 5.2 (b) Percentage improvement of TI-PIDN over other controllers.

Responses		% improvement of TI-PIDN over other controllers			
		PI	TI	PID	TID
Δf_1	M.U	-1	-16	4	-11
	M.O	88	80	89	57
	S.T	88	88	88	25
Δf_2	M.U	3	-28	1.5	-24
	M.O	90	68	89	56
	S.T	88	82	88	40
Δf_3	M.U	-4	-28	0.5	-33
	M.O	77	48	79	28
	S.T	88	88	88	33

Table 5.2 (b) (contd.) Percentage improvement of TI-PIDN over other controllers.

Responses		% Improvement of TI-PIDN over other controllers			
		PI	TI	PID	TID
Δf_4	M.U	-8	-27	10	-30
	M.O	84	74	89	62
	S.T	88	88	88	25
ΔP_{tie1}	M.U	85	87	86	68
	M.O	20	-42	24	-36
	S.T	84	73	84	33
ΔP_{tie2}	M.U	60	-76	-48	14
	M.O	61	80	82	-78
	S.T	80	80	80	56
ΔP_{tie3}	M.U	19	21	-7	-18
	M.O	93	89	93	72
	S.T	78	78	78	59
ΔP_{tie4}	M.U	94	96	98	50
	M.O	-67	-58	-26	-65
	S.T	84	84	84	46
ΔV_1	M.O	13	20	12	12
	S.T	55	77	69	76
ΔV_2	M.O	13	15	8	17
	S.T	40	71	40	40
ΔV_3	M.O	5	16	7	15
	S.T	33	76	33	25
ΔV_4	M.O	11	15	30	13
	S.T	44	66	50	50

Analysis: Based on the detailed results presented in the table, a clear comparative assessment of the controller performances can be drawn. The PI, TI, PID, TID, and TI-PIDN controllers exhibit distinct trends in terms of maximum undershoot (M.U), maximum overshoot (M.O), and settling time (S.T). Traditional controllers such as PI, TI, and PID generally show acceptable performance in terms of stability, but their settling times are consistently high (often around or beyond 50s), making them slower in dynamic adjustment. Among them, the PI controller maintains moderate undershoot and overshoot values but at the expense of slow response. The TI controller reduces overshoot in several cases compared to PI and PID, yet its longer settling time limits practical effectiveness.

The PID controller demonstrates improved damping and better overshoot control in some instances, though it still suffers from relatively slower convergence. On the other hand, the TID controller shows a notable improvement with shorter settling times (8–27 s in most cases), reduced oscillatory behavior, and smaller overshoot values, which indicates better adaptability to dynamic changes. However, the most significant improvement is achieved with the proposed TI-PIDN controller, which consistently records the lowest overshoot and undershoot values across the scenarios and, most importantly, achieves a drastically reduced settling time (as low as 4–6 s in several cases).

This suggests that the TI-PIDN controller not only ensures stability and precision but also enhances the speed of dynamic response, outperforming conventional controllers. In conclusion, the results decisively highlight the superiority of the TI-PIDN controller in terms of robustness, stability, and rapid convergence, making it the most suitable choice for advanced AGC applications.

5.4.1.2 Sensitivity analysis

5.4.1.2.1 Random load perturbation

When the system is operating in real-time, it undergoes a continuous change throughout the day. As a result, even in the face of erratic fluctuating load conditions, the proposed controller's ability to regulate system frequency is essential. The working of the proposed controller is checked by these randomly changing load settings for t=100s, as explained in the previously discussed scenarios, and it performs admirably under these circumstances.

To simulate the random load conditions, Figure 5.9 displays the applied load variations graphically. Figure 5.8 illustrates the system's dynamic reaction, which demonstrates that the proposed TI-PIDN controller can effectively operate the system even when load fluctuation occurs in a real-world power system scenario. Table 5.3 offers detailed information on the controller settings' adjusted gain values. Since numerical data for the dynamic system responses is not applicable to a random load fluctuation, the graphs presented are considered as the proof of the stable system.

Table 5.3 ZOA Optimized TI-PIDN Controller gain values for random load variation analysis for LFC-AVR system.

TI-PIDN	K_{t1}=0.8416, n_1=2.5642, K_{i1}=0.8003, K_{p1}=0.5406, K_{i11}=0.3029, K_{d1}=0.6932, N_1=52.463: K_{t2}=0.2791, n_2=2.6503, K_{i2}=0.8333, K_{p2}=0.6818, K_{i22}=0.3350, K_{d2}=0.9996, N_2=52.762: K_{t3}=0.5173, n_3=2.6229, K_{i3}=0.3526, K_{p3}=0.6043, K_{i33}=0.3203, K_{d3}=0.8893, N_3=30.236, K_{t4}=0.5271, n_4=2.7691, K_{i4}=0.4310, K_{p4}=0.8433, K_{i44}=0.4145, K_{d4}=0.9999, N_4=55.801, K_{t5}=0.7993, n_5=2.7443, K_{i5}=0.2076, K_{p5}=0.8303, K_{i55}=0.6187, K_{d5}=0.9994, N_5=79.480, K_{t6}=0.7739, n_6=2.9294, K_{i6}=0.3353, K_{p6}=0.3380, K_{i66}=0.3466, K_{d6}=0.9999, N_6=98.256, K_{t7}=0.3425, n_7=2.4411, K_{i7}=0.3816, K_{p7}=0.8040, K_{i77}=0.5780, K_{d7}=0.9997, N_7=96.810, K_{t8}=0.3694, n_8=2.3823, K_{i8}=0.4112, K_{p8}=0.9807, K_{i88}=0.2624, K_{d8}=0.9999, N_8=94.01 Numerical 1-4 represents area 1-4 LFC control While, 5-8 represent area 1-4 AVR control

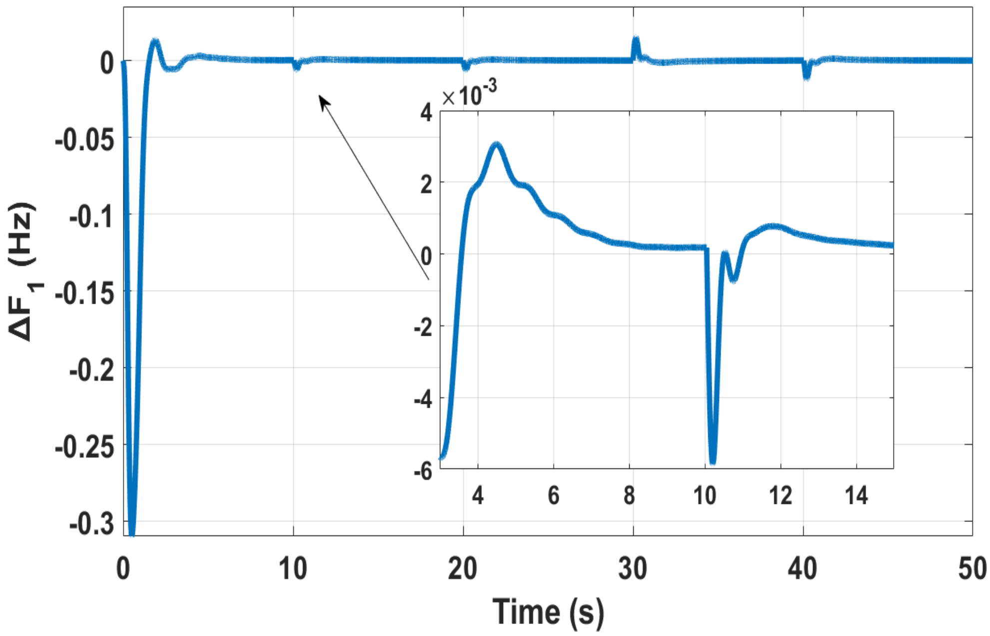

Figure 5.8 (a) System dynamic response of LFC and AVR obtained from random load analysis: Area-1 deviation in frequency.

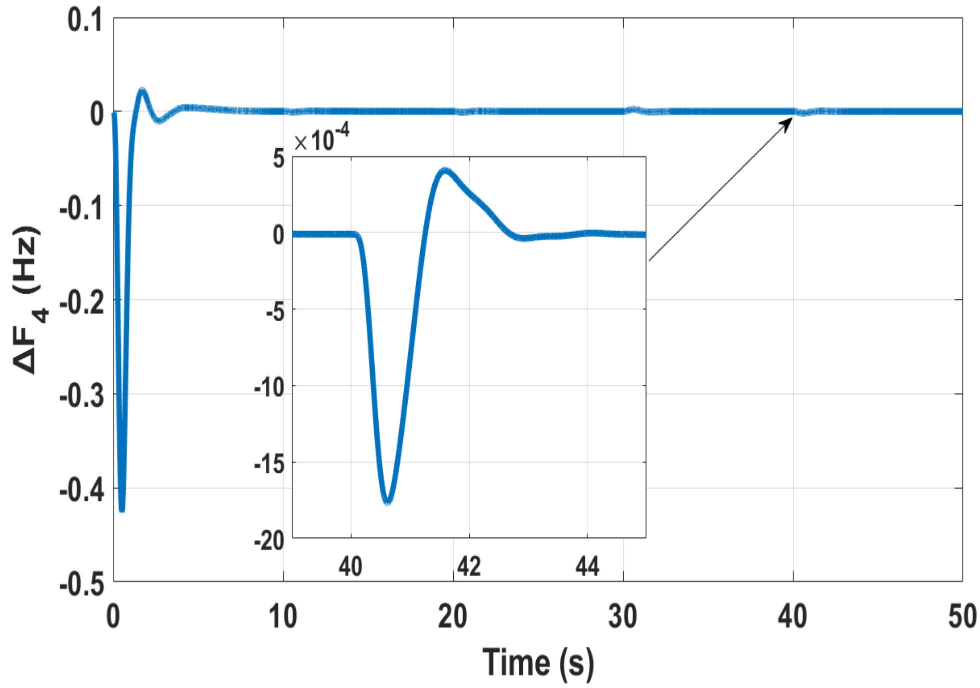

Figure 5.8 (b) System dynamic response of LFC and AVR obtained from random load analysis: Area-4 deviation in frequency.

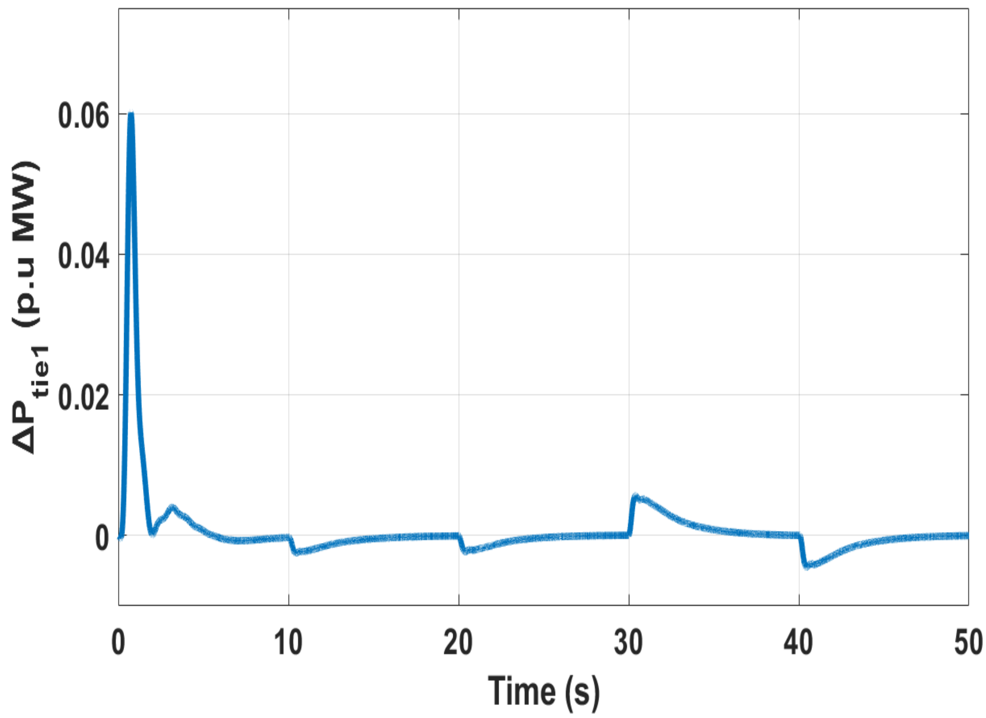

Figure 5.8 (c) System dynamic response of LFC and AVR obtained from random load analysis: Deviation in tie line power-1.

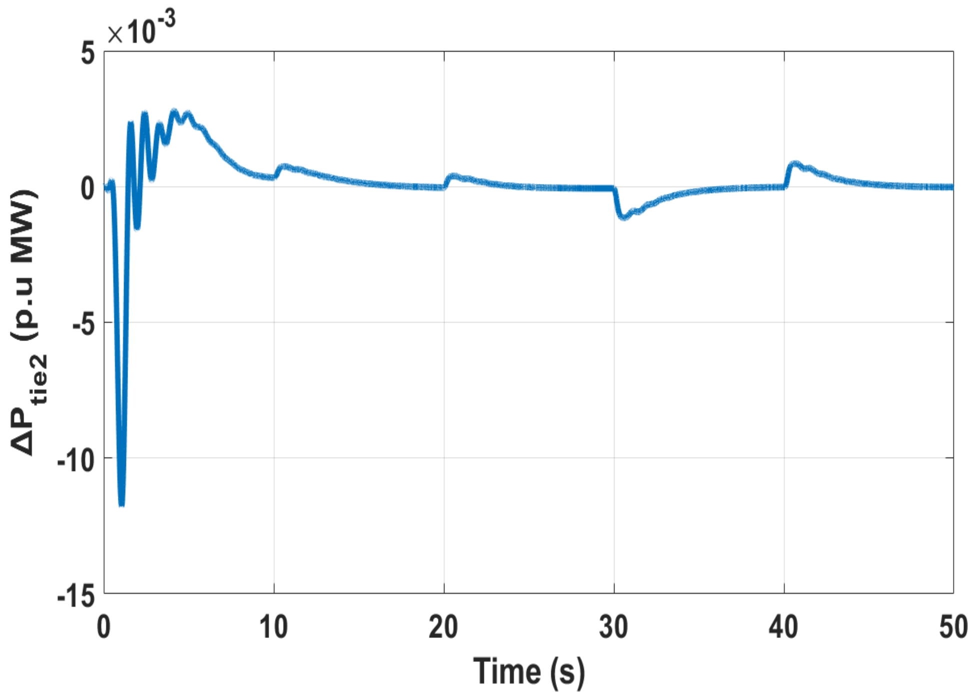

Figure 5.8 (d) System dynamic response of LFC and AVR obtained from random load analysis: Deviation in tie line power-2.

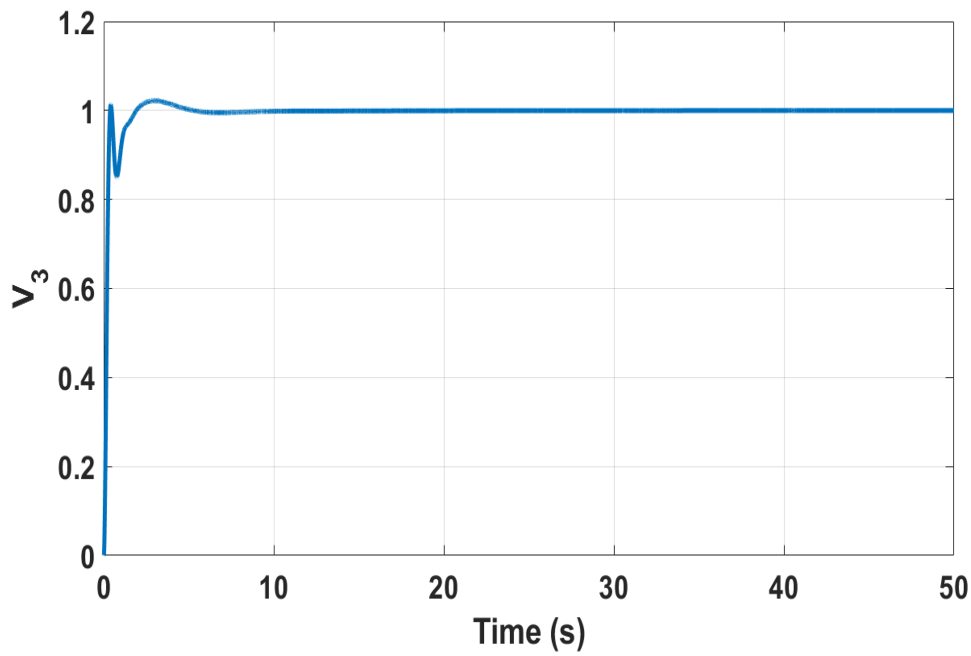

Figure 5.8 (e) System dynamic response of LFC and AVR obtained from random load analysis: Area-3 voltage in p.u.

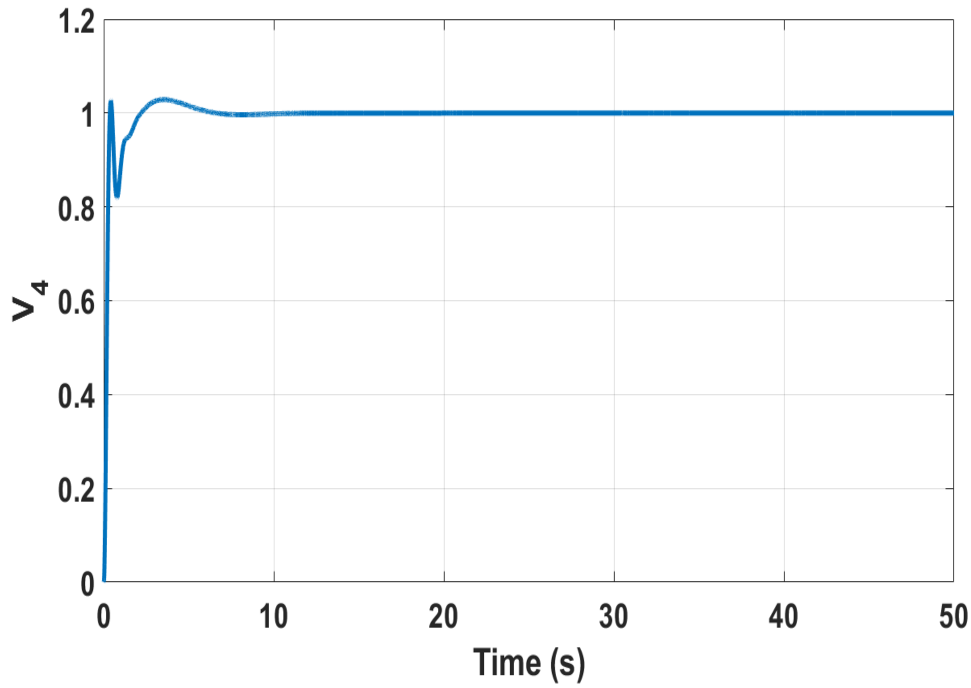

Figure 5.8 (f) System dynamic response of LFC and AVR obtained from random load analysis: Area-4 voltage in p.u.

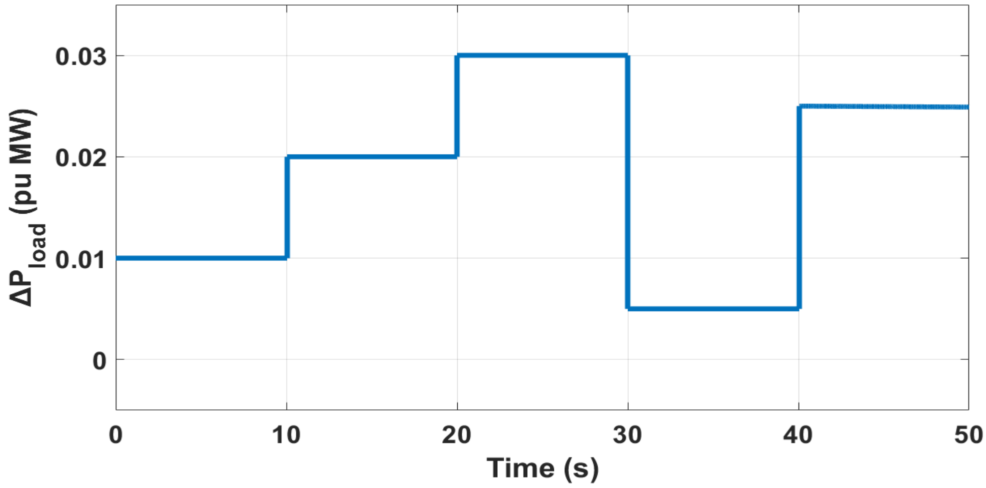

Figure 5.9 Change in step load perturbation for LFC-AVR system.

Analysis: The stability responses depicted in the presented figures clearly validate the effectiveness of the proposed control strategy in ensuring secure and reliable operation of the interconnected power system. The frequency deviations in both areas initially experience sharp transients, yet the system demonstrates rapid damping characteristics with minimal residual oscillations, thereby highlighting the robustness of the controller in maintaining frequency stability even under sudden disturbances. Similarly, the tie-line power deviations exhibit noticeable spikes during load perturbations; however, these oscillations are quickly attenuated, and the steady-state values converge close to zero, confirming the controller's capability to regulate inter-area power exchanges effectively. Furthermore, the voltage responses show only minor overshoots during the initial transients and then settle tightly around the nominal voltage, ensuring secure voltage stability. Collectively, these results emphasize that the proposed controller not only stabilizes dynamic frequency and tie-line power fluctuations but also preserves voltage quality, thereby providing a comprehensive and reliable solution for modern interconnected systems operating under uncertain and varying conditions.

5.4.1.2.2 System with non-linearities

These days, AGC's primary problems are related to the increasing complexity of power systems caused by physical constraints such as generation rate constraints (GRC), boiler dynamics (BD), and communication time delay (TD). For this reason, a closed-loop type GRC of ± 0.03MW/min and a TD of 0.5 s are used to test the suggested control scheme at the output of each secondary controller in each area. Analysis shows that fluctuations are caused by non-linearities in the system; however, by combining the suggested method with the FACTs device, the oscillations can be reduced and the system can approach stability. Figure 5.10 shows the responses of the system.

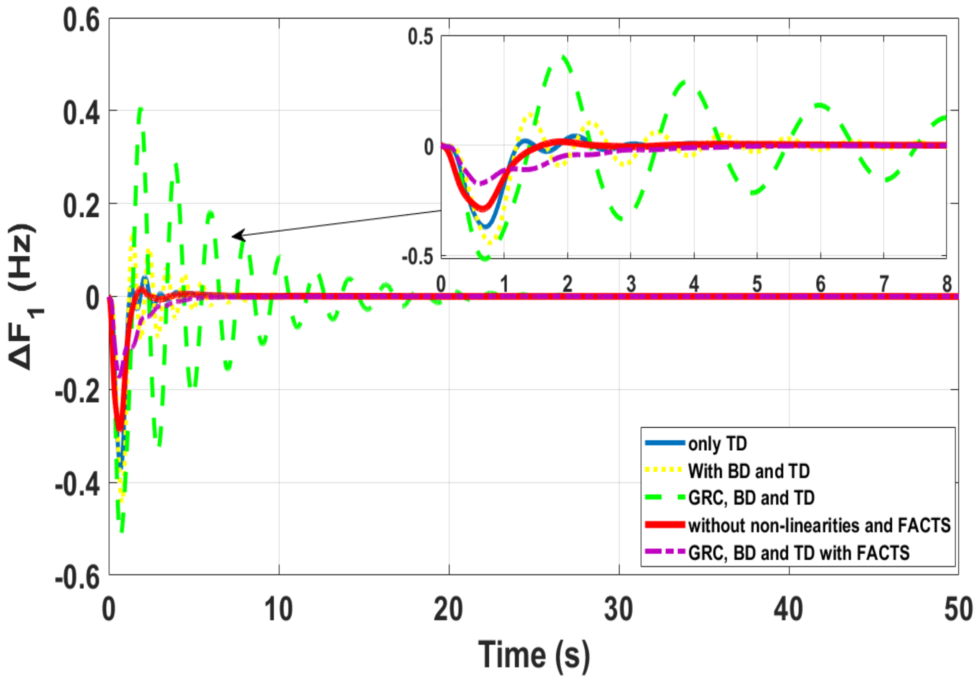

Figure 5.10 (a) System dynamic response of LFC and AVR obtained from analysis of system with non-linearities: Area-1 change in frequency.

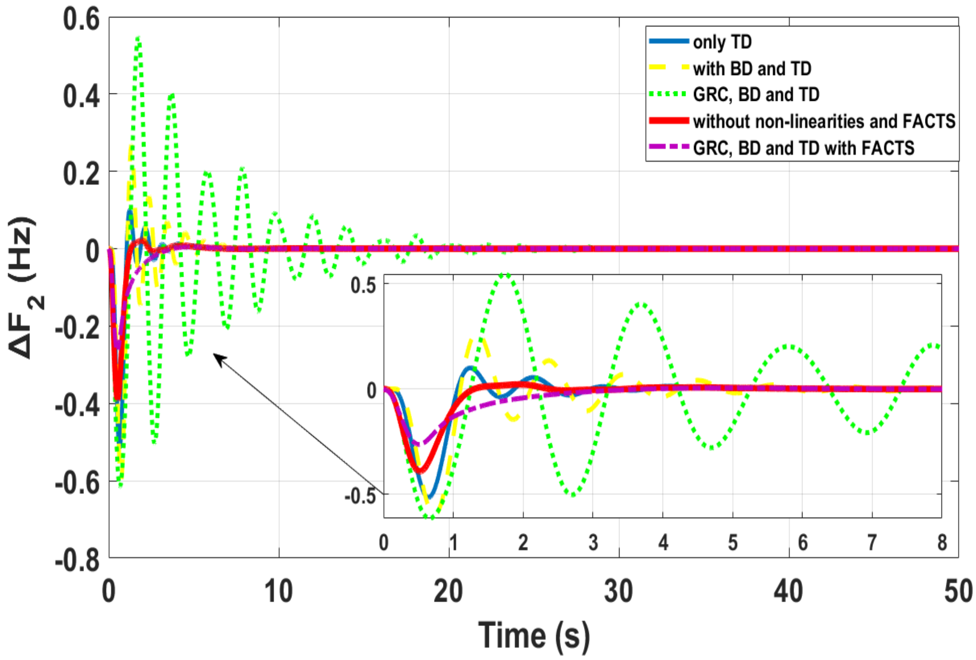

Figure 5.10 (b) System dynamic response of LFC and AVR obtained from analysis of system with non-linearities: Area-2 change in frequency.

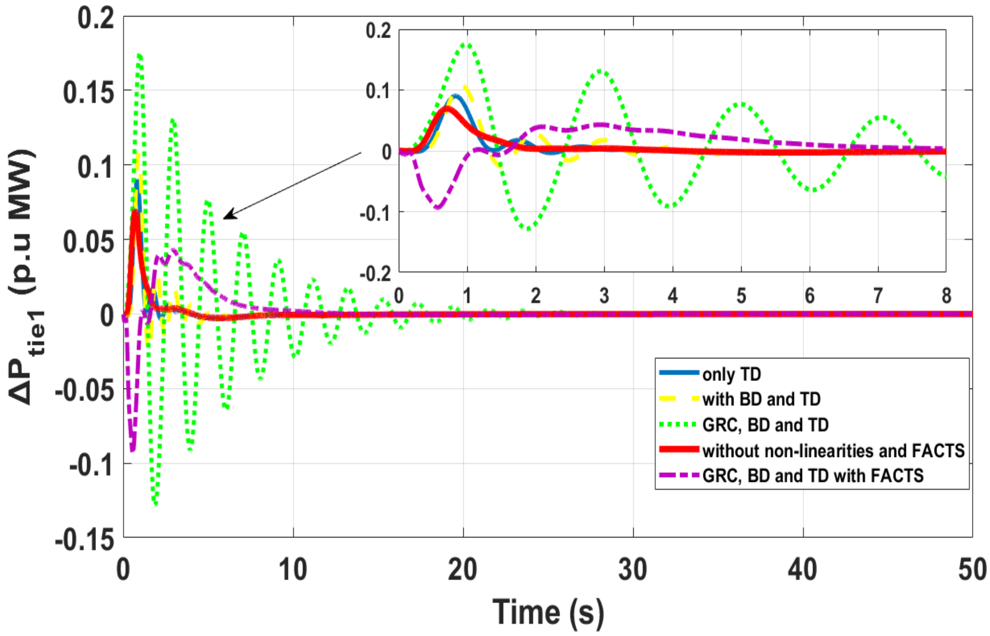

Figure 5.10 (c) System dynamic response of LFC and AVR obtained from analysis of system with non-linearities: Deviation in tie line power-1.

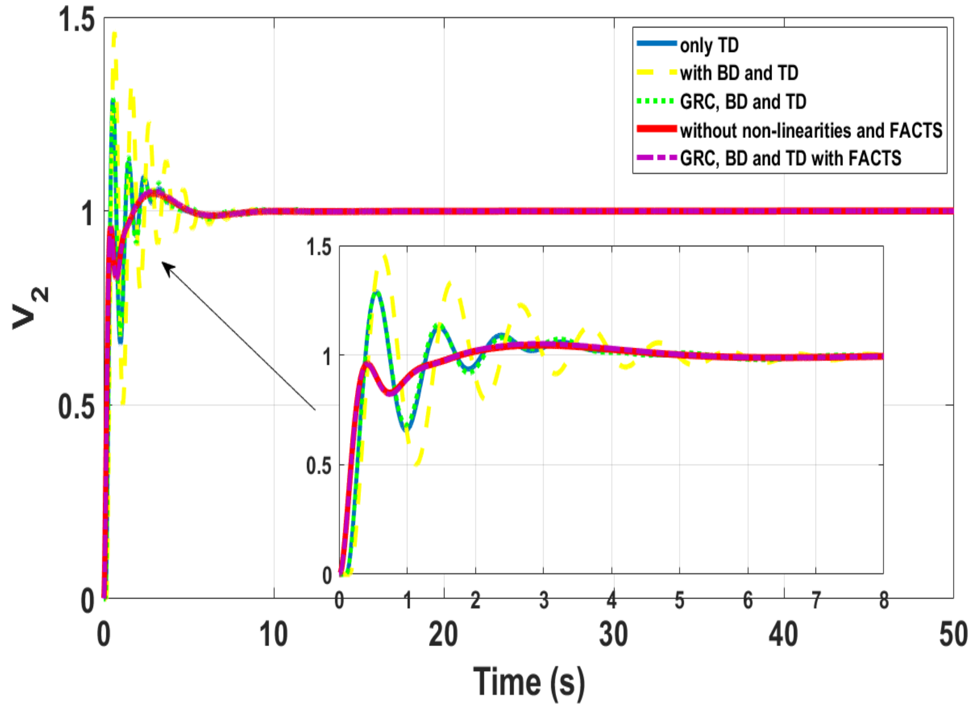

Figure 5.10 (d) System dynamic response of LFC and AVR obtained from analysis of system with non-linearities: Area-2 voltage in p.u.

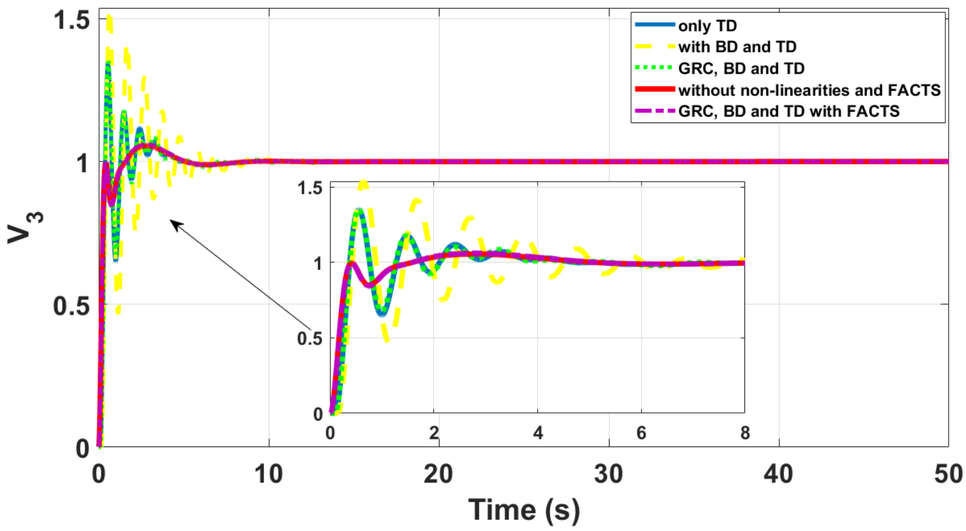

Figure 5.10 (e) System dynamic response of LFC and AVR obtained from analysis of system with non-linearities: Area-3 voltage in p.u.

Analysis: The presented figures illustrate the performance of the system under nonlinearities such as Generation Rate Constraint (GRC), Boiler Dynamics (BD), and Turbine Dynamics (TD), and further assess the impact of incorporating FACTS devices. From the frequency deviation plots, it is evident that the presence of nonlinearities causes larger oscillations and slower damping, particularly under GRC conditions, which significantly distort system stability. Similarly, the tie-line power deviations highlight that nonlinear effects lead to persistent oscillations and poor settling characteristics when left uncompensated. However, once the proposed controller is integrated with FACTS devices, the system response is notably improved, showing rapid damping of oscillations, reduced overshoot, and faster stabilization compared to the cases without FACTS. Moreover, the voltage profiles confirm that although initial transients are amplified by nonlinearities, the controller successfully restores voltages to nominal levels with minimal steady-state error when FACTS are included.

5.4.1.2.3 Change in system parameter

To determine how resilient the controller is to changes in parameters brought on by unknown variables, a sensitivity analysis is carried out. The objective is to make sure that even with minor changes to the system parameters, the controller's performance stays constant. The system parameters are changed by ±20% from nominal H and ±25% from their nominal loading of the system in all areas for this study. The controller optimized values are presented in Table 5.4. The dynamic responses of the system are shown in Figure 5.11.

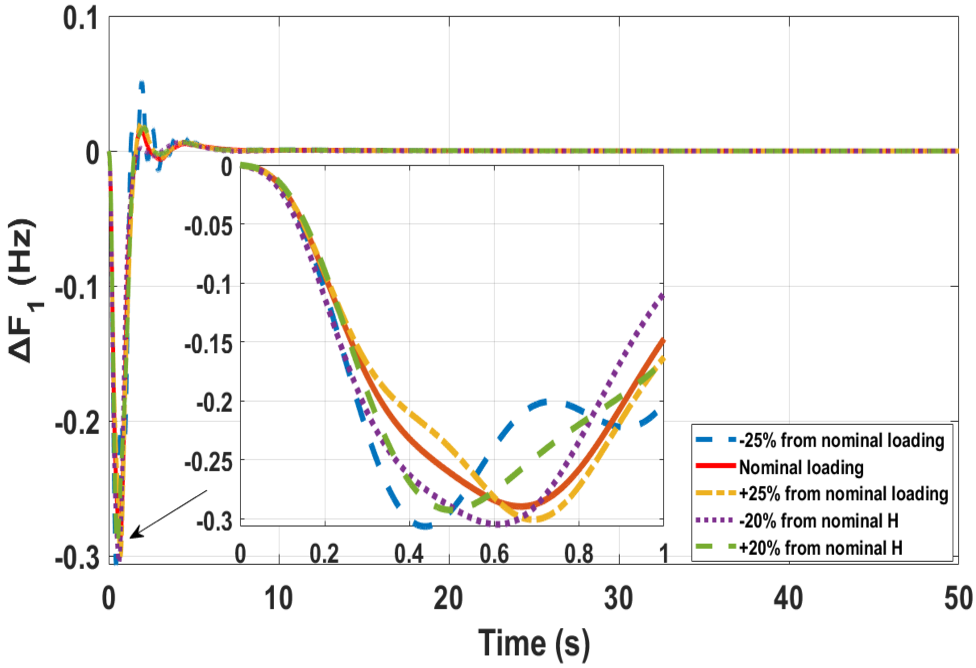

Figure 5.11 (a) System dynamic response of LFC and AVR obtained from analysis of change in system parameters: Area-1 change in frequency.

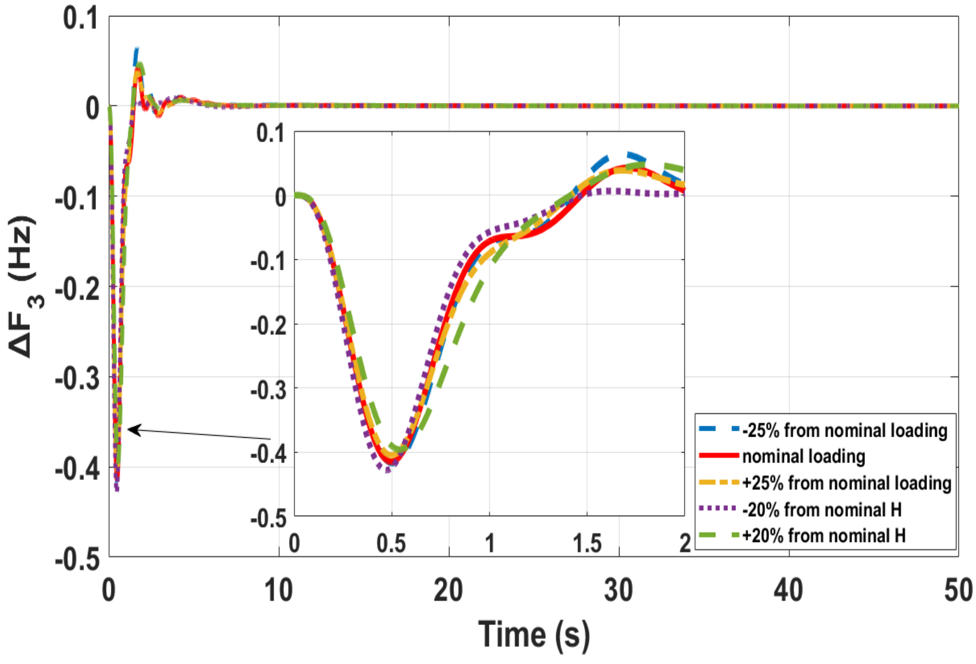

Figure 5.11 (b) System dynamic response of LFC and AVR obtained from analysis of change in system parameters: Area-3 change in frequency.

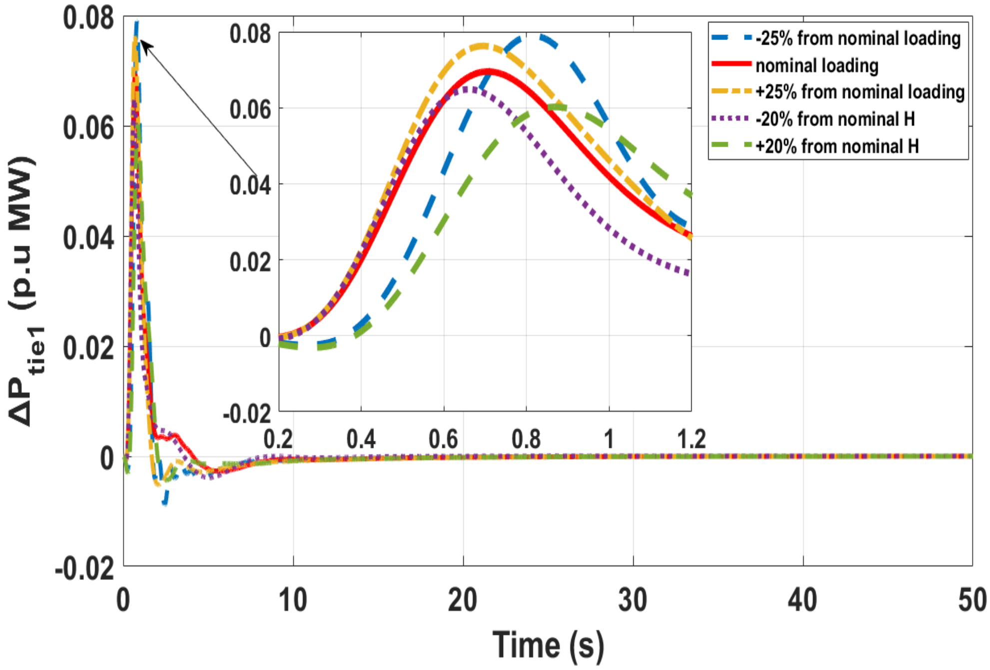

Figure 5.11 (c) System dynamic response of LFC and AVR obtained from analysis of change in system parameters: Deviation in tie line power-1.

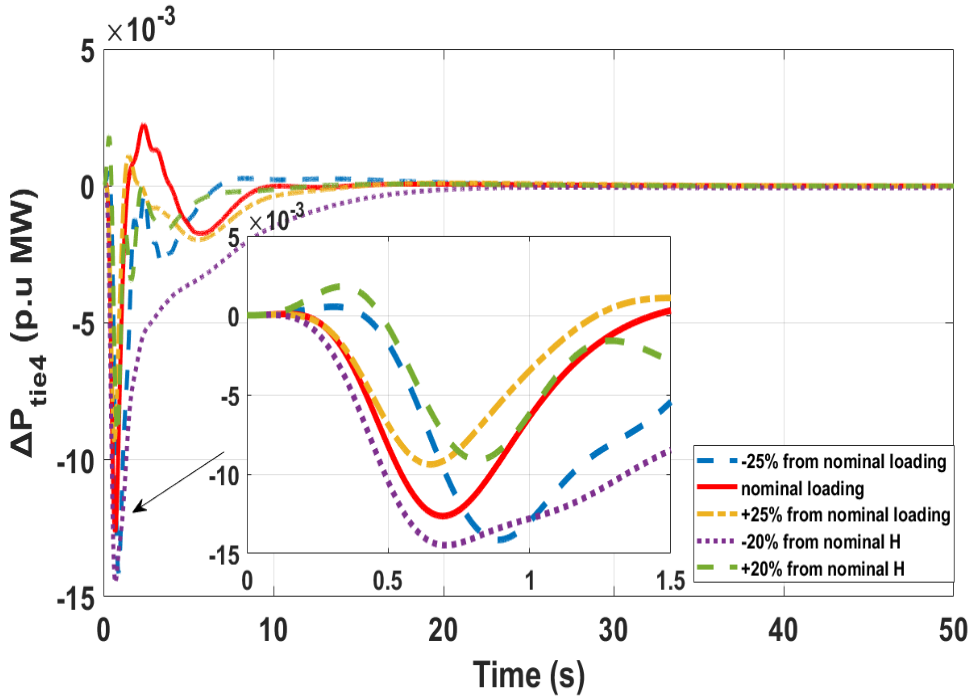

Figure 5.11 (d) System dynamic response of LFC and AVR obtained from analysis of change in system parameters: Deviation in tie line power-4.

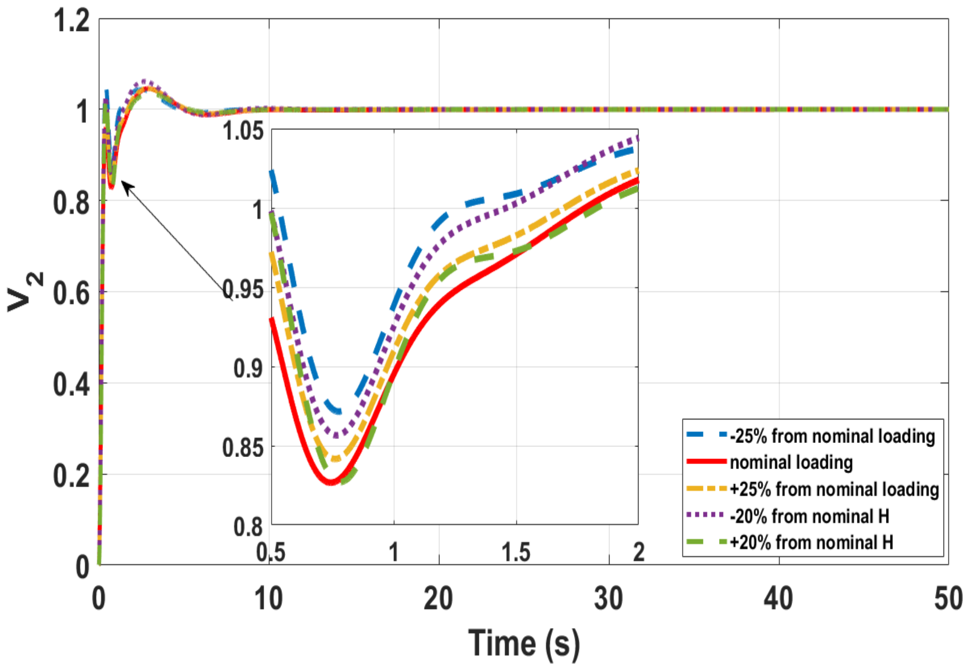

Figure 5.11 (e) System dynamic response of LFC and AVR obtained from analysis of change in system parameters: Area-2 voltage in p.u.

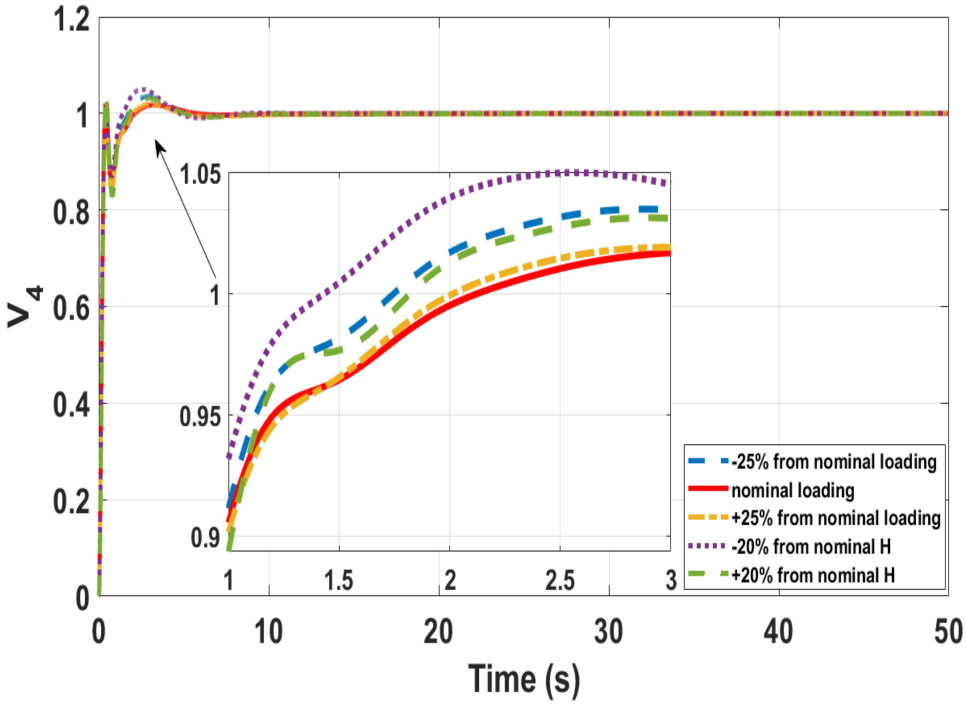

Figure 5.11 (f) System dynamic response of LFC and AVR obtained from analysis of change in system parameters: Area-4 voltage in p.u.

Table 5.4 Controller parameters for change in system parameter for LFC-AVR

Parameters	-25% loading	+25% loading	-20% H	+20% H
K_{t1}	0.2854	0.5284	0.2114	0.4781
n_1	2.3258	2.2113	2.4302	2.3624
K_{i1}	0.5263	0.3929	0.7126	0.4590
K_{p1}	0.5284	0.8227	0.7479	0.4688
K_{i11}	0.6984	0.4416	0.1911	0.5426
K_{d1}	0.4028	0.8066	0.5852	0.3459
N_1	12.838	32.497	58.380	52.580
K_{t2}	0.3470	0.3889	0.7031	0.2332
n_2	2.8534	2.1208	2.8653	2.2602
K_{i2}	0.6099	0.6272	0.6622	0.5519
K_{p2}	0.2526	0.4975	0.9061	0.8212
K_{i22}	0.9766	0.5356	0.5599	0.6799
K_{d2}	0.9999	0.9999	0.9985	0.9999
N_2	47.622	73.562	79.054	50.028
K_{t3}	0.7470	0.9020	0.2750	0.3760
n_3	2.4575	2.5791	2.1922	2.8843
K_{i3}	0.5920	0.1891	0.6135	0.5158
K_{p3}	0.9813	0.3531	0.9519	0.9985
K_{i33}	0.5543	0.5893	0.5817	0.4650
K_{d3}	0.9993	0.9997	0.9507	0.9999
N_3	50.054	58.633	67.018	76.699
K_{t4}	0.4411	0.6410	0.6126	0.3439
n_4	2.6085	2.8920	2.0187	2.4002
K_{i4}	0.7069	0.4484	0.4548	0.4990
K_{p4}	0.3742	0.7809	0.6622	0.9151
K_{i44}	0.4940	0.4376	0.0747	0.5530
K_{d1}	0.9997	0.9999	0.9999	0.9999
N_4	55.213	66.417	40.200	28.905
K_{t5}	0.6318	0.7263	0.6524	0.3384
n_5	2.6985	2.6924	2.3862	2.6430
K_{i5}	0.5521	0.4009	0.3857	0.3727
K_{p5}	0.7456	0.5963	0.9806	0.9968
K_{i55}	0.2252	0.3204	0.2810	0.7545
K_{d5}	0.9999	0.9996	0.9999	0.9999
N_5	70.334	76.603	78.468	86.576
K_{t6}	0.4626	0.4271	0.1415	0.5506
n_6	2.7521	2.3596	2.4124	2.7059
K_{i6}	0.5906	0.4928	0.6937	0.3825
K_{p6}	0.8977	0.7578	0.9965	0.6407
K_{i66}	0.4335	0.2457	0.4641	0.3468
K_{d6}	0.9999	0.9999	0.9999	0.9998
N_6	58.2443	74.809	71.925	43.686
K_{t7}	0.5217	0.3689	0.9978	0.9308
n_7	2.2898	2.3297	2.9835	2.5372
K_{i7}	0.2588	0.4710	0.3966	0.6154
K_{p7}	0.9329	0.9214	0.2108	0.9437

Table 5.4 (contd.) Controller parameters for change in system parameter for LFC-AVR.

Parameters	-25% loading	+25% loading	-20% H	+20% H
K_{i77}	0.5819	0.3661	0.5178	0.4011
K_{d7}	0.9999	0.9999	0.9999	0.9999
N_7	62.814	82.276	66.770	75.968
K_{t8}	0.5013	0.7445	0.5623	0.7251
n_8	2.5932	2.8988	2.8936	2.9323
K_{i8}	0.4026	0.0696	0.3574	0.2516
K_{p8}	0.7609	0.5565	0.7218	0.5129
K_{i88}	0.3656	0.5094	0.6020	0.4292
K_{d8}	0.9988	0.9999	0.9999	0.9998
N_8	60.467	92.364	99.590	34.842

Analysis: The stability analysis presented in the given figures demonstrates the dynamic performance of the system under varying operating conditions, including changes in loading levels (±25% from nominal) and system inertia (±20% from nominal H). The frequency responses reveal that although initial deviations are noticeable, the system is capable of regaining stability within a relatively short duration, highlighting robustness against parameter variations. The tie-line power deviations exhibit transient oscillations that settle smoothly, confirming the effectiveness of the control mechanism in maintaining power exchange balance even under stressed conditions. Additionally, the voltage responses reflect minor dips and overshoots during disturbances, but they recover quickly and converge close to the nominal value, ensuring secure voltage stability. Overall, the results confirm that the system remains dynamically stable across all tested perturbations, proving the resilience of the proposed control strategy to uncertainties in load demand and system inertia. This robustness indicates suitability for modern interconnected power systems operating under diverse and deregulated environments.

5.4.2 Deregulated environment

In order to refine the gain values of the controller from a power system containing a deregulated network, we have used the ZOA algorithm. As shown in Figure 5.3, two GENCOs and two DISCOs are assumed to be present for each particular area in this study model of combined LFC and AVR. The appendix provides the values of the parameters of the system. In this part, deregulated environment is analysed in three different types of transaction known as contract violation, unilateral, and bilateral using the following two scenarios of system without FACTs device and system with FACTs device. Here, the FACTS devices are connected in each area for the study. In situation 2, the Facts device (FD) is present, whereas in scenario 1, it is not. For clarity, we display the simulation findings using a format that incorporates pertinent figures and tables.

5.4.2.1 Unilateral transaction

Under this kind of organizational structure, DISCOs can only enter into electricity contracts with GENCOs that operate in their respective assigned areas. In particular, each DISCO demands the GENCOs of 0.01 p.u. load in their respective areas. In (5.14), the DPM matrix is displayed. The specific areas local load demand is:

$$\Delta P_D = 0.01 + 0.01 = 0.02 \tag{5.18}$$

For both cases, with and without FD, the overall system performance is shown in Figure 5.12. It has been observed that when FD is present, the system performs better after a disruption than when FD is absent. Furthermore, ZOA-tuned controllers gain values for scenarios 1 and 2 are shown in Table 5.6. The dynamic response of the system is shown in Table 5.7 (a) with percentage improvement in Table 5.7 (b).

$$DPM = \begin{bmatrix} 0.7 & 0.3 & cpf_{13} & cpf_{14} & cpf_{15} & cpf_{16} & cpf_{17} & cpf_{18} \\ 0.3 & 0.7 & cpf_{23} & cpf_{24} & cpf_{25} & cpf_{26} & cpf_{27} & cpf_{28} \\ cpf_{31} & cpf_{32} & 0.4 & 0.6 & cpf_{35} & cpf_{36} & cpf_{37} & cpf_{38} \\ cpf_{41} & cpf_{42} & 0.6 & 0.4 & cpf_{45} & cpf_{46} & cpf_{47} & cpf_{48} \\ cpf_{51} & cpf_{52} & cpf_{53} & cpf_{54} & 0.5 & 0.5 & cpf_{57} & cpf_{58} \\ cpf_{61} & cpf_{62} & cpf_{63} & cpf_{64} & 0.5 & 0.5 & cpf_{67} & cpf_{68} \\ cpf_{71} & cpf_{72} & cpf_{73} & cpf_{74} & cpf_{75} & cpf_{76} & 0.6 & 0.4 \\ cpf_{81} & cpf_{82} & cpf_{83} & cpf_{84} & cpf_{85} & cpf_{86} & 0.4 & 0.6 \end{bmatrix} \tag{5.19}$$

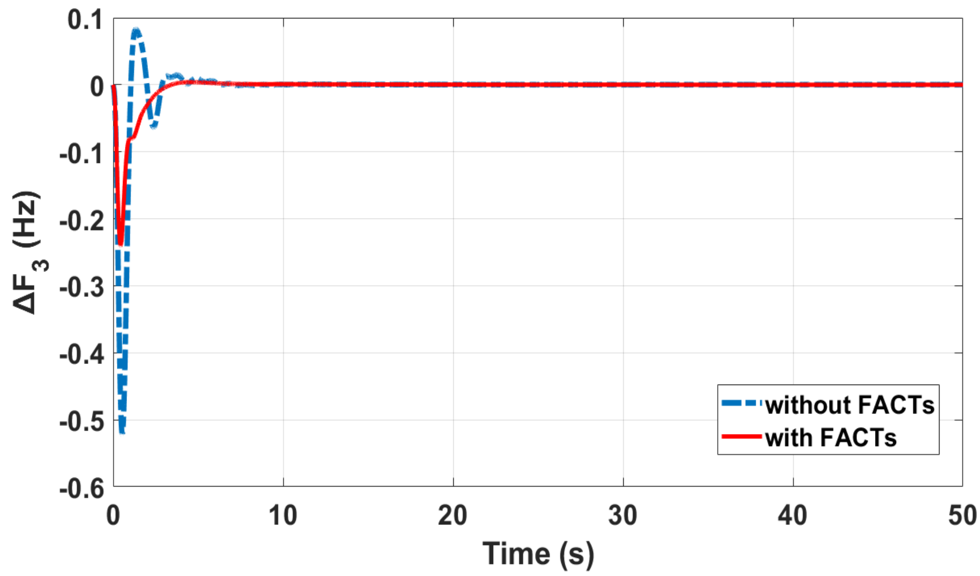

Figure 5.12 (a) System dynamic response of LFC and AVR obtained from analysis of Unilateral transaction: Area-3 change in frequency.

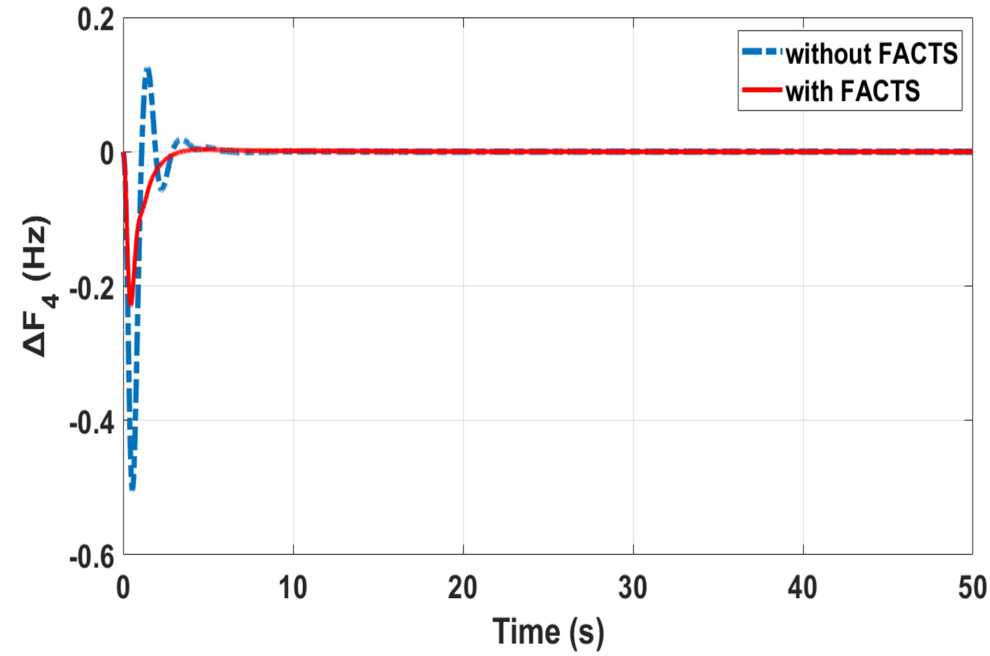

Figure 5.12 (b) System dynamic response of LFC and AVR obtained from analysis of Unilateral transaction: Area-4 change in frequency.

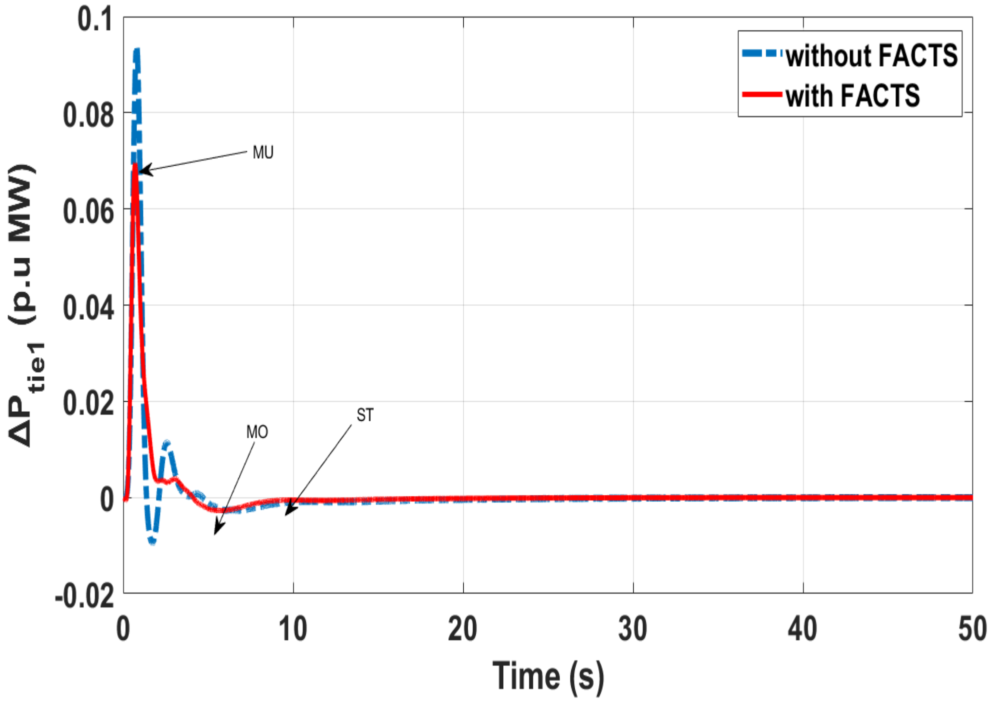

Figure 5.12 (c) System dynamic response of LFC and AVR obtained from analysis of Unilateral transaction: Deviation in tie line power-1.

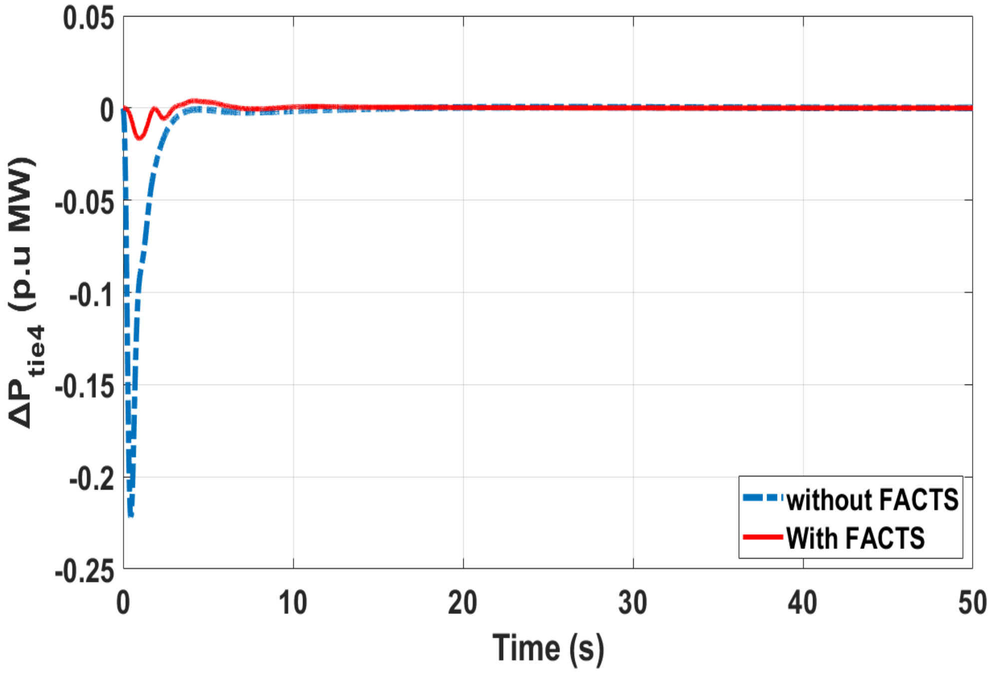

Figure 5.12 (d) System dynamic response of LFC and AVR obtained from analysis of Unilateral transaction: Deviation in tie line power-4.

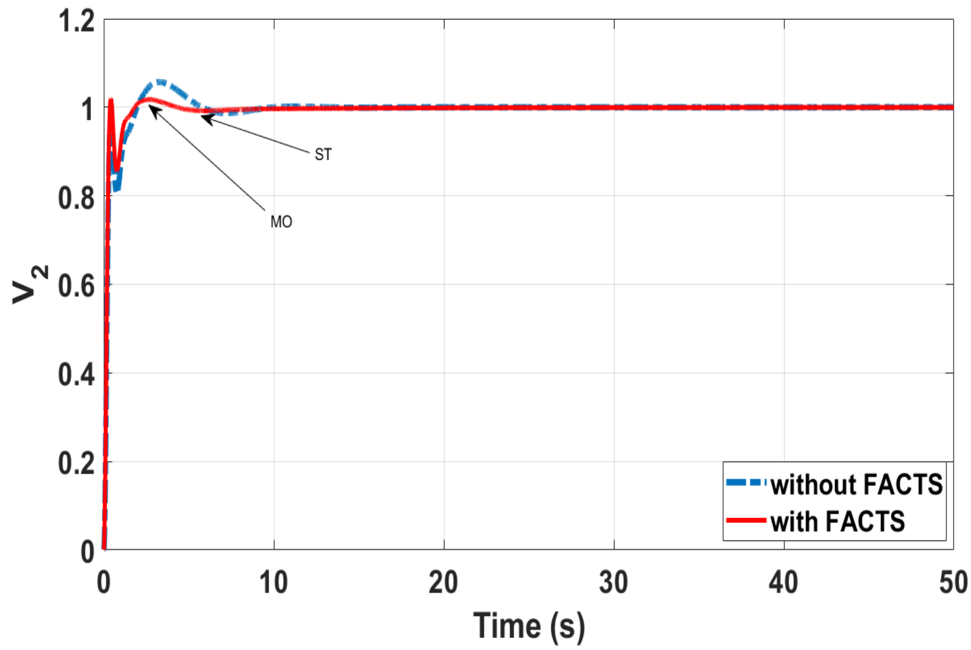

Figure 5.12 (e) System dynamic response of LFC and AVR obtained from analysis of Unilateral transaction: Area-2 voltage in p.u.

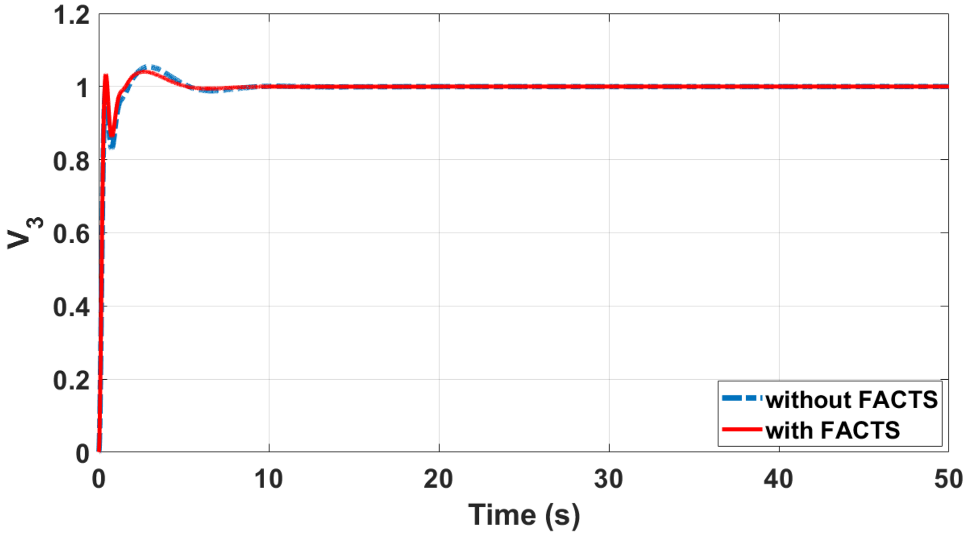

Figure 5.12 (f) System dynamic response of LFC and AVR obtained from analysis of Unilateral transaction: Area-3 voltage in p.u.

5.4.2.2 Bilateral transaction

Each disco in a distinct area can demand power from each Genco's in a different area in this scenario, which examines a bilateral transaction. The DPM matrix shown in (5.16) is for the bilateral transaction context. Assuming that each DISCO asks the GENCOs for 0.01 per unit (p.u.) of power, the cumulative area load demand would be as follows:

$$\Delta P_D = 0.01 + 0.01 = 0.02 \tag{5.20}$$

The system's performance under the two scenarios "with FD" and "without FD" is depicted in Figure 5.13. Tables 5.6 and 5.7 display the optimal controller gain levels as well as the associated system performance in numerical data.

$$DPM = \begin{bmatrix} 0.1 & 0.1 & 0.1 & 0.2 & 0.1 & 0.1 & 0.1 & 0.2 \\ 0.1 & 0.1 & 0.1 & 0.2 & 0.1 & 0.1 & 0.1 & 0.2 \\ 0.1 & 0.1 & 0.2 & 0.1 & 0.1 & 0.1 & 0.2 & 0.1 \\ 0.1 & 0.1 & 0.2 & 0.1 & 0.1 & 0.1 & 0.2 & 0.1 \\ 0.1 & 0.2 & 0.1 & 0.1 & 0.1 & 0.2 & 0.1 & 0.1 \\ 0.1 & 0.2 & 0.1 & 0.1 & 0.1 & 0.2 & 0.1 & 0.1 \\ 0.2 & 0.1 & 0.1 & 0.1 & 0.2 & 0.1 & 0.1 & 0.1 \\ 0.2 & 0.1 & 0.1 & 0.1 & 0.2 & 0.1 & 0.1 & 0.1 \end{bmatrix} \tag{5.21}$$

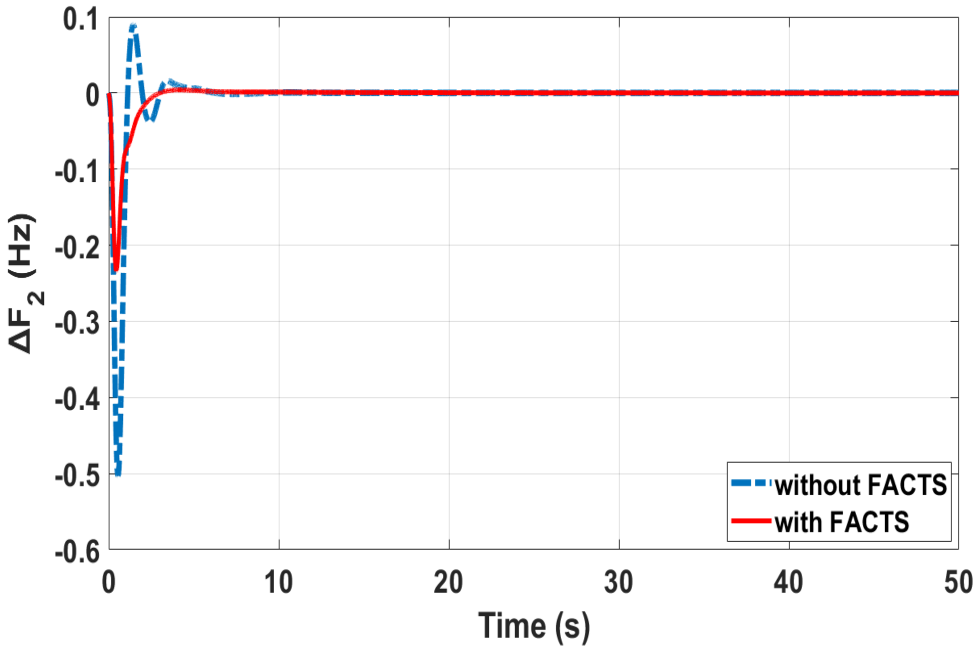

Figure 5.13 (a) System dynamic response of LFC and AVR obtained from analysis of Bilateral transaction: Area-2 change in frequency.

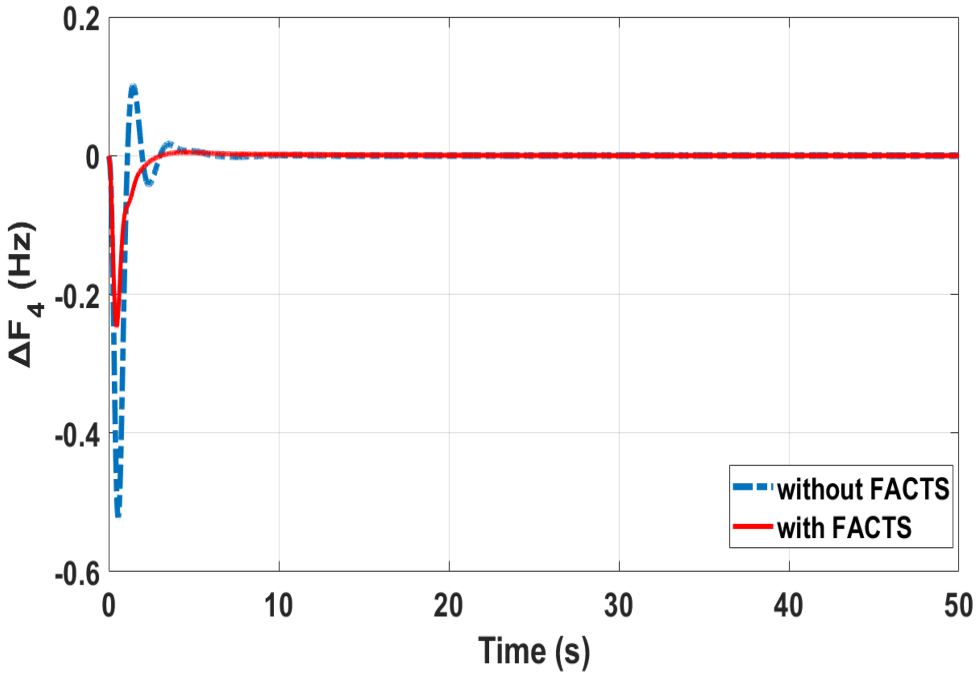

Figure 5.13 (b) System dynamic response of LFC and AVR obtained from analysis of Bilateral transaction: Area-4 change in frequency.

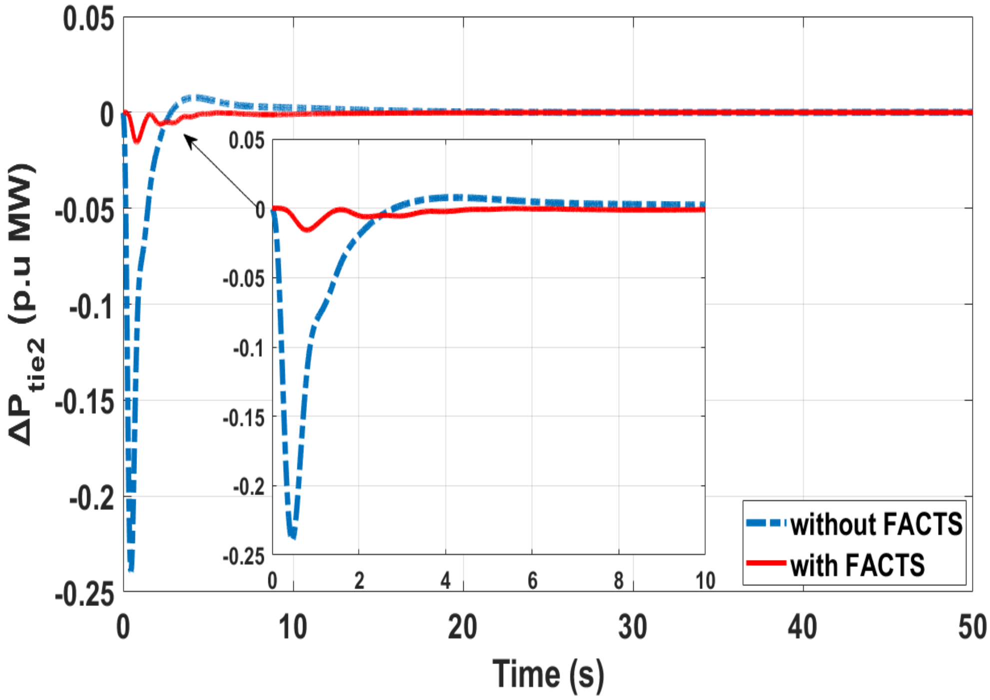

Figure 5.13 (c) System dynamic response of LFC and AVR obtained from analysis of Bilateral transaction: Change in tie line power-2.

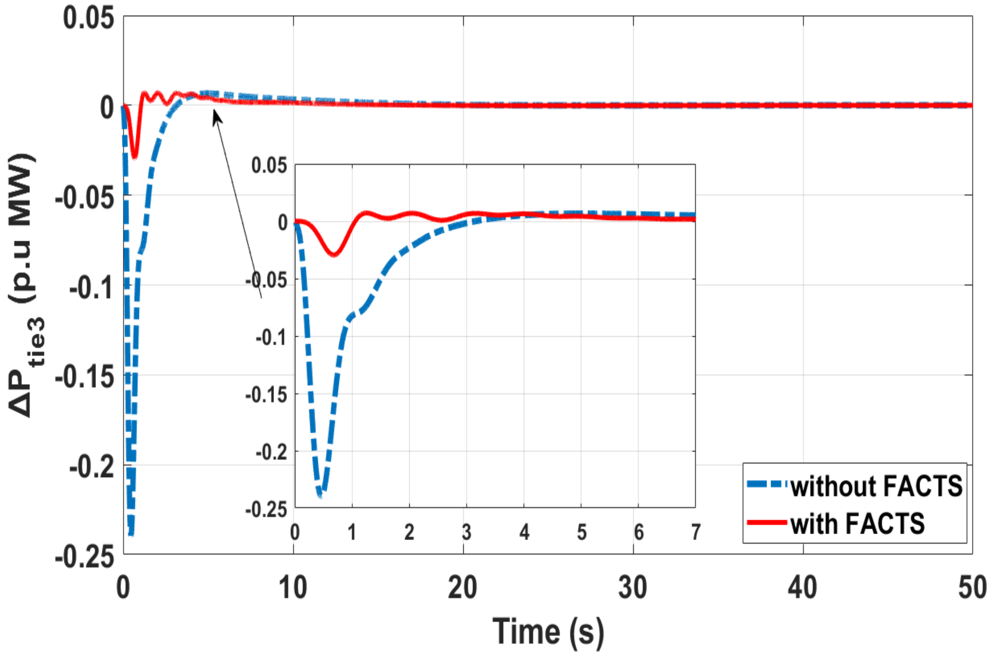

Figure 5.13 (d) System dynamic response of LFC and AVR obtained from analysis of Bilateral transaction: Change in tie line power-3.

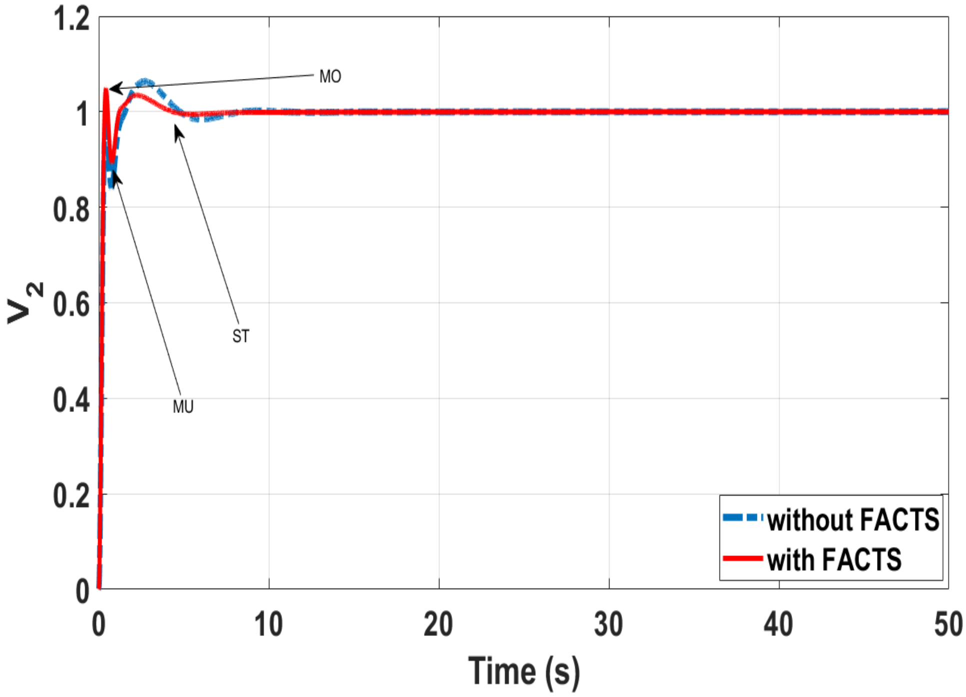

Figure 5.13 (e) System dynamic response of LFC and AVR obtained from analysis of Bilateral transaction: Area-2 voltage in p.u.

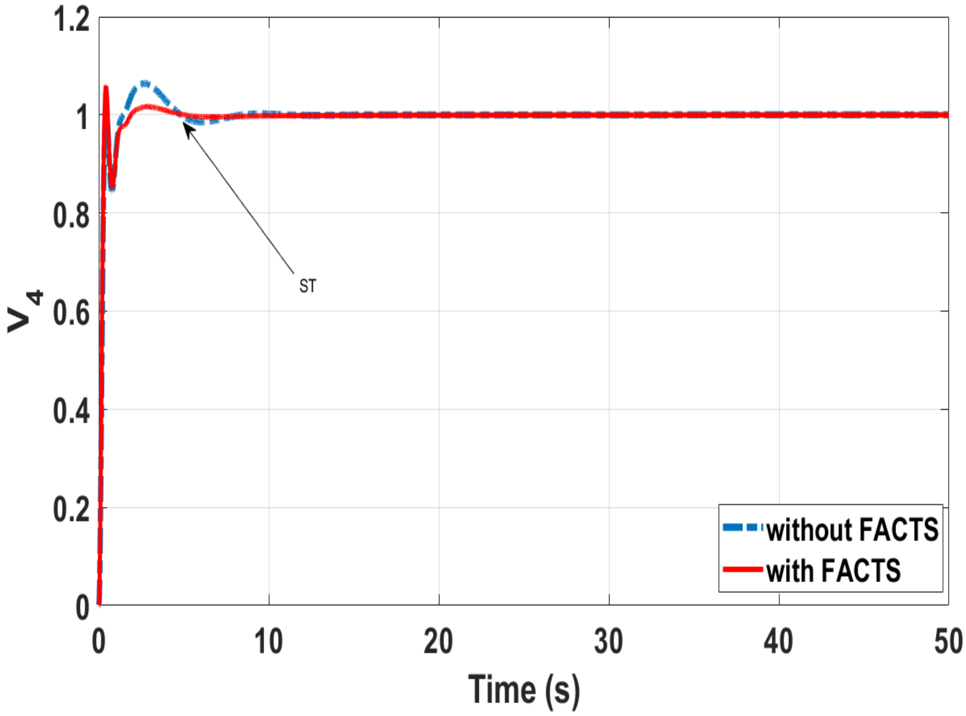

Figure 5.13 (f) System dynamic response of LFC and AVR obtained from analysis of Bilateral transaction: Area-4 voltage in p.u.

5.4.2.3 Contract violation

This scenario stands out from the others because the DISCOs broke their obligations. In this instance, the GENCO, which is situated in the same vicinity as the DISCO, satisfies the uncontract power demand. By failing to adhere to the rules of the contract, DISCO 1 in area 1 requests an extra 0.005 p.u. in a case study on a pool-based transaction. Consequently, area 1 local load is modified as:

$$\Delta P_D = (0.01 + 0.01) + 0.005 = 0.025 \qquad (5.22)$$

In Figure 5.14, the system's overall performance is displayed. The optimized controller gain settings are displayed in Table 5.6, and the system response statistics. are listed in Table 5.7. The change in apfs is shown in Table 5.5.

Table 5.5 Power generation table for contract violation case of LFC-AVR system

Areas	Power Generation (Source)	apfs	Generated power (P.u. MW)
Area 1	GENCO 1	0.6	0.015
	GENCO 2	0.4	0.01
Area 2	GENCO 3	0.5	0.01
	GENCO 4	0.5	0.01
Area 3	GENCO 5	0.5	0.01
	GENCO 6	0.5	0.01
Area 4	GENCO 7	0.5	0.01
	GENCO 8	0.5	0.01

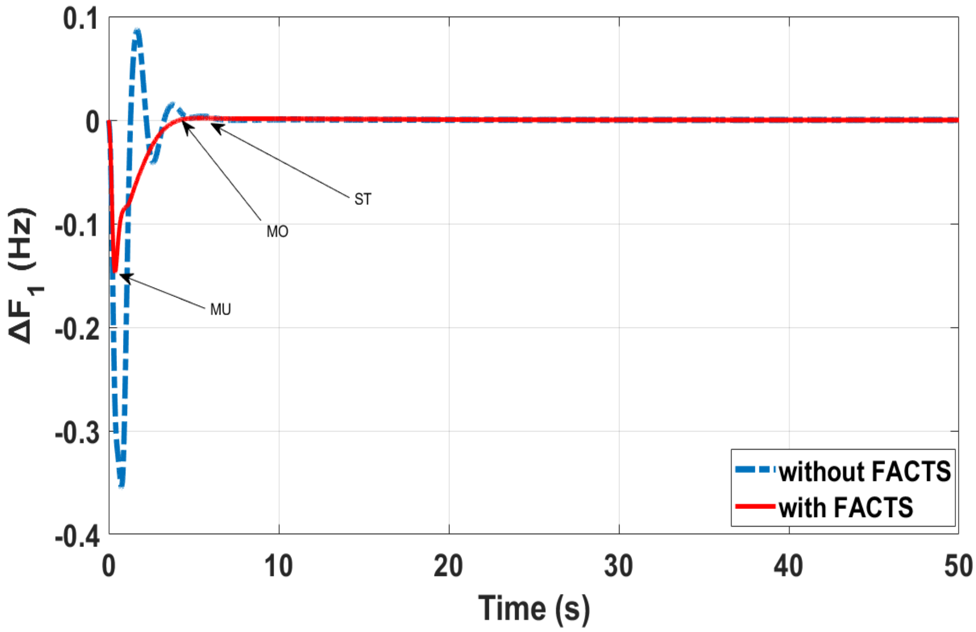

Figure 5.14 (a) System dynamic response of LFC and AVR obtained from analysis of Contract violation transaction: Area-1 change in frequency.

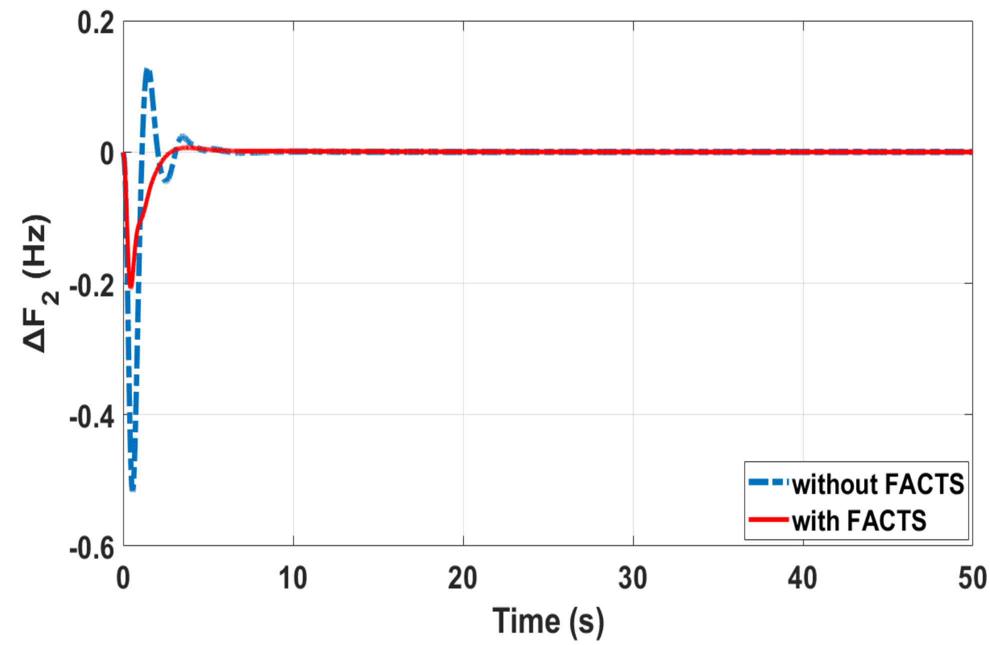

Figure 5.14 (b) System dynamic response of LFC and AVR obtained from analysis of Contract violation transaction: Area-2 change in frequency.

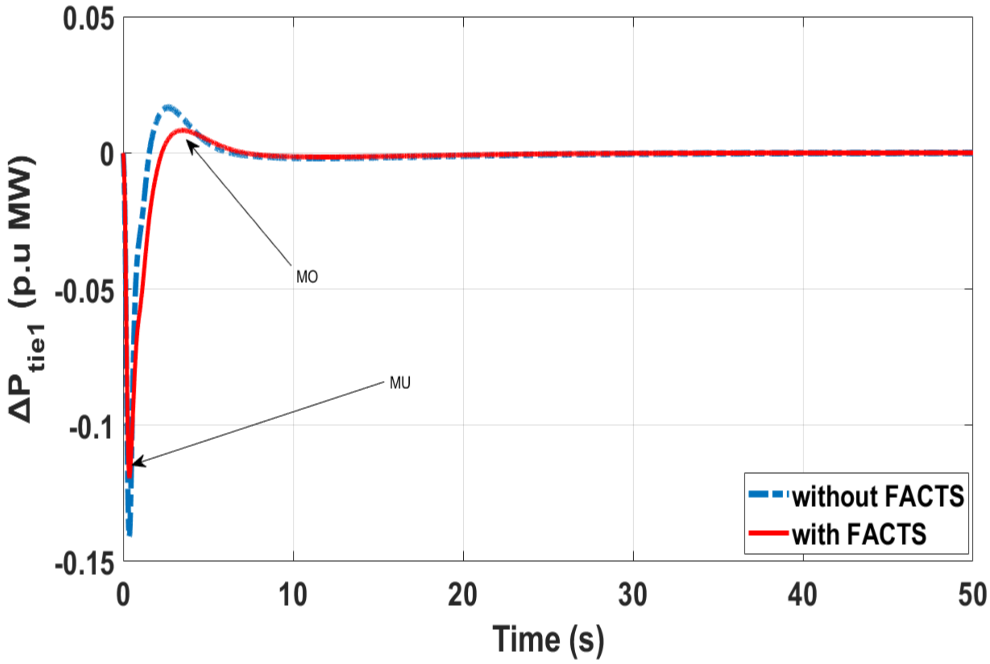

Figure 5.14 (c) System dynamic response of LFC and AVR obtained from analysis of Contract violation transaction: Change in tie line power 1.

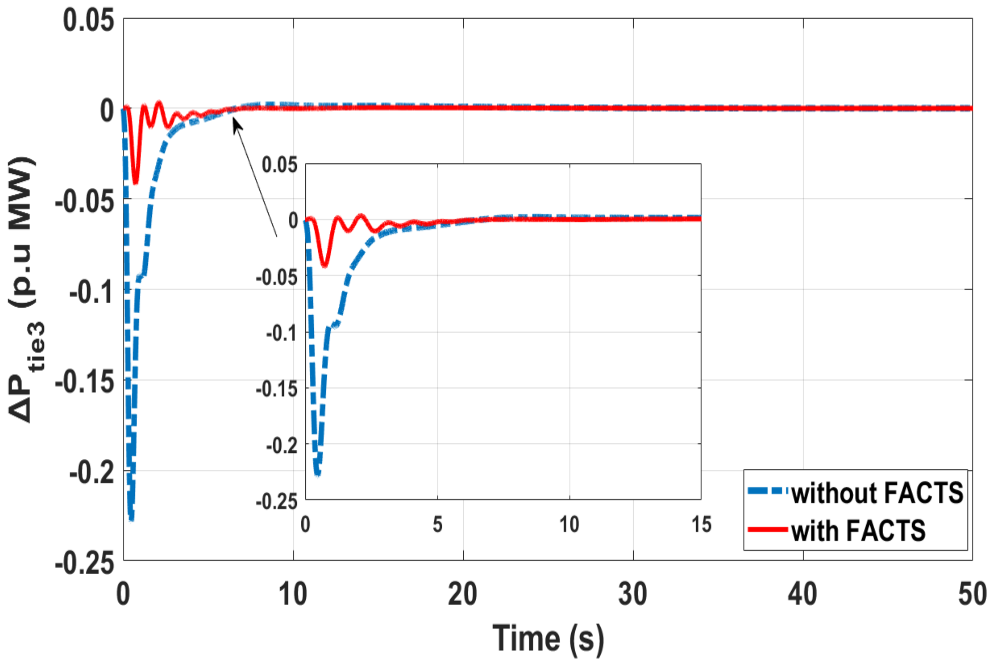

Figure 5.14 (d) System dynamic response of LFC and AVR obtained from analysis of Contract violation transaction: Change in tie line power 3.

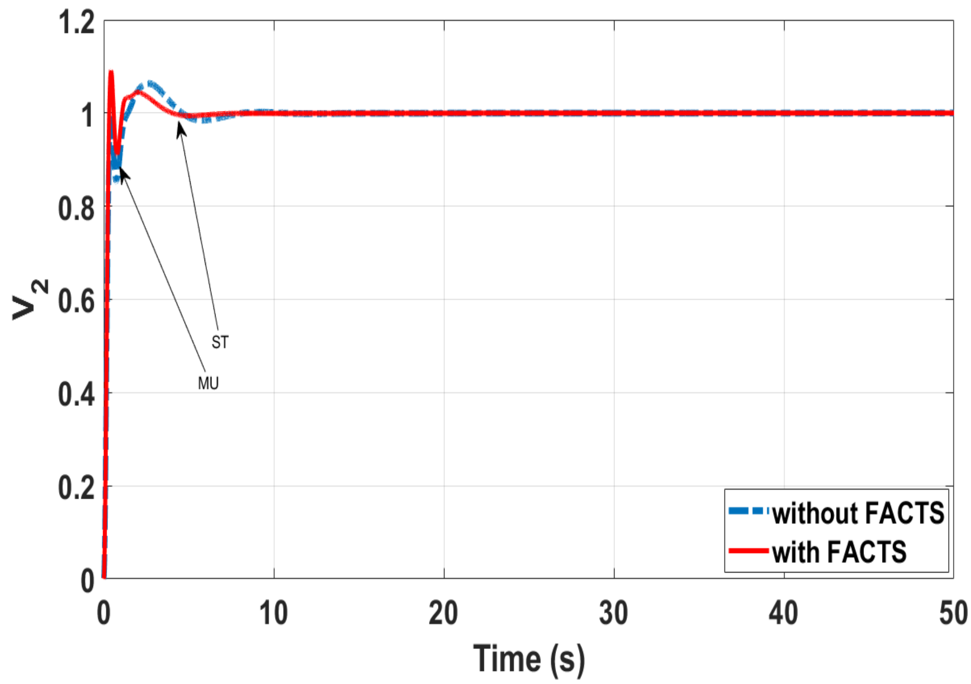

Figure 5.14 (e) System dynamic response of LFC and AVR obtained from analysis of Contract violation transaction: Area-2 voltage in p.u.

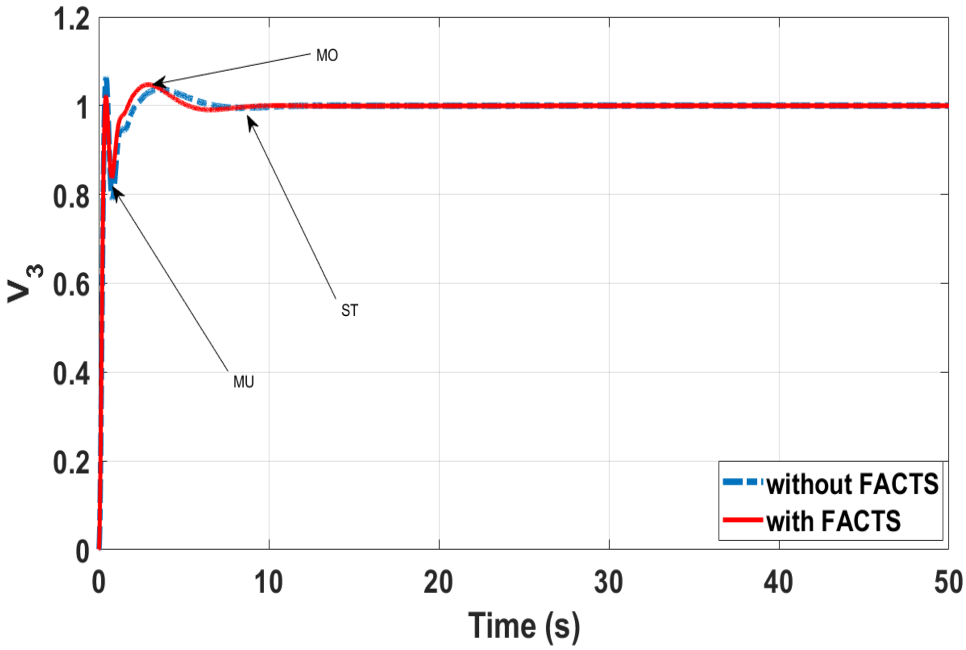

Figure 5.14 (f) System dynamic response of LFC and AVR obtained from analysis of Contract violation transaction: Area-3 voltage in p.u.

Table 5.6 Optimized controller gain values for different modes of deregulated environment for system with and without Facts Device for LFC-AVR system.

Gain	Unilateral		Bilateral		Contract violation	
	Without FD	With FD	Without FD	With FD	Without FD	With FD
K_{t1}	0.9395	0.6106	0.4519	0.3560	0.5584	0.7903
n_1	2.2516	2.8083	2.5416	2.1621	2.6111	2.2136
K_{i1}	0.4743	0.6127	0.5954	0.3997	0.6951	0.2333
K_{p1}	0.3410	0.3400	0.7218	0.4462	0.5183	0.8755
K_{i11}	0.3526	0.2766	0.5915	0.4477	0.5609	0.6708
K_{d1}	0.6631	0.7450	0.9215	0.5197	0.9907	0.3123
N_1	41.626	28.787	40.923	40.173	27.442	35.191
K_{t2}	0.5917	0.1673	0.4121	0.5168	0.3869	0.5649
n_2	2.4384	2.6716	2.3860	2.2003	2.5183	2.6845
K_{i2}	0.9168	0.9749	0.3256	0.7933	0.4727	0.6816
K_{p2}	0.6461	0.4102	0.9218	0.6012	0.3236	0.3353
K_{i22}	0.8498	0.4763	0.2890	0.6136	0.8681	0.4130
K_{d2}	0.9998	0.2906	0.9992	0.4060	0.9999	0.9930
N_2	23.346	49.717	43.809	40.304	45.574	50.5674
K_{t3}	0.5900	0.5150	0.7304	0.5770	0.5077	0.4334
n_3	2.5714	2.2556	2.8580	2.5248	2.7959	2.9962
K_{i3}	0.2006	0.3476	0.6300	0.8337	0.7265	0.3631
K_{p3}	0.6856	0.6060	0.6842	0.5746	0.1021	0.3844

Table 5.6 (Contd.) Optimized controller gain values for different modes of deregulated environment for system with and without Facts Device for LFC-AVR system.

Gain	Unilateral		Bilateral		Contract violation	
	Without FD	With FD	Without FD	With FD	Without FD	With FD
K_{i33}	0.4567	0.1814	0.3568	0.5824	0.2227	0.5904
K_{d3}	0.8864	0.3264	0.9993	0.5277	0.9999	0.7582
N_3	31.842	30.348	73.425	51.874	48.010	37.812
K_{t4}	0.6240	0.3765	0.3459	0.3657	0.7858	0.4564
n_4	2.2496	2.4029	2.9129	2.3756	2.6677	2.5988
K_{i4}	0.5480	0.4048	0.5989	0.7216	0.5514	0.7388
K_{p4}	0.9657	0.7180	0.5984	0.4642	0.2540	0.1834
K_{i44}	0.6133	0.3887	0.1188	0.5374	0.5391	0.3900
K_{d1}	0.9999	0.5499	0.9999	0.3687	0.9999	0.9076
N_4	61.181	89.461	48.707	44.036	50.736	16.916
K_{t5}	0.9780	0.9902	0.3275	0.5904	0.5365	0.9088
n_5	2.9150	2.7747	2.1348	2.8754	2.6716	2.9993
K_{i5}	0.4697	0.2937	0.4953	0.2022	0.4955	0.5948
K_{p5}	0.3643	0.8145	0.8501	0.9999	0.9264	0.9357
K_{i55}	0.2960	0.5223	0.0615	0.7126	0.3681	0.3222
K_{d5}	0.9998	0.9999	0.9998	0.9999	0.9999	0.9999
N_5	76.047	85.355	71.2349	76.713	93.860	98.933
K_{t6}	0.4024	0.8339	0.7108	0.7388	0.6798	0.7404
n_6	2.6419	2.5642	2.9029	2.9224	2.7674	2.9778
K_{i6}	0.5872	0.3258	0.5494	0.4144	0.3416	0.6593
K_{p6}	0.5122	0.6840	0.3925	0.8839	0.4766	0.9991
K_{i66}	0.1427	0.2594	0.3134	0.5441	0.5813	0.5254
K_{d6}	0.9805	0.9999	0.9999	0.9999	0.9986	0.9998
N_6	47.468	76.040	56.515	93.878	67.076	64.811
K_{t7}	0.4138	0.3622	0.8198	0.5253	0.4276	0.0716
n_7	2.3724	2.7232	2.3798	2.9511	2.3945	2.3811
K_{i7}	0.4240	0.4154	0.4212	0.7246	0.3627	0.6589
K_{p7}	0.6668	0.9992	0.4711	0.9264	0.7276	0.9999
K_{i77}	0.4017	0.5602	0.2420	0.1763	0.4652	0.1313
K_{d7}	0.9998	0.9999	0.9999	0.9997	0.9999	0.9995
N_7	57.224	86.110	72.453	50.413	48.109	32.005
K_{t8}	0.6740	0.6597	0.5285	0.5584	0.4323	0.9341
n_8	2.5422	2.8738	2.9618	2.7821	2.3424	2.9710
K_{i8}	0.4098	0.4700	0.2995	0.4140	0.3383	0.5746
K_{p8}	0.5726	0.9999	0.5629	0.9310	0.7668	0.6560
K_{i88}	0.5598	0.2356	0.6602	0.3005	0.3318	0.3655
K_{d8}	0.9999	0.9999	0.9825	0.9997	0.9999	0.9999
N_8	68.246	89.727	40.380	53.0080	89.338	72.455

Table 5.7 (a) Dynamic response of system under deregulation with and without FD for LFC-AVR system.

Responses		C1: Unilateral		C2: Bilateral		C3: Contract	
		S1	S2	S1	S2	S1	S2
Δf_1	M.U	-0.3452	-0.1360	-0.3355	-0.1417	-0.3527	-0.1455
	M.O	0.0806	0.0003	0.0641	0.0020	0.0863	0.0014
	S.T	7	4	10	5	7	5
Δf_2	M.U	-0.5060	-0.2380	-0.5003	-0.2341	-0.5142	-0.2045
	M.O	0.1187	0.0024	0.0889	0.0037	0.1288	0.0063
	S.T	8	5	9	6	8	6
Δf_3	M.U	-0.5187	-0.2397	-0.4943	-0.2326	-0.5287	-0.2177
	M.O	0.0827	0.0038	0.0758	0.0043	0.1011	0.0056
	S.T	11	6	8	6	9	7
Δf_4	M.U	-0.5035	-0.2279	-0.5162	-0.2442	-0.5038	-0.2094
	M.O	0.1241	0.0034	0.1006	0.0047	0.1247	0.0099
	S.T	9	5	9	7	7	6
ΔP_{tie1}	M.U	-0.009	-0.0026	-0.1185	-0.0812	-0.1405	-0.1177
	M.O	0.0938	0.0692	0.0082	0.0268	0.0166	0.0082
	S.T	10	9	20	16	20	20
ΔP_{tie2}	M.U	-0.2478	-0.0121	-0.2393	-0.0157	-0.2074	-0.0194
	M.O	0.0155	0.0145	0.0076	0.0001	0.0102	0.0037
	S.T	20	10	19	7	13	8
ΔP_{tie3}	M.U	-0.2540	-0.0402	-0.2380	-0.0285	-0.2280	-0.0411
	M.O	0.0001	0.0027	0.0065	0.0071	0.0018	0.0030
	S.T	16	13	18	11	12	6
ΔP_{tie4}	M.U	-0.2217	-0.0165	-0.2403	-0.0243	-0.2099	-0.0142
	M.O	0.0008	0.0037	0.0013	0.0008	0.0111	0.0087
	S.T	12	8	6	5	8	7
ΔV_1	M.O	1.046	1.057	1.018	1.057	1.029	1.069
	S.T	9	5	7	6	6	4
ΔV_2	M.O	1.056	1.017	1.063	1.049	1.063	1.087
	S.T	13	7	10	5	10	4
ΔV_3	M.O	1.053	1.0406	1.043	1.065	1.063	1.047
	S.T	9	6	7	5	8	8
ΔV_4	M.O	1.063	1.052	1.063	1.059	1.030	1.043
	S.T	11	6	11	5	7	6

Table 5.7 (b) Percentage improvement of using FD over system without FD for different cases of deregulation.

Responses		% improvement of S2 over S1		
		C1	C2	C3
Δf_1	M.U	60	57	58
	M.O	99	96	98
	S.T	42	50	28
Δf_2	M.U	52	53	60
	M.O	97	95	95
	S.T	37	33	25
Δf_3	M.U	53	52	58
	M.O	95	94	94
	S.T	45	25	22
Δf_4	M.U	54	52	58
	M.O	97	95	92
	S.T	44	22	14
ΔP_{tie1}	M.U	71	31	16
	M.O	26	67	50
	S.T	10	20	0
ΔP_{tie2}	M.U	95	93	90
	M.O	6	98	63
	S.T	50	63	38
ΔP_{tie3}	M.U	84	88	81
	M.O	-96	-9	-66
	S.T	18	38	50
ΔP_{tie4}	M.U	92	89	93
	M.O	-78	38	21
	S.T	33	16	12
ΔV_1	M.O	-1	-3	-3
	S.T	44	14	3.3
ΔV_2	M.O	3	1	-2
	S.T	46	50	60
ΔV_3	M.O	1	-2	1
	S.T	33	28	0
ΔV_4	M.O	1	0.3	1
	S.T	45	54	14

Analysis: The results highlight that the inclusion of a FACTS device in a unilateral transaction significantly improves system performance. The data clearly show reduced maximum undershoot and overshoot values, indicating better damping and enhanced stability margins. For example, overshoot values, which are noticeable without FACTS, drop almost to zero with its integration, while undershoot levels are also considerably minimized. Another key benefit is the marked reduction in settling time: without FACTS, stabilization often takes 7–20 seconds, whereas with FACTS it reduces to 4–10 seconds, ensuring much faster dynamic response. In summary, FACTS devices in unilateral transactions enhance transient stability, minimize oscillations, and accelerate settling, thereby strengthening both reliability and dynamic efficiency of the power system

The analysis of the bilateral transactions case with FACTS devices further confirms their positive impact on system dynamics. Across the results, the maximum undershoots and overshoot values are significantly reduced when FACTS is applied, indicating improved damping and enhanced stability. For example, overshoot values that are noticeable without FACTS (0.0641, 0.0889) drop to near-zero levels (0.0020, 0.0037), while undershoot values also decrease substantially.

A major advantage is observed in the settling time, where stabilization that would otherwise require 9-20 seconds without FACTS is shortened to just 5–7 seconds with the device. This demonstrates a much faster convergence and reduced oscillatory behavior, even under bilateral power exchanges. In summary, the integration of FACTS devices in bilateral transactions ensures quicker settling, minimized oscillations, and improved transient stability, thereby enhancing the reliability and dynamic performance of the deregulated power system

In contract violation cases, the comparative outcomes indicate that the maximum undershoot (M.U) and maximum overshoot (M.O) are consistently reduced when the proposed method is applied, demonstrating its robustness and ability to limit frequency deviations effectively. Furthermore, the settling time (S.T) is notably shortened in most cases, confirming faster dynamic response and quicker stabilization of the system. These improvements highlight the capability of the controller to handle uncertainties and maintain system reliability even in deregulated and stressed operating conditions. Overall, the findings validate that the adopted approach offers superior transient and steady-state performance, making it a promising solution for modern automatic generation control frameworks in interconnected power systems.

5.4.3 Eigen value analysis

The analysis is carried out to show that the proposed controller is able to provide stability to the system. The controlled environment is used to analyze the various controller types, including integral, PI, TI, PID, TID, and the suggested TI-PIDN controllers. Table 5.8 displays the Eigen values that were found. According to analysis, it can be said that the system is stable because the eigen values of the proposed controllers are negative that is, it remains on the left side of the s-plane. In comparison to the other controllers examined, the suggested controller's minimum damping ratio is likewise larger.

Table 5.8 Eigen values of different controllers for combined LFC and AVR.

Controllers	Eigen values	Minimum damping ratio
PI	0.0000, -0.1954, -0.1967, -0.1970, -0.1972, -0.1466, -0.1317, -0.1233,-0.1294, -0.1290, -0.1166, -0.1127, -0.1116, -0.1112,-0.0017, 0.0017,- 0.0000,- 0.0000, 0.0004, 0.0004, -0.0543, -0.0038, -0.0038, -0.0086, -0.0086, -0.0295, -0.0287, -0.0261, -0.0218, -0.0096, -0.0096, -0.0099, -0.0099, -0.0099, -0.0099, -0.0050, -0.0032, -0.0030, -0.0029, -0.0023, -0.0010, -0.0010, -0.0015, -0.0008,- 0.0008, -0.0010, 0.0000, 0.0000, 0.0000, 0.0000, 0.0000, 0.0000, 0.0000, -0.1250, -1.0000, 0.0033, -0.0100, -0.0100, -1.0000, -0.0333	0.0009254
TI	0.0000,-1.0000,-1.0000,-1.0000,-1.0000,-1.0000,-1.1111, -1.1111, -1.1111, -1.1111, -1.1111, -1.1111, -1.1111, -1.1111,-0.3945, -0.3909, -0.4002, -0.4005, -0.4329, -0.4329, -0.4329, -0.4329, -1.0000, -1.0000, -1.0000, -0.1123, -0.1113, -0.1140, -0.1141, -0.1233, -0.1233, -0.1233, -0.1233, -0.0320, -0.0317, -0.0325, -0.0325, -0.0351, -0.0351, -0.0351, -0.0351, -0.0199, -0.0200, -0.0199, -0.0199, -0.0142, -0.0123, -0.0128, -0.0129, -0.0129, -0.0002, -0.0002, -0.0000, -0.0000, -0.0000, -0.0000, -0.0055, -0.0103, -0.0103, -0.0102, -0.0102, -0.0102, -0.0102, -0.0102, -0.0102, -0.0095, -0.0094, -0.0093, -0.0090, -0.0003, -0.0003, -0.0038, -0.0037, -0.0037, -0.0037, -0.0005, -0.0005, -0.0026, -0.0026, -0.0030, -0.0028, -0.0028, -0.0021, -0.0028, -0.0027, -0.0005, -0.0005,-0.0005, -0.0005,-0.0005, -0.0005, -0.0009, -0.0008, -0.0013, -0.0014, -0.0014, -0.0014, -0.0008, -0.0007, -0.0003, -0.0004, -0.0004, -0.0004, -0.0004, -0.0001, -0.0001, -0.0002, -0.0002 + 0.0000i, -0.0002, -0.0002, -0.0002, -0.0001, -0.0001, -0.0001, -0.0001, -0.0001, -0.0001, -0.0001, -0.0001, -0.0001, -0.0001, -0.0000, -0.0000, -0.0000, -0.0000, -0.0000, -0.0000, -0.0000, -0.0000, -0.0000, -0.0000, -0.0000, -0.0125, -0.1000, -0.0003, -0.0010, -0.0010, -0.1000,-0.0033	0.0030
PID	0.0000, -0.1956, -0.1971, -0.1968, -0.1969, -0.1472, -0.1310, -0.1303, -0.1290, -0.1233, -0.1161, -0.1110, -0.1124, -0.1120, -0.0026, -0.0026, 0.0003, 0.0003, 0.0003, 0.0003, -0.0540, -0.0038, -0.0038, -0.0089, -0.0089, -0.0060, -0.0060, -0.0097, -0.0097, -0.0098, -0.0098, -0.0299, -0.0288, -0.0270, -0.0213, -0.0113, -0.0030, -0.0028, -0.0024, -0.0018, -0.0018, -0.0011, -0.0011, -0.0008, -0.0008, -0.0010, -0.0000, -0.0000, 0.0000, -0.0000, 0.0000, 0.0000, 0.0000 - 0.0000i, -0.1250, 0.0000, 0.0000, -1.0000, 0.0000, 0.0000, 0.0000, 0.0000, 0.0000, 0.0000, -0.0033, -0.0100, -0.0100, -1.0000, -0.0333	0.0048

Table 5.8 (Contd.) Eigen values of different controllers for combined LFC and AVR

Controllers	Eigen values	Minimum damping ratio
TID	0.0000, -0.3964, -0.4080, -0.4032, -0.4006, -1.1111, -1.1111, -1.1111, -1.1111, -0.4329, -0.4328, -0.4329, -0.4329, -1.1111, -1.1111, -1.1111, -1.0000, -1.0000, -1.0000, -1.0000, -1.0000, -1.0000, -1.0000, -1.0000, -1.111, -0.1129, -0.1162, -0.1148, -0.1141, -0.1233, -0.1233, -0.1233, -0.1233, -0.0321, -0.0331, -0.0327, -0.0325, -0.0351, -0.0351, -0.0351, -0.0351, -0.0199, -0.0199, -0.0199, -0.0199, -0.0143, -0.0123, -0.0129, -0.0128, -0.0128, -0.0003, -0.0003, 0.0000, 0.0000, 0.0000, 0.0000, -0.0055, -0.0095, -0.0093, -0.0094, -0.0093, -0.0104, -0.0104, -0.0104, -0.0104, -0.0104, -0.0104, -0.0104, -0.0104, -0.0002, -0.0002, -0.0031, -0.0039, -0.0039, -0.0039, -0.0039, -0.0002, -0.0002, -0.0002, -0.0002, -0.0003, -0.0003, -0.0003, -0.0003, -0.0028, -0.0028, -0.0026, -0.0026, -0.0027, -0.0027, -0.0022, -0.0009, -0.0014, -0.0014, -0.0013, -0.0013, -0.0008, -0.0008, -0.0007, -0.0004, -0.0004, -0.0004, -0.0004, -0.0004, -0.0002, -0.0002, -0.0001, -0.0001, -0.0002, -0.0002, -0.0002, -0.0002, -0.0002, -0.0002, -0.0001, -0.0001, -0.0001, -0.0001, -0.0001, -0.0001, -0.0001, -0.0001, -0.0001, -0.0001, -0.0000, -0.0000, -0.0125, -0.1000, -0.0003, -0.0010, -0.0010, -0.1000, -0.0033	0.0007517
TI-PIDN	-0.4177, -0.4200, -0.4211, -0.4254, -0.4245, -0.4307, -0.4126, -0.4100, -1.1111, -0.1190, -1.0000, -1.1111, -1.1111, -1.1111, -1.1111, -1.1111, -1.1111, -1.1111, -1.0000, -1.0000, -1.0000, -1.0000, -1.0000, -1.0000, -1.0000, -0.1227, -0.1212, -0.1209, -0.1196, -0.1199, -0.1168, -0.1175, -0.0980, -0.0966, -0.0938, -0.0791, -0.0571, -0.0570, -0.0540, -0.0040, -0.0040, -0.0323, -0.0349, -0.0345, -0.0344, -0.0339, -0.0341, -0.0342, -0.0335, -0.0333, -0.0258, -0.0255, -0.0255, -0.0255, -0.0124, -0.0009, -0.0009, -0.0048, -0.0048, -0.0017, -0.0017, -0.0038, -0.0038, -0.0036, -0.0036, -0.0035, -0.0035, -0.0036, -0.0036, -0.0060, -0.0050, -0.0090, -0.0099, -0.0099, -0.0094, -0.0094, -0.0094, -0.0098, -0.0096, -0.0097, -0.0095, -0.0014, -0.0014, -0.0016, -0.0016, -0.0021, -0.0022, -0.0025, -0.0025, -0.0027, -0.0025, -0.0025, -0.0026, -0.0026, -0.0026, -0.0008, -0.0008, -0.0005, -0.0005, -0.0005, -0.0005, -0.0006, -0.0006, -0.0009, -0.0008, -0.0008, -0.0007, -0.0005, -0.0006, -0.0006, -0.0006, -0.0002, -0.0002, -0.0002, -0.0002, -0.0001, -0.0002, -0.0002, -0.0002, -0.0002, -0.0002, -0.0002, -0.0002, -0.0002, -0.0002, -0.0001, -0.0001, -0.0001, -0.0001, -0.0001, -0.0001, -0.0001, -0.0001, -0.0125, -0.1000, -0.0003, -0.0010, -0.0010, -0.1000, -0.0033	0.0282

Analysis: The eigenvalue analysis provides a rigorous foundation for evaluating the stability and damping performance of different controllers in the AGC framework. The comparative results reveal that the classical PI, PID, and TID controllers yield relatively low minimum damping ratios (0.0009, 0.0048, and

0.00075, respectively), indicating limited robustness in suppressing oscillatory modes. The TI controller exhibits some improvement with a slightly higher damping ratio (0.0030), but it still remains within a marginal range. In contrast, the proposed hybrid TI-PIDN controller achieves a significantly superior minimum damping ratio of 0.0282, clearly surpassing all other schemes and demonstrating its enhanced capability to improve system damping and ensure better transient stability.

5.5 Conclusion

The study thoroughly investigates and analyses the effectiveness of combined LFC and AVR in four interconnected areas managing both traditional power sources and renewable energy sources like GTPP, STPP, TEG and AWEC in a regulated and deregulated scenarios with the presence of non-linearities like GRC, TD and BD in the later. A novel TI-PIDN controller is proposed and designed for the control of the combined LFC and AVR model whose performance is compared to other classical controllers like PI, TI, PID and TID in which analysis reveals that the proposed controller outperforms the existing controller. A recent Zebra optimization algorithm is utilized for the optimization of the gain values of the controller with ISE as an objective function. Comparisons of the objective functions are done and ISE appears to be most suitable for the study system. Different case studies within the deregulated environment are carried out with the presence of FD and without FD in which the presence of FDs help achieving the stability of the system. Sensitivity analysis along with Eigen value analysis is carried out to show the robustness of the proposed technique in maintaining system stability when disturbances occurred in the power system. The analysis reveals that the proposed TI-PIDN optimized with ZOA algorithm and ISE as an objective function with the presence of FDs can achieve in obtaining system stability in the combined LFC and AVR power system.

Chapter 6 Conclusion

6.1 Introduction

AGC is an ancillary service used in power system management and control that maintains determined frequency and tie-line power, which may vary as a result of imbalances between power generation and demands. AGC performs a crucial control role in preserving the selected nominal frequency and tie-line power exchange within interconnected areas in the event of unexpected load interruptions. Around the world, a variety of studies and methods have been developed on AGC, considering traditional energy sources like natural gas, hydroelectric, thermal, etc. in single or multi-area systems. RESs-based power plants are gaining increased attention in research and applications to generate electricity to combat rising power demand as fossil fuels become more expensive and less available. RESs are abundant in nature, and as technology advances, so does their energy conversion efficiency. The different sources-thermal, STPP, AWEC, biogas, hydro, biodiesel, wind, SPV, TPP and GTP are integrated into a multi-area system in this study, which has been thoroughly examined in both a traditional and deregulated market. This thesis presents a number of methods for demonstrating the AGC in conventional and deregulated environments in multi-source based multi-area interconnected power systems. In order to address AGC issues in both conventional and deregulated power systems, this thesis suggests a few novel control techniques. The suggested controllers are contrasted with the traditional controller found in the literature in order to assess the efficacy of the suggested control system. Various optimization methods are applied to adjust the gains of controllers. Compared to other widely used optimization techniques like FA, GWO, PSO, SMA, etc., ZOA has been found to produce superior results, a minimum cost function, and a faster rate of convergence. Therefore, to adjust the gains of controllers and other related factors, the ZOA optimization technique has been applied. The dynamic performance of multi-area multi-source systems that integrate EVs and DGs is examined in both conventional and deregulated settings. Multi-area power systems integrating renewable energy sources are examined in relation to the impact of virtual inertia control. Additionally, the impact of AVR on the LFC is examined through the incorporation of the FACTs device. Various shifting situations and system parameter variations have been taken into consideration while conducting the stability analysis of the proposed system and the sensitivity analysis of the proposed controllers.

6.2 Conclusion

The following are the novel contributions of this thesis:

1. The study thoroughly investigates and analyzes the effectiveness of AGC in managing both traditional power sources and distributed generation, particularly focusing on enhancing frequency regulation under various conditions and deregulation scenarios. The research delves into the comprehensive evaluation of Distributed Generation (DG) units in the face of unpredictable weather conditions and fluctuating load demands. To provide a realistic assessment of the AGC framework, the study also considers and examines non-linearities, such as the GDB and GRC of 3% per minute in each reheat-thermal plant. Analysis of the performance index selection revealed that, in comparison to IAE, ITSE, and ITAE, ISE is more suitable for the system under study. An innovative approach is introduced, utilizing the cascaded 2DOFTIDN-FOTI controller whose dynamic responses of the system obtained using ZOA are compared with existing controllers like I, PI, TID and TID-FOTI in which the proposed technique shows better results than the other. It also introduces ZOA to optimize the control parameters for the employed controllers in the test system. Comparison is done between the proposed and different types of algorithms like FA, GWO, PSO, SMA that are found in the literature, demonstrating its efficacy and superiority. A comprehensive performance evaluation shows its superiority under the analyzed scenario. Furthermore, the study incorporates Electric Vehicles. It also introduces ZOA to optimize the control parameters for the employed controllers in the test system. Ultimately, the study conclusively shows that the proposed AGC controller significantly improves the deviation in frequency and fluctuations in tie-line power within the test system. The research presents distinct and improved results to validate frequency response of the system. Through different deregulation scenarios, comparative analyses with alternative controllers, sensitivity assessments in response to random load changes and eigen-value analysis, robustness is verified.
2. The effectiveness of VIC in managing distributed generation and conventional power sources in a four area AGC is comprehensively examined and analysed in this chapter, with a special emphasis on improving frequency control in

deregulated scenarios and under different situations. The system is designed utilizing a virtual inertia control method, and a new TI-IDN controller is proposed for controlling the VIC, whose gain values are analysed using ZOA. A variety of case studies are conducted to demonstrate how well the VIC and suggested controller work together to keep the system stable. In order to find the optimal solution for the system, several objective function formulations are compared where ISE is selected for the research. Analysis reveals that the suggested controller outperforms the other controllers in the cases of oscillations and settling time. The damping ratio of the eigen value using proposed controller is compared with other existing controllers such as the I, TI, and TIDN controllers. By comparing two scenarios—one with and without VIC—the influence of VIC on the system is further examined. The results indicate that the system with VIC performs better in preserving system stability in the three different kinds of deregulated environments. The suggested approach for the VIC is shown to be resilient by examining the system under random load fluctuation and doing a sensitivity analysis of changes in system loading. The Eigen value analysis for the different types of controllers and system without VIC is analysed comparing with the proposed controller to show the robustness of the proposed technique. According to the analysis, the proposed VIC can greatly improve the dynamics of the whole system under deregulation by improving dipping frequency, tie- power oscillations, and settling time.

3. The study thoroughly investigates and analyses the effectiveness of combined LFC and AVR in four interconnected areas managing both traditional power sources and renewable energy sources like GTP, STP, TPP and AWEC in a regulated and deregulated scenarios with the presence of non-linearities like GRC, TD and BD in the later. A novel TI-PIDN controller is proposed and designed for the control of the combined LFC and AVR model whose performance is compared to other classical controllers like PI, TI, PID and TID in which analysis reveals that the proposed controller outperforms the existing controller. A recent Zebra optimization algorithm is utilized for the optimization of the gain values of the controller with ISE as an objective function. Comparisons of the objective functions are done and ISE appears to be most suitable for the study system. Different case studies within the deregulated environment are carried out with the presence of FD and without FD in which the presence of FDs help achieving the stability of the system. Sensitivity analysis along with eigen value analysis is carried out to show the robustness of the proposed technique in maintaining system stability when disturbances occurred in the power system. The analysis reveals that the proposed TI-PIDN

optimized with ZOA algorithm and ISE as an objective function with the presence of FDs can achieve in obtaining system stability in the combined LFC and AVR power system.

6.3 Scope for the Future Work

In the presence of diverse renewable energy sources, the current study suggests several effective controller designs for the AGC of power systems connected in both regulated and unregulated markets. The controllers used in this study have shown extremely encouraging results. However, more study is needed in a few areas to produce improved AGC controller designs for different types of power system topologies.

The following points out the scope for further study:

1. Only conventional/deregulated interconnected power networks in three and four area are currently included in this analysis. This effort could be expanded to five or more areas.
2. Although ZOA is used in this study to optimize the gain values of the controllers, other intelligent optimization strategies may yield better outcomes.
3. In addition to new tuning methods, future research on restructured and conventional power systems may use other controller types such as neural, neural fuzzy, fuzzy tilt integral derivative, deep learning, machine learning, etc.
4. In order to investigate the efficacy of the suggested control strategies, renewable resources such as TPP, AWEC, STPP, GTP, BDP, BGP, WTP, and SPV are taken into account in a linked power system. Therefore, by incorporating additional RESs, this study can be further expanded to large traditional and deregulated multi-area electricity systems.
5. The study can be further extended by including cyber-attacks that happen in a power system for more realistic study.

Appendices

Appendix-I (Chapter-3)

System	Values
Power system	f=60 Hz, Initial loading=50%, K_p=120 Hz/p.u. MW, T_p=20s, H_k=5s, D_k=0.00833p.u. MW/Hz, β_k=0.425 p.u MW/Hz, R_k=2.4 Hz/p.u MW, T_{kl}=0.086s.
Thermal unit	T_g=0.08s, T_t=0.3s, T_r=10s, K_r=0.5, N_{g1}=0.8, N_{g2}=-0.2/π
SPV unit	T_{SPV}=1.8s, K_{SPV}=1
GTPP unit	T_{gt}=0.1s, T_{sg}=0.1s
HPP unit	T_r=5, T_{rh}=28.75s, T_w=1, T_h=0.2s
WTG unit	K_h=1.25, T_a=0.6s,K_p=1.4, T_h=0.041s, K_{bl}=0.8
BGPP unit	X_c=0.6s, Y_c=1, b_B=0.05, T_{CR}=1, T_{BG}=0.23s, T_{BT}=0.2s
BDPP unit	K_{VA}=1, T_{VA}=0.05s, K_{BE}=1, T_{BE}=0.05s
EV unit	K_{EV}=1, N_{EV1}=2000, N_{EV2}=4000, N_{EV3}=2000, charging and discharging= ±30KW, Δf_{ul} and Δf_{ll}=±10mHz

Appendix-II (Chapter-4)

System	Values
Power system	f=60 Hz, Initial loading=50%, K_p=120 Hz/p.u. MW, T_p=20s, H_k=5s, D_k=0.00833p.u. MW/Hz, β_k=0.425 p.u MW/Hz, R_k=2.4 Hz/p.u MW, T_{kl}=0.086s.
Thermal unit	T_g=0.08s, T_t=0.3s, T_r=10s, K_r=0.5
SPV unit	T_{SPV}=1.8s, K_{SPV}=1
GTPP unit	T_{gt}=0.1s, T_{sg}=0.1s
WTG unit	K_{wtg}=1, T_{wtg}=0.5s
BGPP unit	X_c=0.6s, Y_c=1, b_B=0.05, T_{CR}=1, T_{BG}=0.23s, T_{BT}=0.2s
BES parameter	K_{bes}=-0.003, T_{bes}=0.1s,
FES parameter	K_{fes}=-0.01, T_{fes}=0.1s,
UC parameter	K_{uc}=-0.7, T_{uc}=0.9s,

Appendix-III (Chapter-5)

System	Values
Power system	T_{kl}= 0.086s, H_k=5s, Initial loading=50%, β_k=0.425 p.u MW/Hz, K_p=120 Hz/p.u. MW, T_p=20s, D_k=0.00833p.u. MW/Hz, R_k=2.4 Hz/p.u MW, f=60 Hz, voltage in p.u=1.
Thermal unit	T_g=0.08s, T_t=0.3s, T_r=10s, K_r=0.5
GTPP unit	T_{gt}=0.1s, T_{sg}=0.1s
TEG unit	K_{TEG}= 1, T_{TEG}= 0.08s
STPP unit	K_{sf}=1.8, T_{sf}=1.8s, T_{stg}=1s, T_{st}=3s
AWEC unit	K_{aw}=1, T_{aw}= 0.3s, $K_c = K_i$=1, $T_c = T_i$=0.01s
AVR unit	P_s=1.5, T_{am}=0.1s, T_{ex}=0.4s, K_{gf}=0.8, T_{gf}=0.4s, K_{se}=1, T_{se}=0.05s, K_1=0.2, K_2=-0.01, K_3=0.5, K_4=1.4
IPFC parameter	T_{IPFC}= 0.01s

References

Abazari, A., Monsef, H., & Wu, B. (2019). Load frequency control by de-loaded wind farm using the optimal fuzzy-based PID droop controller. *IET Renewable Power Generation*, 13(1), 180–190.

Abd-Elazim, S. M., & Ali, E. S. (2018). Load frequency controller design of a two-area system composing of PV grid and thermal generator via firefly algorithm. *Neural Computing and Applications*, 30(2), 607–616.

Abdolrasol, M. G. (2021). Optimal PI controller based PSO optimization for PV inverter using SPWM techniques. *Energy Reports*, 8, 1003–1011

Abumeteir, H. A., & Vural, A. M. (2022). Design and optimization of fractional order PID controller to enhance energy storage system contribution for damping low-frequency oscillation in power systems integrated with high penetration of renewable sources. *Sustainability*, 14(9), 5095.

Acharyulu, B. V. S., Mohanty, B., & Hota, P. K. (2020). Analysis of moth flame optimization optimized cascade proportional-integral-proportional-derivative controller with filter for automatic generation control system incorporating solar thermal power plant. *Optimal Control Applications and Methods*, 41(3), 866–881.

Alam, M. S., Al-Ismail, F. S., Salem, A., & Abido, M. A. (2020). High-level penetration of renewable energy sources into grid utility: Challenges and solutions. *IEEE Access*, 8, 190277–190299.

Aldeen, M., & Marsh, J. (1991). Decentralised proportional-plus-integral design method for interconnected power systems. *IEE Proceedings C Generation Transmission and Distribution*, 138(4), 263.

Alharbi, M., Ragab, M., AboRas, K. M., Kotb, H., Dashtdar, M., Shouran, M., & Elgamli, E. (2023). Innovative AVR-LFC design for a multi-area power system using hybrid fractional-order PI and PIDD2 controllers based on dandelion optimizer. *Mathematics*, 11, 1–45.

Alhelou, H. H., Hamedani-Golshan, M., Zamani, R., Heydarian-Forushani, E., & Siano, P. (2018). Challenges and opportunities of load frequency control in conventional, modern and future smart power systems: A comprehensive review. *Energies*, 11(10), 2497.

Ali, H., Magdy, G., Elsamaly, A., Jurado, F., & Bevrani, H. (2019). A new frequency control strategy in an islanded microgrid using virtual inertia control-based coefficient diagram method. *IEEE Access*, 7, 16979–16990.

Ali, T., Malik, S. A., Daraz, A., Adeel, M., Aslam, S., & Herodotou, H. (2023). Load frequency control and automatic voltage regulation in four-area interconnected power systems using a gradient-based optimizer. *Energies*, 16(5), 1–27.

Ali, T., Malik, S. A., Daraz, A., Adeel, M., Aslam, S., & Herodotou, H. (2024). Terminal voltage and load frequency control in a real four-area multi-source interconnected power system with nonlinearities via OOBO algorithm. *IEEE Access*, 12, 123782–123803.

Ali, T., Malik, S. A., Daraz, A., Aslam, S., & Alkhalifah, T. (2022). Dandelion optimizer-based combined automatic voltage regulation and load frequency control in a multi-area, multi-source interconnected power system with nonlinearities. *Energies*, 15(22), 1–34.

Ali, T., Malik, S. A., Hameed, I. A., Daraz, A., Mujlid, H., & Azar, A. T. (2022). Load frequency control and automatic voltage regulation in a multi-area interconnected power system using nature-inspired computation-based control methodology. *Sustainability*, 14(19), 1–30.

Altbawi, S. M. A., Mokhtar, A. S. B., Jumani, T. A., Khan, I., Hamadneh, N. N., & Khan, A. (2024). Optimal design of fractional order PID controller based automatic voltage regulator system using gradient-based optimization algorithm. Journal of King Saud University - *Engineering Sciences*, 36(1), 32–44.

Anusha, P., Patra, S., Roy, A., & Saha, D. (2021). Combined frequency and voltage control of a deregulated hydro-thermal power system employing FA based industrial controller. *In Proceedings of the International Conference on Computing Performance Evaluation (ComPE)*, 848–853.

Arya, Y. (2019a). A new optimized fuzzy FOPI-FOPD controller for automatic generation control of electric power systems. *Journal of the Franklin Institute*, 356(11), 5611–5629.

Arya, Y. (2019b). Effect of energy storage systems on automatic generation control of interconnected traditional and restructured energy systems including renewables. *International Journal of Energy Research*, 43(16), 6475–6493.

Arya, Y. (2020a). A novel CFFOPI-FOPID controller for AGC performance enhancement of single and multi-area electric power systems. *ISA Transactions*, 100, 126–135.

Arya, Y. (2020b). Effect of electric vehicles on load frequency control in interconnected thermal and hydrothermal systems utilizing CF-FOIDF controller. *IET Generation, Transmission & Distribution*, 14(14), 2666–2675.

Arya, Y. (2023). ICA assisted FTIλDN controller for AGC performance enrichment of interconnected reheat thermal power systems. *Journal of Ambient Intelligence and Humanized Computing*, 14(3), 1919–1935.

Arya, Y., & Kumar, N. (2015). AGC of a multi-area multi-source hydrothermal power system interconnected via AC/DC parallel links under deregulated environment. *International Journal of Electrical Power & Energy Sys*tems, 75, 127–138.

Arya, Y., & Kumar, N. (2016). Design and analysis of BFOA-optimized fuzzy PI/PID controller for AGC of multi-area traditional/restructured electrical power systems. *Soft Computing*, 21(21), 6435–6452.

Arya, Y., & Kumar, N. (2017). BFOA-scaled fractional-order fuzzy PID controller applied to AGC of multi-area multi-source electric power generating systems. *Swarm and Evolutionary Computation*, 32, 1–16.

Arya, Y., Dahiya, P., Çelik, E., Sharma, G., Gözde, H., & Nasiruddin, I. (2020). AGC performance amelioration in multi-area interconnected thermal and thermal-hydro-gas power systems using a novel controller. *Engineering Science and Technology, an International Journal*, 24(2), 384–396.

Arya, Y., Kumar, N., Dahiya, P., Sharma, G., Çelik, E., Dhundhara, S., & Sharma, M. (2021). Cascade-IλDμN controller design for AGC of thermal and hydro-thermal power systems integrated with renewable energy sources. *IET Renewable Power Generation*, 15(3), 504–520.

Audomsi, S., & Sa-ngiamvibool, W. (2023). Development and design of an optimal fuzzy logic 2DOF-PID controller for a two-area power system using bee algorithm. Preprints, Article 2025010161.

Babaei, M., & Hadian, M. (2022). Learning-based fractional order PID controller for load frequency control of distributed energy resources including PV and wind turbine generator. *Distributed Generation & Alternative Energy Journal*, 37(6), 1755–1772.

Babaei, M., Abazari, A., & Muyeen, S. M. (2020). Coordination between demand response programming and learning-based FOPID controller for alleviation of frequency excursion of hybrid microgrid. *Energies*, 13(2), Article 442.

Babu, N. R., & Saikia, L. C. (2019). AGC of a multiarea system incorporating accurate HVDC and precise wind turbine systems. *International Transactions on Electrical Energy Systems*, 30(4), Article e12277.

Babu, N. R., & Saikia, L. C. (2021). Load frequency control of a multi-area system incorporating realistic high-voltage direct current and dish-Stirling solar thermal system models under deregulated scenario. *IET Renewable Power Generation*, 15(5), 1116–1132.

Barakat, M. (2022). Optimal design of fuzzy-PID controller for automatic generation control of multi-source interconnected power system. *Neural Computing and Applications*, 34(21), 18859–18880.

Babu, N. R., Bhagat, S. K., Chiranjeevi, T., Pushkarna, M., Saha, A., Kotb, H., AboRas, K. M., Alsaif, F., Alsulamy, S., Ghadi, Y. Y., & Hermann, D. T. (2023). Frequency control of a realistic dish stirling solar thermal system and accurate HVDC models using a cascaded FOPI-IDDN-based crow search algorithm. *International Journal of Energy Research*, 2023, Article 9976375.

Barik, A. K., & Das, D. C. (2018). Expeditious frequency control of solar photovoltaic/biogas/biodiesel generator-based isolated renewable microgrid using grasshopper optimisation algorithm. *IET Renewable Power Generation*, 12(14), 1659–1669.

Barisal, A. K., & Mishra, S. (2018). Improved PSO based automatic generation control of multi-source nonlinear power systems interconnected by AC/DC links. *Cogent Engineering*, 5(1), Article 1422228.

Behera, S. P., Biswal, A., Swain, B., & Samantray, S. S. (2018). Hybrid power systems frequency regulation using TID based robust controller design and differential evolution (DE) algorithm. *In 2018 Technologies for Smart-City Energy Security and Power (ICSESP)*, 1–6.

Bevrani, H., Golpîra, H., Messina, A. R., Hatziargyriou, N., & Ise, T. (2010). Renewable energy sources and frequency regulation: Survey and new perspectives. *IET Renewable Power Generation*, 4(5), 438–457.

Bevrani, H., Golpîra, H., Messina, A. R., Hatziargyriou, N., & Milano, F. (2021). Power system frequency control: An updated review of current solutions and new challenges. *Electric Power Systems Research*, 194, Article 107114.

Bevrani, H., Ise, T., & Miura, Y. (2014). Virtual synchronous generators: A survey and new perspectives. *International Journal of Electrical Power & Energy Systems*, 54, 244–254.

Bevrani, H., Ghosh, A., & Ledwich, G. (2010). Renewable energy sources and frequency regulation: Survey and new perspective. *IET Renewable Power Generation*, 4(5), 438–457.

Bhagat, S. K., Saikia, L. C., Babu, N. R., & Saha, D. (2021). Impact of PLL and virtual inertia on deregulated AGC system integrated with parallel AC/HVDC. *IETE Journal of Research*, 69(4), 1–14.

Bhatt, P., Roy, R., & Ghoshal, S. (2009). Optimized multi area AGC simulation in restructured power systems. *International Journal of Electrical Power & Energy Systems*, 32(4), 311–322.

Brinda, M. D., Suresh, A., & Rashmi, M. R. (2018). A literature survey on LFC in a deregulated electricity environment. *World Review of Science, Technology and Sustainable Development*, 14(1), 1–10.

Buzas, J. and Kicsiny, R. (2014). Transfer functions of solar collectors for dynamical analysis and control design. *Renewable Energy*, 68, 146-155.

Celik, E. (2018). Incorporation of stochastic fractal search algorithm into efficient design of PID controller for an automatic voltage regulator system. *Neural Computing and Applications*, 30(6), 1991–2002.

Chan, W., & Hsu, Y. (1981). Automatic generation control of interconnected power systems using variable-structure controllers. *IEE Proceedings C Generation Transmission and Distribution*, 128(5), 269.

Chandrakala, K. V., & Balamurugan, S. (2016). Simulated annealing based optimal frequency and terminal voltage control of multi-source multi area system. *International Journal of Electrical Power & Energy Systems*, 78, 823–829.

Chauhan, A., Upadhyay, S., Khan, M. T., Hussain, S. M. S., & Ustun, T. S. (2021). Performance investigation of a solar photovoltaic/diesel generator-based hybrid system with cycle charging strategy using BBO algorithm. *Sustainability*, 13(13), 7202. https://doi.org/10.3390/su13137202

Chidambaram, I., & Paramasivam, B. (2019). Optimized load-frequency control in a deregulated power system using predictive controllers. *IET Generation, Transmission & Distribution*, 13(13), 2474–2487.

Chintu, J. M. R., & Sahu, R. K. (2020). Differential evolution optimized fuzzy PID controller for automatic generation control of interconnected power system. *In Advances in Intelligent Systems and Computing*,123–132

Christie, R. D., & Bose, A. (1996). Load frequency control issues in power system operations after deregulation. *IEEE Transactions on Power Systems*, 11(3), 1191–1200.

Cohn, N. (1956). Some aspects of tie-line bias control on interconnected power systems [includes discussion]. Transactions of the American Institute of Electrical Engineers. Part III: *Power Apparatus and Systems*, 75(3), 1415–1436.

Concordia, C., & Kirchmayer, L. K. (1954). Tie-line power and frequency control of electric power systems - Part II [includes discussion]. *Transactions of the American Institute of Electrical Engineers*. Part III: *Power Apparatus and Systems*, 73(2), 133–146.

Daraz, A., Malik, S. A., Azar, A. T., Aslam, S., Alkhalifah, T., & Alturise, F. (2022). Optimized fractional order integral-tilt derivative controller for frequency regulation of interconnected diverse renewable energy resources. *IEEE Access*, 10, 43514–43527.

Daraz, A., Malik, S. A., Waseem, A., Azar, A. T., Haq, I. U., Ullah, Z., & Aslam, S. (2021). Automatic generation control of multi-source interconnected power system using FOI-TD controller. *Energies*, 14(18), 1–17.

Das, D., Kothari, M.L., Kothari, D.P. and Nanda, P.J. (1991). Variable structure control strategy to automatic generation control of interconnected reheat thermal system. *IET Proceedings D- Control Theory and Applications*, 138(6), 579-585

Das, D., Aditya, S. K., & Kothari, D. P. (1999). Dynamics of diesel and wind turbine generators on an isolated power system. *International Journal of Electrical Power & Energy Systems*, 21(3), 183–189.

Das, D. C., Roy, A. K., & Sinha, N. (2012). GA based frequency controller for solar-thermal-wind hybrid energy generation/energy storage system. *International Journal of Electrical Power & Energy Systems*, 43(1), 262–279.

Das S., Saikia L.C. & Datta S. (2021) Maiden application of TIDN-(1+PI) cascade controller in LFC of a multi-area hydro-thermal system incorporating EV–Archimedes wave energy-geothermal-wind generations under deregulated scenario. *International transactions on electrical energy systems*, 31, 1-23.

Das, S., Datta, S., & Saikia, L. C. (2022). Effect of PI-TI based virtual inertia controller with virtual damping on a renewable energy-based multi-area power system under deregulation. *Arabian Journal for Science and Engineering*, 48, 6431–6452.

Das, S., Datta, S., & Saikia, L. C. (2023). A novel mine blasting algorithm optimized DFOPI-TIDN controller for VIC of multi-area power systems. *Iranian Journal of Science and Technology, Transactions of Electrical Engineering*, 47, 1–22.

Das, S., Nayak, P. C., Prusty, R. C., & Panda, S. (2024). Design of fractional order multistage controller for frequency control improvement of a multi-microgrid system using equilibrium optimizer. *Multiscale and Multidisciplinary Modeling, Experiments and Design*, 7, 1357–1373.

Dash, P., Saikia, L. C., & Sinha, N. (2014). Comparison of performances of several FACTS devices using Cuckoo search algorithm optimized 2DOF controllers in multi-area AGC. *International Journal of Electrical Power & Energy Systems*, 65, 316–324.

Datta, M., et al. (2012). Frequency control improvement in a PV-diesel hybrid power system with a virtual inertia controller. *In 2012 7th IEEE Conference on Industrial Electronics and Applications (ICIEA)*, 1–6.

Datta, M., & Senjyu, T. (2013). Fuzzy control of distributed PV inverters/energy storage systems/electric vehicles for frequency regulation in a large power system. *IEEE Transactions on Smart Grid*, 4(1), 479–488.

Debbarma, S., Dutta, A., & Saikia, L. C. (2017). Utilizing electric vehicles for LFC in restructured power systems using fractional order controller. *IEEE Transactions on Smart Grid*, 8(6), 2554–2564.

Debbarma, S., Saikia, L. C., & Sinha, N. (2012). AGC of a multi-area thermal system under deregulated environment using a non-integer controller. *Electric Power Systems Research*, 95, 175–183.

Debnath, M. K., Jena, T., & Mallick, R. K. (2017a). Application of fuzzy-PIDF controller for automatic generation control using termite correlation PSO algorithm. *International Review of Automatic Control*, 10(5), 380–387.

Debnath, M. K., Jena, T., & Mallick, R. K. (2017b). Optimal design of PD-Fuzzy-PID cascaded controller for automatic generation control. *Cogent Engineering*, 4(1), Article 1416535.

Dekaraja, B., & Saikia, L. C. (2022). Impact of electric vehicles and realistic dish-Stirling solar thermal system on combined voltage and frequency regulation of multiarea hydrothermal system. *Energy Storage*, 4(6), e370.

Dekaraja, B., Saikia, L. C., & Ramoji, S. K. (2022). Combined ALFC-AVR control of diverse energy source-based interconnected power system using cascade controller. *In Proceedings of the International Conference on Intelligent Controller Computing for Smart Power (ICICCSP)*,1–6.

Dekaraja, B., Saikia, L. C., Ramoji, S. K., Behera, M. K., & Bhagat, S. K. (2021). Performance analysis of diverse energy storage on combined ALFC and AVR control of multiarea multiunit system with AC/HVDC interconnection. *IFAC-PapersOnLine*, 55(1), 479–485.

Dey, P. P. (2020). Active power management of virtual power plant under penetration of central receiver solar thermal-wind using butterfly optimization technique. *Sustainability*, 12(17), 6979.

Dhawane, V., & Bichkar, R. (2020). Automatic generation control of a thermal power plant with reheat turbine using PSO optimized integral controller. *International Journal of Electrical Engineering and Technology*, 11(4), 318-330.

Dutta, A., & Debbarma, S. (2018). Frequency regulation in deregulated market using vehicle-to-grid services in residential distribution network. *IEEE Systems Journal*, 12(3), 2812–2820

El-Bahay, M. H., El-Morshedy, M., & El-Bahy, A. (2023). Effective participation of wind turbines in frequency control of a renewable-rich two-area power system. *Protection and Control of Modern Power Systems*, 8, Article 29.

El-Shimy, M. E., AbdelMeguid, H., & Manqarah, B. (2023). A new intelligent fractional-order load frequency control for interconnected modern power systems with virtual inertia control. *Fractal and Fractional*, 7(1), Article 62.

Elgerd, O. I., & Fosha, C. E. (1970). Optimum megawatt-frequency control of multiarea electric energy systems. *IEEE Transactions on Power Apparatus and Systems*, PAS-89(4), 556–563.

Elmenfy, T. H. (2020). Gain schedule PI fuzzy load frequency control for two-area electric power system. *International Journal of Energy Optimization and Engineering*, 9(3), 39–50.

Elsaied, M. M., Hameed, W. H. A., & Hasanien, H. M. (2022). Frequency stabilization of a hybrid three-area power system equipped with energy storage units and renewable energy sources. *IET Renewable Power Generation*, 16(15), 3267–3286.

Esmail, M., Tzoneva, R., & Krishnamurthy, S. (2017). Review of automatic generation control in deregulated environment. *IFAC-PapersOnLine*, 50(2), 88–93.

Falahati, S., Taher, S. A., & Shahidehpour, M. (2016). Grid frequency control with electric vehicles by using of an optimized fuzzy controller. *Applied Energy*, 178, 918–928.

Fan, H., Jiang, L., Zhang, C., & Mao, C. (2016). Frequency regulation of multi-area power systems with plug-in electric vehicles considering communication delays. *IET Generation, Transmission & Distribution*, 10(14), 3481–3491.

Fathy, A., Yousri, D., Rezk, H., Thanikanti, S. B., & Hasanien, H. M. (2022). A robust fractional-order PID controller-based load frequency control using modified hunger games search optimizer. *Energies*, 15(1), 361.

Farooq, Z., Rahman, A., & Hussain, S. M. S. (2022). Power generation control of renewable energy-based hybrid deregulated power system. *Energies*, 15(1), 1–21.

Fayek, H. H., & Rusu, E. (2022). Novel combined load frequency control and automatic voltage regulation of 100% sustainable energy interconnected microgrids. *Sustainability*, 14(15), 1–16.

Feng, J., et al. (2011). Applying flywheel energy storage system to integrated power system for power quality and stability enhancement. *In 2011 International Conference on Electrical Machines and Systems*, 1–5).

Franklin, R. V. R., & Abdul Kareem, P. F. (2023). Frequency regulation for state-space model-based renewables integrated to multi-area microgrid systems. *Sustainability*, 15(3), 2552.

Franklin, R. V. R., & Kareem, P. F. A. (2022). Frequency regulation in conventional, deregulated and microgrid systems: A review on designs, strategies, techniques and related aspects. *IETE Journal of Research*, 69(10), 7476–7494.

Gbadega, P. A., & Sun, Y. (2023). Multi-area automatic generation control of a renewable energy-based hybrid power systems using JAYA optimized model predictive control. *Energy Reports*, 9, 74–84.

Ghasemi-Marzbali, A. (2020). Multi-area multi-source automatic generation control in deregulated power system. *Energy*, 201, Article 117667.

Gorripotu, T. S., Sahu, R. K., & Panda, S. (2015). AGC of a multi-area power system under deregulated environment using redox flow batteries and interline power flow controller. *Engineering Science and Technology, an International Journal*, 18(4), 555–578.

Guha, D., Roy, P. K., & Banerjee, S. (2016). Load frequency control of interconnected power system using grey wolf optimization. *Swarm and Evolutionary Computation*, 27, 97–115.

Gulzar, M. M., Iqbal, M., Shahzad, S., Muqeet, H. A., Shahzad, M., & Hussain, M. M. (2022). Load frequency control (LFC) strategies in renewable energy-based hybrid power systems: A review. *Energies*, 15(10), 3488.

Gulzar, M. M., Iqbal, M., Shahzad, S., Muqeet, H. A., Shahzad, M., & Hussain, M. M. (2023). Designing robust frequency stabilization using optimized MPC-(1+PIDN) controller for high-order interconnected renewable energy-based power systems. *Protection and Control of Modern Power Systems*, 8, Article 286.

Gupta, M., Srivastava, S., & Gupta, J. R. P. (2016). A novel controller for model with combined LFC and AVR loops of single area power system. *Journal of the Institution of Engineers* (India): Series B, 97(1), 21–29.

Gupta, N. K., Kar, M. K., & Singh, A. K. (2022). Design of a 2-DOF-PID controller using an improved sine-cosine algorithm for load frequency control of a three-area system with nonlinearities. *Protection and Control of Modern Power Systems*, 7(3), 1–18.

Habib, S., Abbas, G., Jumani, T. A., Bhutto, A. A., Mirsaeidi, S., & Ahmed, E. M. (2022). Improved whale optimization algorithm for transient response, robustness, and stability enhancement of an automatic voltage regulator system. *Energies*, 15(14), 1–18.

Hakimuddin, N., Nasiruddin, I., Bhatti, T. S., & Arya, Y. (2020). Optimal automatic generation control with hydro, thermal, gas, and wind power plants in 2-area interconnected power system. *Electric Power Components and Systems*, 48(6–7), 558–571.

Hasanien, H. M. (2017). Whale optimisation algorithm for automatic generation control of interconnected modern power systems including renewable energy sources. *IET Generation, Transmission & Distribution*, 12(3), 607–614.

Hasen, S. A., Aydın, Ö., Ayasun, S., & Sönmez, Ş. (2024). Impact of virtual inertia and damping control on stability delay margins of load frequency control systems with renewable energy sources. *Electrical Engineering*, 106(2), 323–341.

Hota, P., & Mohanty, B. (2015). Automatic generation control of multi-source power generation under deregulated environment. *International Journal of Electrical Power & Energy Systems*, 75, 205–214.

Hussain, I., et al. (2020). Performance assessment of an islanded hybrid power system with different storage combinations using an FPA-tuned two-degree-of-freedom (2DOF) controller. *Energies*, 13(22), 5610.

Ibraheem, Kumar, P., & Kothari, D. P. (2005). Recent philosophies of automatic generation control strategies in power systems. *IEEE Transactions on Power Systems*, 20(1), 346–357.

Izci, D., Ekinci, S., Zeynelgil, H. L., & Hedley, J. (2021). Fractional order PID design based on novel improved slime mould algorithm. *Electric Power Components and Systems*, *49*(9–10), 901–918

Jagatheesan, K., Anand, B., & Dey, N. (2016). Evolutionary algorithm based LFC of single area thermal power system with different steam configurations and non-linearity. *Information Systems Design and Intelligent Applications*, *New Delhi Springer*, 435, 185-194.

Jagatheesan, K., Anand, B., Dey, N., & Amira, S. A. (2016). Ant colony optimization algorithm based PID controller for LFC of single area thermal system. *World Journal of Modelling and Simulation*, 12(1), 3–14.

Jagatheesan, K., Anand, B., Samanta, S., Dey, N., Ashour, A. S., & Balas, V. E. (2019). Design of a proportional-integral-derivative controller for an automatic generation control of multi-area power thermal systems using firefly algorithm. *IEEE/CAA Journal of Automatica Sinica*, 6(2), 503–515.

Jain, S., & Hote, Y. V. (2018). Design of fractional order PID for load frequency control via IMC and Big Bang-Big Crunch. *IFAC-PapersOnLine*, 51(6), 65–71.

Jampeethong, P., & Khomfoi, S. (2020). Coordinated control of electric vehicles and renewable energy sources for frequency regulation in microgrids. *IEEE Access*, 8, 141967–141976.

Jena, N. K., Sahoo, S., Sahu, B. K., et al. (2022). Design of fractional order cascaded controller for AGC of a deregulated power system. *Journal of Control, Automation and Electrical Systems*, 33, 1389–1405.

Kalyan, C. N. S. (2021). UPFC and SMES based coordinated control strategy for simultaneous frequency and voltage stability of an interconnected power system. *In Proceedings of the 1st International Conference on Power Electronics and Energy (ICPEE)*, 1–6.

Kalyan, C. N. S., & Rao, G. S. (2020). Frequency and voltage stabilization in combined load frequency control and automatic voltage regulation of multiarea system with hybrid generation utilities by AC/DC links. *International Journal of Sustainable Energy*, 39(10), 1009–1029.

Kalyan, C. N. S., & Rao, G. S. (2021). Impact of communication time delays on combined LFC and AVR of a multi-area hybrid system with IPFC-RFBs coordinated control strategy. *Protection and Control of Modern Power Systems*, 6, 1–20.

Kalyan, C. N. S., & Rao, G. S. (2022). Combined frequency and voltage stabilization of multi-area multisource system by DE-AEFA optimized PID controller with coordinated performance of IPFC and RFBs. *International Journal of Ambient Energy*, 43(1), 3815–3831.

Kalyan, C. N. S., Goud, B. S., Reddy, C. R., Bajaj, M., Sharma, N. K., Alhelou, H. H., Siano, P., & Kamel, S. (2022). Comparative performance assessment of different energy storage devices in combined LFC and AVR analysis of multi-area power system. *Energies*, 15(2), 1–22.

Kalyan, N., Sai, G., & Sambasiva Rao, P. (2020). Frequency and voltage stabilisation in combined load frequency control and automatic voltage regulation of a multiarea system with hybrid generation utilities by AC/DC links. *International Journal of Sustainable Energy*, 39(10), 1009–1029.

Karanam, A. N., & Shaw, B. (2022). A new two-degree-of-freedom combined PID controller for automatic generation control of a wind-integrated interconnected power system. *Protection and Control of Modern Power Systems*, 7, 20.

Kassem, A. M. (2010). Neural predictive controller of a two-area load frequency control for interconnected power system. *Ain Shams Engineering Journal*, 1(1), 49–58.

Kerdphol, T., Rahman, F., & Mitani, Y. (2018). Virtual inertia control application to enhance frequency stability of interconnected power systems with high renewable energy penetration. *Energies*, 11(4), Article 981.

Kerdphol, T., Rahman, F. S., Matani, Y., Watanabe, M., & Kufeoglu, S. (2018). Robust virtual inertia control of an islanded microgrid considering high penetration of renewable energy. *IEEE Access*, 6, 625–636.

Kerdphol, T., et al. (2019). Enhanced virtual inertia control based on derivative technique to emulate simultaneous inertia and damping properties for microgrid frequency regulation. *IEEE Access*, 7, 14422–14433.

Khamari, D., Sahu, R. K., Gorripotu, T. S., & Panda, S. (2019). Automatic generation control of power system in deregulated environment using hybrid TLBO and pattern search technique. *Ain Shams Engineering Journal*, 11(3), 553–573.

Khan, I. A., Mokhlis, H., Mansor, N. N., Illias, H. A., Awalin, L. J., & Wang, L. (2023). New trends and future directions in load frequency control and flexible power system: A comprehensive review. *Alexandria Engineering Journal*, 71, 263–308.

Khan, M., Sun, H., Xiang, Y., & Shi, D. (2021). Electric vehicles participation in load frequency control based on mixed H2/H∞. *International Journal of Electrical Power & Energy Systems*, 125, 106446

Khodabakhshian, A., & Hooshmand, R. (2009). A new PID controller design for automatic generation control of hydro power systems. *International Journal of Electrical Power & Energy Systems*, 32(5), 375–382.

Khokhar, B., Dahiya, S., & Parmar, K. P. S. (2020). A robust cascade controller for frequency regulation of a standalone microgrid incorporating electric vehicles. *Electric Power Components and Systems*, 48(6–7), 711–726.

Khooban, M. H., Niknam, T., Shasadeghi, M., Dragicevic, T., & Blaabjerg, F. (2018). Load frequency control in microgrids based on a stochastic non-integer controller. *IEEE Transactions on Sustainable Energy*, 9(2), 853–861.

Kothari, M.L., Satsangi, P.S. and Nanda, J. (1981). Sampled-Data automatic generation control of interconnected reheat thermal systems considering generation rate constraints. *IEEE transactions on power apparatus and systems*, 100(5), 2334-2342.

Kumar, A. G. D., & Ramana, N. V. (2017). A fuzzy sliding mode controller for AGC of multi area deregulated power system. *International Journal of Electronics Engineering Research*. 9(7), 1079-1094

Kumar, A., & Singh, O. (2021). Recent strategies for automatic generation control of power systems with diverse energy sources. *International Journal of System Dynamics Applications*, 10(4), 1–26.

Kumar, A., Gupta, D. K., Ghatak, S. R., Appasani, B., Bizon, N., & Thounthong, P. (2022). A novel hybrid GSA-BPSO-driven PID controller for load frequency control of multi-source deregulated power system. *Mathematics*, 10(18), 3255.

Kumar, N., Alotaibi, M. A., Singh, A., Malik, H., & Nassar, M. E. (2022). Application of fractional order-PID control scheme in automatic generation control of a deregulated power system in the presence of SMES unit. *Mathematics*, 10(3), 521.

Kumar, R., & Prasad, L. B. (2023). Optimal load frequency control of multi-area multi-source deregulated power system with electric vehicles using teaching learning-based optimization: A comparative efficacy analysis. *Electrical Engineering*, 105, 4265–4282.

Kumar, V., Sharma, V., & Naresh, R. (2021). HHO-based model predictive controller for combined voltage and frequency control problem including SMES. *IETE Journal of Research*, 69(5), 2926–2940.

Kumar, V., Sharma, V., & Naresh, R. (2022). Model predictive controller-based voltage and frequency regulation in renewable energy integrated power system coordinated with virtual inertia and redox flow battery. *Iranian Journal of Science and Technology Transactions of Electrical Engineering*, 47(1), 159–176.

Kundur, P. (1994). Power system stability and control. McGraw-Hill.

Lal, D. K., & Barisal, A. K. (2017). Comparative performance evaluation of FACTS devices on AGC with diverse energy sources and SMES. *Cogent Engineering*, 4(1), Article 1318466.

Lal, D. K., & Barisal, A. K. (2019). Combined load frequency and terminal voltage control of power systems using moth flame optimization algorithm. *Journal of Electrical Systems and Information Technology*, 6(1), 1–24.

Lam, A. Y. S., Leung, K.-C., & Li, V. O. K. (2016). Capacity estimation for vehicle-to-grid frequency regulation services with smart charging mechanism. *IEEE Transactions on Smart Grid*, 7(1), 156–166.

Latif, A., Hussain, S. M. S., & Das, D. C. (2021). Optimization of two-stage IPD-(1+I) controllers for frequency regulation of sustainable energy-based hybrid microgrid network. *Electronics*, 10(8), 919.

Latif, A., Hussain, S. S., Das, D. C., & Ustun, T. S. (2021). Double stage controller optimization for load frequency stabilization in hybrid wind-ocean wave energy-based maritime microgrid system. *Applied Energy*, 282, 116171.

Latif, A., Paul, M., & Das, D. C. (2020). Price based demand response for optimal frequency stabilization in ORC solar thermal based isolated hybrid microgrid under salp swarm technique. *Electronics*, 9(12), 2209.

Latif, A., Padhee, S., Saikia, L. C., & Sinha, N. (2019). Maiden coordinated load frequency control strategy for solar tower-Archimedes wave energy conversion-geothermal energy conversion systems. *IET Renewable Power Generation*, 13(15), 2921–2931.

Lemeski, A. T., Ebrahimi, R., & Zakariazadeh, A. (2022). Optimal decentralized coordinated operation of electric vehicle aggregators enabling vehicle to grid option using distributed algorithm. *Journal of Energy Storage*, 54, Article 105213.

Li, D., et al. (2016). A self-adaptive inertia and damping combination control of VSG to support frequency stability. *IEEE Transactions on Energy Conversion*, 32(1), 397–398.

Liu, H., Hu, Z., Song, Y., Wang, J., & Xie, X. (2015). Vehicle-to-grid control for supplementary frequency regulation considering charging demands. *IEEE Transactions on Power Systems*, 30(6), 3110–3119.

Liu, W., Xu, Y., Feng, X., & Wang, Y. (2022). Research on the frequency regulation strategy of large-scale battery energy storage in the power grid system. *International Transactions on Electrical Energy Systems*, 2022, 4611426.

Longatt, F. G., et al. (2012). Effects of the synthetic inertia from wind power on the total system inertia after a frequency disturbance. *In 2012 IEEE PES Conference on Innovative Smart Grid Technologies–Africa (ISGT Africa)*, 1–7.

Lurie, B. J. (1994). Three parameters tunable tilt–integral–derivative (TID) controller. U.S. Patent No. 5,371,670.

Ma, M., Zhang, C., Liu, X., & Chen, H. (2017). Distributed model predictive load frequency control of the multi-area power system after deregulation. *IEEE Transactions on Industrial Electronics*, 64(6), 5129–5139.

Masuta, T., & Yokoyama, A. (2012). Supplementary load frequency control by use of a number of both electric vehicles and heat pump water heaters. *IEEE Transactions on Smart Grid*, 3(3), 1253–1262

Mahmoud, M. S. (2017). Microgrid: Advanced control methods and renewable energy system integration. *Elsevier*.

Magdy, G., et al. (2019). A novel coordination scheme of virtual inertia control and digital protection for microgrid dynamic security considering high renewable energy penetration. *IET Renewable Power Generation*, 13(3), 462–474.

Mahto, T., Kumar, R., Malik, H., & Hussain, S. M. S. (2021). Fractional order fuzzy-based virtual inertia controller design for frequency stability in isolated hybrid power systems. *Energies*, 14(12), 3456.

Mansour, S., Badr, A. O., Attia, M. A., Sameh, M. A., Kotb, H., & Shouran, M. (2022). Fuzzy logic controller equilibrium base to enhance AGC performance with renewable energy disturbances. *Energies*, 15(18), Article 6709.

Menteisidi, K., et al. (2015). Implementation of a fuzzy logic controller for virtual inertia emulation. *In 2015 International Symposium on Smart Electric Distribution Systems and Technologies (EDST)*, 606–611.

Meseret, G. M., Kumar, N., Mahato, T. K., Kumhar, R., Lakra, P., & Alam, M. D. M. (2025). AGC of a Multi-Area Hydrothermal Interconnected Diverse Deregulated Power System Using a Proposed Novel SBOA-Multi-Level Fuzzy Logic-Tilt Controller Incorporated With IPFC. *Engineering Reports*, 7(6), Article e70236.

Mirjalili, S., Mirjalili, S. M., & Lewis, A. (2014). Grey wolf optimizer. *Advances in Engineering Software*, 69, 46–61.

Mishra, D. K., Panigrahi, T. K., Mohanty, A., Ray, P. K., & Sahoo, A. K. (2018). Robustness and stability analysis of renewable energy based two-area automatic generation control. *International Journal of Renewable Energy Research*, 8(4), 1951–1961.

Mishra, D. K., Złotecka, D., & Li, L. (2022). Significance of SMES devices for power system frequency regulation scheme considering distributed energy resources in a deregulated environment. *Energies*, 15(5), Article 1766.

Mohammadi, S., Izadfar, H. R., & Eskandarian, N. (2020). Performance optimisation of the grid-connected flyback inverter under improved hybrid conduction mode. *IET Renewable Power Generation*, *14*(13), 2437–2446

Mokhtar, M., Azmy, A. M., & Abdelaziz, A. Y. (2022). An adaptive load-frequency control for power systems with high renewable penetration. *Energies*, 15(2), Article 573.

Morsali, J., & Esmaeili, Z. (2020, August). Proposing a new hybrid model for LFC and AVR loops to improve effectively frequency stability using coordinative CPSS. *In Proceedings of the 28th Iranian Conference on Electrical Engineering (ICEE)*,1–7.

Morsali, J., Zare, K., & Hagh, M. T. (2016). Applying fractional order PID to design TCSC-based damping controller in coordination with automatic generation control of interconnected multi-source power system. *Engineering Science and Technology an International Journal*, 20(1), 1–17.

Mu, Y., Wu, J., Ekanayake, J., Jenkins, N., & Jia, H. (2013). Primary frequency response from electric vehicles in the Great Britain power system. *IEEE Transactions on Smart Grid*, 4(2), 1142–1150.

Nadimi-Shahraki, M. H., Taghian, S., & Mirjalili, S. (2021). An improved grey wolf optimizer for solving engineering problems. *Expert Systems with Applications*, 166, Article 113917.

Nahas, N., Abouheaf, M., Darghouth, M. N., & Sharaf, A. (2021). A multi-objective AVR-LFC optimization scheme for multi-area power systems. *Electric Power Systems Research*, 200, 107463.

Nanda J, Mangla A & Suri S. (2006). Some new findings on automatic generation control of an interconnected hydrothermal system with conventional controllers. *IEEE Trans Energy Convers*. 21(1), 187-194.

Nanda, J., & Kaul, B. (1978). Automatic generation control of an interconnected power system. *Proceedings of the Institution of Electrical Engineers*, 125(5), 385.

Nayak, J. R., Shaw, B., & Sahu, B. K. (2020). Implementation of hybrid SSA–SA based three-degree-of-freedom fractional-order PID controller for AGC of a two-area power system integrated with small hydro plants. *IET Generation, Transmission & Distribution*, 14(13), 2430–2440.

Nayak, P. C., Prusty, R. C., & Panda, S. (2021). Grasshopper optimization algorithm optimized multistage controller for automatic generation control of a power system with FACTS devices. *Protection and Control of Modern Power Systems*, 6(1), 1–15.

Niu, S., Qu, L., Lin, H. C., & Fang, W. (2021). Effective virtual inertia control using inverter optimization method in renewable energy generation. *Energy Exploration & Exploitation*, 39(6), 2103–2125.

Oladipo, S., Sun, Y., & Wang, Z. (2021). An effective hFPAPFA for a PIDA-based hybrid loop of load frequency and terminal voltage regulation system. *In 2021 IEEE PES/IAS PowerAfrica*, 1–5.

Oshnoi, B., et al. (2023). A novel virtual inertia control strategy for frequency regulation of islanded microgrid using two-layer multiple model predictive control. *Applied Energy*, 343, 121016.

Padhy, S., Panda, S., & Mahapatra, S. (2017). A modified GWO technique based cascade PI-PD controller for AGC of power systems in presence of plug in electric vehicles. *Engineering Science and Technology, an International Journal*, 20(2), 427–442.

Pappachen, A., & Fathima, A. P. (2017). Critical research areas on load frequency control issues in a deregulated power system: A state-of-the-art-of-review. *Renewable and Sustainable Energy Reviews*, 72, 163–177.

Parmar, K. S., Majhi, S., & Kothari, D. (2012). Load frequency control of a realistic power system with multi-source power generation. *International Journal of Electrical Power & Energy Systems*, 42(1), 426–433.

Pathak, N., Verma, A., Bhatti, T. S., & Nasiruddin, I. (2019). Modeling of HVDC tie links and their utilization in AGC/LFC operations of multiarea power systems. *IEEE Transactions on Industrial Electronics*, 66(3), 2185–2197.

Peddakapu, K., Mohamed, M. R., Srinivasarao, P., Arya, Y., Leung, P., & Kishore, D. (2022). A state-of-the-art review on modern and future developments of AGC/LFC of conventional and renewable energy-based power systems. *Renewable Energy Focus*, 43, 146–171.

Pradhan, P. C., Sahu, R. K., & Panda, S. (2015). Firefly algorithm optimized fuzzy PID controller for AGC of multi-area multi-source power systems with UPFC and SMES. *Engineering Science and Technology, an International Journal*, 19(1), 338–354.

Prakash, E., Chidambaram, I. A., & Paramasivam, B. (2022). Cascade 2DOF-PIDN-FOPIDN controller-based AGC system of a multi-source restructured power system with HES and IPFC. *Indian Journal of Science and Technology*, 14(47), 3442–3455.

Prakash, K., Ali, M., Siddique, M. N. I., Chand, A. A., Kumar, N. M., Dong, D., & Pota, H. R. (2022). A review of battery energy storage systems for ancillary services in distribution grids: Current status, challenges and future directions. *Frontiers in Energy Research*, 10, 971704.

Priyadarshani, S., Subhashini, K. R., & Satapathy, J. K. (2020). Pathfinder algorithm optimized fractional order tilt-integral-derivative (FOTID) controller for automatic generation control of multi-source power system. *Microsystem Technologies*, 27(1), 23–35.

Rahman, A., Saikia, L. C., & Sinha, N. (2016a). AGC of dish-Stirling solar thermal integrated thermal system with biogeography based optimised three degree of freedom PID controller. *IET Renewable Power Generation*, 10(8), 1161–1170.

Rahman, A., Saikia, L. C., & Sinha, N. (2016b). Automatic generation control of an interconnected two-area hybrid thermal system considering dish-stirling solar thermal and wind turbine system. *Renewable Energy*, 105, 41–54.

Rahmat, K., Arman, O., Hagh, T. M., & Muyeen, S. M. (2018). Coordination of heat pumps, electric vehicles and AGC for efficient LFC in a smart hybrid power system via SCA-based optimized FOPID controllers. *Energies*, 11(2), Article 420.

Raj, U., & Shankar, R. (2020). Deregulated automatic generation control using novel opposition-based interactive search algorithm cascade controller including distributed generation and electric vehicle. *Iranian Journal of Science and Technology, Transactions of Electrical Engineering*, 44, 1233–1251.

Raj, U., & Shankar, R. (2023). Optimally enhanced fractional-order cascaded integral derivative tilt controller for improved load frequency control incorporating renewable energy sources and electric vehicle. *Soft Computing*, 27, 16989–17012.

Rajbongshi, R., & Saikia, L. C. (2017). Combined control of voltage and frequency of multi-area multi-source system incorporating solar thermal power plant using LSA optimized classical controllers. *IET Generation, Transmission & Distribution*, 11, 2489–2498.

Rajbongshi, R., & Saikia, L. C. (2017a). Combined voltage and frequency control of a multi-area multisource system incorporating dish-Stirling solar thermal and HVDC link. *IET Renewable Power Generation*, 12(3), 323–334.

Rajbongshi, R., & Saikia, L. C. (2017b). Performance of coordinated FACTS and energy storage devices in combined multiarea ALFC and AVR system. *Journal of Renewable and Sustainable Energy*, 9(6), Article 064101.

Rajbongshi, R., & Saikia, L. C. (2018). Coordinated performance of interline power flow controller and superconducting magnetic energy storage in combined ALFC and AVR system under deregulated environment. *Journal of Renewable and Sustainable Energy*, 10(4), Article 044102.

Raju, M., Saikia, L. C., & Sinha, N. (2018). Load frequency control of a multi-area system incorporating distributed generation resources, gate controlled series capacitor along with high-voltage direct current link using hybrid ALO-pattern search optimised fractional order controller. *IET Renewable Power Generation*, 13(2), 330–341.

Rakhshani, E., & Sadeh, J. (2010). Practical viewpoints on load frequency control problem in a deregulated power system. *Energy Conversion and Management*, 51(6), 1148–1156.

Rakhshani, E., Remon, D., Cantarellas, A. M., & Rodriguez, P. (2016). Analysis of derivative control based virtual inertia in multi-area high-voltage direct current interconnected power systems. *IET Generation, Transmission & Distribution*, 10(6), 1458–1469.

Ramoji, S. K., & Saikia, L. C. (2021). Optimal coordinated frequency and voltage control of CCGT-thermal plants with TIDF controller. *IETE Journal of Research*, 69(7), 4836–4853.

Ramoji, S. K., & Saikia, L. C. (2022). Comparative performance of multiple energy storage systems in unified voltage and frequency regulation of power system including electric vehicles. *Energy Storage*, 4(6), e360.

Ramoji, S. K., & Saikia, L. C. (2023). Optimal coordinated frequency and voltage control of CCGT-thermal plants with TIDF controller. *IETE Journal of Research*, 69(7), 4836–4853.

Ramoji, S. K., Saikia, L. C., Dekaraja, B., Behera, M. K., & Bhagat, S. K. (2022). Performance comparison of various tilt controllers in coalesced voltage and frequency regulation of multi-area multi-unit power system. *In Proceedings of the IEEE Delhi Section Conference (DELCON)*, 1–7.

Ranjan, M., & Shankar, R. (2021). A literature survey on load frequency control considering renewable energy integration in power system: Recent trends and future prospects. Journal of Energy Storage, 45, *Article* 103717.

Rerkpreedapong, D., Hasanovic, A., & Feliachi, A. (2003). Robust load frequency control using genetic algorithms and linear matrix inequalities. *IEEE Transactions on Power Systems*, 18(2), 855–861.

Rezkalla, M., Pertl, M., & Marinelli, M. (2018). Electric power system inertia: Requirements, challenges and solutions. *Electrical Engineering*, 100, 2677–2693.

Saadat, H. (1999). Power system analysis. McGraw-Hill.

Saha, A., & Saikia, L. C. (2018a). Combined application of redox flow battery and DC link in AGC of interconnected power system with diverse sources. *IET Generation, Transmission & Distribution*, 12(12), 3023–3032.

Saha, A., & Saikia, L. C. (2018b). Combined application of redox flow battery and DC link in restructured AGC system in the presence of WTS and DSTS in distributed generation unit. *IET Generation, Transmission & Distribution*, 12(9), 2072–2085.

Saha, A., & Saikia, L. C. (2019). Renewable energy source-based multiarea AGC system with integration of EV utilizing cascade controller considering time delay. *International Transactions on Electrical Energy Systems*, 29(2), e2755.

Saha, A., Dash, P., & Babu, N. R. (2023). Influence of solar and solid oxide fuel cell in AGC learning by utilizing spotted hyena optimized cascade controller. *International Journal of Energy and Environmental Engineering*, 14, 757–776.

Saha, D., Saha, A., & Saikia, L. C. (2022). Cascade controller-based modelling of a four-area hybrid system with additional generation under restructured AGC. *Protection and Control of Modern Power Systems*, 7, Article 26.

Saha, D., Saikia, L. C., & Rahman, A. (2022). Cascade controller-based modelling of a four-area thermal–gas AGC system with dependency of wind turbine generator and PEVs under restructured environment. *Protection and Control of Modern Power Systems*, 7(4), 1-18.

Sahib, M. A. (2015). A novel optimal PID plus second order derivative controller for AVR system. *Engineering Science and Technology, an International Journal*, 18(2), 194–206.

Sahoo, D. K., Sahu, R. K., & Panda, S. (2021). Fractional order fuzzy PID controller for automatic generation control of power systems. *ECTI Transactions on Electrical Engineering, Electronics and Communications*, 19(1), 71–82.

Sahu, R. K., Gorripotu, T. S., & Panda, S. (2015). Automatic generation control of multi-area power systems with diverse energy sources using teaching learning based optimization algorithm. *Engineering Science and Technology, an International Journal*, 19(1), 113–134.

Sahu, R. K., Panda, S., & Rout, U. K. (2013). DE optimized parallel 2-DOF PID controller for load frequency control of power system with governor dead-band nonlinearity. *International Journal of Electrical Power & Energy Systems*, 49, 19–33.

Sahu, R. K., Panda, S., & Sekhar, G. C. (2014). A novel hybrid PSO-PS optimized fuzzy PI controller for AGC in multi area interconnected power systems. *International Journal of Electrical Power & Energy Systems*, 64, 880–893.

Sahu, R. K., Panda, S., Biswal, A., & Sekhar, G. T. C. (2016). Design and analysis of tilt integral derivative controller with filter for load frequency control of multi-area interconnected power systems. *ISA Transactions*, 61, 251–264.

Sahu, R. K., Sekhar, G. T. C., & Priyadarshani, S. (2019). Differential evolution algorithm tuned tilt integral derivative controller with filter controller for automatic generation control. *Evolutionary Intelligence*, 14(1), 5–20.

Saikia, L. C., Sinha, N., & Nanda, J. (2013). Maiden application of bacterial foraging based fuzzy IDD controller in AGC of a multi-area hydrothermal system. *International Journal of Electrical Power & Energy Systems*, 45(1), 98–106. https://doi.org/10.1016/j.ijepes.2012.08.063

Saikia, L. C., Nanda, J., & Mishra, S. (2010). Performance comparison of several classical controllers in AGC for multi-area interconnected thermal system. *International Journal of Electrical Power & Energy Systems*, 33(3), 394–401.

Saranyaa, J. S., & Kareem, P. F. A. (2023). A comprehensive survey on the current trends in improvising the renewable energy incorporated global power system market. *IEEE Access*, 11, 24016–24038.

Sariki, M., & Shankar, R. (2022). Optimal CC-2DOF(PI)-PDF controller for LFC of restructured multi-area power system with IES-based modified HVDC tie-line and electric vehicles. *Engineering Science and Technology, an International Journal*, 32, 101058.

Saxena, A., & Shankar, R. (2022). Improved load frequency control considering dynamic demand regulated power system integrating renewable sources and hybrid energy storage system. *Sustainable Energy Technologies and Assessments*, 52, 102245.

Saxena, P., et al. (2020). Enhancing the dynamic performance of microgrid using derivative controlled solar and energy storage based virtual inertia system. *Journal of Energy Storage*, 31, 101579.

Saxena, S., & Hote, Y. V. (2018). PI controller-based load frequency control approach for single-area power system having communication delay. *IFAC-PapersOnLine*, 51(4), 622–626.

Shang, L., Dong, X. Z., Liu, C. X., & Gong, Z. (2022). Fast grid frequency and voltage control of battery energy storage system based on the amplitude-phase-locked-loop. *IEEE Transactions on Smart Grid*, 13(2), 941–953.

Sharma, D. (2020). Automatic generation control of multi source interconnected power system using adaptive neuro-fuzzy inference system. *International Journal of Engineering Science and Technology*, 12(3), 66–80.

Sharma, D., & Yadav, N. K. (2019). Lion algorithm with Levy update: Load frequency controlling scheme for two-area interconnected multi-source power system. *Transactions of the Institute of Measurement and Control*, 41(14), 4084–4099.

Sharma, D., Kushwaha, V., Pandey, K., & Rani, N. (2018). Intelligent AVR control of a single thermal area combined with LFC loop. *In Intelligent Communication, Control and Devices (Advances in Intelligent Systems and Computing*, 779–789. Springer.

Sharma, P., Prakash, A., Shankar, R., & Parida, S. K. (2020). A novel hybrid salp swarm differential evolution algorithm based 2DOF tilted-integral-derivative controller for restructured AGC. *Electric Power Components and Systems*, 47(19–20), 1775–1790.

Sharma, Y., & Saikia, L. C. (2015). Automatic generation control of a multi-area ST–Thermal power system using Grey Wolf Optimizer algorithm based classical controllers. *International Journal of Electrical Power & Energy Systems*, 73, 853–862.

Shayeghi, H., Shayanfar, H., & Jalili, A. (2008). Load frequency control strategies: A state-of-the-art survey for the researcher. *Energy Conversion and Management*, 50(2), 344–353.

Shiva, C. K., & Mukherjee, V. (2016). Design and analysis of multi-source multi-area deregulated power system for automatic generation control using quasi-oppositional harmony search algorithm. *International Journal of Electrical Power & Energy Systems*, 80, 382–395.

Shouran, M., & Alsseid, A. (2022). Particle swarm optimization algorithm-tuned fuzzy cascade fractional-order PI-fractional-order PD for frequency regulation of dual-area power system. *Processes*, 10(3), 477.

Simhadri, K., Mohanty, B., & Rao, U. M. (2018). Optimized 2DOF PID for AGC of multi-area power system using dragonfly algorithm. *In Advances in Intelligent Systems and Computing*, 11–22.

Simpson-Porco, J. W. (2021). On area control errors, area injection errors, and textbook automatic generation control. *IEEE Transactions on Power Systems*, 36(1), 557–560.

Singh, K., Zaheeruddin, & Singh, P. (2020). Load frequency regulation by de-loaded tidal turbine power plant units using fractional fuzzy-based PID droop controller. *Applied Soft Computing*, 92, Article 106338.

Skiparev, E., et al. (2023). Virtual inertia control of isolated microgrids using an NN-based VFOPID controller. *IEEE Transactions on Renewable Energy*, 13(14), 1–10.

Spahic, E., et al. (2016). Impact of reduced system inertia on stable power system operation and an overview of possible solutions. *In 2016 IEEE Power and Energy Society General Meeting (PESGM)*, 1–5.

Sockeel, N., et al. (2020). Virtual inertia emulator-based model predictive control for grid frequency regulation considering high penetration of inverter-based energy storage system. *IEEE Transactions on Sustainable Energy*, 11(4), 2932–2939.

Tabak, A. (2021a). Maiden application of fractional order PID plus second order derivative controller in automatic voltage regulator. *International Transactions on Electrical Energy Systems*, 31(12), 1–22.

Tabak, A. (2021). A novel fractional order PID plus derivative (PIλDμDμ2) controller for AVR system using equilibrium optimizer. COMPEL - *The International Journal for Computation and Mathematics in Electrical and Electronic Engineering*, 40(3), 722–743.

Taha, M. Q., Elhassene, I. C., & El Heiba, B. (2024). Gray Wolf Algorithm optimization of automatic generation control for deregulated multi-area power system. *In 2024 International Congress on Human-Computer Interaction, Optimization and Robotic Applications (HORA)*,1–4.

Tamrakar, U., Shrestha, D., Maharjan, M., Bhattarai, B. P., Hansen, T. M., & Tonkoski, R. (2017). Virtual inertia: Current trends and future directions. *Applied Sciences*, 7(7), Article 654.

Tasnin, W., & Saikia, L. C. (2018). Performance comparison of several energy storage devices in deregulated AGC of a multi-area system incorporating geothermal power plant. *IET Renewable Power Generation*, 12(7), 761–772.

Tasnin, W., & Saikia, L. C. (2018a). Comparative performance of different energy storage devices in AGC of multi-source system including geothermal power plant. *Journal of Renewable and Sustainable Energy*, 10(2), Article 024101.

Tasnin, W., & Saikia, L. C. (2018b). Deregulated AGC of multi-area system incorporating dish-Stirling solar thermal and geothermal power plants using fractional-order cascade controller. *International Journal of Electrical Power & Energy Systems*, 100, 367–379.

Torres, J., et al. (2014). Self-tuning virtual synchronous machine: A control strategy for energy storage system to support dynamic frequency control. *IEEE Transactions on Energy Conversion*, 29(4), 833–840.

Tebib, A., & Boudour, M. (2021). Stability improvement of interconnected AC/DC multi-area AGC systems using optimized virtual synchronous power strategy based on eigenvalue sensitivity and adaptive GWO. *International Transactions on Electrical Energy Systems*, 31(4), Article e12725.

Trojovská, E., Dehghani, M., & Trojovský, P. (2022). Zebra optimization algorithm: A new bio-inspired optimization algorithm for solving optimization problems. *IEEE Access*, 10, 49445–49473.

Ullah, K., Basit, A., Ullah, Z., Aslam, S., & Herodotou, H. (2021). Automatic generation control strategies in conventional and modern power systems: A comprehensive overview. *Energies*, 14(9), Article 2376.

Vachirasricirikul, S., & Ngamroo, I. (2014). Improved H2/H∞ control-based robust PI controller design of SMES for suppression of power fluctuation in microgrid. *In 2014 International Electrical Engineering Congress (iEECON)*, 1–4.

Xia, S., Bu, S. Q., Luo, X., Chan, K. W., & Lu, X. (2018). An autonomous real-time charging strategy for plug-in electric vehicles to regulate frequency of distribution system with fluctuating wind generation. *IEEE Transactions on Sustainable Energy*, 9(2), 511–524.

Xu, Y., Li, C., Wang, Z., Zhang, N., & Peng, B. (2018). Load frequency control of a novel renewable energy integrated micro-grid containing pumped hydropower energy storage. *IEEE Access*, 6, 29067–29077.

Yan, R., & Saha, T. K. (2015). Frequency response estimation method for high wind penetration considering wind turbine frequency support functions. *IET Renewable Power Generation*, 9(7), 775–782.

Yao, E., Wong, V. W. S., & Schober, R. (2017). Robust frequency regulation capacity scheduling algorithm for electric vehicles. *IEEE Transactions on Smart Grid*, 8(2), 984–997.

Yin, L., Cao, X., & Chen, L. (2022). High-dimensional multiple fractional order controller for automatic generation control and automatic voltage regulation. *International Journal of Control, Automation and Systems*, 20(12), 3979–3995.

Yusuf, S. S., Kunya, A. B., Abubakar, A. S., & Salisu, S. (2024). Review of load frequency control in modern power systems: A state-of-the-art review and future trends. Electrical Engineering. *Electrical Engineering* 107, 5823–5848

Zamani, A., Barakati, S. M. S., & Yousofi-Darmian, S. (2016). Design of a fractional-order PID controller using GBMO algorithm for load-frequency control with governor saturation. *ISA Transactions,* 64, 56–66.

Zare, P., Davoudkhani, I. F., Zare, R., Ghadimi, H., Mohajeri, R., & Babaei, A. (2023). Maiden application of zebra optimization algorithm for design PIDN-TIDF controller for frequency control in offshore fixed platforms microgrid in the presence of tidal energy. *2023 8th International Conference on Technology and Energy Management (ICTEM)*, 1–7.

Zhao, H., et al. (2017). Multi-loop virtual synchronous generator control of inverter-based DGs under microgrid dynamics. *IET Generation, Transmission & Distribution*, 11(3), 795–803.

Zhang, Z. S., Sun, Y. Z., Lin, J., & Li, G. J. (2012). Coordinated frequency regulation by doubly fed induction generator-based wind power plants. *IET Renewable Power Generation*, 6(1), 38–47.

Zhong, Q. C., & Hornik, T. (2013). Control of power inverters in renewable energy and smart grid integration. *Wiley*.

BIO-DATA OF THE CANDIDATE

Name of Candidate	:	Samuel Lalngaihawma
Contact	:	8119868835 samuelchenkual05@gmail.com
Permanent Address	:	B-35, Durtlang Mel-5, Aizawl, Mizoram 796015
Marital Status	:	Unmarried
Educational Details	:	
a) B.Tech	:	Electrical Engineering CGPA of 6.77
b) M.Tech	:	Electrical Engineering CGPA of 8.3
c) Ph.D. Course Work	:	SGPA of 7.71

List of Research Publications

Journal Papers:

1. S. Lalngaihawma, S. Datta, S. Das, F. Alsaif and T. S. Ustun, "Automatic Generation Control of Hybrid Sources Incorporating Renewable Energy Sources and Electric Vehicles in an Interconnected Power System Considering a Deregulated Environment," *IEEE Access*, vol. 12, pp. 124764-124789, 2024. https://dx.doi.org/10.1109/ACCESS.2024.3454229. IF=3.6 (Published) SCIE
2. S. Lalngaihawma, S. Das, S. Datta, T.S. Ustun and U. Cali, "Enhancing grid stability through virtual inertia control in automatic generation control of a multi area system", *Energy Reports*, Volume 13, Pages 2764-2789, ISSN 2352-4847, 2025. https://doi.org/10.1016/j.egyr.2025.01.050. IF=5.1 (Published) SCIE
3. S. Lalngaihawma, S. Das, S. Datta, "FACTs Integrated multi source multi-area power system considering combined load frequency control and automatic voltage regulator under deregulated environment". (Under Review)
4. S. Lalngaihawma, S. Das and S. Datta, "Automatic Generation Control of a multi area system with the integration of FACTS device and energy storage". (Under Review)

Conference Papers:

1. S. Lalngaihawma and S. Datta, "Performance Analysis of an Electric Vehicle Fleet for Automatic Generation Control of a Multi Area Multi Source Power System Using a Cascaded Controller Tuned with a Recent Mayfly Optimization Algorithm," *2023 IEEE 3rd International Conference on Sustainable Energy and Future Electric Transportation (SEFET)*, Bhubaneswar, India, 2023, pp. 1-6, doi: 10.1109/SeFeT57834.2023.10245409. (Published).
2. S. Lalngaihawma, S. Datta and S. Das, "Automatic Generation Control with a Recent ZOA Algorithm Optimized TIDN Controller," *2024 IEEE 4th International Conference on Sustainable Energy and Future Electric Transportation (SEFET)*, Hyderabad, India, 2024, pp. 1-6, doi: 10.1109/SEFET61574.2024.10718195. (Published).

PARTICULARS OF THE CANDIDATE

Name of the Candidate	:	Samuel Lalngaihawma
Degree	:	Ph.D.
Department	:	Electrical Engineering
Title of Thesis	:	Study on Automatic Generation Control of Renewable Energy Sources based multi-area, multi-source system under Deregulated Environment.
Date of Admission	:	30/10/2020
Approval of Research Proposal	:	
1. DRC	:	24/04/2021
2. BOS	:	04/05/2021
3. School Board	:	20/05/2021
MZU Registration Number	:	6850 of 2014
Ph.D. Registration Number	:	MZU/Ph.D./1553 of 30.10.2020
Extension	:	None

Dr. Subir Datta

Head

Department of Electrical Engineering

ABSTRACT

STUDY ON AUTOMATIC GENERATION CONTROL OF RENEWABLE ENERGY SOURCES BASED MULTI-AREA, MULTI-SOURCE SYSTEM UNDER DEREGULATED ENVIRONMENT

AN ABSTRACT SUBMITTED IN PARTIAL FULFILLMENT OF

THE REQUIREMENT FOR THE DEGREE OF

DOCTOR OF PHILOSOPHY

SAMUEL LALNGAIHAWMA

MZU REGN NO: 6850 of 2014

PH.D. REGN NO: MZU/PH.D./1553 OF 30/10/2020

DEPARTMENT OF ELECTRICAL ENGINEERING

SCHOOL OF ENGINEERING AND TECHNOLOGY

NOVEMBER 2025

STUDY ON AUTOMATIC GENERATION CONTROL OF RENEWABLE ENERGY SOURCES BASED MULTI-AREA, MULTI-SOURCE SYSTEM UNDER DEREGULATED ENVIRONMENT

BY

Samuel Lalngaihawma

Department of Electrical Engineering

Name of Supervisor: Dr. Subir Datta

Submitted

In partial fulfillment of the requirement for the degree of Doctor of Philosophy in Electrical Engineering of Mizoram University, Aizawl

ABSTRACT

Automatic Generation Control (AGC) keeps system frequency and tie-line power variations within predetermined bounds while balancing generation and load in an interconnected power system. Large-scale integration of intermittent renewables (wind, solar PV, etc.) and the transition from vertically integrated (controlled) to deregulated markets significantly enhance the complexity of AGC in the contemporary grid. While deregulation change the network into several organizations (GENCOs, DISCOs, etc.), increasing competition and congestion, high renewable penetration adds unpredictability in power output and effectively lowers system inertia. Strong, flexible AGC tactics are crucial in light of these tendencies. The study examines the principles of AGC and current developments, pointing out that traditional PID and model-predictive controllers are frequently insufficient in situations with significant renewable energy and market volatility. It examines the difficulties of frequency management in deregulated systems and shows how novel control techniques, electric vehicles, storage, and FACTS devices have been suggested to support AGC. The research establishes the foundation for the remaining work by highlighting the necessity of sophisticated controller design to manage renewable intermittency and structural market shifts.

Detailed mathematical models of every generating and load component in the study system are developed in a MATLAB/SIMULINK environment. A reheat thermal power plant is integrated in each area of the whole study since maximum generation of power is still based on the conventional plant in the modern world. Renewable energy sources such as hydropower plant, wind turbine plant, geothermal plant, biodiesel and biogas plant, tidal power plant, archimedes wave energy conversion, solar photovoltaic plant and solar thermal power plant are integrated in the study system. Here, Electric Vehicles (EVs) are included in the model as a distributed energy resources. The batteries and power converters are designed to respond to frequency changes by either absorbing or injecting electricity. Recognizing that the power system is a highly non-linear process whose dynamics are heavily influenced by its individual equipment, these component models include non-linearities such as regulator dead bands and generating rate restrictions. The study offers a library of dynamics that describes how thermal and renewable units behave under load variations by obtaining linearized state space or transfer functions for each element. In subsequent studies, hybrid multi-area systems may be simulated using these composite models.

A study is done on a three-area interconnected hybrid power system. Each of the three areas has a reheat steam turbine plant combined with embedded distributed generation, such as EV aggregations, and many renewable energy sources, such as solar PV, wind, hydropower, geothermal, biogas units, etc. Study is done in both traditional or regulated and deregulated market situations. For instance, under

deregulation, each area may be seen as a distinct GENCO with its own control goal. A unique control architecture for AGC—a cascaded two-stage controller in each area—is the main contribution. Together, they are referred to as a 2DOFTIDN–FOTI cascade. The inner loop is a fractional-order tilt integral (FOTI) controller, while the outer loop is a two-degree-of-freedom tilt integral-derivative with filter (2DOFTID) controller. In an effort to enhance transient responsiveness, this controller form expands upon the traditional PID by including an additional "tilt" term (fractional-exponent integral) and filter dynamics. A recently developed Zebra Optimization Algorithm (ZOA), a bio-inspired metaheuristic algorithm is used to adjust controller gains. The findings show that this ZOA-based tuning produces high-quality parameters and quick convergence. The suggested cascade controller greatly enhances frequency regulation in this three-area system, according to simulation case studies. For example, adding EV-based storage lowers frequency settling time and overshoots by 40–70% in each area. The study shows that AGC performance is improved under both regulated and unregulated settings when distributed generation and EVs are combined with an optimized fractional-order cascade controller.

Virtual Inertia Control (VIC) is introduced to solve the problem of reduced inertia in grids due to increase use of more renewable energy sources. The previous three-area model is expanded to a four-area linked network, including thermal, renewable, and VIC based storage resources in each areas. High wind and PV generation levels lower the grid's effective rotational inertia, as shown in earlier research, resulting in greater frequency deviations during disturbances. In order to make up for this, a VIC method is used, which involves controlling inverter-interfaced sources such PV or battery converters to simulate inertial response. In particular, a tilt-integral controller paralleled with integral derivative with filter (TI-IDN) VIC controller is created. VIC mimics the governor's inertia by injecting or absorbing power in response to the rate of frequency change. Each areas may once more modify its VIC approach in a deregulated setting. According to simulation findings, the four-area system shows much better stability when VIC is enabled. The simulated inertia reduces the frequency ramp during disturbances, lowering maximum ROCOF (Rate of Change of Frequency) and overshoot. As a result, the study demonstrates that the TI-IDN VIC controller can successfully compensate for the loss of physical inertia, enhancing AGC performance in a highly renewable linked grid.

The combined problem of Load Frequency Control (LFC) and Automatic Voltage Regulation (AVR) in a multi-area system with multiple renewables, non-linearities is examined in this study. In reality, the dynamics of frequency (active power) and voltage (reactive power) interplay, particularly when there are significant disruptions or high DER penetration. The study combines the AVR and LFC loops and looks for a single, cohesive control scheme building on recent research. The tilt-integral combined with proportional integral derivative with filter (TI-PIDN), a multilevel controller is developed for this combined LFC-AVR study. This TI-PIDN controller employs a fractional exponent to enable flexible recollection of previous errors and generalizes the PID form by adding a second integral term for quicker error removal. ZOA adjusts its parameters once more to achieve the best dynamic performance. Step variations in load and generation, including disruptions in renewable production, are applied to the system in simulation studies. The TI-PIDN achieves quicker damping of frequency and voltage oscillations, reduced steady-state errors, and improved resistance to nonlinear generating limitations as compared to a standard controller based LFC-AVR system. The sensitivity analyses demonstrate that the ideal ZOA-tuned fractional controllers offer quick, stable frequency and voltage recovery under a variety of conditions, confirming their efficacy in hybrid power systems and consistent with findings in the literature.

The thesis ends with a summary of the major work's contributions along with its comparative performance. The suggested controllers consistently perform better than traditional designs in every study. Frequency regulation is significantly tightened by including EVs, virtual inertia, and enhanced fractional controllers like frequency deviations settle at 50–70% faster and overshoots are decreased. It is shown that the novel proposed 2DOFTIDN–FOTI, TI-IDN VIC, and TI-PIDN controllers whose parameters are optimized by ZOA are more resilient to changes in parameter and system with non-linearities than the other existing conventional AGC controllers. Furthermore, the Zebra Optimization Algorithm has shown effectiveness in identifying better control parameters in a complicated search spaces often converging more quickly than other metaheuristics algorithm. This study provides an integrated modelling framework for hybrid multi-area systems with a variety of renewables and EVs, innovative fractional-order control structures designed for voltage regulation and AGC, and proof of the advantages of artificial or virtual inertia in contemporary grids. These findings demonstrate enhanced controller resilience and optimization effectiveness in ensuring grid stability, advancing our understanding of frequency management for renewable-rich and deregulated power systems.